699 | November 2016

SCHRIFTENREIHE SCHIFFBAU

Richard C. Hayward

Ultimate Strength of Ship Plating - A Proof of Capacity under Combined In-Plane-Loads

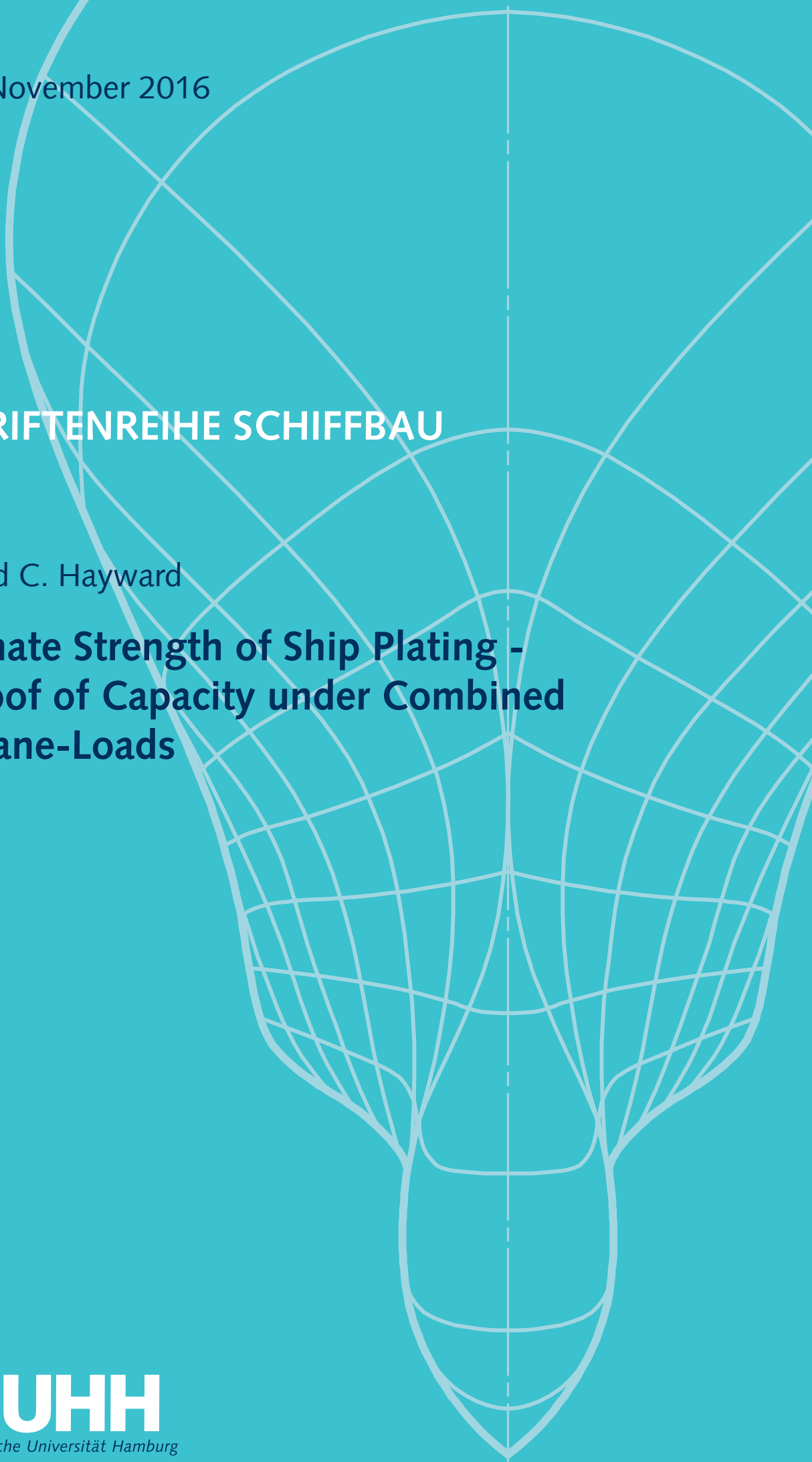

TUHH
Technische Universität Hamburg

Ultimate Strength of Ship Plating

A Proof of Capacity under Combined In-Plane Loads

Vom Promotionsausschuss der
Technischen Universität Hamburg-Harburg

zur Erlangung des akademischen Grades

Doktor-Ingenieur (Dr.-Ing.)

genehmigte Dissertation

von
Richard C. Hayward

aus
Toronto, Kanada

2016

1. Gutachter: Prof. Dr.-Ing. Dr.-Ing. E.h. Dr. h.c. Eike Lehmann
2. Gutachter: Prof. D.Sc. (Tech.) Claude Daley
3. Gutachter: Prof. D.Sc. (Tech.) Sören Ehlers

Tag der mündlichen Prüfung: 18.10.2016

Ultimate Strength of Ship Plating - A Proof of Capacity under Combined In-Plane Loads, Richard C. Hayward, 1. Auflage, Hamburg, Technische Universität Hamburg, 2016, ISBN 978-3-89220-699-6

Schriftenreihe Schiffbau
Am Schwarzenberg – Campus 4
D-21073 Hamburg

http://www.tuhh.de/vss

Abstract

The present work addresses the need for a proof of plate capacity under combined in-plane loads, a need recently highlighted by the loss of the post-panamax container ship *MOL Comfort*. Towards this end, an extensive series of numerical studies based on the finite element method have been performed covering all load combinations and plating configurations relevant for the shipbuilding industry. These studies have been used to investigate the mechanics of plating collapse (including the effects of plate slenderness and aspect ratio) under longitudinal, transverse and shear loads in isolation and in combination. Numerical studies have also been used to quantitatively evaluate existing proofs of plate capacity found in both literature and the shipbuilding industry. In this regard, *quantitative* acceptance criteria have been developed with which to judge whether a proof is (1) precise, (2) accurate and (3) robust. Similarly, *qualitative* criteria have been defined which require an acceptable proof to be (1) concise, (2) physically-based and (3) directly solvable. Because no existing proof was found to satisfy all quantitative and qualitative acceptance criteria, a *hypothetical* proof has been postulated using a generalised form of the von Mises equation (in order to satisfy qualitative acceptance criteria), where the exponents and interaction coefficient have been derived on the basis of observations made in the investigation of plating collapse mechanisms. To satisfy all quantitative acceptance criteria, the exponents and interaction coefficient of the hypothetical proof have subsequently been redefined on the basis of additional numerical studies (in case of biaxial compression only). Design application of the resulting proof has subsequently been explained and demonstrated. Because the new proof is based on numerical studies of simply-supported plates, uniform in-plane loads and idealised initial imperfections, the validity of its application has been demonstrated in case of other boundary conditions, additional load components and more realistic initial imperfections. Moreover, the marginal effect of out-of-plane loads (i.e. lateral pressure) on the in-plane capacity of plating has also been investigated. Finally, two examples of design application have been provided wherein the capacity of stiffened panels in the bottom shell and side shell of a double hull VLCC have been calculated both numerically and according to the new proof. Although the focus of the present work is on the capacity of *plane* plates, a new proof of *curved* plate capacity has been additionally presented. In terms of practical application in the shipbuilding industry, both proofs of plate capacity have been included in the newly harmonised *IACS Common Structural Rules for Bulk Carriers and Oil Tankers*, the new *IACS Longitudinal Strength Standard for Container Ships* as well as the new *DNVGL Rules for Classification* which are applicable to all ship types.

Acknowledgements

It would not have been possible to write this doctoral dissertation without the help and support of the kind people around me, only some of whom it is possible to here give particular mention.

Firstly, I would like to express my sincere gratitude to my academic advisors Professor Eike Lehmann and Professor Claude Daley for their continuous support and guidance. The unending enthusiasm which they exude is indeed infectious.

I also would like to thank my IACS HPT02 colleagues as well as my colleagues at Germanischer Lloyd (now DNV·GL) for their cooperation and valuable feedback. In particular I would like to thank my former supervisor Hans-Joachim Schulte who so kindly mentored me on the buckling and ultimate strengths of ship structures.

Last but not least, I would like to thank my parents and sister for their long-distance support and encouragement. I would especially like to thank my wife Patricia. If kindness and patience are truly virtues then she is without doubt the most virtuous person I know.

Nomenclature

Common notation

a	plate length or frame span [mm]
b	plate breadth or frame spacing [mm]
c	stress ratio σ_y/σ_x [-]
t	nominal plate thickness [mm]
E	modulus of elasticity [N/mm^2]
K	elastic buckling factor [-]
P	axial force [N]
R	normalised axial or shear stress [-]
α	plate aspect ratio [-]
β	plate slenderness parameter [-]
γ	shear strain [-]
δ	deflection [-]
ϵ	axial strain [-]
η	utilisation factor [-]
κ	plate reduction factor [-]
λ	reference degree of slenderness [-]
μ	stress multiplier factor at failure [-]
ν	Poisson's ratio [-]
σ	axial stress [N/mm^2]
τ	shear stress [N/mm^2]
ψ	edge stress ratio [-]
Γ	ratio of (stress) vector magnitudes [-]

Subscripts

cr	critical (elastic) stress
e	reference stress
eq	equivalent stress
i	internal stress
m	effective breadth/length
$proof$	quantity based on proof of capacity
rc	residual compressive stress
rt	residual tensile stress
ult	ultimate strength
x	quantity in the x-direction
xy	quantity in the xy-plane

$_y$	quantity in the y-direction
$_z$	quantity in the z-direction
$_{FEA}$	quantity based on finite element analyses
$_Y$	yield strength
$_0$	initial quantity
$_{1,2,3}$	directions of principal stress

Acronyms

ABS	American Bureau of Shipping
ALS	Accidental Limit State
BV	Bureau Veritas
ClassNK	Nippon Kaiji Kyokai
CSR-BC	IACS Common Structural Rules for Bulk Carriers
CSR BC & OT	IACS Common Structural Rules for Bulk Carriers and Oil Tankers
CSR-OT	IACS Common Structural Rules for Oil Tankers
DIN	Deutsches Institut für Normung (German Institute for Standardization)
DnV	Det norske Veritas
FLS	Fatigue Limit State
GL	Germanischer Lloyd
HPT02	IACS CSR Harmonisation Project Team 02 (Buckling)
IACS	International Association of Classification Societies Ltd.
KPI	Key Performance Indicator
LR	Lloyd's Register
PULS	Panel Ultimate Limit State
SLS	Serviceability Limit State
ULS	Ultimate Limit State
UR	Unified Requirement (IACS)

Contents

1. Introduction

On 17 June 2013 the post-panamax container ship *MOL Comfort* (8,000 TEU class) suffered a fracture amidships during inclement weather en route from Singapore to Jeddah, Saudi Arabia, eventually breaking into two halves. Fortunately all 26 crew members were able to take to lifeboats and thereafter rescued by another ship in the area [1]. Although both halves remained intact and afloat for several days after breaking apart, the aft section sank on 27 June 2013 together with about 1,700 containers and 1,500 metric tons of fuel oil [2]. The bow section, while under tow, caught fire on 06 July 2013 and sank on 11 July 2013 together with another 2,400 containers and 1,600 metric tons of fuel oil [3, 4]. The total loss of ship and cargo (4,382 containers) was evaluated by the insurer Allianz at 83m USD and 440m USD, respectively [5]. Moreover, additional financial claims are being made by the operator against the shipbuilder which include the renovation of sister ships as a safety precaution.

An interim investigative report into the loss of *MOL Comfort* stated that water ingress was first detected by an alarm in the duct keel (i.e. near the centreline of the ship) and a few minutes later in No. 6 cargo hold. Photos of the damaged ship showed a fracture propagating up through the side shell from the bottom of the ship, leading investigators to conclude that the crack which triggered the fracture originated amidships in the bottom shell plating below No. 6 cargo hold [6]. Subsequent surveys of the bottom shell plating of sister ships revealed large buckling deformations in the same area. Based on elasto-plastic analyses using 3-hold finite element models, it was shown that the loss of plating strength led to a reduction in effective breadth of the double bottom girders which in turn led to collapse of the double bottom and subsequently the hull girder [7]. Moreover, it was concluded that the double bottom structure of the *MOL Comfort* and sister ships was relatively weak out-of-plane compared to ships of similar size. The resulting increase in biaxial stresses due to deflection of the double bottom under sea pressure, superimposed on and magnified by axial stresses due to hull girder bending and transverse stresses due to side compression, created an extreme biaxial stress state in the bottom shell plating. Accordingly, although accident investigators struggled to explain the apparent gap between structural demand and capacity, it was concluded with some confidence that the loss of *MOL Comfort* initiated with collapse of the ship's bottom shell plating under biaxial compression.

1.1. Purpose

Although the foregoing is certainly not a singular example of catastrophic failure when the ultimate strength of ship plating is exceeded, it is one of the more recent examples which serves to illustrate the need for a proof of plate capacity under combined in-plane loads. Only with such a proof can ship plating be reliably and efficiently designed so that the demands on structure are met over the service life of a ship without incurring a needless weight penalty. However, five years before the sinking of *MOL Comfort*, the International Associ-

ation of Classification Societies (IACS) had already established a project team (HPT02) to harmonise the disparate buckling strength rules applied at that time to bulk carriers and oil tankers. With respect to the proof of plate capacity under combined in-plane loads, it had become apparent in 2012 that the proof of plate capacity used provisionally by the project team was too non-conservative in case of plating under biaxial compression and too conservative in case of stress states with a tensile component. For this reason, the author of the present work was tasked during the 10^{th} meeting of HPT02 to develop a new proof of plate capacity for inclusion in the newly harmonised *IACS Common Structural Rules for Bulk Carriers and Oil Tankers*. As this proof is intended for use in the design and classification of ships, it was determined that it needs not only to be based on the ultimate strength concept, but needs as well to satisfy certain qualitative and quantitative criteria. In qualitative terms, the proof needs to be (1) concise, (2) physically-based and (3) directly solvable. In quantitative terms, the proof needs to be (1) precise, (2) accurate and (3) robust. The purpose of the present work is to develop a proof of plate capacity which satisfies all of these criteria.

In addition to inclusion in the *IACS Common Structural Rules for Bulk Carriers and Oil Tankers*, the proof presented herein has also been included in the new *IACS Longitudinal Strength Standard for Container Ships* (UR S11A) as well as the new *DNVGL Rules for Classification* which are applicable to all ship types. As a consequence of the loss of *MOL Comfort*, the *IACS Longitudinal Strength Standard for Container Ships* includes additional requirements for the buckling strength assessment of *large* container ships (i.e. breadth $\mathsf{B} > 32.26\mathsf{m}$) for which "(a)ll in-plane stress components (i.e. bi-axial and shear stresses) induced by hull girder loads and local loads are to be considered" [8]. Of course, most classification societies have for many years already considered all in-plane stress components and lateral loads in their assessments of buckling strength for all ship types as a matter of good engineering practice.

1.2. Scope and outline

The present work addresses the need for a proof of plate capacity under combined in-plane loads. Towards this end, an extensive series of numerical studies based on the finite element method have been performed covering all load combinations and plating configurations relevant for the shipbuilding industry. Because the new proof is based on numerical studies of simply-supported plates, uniform in-plane loads and idealised initial imperfections, the validity of its application in case of other boundary conditions, additional load components and more realistic initial imperfections has been demonstrated as is its application to stiffened panels. However, the effects of strain hardening are largely ignored and the plating is assumed to remain ductile throughout loading, i.e. no brittle or fatigue fracture. Finally, although the present work is focussed on a proof of *plane* plate capacity, the DIN 18800 proof of *curved* plate capacity (already used extensively in the shipbuilding industry) has also been revised, the technical background of which is documented in Appendix A.

In Chapter 2 the development of a proof of plate capacity under combined in-plane loads begins with a detailed investigation of the mechanics of plating collapse. Here the collapse of plates are examined under longitudinal, transverse and shear stresses, in isolation and in combination. In this regard, the first three sections of the chapter address the

capacity of plating under uniaxial compression, biaxial loads and in-plane shear (including the reduction in uniaxial/biaxial capacity due to shear). In each of these sections square plating is used to isolate the effects of plate aspect ratio which are subsequently discussed in the last section of the chapter. The purpose of Chapter 2 is to lay the groundwork for a physically-based solution and to thoroughly examine the ultimate strengths of plating under single stress components which are used as reference stresses in most proofs of plate capacity under combined in-plane loads. Accordingly, because the accuracy and precision of these proofs depend extensively on those of the reference stresses, formulations found in literature and the shipbuilding industry for defining the characteristic strength of plates (under single stress components) are thoroughly discussed and compared to numerical results.

In Chapter 3 existing proofs of plate capacity found in literature and the shipbuilding industry are described and quantitatively evaluated over a wide range of load combinations and plating configurations. In this regard, an evaluation scheme is firstly presented which measures bias (or accuracy) and precision (including measures of conservatism and non-conservatism) in terms of five key performance indicators. Each proof is evaluated over a *design space* consisting of 360 evaluation points and a *design subspace* consisting of 56 evaluation points. The former covers load combinations and plating configurations relevant for all ship structures while the latter covers those combinations and configurations largely relevant for cargo hold structures, i.e. those critical to the ultimate strength of the hull girder.

In Chapter 4 a new proof of plate capacity under combined in-plane loads is developed. Towards this end, the problem to be solved is stated quite precisely using quantitative and qualitative criteria which define an *acceptable* proof of plate capacity. On the basis of these criteria, the existing proofs discussed in Chapter 3 are evaluated. Because no existing proof is found to satisfy all quantitative and qualitative acceptance criteria, a *hypothetical* proof of plate capacity under combined in-plane loads is postulated which well reflects the mechanics of plating collapse described in Chapter 2 and the strengths of existing proofs investigated in Chapter 3. In order to satisfy qualitative acceptance criteria, the proof is based on a generalised form of the von Mises equation

$$\left(\frac{\sigma_x}{\kappa_x \cdot \sigma_Y}\right)^{e_0} + \left(\frac{\sigma_y}{\kappa_y \cdot \sigma_Y}\right)^{e_0} - B \cdot \left(\frac{\sigma_x}{\kappa_x \cdot \sigma_Y}\right)^{e_0/2} \cdot \left(\frac{\sigma_y}{\kappa_y \cdot \sigma_Y}\right)^{e_0/2} + \left(\frac{\tau_{xy}}{\kappa_\tau \cdot \tau_Y}\right)^{e_0} = 1.0 \quad (1.1)$$

where the exponent e_0 and interaction coefficient B are derived on the basis of observations made in the investigation of plating collapse mechanisms. Because the hypothetical proof falls just short of satisfying all quantitative acceptance criteria, a new proof of plate capacity is subsequently developed where the exponent e_0 and interaction coefficient B are redefined on the basis of additional numerical studies (in case of biaxial compression only). This new proof is then evaluated followed by a description and evaluation of the proof of plate capacity implemented in the newly harmonised *IACS Common Structural Rules for Bulk Carriers and Oil Tankers* for which the interaction coefficient B is slightly revised when used together with newly harmonised load models.

In Chapter 5 the design application of the newly developed proof as used in the *IACS Common Structural Rules for Bulk Carriers and Oil Tankers* is discussed. In the first section of the chapter, an overview of the proof of stiffened panel capacity is presented where the decoupling of plate strength and stiffener strength is explained and presented. Regard-

ing the former, the new proof of plate capacity is based on numerical studies of simply-supported plates, uniform in-plane loads and idealised initial imperfections. Accordingly, as noted above, the validity of its application in case of other boundary conditions (i.e. free edges and edge pull-in), additional load components (i.e. in-plane bending and lateral pressure) and more realistic initial imperfections (i.e. residual deflections and stresses based on measurements) is demonstrated. The marginal effect of out-of-plane loads (i.e. lateral pressure) on the in-plane capacity of plating is also investigated. The section concludes with a discussion of the proof of stiffener capacity. In the second section of the chapter, two examples of design application are presented where the capacity of stiffened panels in the bottom shell and side shell of a double hull VLCC are calculated both numerically and according to the new proof, the former stiffened panel being particularly relevant to the hull girder collapse of *MOL Comfort*.

2. Mechanics of Plating Collapse

In this chapter the mechanics of plating collapse is examined in detail. Once the behaviour of plating under in-plane loads is thoroughly understood, a physically-based proof of plate capacity is then possible. In §2.1 the simplest case of collapse under uniaxial compression is examined. This is followed in §2.2 by analyses of collapse under biaxial loads and in §2.3 under in-plane shear. In each of these sections square plates are used to isolate the effects of aspect ratio which are discussed in §2.4. Numerical analyses are used throughout this chapter, the description and validation of which are included in Appendix B. All analyses are based on simply-supported plates with edges forced to remain straight, but otherwise free to move in-plane. As explained in Chapter 5, this means that the loads are *strain-based* rather than *stress-based*. Strain-based loads are representative of those arising from hull girder bending where the in-plane displacement of plating is directly proportional to the radius of curvature. Furthermore, in all analyses the loads are uniformly applied and the plates are free of residual welding stresses with initial deflections based on their eigenmodes. In Chapter 5 the effects of other boundary conditions, additional load components and more realistic initial imperfections are investigated. Finally, the concepts of *effective width* and *plate reduction factors* are thoroughly discussed throughout this chapter. Although these concepts only apply to single load types (i.e. σ_x, σ_y or τ_{xy}), they are used to define the *characteristic strength* of plates in several capacity formulations such that their accuracy is a prerequisite for avoiding inaccuracy under combined loading.

2.1. Uniaxial compression

In this section the collapse of square plates under a single compressive load is examined. For plating under single, in-plane loads, "collapse" is best defined using *load-displacement* curves. These curves delineate the relationship between the magnitude of a single applied load and the relative axial or shear displacement of the plate edges. When this relationship is expressed in terms of internal quantities, reference is instead made to *average stress-average strain* curves[1], hereinafter referred to simply as *stress-strain* curves (where the expressions of both stress and strain are usually normalised against yield quantities). The stress and strain corresponding to the peak of the stress-strain curve represents the greatest load which the plate can resist and is therefore referred to as the *collapse strength* (or *ultimate strength*) of the plating[2].

[1] Here the term *strain* does not refer to *true material* strain, but rather *nominal* or *engineering* strain, i.e. the displacement of plate edges relative to the extent of the undeformed plate.

[2] Here the term *strength* refers to both *stress* and *strain*.

2.1.1. Ideal plates

Pre-buckling

A typical stress-strain curve is shown in Figure 2.1 for a square plate without any initial deflections and an elastic buckling stress $\sigma_{x,cr}$ well below its yield stress σ_Y and collapse strength $\sigma_{x,ult}$. With the initial application of a uniaxial load, stresses and strains are uniform throughout the plate with a linear relationship between them defined by the *modulus of elasticity*, $E = \sigma_x/\epsilon_x$. This linear elastic behaviour is referred to as the *pre-buckling* portion of the stress-strain curve and in theory applies only to ideal plates (although in practice the behaviour is also exhibited by plates with large elastic buckling stresses). For the load corresponding to point A on the curve ($\sigma_x/\sigma_Y = 0.3$), the principal stresses in the middle plane of the plate (normalised against the principal stress of greatest magnitude) are plotted in Figure 2.2(a). No Poisson effects are evident in these stresses since the edges of the plate, although straight, are otherwise able to move freely in-plane.

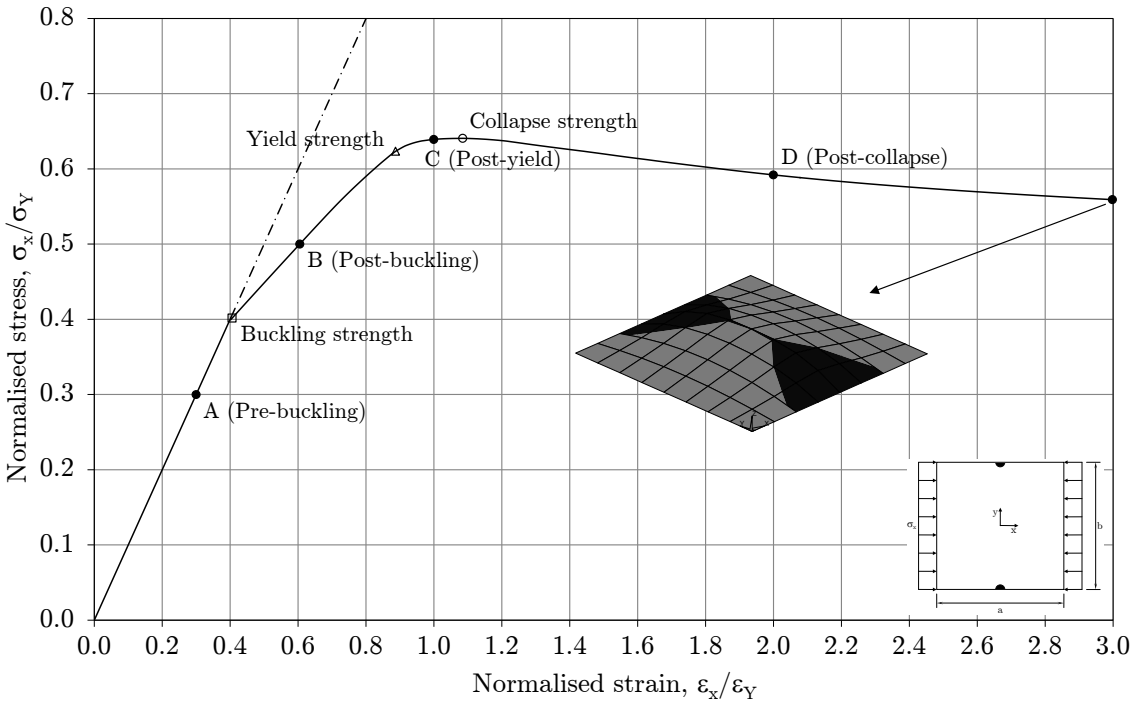

Figure 2.1.: Stress-strain curve of ideal plate under uniaxial compression.

Buckling strength

As the load is increased, the linear relationship between stress and strain continues until the *buckling strength* of the plate is reached. At this point, there exists an alternative (out-of-plane) deflection shape for which the elastic strain energy is equal to that of the compressed, plane plate. In mathematical terms, the critical buckling load is equal to the *1st eigenvalue* and the deformed shape is defined by the *1st eigenmode*. Under the slightest of perturbations, the resulting out-of-plane deflection in the central region of the plate

leads to a redistribution of stresses towards its edges and a lower axial stiffness[3].

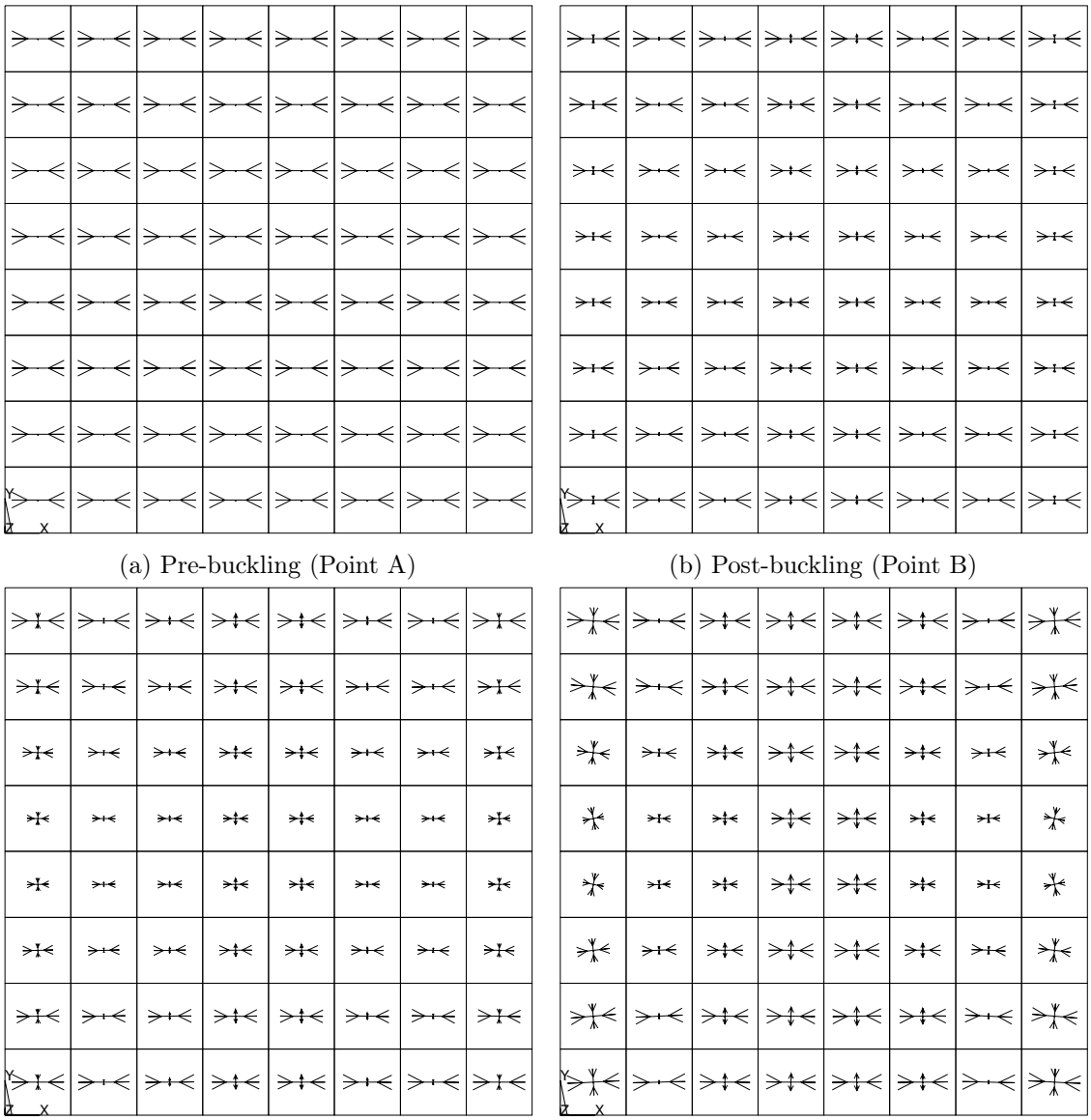

(a) Pre-buckling (Point A)

(b) Post-buckling (Point B)

(c) Post-yield (Point C)

(d) Post-collapse (Point D)

Figure 2.2.: Principle stresses in middle plane of ideal plate.

Post-buckling

Accordingly, the *post-buckling* portion of the stress-strain curve is characterised by a reduced slope ($\mathsf{E}' \simeq 0.49 \cdot \mathsf{E}$). In Figure 2.2(b) the principal stresses associated with point

[3] Plates with or without out-of-plane deflections store about the same amount of membrane strain energy (although this energy is distributed more so towards the edges in plates with out-of-plane deflections). The principle difference is that plates with out-of-plane deflections have additional bending strain energy in the middle region of the plate. This bending strain energy comes from additional external work and accounts for the greater distance over which the load must act, i.e. lower axial stiffness.

B ($\sigma_x/\sigma_Y = 0.5$) are shown. Here the redistribution of longitudinal stresses towards the edges of the plate (i.e. $y = 0$, $y = b$) is clearly evident as is the emergence of stresses in the transverse direction[4]. With respect to the latter, *tensile* stresses form around mid-length of the buckled plate due to the out-of-plane deflection. As a consequence of its straight sides[5], *compressive* stresses arise along the edges of the plate (i.e. $x = 0$, $x = a$)to balance in-plane forces in the transverse direction.

Yield strength

As the load is increased further, the out-of-plane deflections are magnified such that the central region of the plate sheds even more load, leading to an increase in stresses at the edges of the plate (i.e. $y = 0$, $y = b$) until the *yield stress* in the middle plane is eventually reached. Although stresses along the edges of the plate are approximately equal over its length (increasing slightly in the corners of the plate with increasing slenderness), yielding initiates at the mid-length edges of the plate, i.e. $x = a/2$ (see corner inset in Figure 2.1), due to the aforementioned tensile stresses. Here the (compressive) longitudinal stresses and (tensile) transverse stresses are "working together" to deform the plate material. In material failure theory, the opposite signs of these stresses result in a higher equivalent stress $\sigma_{eq,i}$ as reflected, for instance, in the positive interaction term $(-\sigma_{x,i} \cdot \sigma_{y,i})$ defined in the *von Mises* failure criterion[6]

$$\sigma_{eq,i} = \sqrt{{\sigma_{x,i}}^2 - \sigma_{x,i} \cdot \sigma_{y,i} + {\sigma_{y,i}}^2} = \sigma_Y \tag{2.1}$$

Although plasticity first appears at the compression surface of the plate (due primarily to bending strains in the central region), yielding in the middle plane of the plate is indicative of through-thickness plasticity (due primarily to in-plane strains at the edges of the plate) and is typically a precursor to collapse.

Post-yield

With further increases in axial load, plastic flow begins to spread throughout the middle plane, leading to progressive losses in stiffness at the edges of the plate (i.e. $y = 0$, $y = b$) such that the *post-yield* portion of the stress-strain curve is characterised by a rapidly decreasing slope. In Figure 2.2(c) the principal stresses associated with point C ($\epsilon_x/\epsilon_Y = 1.0$) in the post-yield response are shown. Here it can be seen that the axial stresses at the edges of the plate (i.e. $y = 0$, $y = b$) are approximately twice the magnitude of axial stresses in the central region (i.e. $y = b/2$) due to the ever increasing out-of-plane deflection in the buckled plate. This deflection is also reflected in the increased magnitude of transverse stresses.

---

[4] As a matter of convention, the term *longitudinal* refers to quantities in the x-direction and the term *transverse* refers to quantities in the y-direction. Moreover, plate length a is measured locally in the x-direction and plate breadth b in the y-direction such that $a \geqslant b$.

[5] As explained in Appendix B, plate edges remain straight due to reciprocal actions in adjacent plate fields. The effects of pull-in at free edges are discussed in Chapter 5.

[6] To avoid confusion with externally applied (average) stresses, e.g. σ_x, internal stresses distributed throughout the plate are additionally denoted with the subscript i, e.g. $\sigma_{x,i}$.

Collapse strength

Once the slope of the stress-strain curve reaches zero (i.e. the peak of the curve), the *collapse strength* or *ultimate strength* of the plate has been reached. In Figure 2.1 the normalised collapse stress is seen to be approximately $\sigma_{x,ult}/\sigma_Y = 0.64$ which represents a 2.8% increase in stress compared to initial yield. In the nomenclature of ultimate limit state (ULS) design, this value is referred to as the *characteristic measure of capacity* C_k (referred to above as the *characteristic strength* of plates). Alternatively, this capacity may be expressed in terms of strain. In the present example the normalised collapse strain is approximately $\epsilon_{x,ult}/\epsilon_Y = 1.09$ which is an increase of approximately $\Delta\epsilon_x \simeq 0.20 \cdot \epsilon_Y$ compared to initial yield. In the ultimate strength analysis of hull girders, the ultimate strain value may be of particular importance since the applied loads are strain-based. The ratio of $\sigma_{x,ult}$ and $\epsilon_{x,ult}$ is referred to as the secant modulus, $E_s = \sigma_{x,ult}/\epsilon_{x,ult}$, an analogous term to the elastic modulus E. The significance of the secant modulus is explained in §2.1.3.

Post-collapse

After collapse there is, by definition, a reduction in the load resistance of the plate under further straining. This is referred to as the *post-collapse*, *post-ultimate* or *unloading* portion of the stress-strain curve. The last of these terms may lead to some confusion since the plate is certainly not unloaded in the "unloading" portion of the curve. Indeed the strain loading is increasing even if some of the force previously carried by the plate is now "unloaded" onto adjacent structure, without which large axial displacements would ensue. The effects of further post-collapse straining are shown in Figure 2.2(d) for the load associated with point D of the stress-strain curve ($\epsilon_x/\epsilon_Y = 2.0$). Here the development of large axial and transverse stresses spread across the plate at mid-length (i.e. $x = a/2$) is evidence of a plastic mechanism which facilitates large axial straining. Hughes [9] refers to this mechanism as a "pitched roof" configuration, but it is also recognisable as the double-Y plastic formation from hinge line theory. In any case, a plot of this plastic mechanism is shown in Figure 2.1 for $\epsilon_x/\epsilon_Y = 3.0$. This plastic collapse mechanism has also been observed in experiments of stiffened plates carried out by Egge [10], as shown in Figure 2.3, as well as in experiments reported by Faulkner [11].

(a) Panel II (b) Panel III

Figure 2.3.: Plastic collapse mechanisms (reproduced from reference [10] with permission of E.D. Egge and Germanischer Lloyd).

2.1.2. Effective width concept

Plate slenderness

The stress-strain curve shown in Figure 2.1 is for an ideal plate with a slenderness defined by $\beta = 3$, where β is the *plate slenderness parameter*

$$\beta = \frac{b}{t}\sqrt{\frac{\sigma_Y}{E}} \tag{2.2}$$

Stress-strain curves for ideal plates with other slenderness parameters are shown on the left-hand side of Figure 2.4 where three distinct mechanisms of collapse can be identified according to the relationship between the elastic buckling stress $\sigma_{x,cr}$ and collapse stress $\sigma_{x,ult}$.

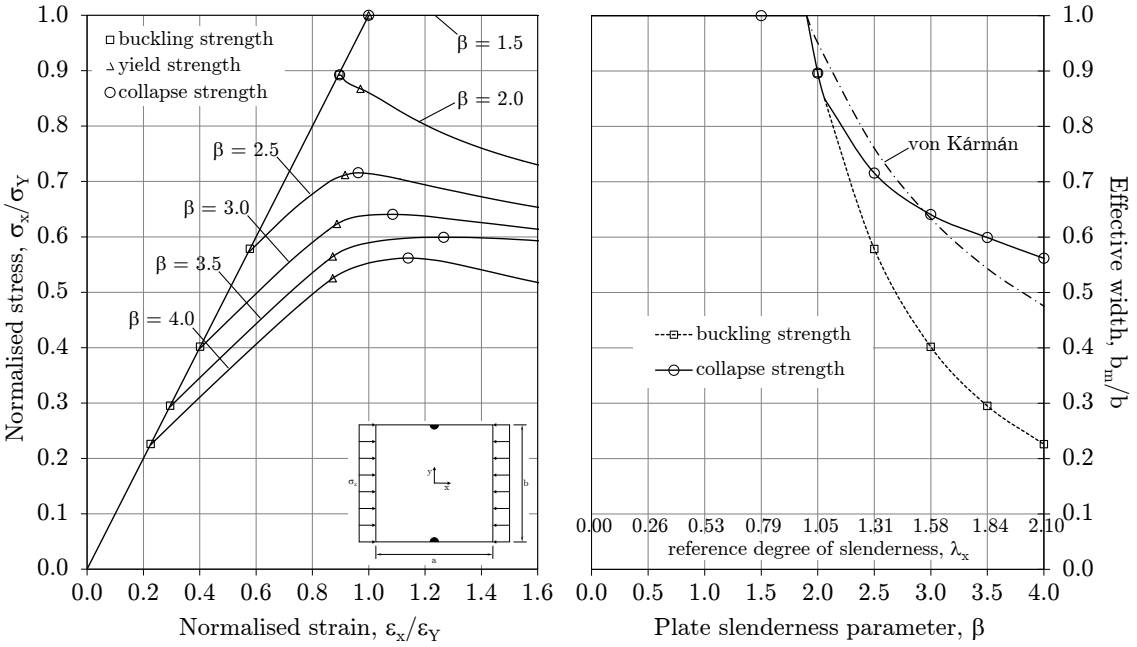

Figure 2.4.: Stress-strain curves and effective width of ideal plates.

$\underline{\sigma_{x,cr} < \sigma_{x,ult}}$

For ideal plates with slenderness parameters $\beta = 2.5$ to $\beta = 4.0$, the buckling stress $\sigma_{x,cr}$ is in each case less than the collapse stress $\sigma_{x,ult}$. For these plates the mechanism of collapse is similar to that described in 2.1.1.

$\underline{\sigma_{x,cr} = \sigma_{x,ult}}$

For ideal plates with a slenderness parameter $\beta = 2.0$, a second mechanism of collapse is observed for which the linear relationship between stresses and strains is maintained until the buckling stress of the plate is reached. At this point the resulting redistribution of stresses leads not only to a *lower* axial stiffness, but a *negative* axial stiffness. In other

words, for such plates the collapse stress $\sigma_{x,ult}$ is defined by their buckling stress $\sigma_{x,cr}$, whereupon the plate begins to unload. Whether or not the yield strain of the plate is reached depends on the stiffness of the adjacent supporting structure.

$\underline{\sigma_{x,cr} > \sigma_{x,ult} = \sigma_Y}$

For ideal plates with a slenderness parameter $\beta = 1.5$, yet a third mechanism of collapse is seen for which the elastic buckling stress $\sigma_{x,cr}$ is greater than the collapse stress $\sigma_{x,ult}$. Here the linear relationship between stresses and strains continues until the yield stress (and yield strain) of the plate is reached, without any buckling whatsoever. Neglecting strain hardening effects, no further increase in stress is possible beyond this point such that the collapse stress of the plate is defined by its yield stress. Because the full cross-section of the plate is yielded at collapse, the post-collapse portion of the stress-strain curve is characterised entirely by plastic flow (i.e. an elastic-perfectly plastic stress-strain curve).

von Kármán

Similar stress-strain curves to those shown on the left-hand side of Figure 2.4 were first determined experimentally in the context of aeronautical research. The seminal work in this regard was carried out in 1930 by Schuman and Back [12] in order to better understand the post-buckling behaviour of thin plates. Simply-supported plates of four different materials were tested to failure under uniaxial compression loads. The plates were $a \sim 600$ mm in length with widths varying between $b \sim 100$ mm and $b \sim 600$ mm ($\Delta b \sim 100$ mm increments) and thicknesses between $t \sim 0.38$ mm and $t \sim 2.41$ mm ($\Delta t \sim 0.38$ mm increments). When plotting the maximum load (i.e. force) carried by each of the plates against their widths, the tests revealed that the loads generally reached a maximum for the $b \sim 200$ mm or $b \sim 300$ mm widths without significant increases in maximum load for larger widths (i.e. for those plates which buckled elastically prior to collapse). As noted by Schuman and Back "(i)t appears that after buckling, the wide plate acts as though it were a narrow plate of a width corresponding to that of the side portions which are taking most of the load".

Indeed, it was precisely this concept of post-buckling behaviour which led von Kármán [13] in 1932 to derive the first effective width expression for thin plates in compression. The sketch used in von Kármán's paper to illustrate this concept is shown in Figure 2.5. As can be seen, it is assumed that the entire axial force P is carried uniformly by two edge strips of width w. For simplicity, von Kármán then assumes "that the deflection is such that horizontal tangents at the inner edges of the two load-supporting strips are parallel to the X-direction, Fig. 2(a). Then the center of the sheet can be disregarded and the two strips can be handled as if they were together".

Accordingly, denoting the effective width of the plating as $b_m = 2 \cdot w$, the critical (elastic) buckling stress of the actual plate

$$\sigma_{x,cr} = K_x \cdot \frac{\pi^2 \cdot E}{12(1-\nu^2)} \left(\frac{t}{b}\right)^2 \tag{2.3}$$

can be rewritten for a fictitious plate of width b_m as

$$\sigma_{x,cr,m} = K_x \cdot \frac{\pi^2 \cdot E}{12(1-\nu^2)} \left(\frac{t}{b_m}\right)^2 \tag{2.4}$$

where K_x is the *elastic buckling factor*.

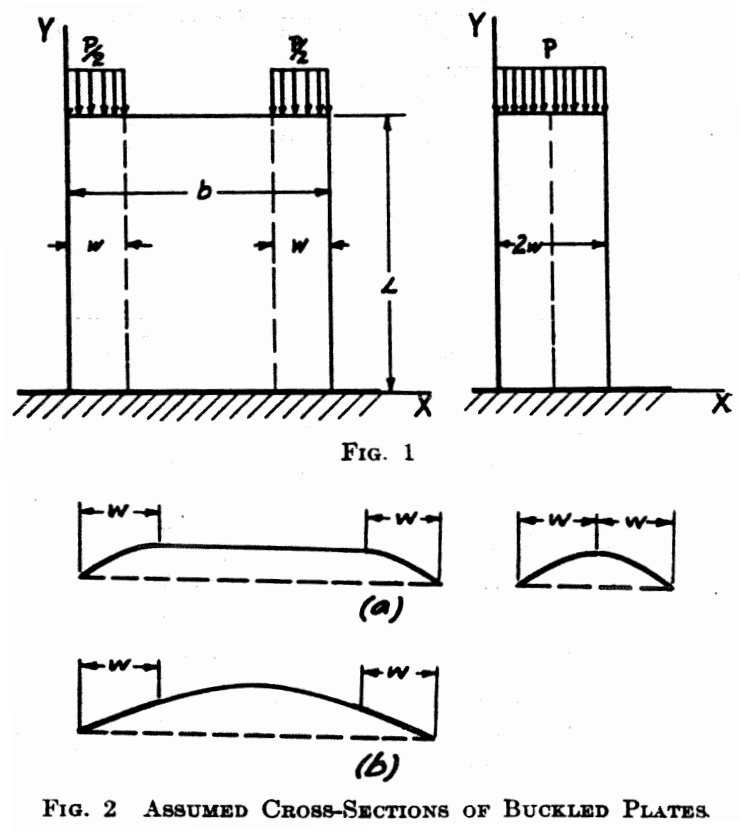

Figure 2.5.: Sketch of effective width concept from von Kármán's paper (reproduced from reference [13] with permission of the American Society of Mechanical Engineers).

However, because the edges of the plate do not buckle elastically before yielding (i.e. $\sigma_{x,cr,m} \geqslant \sigma_Y$), von Kármán is able to define failure of the plate as

$$\sigma_Y = K_x \cdot \frac{\pi^2 \cdot E}{12(1-\nu^2)} \left(\frac{t}{b_m}\right)^2 \tag{2.5}$$

or, in terms of effective width b_m

$$b_m = \sqrt{K_x \cdot \frac{\pi^2 \cdot E}{12(1-\nu^2)} \frac{t^2}{\sigma_Y}} \tag{2.6}$$

which in the modern treatment of the effective width concept is normalised against the actual width of the plating b

$$\frac{b_m}{b} = \sqrt{K_x \cdot \frac{\pi^2 \cdot E}{12(1-\nu^2)} \left(\frac{t^2}{\sigma_Y \cdot b^2}\right)} = \sqrt{\frac{\sigma_{x,cr}}{\sigma_Y}} \tag{2.7}$$

In present-day nomenclature, the inverse ratio of the term on right-hand side of Equation (2.7) is known as the *reference degree of slenderness*, λ_x:

$$\lambda_x = \sqrt{\frac{\sigma_Y}{\sigma_{x,cr}}} = \sqrt{\frac{\sigma_Y}{K_x \cdot \sigma_e}} \tag{2.8}$$

Here the critical buckling stress $\sigma_{x,cr}$ is alternatively expressed as the product $K_x \cdot \sigma_e$, where σ_e is a *reference stress* equal to the Euler buckling stress for a wide column or plate with an infinite aspect ratio (i.e. $\alpha = \infty$)

$$\sigma_e = \frac{\pi^2 \cdot E}{12(1-\nu^2)} \left(\frac{t}{b}\right)^2 \tag{2.9}$$

Accordingly, the *plate slenderness parameter* β is related to the *reference degree of slenderness* λ_x as

$$\lambda_x = \beta \sqrt{\frac{12(1-\nu^2)}{\pi^2 \cdot K_x}} \tag{2.10}$$

and related to the effective width as

$$\frac{b_m}{b} = \frac{1}{\lambda_x} = \frac{1}{\beta} \sqrt{\frac{\pi^2 \cdot K_x}{12(1-\nu^2)}} \simeq \frac{1.9}{\beta} \tag{2.11}$$

where $K_x = 4$ for a square plate. Equation (2.11) is shown on the right-hand side of Figure 2.4 together with buckling and collapse strength curves derived from the stress-strain curves on the left-hand side. Based on numerical analyses it can be seen that von Kármán's effective width expression is somewhat conservative for those plates where the buckling stress is far below the collapse stress, but becoming non-conservative for those plates having comparable buckling and collapse stresses.

2.1.3. Effects of initial deflections

Due primarily to welding during construction, initial deflections of magnitude δ_0 exist in all ship plating. For this reason, stress-strain curves are shown on the left-hand side of Figure 2.6 for initially deflected plating ($\delta_0 = b/200$). Unlike the idealised stress-strain curves shown in Figure 2.4, these curves are characterised from the outset by a loss of in-plane stiffness due to initial out-of-plane deflections which allow the central region of the plate to shirk some of the axial shortening that is occurring fully at the edges. As a result, the stress-strain curves deviate immediately from the elastic modulus curve ($\sigma_x/\epsilon_x = E$) over a wide range of plate slenderness parameters and, although the collapse strengths are about equal for $\beta = 4$, the magnitude of collapse strength for plates with initial deflections becomes progressively smaller with reducing plate slenderness parameters compared to ideal plates. In addition, the peaks of the curves for plates with initial deflections are not as well defined reflecting a more gradual collapse than that for ideal plates.

On the right-hand side of Figure 2.6 the collapse strengths of plates with and without initial deflections are shown. Also shown are three ranges of plate slenderness suggested by Hughes [9] to delineate different types of plating collapse; slender, intermediate and sturdy. As described in §2.1.2, the transitions between these different classes of plating are approximately defined where the collapse strength of plates with initial deflections equals

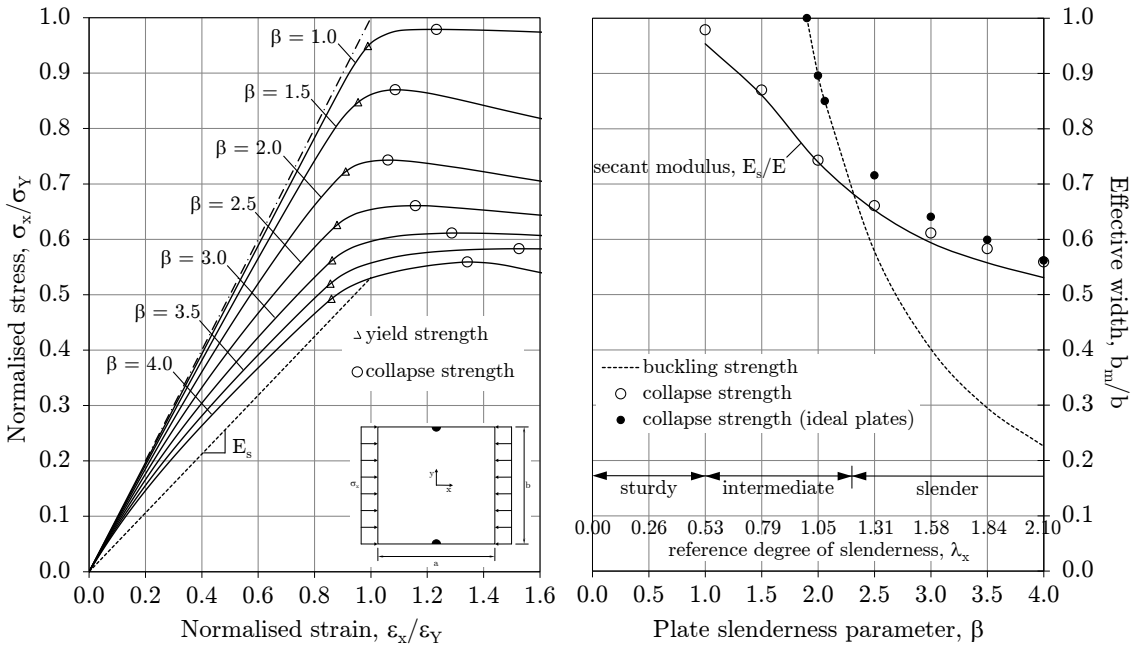

Figure 2.6.: Stress-strain curves and effective width of plates with initial deflections.

the yield strength (i.e. sturdy to intermediate plating) and where the collapse strength equals the elastic buckling strength (i.e. intermediate to slender plating).

Sturdy plating

For sturdy plating ($\beta \leqslant 1.0$) the elastic buckling stress is so large that the magnification of initial deflections is minimal. Accordingly, the stress-strain curves of sturdy plates closely follow the elastic modulus curve and then the yield limit defined by σ_Y, i.e. elastic-perfectly plastic behaviour. This behaviour is evident in the distributions of principal stresses at collapse as shown in Figure 2.7(a) for plating with a slenderness parameter $\beta = 1.0$. The negligible presence of transverse σ_y stresses is due to the (near) absence of out-of-plane deflections. Accordingly, as noted in §2.1.1, sturdy plates (i.e. even those with initial deflections) also exhibit the linear elastic behaviour of pre-buckled, ideal plates and do so until the yield stress is reached.

Slender plating

Conversely, slender plating ($2.3 < \beta$) buckles elastically before either the yield or collapse stresses are reached. However, since the plate continues to support the load after elastic buckling, this is in general acceptable provided serviceability limit state (SLS) and fatigue limit state (FLS) criteria are satisfied (limit states are discussed in §5.1). The elastic buckling behaviour which precedes collapse is clearly evident in the distributions of principal stresses shown in Figures 2.7(c) and 2.7(d) for plating with slenderness parameters $\beta = 3.0$ and $\beta = 4.0$, respectively. These distributions are characterised by a transfer of longitudinal load to the edges of the plate and by significant transverse stresses due to out-of-plane deflections.

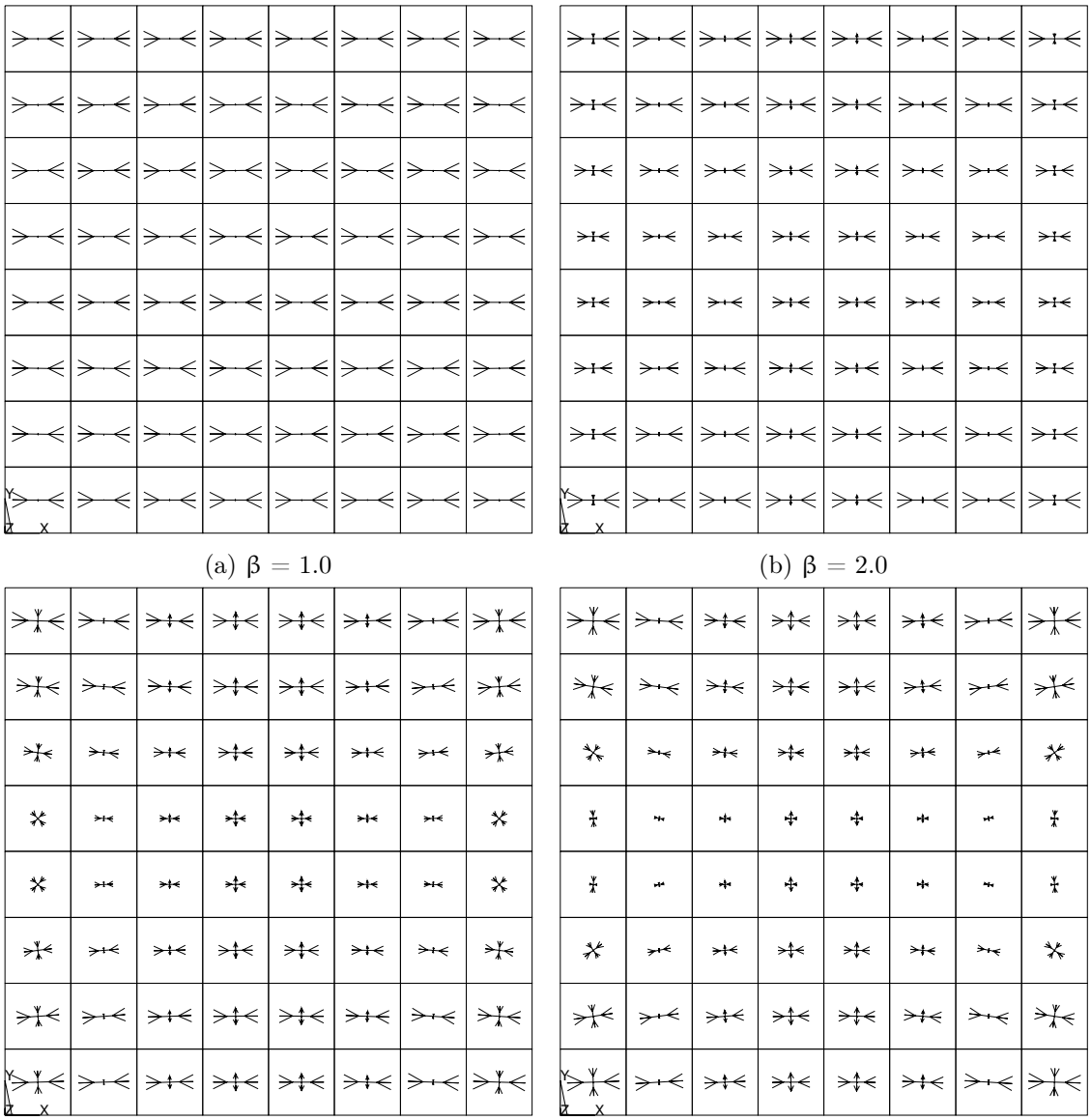

(a) $\beta = 1.0$ (b) $\beta = 2.0$

(c) $\beta = 3.0$ (d) $\beta = 4.0$

Figure 2.7.: Principle stresses at collapse in middle plane of plates with initial deflections.

Intermediate plating

Between these two extremes, intermediate plating ($1.0 < \beta \leqslant 2.3$) is typical of that used in longitudinal strength members and has a collapse stress below both the elastic buckling and yield stresses. Looking at the collapse strength data points on the right-hand side of Figure 2.6, an inflection point can be discerned within the range of slenderness parameters for intermediate plating which marks the steepest portion of the effective width curve, thereby indicating that the collapse strength of intermediate plating is the most sensitive to slenderness under a uniaxial load. As can be seen in Figure 2.7(b), the distribution

of principal stresses displays moderate or "intermediate" levels of both load shedding and transverse stresses.

Plate secant modulus

As illustrated on the left-hand side of Figure 2.6 (for the stress-strain curve associated with plate slenderness $\beta = 4$), a secant intersecting a stress-strain curve at its origin and a point associated with collapse is referred to as the *plate secant stiffness* or *plate secant modulus* E_s. On the left-hand side of Figure 2.6, the yield strain $\epsilon_x/\epsilon_Y = 1.0$ has been chosen as the point associated with collapse. Chatterjee and Dowling [14] showed that if the plate secant modulus E_s is normalised against the plate elastic modulus E, the resulting quantity E_s/E is approximately equal to the normalised ultimate stress $\sigma_{x,ult}/\sigma_Y$ less the magnitude of residual (compressive) stress $\sigma_{x,rc}/\sigma_Y$ [9]. For the stress-strain curves shown on the left-hand side of Figure 2.6, the residual stresses are zero. Accordingly, on the right-hand side of Figure 2.6 the secant modulus curve defined by E_s/E is shown to closely approximate the ultimate stress curve defined by $\sigma_{x,ult}/\sigma_Y$[7]. In general, Chatterjee and Dowling suggest the secant be drawn to the peak of the load-shortening curve or a point on the curve corresponding to an arbitrary strain limit in case there is no clear peak or in case it occurs at a level of strain far beyond yield (e.g. the stress-strain curve for plate slenderness $\beta = 3.5$ shown on the left-hand side of Figure 2.6). On the basis of this procedure, Chatterjee and Dowling have provided curves of secant modulus for plates with and without residual stresses [14].

Winter

Contrary to the foregoing approach, steel-plated structures are generally designed using effective width formulae based on experimental and numerical results. On the left-hand side of Figure 2.8, von Kármán's effective width expression

$$b_m = 1.9\sqrt{\frac{E}{\sigma_Y}} \cdot t \tag{2.12}$$

is plotted as b_m/b together with the collapse strength of plates with and without initial deflections. Unsurprisingly, the detrimental effect of initial deflections on the capacity of plates reveals von Kármán's equation to be even more non-conservative than shown in Figure 2.4 for ideal plates. Nevertheless, this does not diminish von Kármán's effective width concept. As noted by Sechler and Donnell in the Appendix to von Kármán's derivation of effective width, the purpose of von Kármán's derivation was to prove that the capacity of the plate was proportional to the square roots of E and σ_Y as well as the square of plate thickness

$$P_{x,ult} = C\sqrt{E \cdot \sigma_Y} \cdot t^2 \tag{2.13}$$

[7] A useful way to conceptualise this approach is to consider the buckled plate with an elastic modulus E replaced by a plane (unbuckled) plate with a reduced elastic modulus E_s. The collapse strength of the plate is then defined by $\sigma_{x,ult} = \sigma_Y \cdot E_s/E$.

where $P_{x,ult} = b_m \cdot t \cdot \sigma_Y$ and the proportionality constant C accounts for existing boundary conditions.

Accordingly, von Kármán's effective width equation can be rewritten in a more general form as

$$b_m = C\sqrt{\frac{E}{\sigma_Y}} \cdot t \tag{2.14}$$

According to Sechler and Donnell, "(i)n making his analysis, Dr. von Kármán, for simplicity, assumed somewhat artificial conditions, and hence it is not to be expected that the value of C given above is exactly correct even for the case of simply supported sides". In fact, Sechler and Donnell show that for a "perhaps more likely assumption" about the deflected shape (i.e. "Fig. 2(b)" shown in Figure 2.5), the value of C is found to be approximately 1.24. Indeed, Sechler [15] went on to conduct a number tests on thin plates of various metals[8] where he found that the value of $C = 1.9$ is only approached for extremely wide and thin plates, i.e. slender plates. Moreover, Sechler showed that the experimentally determined values of C were not constant, but rather dependent on the parameter $\sqrt{E/\sigma_Y} \cdot (t/b)$, i.e. $1/\beta$.

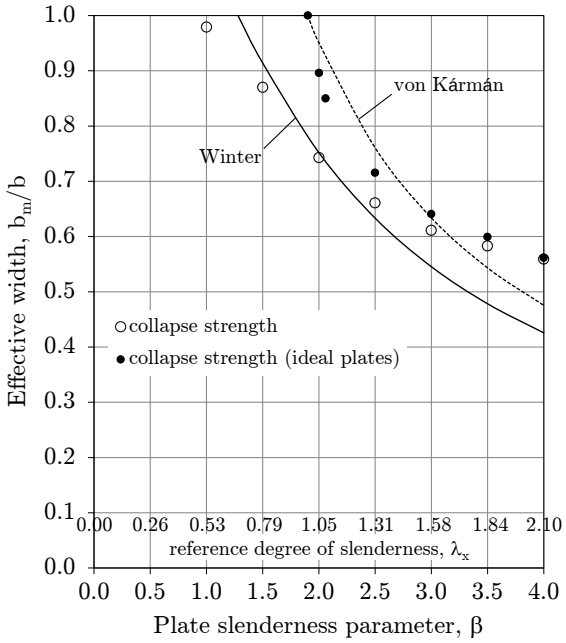

Figure 2.8.: Von Kármán and Winter curves.

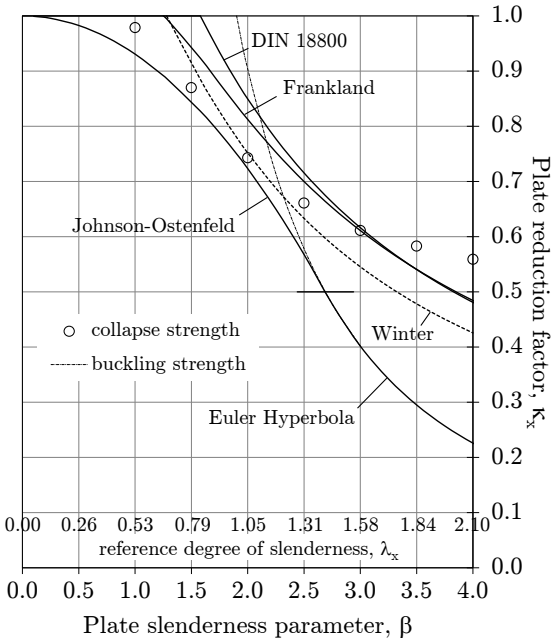

Figure 2.9.: Plate reduction curves.

Building on the work of Sechler, Winter [17] performed additional tests on 25 U-beams to see if von Kármán's effective width concept for individual plates could be applied equally to thin compression plates representing component parts of structural members. Winter concluded that the agreement between the results of the two investigations were "remarkably close" and therefore fit a straight line through the values of C for both sets of tests

[8] Results of these tests are also reported by Timoshenko [16].

$$C = 1.9 - 1.09\sqrt{\frac{E}{\sigma_Y}}\left(\frac{t}{b}\right) \tag{2.15}$$

in which the intercept of the ordinate is equal to von Kármán's initial value of $C = 1.9$. Substituting this equation for C in Equation (2.14), Winter obtained the following equation for effective width

$$b_m = 1.9\sqrt{\frac{E}{\sigma_Y}} \cdot t \left[1 - 0.574\left(\frac{t}{b}\right)\sqrt{\frac{E}{\sigma_Y}}\right] \tag{2.16}$$

where the second term within the square brackets is used to modify von Kármán's original equation. Winter's equation was initially used in the first edition (1946) of the specification for the design of light gage steel structural members published by the American Iron and Steel Institute (AISI) [18], but has since been used widely throughout civil engineering, albeit with modifications over the years to the constant used in the expression for correcting von Kármán's original equation. Today it is most commonly expressed in terms of the reference degree of slenderness as

$$\frac{b_m}{b} = \frac{1}{\lambda_x} - \frac{0.22}{\lambda_x^2} \tag{2.17}$$

and is used to calculate the effective width of compressed plates in Eurocode 3 (EN 1993-1-5) [19]. Accordingly, Winter's equation is also plotted on the left-hand side of Figure 2.8. As expected, Winter's curve lies below that of von Kármán's original curve and is more representative of the collapse strength of intermediate and sturdy plating ($\beta \leqslant 2.3$).

2.1.4. Effective width formulae used in shipbuilding

Plate reduction factors

In the particular case of the classification of ships, three effective width formulae have become prevalent, where the ratio of the collapse stress $\sigma_{x,ult}$ and the material yield stress σ_Y of the plate is alternatively referred to as the *plate reduction factor* κ. In general there is a plate reduction factor corresponding to each stress component,

$$\kappa_x = \sigma_{x,ult}/\sigma_Y \qquad \kappa_y = \sigma_{y,ult}/\sigma_Y \qquad \kappa_\tau = \tau_{xy,ult} \cdot \sqrt{3}/\sigma_Y$$

Not only do plate reduction factors represent the characteristic strength of plates under single stress components, but (as will be seen) they are as well used as reference stresses in interaction equations which define the capacity of plates under multiple stress components. In addition, plate reduction factors are used to define the effective width of plating in proofs of stiffener buckling strength[9].

[9] Generally, the extent of attached plating used in proofs of stiffener buckling strength is the minimum of the effective *width* due to plate buckling and the effective *breadth* due to shear lag effects associated with bending of the plate-stiffener combination (as discussed in §5.1.2).

1. Johnson-Ostenfeld

The Johnson-Ostenfeld correction is used to adjust the (elastic) buckling strength curves shown on the right-hand sides of Figures 2.4 and 2.6 to account for plasticity, i.e. material non-linearity, not geometric non-linearity. It was developed in the context of column buckling, but has also been used for plating since 1989 in the *IACS Longitudinal Strength Standard* UR S11 [20]. In terms of the former, material properties over the cross-section of a column are rarely uniform due to the presence of residual stresses in rolled sections. Those areas under compressive residual stresses $\sigma_{x,rc}$ will begin to yield when the (compressive) axial stress reaches $\sigma_x = \sigma_Y$ - $\sigma_{x,rc}$, while those areas under tensile residual stresses $\sigma_{x,rt}$ will not yield until the (compressive) axial stress reaches $\sigma_x = \sigma_Y + \sigma_{x,rt}$. However, by assuming an elastic-perfectly plastic material, the reduction in the average modulus of elasticity over the cross-section, referred to as the *structural tangent modulus* E_{ts}, becomes linearly proportional to the extent of yielding. On the basis of this assumption, the Ostenfeld-Bleich [21] parabola describes the relationship between the axial stress σ_x and the structural tangent modulus E_{ts}

$$E_{ts} = E\frac{\sigma_x\left(\sigma_Y - \sigma_x\right)}{\sigma_{spl}\left(\sigma_Y - \sigma_{spl}\right)} \tag{2.18}$$

where $\sigma_{spl} = \sigma_Y$ - $\sigma_{x,rc}$ is the *structural proportional limit* which determines where the material stress-strain curve departs from the linear stress-strain relationship defined by the elastic modulus E, i.e. $E_{ts} = E$ when $\sigma_x \leqslant \sigma_{spl}$ [9].

Substituting E_{ts} from Equation (2.18) for E in Equation (2.3) yields the following critical buckling stress corrected for plasticity

$$\sigma_{cr,p} = K_x \cdot \frac{\pi^2 \cdot E}{12(1-\nu^2)}\left(\frac{t}{b}\right)^2 \frac{\sigma_{cr,p}\left(\sigma_Y - \sigma_{cr,p}\right)}{\sigma_{spl}\left(\sigma_Y - \sigma_{spl}\right)} \tag{2.19}$$

which, when taken as the ultimate stress of the plate, becomes

$$\sigma_{x,ult} = \frac{\sigma_Y}{\lambda_x^2}\frac{\sigma_{x,ult}\left(\sigma_Y - \sigma_{x,ult}\right)}{\sigma_{spl}\left(\sigma_Y - \sigma_{spl}\right)} \tag{2.20}$$

If residual compressive stresses $\sigma_{x,rc}$ are assumed to be 50% of yield stress then $\sigma_{spl} = \frac{1}{2}\cdot\sigma_Y$ such that

$$\kappa_x = \frac{\sigma_{x,ult}}{\sigma_Y} = \begin{cases} 1 - \dfrac{\lambda_x^2}{4} & \lambda_x < \sqrt{2} \\ \dfrac{1}{\lambda_x^2} & \lambda_x \geqslant \sqrt{2} \end{cases} \tag{2.21}$$

where $\kappa_x = 1/\lambda_x^2$ is commonly referred to as the *Euler hyperbola* and defines collapse as the critical buckling stress $\sigma_{x,cr}$ (see Equation (2.8)). Equation (2.21) is plotted in Figure 2.9 where the transition from elastic to inelastic buckling occurs at $\kappa_x = 0.5$ (i.e. $\lambda_x = \sqrt{2}$) as defined by the (assumed) structural proportional limit $\sigma_{spl} = \frac{1}{2}\cdot\sigma_Y$. Not surprisingly, the portion of the reduction curve defined by the Euler hyperbola is rather conservative since it does not take the post-buckling strength of the plate into account. The portion of the reduction curve defined by the Johnson-Ostenfeld correction (i.e. $\kappa_x = 1$ - $\lambda_x^2/4$) is also conservative, but generally within 5% of numerical analyses.

2. Frankland

In parallel to the previously referenced experiments by the aircraft industry, similar investigations were undertaken at the U.S. Navy Yard in Washington D.C. Since late 1932 the U.S. Experimental Model Basin conducted strength tests on longitudinally-stiffened plating under in-plane compressive loads (here the unloaded edges of the plate were simply-supported and free to pull in). The results of these tests were documented in a series of confidential reports. However, in a published review of the experimental work written by Frankland in 1940 [22], a figure summarising the buckling and ultimate strength of plates in terms of κ_x and β is reproduced from a report by Vasta (formerly of the Experimental Model Basin staff), together with a fitted curve of "reasonable accuracy". This curve has the equation

$$\kappa_x = \frac{2.25}{\beta} - \frac{1.25}{\beta^2} \tag{2.22}$$

and is included in Figure 2.9. In terms of λ_x, the equation is

$$\kappa_x = \frac{1.18}{\lambda_x} - \frac{0.35}{\lambda_x^2} \tag{2.23}$$

However, Frankland points out that there is a considerable amount of scatter in the data at the high stress end of the curve due to inaccuracies in estimating the *compressive* yield strength of the plates from *tensile* tests. More importantly, Frankland acknowledges the absence of in-plane restraint, without which the depths of plate buckles increase such that the effective width of plates decrease. However, Frankland concludes that this effect is only appreciable for plates with a slenderness $\beta > 2.5$.

Not surprisingly, the U.S. Navy Yard's equation has found its way into commercial shipbuilding as well. In particular, it is used in the hull girder ultimate strength requirements of the CSR BC & OT [23]. Furthermore, it is also used to determine the effective width of the compression flange of corrugations in the IACS unified requirements for the evaluation of corrugated transverse watertight bulkheads (UR S18 [24] and UR S19 [25]).

3. DIN 18800

Using an approach similar to that of the U.S. Navy Yard, ultimate plate strength formulations were also developed in the late 1980's for inclusion in the German construction standard DIN 18800 [26]. The standard was prepared jointly by the *Normenausschuß Bauwesen* (Building and Civil Engineering Standards Committee) and the *Deutscher Ausschuß für Stahlbau* (German Committee for Structural Steelwork). In Part 3 of DIN 18800, equations for reduction factors are provided for buckling cases classified according to boundary conditions and stress types. For a simply-supported plate under longitudinal compression, the equation for $\kappa_x = \sigma_{x,ult}/\sigma_Y$ was determined on the basis of 705 experimentally and numerically derived buckling strength results. However, following critical evaluation of these results, 213 were considered unreliable and discarded (e.g. due to errors/uncertainties concerning boundary conditions, material properties, loading rate etc.) [27]. The resulting equation for the reduction factor κ_x is equal to Winter's Equation (2.17) multiplied by a factor $c = 1.25 - 0.12 \cdot \psi_x \leqslant 1.25$, where $\psi_x = \sigma_{x,max}/\sigma_{x,min}$ is the ratio of edge stresses. Since $\psi_x = 1.0$ for the case of a uniform in-plane load (i.e. no in-plane bending), the resulting equation for the plate reduction factor is

$$\kappa_x = 1.13\left(\frac{1}{\lambda_x} - \frac{0.22}{\lambda_x^2}\right) = \frac{1.13}{\lambda_x} - \frac{0.25}{\lambda_x^2} \tag{2.24}$$

This equation is also plotted in Figure 2.9. In terms of β, the equation is

$$\kappa_x = \frac{2.15}{\beta} - \frac{0.9}{\beta^2} \tag{2.25}$$

which is not too dissimilar from an equation proposed by Faulkner [28] [29] in 1964 on the basis of his own analysis of the tests carried out at the U.S. Navy Yard

$$\kappa_x = \frac{2}{\beta} - \frac{1}{\beta^2} \tag{2.26}$$

The DIN 18800 formulations were first implemented in the buckling strength requirements of the German classification society Germanischer Lloyd (GL) in 1997 [30], but have since been implemented in the buckling strength requirements of the *IACS Common Structural Rules for Bulk Carriers* (CSR BC) [31], the *IACS Common Structural Rules for Double Hull Oil Tankers* (CSR OT) [32], CSR BC & OT [23], UR S11A [8] as well as the new *DNV GL Rules for Classification* [33] which are applicable to all ship types.

2.2. Biaxial loads

In general ship plating is subjected to combined in-plane stresses (as well as lateral pressure). Usually one of the in-plane stress components governs the collapse of the plating (*primary* stress) with another of the in-plane stress components affecting this collapse to some discernible extent (*secondary* stress). A third in-plane stress component may also exist (*tertiary* stress), but often has only a negligible effect on plating collapse. In this section the collapse of square plates under pure biaxial in-plane stresses is examined. Such a stress state is approached, for instance, in the shell and inner bottom plating of double bottom structures due to hull girder bending, transverse compression and double bottom bending[10]. Of sufficient magnitude, either of the axial stresses in isolation would lead to collapse of square plating as described in the preceding section. With the presence of a secondary stress, however, there is an extensive interaction which affects the distribution of stresses and strains within the plate and thereby its collapse strength.

2.2.1. Ideal plates - compressive secondary stress

Loading sequence

In Figure 2.1 a stress-strain curve was shown for a square plate of slenderness $\beta = 3.0$. The plate was without any initial deflections and subjected to a uniaxial load. In Figure 2.10 two stress-strain curves are shown for the same (ideal) plate under a biaxial load $\sigma_y = \sigma_x$. For one curve σ_y and σ_x are applied simultaneously. This is referred to as *proportional loading*. For the other curve σ_y is applied first, followed by σ_x[11]. This is referred to as

[10] The aspect ratio of plating in the shell and inner bottom plating of double bottom structures is typically between $\alpha = 3$ and $\alpha = 5$, although square plates are sometimes found outside the parallel midbody. The effect of plate aspect ratio is examined in §2.4.

[11] In case of $\sigma_y = \sigma_x$ the stress-strain curve for a square plate remains unchanged regardless of which stress is applied first.

sequential loading. In the latter case, the negative strain in the x-direction following the application of σ_y is evidence of the Poisson effect

$$\frac{\epsilon_x}{\epsilon_Y} = -\nu \cdot \frac{\sigma_{y,ult}}{\sigma_Y} = -0.3 \cdot 0.38 = -0.11 \tag{2.27}$$

where $\nu = 0.3$ is Poisson's ratio and $\sigma_{y,ult}/\sigma_Y = 0.38$ is the (normalised) ultimate stress in the y-direction for the biaxial compression case $\sigma_y = \sigma_x$. With the subsequent application of σ_x, the slope of the stress-strain curve is lower, but the load is acting over a greater range of strain. Accordingly, in the present case of a square plate, the two stress-strain curves coincide at the collapse strength. As shown by Valsgård [34] for plates with an aspect ratio $\alpha = 3$, proportional loading leads to lower plate capacity for plates with an aspect ratio greater than $\alpha = 1$. Accordingly, following this subsection, only the critical case of proportional loading will be considered.

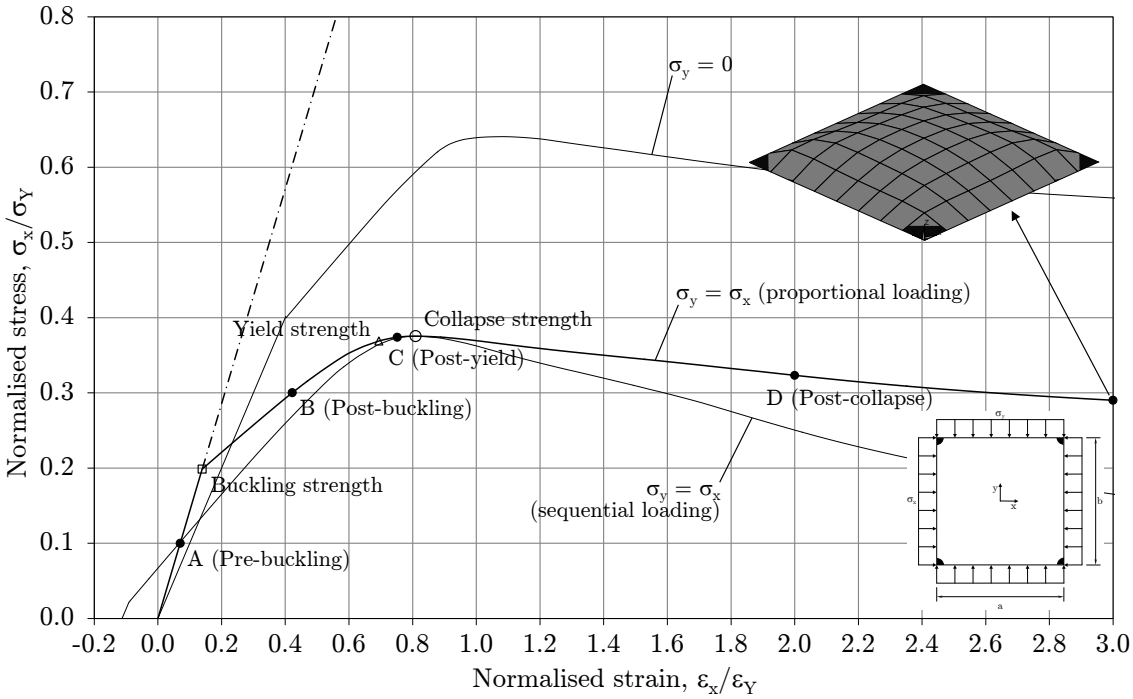

Figure 2.10.: Stress-strain curve of ideal plate under biaxial compression ($\sigma_y = \sigma_x$, $\beta = 3$).

Pre-buckling

Due to symmetry, the stress-strain curve σ_y-ϵ_y under proportional loading has the same shape and height as the σ_x-ϵ_x curve. With the initial application of the biaxial load, stresses and strains in each direction are uniform throughout the plate. However, unlike the uniaxial load case, the linear relationship between them is no longer defined solely by the *modulus of elasticity*, $E = \sigma_x/\epsilon_x$. Rather, due to the presence of the secondary stress σ_y, strain in the x-direction is reduced according to Poisson's equation

$$\epsilon_x = \frac{\sigma_x}{E} - \nu \cdot \frac{\sigma_y}{E} \tag{2.28}$$

When $\sigma_y = \sigma_x$ (as it does in Figure 2.10), this equation can be rewritten as

$$\epsilon_x = \frac{\sigma_x}{E} - \nu \cdot \frac{\sigma_x}{E} = (1 - \nu) \cdot \frac{\sigma_x}{E} \tag{2.29}$$

Rearranging in terms of σ_x/ϵ_x

$$\frac{\sigma_x}{\epsilon_x} = \frac{E}{(1 - \nu)} \tag{2.30}$$

Accordingly, when $\nu = 0.3$, the pre-buckling behaviour of the plate is such that its effective modulus of elasticity is equal to $E' \simeq 1.43 \cdot E$, as reflected in the pre-buckling portion of the curve in Figure 2.10. Again, this linear elastic behaviour applies only to ideal plates or to plates with large elastic buckling stresses. For the load corresponding to point A on the curve ($\sigma_x/\sigma_Y = 0.1$), the principal stresses in the middle plane of the plate are plotted in Figure 2.11(a). As in the uniaxial load case, no Poisson effects are evident in these stresses since the edges of the plate are able to move freely in-plane.

Buckling strength

As the biaxial load $\sigma_y = \sigma_x$ is increased, the linear relationship between stress and strain continues until the *buckling strength* of the plate is reached. Again, with the slightest of perturbations, the resulting out-of-plane deflection in the central region of the plating leads to a redistribution of stresses towards its edges and a lower axial stiffness (in both the x- and y-directions). For a square plate, the 1st eigenmode of the buckled plate under a biaxial load is similar to that under a uniaxial load, although the magnitude of its 1st eigenvalue is lower. In fact, for the biaxial load $\sigma_y = \sigma_x$, the magnitude of the critical buckling stress is exactly half of the critical buckling stress $\sigma_{x,cr}$ in the uniaxial load case (compare the buckling strength in Figure 2.10 to that in Figure 2.1). This is because the elastic strength interaction equation for a square plate has the linear form

$$\frac{\sigma_x}{\sigma_{x,cr}} + \frac{\sigma_y}{\sigma_{x,cr}} = 1 \tag{2.31}$$

when the stresses in both x- and y-directions are compressive.

Post-buckling

Accordingly, the *post-buckling* portion of the stress-strain curve is again characterised by a reduced slope ($E' \simeq 0.36 \cdot E$) which is considerably less compared to the *post-buckling* portion of the curve in the uniaxial load case. In Figure 2.11(b) the principal stresses associated with point B ($\sigma_x/\sigma_Y = 0.3$) are shown. Here the redistribution of applied stresses towards the edges is clearly evident. However, unlike the uniaxial load case, the redistribution of stresses occurs equally in both the x- and y-directions due to the equal magnitudes of σ_x and σ_y. While the stresses parallel and adjacent to the edges of the plate are dominated by the applied compressive stresses, the reduced magnitude of stresses in

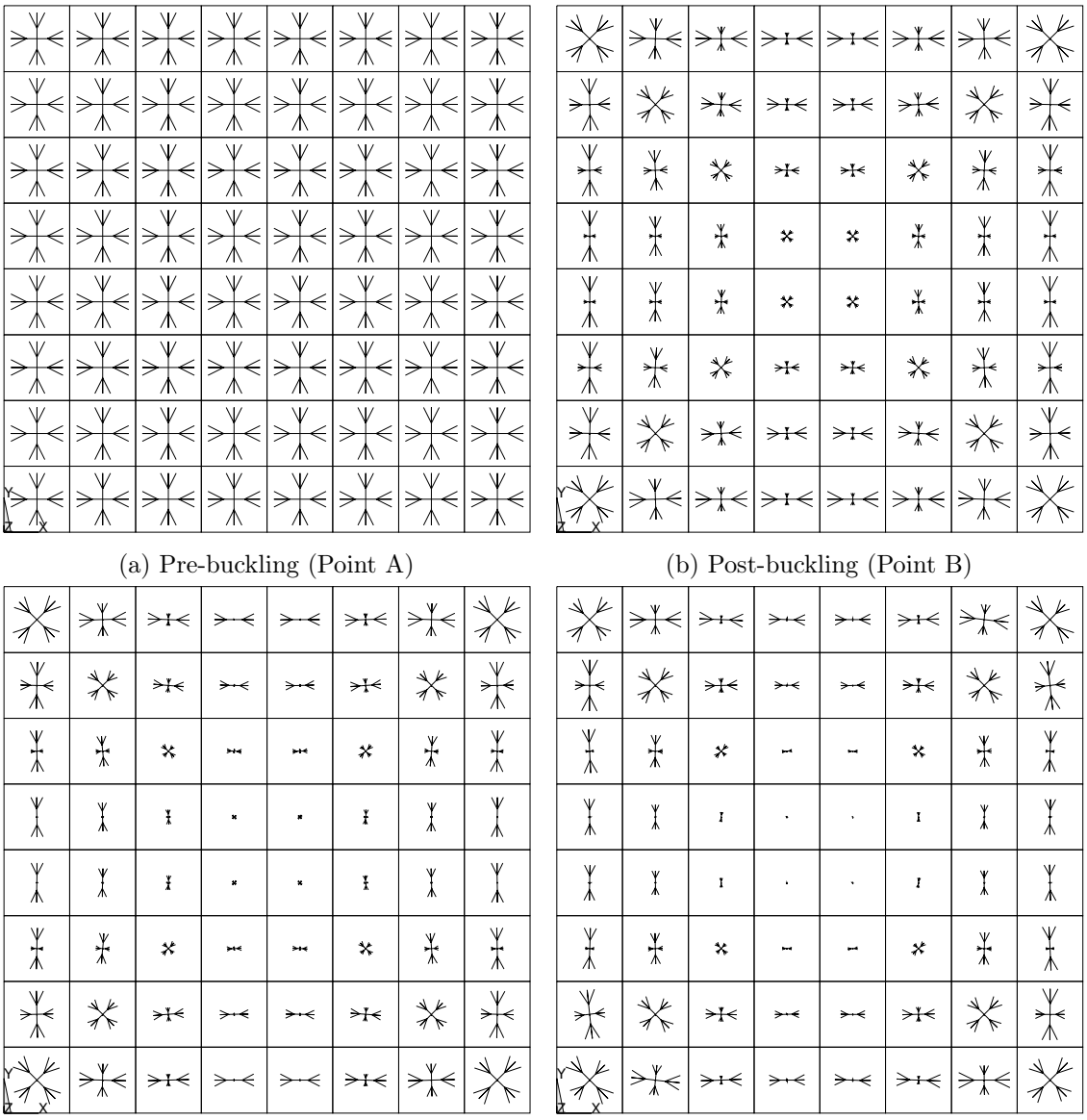

(a) Pre-buckling (Point A)

(b) Post-buckling (Point B)

(c) Post-yield (Point C)

(d) Post-collapse (Point D)

Figure 2.11.: Principle stresses in middle plane of ideal plate ($\sigma_y = \sigma_x$, $\beta = 3$).

the middle of the buckled plate is evidence of tensile stresses caused by the out-of-plane deflections. Accordingly, the magnitude of compressive stresses perpendicular and adjacent to the edges of the plate decrease towards mid-length and mid-breadth.

Yield strength

As the biaxial load is increased further, greater out-of-plane deflections again lead to additional load shedding which results in a further increase in the magnitude of stresses along the edges. In the uniaxial load case, the resulting combination of compressive stresses (due to the applied load) and perpendicular tensile stresses (due to out-of-plane deflections)

leads to initial yielding in the middle plane at the mid-length edges of the plate (see corner inset in Figure 2.1). However, due to the presence of the secondary compressive stress, the tensile stresses at the mid-length edges of the biaxially loaded plate are considerably smaller. Accordingly, initial yielding under the biaxial load $\sigma_y = \sigma_x$ does not occur at the mid-length edges of the plate, but instead in the corners of the plate where the (magnified) applied stresses σ_x and σ_y coalesce (see corner inset in Figure 2.10). In other words, the (compressive) axial and (tensile) transverse stresses at the mid-length edges of the plate are still "working together" to deform the plate material, but the contribution of the tensile stresses is relatively small such that compression-tension yielding at the mid-length edges of the plate is preceded by compression-compression yielding in the corners of the plate. With this sort of mechanism, yielding in the middle plane initiates at a considerably lower level of axial strain compared to the uniaxial load case. Nevertheless, as in the case of a uniaxial load, yielding in the middle plane of the plate is indicative of through-thickness plasticity and is a precursor to collapse.

Post-yield

With further increases in the biaxial load $\sigma_y = \sigma_x$, plastic flow begins to gradually spread from the corners of the plate leading to progressive losses in stiffness. Accordingly, the *post-yield* portion of the stress-strain curve is characterised by a gradually decreasing slope. In Figure 2.11(c) the principal stresses associated with point C ($\epsilon_x/\epsilon_Y \simeq 0.75$) in the post-yield response are shown. At this point it can be seen that the central portion of the plate is approaching a (relatively) stress free state where the compressive stresses due to the applied load and tensile stresses due to out-of-plane deflections are almost equal. Furthermore, the load shedding caused by out-of-plane deflections leads to uniaxial compressive stresses along the sides of the plate with biaxial compressive stress states remaining only in the corners.

Collapse strength

As noted previously, once the slope of the stress-strain curve reaches zero the *collapse strength* of the plate has been reached. In Figure 2.10 the normalised collapse stress is seen to be approximately $\sigma_{x,ult}/\sigma_Y = 0.38$ which represents a 1.7% increase in stress compared to initial yield. Compared to the uniaxial load case ($\sigma_{x,ult}/\sigma_Y = 0.64$), this collapse stress represents a 41% reduction in $\sigma_{x,ult}$. Since $\sigma_{y,ult} = \sigma_{x,ult}$ for the biaxial load case $\sigma_y = \sigma_x$, this reduction represents the maximum decrease of the primary collapse stress due to the presence of a secondary stress (i.e. for $\beta = 3$). As will be shown in §2.2.4, the maximum reduction in the primary collapse stress due to the presence of a secondary stress is 50% for a very slender, square plate. In terms of displacement, the collapse strain has an approximate magnitude of $\epsilon_{x,ult}/\epsilon_Y = 0.81$ which is an additional strain of $\Delta\epsilon_x \simeq 0.12 \cdot \epsilon_Y$ compared to initial yield. Furthermore, compared to the collapse strain under a uniaxial load ($\epsilon_{x,ult}/\epsilon_Y = 1.09$), the collapse under the biaxial load $\sigma_y = \sigma_x$ occurs at a significantly smaller strain ($\Delta\epsilon_x \simeq -0.28 \cdot \epsilon_Y$). As mentioned previously, the ultimate strain value may be of particular importance in the ultimate strength analysis of hull girders since the applied loads are strain-based. For instance, when calculating the ultimate capacity of hull girders according to IACS requirements (e.g. CSR BC & OT),

the stress-strain curves of all elements are assumed to reach ultimate capacity at a strain of $\epsilon_{x,ult}/\epsilon_Y = 1.0$. Accordingly, for plate elements this assumption may be either conservative or non-conservative depending on the stress state.

Post-collapse

Following collapse the *unloading* portion of the stress-strain curve is quite similar to that for a uniaxial load. The effects of further post-collapse straining are shown in Figure 2.11(d) for the load associated with point D of the stress-strain curve ($\epsilon_x/\epsilon_Y = 2.0$). Here the development of the stress state in the pre-collapse portion of the stress-strain curve, i.e. negligible stresses in the central portion of the plate, uniaxial compressive stresses along the sides of the plate and biaxial compressive stresses in the corners, is further intensified. This leads to fully plastified material in the corners of the plate which facilitates its transition into a developable surface. A plot of this plastic mechanism is shown in Figure 2.10 for $\epsilon_x/\epsilon_Y = \epsilon_y/\epsilon_Y = 3.0$, where a gradient exists from the yield stresses in the plastified corners to near zero stresses in the middle of the plate.

2.2.2. Ideal plates - tensile secondary stress

Eigenmodes

Before examining the collapse of an (ideal) square plate under a compressive-tensile biaxial load, it is useful to understand something about the elastic buckling of square plates. In Figure 2.12 the elastic buckling interaction curve for a square plate ($\beta = 3$) is shown based on the following equation [9, 35]

$$\frac{m^2}{a^2}\sigma_x + \frac{n^2}{b^2}\sigma_y - \frac{\pi^2 \cdot D}{t} \cdot \left(\frac{m^2}{a^2} + \frac{n^2}{b^2}\right)^2 = 0 \tag{2.32}$$

where m and n are the *buckling half-wave numbers* in the x- and y-directions, respectively, and D is the *flexural rigidity* of the plate

$$D = \frac{E \cdot t^3}{12 \cdot (1 - \nu^2)} \tag{2.33}$$

The elastic buckling interaction curve shows the combinations of σ_x and σ_y under which an ideal plate buckles elastically. When σ_x and σ_y are both compressive (i.e. Quadrant 1), the plate buckles into a mode characterised by a single half-wave in each direction. However, when either σ_x or σ_y is tensile, the plate may buckle into a mode characterised by a single half-wave in the direction of the tensile stress and two half-waves in the direction of the compressive stress. This transition in mode shape occurs at the discontinuities in the elastic buckling interaction curve (i.e. in Quadrants 2 and 4). Also shown in Figure 2.12 is the von Mises ellipse. For the combinations of σ_x and σ_y which lie on this ellipse, a plane plate yields according to the von Mises failure criterion provided it does not first buckle elastically. Accordingly, for the stress ratio $\sigma_y/\sigma_x = -1/4$, the plate buckles at point A into an eigenmode characterised by a single half-wave in each direction. However, for the stress ratio $\sigma_y/\sigma_x = -1/2$, the plate buckles at point B into an eigenmode which is characterised by two half-waves in the (compressive) x-direction. This mode shape is shown on the right hand side of Figure 2.12 together with the eigenmode of the plate at

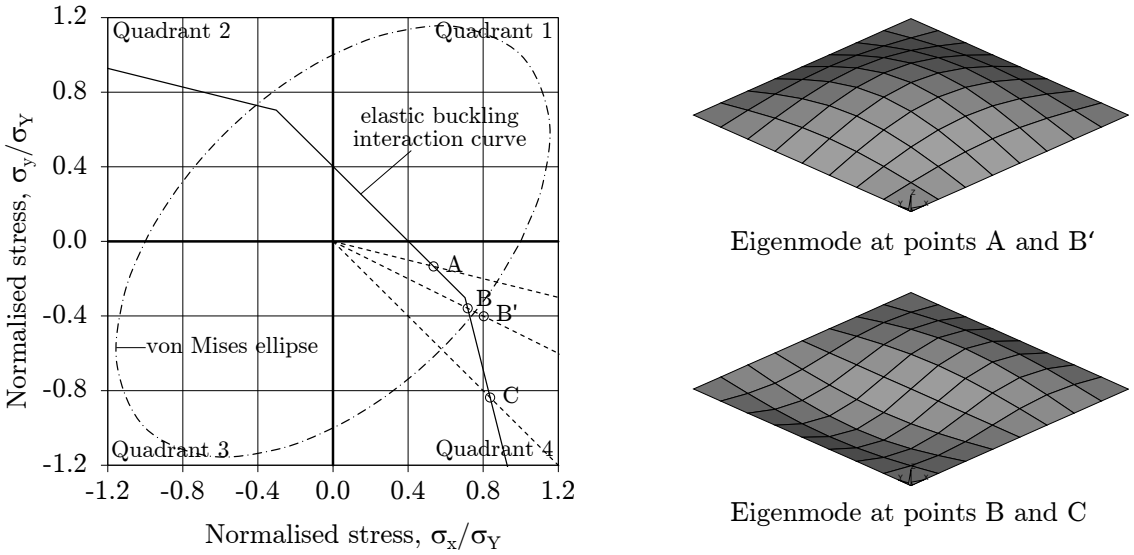

Figure 2.12.: Elastic buckling interaction curve and eigenmodes of ideal square plate.

point B'. This latter eigenmode is a more likely shape for an initially deflected plate, but the biaxial stress combination at which it occurs for an ideal plate (assuming that the eigenmode at point B fails to develop) lies outside the von Mises ellipse such that the plate would fail in yielding before the stresses required for this eigenmode could develop. For the stress ratio $\sigma_y/\sigma_x = -1$, the eigenmode of the plate is also characterised by two half-waves in the (compressive) x-direction (point C). However, as can be seen, the plate would also fail in yielding before reaching the stresses required for this eigenmode to develop.

Loading sequence

On the basis of the foregoing, the stress-strain curve shown in Figure 2.13 is for an ideal square plate ($\beta = 3.0$) under proportional loading with a secondary stress $\sigma_y = -\sigma_x/4$. A second curve for sequential loading is shown for comparison where σ_y is again applied first, followed by σ_x. Here the positive strain in the x-direction following the application of $\sigma_{y,ult}$ is again evidence of the Poisson effect

$$\frac{\epsilon_x}{\epsilon_Y} = -\nu \cdot \frac{\sigma_{y,ult}}{\sigma_Y} = \nu \cdot \frac{\sigma_x}{4 \cdot \sigma_Y} = 0.3 \cdot \frac{0.7}{4} = 0.0525 \tag{2.34}$$

In this case, the resulting initial strain is compensated by a greater slope in the stress-strain curve with the subsequent application of σ_x. Accordingly, the two stress-strain curves coincide at the yield strength with the post-yield portion of the curve similar to that for proportional loading. For the sake of comparison, the stress-strain curve for the uniaxial load case ($\sigma_y = 0$) is also shown.

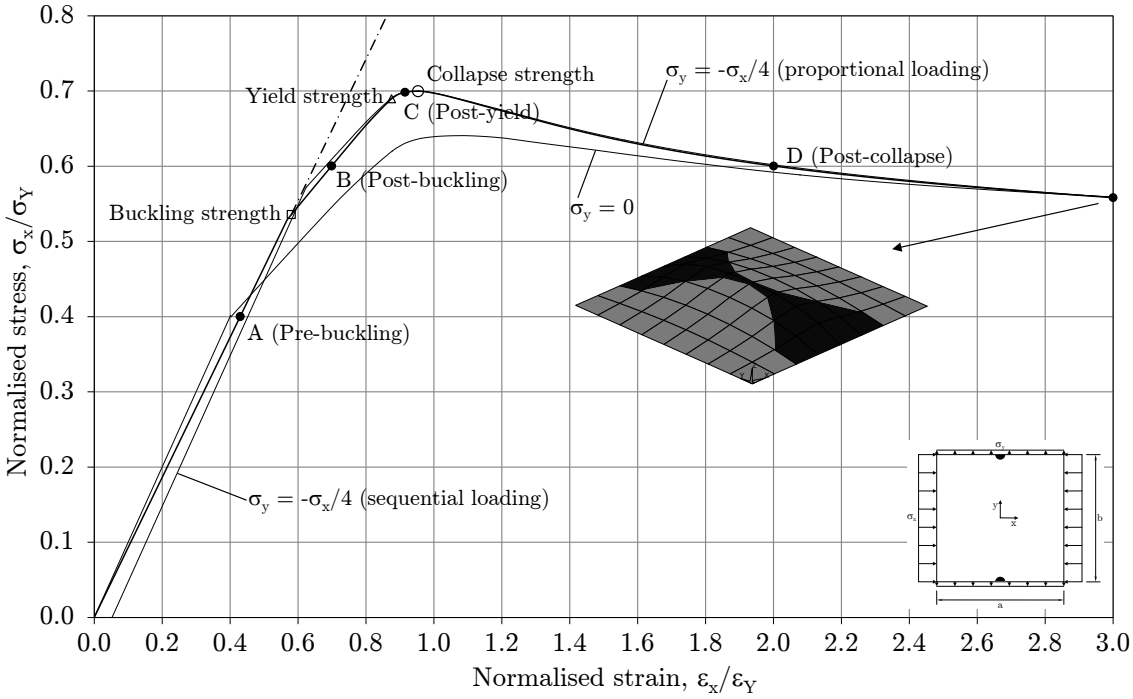

Figure 2.13.: Stress-strain curve of ideal plate under biaxial compression ($\sigma_y = -\sigma_x/4$, $\beta = 3$).

Pre-buckling

With the proportional application of the biaxial load, the linear relationship between stresses and strains is again defined according to Poisson's equation

$$\epsilon_x = \frac{\sigma_x}{E} - \nu \cdot \frac{\sigma_y}{E} \tag{2.35}$$

When $\sigma_y = -\sigma_x/4$, this equation can be rewritten as

$$\epsilon_x = \frac{\sigma_x}{E} + \nu \cdot \frac{\sigma_x}{4 \cdot E} = \frac{\sigma_x}{E} \cdot (1 + \frac{\nu}{4}) \tag{2.36}$$

Rearranging in terms of σ_x/ϵ_x

$$\frac{\sigma_x}{\epsilon_x} = \frac{E}{(1 + \frac{\nu}{4})} \tag{2.37}$$

Accordingly, for a Poisson's ratio of $\nu = 0.3$ the pre-buckling behaviour of the plate is such that its effective modulus of elasticity is equal to $E' \simeq 0.93 \cdot E$, as reflected in the pre-buckling portion of the curve in Figure 2.13. For the load corresponding to point A on the curve ($\sigma_x/\sigma_Y = 0.4$), the principal stresses in the middle plane of the plate are plotted in Figure 2.14(a). Unsurprisingly, these stresses are uniform throughout the plate, reflecting the magnitudes of the applied stresses, i.e. $\sigma_y = -\sigma_x/4$. As in previous cases,

no Poisson effects are evident in these stresses since the edges of the plate are able to move freely in-plane.

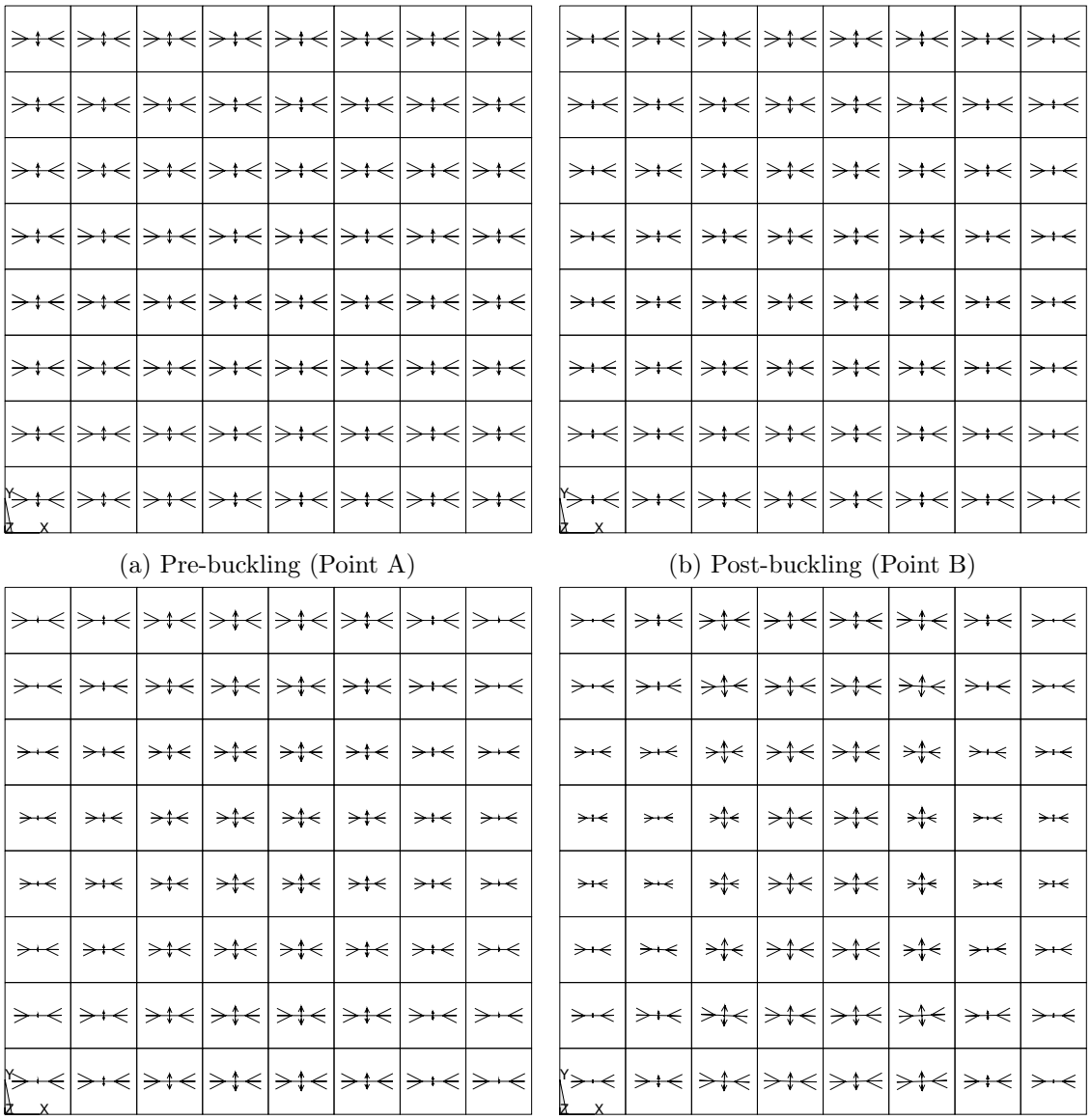

(a) Pre-buckling (Point A)

(b) Post-buckling (Point B)

(c) Post-yield (Point C)

(d) Post-collapse (Point D)

Figure 2.14.: Principle stresses in middle plane of ideal plate ($\sigma_y = -\sigma_x/4$, $\beta = 3$).

Buckling strength

As the biaxial load $\sigma_y = -\sigma_x/4$ is increased, the linear relationship between stress and strain continues until the *buckling strength* of the plate is reached. Again, with the slightest of perturbations, the resulting out-of-plane deflection in the central region of the plating leads to a redistribution of stresses towards its edges and a lower axial stiffness in the x-direction. As shown by point A in Figure 2.12, the magnitude of the critical buckling

stress $\sigma_{x,cr}$ is greater than that for the case $\sigma_y = 0$ with the plate buckling into a mode characterised by a single half-wave in each direction.

Post-buckling

Accordingly, the *post-buckling* portion of the stress-strain curve is again characterised by a reduced slope ($E' \simeq 0.54 \cdot E$). However, this slope is still greater than that for the *post-buckling* portion of the curve in the uniaxial load case. This is due to the tensile stresses applied in the y-direction which restrain the out-of-plane deflections of the buckled plate, thereby making the plate effectively stiffer in the x-direction. Accordingly, the post-buckling effects are not as pronounced as in the uniaxial load case. In Figure 2.14(b) the principal stresses associated with point B ($\sigma_x/\sigma_Y = 0.6$) confirm this effect (i.e. compared to Figure 2.2(b)). Similar to the uniaxial load case, the out-of-plane deflections cause load shedding of compressive stresses in the x-direction towards the edges of the plate and induce tensile stresses in the y-direction around mid-length of the buckled plate with associated compressive stresses at the ends of the plate to balance in-plane forces, i.e. tensile stresses in the y-direction still exist in the corners of the plate, but they are less than those at mid-length. However, redistribution of both compressive stresses towards the edges and tensile stresses towards mid-length is generally mitigated compared to the uniaxial load case, again due to restrained out-of-plane deflections.

Yield strength

As the load is increased further, greater out-of-plane deflections again lead to additional load shedding which results in a further increase in the magnitude of stresses along the edges. As in the uniaxial load case, the resulting combination of compressive stresses (due to the applied load) and perpendicular tensile stresses (due to out-of-plane deflections) leads to initial yielding in the middle plane at the mid-length edges of the plate (see corner inset in Figure 2.13). However, because the restrained out-of-plane deflections mitigate the redistribution of stresses, the (applied) axial stress σ_x at which the plate yields is *greater* than that in the uniaxial load case although yielding in the middle plane initiates at a comparable level of axial strain ϵ_x. As in the case of a uniaxial load, yielding in the middle plane of the plate is indicative of through-thickness plasticity and is a precursor to collapse.

Post-yield

With further increases in the biaxial load $\sigma_y = -\sigma_x/4$, plastic flow begins to spread throughout the middle plane, leading to progressive losses in stiffness at the edges of the plate such that the *post-yield* portion of the stress-strain curve is again characterised by a rapidly decreasing slope. In Figure 2.14(c) the principal stresses associated with point C ($\epsilon_x/\epsilon_Y = 0.92$) in the post-yield response are shown. Here it can be seen that the axial stresses at the edges of the plate are greater than those in the central region due to the ever increasing out-of-plane deflection in the buckled plate. This deflection is also reflected in the increased magnitude of transverse stresses. However, it can be seen that the redistribution of stresses is clearly less than that in the uniaxial load case (see Figure 2.2(c)).

Collapse strength

As noted previously, once the slope of the stress-strain curve reaches zero the *collapse strength* of the plate has been reached. In Figure 2.13 the normalised collapse stress is seen to be approximately $\sigma_{x,ult}/\sigma_Y = 0.70$ which represents a 1.5% increase in stress compared to initial yield. Compared to the uniaxial load case ($\sigma_{x,ult}/\sigma_Y = 0.64$), this collapse stress represents a 9.2% increase in $\sigma_{x,ult}$. In terms of displacement, the collapse strain has an approximate magnitude of $\epsilon_{x,ult}/\epsilon_Y = 0.95$ which is an additional $\Delta\epsilon_x \simeq 0.078 \cdot \epsilon_Y$ compared to initial yield. Furthermore, compared to the collapse strain under a uniaxial load ($\epsilon_{x,ult}/\epsilon_Y = 1.09$), collapse under the biaxial load $\sigma_y = -\sigma_x/4$ occurs at a smaller strain ($\Delta\epsilon_x \simeq -0.13 \cdot \epsilon_Y$).

Post-collapse

Following collapse the *unloading* portion of the stress-strain curve is very similar to that for a uniaxial load. The effects of further post-collapse straining are shown in Figure 2.14(d) for the load associated with point D of the stress-strain curve ($\epsilon_x/\epsilon_Y = 2.0$). Here the development of large axial and transverse stresses spread across the plate at mid-length is the same as that for the uniaxial load case. This growth of plasticity again leads to a plastic mechanism which facilitates large axial straining. A plot of this plastic mechanism is shown in Figure 2.13 for $\epsilon_x/\epsilon_Y = 3.0$.

2.2.3. Internal stress distributions

Hot spots

In Figure 2.12 the elastic buckling interaction curve was shown for an ideal square plate ($\beta = 3$) together with the von Mises ellipse. As explained, whether elastic buckling precedes gross yielding depends on the *stress ratio* designated hereafter as $c = \sigma_y/\sigma_x$. For plates with a slenderness $\beta < 3$, the elastic buckling interaction curve lies outside that shown in Figure 2.12 (i.e. further from the origin). Accordingly, for very sturdy plates where the elastic buckling curve lies completely outside the von Mises ellipse, failure occurs by gross yielding for all values of c.

In addition to the foregoing, the stress ratio $c = \sigma_y/\sigma_x$ also determines the location of initial yield in plates (i.e. in case of buckling). So far initial yielding in a plate has been shown for two sets of locations; yielding at the mid-length edges in the x-direction ($c = 0$ and $c = -0.25$) and yielding in the corners of the plate ($c = 1.0$). Each of these location sets, or "hot spots", are shown in Figure 2.15(a) and Figure 2.15(b), respectively. The hot spots shown in Figure 2.15(c) (i.e. mid-breadth edges) are analogous to those shown in Figure 2.15(a) where σ_y is the primary stress, i.e. $\sigma_y > \sigma_x$. As noted previously, initial yielding in the middle plane of the plate is a precursor to collapse. Accordingly, the mechanism of collapse depends on where yielding initiates which in turn depends on the stress ratio $c = \sigma_y/\sigma_x$.

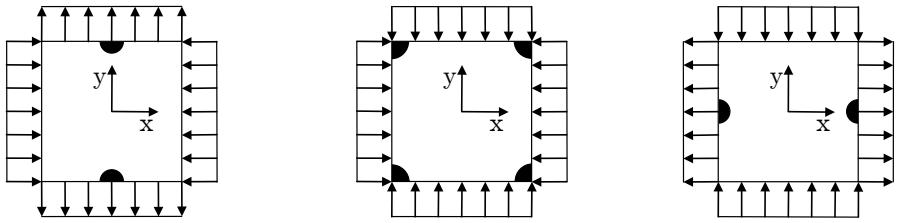

(a) mid-length edges (b) corners (c) mid-breadth edges

Figure 2.15.: Location of plasticity "hot spots".

Qualitatively there are two basic types of effects on the distribution of stresses within a plate due to the presence of a secondary stress σ_y. There are, of course, the *first order effects* of changes to the internal stresses as a result of the stress application, i.e. direct effect on internal stresses $\sigma_{y,i}$ and an indirect effect on internal stresses $\sigma_{x,i}$ due to the Poisson effect. In addition, there is the *second order effect* of load shedding towards the edges in both directions associated with the magnitude of out-of-plane deflections.

$\underline{c \lesssim -0.6}$

In order to obtain a better understanding of how the stress ratio $c = \sigma_y/\sigma_x$ affects the location of initial yielding (and therefore the collapse mechanism), Figure 2.16(a) shows the normalised equivalent stresses at the point of initial yield for each of the hot spots shown in Figure 2.15 for an ideal square plate of slenderness $\beta = 3$ (based on numerical analyses). As can be seen, when $c \lesssim -0.6$, the normalised equivalent stress $\sigma_{eq,i}/\sigma_Y = 1.0$ at each of the hot spots. This is indicative of gross yielding and is in approximate agreement with Figure 2.12. Evidence of gross yielding can also be seen in Figure 2.16(b) and Figure 2.16(c) which show the normalised internal stresses ($\sigma_{x,i}/\sigma_Y$ and $\sigma_{y,i}/\sigma_Y$) and normalised applied stresses (σ_x/σ_Y and σ_y/σ_Y), respectively, for various values of $c = \sigma_y/\sigma_x$. In the former, it can be seen that $\sigma_{x,i}/\sigma_Y$ and $\sigma_{y,i}/\sigma_Y$ are the same in each of the hot spots and that the relationship between them is defined by c. Furthermore, it can be seen that $\sigma_{x,i}/\sigma_Y = \sigma_x/\sigma_Y$ and $\sigma_{y,i}/\sigma_Y = \sigma_y/\sigma_Y$. This shows that no stress redistribution is occurring and is further evidence of gross yielding. The absence of any stress redistribution is explained by the lack of out-of-plane deflections. This is shown in Figure 2.17 where the maximum out-of-plane deflections are normalised against a representative magnitude of initial deflections $\delta_0 = b/200$ for *real* plates.

$\underline{-0.6 \lesssim c \leqslant 0}$

When the stress ratio is between $-0.6 \lesssim c \leqslant 0$, Figure 2.16(a) shows that the equivalent stress $\sigma_{eq,i}$ is critical at the mid-length edges of the plate. Accordingly, yielding initiates at these locations. As already discussed in §2.1.1 (i.e. the uniaxial load case $c = 0$), yielding in the middle plane of the plate initiates at the mid-length edges due to compressive stresses in the x-direction combined with tensile stresses in the y-direction. Here out-of-plane displacements magnify the compressive stresses due to load shedding and induce the tensile stresses. In case of tensile secondary stresses (i.e. $c < 0$), the out-of-plane deflections are *smaller* compared to those in the absence of tensile stresses (i.e. $c = 0$) as shown in Figure 2.17. This means that the degree of load shedding is lessened

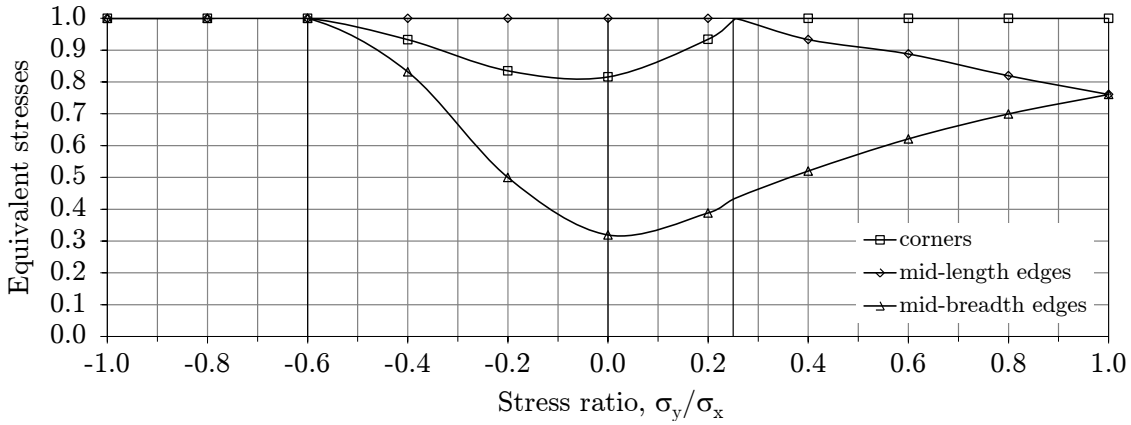

(a) Normalised equivalent stresses, $\sigma_{eq,i}/\sigma_Y$

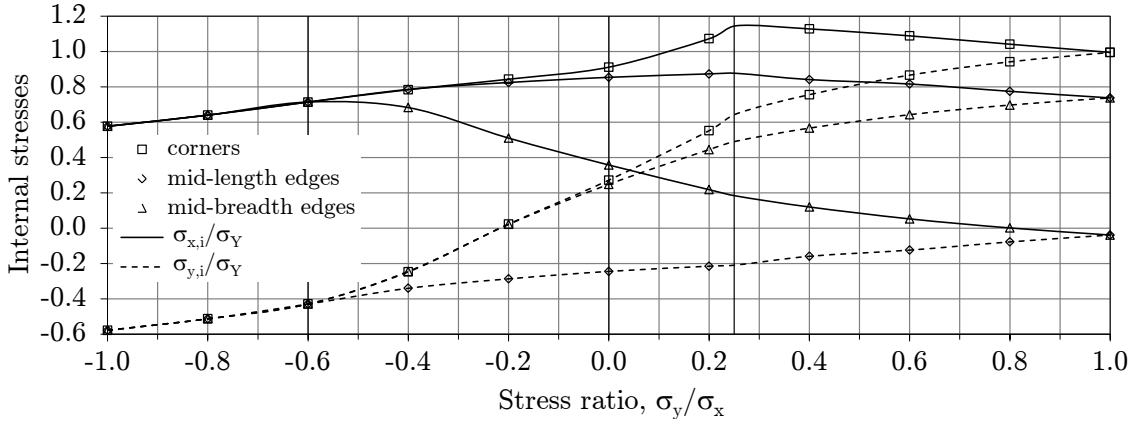

(b) Normalised internal stresses, $\sigma_{x,i}/\sigma_Y$, $\sigma_{y,i}/\sigma_Y$

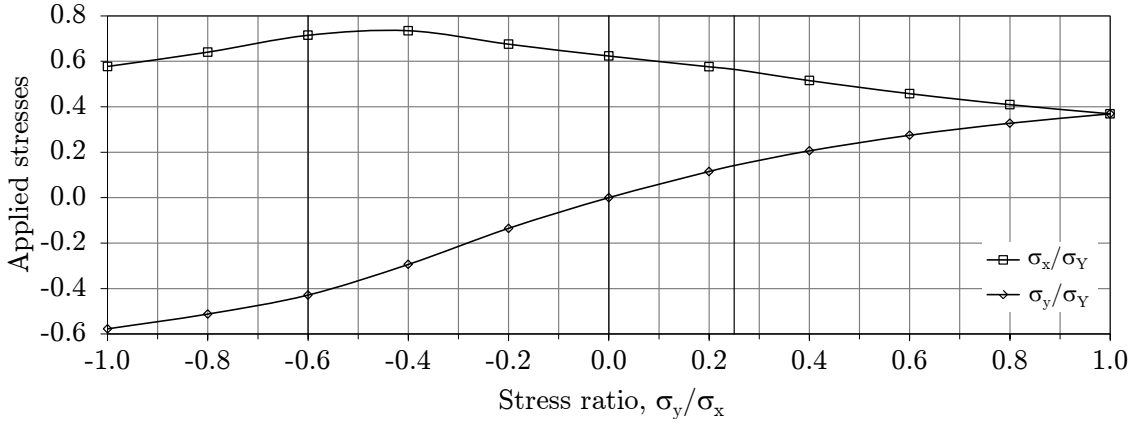

(c) Normalised applied stresses, σ_x/σ_Y, σ_y/σ_Y

Figure 2.16.: Stress distributions at initial yield ($\alpha = 1$, $\beta = 3$).

which effectively retards the development of plasticity at the mid-length edges. This can be seen in the decreasing ratios of $\sigma_{x,i}/\sigma_x$ at the mid-length edges with increasing tensile stresses (i.e. with decreasing values of c as shown in Figures 2.16(b) and 2.16(c)). It is this increase in the effective width of plating which permits greater applied compressive stresses in the x-direction under applied tensile stresses in the y-direction, i.e. compared

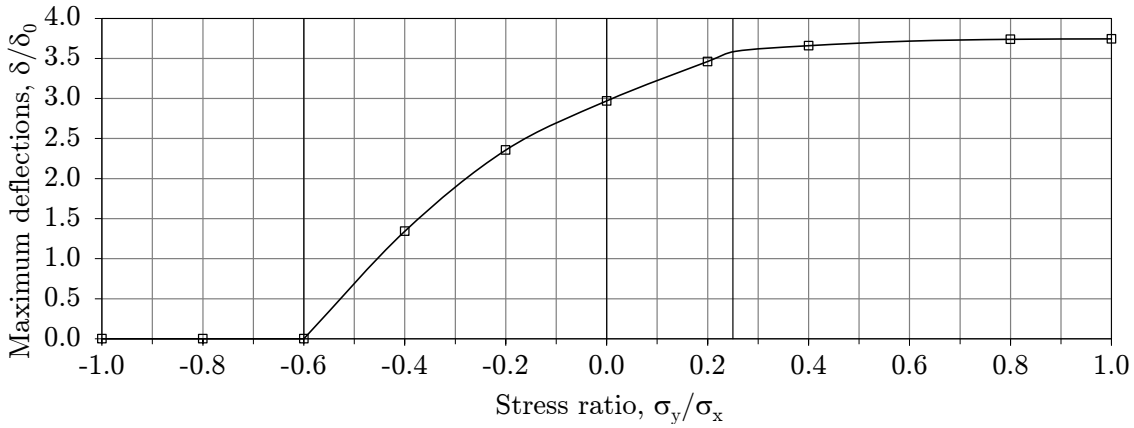

Figure 2.17.: Normalised maximum (out-of-plane) deflections at initial yield, δ/δ_0 ($\alpha = 1$, $\beta = 3$).

to the uniaxial load case $\sigma_y = 0$. Here the second order effect of tensile stresses is more significant than their first order effect.

$0 < c \lesssim 0.25$

When the stress ratio is between $0 < c \lesssim 0.25$, Figure 2.16(a) shows that the equivalent stress $\sigma_{eq,i}$ remains critical at the mid-length edges of the plate (this is contrary to the widely held assumption that yielding always initiates in the corners of a plate whenever $c > 0$). In this case the out-of-plane deflections are *larger* compared to those in the absence of tensile stresses (i.e. $c = 0$) as shown in Figure 2.17. This means that the degree of load shedding is increased which effectively promotes the development of plasticity at the mid-length edges. This can be seen in the increasing ratios of $\sigma_{x,i}/\sigma_x$ at the mid-length edges with increasing compressive stresses (i.e. with increasing values of c as shown in Figures 2.16(b) and 2.16(c)). It is this decrease in the effective width of plating which prohibits higher applied compressive stresses in the x-direction under applied compressive stresses in the y-direction, i.e. again compared to the uniaxial load case $\sigma_y = 0$. Here the second order effect of compressive stresses is again more significant than their first order effect.

$0.25 \lesssim c \leqslant 1.0$

In the presence of a (significant) compressive secondary stress, both its first and second order effects increase the magnitude of equivalent stress $\sigma_{eq,i}$ in the corners of the plate. In this regard, the internal (compressive) stresses $\sigma_{x,i}$ remain above yield such that plasticity is only prevented in the corners of the plate by the contrary action of internal (compressive) stresses $\sigma_{y,i}$. Accordingly, the increase in the equivalent stresses in the corners of the plate is such that they become the critical hot spots for stress ratios $0.25 \lesssim c \leqslant 1.0$ (for values $c > 1.0$, σ_y becomes the primary stress such that $c > 1/0.25 = 4.0$ is the stress ratio where the mid-breadth edges in the y-direction become the critical hot spots). For stress ratios in this range the out-of-plane displacements remain (relatively) constant as shown in Figure 2.17. Accordingly, as can be seen in Figures 2.16(b) and 2.16(c), the rate of decreasing internal stress $\sigma_{x,i}$ is rather similar to the rate of decreasing applied stresses σ_x. Only the values of $\sigma_{y,i}$ increase markedly due to the direct effects of increasing σ_y. Finally, since a

plate supported on all edges is a non-developable surface, shear stresses $\tau_{xy,i}$ arise near the corners of the plate under biaxial loading. However, by calculating the equivalent stresses in Figure 2.16(a) using the internal stresses in the x- and y-directions from Figure 2.16(b), it can be seen that these shear stresses are negligible.

2.2.4. Capacity curves

Concept of capacity curves

In ship design it is usual to express the interaction between primary and secondary stresses in terms of a *capacity curve* (alternatively referred to as an *interaction curve*). As shown above, the strength of the plate under the primary stress depends on the magnitude of the secondary stress. Accordingly, capacity curves are used to delineate the combinations of applied stresses that result in plate failure (e.g. initial yield, collapse etc.). In this way capacity curves are analogous to reduction curves for uniaxially loaded plates except that separate capacity curves need to be plotted for plates of different slenderness (i.e. due to graphical restrictions in two dimensions).

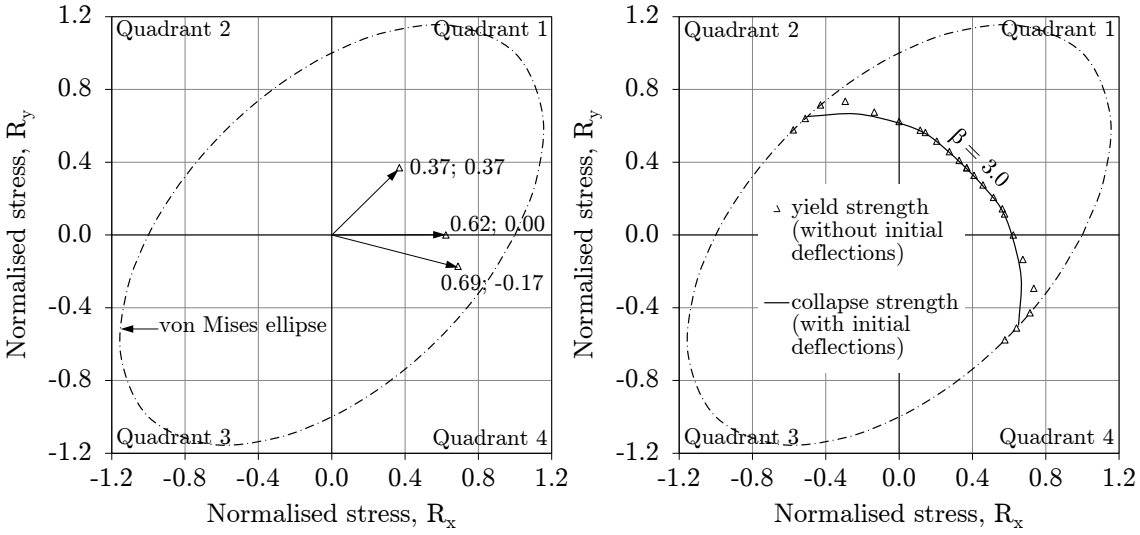

Figure 2.18.: Construction of capacity curve ($\beta = 3$).

To illustrate, three combinations of normalised stresses resulting in the initial yield of an ideal square plate ($\beta = 3$) have been plotted on the left-hand side of Figure 2.18 together with the von Mises ellipse. These combinations are based on the stress-strain curves shown for $c = \sigma_y/\sigma_x = 0$ (Figure 2.1), $c = \sigma_y/\sigma_x = 1.0$ (Figure 2.10) and $c = \sigma_y/\sigma_x = -0.25$ (Figure 2.13). For the sake of simplicity, the nomenclature $R_x = \sigma_x/\sigma_Y$ and $R_y = \sigma_y/\sigma_Y$ is introduced for designating normalised stress ratios. Accordingly, when written in vector notation, biaxial stress combinations are designated

$$\mathbf{R} = R_x\mathbf{i} + R_y\mathbf{j} \tag{2.38}$$

where $\mathbf{i}$ and $\mathbf{j}$ are the unit vectors in the x- and y-directions, respectively. As a result, the biaxial stress combination $\sigma_y/\sigma_x = 1.0$ on the left-hand side of Figure 2.18 would be written as

$$\mathbf{R} = R_x\mathbf{i} + R_y\mathbf{j} = 0.37\mathbf{i} + 0.37\mathbf{j} \tag{2.39}$$

where the vector magnitude is equal to

$$R = \sqrt{0.37^2 + 0.37^2} = 0.52 \tag{2.40}$$

As will be explained in Chapter 3, vectors are often used in shipbuilding to calculate the utilisation factor η which is the ratio of the vector magnitudes of applied loads to those associated with ultimate plate capacity.

When constructing a capacity curve, it is only necessary to identify the stress combinations which do not coincide with the von Mises ellipse. These combinations are mostly found in Quadrant 1 where both primary and secondary stresses are compressive although some additional combinations may be needed in Quadrants 2 and 4 for intermediate and slender plates. Furthermore, the R_x- and R_y-intercepts in Quadrant 1 can be obtained directly from the plate reduction factors κ_x and κ_y, respectively (see §2.1.4). Although the three points shown on the left-hand side of Figure 2.18 are sufficient for an approximate representation of the capacity curve (i.e. due to symmetry of the capacity curve for a square plate), additional combinations have been obtained from Figure 2.16(c) and plotted on the right-hand side of Figure 2.18. Since these data points are associated with the initial yield of an ideal plate, the ultimate capacity curve of a square plate with initial deflections $\delta_0 = b/200$ has also been plotted for the sake of comparison. As can be seen, for a square plate ($\beta = 3$) the curve of collapse strength (with initial deflections) is rather close to the data points of yield strength (without initial deflections).

Effect of slenderness on plate capacity

As shown above, the capacity of plates under biaxial loads is determined by the degree of load shedding which in turn depends on the magnitude of out-of-plane deflections. Since the magnification of deflections are directly related to the elastic buckling strength of the plate, it should be of no surprise that the capacity of biaxially loaded plates are strongly dependent on plate slenderness β. Evidence of this can be seen in the principal stress plots shown in Figure 2.19 for square plates of slenderness $\beta = 0.5$, $\beta = 1.0$, $\beta = 2.0$ and $\beta = 4.0$. Each of the plates have initial deflections ($\delta_0 = b/200$) and are under a biaxial load $\sigma_y = \sigma_x$. The stress-strain curves for these plates are shown on the left-hand side of Figure 2.20 and in both figures it can be seen that the most slender plate ($\beta = 4$) is dominated by elastic buckling while collapse of the sturdiest plate ($\beta = 0.5$) approaches that of gross yielding.

As a result, the right-hand side of Figure 2.20 shows that the capacity curves for slender plates approach the linear form of the elastic buckling interaction curve for a square plate which was shown in Figure 2.12, i.e. the lower bound of the capacity of square plates has the form

$$\frac{\sigma_x}{\sigma_Y} + \frac{\sigma_y}{\sigma_Y} = R_x + R_y = 1 \tag{2.41}$$

Conversely, as shown on the right-hand side of Figure 2.20, the capacity curves for sturdy plates approach the quadratic form of the von Mises ellipse, i.e. the upper bound of the capacity of square plates (in fact, all plates) has the form

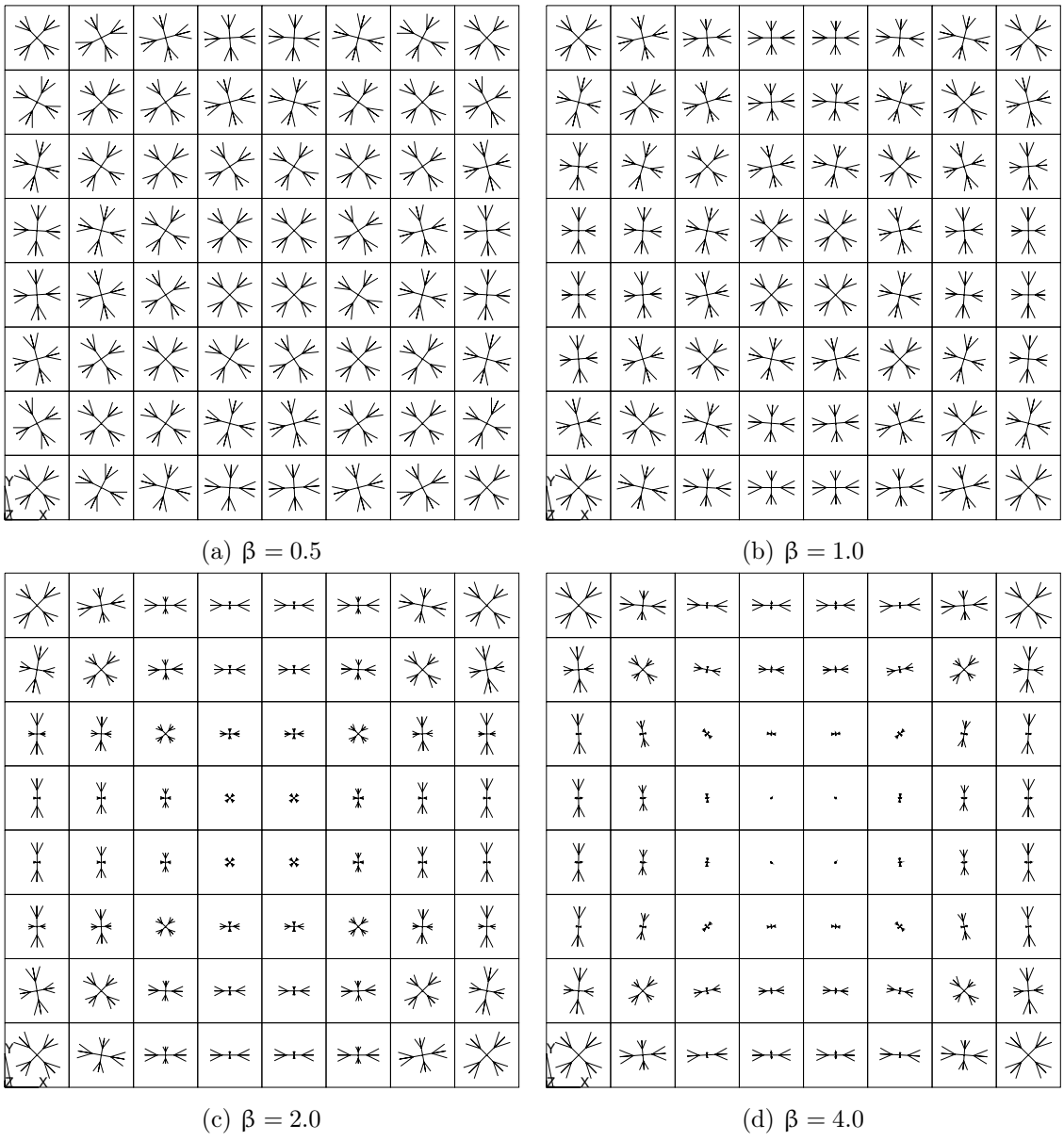

(a) $\beta = 0.5$ (b) $\beta = 1.0$

(c) $\beta = 2.0$ (d) $\beta = 4.0$

Figure 2.19.: Principle stresses at collapse in middle plane of plates with initial deflections ($c = 1$).

$$\left(\frac{\sigma_x}{\sigma_Y}\right)^2 - \left(\frac{\sigma_x}{\sigma_Y}\right) \cdot \left(\frac{\sigma_y}{\sigma_Y}\right) + \left(\frac{\sigma_y}{\sigma_Y}\right)^2 = R_x^2 - R_x \cdot R_y + R_y^2 = 1 \tag{2.42}$$

In between these two limits, the interaction is a mixture of elastic buckling and yielding (i.e. inelastic buckling). Based on this observation, Hughes [9] developed the following interaction equation for square plates

$$R_x^2 - R_x \cdot R_y + R_y^2 + \left(\beta - \frac{4}{9 \cdot \beta}\right) \cdot (R_x + R_y - 1) = 1 \tag{2.43}$$

As can be seen, this equation employs a weighting factor

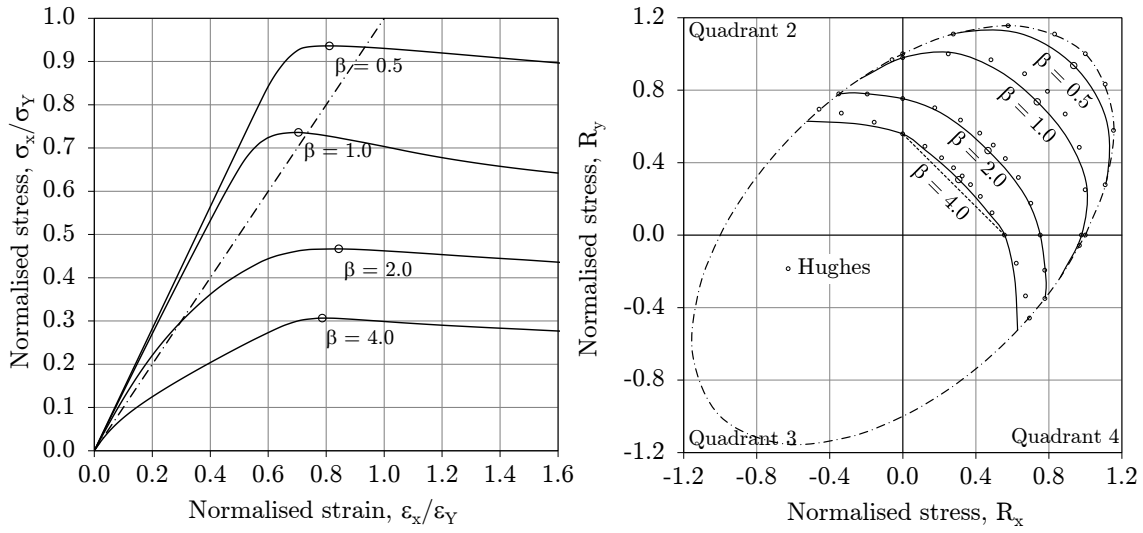

Figure 2.20.: Capacity curves under biaxial compression ($c = 1$).

$$\left(\beta - \frac{4}{9 \cdot \beta}\right) \tag{2.44}$$

which determines where the capacity lies between the upper and lower bounds as a function of plate slenderness β, i.e. based on the assumption that gross yielding occurs when the plate slenderness $\beta \leqslant 2/3$. For the sake of comparison, data points based on Equation (2.43) are plotted on the right-hand side of Figure 2.20 and show reasonably good agreement with numerical analyses. Other interaction equations suitable for square plates under biaxial loads will be presented in Chapter 3.

2.3. In-plane shear

If plating is subjected to large shear loads, collapse may occur whether axial stresses are present or not. In such cases, shear stress is designated the primary stress. High shear loads generally exist in the webs of ship structures whether that be the web of a hull girder (e.g. side shell plating, longitudinal bulkheads etc.) or the web in a more local structure (e.g. floors, longitudinal girders etc.). In this section the collapse of square plates under a pure shear load is examined as well as the capacity reduction in plating due to shear as a secondary or tertiary stress. In case of the former, collapse under pure shear is still best defined using stress-strain curves which delineate the relationship between the applied shear stress and the resulting *angular* strain. Once again the stress and strain corresponding to the peak of the stress-strain curve represents the greatest shear load which the plate can resist and is therefore referred to as the collapse (or ultimate) strength of the plating.

2.3.1. Ideal plates

For pre-buckled plates subjected to a pure shear load τ_{xy}, in-plane *principal* stresses are oriented $\pm 45°$ to the x-axis with magnitudes $\sigma_1 = \tau_{xy}$ (compression) and $\sigma_2 = -\tau_{xy}$

(tension). Accordingly, with the stabilising influence of a tensile stress perpendicular to the compression stress (and of equal magnitude), it is not surprising that the buckling strength of plates under pure shear is generally higher than that under a uniaxial load for which $\sigma_1 = \sigma_x$ and $\sigma_2 = 0$. This is reflected in the elastic buckling factor of plates under shear, $K_\tau = 5.34 + 4/\alpha^2$, compared to that under a uniaxial load, $K_x \simeq 4$. Accordingly, the shear buckling stress for a square plate is greater than that under a uniaxial load by a factor of $9.34/4 \simeq 2.3$. Moreover, while the shear buckling strength of plating is relatively high compared to its uniaxial buckling strength, the shear yield strength is relatively low. Given that the (von Mises) equivalent stress in terms of principal in-plane stresses is equal to

$$\sigma_{eq} = \sqrt{\sigma_1^2 + \sigma_2^2 - \sigma_1 \cdot \sigma_2} \tag{2.45}$$

it can be seen from the above quantities for σ_1 and σ_2 that a plate under a uniaxial load yields when $\sigma_{eq} = \sigma_1 = \sigma_x = \sigma_Y$ while under a pure shear load the plate yields when $\sigma_{eq} = \sqrt{3} \cdot \sigma_1 = \sqrt{3} \cdot \tau_{xy} = \sigma_Y$, i.e. $\tau_Y = \sigma_Y/\sqrt{3}$. Consequently, although the square plate shown in Figure 2.1 buckles well before yield under a uniaxial load ($\beta = 3$), as shown in Figure 2.21 the same plate under pure shear is characterised by elastic-perfectly plastic behaviour (at least for $\gamma_{xy}/\gamma_Y < 2$). In case of a square plate with slenderness $\beta = 4$, there is an immediate unloading of the plate once it buckles elastically such that the ultimate shear stress $\tau_{xy,ult}$ equals the elastic buckling stress $\tau_{xy,cr}$. Accordingly, in order to obtain an *illustrative* stress-strain curve under pure shear, the slenderness of an (ideal) square plate needs to be more than that permitted in the shipbuilding industry.

Pre-buckling

Given the foregoing, the stress-strain curve for a square plate of slenderness $\beta = 5$ is shown in Figure 2.21. The plate is without initial deflections and subjected to a pure shear load. With the initial application of the load, stresses and strains are uniform throughout the plate with a linear relationship between them defined by the *shear modulus of elasticity*

$$G = \frac{E}{2 \cdot (1 + \nu)} \tag{2.46}$$

This linear elastic behaviour is referred to as the *pre-buckling* portion of the stress-strain curve and theoretically applies only to ideal plates. For the load corresponding to point A on the curve ($\tau_{xy}/\tau_Y = 0.5$), the principal stresses in the middle plane of the plate are plotted in Figure 2.22(a). As noted above, the tensile stresses are oriented 45° to the x-axis and the compressive stresses −45° to the x-axis with both tensile and compressive components having the same magnitude as the applied shear stress[12].

Buckling strength

As the shear load is increased, the linear relationship between stress and strain continues until the *buckling strength* of the plate is reached. At this point, due to the compressive

[12] The orientation of the principal stresses are reversed in case the shear load is applied in the opposite direction.

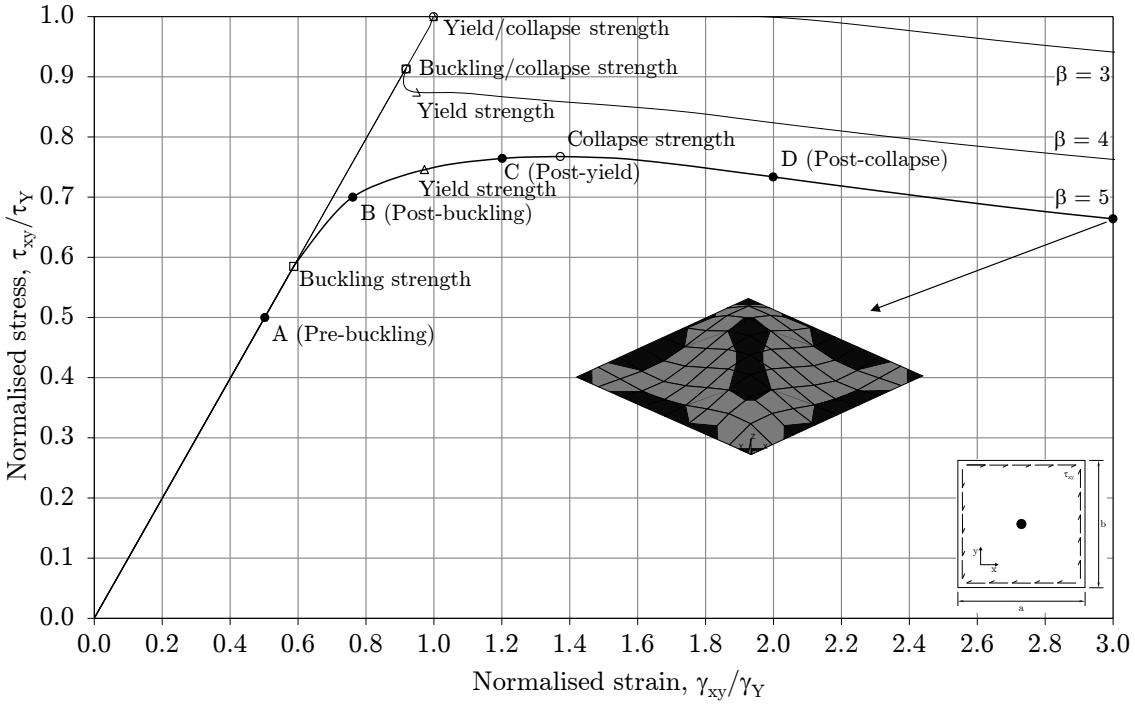

Figure 2.21.: Stress-strain curves of ideal plates under shear.

stresses, a shear buckle develops (under the slightest of perturbations) with its axis oriented 45° to the x-axis, i.e. from plate corner to plate corner. Shear buckling of an ideal plate causes a redistribution of stresses which marks the beginning of a distinctly different phase of its response to the shear load.

Post-buckling

The *post-buckling* portion of the stress-strain curve is characterised by a constantly reducing slope. In Figure 2.22(b) the principal stresses associated with point B ($\tau_{xy}/\tau_Y = 0.7$) are shown. As can be seen, these principal stresses are no longer comprised of pure (internal) shear stresses, i.e. axial stresses are now present as evidenced by changes in the relative magnitude of principal stresses and slight changes in their orientation. Despite these changes, stresses remain symmetric about an axis oriented 45° to the x-axis. This newly formed stress distribution marks the emergence of a stable arrangement of stresses called the *tensile field* or *tension band*. The development of such a field or band is only possible if the plate is bounded by structure of sufficient in-plane stiffness which enables the plate to carry additional (post-buckling) shear load. Within the tension band the magnitude of tensile stresses increase with their proximity to the axis of symmetry while the opposite is true for compressive stresses due to out-of-plane deflections in the plate.

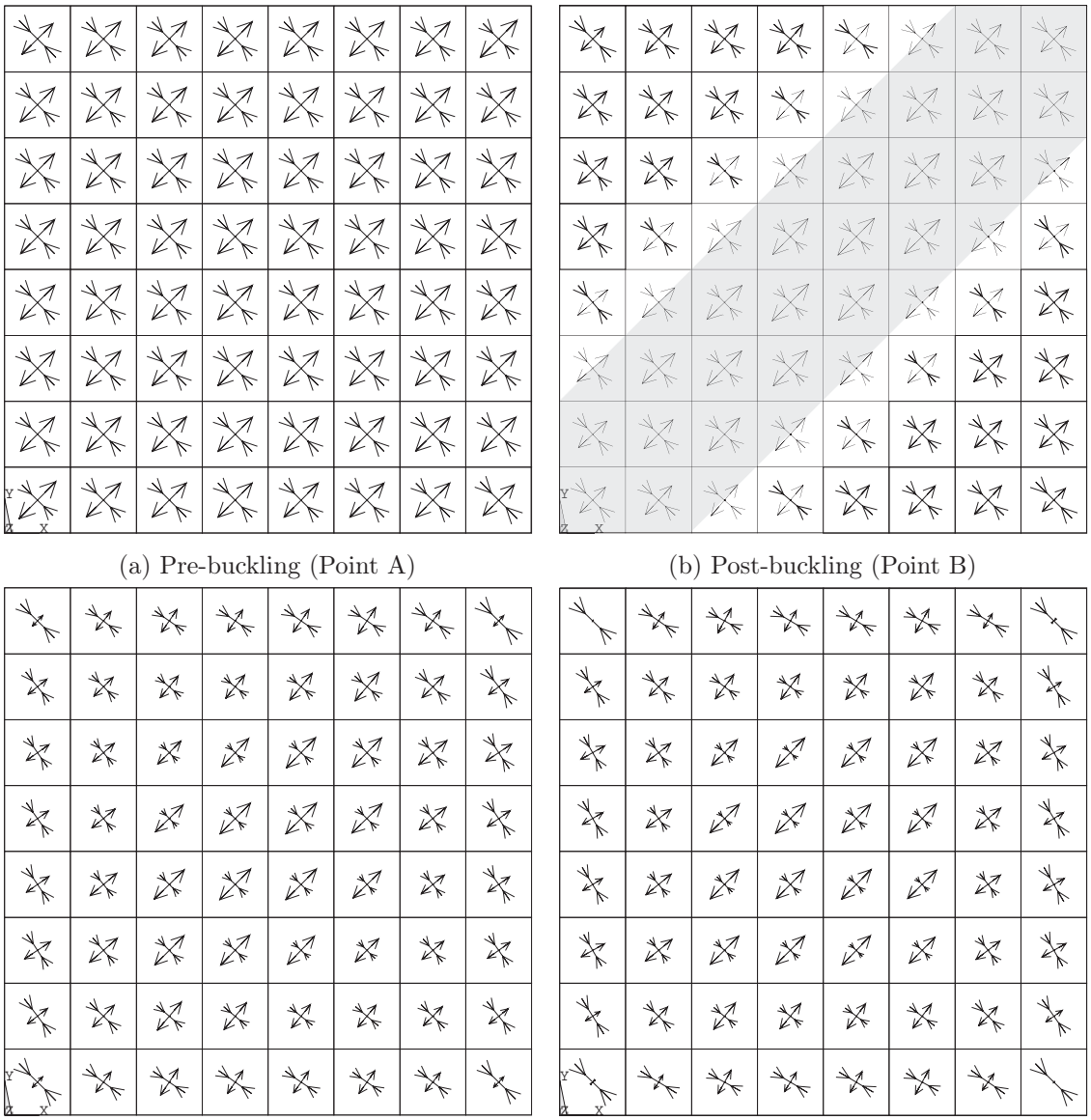

(a) Pre-buckling (Point A)

(b) Post-buckling (Point B)

(c) Post-yield (Point C)

(d) Post-collapse (Point D)

Figure 2.22.: Principle stresses in middle plane of ideal plate ($\beta = 5$).

Yield strength

As the shear load is increased further, the out-of-plane deflections are magnified (albeit mitigated by the tensile stresses) leading to an increase in the polarisation of tensile and compressive stresses. Yielding in the middle plane of the plate eventually initiates in the centre of the plate, i.e. $x = a/2$, $y = b/2$. Because the centre of the plate is located within the tension band, the stress state is dominated by tensile stresses although the magnitude of compressive stresses remain significant (about 73% of the tensile stress). Accordingly, similar to the mid-length edges of the plate under a uniaxial load, tensile and compressive stresses at the centre of the plate are "working together" to deform the plate material. As always, yielding in the middle plane of the plate is indicative of through-thickness plasticity

and is typically a precursor to collapse.

Post-yield

With further increases in shear load, plastic flow begins to spread throughout the middle plane as evidenced by the near-zero slope of the stress-strain curve following yield (see Figure 2.21). In particular, plasticity begins to appear in the central portion of the tension band, all four corners of the plate and near the mid-length and mid-breadth edges of the plate. In Figure 2.22(c) the principal stresses associated with point C ($\gamma_{xy}/\gamma_Y = 1.2$) in the post-yield response are shown. Here the polarisation of tensile and compressive stresses is more pronounced as is the formation of the tension band. Corresponding to the latter, the edges of the plate begin to take on a role similar to compression posts of a *Pratt* truss as reflected in the magnitude and orientation of stresses, i.e. except in the corners of the plate, the magnitude of angles between the x-axis and compressive principal stresses at the edges of the plate are markedly more than 45°.

Collapse strength

With a small increase in shear load the slope of the stress-strain curve reaches zero. In Figure 2.21 the normalised collapse stress is seen to be approximately $\tau_{xy,ult}/\tau_Y = 0.77$ which represents a 2.9% increase in shear stress compared to initial yield. In terms of displacement, the normalised collapse strain is approximately $\gamma_{xy,ult}/\gamma_Y = 1.37$ which is an increase of approximately $\Delta\gamma_{xy} \simeq 0.40 \cdot \gamma_Y$ compared to initial yield. This increase is twice that compared to the uniaxial load case and is due to the near-zero (post-yield) stiffness of the plate.

Post-collapse

After collapse the load resistance of the plate under further shear straining is reduced through the spread of plasticity throughout the tension band. The effects of post-collapse straining on principal stresses are shown in Figure 2.22(d) for the load associated with point D of the stress-strain curve ($\gamma_{xy}/\gamma_Y = 2.0$). Here the redistribution of stresses which initiated under buckling are further accentuated. Accordingly, tensile stresses in the tension band continue to grow as do compressive stresses along the edges of the plate. A plot of the plastic collapse mechanism which permits large shear straining is shown in Figure 2.21 for $\gamma_{xy}/\gamma_Y = 3.0$. Photos of collapse mechanisms under pure shear are shown by Rockey et al. in reference [36] and reproduced in Figure 2.23. In case of both girders evidence of finite in-plane edge restraint can be seen. In Figure 2.23(a) neither of the shear buckles are anchored in the corners of the plate and in Figure 2.23(b) a well-developed plastic mechanism in the compression flange is clearly evident.

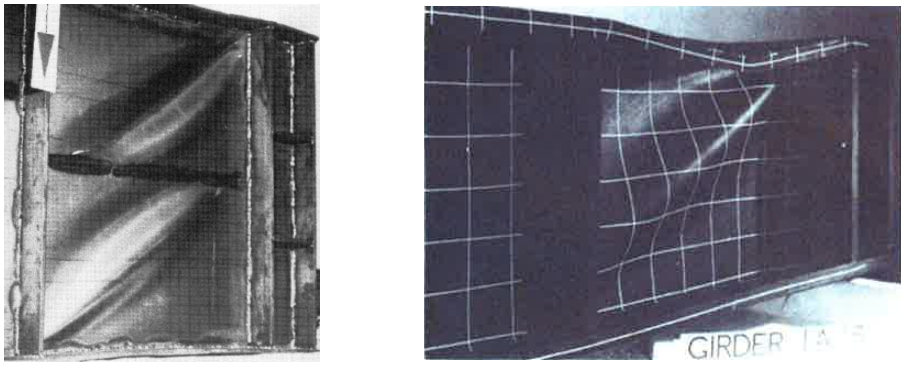

(a) Girder SH1 (b) Girder 1AS1-5

Figure 2.23.: Collapse mechanism under pure shear (reproduced from reference [36] with permission of the Institution of Civil Engineers).

2.3.2. Tension field analysis

In parallel to the early work being carried out to study plating under pure axial loads, the aeronautical industry was also studying the collapse of plating under pure shear loads. A pioneer in this regard was Wagner who in 1931 described the post-buckling capacity of a plate under pure shear in terms of the tension band[13] [37]. Wagner explained his concept using a square truss comprised of four perfectly rigid members and two cross diagonals (pinned at the corners) as shown in Figure 2.24(a). Under low levels of shear the two cross diagonals D_1 and D_2 carry equal and opposite stresses. However, at a critical level of shear the cross diagonal under compression D_2 will buckle such that it is unable to carry further increases in stress. Accordingly, with further increases in the applied shear stress, Wagner writes "we can assume that the stress in the buckled D_2 remains constant but that thereby the tension in D_1 raises twice as fast, so that finally the tension diagonal D_1 transmits the principal portion of the cross stress". By analogy, the same state of stress results when shear resistance is provided by a thin plate instead of the cross diagonals D_1 and D_2 (although Wagner acknowledges that the buckling of the plate under compression stress $\sigma_{2,i}$ will be somewhat delayed by the presence of the tensile stress $\sigma_{1,i}$). When the tensile stress $\sigma_{1,i}$ is so large that the compression stress $\sigma_{2,i}$ can be neglected, the plate is said to be in a state of *pure* diagonal tension.

Accordingly, there are two analytical models describing two separate states of internal stress in a plate under an applied shear load. One model is of a state of pure shear (see Figure 2.24(b)) and the other a state of pure (diagonal) tension (see Figure 2.24(c)). Of course, in reality the state of stress in plating under pure shear lies somewhere between these two limits. For this reason, Wagner suggested to include the effects of buckling stiffness in his tension field analysis of curved plates [38] (i.e. due to their increased buckling strength compared to plane plates). However, this idea was subsequently adopted by others for plane plates and further refined by Kuhn et al. [39] in their theory of *incomplete diagonal*

[13] To be precise, 1931 was the publication year of Wagner's technical memorandums for the National Advisory Committee for Aeronautics. However, he had previously published his work under the title "Ebene Blechwandträger mit sehr dünnem Stegblech" in the German language publication *Zeitschrift für Flugtechnik und Motorluftschiffahrt* (Vol. 20, No. 8, 29 April 1929, pp. 200-207 and Vol. 20, No. 9, 14 May 1929, pp. 227-231).

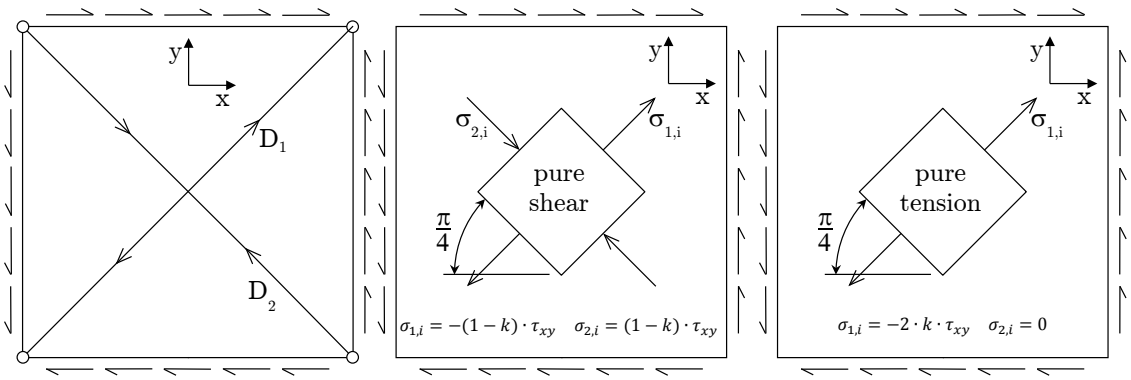

(a) Truss with cross diagonals (b) Pure shear component (c) Pure tension component

Figure 2.24.: Wagner's truss and plate models.

tension. In its mathematical form, Kuhn et al. defined a *diagonal tension factor*

$$k = 1 - \frac{\tau_{xy,cr}}{\tau_{xy}} \tag{2.47}$$

In this definition of k it is assumed that the plate is in an internal state of pure shear stress only so long as $\tau_{xy} < \tau_{xy,cr}$, although Kuhn et al. suggested lower values for k based on empirical evidence, noting "it does not seem reasonable to assume that the hardly perceptible buckles which form in a web loaded just beyond the critical stress deprive the sheet immediately of all ability to carry any further increase in diagonal compressive stress and consequently any increase in true shear stress" [39]. In any case, the diagonal tension factor k works like a weighting factor between two extreme stress states where the principal stresses of the pure shear component are defined by[14]

$$\sigma_{1,i} = -(1-k) \cdot \tau_{xy} \tag{2.48a}$$
$$\sigma_{2,i} = \quad (1-k) \cdot \tau_{xy} \tag{2.48b}$$

and the principal stresses of the pure tension component are defined by

$$\sigma_{1,i} = -2 \cdot k \cdot \tau_{xy} \tag{2.49a}$$
$$\sigma_{2,i} = \quad 0 \tag{2.49b}$$

Equation (2.49a) is based on the assumption of infinitely rigid edges (i.e. no edge pull-in) for which the tensile stress $\sigma_{1,i}$ is inclined 45° to the x-axis (otherwise the tensile stress $\sigma_{1,i}$ is to be reduced by a factor of $\sin(2\phi)$, where ϕ is the angle of inclination).

Accordingly, the total (mixed) stress state of a plate in incomplete diagonal tension is defined by summing the principal stresses defined in Equations (2.48) and (2.49)

$$\sigma_{1,i} = -(1-k) \cdot \tau_{xy} - 2 \cdot k \cdot \tau_{xy} \tag{2.50a}$$
$$\sigma_{2,i} = \quad (1-k) \cdot \tau_{xy} \tag{2.50b}$$

[14] Although it is usual in stress analyses that the greatest of the principal stresses be positive, it is a convention in buckling analyses literature that tensile stresses be negative.

which can be rewritten as

$$\sigma_{1,i} = -(1+k)\cdot\tau_{xy} \tag{2.51a}$$
$$\sigma_{2,i} = \quad (1-k)\cdot\tau_{xy} \tag{2.51b}$$

Substituting Equation (2.51) into that defining the (von Mises) equivalent stress

$$\sigma_{eq,i} = \sqrt{\sigma_{1,i}^2 + \sigma_{2,i}^2 - \sigma_{1,i}\cdot\sigma_{2,i}} \tag{2.52a}$$
$$= \tau_{xy}\cdot\sqrt{3+k^2} \tag{2.52b}$$

As a result, if the ultimate shear strength of the plate $\tau_{xy,ult}$ is defined by initial yield, i.e. $\sigma_{eq,i} = \sigma_Y$,

$$\tau_{xy,ult} = \frac{\sigma_Y}{\sqrt{3+k^2}} \tag{2.53}$$

As a result,

$$\tau_{xy,ult} = \frac{\sigma_Y}{\sqrt{3}} \quad (=\tau_Y) \tag{2.54}$$

for relatively thick plates where $k \to 0$ (pure shear) and

$$\tau_{xy,ult} = \frac{\sigma_Y}{2} \tag{2.55}$$

for very thin plates where $k \to 1$ (pure tension). This means that the minimum ultimate shear capacity of a very thin plate under pure diagonal tension is about 87% of that for a thick "shear resistant" plate, i.e. $\sqrt{3}/2 \sim 0.866$, such that $0.866\cdot\tau_Y \leqslant \tau_{xy,ult} \leqslant \tau_Y$ according to tension field theory for plating with perfect in-plane edge restraint.

In the case of the square plate shown in Figure 2.21 ($\beta = 5$), the development of internal stresses obtained using tension field theory (for plating with perfect in-plane edge restraint) will now be compared to that obtained using finite element analysis. In this regard, the growth of internal stresses $\sigma_{x,i}$, $\sigma_{y,i}$, $\tau_{xy,i}$ and $\sigma_{eq,i}$ with the application of the applied shear stress τ_{xy} is shown on the left-hand side of Figure 2.25 and in terms of principal stresses on the right-hand side of Figure 2.25[15]. Also shown on the right-hand side of Figure 2.25 is the growth of principal stresses according to tension field theory. On both sides of Figure 2.25 the elastic buckling stress for the plate ($\tau_{xy,cr} \simeq 0.59\cdot\tau_Y$) is indicated. As noted above, the magnitudes of principal stresses $\sigma_{1,i}$ and $\sigma_{2,i}$ in the pre-buckled state are equal to $\sigma_{1,i} = -\tau_{xy}$ and $\sigma_{2,i} = \tau_{xy}$. In the post-buckled state, $\Delta\sigma_{1,i} = -2\cdot\Delta\tau_{xy}$ and $\Delta\sigma_{2,i} = 0$. Therefore, according to tension field theory, the plate yields under an applied shear stress of $\tau_{xy} = 0.97\cdot\tau_Y$, where $\sigma_{1,i} = -(0.59 + 2\cdot(0.97-0.59))\cdot\tau_Y = -0.78\cdot\sigma_Y$ and $\sigma_{2,i} = 0.59\cdot\tau_Y = 0.34\cdot\sigma_Y$. Here the applied shear stress $\tau_{xy} = 0.97\cdot\tau_Y$ initiating yield in plating of slenderness $\beta = 5$ is near the upper limit of the above condition $0.866\cdot\tau_Y \leqslant \tau_{xy,ult} \leqslant \tau_Y$ for tension field theory.

However, as can be seen in Figure 2.21, yielding occurs under an applied shear stress of $\tau_{xy} = 0.75\cdot\tau_Y$ according to finite element analysis. Here it is important to reiterate

[15] For the purpose of representation the first principal stress σ_1 is plotted as $|\sigma_1|$.

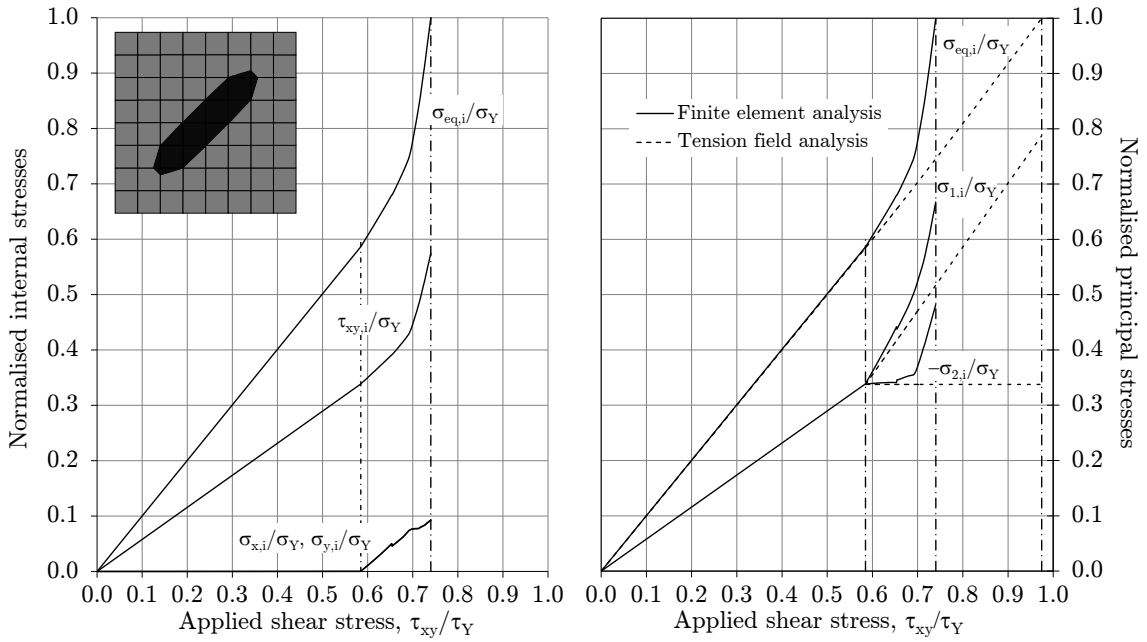

Figure 2.25.: Mid-plane stresses at centre of square plate shown in Figure 2.21 ($\beta = 5$).

that in this analysis the edges of the plate, although straight, are otherwise able to move freely in-plane. At the point of initial yield, the finite element analysis shows that all areas of the plate carry shear stress in excess of $\tau_{xy,cr}$ and the dark area shown in the inset on the left-hand side of Figure 2.25 carries shear stresses greater than $0.9 \cdot \tau_Y$. In particular, the shear stress at the centre of the plate (where initial yielding takes place) is equal to $\tau_{xy,i} = 0.575 \cdot \sigma_Y = 0.995 \cdot \tau_Y$ as shown on the left-hand side of Figure 2.25. As shown on the right-hand side of Figure 2.25, the principal stresses at the point of yield are equal to $\sigma_{1,i} = -0.66 \cdot \sigma_Y$ and $\sigma_{2,i} = 0.49 \cdot \sigma_Y$.

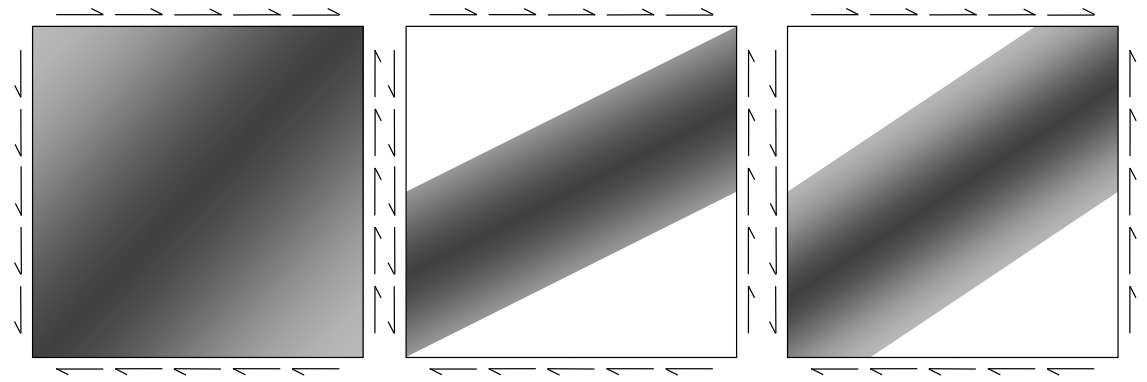

(a) Wagner and Kuhn et al. (b) Basler (c) Rockey and Skaloud

Figure 2.26.: Tension field models.

As noted above, the tension field theory presented so far assumes that the edges of the plate have perfect in-plane edge restraint. This results in a tension field which covers the entire plate and which is inclined 45° to the x-axis (see Figure 2.26(a)). In case

of aeronautical engineering, this assumption may well be valid given the high strength aluminium alloys used in aircraft structure which lead to thin webs and relatively strong flanges [40, 41]. However, in the case of steel plate girders used in civil engineering applications, the bending stiffness of flanges is usually insufficient to prevent in-plane displacement of the plate edges. If this displacement is of an extent that the tensile stresses in the diagonal of the plate are appreciably relieved, then both the width and inclination of the tension field are affected. In this regard, Basler (as referenced in [40]) assumed that the flanges of most plate girders were too flexible to withstand the lateral load caused by a *perfectly* diagonal tension field. Accordingly, he postulated an *off* diagonal tension field which is not anchored to any part of the flange (see Figure 2.26(b)). Rockey and Skaloud (as referenced in [40]) subsequently showed the foregoing assumption to be overly conservative and postulated tension fields which took into explicit account the stiffness of the flanges (see Figure 2.26(c)). Such models may be more appropriate for ship structures such as floors and longitudinal girders where in-plane edge restraint is negligible.

2.3.3. Effects of initial deflections

In order to study the effect of welding distortions, stress-strain curves are shown on the left-hand side of Figure 2.27 for initially deflected plating ($\delta_0 = b/200$). Here the nomenclature of the plate reduction factor $\kappa_\tau = \tau_{xy,ult} \cdot \sqrt{3}/\sigma_Y = \tau_{xy,ult}/\tau_Y$ is reintroduced (see §2.1.4). Unlike the uniaxial load case (see the left-hand side of Figure 2.6), these curves deviate only slightly from the shear modulus curve ($G = \tau_{xy}/\gamma_{xy}$) due to the mitigating influence of tensile stresses on out-of-plane deflections. Accordingly, the magnitudes of collapse strength normalised against yield are clearly higher in the case of shear loading. Furthermore, regardless of plate slenderness, the stress-strain curves approach elastic-perfectly plastic behaviour where plasticity is defined by the ultimate stress $\tau_{xy,ult}$ rather than the yield stress τ_Y. This stable response is again due to the presence of the tension field.

Ranges of plate slenderness

On the right-hand side of Figure 2.27 the collapse strengths of plates with and without initial deflections are shown. Also shown are the ranges of the plate slenderness parameter β defined by Hughes to delineate different types of plating collapse (because the shear buckling factor K_τ is a function of the plate aspect ratio α, the reference degrees of slenderness λ_τ shown in Figure 2.27 are only valid for $\alpha = 1$). Here it may be recalled that the transitions between these different classes of plating are approximately defined where the collapse strength equals the yield strength (i.e. sturdy to intermediate plating) and where the collapse strength equals the elastic buckling strength (i.e. intermediate to slender plating). Applying these same criteria to square plates under a pure shear load, it can be seen that there is no "slender" plating for the range of plate slenderness parameters typically found in shipbuilding since the elastic buckling strength always exceeds the ultimate strength. Moreover, the transition between sturdy and intermediate plating occurs not in the vicinity of $\beta = 1$ but rather $\beta = 2$. As can be seen in Figure 2.28, there is little evidence of buckling behaviour in the principal stress plots at collapse for plating of slenderness $\beta = 2$.

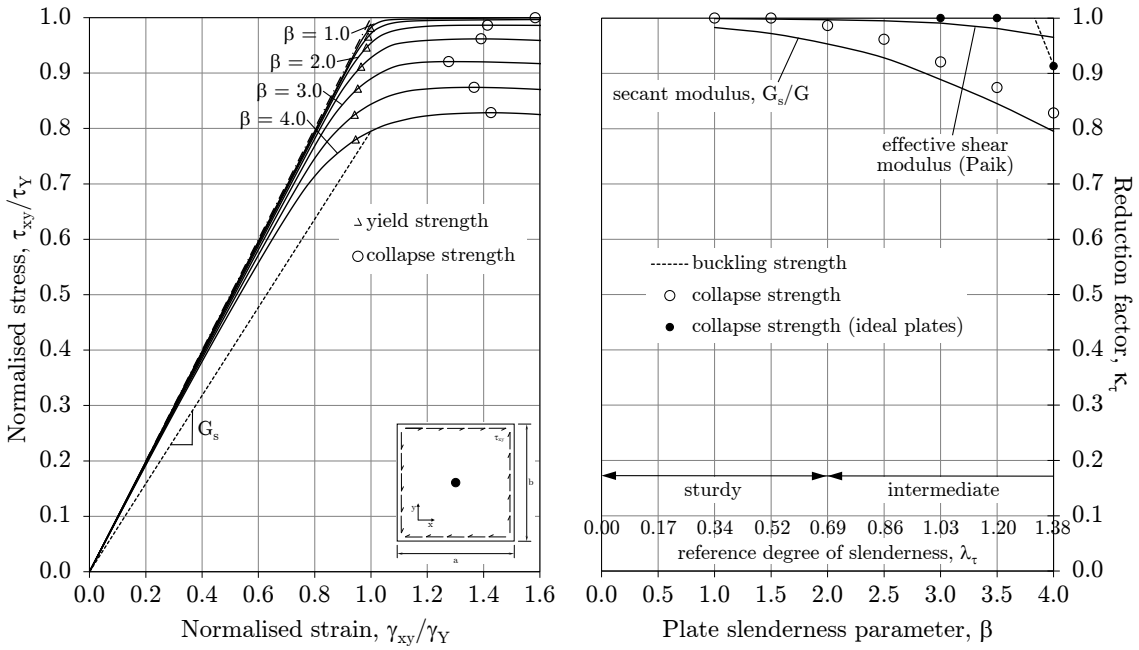

Figure 2.27.: Stress-strain curves and effective width of plates with initial deflections.

Effective shear modulus

On the left-hand side of Figure 2.27, a secant intersecting the stress-strain curve at its origin and the yield strain $\gamma_{xy}/\gamma_Y = 1$ is shown for $\beta = 4$. The corresponding *plate secant shear modulus* G_s is again normalised against the plate elastic modulus G and the resulting quantity G_s/G is plotted on the right-hand side of Figure 2.27 for all plate slenderness parameters. In this regard, Paik has provided empirical formulae for the plate secant shear modulus G_s (or *effective shear modulus*, G_e, in his nomenclature) [42]. Paik claims that this concept has quite similar characteristics and advantages to von Kármán's concept of effective width in the case of uniaxial stress. Paik based his empirical formulae on elastic large deflection analyses through an application of the incremental Galerkin method. The formulae are functions of applied shear stress normalised against critical buckling stress ($\tau_{xy}/\tau_{xy,cr}$) and initial deflections normalised against plate thickness (δ_0/t). Unfortunately, the results of the analyses presented in [42] are rather non-conservative compared to those based on the finite element method as shown on the right-hand side of Figure 2.27.

2.3.4. Formulae for plate reduction factors

Formulae from literature

Because the deformation of plates under pure shear is relatively complex compared to uniaxial stresses, many authors have offered formulae which have been derived from fitting curves to numerical results. Perhaps given the difficulties with his effective shear modulus approach, Paik subsequently derived the following formulae based on a series of non-linear finite element calculations for simply supported plates (with straight edges) where both slenderness parameters and aspect ratios were varied (described in a confidential report to

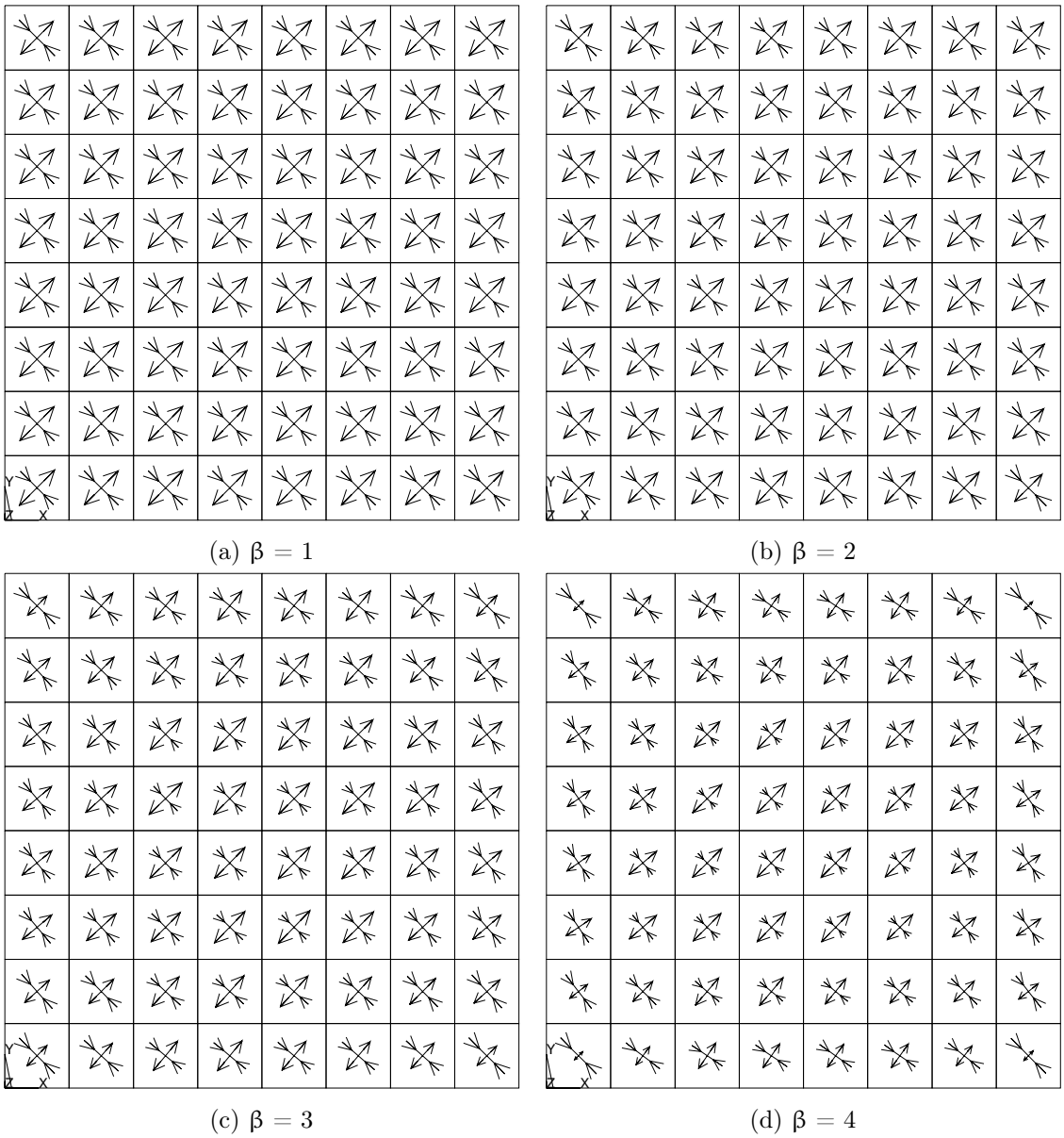

(a) $\beta = 1$ (b) $\beta = 2$

(c) $\beta = 3$ (d) $\beta = 4$

Figure 2.28.: Principle stresses at collapse in middle plane of plates with initial deflections.

the American Bureau of Shipping (ABS) [43], but referenced in [44])

$$\kappa_\tau = \frac{\tau_{xy,ult}}{\tau_Y} = \begin{cases} 1.324/\lambda_\tau^2 & \lambda_\tau \geqslant \sqrt{2} \\ 0.039/\lambda_\tau^6 - 0.274/\lambda_\tau^4 + 0.676/\lambda_\tau^2 + 0.388 & \sqrt{2} > \lambda_\tau \geqslant \sqrt{0.5} \\ 0.956 & \lambda_\tau < \sqrt{0.5} \end{cases} \tag{2.56}$$

where $\lambda_\tau = \sqrt{\tau_Y/\tau_{cr}}$. In Paik's solution, τ_{cr} is calculated for a plate aspect ratio $\alpha = 1$ because he found that the ultimate shear strength of plates decreases only slightly with aspect ratios $\alpha > 1$. Similarly, Nara et al. (referenced in [35] and [45]) proposed the following which was also obtained by fitting a curve to non-linear finite element results

$$\kappa_\tau = \frac{\tau_{xy,ult}}{\tau_Y} = \left(\frac{0.486}{\lambda_\tau}\right)^{\frac{1}{3}} \leqslant 1.0 \tag{2.57}$$

and which is valid for $\lambda_\tau \leqslant 2.0$. Results obtained with the proofs of Paik and Nara et al. are compared in Figure 2.29 to those obtained by finite element analyses.

Because formulae based on curve fitting can be devoid of physical meaning, Zhang et al. sought a format which more closely resembled established expressions for ultimate *compressive* strength. Towards this end, Faulkner's well-known Equation (2.26) for the ultimate strength of plates under a uniaxial load was considered both accurate and simple to apply. Accordingly, "(t)hrough analyses and application of engineering experience", Zhang et al. [45] proposed the following similarly constructed formula

$$\kappa_\tau = \frac{\tau_{xy,ult}}{\tau_Y} = \begin{cases} \dfrac{2}{\sqrt{\beta_\tau}} - \dfrac{1}{\beta_\tau} & \beta_\tau \geqslant 1 \\ 1 & \beta_\tau < 1 \end{cases} \tag{2.58}$$

where $\beta_\tau = \beta / \left(1 + (b/a)^{3/2}\right)$. Results obtained with the proof of Zhang et al. are also shown in Figure 2.29.

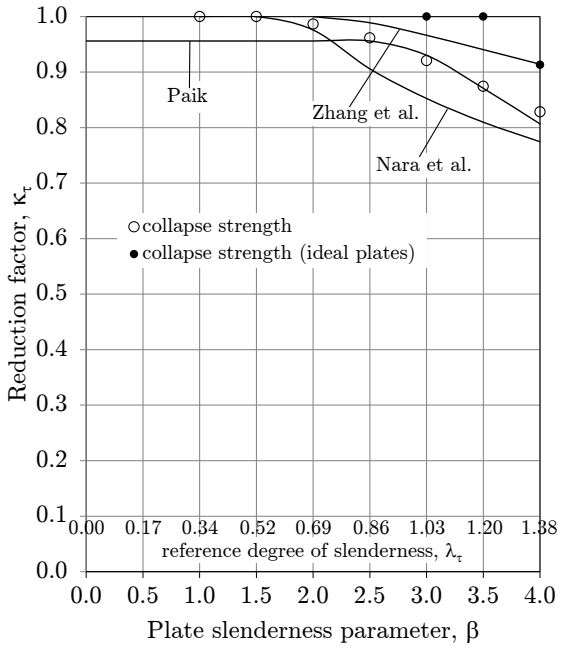

Figure 2.29.: Formulae from literature.

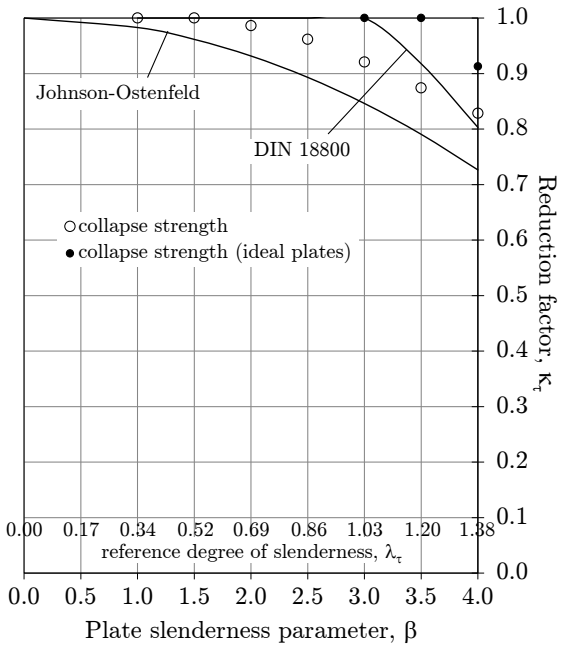

Figure 2.30.: Formulae used in shipbuilding.

Formulae used in shipbuilding

In terms of the classification of ships, two proofs for the ultimate shear strength of plates are widely used in the shipbuilding industry. The first proof is again based on the Johnson-Ostenfeld correction which is used to adjust the elastic shear buckling curve to account for plasticity (as presented in §2.1.4. for the uniaxial load case)

$$\kappa_\tau = \frac{\tau_{xy,ult}}{\tau_Y} = \begin{cases} 1 - \dfrac{\lambda_\tau^2}{4} & \lambda_\tau < \sqrt{2} \\ \dfrac{1}{\lambda_\tau^2} & \lambda_\tau \geqslant \sqrt{2} \end{cases} \tag{2.59}$$

Results using this proof are compared to those obtained by finite element analyses in Figure 2.30. However, due to the relatively low (shear) yield strength τ_Y and high (shear) buckling stress $\tau_{xy,cr}$ mentioned above, the reference degrees of slenderness $\lambda_\tau = \sqrt{\tau_Y/\tau_{xy,cr}}$ do not exceed $\sqrt{2} = 1.41$ in Figure 2.30 (i.e. for a plate aspect ratio $\alpha = 1$). Accordingly, only the first case of Equation (2.59) is here relevant and leads to an estimate of shear strength which is increasingly conservative with plate slenderness (i.e. 1.7% for $\beta = 1$ to 12.3% for $\beta = 4$). This proof is used most notably in the *IACS Longitudinal Strength Standard* UR S11 [20].

The second proof widely used in the shipbuilding industry is based on the ultimate plate strength formulations developed in the late 1980's for inclusion in the German construction standard DIN 18800 [26]. For the case of a simply-supported plate under pure shear stress, the equation for the plate reduction factor is

$$\kappa_\tau = \frac{\tau_{xy,ult}}{\tau_Y} = \begin{cases} 1 & \lambda_\tau \leqslant 0.84 \\ \dfrac{0.84}{\lambda_\tau} & \lambda_\tau > 0.84 \end{cases} \tag{2.60}$$

This equation is also plotted in Figure 2.30. A similar equation is used in Eurocode 3 (Design of steel structures - Part 1-5: Plated structural elements) where a constant of 0.83 is used instead of 0.84 [19]. As noted in §2.1.4, the DIN 18800 formulations were first implemented in the buckling strength requirements of the German classification society Germanischer Lloyd (GL) in 1997 [30], but have since been implemented in the buckling strength requirements of CSR BC [31], CSR OT [32], CSR BC & OT [23], UR S11A [8] as well as the new *DNV GL Rules for Classification* [33] which are applicable to all ship types.

2.3.5. Reduction in uniaxial/biaxial capacity due to shear

In case the collapse of plating under combined uniaxial and shear loads is dominated by the former, the essential effect of the latter is to hasten collapse of the plate with little change in the shape of the stress-strain curve. The same is true in case of plates subjected to combined biaxial and shear loads, whether the secondary biaxial load is compressive or tensile. For this reason, some authors have attempted to account for shear by using a reduced yield strength [9, 34].

Uniaxial load case

Continuing with the example used in previous sections, Figure 2.31 shows the stress-strain curve for an ideal square plate with slenderness $\beta = 3$ under uniaxial compression, i.e. the curve shown for $\tau_{xy} = 0$ is the same as that shown in Figure 2.1. In addition, stress-strain curves are shown for the same plate under three levels of shear, $\tau_{xy} = 0.25 \cdot \tau_{xy,ult}$,

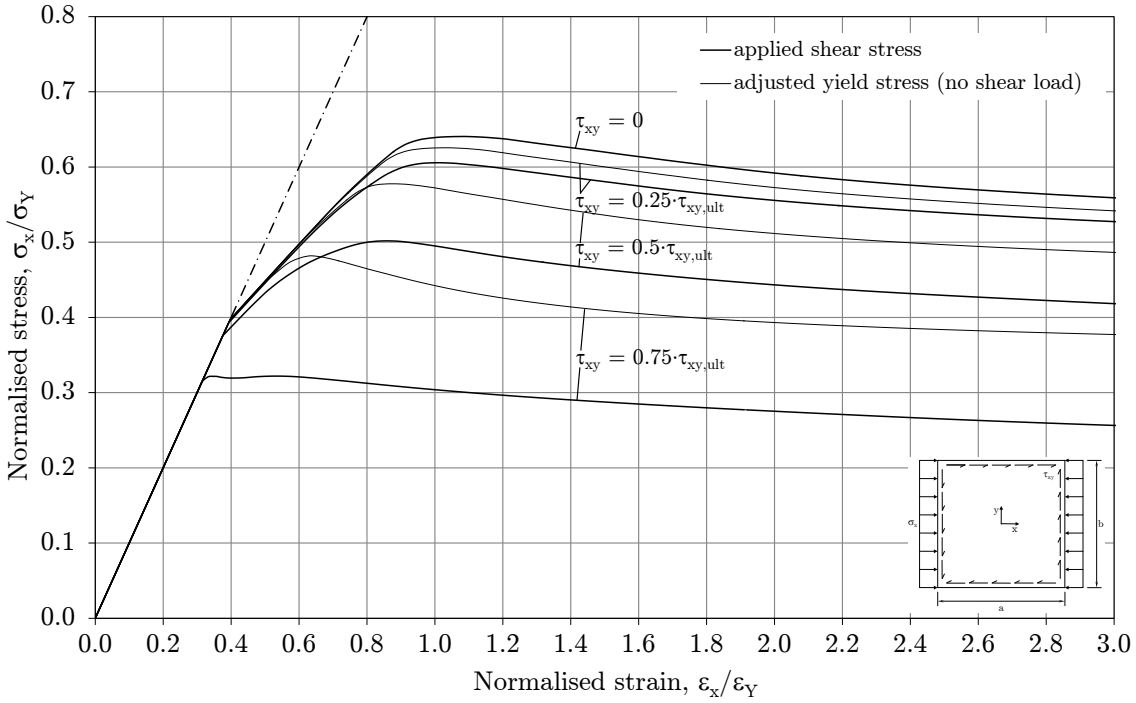

Figure 2.31.: Stress-strain curves under influence of shear ($\sigma_y = 0$, $\beta = 3$).

$\tau_{xy} = 0.5 \cdot \tau_{xy,ult}$ and $\tau_{xy} = 0.75 \cdot \tau_{xy,ult}$. Compared to the ultimate strength under uniaxial compression only, there is a non-linear decrease in the capacity of the plate with increasing levels of shear, i.e. 5.4%, 21.7% and 49.7%, respectively. However, there is little change in the shape of the stress-strain curves, except for the shear dominant case $\tau_{xy} = 0.75 \cdot \tau_{xy,ult}$ (the stress-strain curve of which resembles that for pure shear). Accordingly, also shown in Figure 2.31 are stress-strain curves for a uniaxially loaded plate using a reduced yield stress σ'_Y in lieu of applied shear loads. The reductions in yield stress are calculated according to the following commonly used equation

$$\sigma'_Y = \sqrt{\sigma_Y^2 - 3 \cdot \tau_{xy}^2} \tag{2.61}$$

However, as can be seen, this approach generally overestimates the collapse strength of the plate with errors increasing with levels of shear, i.e. 3.3%, 15.1% and 49.7% for $\tau_{xy} = 0.25 \cdot \tau_{xy,ult}$, $\tau_{xy} = 0.5 \cdot \tau_{xy,ult}$ and $\tau_{xy} = 0.75 \cdot \tau_{xy,ult}$, respectively.

To better understand the collapse of plating under combined uniaxial and shear loads, Figure 2.32 shows principal stresses in the middle plane of an ideal plate at the point of collapse under various levels of shear. In Figure 2.32(a) the principal stresses are shown for collapse in the absence of shear. As noted in §2.1.1, although longitudinal stresses along the edges of the plate are approximately equal over its length, yielding initiates at the mid-length edges of the plate (i.e. $x = a/2$), because of transverse tensile stresses which arise due to out-of-plane deflections. As noted previously, the (compressive) longitudinal stresses and (tensile) transverse stresses are here "working together" to deform the plate material. This is reflected in Figure 2.33 which shows the internal equivalent stresses at the mid-length edges, mid-breadth edges, corners within the tension band and centre of the plate under various levels of shear. As can be seen, equivalent stresses in the corners

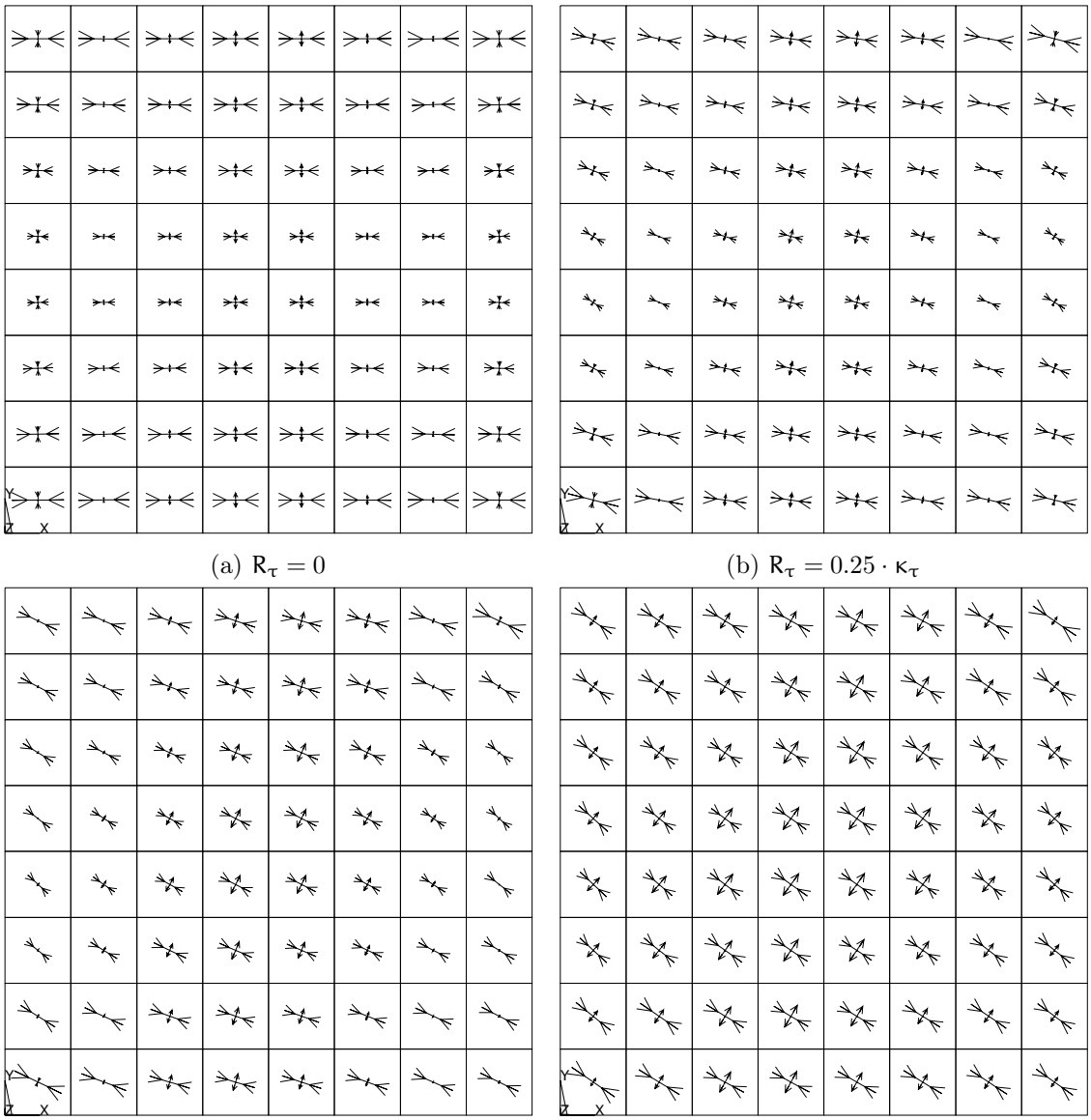

(a) $R_\tau = 0$ (b) $R_\tau = 0.25 \cdot \kappa_\tau$

(c) $R_\tau = 0.5 \cdot \kappa_\tau$ (d) $R_\tau = 0.75 \cdot \kappa_\tau$

Figure 2.32.: Principle stresses at collapse in middle plane of ideal plate ($\sigma_y = 0$, $\beta = 3$).

of the plate are about 82% of those at the mid-length edges (where yielding initiates) in the absence of shear. However, in the presence of a shear stress $\tau_{xy} = 0.25 \cdot \tau_{xy,ult}$, the tensile stresses which develop are such that yielding initiates instead in the corners of the plate within the tension band. As the level of shear increases, the principal stresses shown in Figure 2.32 progressively approach those shown in Figure 2.22 ((c) and (d)) for the pure shear case. In other words, as the level of shear increases, the locations of initial yield gradually move from the mid-length edges of the plate, to the corners of the plate (within the tension band) to the centre of the plate. This transition is reflected in the internal equivalent stresses shown in Figure 2.33. Moreover, as discussed in §2.3.1, Figure 2.33 confirms that collapse of an ideal (square) plate ($\beta = 3$) under pure shear ($\tau_{xy}/\tau_{xy,ult} = 1.00$)

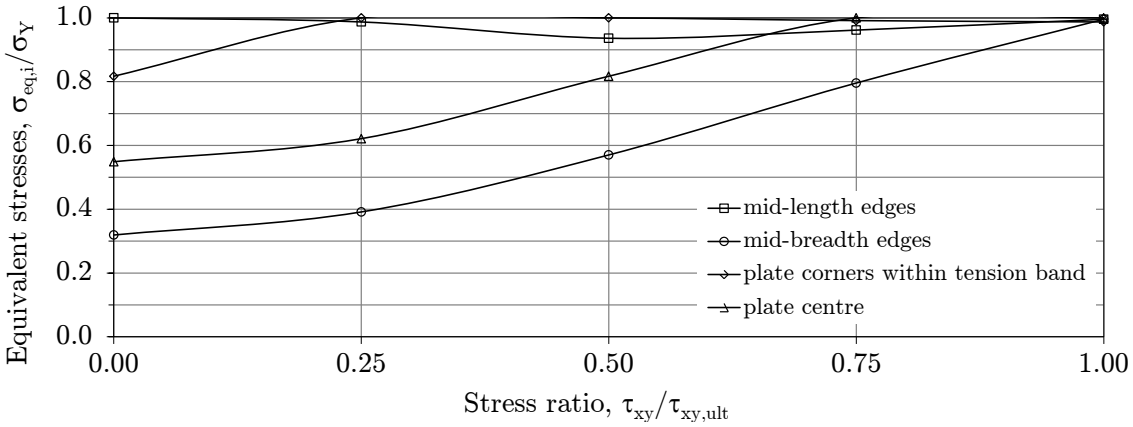

Figure 2.33.: Internal equivalent stresses at collapse ($\sigma_y = 0$, $\beta = 3$).

occurs by gross yielding.

Compressive secondary stress, c = 1

Continuing further with the example used in previous sections, Figure 2.34 shows the stress-strain curve for an ideal square plate with slenderness $\beta = 3$ under biaxial compression where $\sigma_y = \sigma_x$, i.e. the curve shown for $\tau_{xy} = 0$ is the same as that shown in Figure 2.10. In addition, stress-strain curves are again shown for the same plate under three levels of

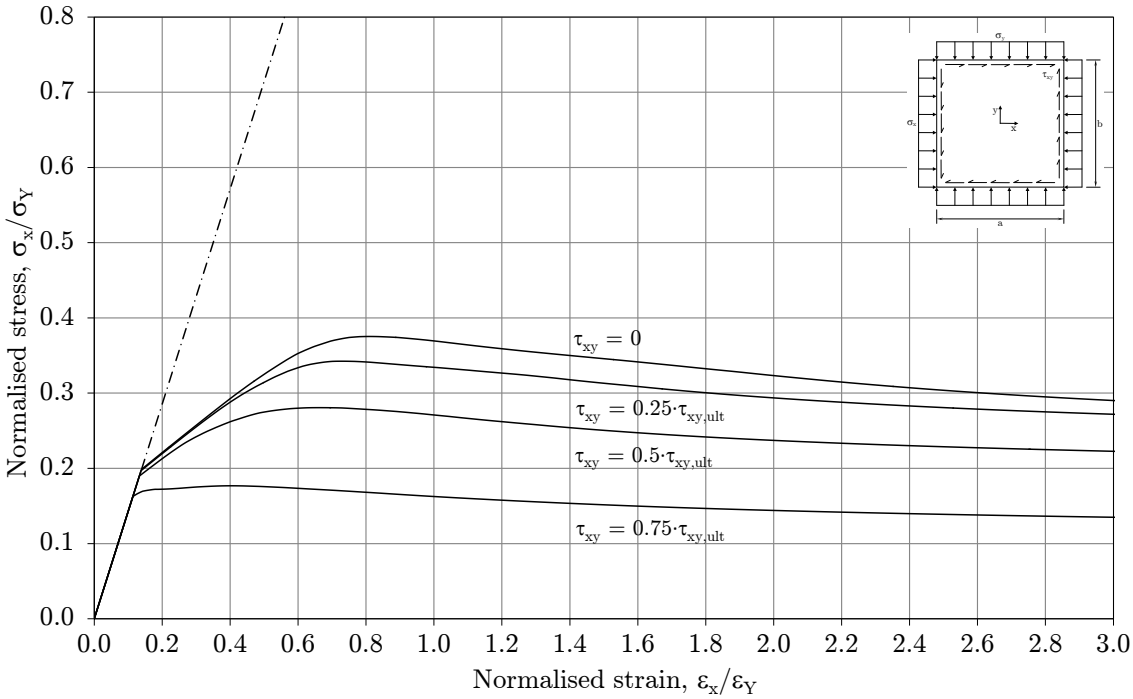

Figure 2.34.: Stress-strain curves under influence of shear ($\sigma_y = \sigma_x$, $\beta = 3$).

shear, $\tau_{xy} = 0.25 \cdot \tau_{xy,ult}$, $\tau_{xy} = 0.5 \cdot \tau_{xy,ult}$ and $\tau_{xy} = 0.75 \cdot \tau_{xy,ult}$. Compared to the ultimate strength under biaxial compression alone (i.e. $\sigma_y = \sigma_x$), there is again a non-linear decrease in the capacity of the plate with increasing levels of shear, i.e. 8.8%, 25.2% and 52.9%, respectively. Likewise, there is again little change in the shape of the stress-strain curves, except for the shear dominant case $\tau_{xy} = 0.75 \cdot \tau_{xy,ult}$ (the stress-strain curve of which again resembles that for pure shear).

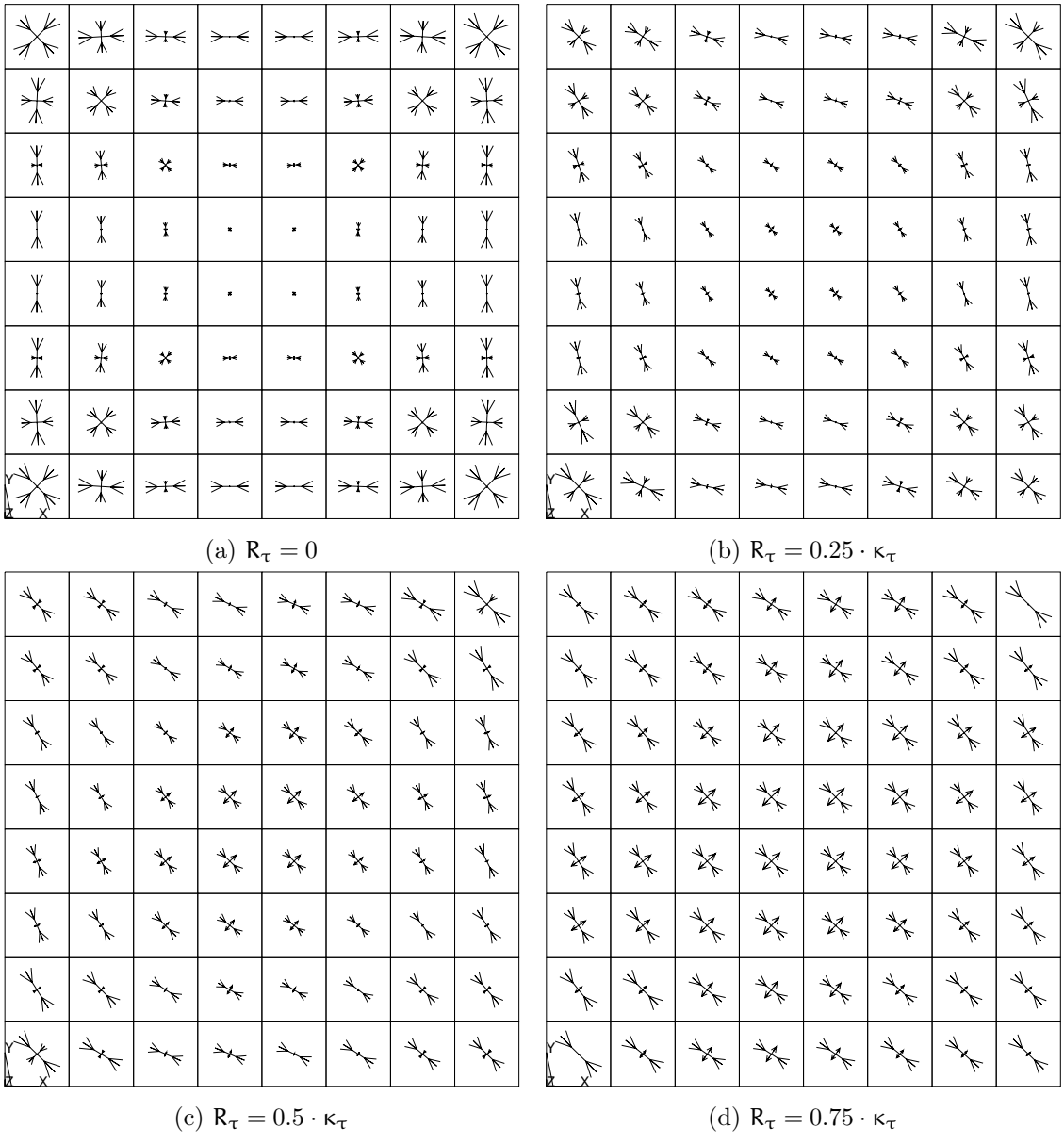

(a) $R_\tau = 0$ (b) $R_\tau = 0.25 \cdot \kappa_\tau$

(c) $R_\tau = 0.5 \cdot \kappa_\tau$ (d) $R_\tau = 0.75 \cdot \kappa_\tau$

Figure 2.35.: Principle stresses at collapse in middle plane of ideal plate ($\sigma_y = \sigma_x$, $\beta = 3$).

To better understand the collapse of plating under combined biaxial ($\sigma_y = \sigma_x$) and shear loads, Figure 2.35 shows principal stresses in the middle plane of the plate at the point of collapse. In Figure 2.35(a) the principal stresses are again shown for collapse in the absence of shear. As noted in §2.2.1, initial yielding under a biaxial load $\sigma_y = \sigma_x$ does

not occur at the mid-length edges of the plate, but rather in the corners of the plate where the (magnified) applied stresses σ_x and σ_y coalesce. This is reflected in Figure 2.36 which again shows the internal equivalent stresses at the mid-length edges, mid-breadth edges, corners in the tension band and centre of the plate under various levels of shear. As can be seen, equivalent stresses in the corners of the plate (within the tension band) are the first to reach yield under all levels of shear. As the level of shear increases, the principal stresses shown in Figure 2.35 once again progressively approach those shown in Figure 2.22 ((c) and (d)) for the pure shear case. Moreover, Figure 2.36 again confirms that collapse of an ideal (square) plate ($\beta = 3$) under pure shear ($\tau_{xy}/\tau_{xy,ult} = 1.00$) occurs by gross yielding.

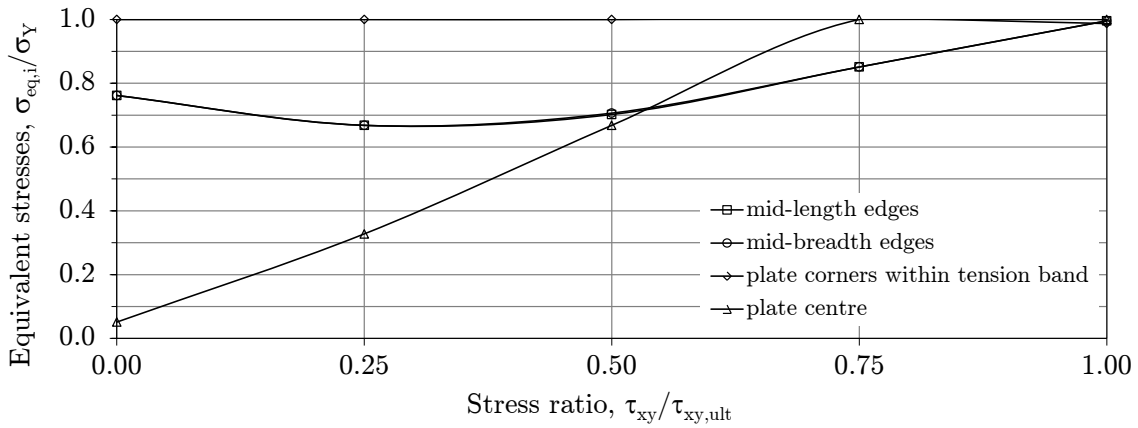

Figure 2.36.: Internal equivalent stresses at collapse ($\sigma_y = \sigma_x$, $\beta = 3$).

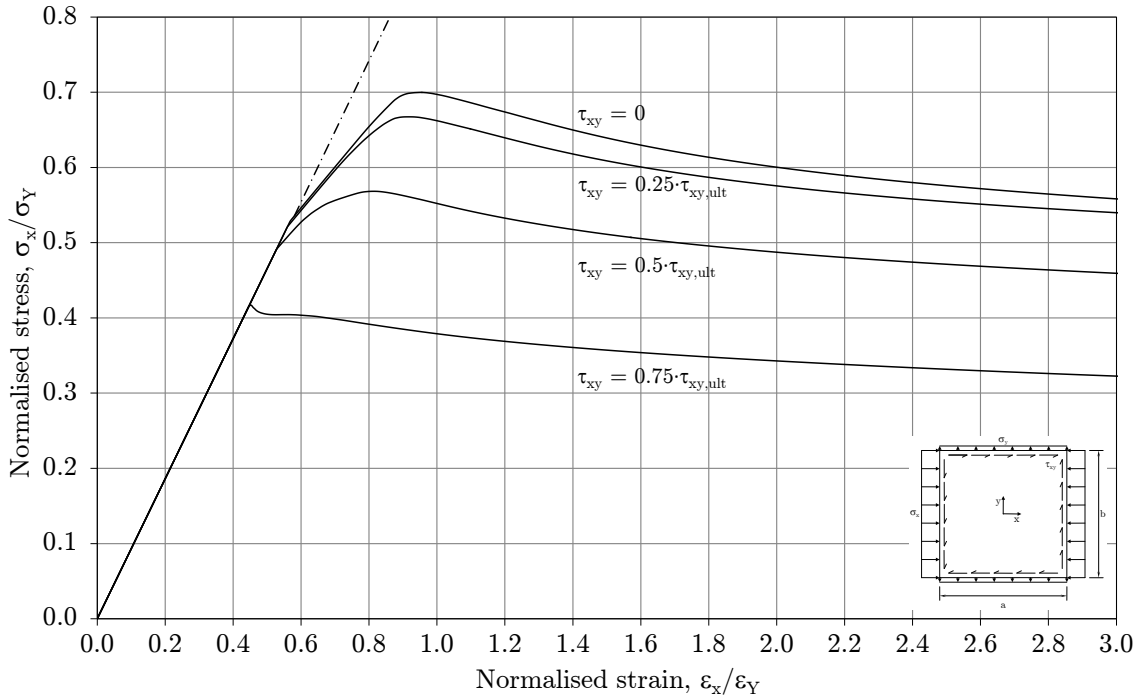

Figure 2.37.: Stress-strain curves under influence of shear ($\sigma_y = -\sigma_x/4$, $\beta = 3$).

Compressive secondary stress, c = -0.25

Lastly, continuing even further with the example used in previous sections, Figure 2.37 shows the stress-strain curve for an ideal square plate with slenderness $\beta = 3$ under biaxial compression where $\sigma_y = -\sigma_x/4$, i.e. the curve shown for $\tau_{xy} = 0$ is the same as that shown in Figure 2.13. In addition, stress-strain curves are again shown for the same plate under three levels of shear, $\tau_{xy} = 0.25 \cdot \tau_{xy,ult}$, $\tau_{xy} = 0.5 \cdot \tau_{xy,ult}$ and $\tau_{xy} = 0.75 \cdot \tau_{xy,ult}$. Compared to the ultimate strength under biaxial compression alone (i.e. $\sigma_y = -\sigma_x/4$), there is again a non-linear decrease in the capacity of the plate with increasing levels of shear, i.e. 4.6%, 18.8% and 40.4%, respectively. Likewise, there is again little change in the

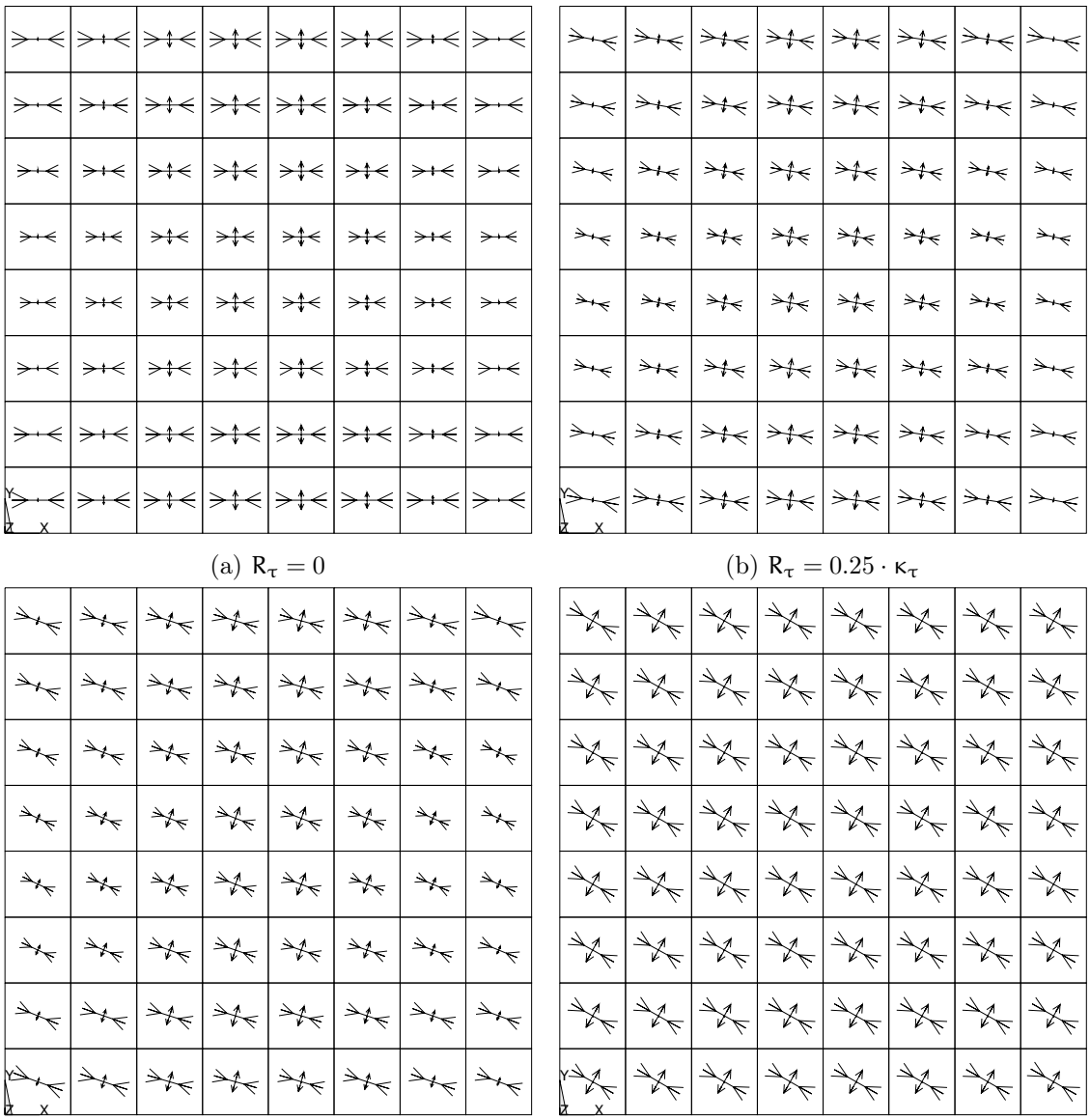

(a) $R_\tau = 0$ (b) $R_\tau = 0.25 \cdot \kappa_\tau$

(c) $R_\tau = 0.5 \cdot \kappa_\tau$ (d) $R_\tau = 0.75 \cdot \kappa_\tau$

Figure 2.38.: Principle stresses at collapse in middle plane of ideal plate ($\sigma_y = -\sigma_x/4$, $\beta = 3$).

shape of the stress-strain curves, except for the shear dominant case $\tau_{xy} = 0.75 \cdot \tau_{xy,ult}$ (the stress-strain curve of which again resembles that for pure shear).

To better understand the collapse of plating under combined biaxial ($\sigma_y = -\sigma_x/4$) and shear loads, Figure 2.38 shows principal stresses in the middle plane of the plate at the point of collapse. In Figure 2.38(a) the principal stresses are again shown for collapse in the absence of shear. As noted in §2.2.2, the resulting combination of compressive stresses (due to the applied load) and perpendicular tensile stresses (due to out-of-plane deflections) leads to initial yielding in the middle plane at the mid-length edges of the plate. However, because the restrained out-of-plane deflections mitigate the redistribution of stresses, the (applied) axial stress σ_x at which the plate yields is *greater* than that in the uniaxial load case. This is reflected in Figure 2.39 which once again shows the internal equivalent stresses at the mid-length edges, mid-breadth edges, corners within the tension band and centre of the plate under various levels of shear. As can be seen, equivalent stresses in the corners of the plate are approximately 85% of those at the mid-length edges (where yielding initiates) in the absence of shear. Moreover, due to the effect of the tensile stress in the y-direction, a shear stress of $\tau_{xy} = 0.5 \cdot \tau_{xy,ult}$ is needed before yielding initiates in the corners of the plate within the tension band. As the level of shear increases, the principal stresses shown in Figure 2.38 once again progressively approach those shown in Figure 2.22 ((c) and (d)) for the pure shear case. Moreover, Figure 2.39 again confirms that collapse of an ideal (square) plate ($\beta = 3$) under pure shear ($\tau_{xy}/\tau_{xy,ult} = 1.00$) occurs by gross yielding.

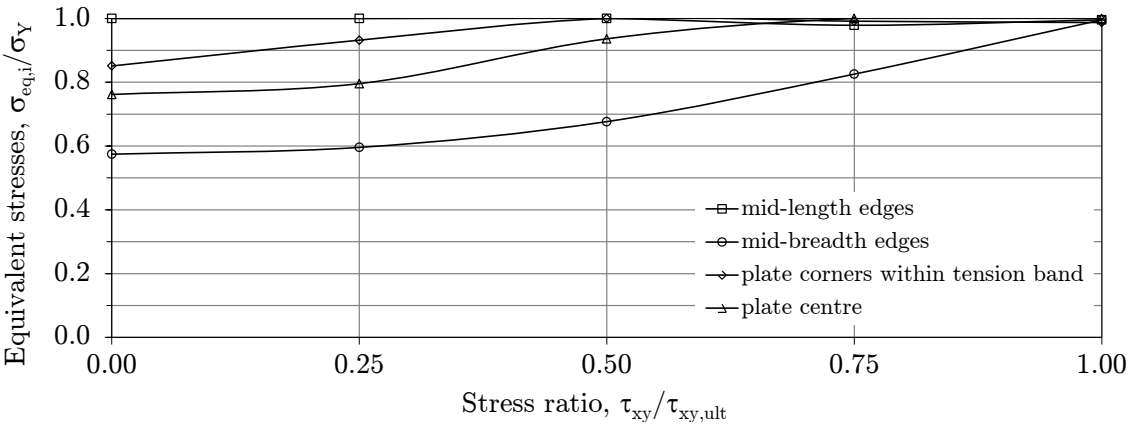

Figure 2.39.: Internal equivalent stresses at collapse ($\sigma_y = -\sigma_x/4$, $\beta = 3$).

Concept of capacity surfaces

In the context of plates under biaxial loads, the concept of capacity curves was introduced in §2.2.4. As noted therein, it is usual in ship design to delineate the combinations of biaxial stresses associated with plating collapse in terms of a *capacity curve* (alternatively referred to as an *interaction curve*). In this section the concept is extended to include the effects of shear, where separate capacity curves are shown for different levels of shear loads. For example, in Figure 2.40 a stress combination is shown in the x-y plane corresponding to collapse of a square plate ($\beta = 3$) with initial deflections under a shear load of $\tau_{xy} = 0.50 \cdot \tau_{xy,ult}$. In terms of vector notation this combination is written as

$$\mathbf{R} = \mathsf{R}_{\mathsf{x}}\,\mathbf{i} + \mathsf{R}_{\mathsf{y}}\,\mathbf{j} + \mathsf{R}_{\tau}\,\mathbf{k} = 0.34\,\mathbf{i} + 0.20\,\mathbf{j} + 0.46\,\mathbf{k} \tag{2.62}$$

By developing capacity curves for several values of τ_{xy}, the effects of shear can be represented as shown in Figure 2.41. If each of these capacity curves are plotted on a shear plane, then reference is instead made to a *capacity* or *failure surface*. Formulations or proofs to describe such failure surfaces will be presented in Chapters 3 and 4.

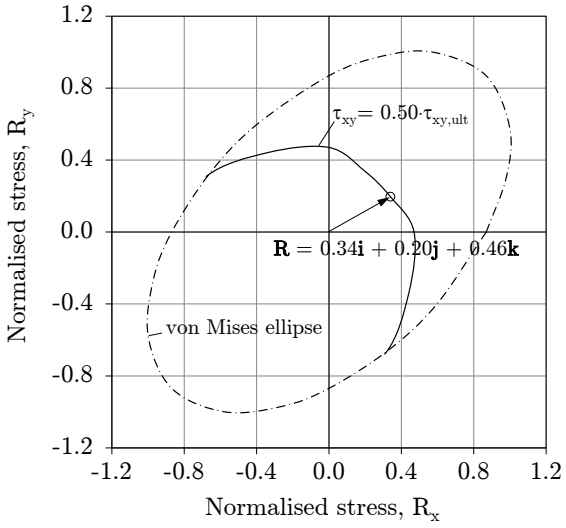

Figure 2.40.: Biaxial capacity vector under shear ($\beta = 3$).

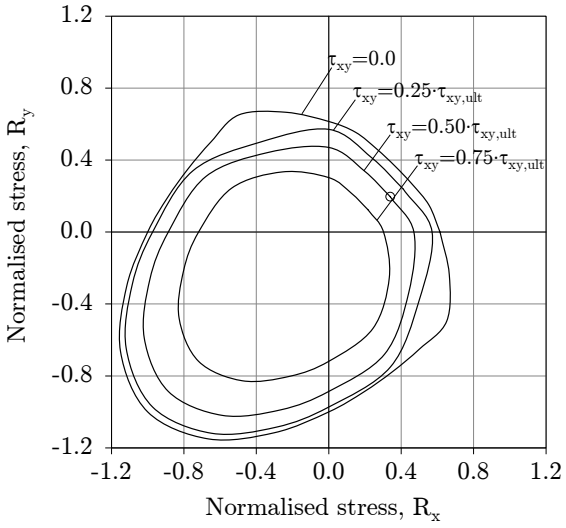

Figure 2.41.: Biaxial capacity curves under shear ($\beta = 3$).

2.4. Effects of plate aspect ratio

In order to isolate the effects of plate aspect ratio α, the mechanics of plating collapse in the preceding sections has been studied using square plates. In this section the effects of the plate aspect ratio on the mechanics of collapse under uniaxial, biaxial and shear loads is now examined. As shown below, the elastic buckling strength of longitudinally-stiffened plating is up to four times that for transversely-stiffened plating. For this reason, ship structures are generally made more weight-efficient (i.e. lighter) when plating is stiffened in the direction of the primary axial stress. Although the aspect ratio of ship plating is usually between the minimum value of $\alpha = 1$ and a maximum of about $\alpha = 8$ in (transversely-stiffened) shell plating of single-side skin bulk carriers, the usual range of aspect ratio for plates in the cargo hold regions of ships is between $\alpha = 3$ and $\alpha = 5$.

2.4.1. Uniaxial loads

Ideal plates

A typical stress-strain curve is shown in Figure 2.42 for a plate without any initial deflections and an aspect ratio of $\alpha = 3$ ($\beta = 3$). For the sake of comparison, plates with aspect ratios $\alpha = 1$ and $\alpha = 5$ are also shown. Here the stresses are applied along the

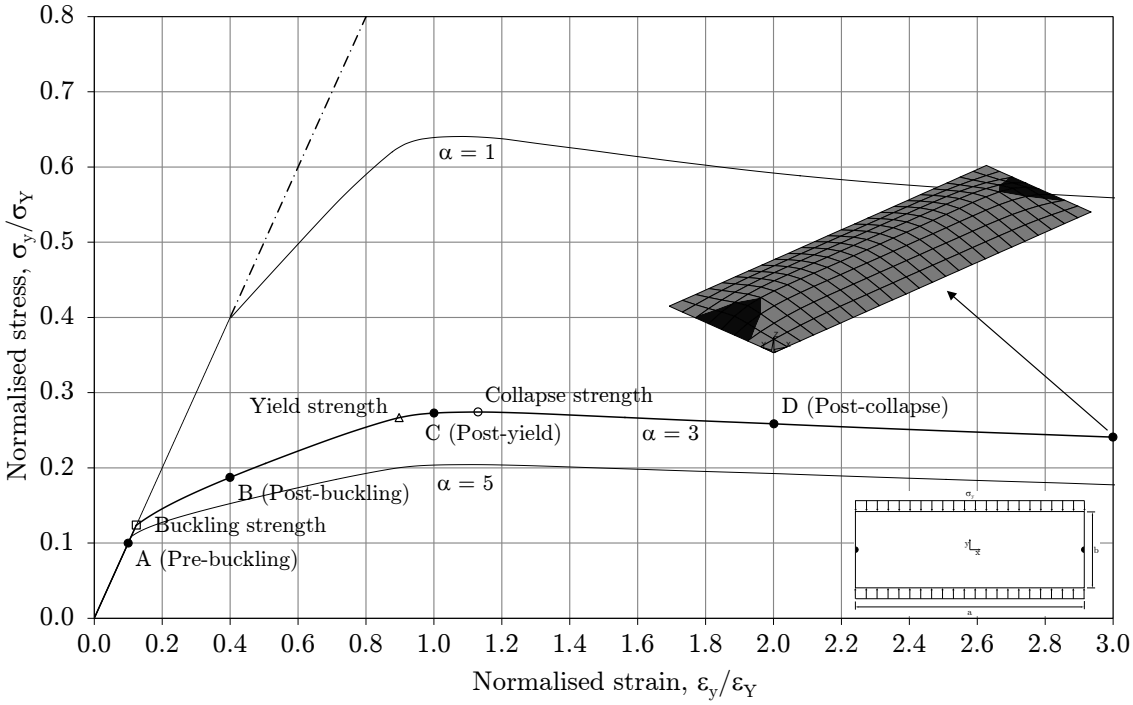

Figure 2.42.: Stress-strain curve of ideal plate under transverse compression ($\beta = 3$).

longer edges of the plate, i.e. transverse stresses σ_y. Once again, the plate has an elastic buckling stress $\sigma_{y,cr}$ which is well below its yield stress σ_Y and collapse strength $\sigma_{y,ult}$. When longitudinal stresses σ_x are applied to the shorter edges, the plate deflects into $\alpha = 3$ square buckles with the response within each buckle as described for a square plate in §2.1.1. In case the length of the plate is not an exact multiple of its width, then the plate deflects into the number of buckles which minimises the deflection energy. Because the energy of *nearly* square buckles will always be slightly higher than that for *perfectly* square buckles, the ultimate strength of the former under a single longitudinal stress is always slightly higher. Accordingly, in terms of their longitudinal strength, plates may generally be regarded as square. For this reason, only rectangular plates under transverse stresses are discussed in this section.

Pre-buckling

With the initial application of a uniaxial (transverse) load, stresses and strains are uniform throughout the plate with a linear relationship between them defined by the *modulus of elasticity*, $E = \sigma_y/\epsilon_y$. For the load corresponding to point A on the curve ($\sigma_y/\sigma_Y = 0.1$), the principal stresses in the middle plane of the plate are plotted in Figure 2.43(a). During this phase of the response, the stress-strain curve is exactly the same as for a square plate. Once again, no Poisson effects are evident in these stresses since the edges of the plate, although straight, are otherwise able to move freely in-plane.

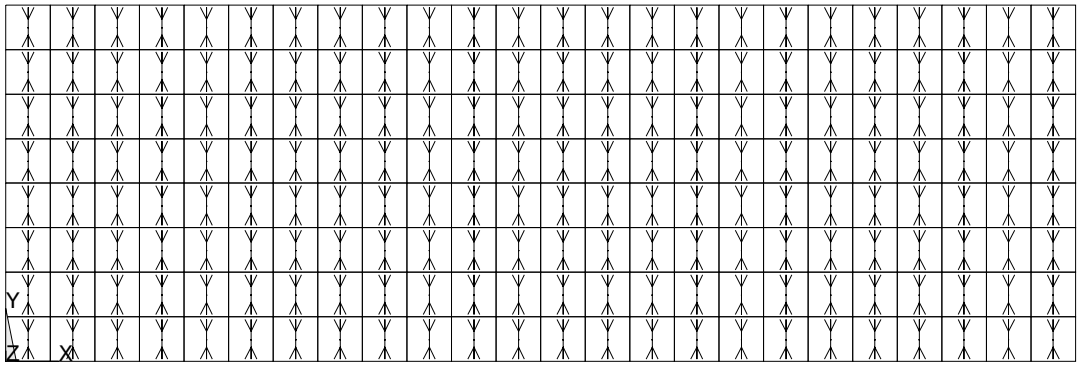

(a) Pre-buckling (Point A)

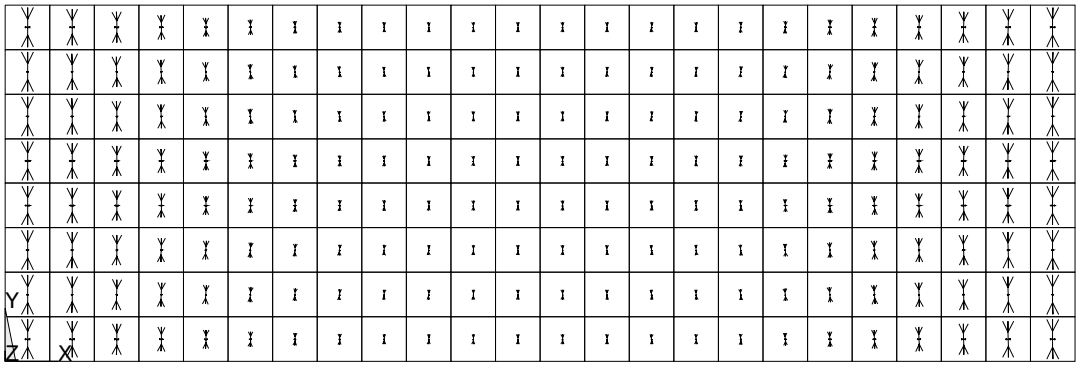

(b) Post-buckling (Point B)

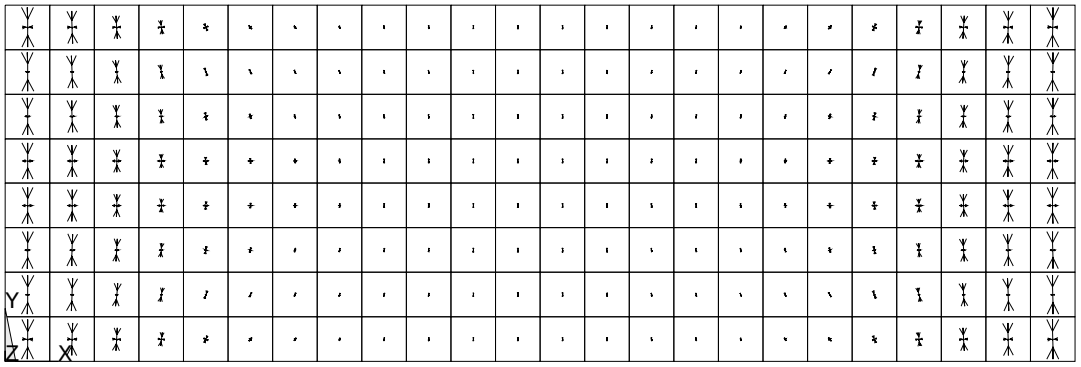

(c) Post-yield (Point C)

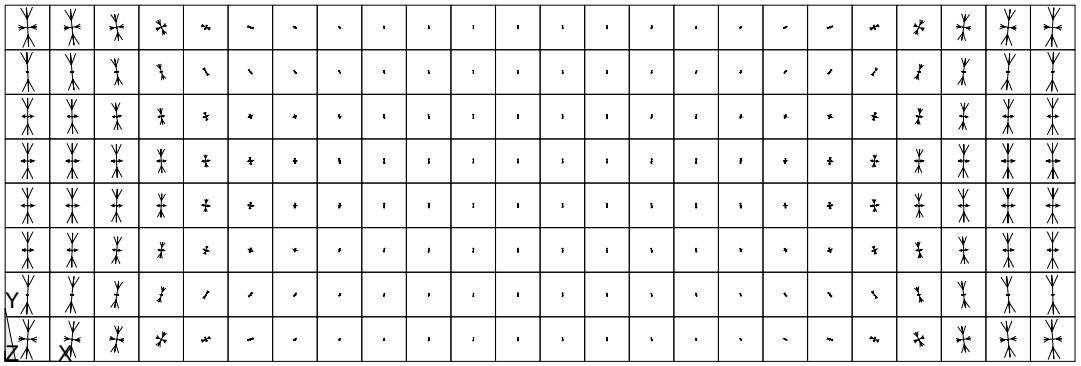

(d) Post-collapse (Point D)

Figure 2.43.: Principle stresses in middle plane of ideal plate ($\alpha = 3$, $\beta = 3$).

Buckling strength

As the load is increased, the linear relationship between stress and strain continues until the *buckling strength* of the plate is reached. At this point, as explained in the case of square plates, there exists an alternative (out-of-plane) deflection shape for which the elastic strain energy is equal to that of the compressed plane plate. Upon buckling (under the slightest of perturbations), the so-called *non-developable* deflection seen in §2.1.1 for a square plate occurs at the ends of rectangular plates. However, the central portion of rectangular plates is far enough removed from the out-of-plane restraint at the ends to permit *developable* deflection. This type of deflection is often referred to as *beam* bending although *wide column* (or *cylindrical*) bending is more correct since the anticlastic curvature which occurs in beam bending (due to Poisson effects) is prevented in continuous plating [9] (it is for this reason that the *effective* modulus of elasticity for buckled plates is defined as $E/(1-\nu^2)$). As the relative amount of *developable* bending increases, the relative amount of deflection energy decreases. Accordingly, as shown in Figure 2.42, the critical transverse buckling stress of a plate $\sigma_{y,cr}$ decreases with increasing aspect ratio α. This is reflected in the equation for the buckling factor $K_y = (1+1/\alpha^2)^2$ under a transverse load which for a plate aspect ratio $\alpha = \infty$ results in an elastic buckling strength which is 25% of that for a square plate or a rectangular plate under a longitudinal load. The resulting out-of-plane deflection in the central region of post-buckled plating leads expectedly to a redistribution of stresses towards its ends and a lower axial stiffness.

Post-buckling

Accordingly, the *post-buckling* portion of the stress-strain curve is characterised by a reduced slope which, again due to increased cylindrical bending, decreases with increasing plate aspect ratio. In Figure 2.43(b) the principal stresses associated with point B ($\epsilon_y/\epsilon_Y = 0.4$) are shown. Here the redistribution of transverse stresses towards the short edges of the plate is clearly evident as is the emergence of stresses in the longitudinal direction. As in the case of square plates, *tensile* stresses in the longitudinal direction form around mid-breadth of the buckled plate due to the out-of-plane deflection and *compressive* stresses arise along the long edges of the plate to balance in-plane forces. However, as can be seen, these effects are limited to the ends of the plate (i.e. $0 \leqslant x \lesssim b/2$ and $a - b/2 \lesssim x \leqslant a$) where the deflection is *non-developable*.

Yield strength

As the transverse load is increased further, the out-of-plane deflections are magnified leading to a non-linear increase in stresses at the ends of the plate until the *yield stress* in the middle plane is reached. Here again yielding initiates at the mid-breadth edges of the plate, i.e. $y = b/2$ (see corner inset in Figure 2.42), where the (compressive) transverse stresses and (tensile) longitudinal stresses are working together to deform the plate material. As always, yielding in the middle plane of the plate is indicative of through-thickness plasticity and is typically a precursor to collapse. In case of very thick plates (e.g. $\beta = 1$), the out-of-plane deflections are only slightly magnified (i.e. due to the comparatively high elastic buckling stress) such that the (tensile) longitudinal stresses at the mid-breadth edges

of the plate are quite small. Accordingly, initial yielding may occur towards the corners of the plate where shear stresses (particularly in the y-z and x-z planes due to rotations) contribute more to the equivalent stresses (i.e. the assumptions of plane stress are no longer valid). However, in such cases the equivalent stress at the mid-breadth edges of the plate is only slightly less than that at the location of initial yield (i.e. approximately 1% in case of $\alpha = 3$ and $\beta = 1$).

Post-yield

With further increases in transverse load, plastic flow begins to spread throughout the middle plane, leading to progressive losses in stiffness at the short edges of the plate such that the *post-yield* portion of the stress-strain curve is characterised by a decreasing slope. In Figure 2.43(c) the principal stresses associated with point C ($\epsilon_y/\epsilon_Y = 1.0$) in the post-yield response are shown. Here it can be seen that the transverse stresses at the short edges of the plate are several times the magnitude of transverse stresses in the central region due to the ever increasing out-of-plane deflection in the buckled plate. This deflection is also reflected in the increased magnitude of longitudinal stresses at the short edges of the plate.

Collapse strength

Eventually the slope of the stress-strain curve reaches zero, thereby defining the *collapse strength* or *ultimate strength* of the plate. In Figure 2.42 the normalised collapse stress is seen to be approximately $\sigma_{y,ult}/\sigma_Y = 0.27$ which represents a 57% decrease in the collapse stress compared to a plate with an aspect ratio $\alpha = 1$. For a plate with an aspect ratio $\alpha = 5$, the normalised collapse stress is seen to be approximately $\sigma_{y,ult}/\sigma_Y = 0.20$ which represents a 25% decrease in the collapse stress compared to a plate with an aspect ratio $\alpha = 3$ and a 68% decrease in the collapse stress compared to a plate with an aspect ratio $\alpha = 1$.

Post-collapse

After collapse there is of course a reduction in the load resistance of the plate under further straining. As mentioned previously, in this *post-collapse* phase of plating response some of the load previously carried by plate must now be taken by adjacent structure if large (unrestrained) transverse displacements are to be avoided. The effects of further post-collapse straining are shown in Figure 2.43(d) for the load associated with point D of the stress-strain curve ($\epsilon_y/\epsilon_Y = 2.0$) with a plot of the yielded portion of the plate shown in Figure 2.42 for $\epsilon_y/\epsilon_Y = 3.0$.

Plates with initial deflections

Influence of plate aspect ratio

On the left-hand side of Figure 2.44, stress-strain curves are shown for initially deflected plating ($\delta_0 = b/200$) with an aspect ratio $\alpha = 3$. As for the square plates examined in §2.1.3, these curves are characterised from the outset by a loss of in-plane stiffness due to

initial deflections which allow regions away from the short edges of the plate to shirk some of the transverse shortening that is occurring fully at the short edges. As a result, the stress-strain curves deviate immediately from the elastic modulus curve ($\sigma_y/\epsilon_y = E$) over a wide range of plate slenderness parameters. Corresponding to the peaks of these curves, the curve of *effective lengths* (or *plate reduction factors*) is shown on the right-hand side of Figure 2.44 as a function of the plate slenderness parameter β. Similar curves are also shown for $\alpha = 1$, $\alpha = 5$ and $\alpha = \infty$, the latter representing 100% cylindrical bending. Here the influence of aspect ratio on the collapse strength of plates under transverse loads can be seen (especially for slender plates). As shown, this influence is clearly non-linear with the influence of plate aspect ratio diminishing rapidly beyond $\alpha = 3$ as cylindrical bending becomes increasingly dominant.

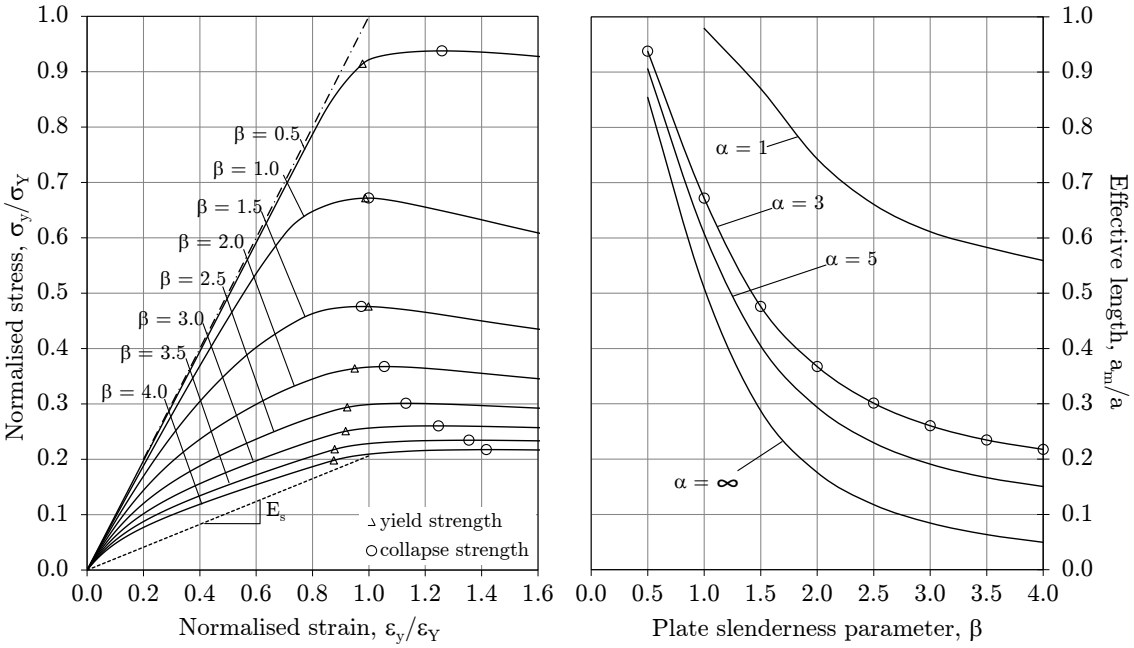

Figure 2.44.: Stress-strain curves ($\alpha = 3$) and effective length of plates with initial deflections.

Effective length curves from literature

As described in §2.1.3, the *plate secant modulus* E_s has been calculated for each of the stress-strain curves on the left-hand side of Figure 2.44 (as shown for $\beta = 4$) and normalised against the plate elastic modulus E. The resulting curves of effective length are shown in Figures 2.45 and 2.46 for $\alpha = 3$ and $\alpha = 5$, respectively, based on the approach of Chatterjee and Dowling [14]. As can be seen, this approach once again yields good results.

Alternative approaches to deriving effective length curves for plates under transverse loading can be found in the literature such as that provided by Faulkner et al. [46], but for which the French classification society Bureau Veritas (BV) is credited

$$\kappa_y = \frac{a_m}{a} = \frac{0.9}{\beta^2} + \frac{1.9}{\alpha \cdot \beta}\left(1 - \frac{0.9}{\beta^2}\right) \tag{2.63}$$

Results using this formulation are also shown in Figures 2.45 and 2.46 and are shown to

be rather non-conservative.

However, a more physical approach to deriving effective length curves has been suggested by Valsgård [34]. As shown on the left-hand side of Figure 2.47, Valsgård assumes that the collapse strength at the ends of a rectangular plate is equal to that of a square plate (i.e. $\kappa_x \cdot \sigma_Y$) while the collapse strength of the remaining central portion is equal to that for cylindrical bending. Accordingly, the normalised difference between plate length and width, i.e. $\rho = (a-b)/a = 1-b/a$, acts as a weighting factor ρ for *cylindrical* bending

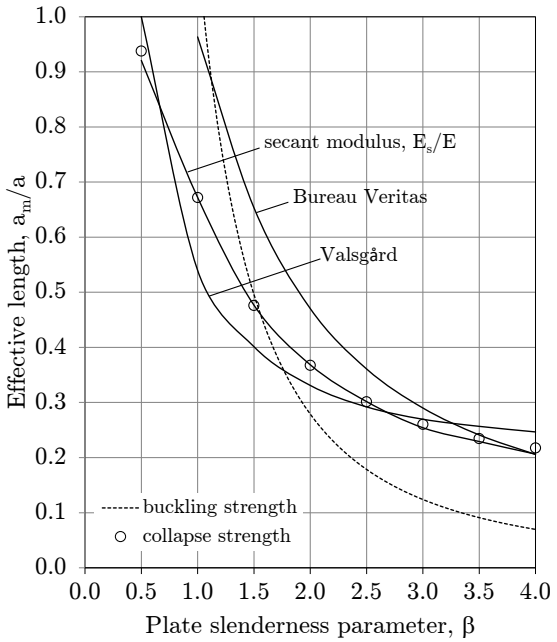

Figure 2.45.: Effective length curves from literature ($\alpha = 3$).

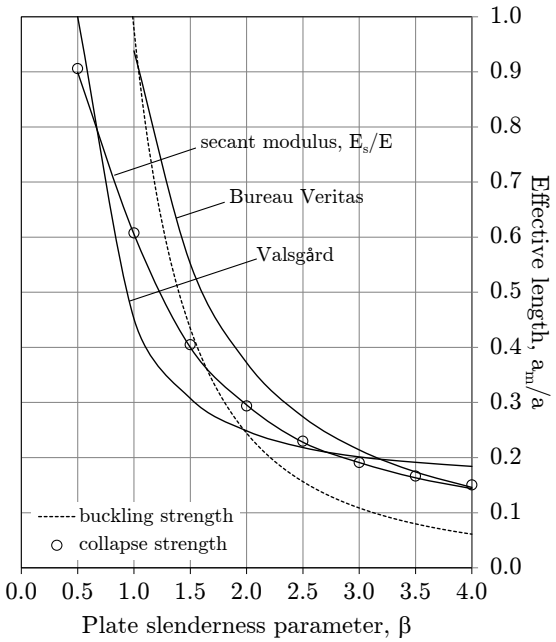

Figure 2.46.: Effective length curves from literature ($\alpha = 5$).

$$\kappa_y = \frac{a_m}{a} = \frac{b}{a} \cdot \kappa_x + \left(1 - \frac{b}{a}\right) \cdot \kappa_{wc} \tag{2.64}$$

where κ_{wc} equals the normalised collapse stress of a wide column, for which Valsgård worked backwards from reference solutions based on finite element analyses to obtain

$$\kappa_{wc} = 0.08 \cdot \left(1 + \frac{1}{\beta^2}\right)^2 \tag{2.65}$$

For the collapse strength of a square plate, Valsgård used Equation (2.26) of Faulkner as presented in §2.1.4

$$\kappa_x = \frac{2}{\beta} - \frac{1}{\beta^2} \tag{2.66}$$

Results based on Valsgård's approach are shown in Figures 2.45 and 2.46.[16] As can be seen, the formulation works well for plating of slenderness $2.5 \leqslant \beta \leqslant 3.0$, but becomes

[16] In order to eliminate any errors associated with the collapse strength of plates, the values of κ_x obtained with finite element analyses are here used in lieu of those calculated with Equation (2.66).

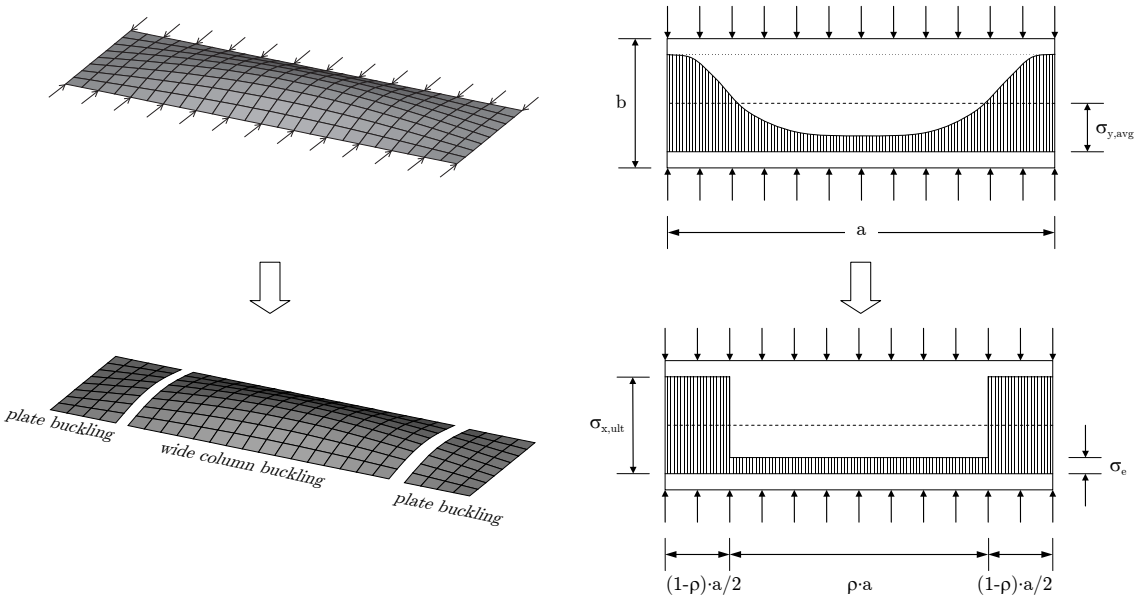

Figure 2.47.: Effective length concept for transverse stresses.

non-conservative for more slender plating and conservative for more sturdy plating. To generalise the approach of Valsgård for any ratio of plate and wide column collapse, Equation (2.64) can be rewritten as

$$\kappa_y = \frac{a_m}{a} = (1-\rho)\cdot\kappa_x + \rho\cdot\kappa_{wc} \tag{2.67}$$

as illustrated on the right-hand side of Figure 2.47, where $\rho = 1 - b/a$ in case of Valsgård's approach.

Effective length formulae used in shipbuilding

In the particular case of the classification of ships, two effective length formulae have become prevalent, one based on the Johnson-Ostenfeld correction and the other based on the German construction standard DIN 18800 [26]. As shown in §2.1.4, the Johnson-Ostenfeld correction is used to adjust the elastic buckling curve to account for plasticity. This approach is most prominently used in the *IACS Longitudinal Strength Standard* UR S11 [20]. The calculation proceeds by obtaining the buckling factor K_y from which the reference degree of slenderness λ_y can be determined

$$\lambda_y = \beta\sqrt{\frac{12(1-\nu^2)}{\pi^2\cdot K_y}} \tag{2.68}$$

The Johnson-Ostenfeld correction is then calculated as described previously

$$\kappa_y = \frac{\sigma_{y,ult}}{\sigma_Y} = \begin{cases} 1 - \dfrac{\lambda_y^2}{4} & \lambda_y < \sqrt{2} \\ \dfrac{1}{\lambda_y^2} & \lambda_y \geqslant \sqrt{2} \end{cases} \tag{2.69}$$

Capacity curves obtained using this approach are shown in Figures 2.48 and 2.49 for plates with aspect ratios $\alpha = 3$ and $\alpha = 5$, respectively, where the shipbuilding nomenclature *plate reduction factor* κ_y is reintroduced. As can be seen, reduction factors obtained with the Johnson-Ostenfeld correction are rather conservative for slender plates.

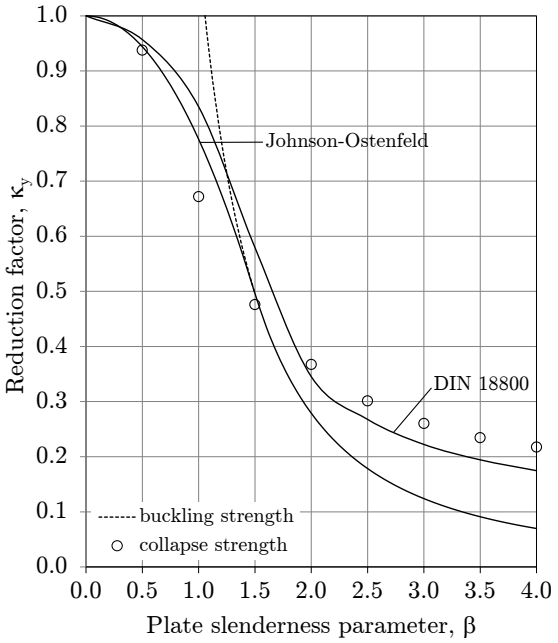

Figure 2.48.: Reduction factor curves from shipbuilding industry ($\alpha = 3$).

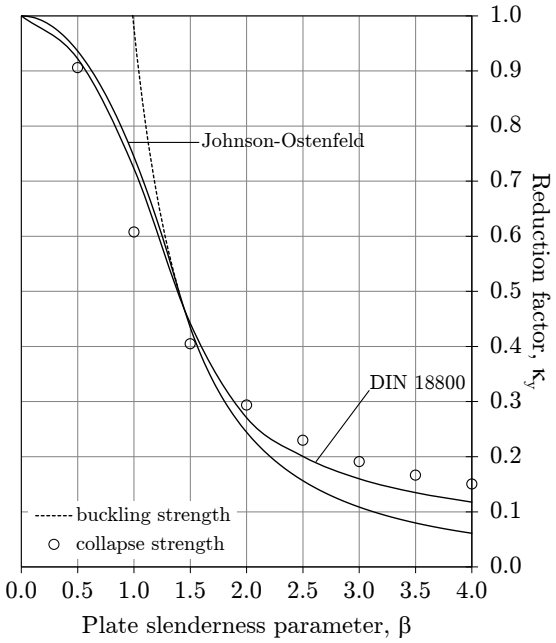

Figure 2.49.: Reduction factor curves from shipbuilding industry ($\alpha = 5$).

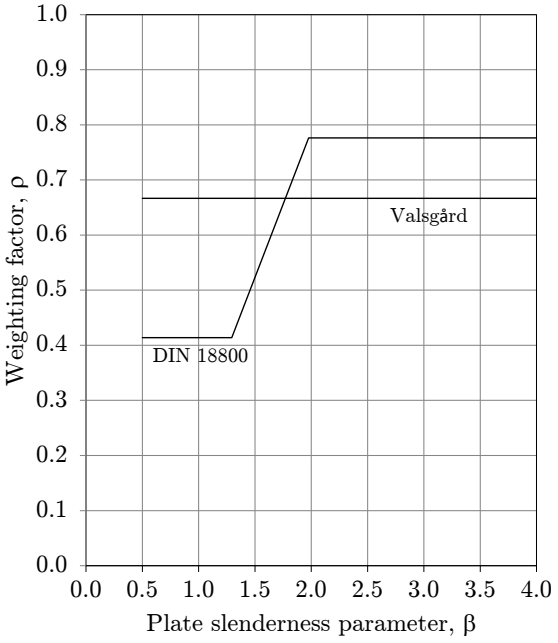

Figure 2.50.: Weighting factors ($\alpha = 3$).

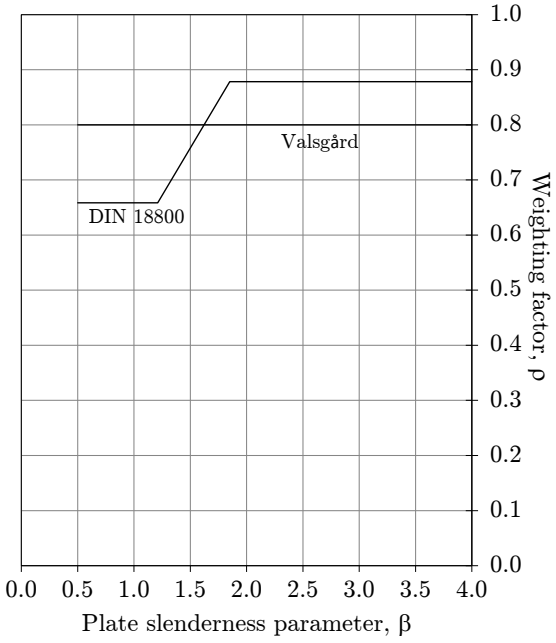

Figure 2.51.: Weighting factors ($\alpha = 5$).

In DIN 18800 the approach used in obtaining the transverse strength of plates is similar to that used by Valsgård, but the calculation of the reduction factors κ_x and κ_{wc}, as well as the weighting factor ρ, are different. While the plate reduction factor κ_x is of course based on the experimentally and numerically derived expression shown in Equation (2.24) as found in Part 3 of DIN 18800 (Analysis of safety against buckling of plates), the reduction factor for wide column buckling κ_{wc} is based on an expression found in Part 2 (Analysis of safety against buckling of linear members and frames) [47]

$$\kappa_{wc} = \begin{cases} 1 & \lambda_y \leqslant 0.2 \\ \dfrac{1}{k + \sqrt{k^2 - \lambda_y^2}} & \lambda_y > 0.2 \end{cases} \tag{2.70}$$

where $k = 0.5[1 + \zeta \cdot (\lambda_y - 0.2) + \lambda_y^2]$. In case $\lambda_y > 3.0$, Equation (2.70) may be simplified to

$$\kappa_{wc} = \frac{1}{\lambda_y \cdot (\lambda_y + \zeta)} \tag{2.71}$$

where the value of ζ is based on the type of cross-section and the axis about which it buckles[17]. When the German classification society Germanischer Lloyd (GL) revised its proof of buckling strength on the basis of DIN 18800, a value of $\zeta = 0.34$ was used. Finally, in terms of Equation (2.67), the weighting factor ρ is calculated as follows

$$\rho = \left(\frac{\Lambda - K_y/(1-\nu^2)}{\Lambda - 1} \right)^2 \geqslant 0 \tag{2.72}$$

where $\Lambda = \lambda_y^2 + 0.5$, with $2 \leqslant \Lambda \leqslant 4$. Weighting factors obtained with this equation are compared to those obtained with Valsgård's approach in Figures 2.50 and 2.51. Results obtained with the DIN 18800 formulae are also shown in Figures 2.48 and 2.49. As can be seen, the results are more accurate for slender plating compared to the Johnson-Ostenfeld plasticity correction, but are slightly more non-conservative for sturdy plates (in case $\alpha = 3$). The DIN 18800 formulations, first implemented in the buckling strength requirements of GL [30], have since been implemented in the buckling strength requirements of CSR BC [31], CSR OT [32], CSR BC & OT [23], UR S11A [8] as well as the new *DNVGL Rules for Classification* [33] which are applicable to all ship types.

2.4.2. Biaxial loads

Compressive secondary stresses

For a plate with an aspect ratio $\alpha = 3$, three fundamental eigenmodes[18] are possible under biaxial compression as shown in Figure 2.52, where m equals the number of half-waves in the longitudinal direction of the plate, i.e. in the x-direction. For a perfect plate without any initial deflections, the plate will deflect into one of these eigenmodes upon reaching the elastic buckling stress (again with the slightest of perturbations) depending on the ratio

[17] As can be seen, Equation (2.71) reduces to the Euler hyperbola in case $\zeta = 0$.

[18] The *fundamental eigenmode* or *first eigenmode* is the mode of deflection associated with the lowest *eigenvalue*.

of stresses in the x- and y-directions ($c = \sigma_y/\sigma_x$). In case of real plates (which always have some level of initial deflections), the plate may snap into its fundamental eigenmode provided the magnitude of initial deflection is sufficiently small. With initial deflections of greater magnitude, the energy required for this to occur may be too great for any mode change to occur. This in turn leads to a higher plate capacity than if the plate deflects according to its fundamental eigenmode, a fact which has implications for choosing initial deflection shapes and magnitudes in finite element analyses (as discussed in Appendix B).

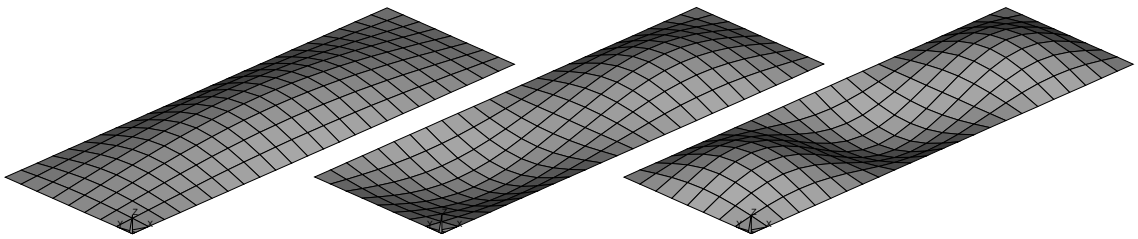

(a) $m = 1$ (b) $m = 2$ (c) $m = 3$

Figure 2.52.: Fundamental eigenmode shapes.

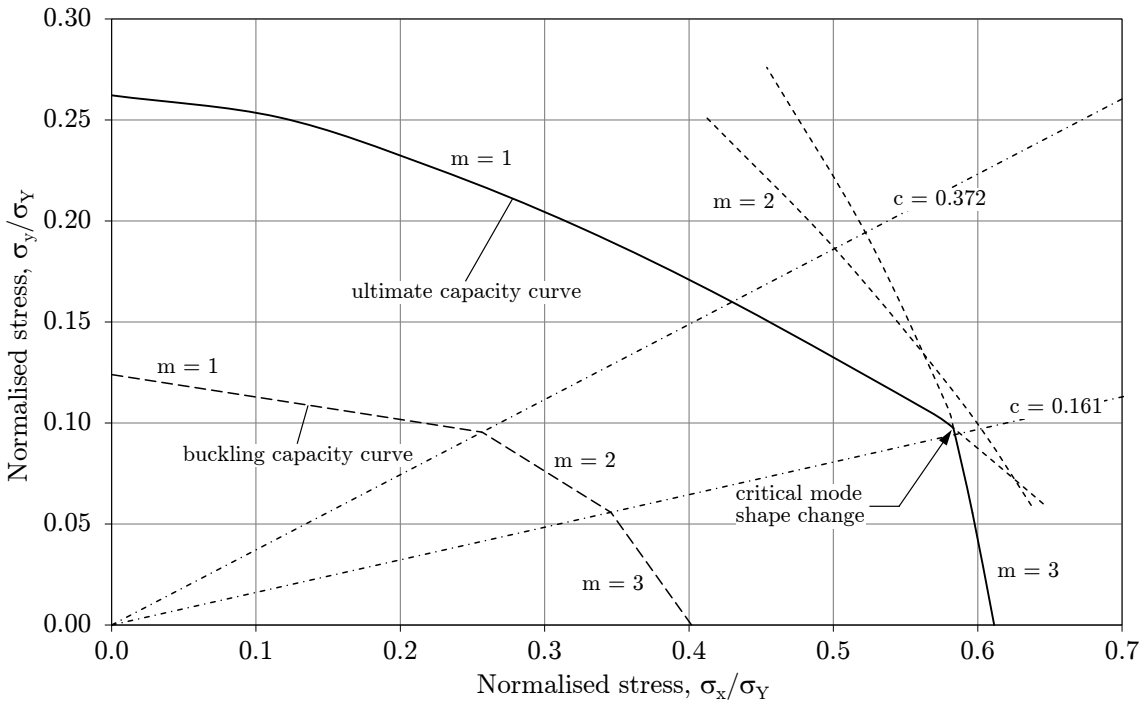

Figure 2.53.: Ultimate capacity curve for rectangular plate ($\alpha = 3$, $\beta = 3$).

In Figure 2.53 the tangent $c = \sigma_y/\sigma_x = 0.161$ indicates the transition ratio between eigenmodes with $m = 1$ half-wave and $m = 2$ half-waves. Similarly, the tangent $c = \sigma_y/\sigma_x = 0.372$ indicates the transition ratio between eigenmodes with $m = 2$ half-waves and $m = 3$ half-waves. These transition values of c remain constant for all plates with an aspect ratio $\alpha = 3$, regardless of the plate slenderness parameter β. This is evident in the following condition provided by Paik and Thayamballi [35] with which to determine the buckling half-wave number, m

$$\frac{(m^2/a^2 + 1/b^2)^2}{m^2/a^2 + c/b^2} \leqslant \frac{[(m+1)^2/a^2 + 1/b^2]^2}{(m+1)^2/a^2 + c/b^2} \tag{2.73}$$

For a plate of slenderness $\beta = 3$, Figure 2.53 also shows the buckling capacity curve as well as segments of the capacity curves using initial deflection shapes based on the three fundamental eigenmodes shown in Figure 2.52 ($\delta_0 = b/200$). As can be seen, for an ideal plate (or plate with small initial deflections), the plate will buckle into three half-waves in the x-direction when $c \leqslant 0.161$, which is then the critical deflection shape at collapse. Similarly, an ideal plate (or plate with small initial deflections) will buckle into one half-wave in the x-direction when $c \geqslant 0.372$, which is then the critical deflection shape at collapse. However, although an ideal plate (or plate with small initial deflections) will buckle into two half-waves in the x-direction when $0.161 < c < 0.372$, this is not the critical deflection shape at collapse. Rather, the critical deflection shape is either $m = 1$ or $m = 3$ depending on the value of c. Here the change in critical mode shape at collapse (i.e. between $m = 3$ and $m = 1$) occurs at $c = \sigma_y/\sigma_x = 0.167$. Accordingly, whereas the ultimate capacity curve for square plates are always symmetric (see the right-hand side of Figure 2.18), plates with an aspect ratio $\alpha > \sqrt{2}$ (according to Equation (2.73) when $c = 0$) will in general have a discontinuity in the ultimate capacity curve where the critical mode shape changes. Plates with irregular initial deflections of large magnitudes will be discussed in Chapter 5.

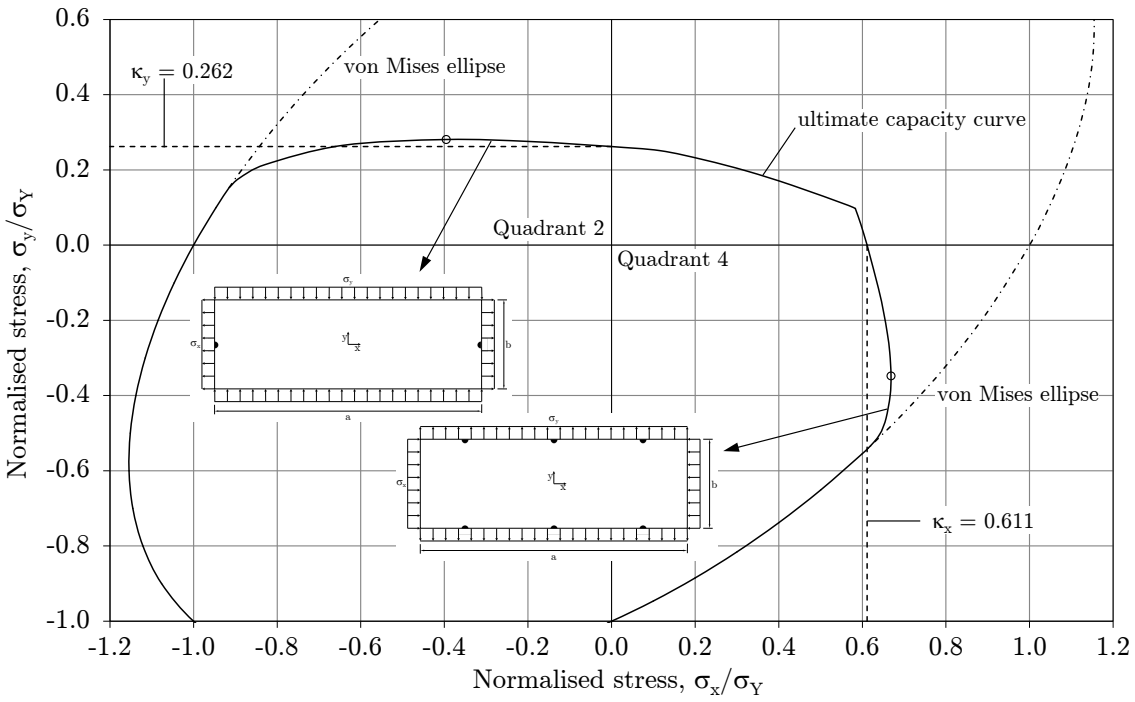

Figure 2.54.: Capacity curves for rectangular plate under tension ($\alpha = 3$, $\beta = 3$).

Tensile secondary stresses

In case of tensile secondary stresses, the capacity curves of plates with an aspect ratio $\alpha = 3$ are shown in Figure 2.54 where the ultimate capacity curve shown in Figure 2.53

is extended beyond Quadrant 1 to show the effects of tensile stresses. To help illustrate the effect of tensile stresses, reference lines are drawn for the capacity of the plate under uniaxial compressive loads (i.e. $\kappa_x = 0.611$ and $\kappa_y = 0.262$). Under a uniaxial compressive load in the y-direction, as explained in §2.4.1, yielding initiates at the mid-breadth edges of the plate (i.e. $y = b/2$, see inset in Figure 2.54), where the (compressive) transverse stresses $\sigma_{y,i}$ and (tensile) longitudinal stresses $\sigma_{x,i}$ are working together to deform the plate material. With the application of a tensile secondary stress in the x-direction, the first order effect is an increase of tensile stresses $\sigma_{x,i}$ in the middle plane of the plate. However, in terms of plate capacity, the more significant second order effect of applied tensile stresses in the x-direction is to restrain out-of-plane deflections, thereby mitigating the redistribution of compressive stresses $\sigma_{y,i}$ towards the short edges of the plate, i.e. increasing the effective length a_m of the plate.

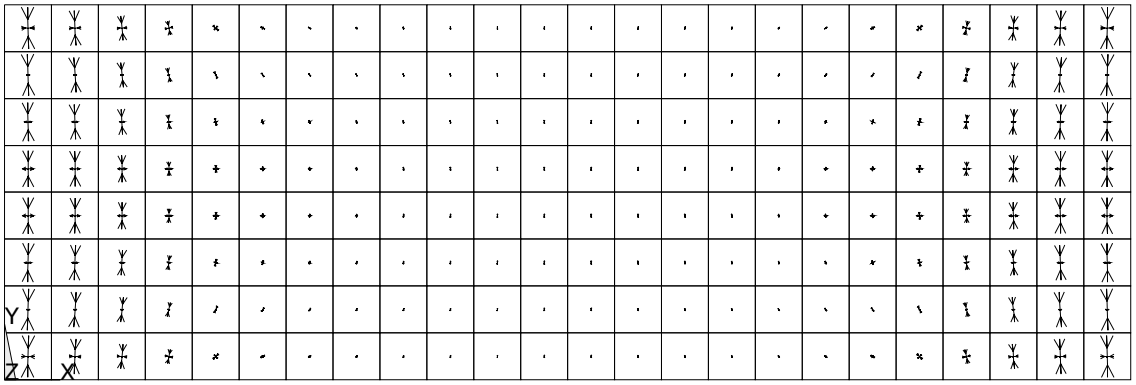

(a) $R_x = 0$

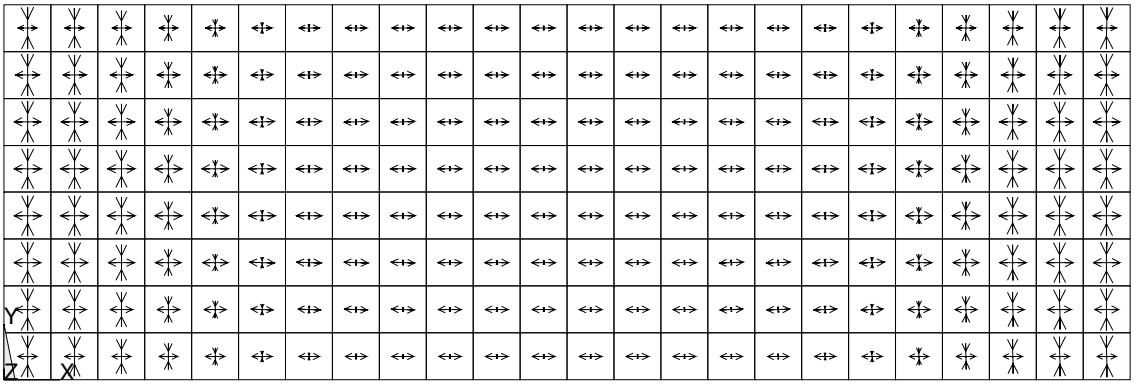

(b) $R_x = -0.40$

Figure 2.55.: Principle stresses in middle plane of rectangular plate ($\alpha = 3$, $\beta = 3$) - Quadrant 2.

This can be seen in the distribution of principal stresses in the middle plane of the plate at collapse. In Figure 2.55(a), these stresses show that the transverse load is taken by an effective length of plating concentrated at the short edges of the plate. For the plate under consideration ($\alpha = 3$, $\beta = 3$), capacity increases with tensile stresses applied in the x-direction, reaching a maximum at about $\sigma_x \sim -0.40 \cdot \sigma_Y$. For this stress combination, the distribution of principal stresses in the middle plane of the plate at collapse are shown in Figure 2.55(b). As can be seen in the distribution of principal stresses (normalised

against the principal stress of greatest magnitude), the effective length of the plate a_m is significantly greater compared to that in Figure 2.55(a), i.e. more of the plating away from the short edges is carrying the applied transverse load. For tensile stresses $\sigma_x < -0.40 \cdot \sigma_Y$, the incremental (second order) effect of lower compressive stresses in the y-direction (due to restrained out-of-plane deflections) become increasingly smaller relative to the first order effect of increased tensile stresses in the x-direction. In fact, once the applied tensile stresses reach approximately $\sigma_x = -0.65 \cdot \sigma_Y$, the capacity of the plate in the y-direction is again equal to that under a uniaxial compressive stress, i.e. $\sigma_x = 0$. Beyond this point, increasing tensile stresses in the x-direction continue to lower the capacity of the plate in the y-direction. As compressive stresses in the y-direction are reduced, so too are the out-of-plane deflections and accompanying redistribution of stresses until the capacity curve eventually merges into the von Mises ellipse which defines gross yielding of a perfectly plane plate.

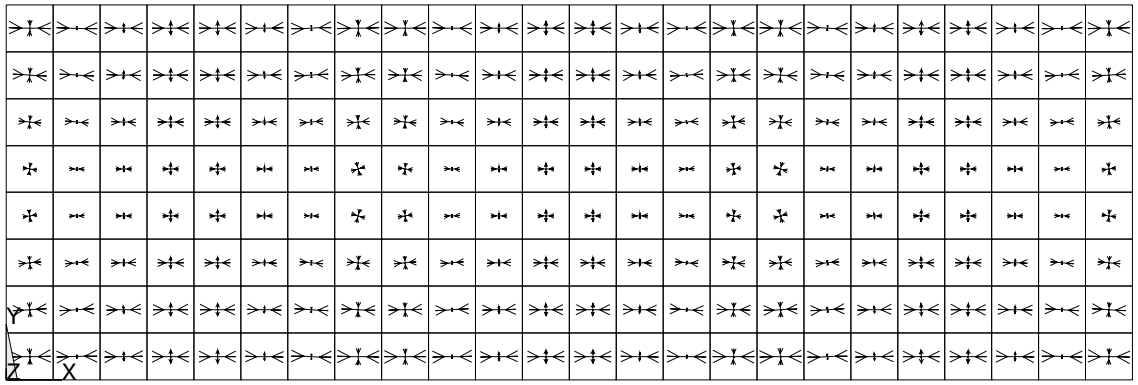

(a) $R_y = 0$

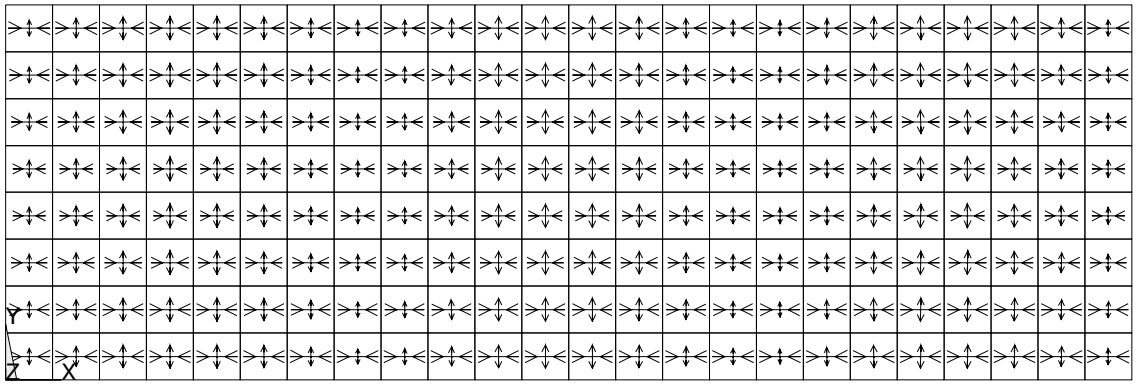

(b) $R_y = -0.35$

Figure 2.56.: Principle stresses in middle plane of rectangular plate ($\alpha = 3$, $\beta = 3$) - Quadrant 4.

Similarly, under a uniaxial compressive load in the x-direction, yielding initiates at the mid-length edges of the (square) buckles in the plate, i.e. $x = b/2$, $x = 3 \cdot b/2$ and $x = 5 \cdot b/2$ (see inset in Figure 2.54), where the (compressive) longitudinal stresses $\sigma_{x,i}$ and (tensile) transverse stresses $\sigma_{y,i}$ are working together to deform the plate material. With the application of a tensile secondary stress in the y-direction, the first order effect is again an increase of tensile stresses $\sigma_{y,i}$ in the middle plane of the plate. More significantly, in

terms of plate capacity, the second order effect of applied tensile stresses in the y-direction is to restrain out-of-plane deflections, thereby mitigating the redistribution of compressive stresses $\sigma_{x,i}$ towards the long edges of the plate (i.e. increasing the effective width b_m of the plate). In fact, because *transverse* tensile stresses are more effective at restraining out-of-plane deflections (i.e. acting along the entire length of the plate and across its relatively short breadth), the second order effects in Quadrant 4 are even greater than those in Quadrant 2. Accordingly, as shown in Figure 2.54, the corresponding increase in capacity is markedly greater with the maximum increase under a tensile stress of $\sigma_y \sim -0.35 \cdot \sigma_Y$ occurring comparably close to the von Mises ellipse.

The foregoing effects of tensile secondary stresses can again be seen in the distribution of principal stresses in the middle plane of the plate at collapse. In the absence of tensile secondary stresses, the redistribution of compression stresses $\sigma_{x,i}$ towards the long edge of the plate is clearly visible in Figure 2.56(a). Moreover, the out-of-plane deflections associated with a buckled plated are clearly reflected in the redistribution of transverse stresses $\sigma_{y,i}$. Conversely, in the presence of tensile secondary stresses ($\sigma_y \sim -0.35 \cdot \sigma_Y$), the mitigation of out-of-plane deflections is such that the distribution of principal stresses in the middle plane of the plate look similar to those of a plate which has collapsed under gross yielding without any buckling. Accordingly, in Quadrant 4 the capacity of plating in the x-direction is generally greater under tensile secondary stresses, excluding those stress combinations lying on the von Mises ellipse. As will be shown in Chapter 4, this demonstrable increase of capacity under tensile loads enables an approach to calculating ultimate plate capacity in Quadrants 2 and 4 which has heretofore not been used in the shipbuilding industry.

2.4.3. In-plane shear

Description of collapse

As in the case of ideal square plates, the principal in-plane stresses of ideal (pre-buckled) rectangular plates under a pure shear load τ_{xy} are again oriented $\pm 45°$ to the x-axis with magnitudes $\sigma_1 = -\tau_{xy}$ (tension) and $\sigma_2 = \tau_{xy}$ (compression). Although the stabilising influence of a tensile stress perpendicular to the compression stress (and of equal magnitude) again ensures that the elastic buckling strength of plates under pure shear is generally higher than that under a uniaxial load, it does decrease with the plate aspect ratio α according to the equation for the buckling factor $K_\tau = 5.34 + 4/\alpha^2$. As in the case of rectangular plates under transverse compression, this loss of strength reflects the diminishing effect of the out-of-plane restraint at the short edges of the plate, i.e. a function of the plate aspect ratio α. Once the shear buckling strength is exceeded, the post-buckled deflection shape of rectangular plates is generally characterised by multiple shear buckles rather than a single shear buckle as in the case of square plates. The number of shear buckles depends on the plate aspect ratio α, where shear buckles with an aspect ratio of 1.25 generally minimise the internal strain energy of the plate [9]. Accordingly, as shown in Figure 2.57, plates with an aspect ratio of $\alpha = 3$ develop $3/1.25 \sim 2$ buckles while plates with an aspect ratio of $\alpha = 5$ develop $5/1.25 = 4$ buckles.

Therefore, because rectangular plates under pure shear behave as a series of plates with an aspect ratio $\alpha = 1.25$, the post-buckling, post-yield and post-collapse phases of the response are similar to that for a square plate (as described in §2.3), including the development of influential tension bands. Initial yield of rectangular plates again occurs in

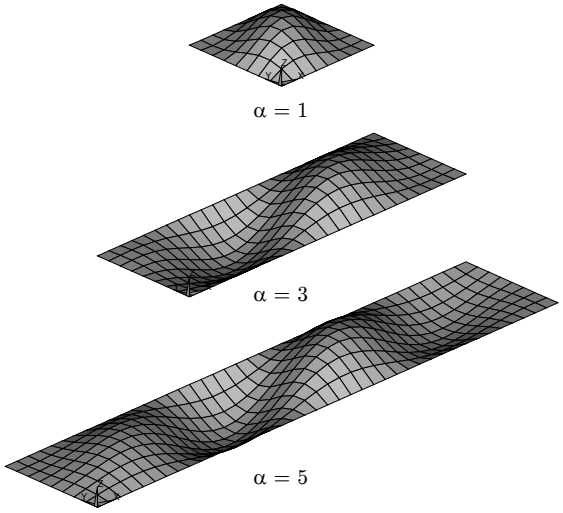

Figure 2.57.: Eigenmodes under pure shear.

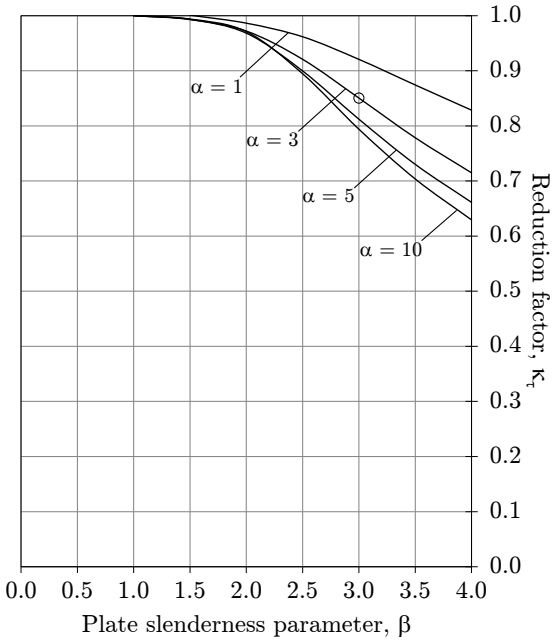

Figure 2.58.: Reduction factor curves.

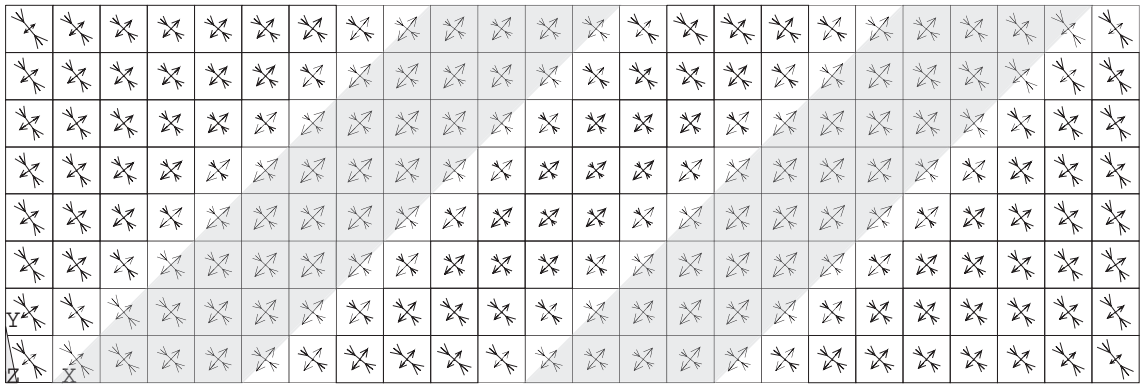

Figure 2.59.: Principle stresses at collapse in middle plane of rectangular plate under pure shear ($\alpha = 3$, $\beta = 3$).

the centre of these bands where tensile stresses are dominant and working together with (perpendicular) compressive stresses to deform the material. With further increases in shear load, plastic flow again begins to spread throughout the middle plane of the plate, particularly in the central portion of the tension band, until the collapse strength of the plate is reached. The influence of aspect ratio α on this strength is shown in Figure 2.58 for plates with initial deflections ($\delta_0 = b/200$). As reflected in the buckling factor K_τ, it can be seen that the effect of the plate aspect ratio α diminishes exponentially (as in the case of rectangular plates under pure transverse loads). For a plate with an aspect ratio $\alpha = 3$ and slenderness $\beta = 3$ (indicated by the marker in Figure 2.58), the principal stresses in the middle plane of the plate at collapse are shown in Figure 2.59. Here the tension bands

which develop throughout plating response are again highlighted.

Formulae for reduction factors from literature

In §2.3.4 formulae for deriving plate reduction factors associated with pure shear were described and compared to numerical results for square plates. In terms of formulae found in the literature, those of Paik (Equation (2.56)), Nara et al. (Equation (2.57)) and Zhang et al. (Equation (2.58)) are compared in Figures 2.60 and 2.61 to numerical results for plates with aspect ratios $\alpha = 3$ and $\alpha = 5$, respectively. As noted previously, Paik's solution is always calculated for a plate aspect ratio $\alpha = 1$ such that results using his solution become progressively non-conservative with increasing plate aspect ratios. Conversely, whereas the solution of Nara et al. is rather conservative for square plates, results using this solution gradually approach those of the numerical results with increasing values of the plate aspect ratio α. Similarly, results using the solution of Zhang et al. also approach those of the numerical results for plate aspect ratios $\alpha > 1$, although the slope of the reduction curve is somewhat low (compared to that of the numerical results) such that results for slender plates tend to become non-conservative.

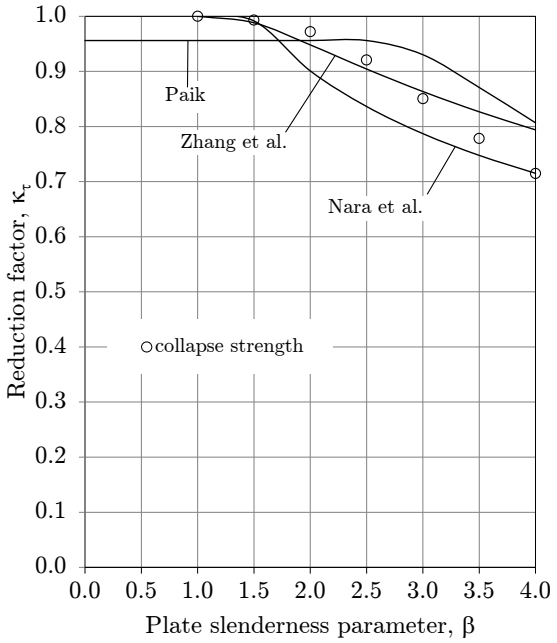

Figure 2.60.: Reduction factor curves from literature ($\alpha = 3$).

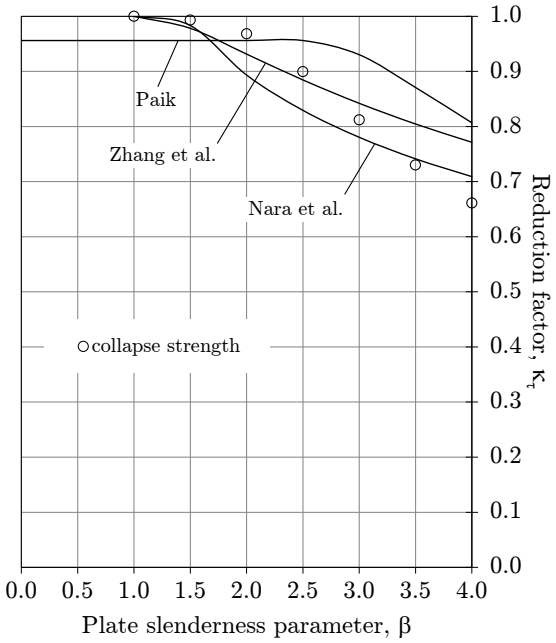

Figure 2.61.: Reduction factor curves from literature ($\alpha = 5$).

Formulae for reduction factors used in shipbuilding

In terms of the classification of ships, two proofs for the ultimate shear strength of plates widely used in the shipbuilding industry were presented in §2.3.4. The first proof is based on the Johnson-Ostenfeld correction which is used to adjust the elastic shear buckling curve to account for plasticity (Equation (2.59)) and the second proof is based on the ultimate

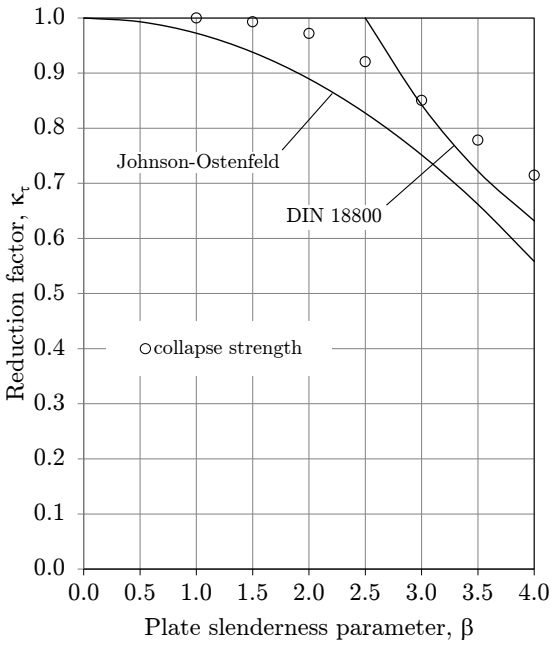

Figure 2.62.: Reduction factor curves from shipbuilding industry ($\alpha = 3$).

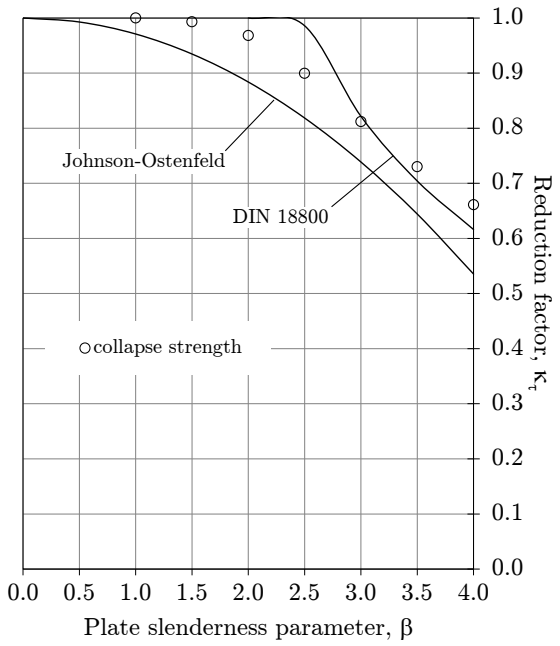

Figure 2.63.: Reduction factor curves from shipbuilding industry ($\alpha = 5$).

plate strength formulations developed for inclusion in the German construction standard DIN 18800 (Equation (2.60)). Both of these equations are compared in Figures 2.62 and 2.63 to numerical results for plates with aspect ratios $\alpha = 3$ and $\alpha = 5$, respectively. As in the case of square plates, results using the Johnson-Ostenfeld correction are relatively conservative, but follow the influence of the plate slenderness β quite well. Results obtained with the DIN 18800 formulation are slightly conservative for slender plates, but become non-conservative for sturdy plates due to the comparatively steep slopes of the associated plate reduction curves.

3. Existing Proofs

In Chapter 1 the need for a proof of plate capacity with which to reliably and efficiently design ship plating was discussed. The purpose of this chapter is to describe existing proofs of plate capacity found in literature and the shipbuilding industry, as well as to measure the accuracy and precision of each. With respect to the latter, an evaluation scheme is presented in §3.1 which measures both accuracy (or bias) and precision over a wide range of load combinations and plating configurations relevant for the shipbuilding industry. Since proofs of plate capacity are normally used for assessing structures anywhere in the ship, it is important that they be robust as well as precise and without bias. Using this evaluation scheme, existing proofs from literature are assessed in §3.2, followed by proofs from the shipbuilding industry in §3.3.

3.1. Quantitative evaluation scheme

In this section the quantitative evaluation scheme used to assess existing proofs of plate capacity in subsequent sections is described. Here the capacity according to the proofs is compared against the capacity according to finite element analyses. Firstly, the aspects of bias and precision are discussed (§3.1.1), followed by the aspect of robustness (§3.1.2). The evaluation scheme presented in this section is also used later in Chapter 4 to assess the accuracy and precision of the new proof of plate capacity.

3.1.1. Precision and bias

As noted in §2.3.5, the capacity of plates under combined axial, transverse and shear loads is described by a *failure surface* in three dimensions. Each point on the failure surface is expressed in terms of a stress vector with three components

$$\mathbf{R} = R_x\,\mathbf{i} + R_y\,\mathbf{j} + R_\tau\,\mathbf{k} \tag{3.1}$$

where $\mathbf{i}$, $\mathbf{j}$ and $\mathbf{k}$ are unit vectors and the magnitude of the stress vector $\mathbf{R}$ is *normally* defined by

$$R = \sqrt{R_x^2 + R_y^2 + R_\tau^2} \tag{3.2}$$

However, in the definition of the *buckling utilisation factor* within the *IACS Common Structural Rules for Bulk Carriers and Oil Tankers* [23], stresses are not first normalised against yield before calculating the magnitude of stress vectors. Accordingly, in order to be consistent with this approach, the magnitude of $\mathbf{R}$ in the present work is defined by

$$R = \sqrt{R_x^2 + R_y^2 + R_\tau^2/3} \tag{3.3}$$

i.e. since $R_\tau = \tau_{xy}/\tau_Y = \sqrt{3}\cdot\tau_{xy}/\sigma_Y$.

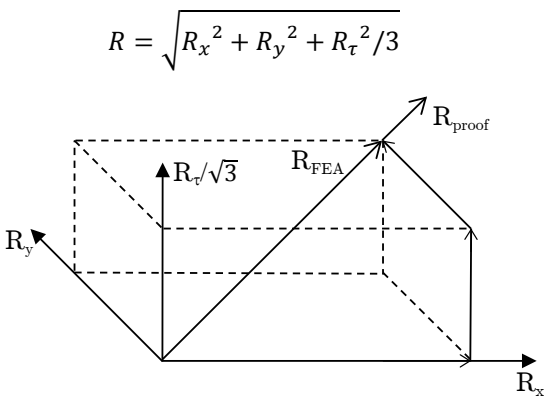

Figure 3.1.: Magnitude of stress vectors.

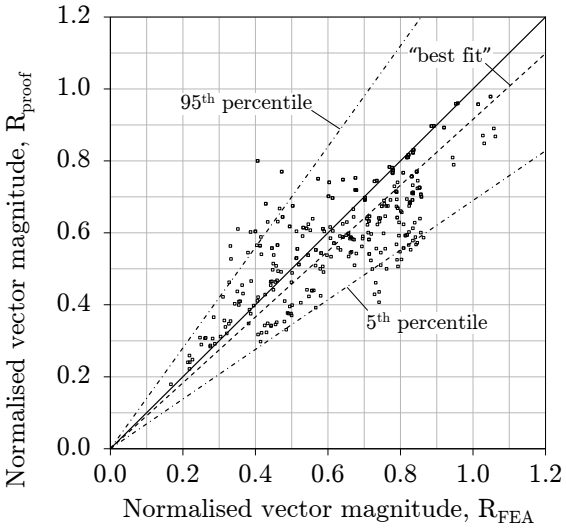

Figure 3.2.: Scatter of results.

As shown in Figure 3.1, when comparing the plate capacity according to a proof with the plate capacity according to finite element analyses, the direction cosines of the stress vector associated with the proof are defined by those of the stress vector associated with the finite element analyses, i.e. both stress vectors have the same unit vector

$$\mathbf{u}_R = \frac{\mathbf{R}}{R} = \frac{R_x}{R}\,\mathbf{i} + \frac{R_y}{R}\,\mathbf{j} + \frac{R_\tau/\sqrt{3}}{R}\,\mathbf{k} \tag{3.4}$$

such that error evaluation can be based solely on the relative magnitudes of the stress vector associated with the proof (R_{proof}) and the stress vector associated with the finite element analyses (R_{FEA}). This ratio of vector magnitudes Γ is used extensively in the quantitative evaluation scheme to measure bias and precision:

$$\Gamma = \frac{R_{proof}}{R_{FEA}} \tag{3.5}$$

such that a proof is said to be non-conservative if $\Gamma > 1.0$.

Accordingly, both bias and precision of a given proof can be quantified by evaluating the ratio of stress vector magnitudes Γ for all load combinations and plating configurations. This is represented graphically in Figure 3.2 by the scatter of R_{proof} against R_{FEA}. Here the curve of "best fit" is shown together with curves showing the 5^{th} and 95^{th} percentiles of the ratios Γ. In Figure 3.3, four broad characterisations of precision and bias are shown. On the basis of such plots, five key performance indicators (KPI's) are used to measure precision and bias for each proof.

1. Average of the squares of the residuals, S_r/n_s

The first KPI is based on the differences between R_{proof} and R_{FEA}. By taking the average of the squares of these residuals, a combined measure of precision and bias is obtained

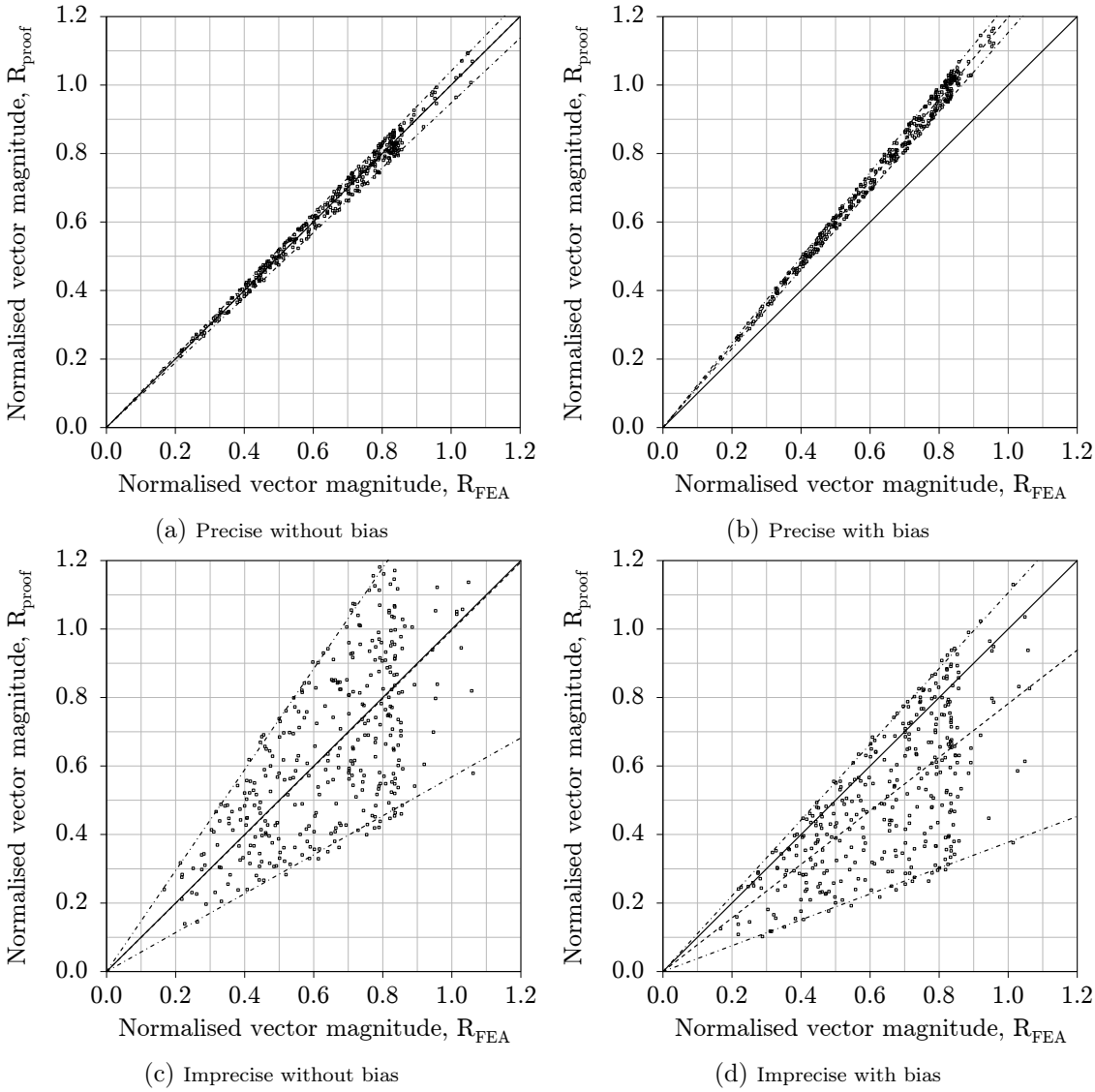

(a) Precise without bias

(b) Precise with bias

(c) Imprecise without bias

(d) Imprecise with bias

Figure 3.3.: Precision and bias.

$$KPI_1 = S_r/n_s = \frac{\sum_{i=1}^{n_s} (R_{proof,i} - R_{FEA,i})^2}{n_s} \tag{3.6}$$

where n_s is the number of evaluation points (i.e. sample size). For this KPI the target is to be as close to zero as possible, i.e. $S_r/n_s \to 0$. This KPI is not very informative in absolute terms, but becomes so when compared to those of other proofs.

2. Slope, m_{lsr}

By using least square regression (without an intercept term), the second KPI is defined by the slope of the resulting straight line through the R_{FEA} - R_{proof} evaluation points, thereby providing a measure of bias

$$KPI_2 = m_{lsr} = \frac{\sum_{i=1}^{n_s} (R_{FEA,i} \cdot R_{proof,i})}{\sum_{i=1}^{n_s} (R_{FEA,i})^2} \tag{3.7}$$

For this KPI the target is to be as close to unity as possible, i.e. $m_{lsr} \to 1$.

3. Coefficient of determination, R_D^2

On the basis of the foregoing regression, the third KPI is defined as the coefficient of determination R_D^2 which provides a measure of precision

$$KPI_3 = R_D^2 = 1 - \frac{\sum_{i=1}^{n_s} (R_{proof,i} - m_{lsr} \cdot R_{FEA,i})^2}{\sum_{i=1}^{n_s} (R_{proof,i} - R_{proof,mean})^2} \tag{3.8}$$

For this KPI the target is also to be as close to unity as possible, i.e. $R_D^2 \to 1$.

4. Slope of 95th percentile, m_{95}

Although the preceding KPI's provide useful information about bias and precision in a proof, neither gives any direct measure of *non-conservatism*. In shipbuilding it is important to know the magnitude of any inherent *non-conservatism* in plate capacity formulations. Accordingly, the fourth KPI is the slope of a straight line through the 95th percentile of the R_{FEA} - R_{proof} evaluation points, m_{95}, which excludes the undue influence of outliers. This measure is useful in the determination of partial safety factors, the target of which is to be as close to unity as possible, i.e. $m_{95} \to 1$.

5. Slope of 5th percentile, m_5

Conversely, in shipbuilding it is also important to know the magnitude of any inherent *conservatism* in plate capacity formulations. Accordingly, the fifth KPI is the slope of a straight line through the 5th percentile of the R_{FEA} - R_{proof} evaluation points, m_5. This measure is useful in gauging the over-design inherent in a proof of plate capacity which leads to a weight penalty that must be borne throughout the ship's service life. The target of this KPI is again to be as close to unity as possible, i.e. $m_5 \to 1$.

3.1.2. Robustness

Measurements of bias and precision are meaningless unless the sample upon which they are based is representative of the design space. Since proofs of plate capacity are used by shipbuilders for a wide variety of ship structures, it is imperative that they are sufficiently robust (unfortunately history is replete with catastrophic structural failures due to the use of engineering formulae beyond the boundaries of their validity [9]). In the context of

a capacity equation for ship plating, this design space is defined by the intersection of a continuous set of load combinations and a continuous set of plating configurations, both of which need to be delimited and discretised within the quantitative evaluation scheme.

Load combinations

Because axial, transverse and shear stresses combine in an infinite number of ways to form a three-dimensional failure surface, the first step in the discretisation of this surface is to equally divide the surface into four discrete levels of shear; $R_\tau = 0$, $R_\tau = 0.25 \cdot \kappa_\tau$, $R_\tau = 0.50 \cdot \kappa_\tau$ and $R_\tau = 0.75 \cdot \kappa_\tau$. The shear value $R_\tau = \kappa_\tau$ is omitted since in this case $R_x = R_y = 0$, i.e. the capacity of the plate under pure shear is (by definition) directly defined by the plate reduction factor κ_τ. Furthermore, negative values of shear are omitted since failure surfaces are symmetric about the R_x-R_y plane[1].

This discretisation results in four concentric capacity curves in the R_x-R_y plane (i.e. four levels of shear) as shown in Figure 3.4. Accordingly, in the second step of the discretisation, each capacity curve for a given level of shear is further divided into 12 combinations of biaxial stresses (R_x-R_y). Four of these combinations coincide with positive and negative values of the x- and y-axes where $R_y = 0$ and $R_x = 0$, respectively. Taken collectively with $R_\tau = \kappa_\tau$, each set of points at $R_x = 0$ and $R_y = 0$ constitute the $R_y - R_\tau$ and $R_x - R_\tau$ capacity curves, respectively.

The foregoing discretisation steps result in 4 x 12 = 48 evaluation points for each plating configuration. However, in order to avoid an artificial increase in the accuracy of the evaluated proofs, the 16 data points representing only yielding behaviour are not included in the evaluation scheme. The capacity of these data points, shown as open in Figure 3.4, can be calculated using the von Mises failure criterion and are therefore assumed to have no error. Furthermore, the capacity of the two additional evaluation points representing $R_x = R_\tau = 0$ and $R_y = R_\tau = 0$ are also omitted since they can be directly calculated from the plate reduction factors κ_y and κ_x, respectively (determined in the present work by finite element analyses). Accordingly, there remain 48 - 16 - 2 = 30 evaluation points for each plating configuration.

Plating configurations

The configurations of simply-supported, plane and rectangular plating can be described by two parameters; the plate aspect ratio α and the plate slenderness parameter β. In shipbuilding the aspect ratios of plates range from $\alpha = 1$ up to a maximum of about $\alpha = 10$. However, reductions in capacity above $\alpha = 5$ become increasing small and are, in any case, usually confined to the shell plating of (transversely-framed) single side skin bulk carriers. Accordingly, three plate aspect ratios are included in the quantitative evaluation scheme used in the present work; $\alpha = 1$, $\alpha = 3$ and $\alpha = 5$.

With respect to plate slenderness, most shipbuilding rules provide minimum slen-

[1] For this reason all references to τ_{xy} and R_τ throughout the present work are to be understood as $|\tau_{xy}|$ and $|R_\tau|$, respectively.

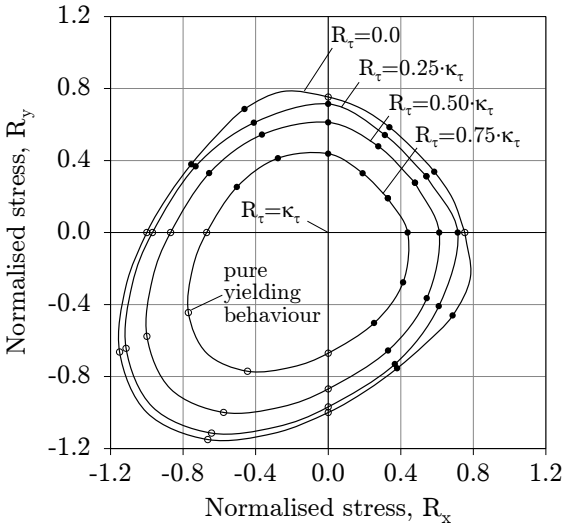

Figure 3.4.: Load combinations.

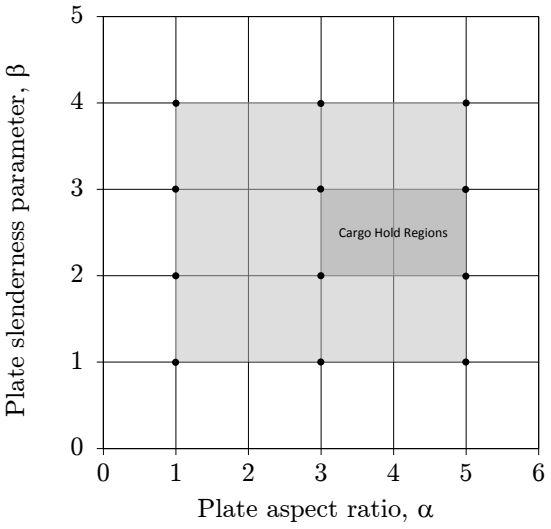

Figure 3.5.: Plating configurations.

derness requirements to 1) avoid excessive welding distortions, 2) avoid excessive elastic deflections and 3) promote good vibration behaviour. For example, in the CSR BC & OT [23], IACS requires that the net thickness of plates satisfy the following criteria

$$t \geqslant \frac{b}{C}\sqrt{\frac{\sigma_Y}{235}} \tag{3.9}$$

where $C = 100$ for hull envelope as well as cargo and tank boundaries and $C = 125$ for other structures. Rewriting Equation (3.9) in terms of β results in maximum values of $\beta = 3.4$ for hull envelope as well as cargo and tank boundaries and $\beta = 4.2$ for other structures. Accordingly, the maximum value of plate slenderness used in the quantitative evaluation scheme is $\beta = 4$. Regarding the minimum value of β, it has been shown in Chapter 2 that yielding behaviour begins for various stress combinations when plate slenderness approaches $\beta = 1$. For this reason, four plate slenderness parameters are included in the evaluation scheme; $\beta = 1$, $\beta = 2$, $\beta = 3$ and $\beta = 4$. Accordingly, with three plate aspect ratios and four plate slenderness parameters, there are a total of 3 x 4 = 12 plating configurations in the evaluation scheme as shown in Figure 3.5.

Evaluation design space and subspace

On the basis of the foregoing, 30 load combinations combined with 12 plating configurations means that the bias and precision of each proof is to be assessed on the basis of 30 x 12 = 360 evaluation points. These load combinations together with plating configurations are hereinafter referred to as the *design space*. The results of finite element analyses for the design space are tabulated and plotted in Appendix C preceded by a description of these numerical studies in Appendix B. Furthermore, it is usual in the shipbuilding industry to differentiate structures based on the consequences of their failure. For this reason, each proof is additionally evaluated using a subset of load combinations and plating configurations which is representative of the hold regions of cargo ships. Plating within the hold regions is critical to longitudinal strength which is a fundamental aspect of ship safety. Compared to localised damages in the superstructure, forecastle deck, hatch covers etc.,

failure of plating in the cargo hold regions may endanger the structural integrity of the ship. Typically, plating in the hold regions is characterised by an aspect ratio between $\alpha = 3$ and $\alpha = 5$ and a slenderness parameter between $\beta = 2$ and $\beta = 3$ (see Figure 3.5). Moreover, the critical stress combinations for plating in these regions usually involve compressive biaxial stresses (i.e. Quadrant 1). As a result, each proof is additionally assessed for a subset of load combinations and plating configurations represented by 2 x 2 x 14 = 56 evaluation points, hereinafter referred to as the *design subspace*.

3.2. Proofs from literature

In 1969 the Ship Structure Committee (SSC) released a feasibility study for a programme of ultimate strength tests on ship structural elements (i.e. unstiffened plates, stiffened plates and grillages) [48]. Following a detailed review of the state-of-the-art, it was therein concluded that there was no published theoretical or experimental material on the ultimate strength of any structural elements under biaxial compression. In the following year results from the initial phase of an ensuing SSC project were reported where the compressive strength of unstiffened plates was addressed (the effects of shear were listed among the topics to be investigated after the initial phase was completed) [49]. Within this initial phase, compression tests on square tubes were conducted in order to obtain a large amount of experimental data on the ultimate strength of plating under various combinations of biaxial loading (sometimes with lateral pressure).

In order to support the experimental data with theoretical explanations, the report included *biaxial strength hypotheses*. For small b/t ratios (in this case $b/t = 30$ and $b/t = 50$), biaxial failure was expected to occur under plastic buckling involving the entire plate. Accordingly, a modified (elastic) buckling interaction curve was used where the y-axis was left unchanged (since transverse buckling was assumed to result in failure) and the x-axis was divided by four (thereby transforming the elastic buckling factor $K_x = 4.0$ into the stress ratio $R_x = 1.0$). However, on the basis of the test results, a different hypothesis was required for plates of larger b/t ratios (in this case $b/t = 70$ and $b/t = 90$). As noted in §2.4.2, plating with an aspect ratio $\alpha > \sqrt{2}$ develops a number of buckle-induced node or ridge lines in the transverse direction depending on the ratio of σ_x and σ_y (acting like "invisible stiffeners" in the words of the authors). The effective breadth of plating on each side of these ridge lines (in addition to that on the ends of the plate) theoretically gives slender plating the post-buckling strength needed to agree with observed test results. However, the authors concede that "(t)he hypothesis of multiple flange failure modes represents an attempt to characterize the ultimate load behaviour of a biaxially compressed plate in terms of well known phenomena. At present it is an engineering approach of a conceptual nature. The evolution of a rigorous solution must be deferred to a subsequent investigation".

Indeed several authors in subsequent years investigated the capacity of plating under combined in-plane loads with solutions almost always expressed in terms of a generalised form of the von Mises failure criterion

$$\left(\frac{\sigma_x}{\kappa_x \cdot \sigma_Y}\right)^{e_1} + \left(\frac{\sigma_y}{\kappa_y \cdot \sigma_Y}\right)^{e_2} - B \cdot \left(\frac{\sigma_x}{\kappa_x \cdot \sigma_Y}\right) \cdot \left(\frac{\sigma_y}{\kappa_y \cdot \sigma_Y}\right) + \left(\frac{\tau_{xy}}{\kappa_\tau \cdot \tau_Y}\right)^{e_3} = 1.0 \quad (3.10)$$

or

$$\left(\frac{R_x}{\kappa_x}\right)^{e_1} + \left(\frac{R_y}{\kappa_y}\right)^{e_2} - B \cdot \left(\frac{R_x}{\kappa_x}\right) \cdot \left(\frac{R_y}{\kappa_y}\right) + \left(\frac{R_\tau}{\kappa_\tau}\right)^{e_3} = 1.0 \tag{3.11}$$

in terms of normalised stresses.

Based on the aforementioned compression tests, Faulkner et al. [46] proposed a parabolic relationship to describe the capacity of plating under compressive biaxial stresses

$$\left(\frac{R_x}{\kappa_x}\right) + \left(\frac{R_y}{\kappa_y}\right)^2 = 1.0 \tag{3.12}$$

where $e_1 = 1$, $e_2 = 2$ and $B = 0$ in terms of Equation (3.11). Typical of earlier efforts, the solution accounts neither for the effects of shear loading nor tensile stresses. Nevertheless, Valsgård [34] notes that Equation (3.12) was incorporated in the offshore design code of Det norske Veritas (DnV) [50] (although this could not be confirmed by the author). By choosing various values for $B > 0$, Valsgård produced skewed variations of Faulkner's parabolic interaction equation. Comparing these variations to his own numerical results for plates with an aspect ratio $\alpha = 3$, Valsgård concluded that $B = 0.25$ fits the numerical data "reasonably well", i.e.

$$\left(\frac{R_x}{\kappa_x}\right) + \left(\frac{R_y}{\kappa_y}\right)^2 - 0.25 \cdot \left(\frac{R_x}{\kappa_x}\right) \cdot \left(\frac{R_y}{\kappa_y}\right) = 1.0 \tag{3.13}$$

When incorporating his interaction equation in a design code formulation, Valsgård accounted for the effect of shear loading using a reduced yield stress according to Equation (2.61), i.e.

$$\sigma'_Y = \sqrt{\sigma_Y^2 - 3 \cdot \tau_{xy}^2} \tag{3.14}$$

As noted in §2.3.5, this is a widely used approach whenever plate failure is not dominated by shear buckling.

In this section one of the most recent attempts to derive a capacity equation based on the generalised form of the von Mises failure criterion will be examined. In his report to the American Bureau of Shipping [43], Paik presents a proof that is one of the few to directly account for both shear loading and tensile stresses. Subsequently, a rather unique proof developed by Ueda et al. is also examined [51]. While almost all proofs of plate capacity use a generalised form of the von Mises failure criterion, the proof of Ueda et al. provide so-called *stress coefficients* which enable the calculation of stresses at each of the hot spots identified in Figure 2.15 (but for plates of any aspect ratio α). Knowing how the applied stresses are distributed throughout the plate enables *direct* use of von Mises criterion to calculate yielding (i.e. a precursor to collapse).

3.2.1. Paik

Based on insights gleaned from a series of non-linear finite element analyses where both load ratios and plate aspect ratios were varied, Paik [43] (as referenced in [44]) proposed a proof based on the generalised form of the von Mises failure criterion shown in Equation (3.11) where $e_1 = e_2 = e_3 = 2$ and $B = 0$ when both axial stresses are compressive and $B = 1$ when either are tensile, i.e.

$$\left(\frac{R_x}{\kappa_x}\right)^2 + \left(\frac{R_y}{\kappa_y}\right)^2 + \left(\frac{R_\tau}{\kappa_\tau}\right)^2 = 1.0 \tag{3.15}$$

when $R_x \geqslant 0$ and $R_y \geqslant 0$, and

$$\left(\frac{R_x}{\kappa_x}\right)^2 + \left(\frac{R_y}{\kappa_y}\right)^2 - \left(\frac{R_x}{\kappa_x}\right) \cdot \left(\frac{R_y}{\kappa_y}\right) + \left(\frac{R_\tau}{\kappa_\tau}\right)^2 = 1.0 \tag{3.16}$$

when $R_x < 0$ or $R_y < 0$.

Bias and Precision

In accordance with the evaluation scheme described in §3.1, Paik's proof has been used to calculate the capacity of plating for the 360 evaluation points. The resulting scatter plots for both the design space and design subspace are shown in Figure 3.6. The five key performance indicators used to measure precision and bias are shown in Table 3.1. Regarding the overall measure of error (KPI_1), the average of the squares of the residuals S_r/n_s is somewhat high for the design space ($S_r/n_s = 0.011$), but very low for the design subspace ($S_r/n_s = 0.001$)[2]. With respect to the measure of bias (KPI_2), the least-squares fit of a straight line through the $R_{FEA} - R_{proof}$ data points gives a moderately/significantly conservative slope for the design space ($m_{lsr} = 0.91$) and a slightly non-conservative slope for the design subspace ($m_{lsr} = 1.03$). Concerning the measure of precision (KPI_3), the coefficients of determination reflect a high degree of scatter for the design space (${R_D}^2 = 0.72$), but a very low degree of scatter for the design subspace (${R_D}^2 = 0.95$). Regarding the extent of non-conservatism (KPI_4), a straight line through the 95^{th} percentile gives a significantly non-conservative slope for both the design space ($m_{95} = 1.18$) and design subspace ($m_{95} = 1.13$). With respect to the extent of conservatism (KPI_5), a straight line through the 5^{th} percentile gives an extremely conservative slope for the design space ($m_5 = 0.73$) and a slightly/moderately conservative slope for the design subspace ($m_5 = 0.95$).

KPI		Design space	Design subspace	Target
1	S_r/n_s	0.011	0.001	0.000
2	m_{lsr}	0.91	1.03	1.00
3	${R_D}^2$	0.72	0.95	1.00
4	m_{95}	1.18	1.13	1.00
5	m_5	0.73	0.95	1.00

Table 3.1.: Key performance indicators (Paik).

In order to identify any inherent problems within Paik's proof for specific parameters, the mean and extreme values of the ratio of stress vector magnitudes, $\Gamma = R_{proof}/R_{FEA}$, are shown in Figure 3.7 for each value of plate aspect ratio (α), plate slenderness parameter

[2] The adjectives used throughout all descriptions of bias and precision (e.g. "somewhat high", "very low" etc.) reflect relative degrees of bias and precision. These adjectives are based on the total ranges of bias and precision taken collectively for all existing proofs.

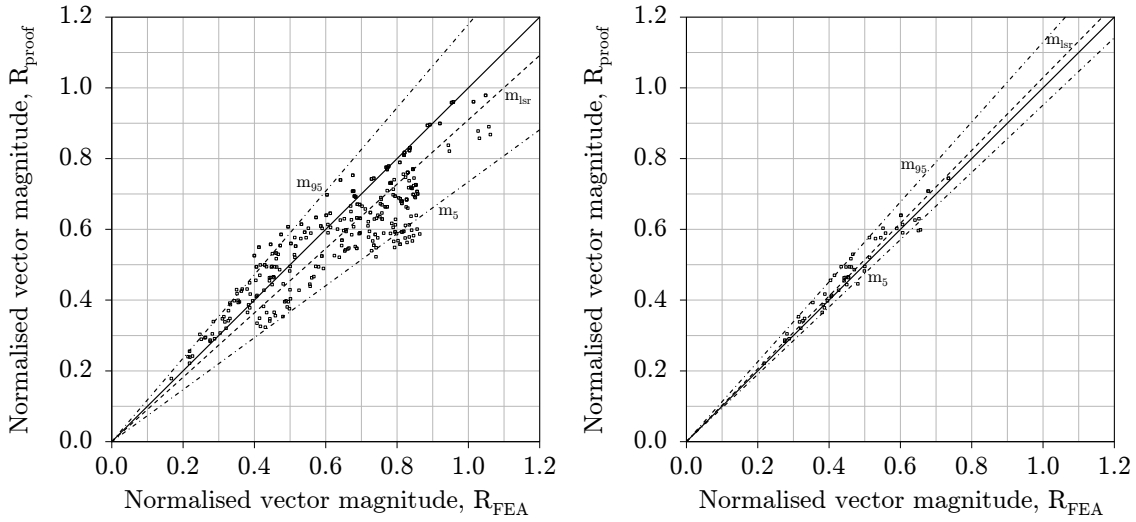

(a) Design space (360 evaluation points) (b) Design subspace (56 evaluation points)

Figure 3.6.: Scatter plots of R_{FEA} - R_{proof} (Paik).

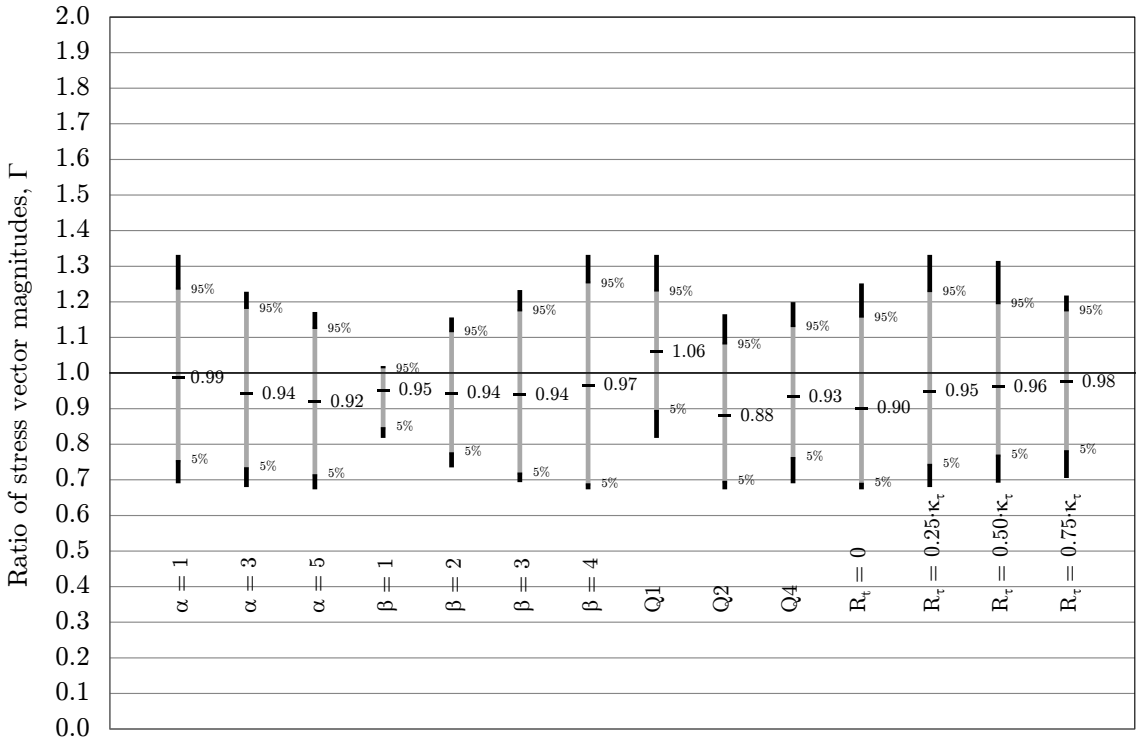

Figure 3.7.: Evaluation of data subsets (Paik).

(β), quadrants of compressive/tensile load combinations (Q1, Q2 and Q4) and levels of shear (R_τ). In case of the plate aspect ratios, the mean values of Γ indicate a slightly non-conservative bias for $\alpha = 1$ and a moderately conservative bias for $\alpha = 3$ and $\alpha = 5$, i.e. increasing conservatism with increasing aspect ratios. The ranges of extreme values indicate poor to somewhat poor precision for all plate aspect ratios. In case of the plate

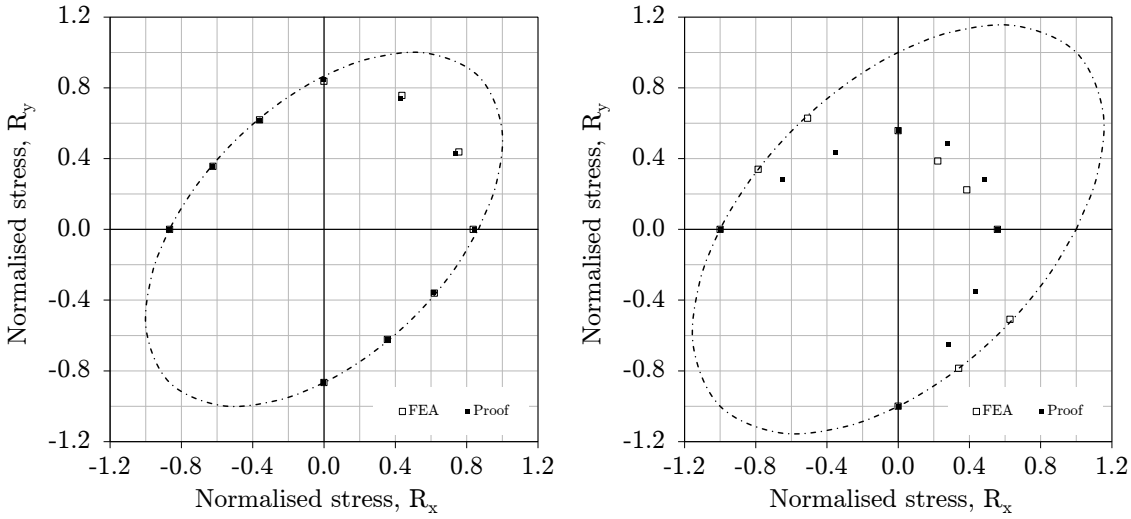

(a) $\alpha = 1,\ \beta = 1,\ R_\tau = 0.5 \cdot \kappa_\tau$ (b) $\alpha = 1,\ \beta = 4,\ R_\tau = 0$

Figure 3.8.: Comparison plots (Paik).

slenderness parameters, the mean values of Γ indicate a slightly/moderately conservative bias for $\beta = 1$, moderately conservative bias for $\beta = 2$ and $\beta = 3$ and a slightly conservative bias for $\beta = 4$. The ranges of extreme values indicate very good precision for $\beta = 1$ to quite poor precision for $\beta = 4$, i.e. decreasing precision with increasing plate slenderness parameters. In case of the compressive/tensile load combinations, the mean values of Γ indicate a moderately non-conservative bias in Q1, a significantly conservative bias in Q2 and a moderately conservative bias in Q4. The ranges of extreme values indicate good to somewhat good precision in all quadrants. In case of shear, the mean values of Γ reveal a moderately/significantly conservative bias in the absence of shear and a slightly to slightly/moderately conservative bias in the presence of shear, i.e. increasing accuracy with increasing levels of shear. The ranges of extreme values indicate poor precision in the absence of shear and poor ($R_\tau = 0.25 \cdot \kappa_\tau$) to somewhat good ($R_\tau = 0.75 \cdot \kappa_\tau$) precision in the presence of shear, i.e. increasing precision with increasing levels of shear (when present).

In order to obtain an impression of the strengths and weaknesses of Paik's proof, the lowest and highest values of the squares of the residuals (S_r/n_s) for each combination of plate aspect ratio (α), plate slenderness parameter (β) and level of shear (R_τ) have been calculated. The lowest value of S_r/n_s is for the combination $\alpha = 1$, $\beta = 1$ and $R_\tau = 0.5 \cdot \kappa_\tau$, the capacity curve of which is plotted in Figure 3.8(a)[3]. Conversely, the highest value of S_r/n_s is for the combination $\alpha = 1$, $\beta = 4$ and $R_\tau = 0$, the capacity curve of which is

[3] The levels of shear indicated in all R_x-R_y plots are those used in the finite element analyses, i.e. $R_\tau = 0.25 \cdot \kappa_\tau$, $R_\tau = 0.50 \cdot \kappa_\tau$ or $R_\tau = 0.75 \cdot \kappa_\tau$. In case of results obtained with the proof, these are *nominal* levels of shear (except of course when $R_\tau = 0$). This is because the unit vectors used in the proof are the same as those used in the finite element analyses. In general this leads to plate capacities obtained with the proof having different magnitudes of shear compared to the fixed values of shear used in the finite element analyses. However, the degree of departure from the fixed value of shear depends on the ratio of stress vector magnitudes $\Gamma = R_{proof}/R_{FEA}$ and as such can be discerned from results plotted in the R_x-R_y plane, i.e. the relative magnitudes of stress vectors of the proof and finite element analyses projected onto the R_x-R_y plane.

plotted in Figure 3.8(b).

3.2.2. Ueda et al.

In §2.2.3 the distribution of internal stresses within a plate were described as a function of the stress ratio $c = \sigma_y/\sigma_x$. There it was described how stresses accumulate in three sets of "hot spots" such that yielding initiates at one or more of them (i.e. all "hot spots" in case of gross yielding). Based on the results of theoretical investigations, Ueda et al. [51] developed *stress coefficients* χ_x and χ_y which enable the calculation of internal stresses at each of the hot spots identified in Figure 2.15 (shown for plates with an aspect ratio $\alpha = 1$). These coefficients have been determined assuming the plate is without initial deflections. As noted above, knowing how the applied stresses are distributed throughout the plate enables direct use of von Mises criterion to calculate yielding (i.e. a precursor to collapse)

$$[R_x \cdot (1+\chi_x)]^2 + [R_y \cdot (1+\chi_y)]^2 - R_x \cdot R_y \cdot (1+\chi_x) \cdot (1+\chi_y) + R_\tau^2 = 1 \tag{3.17}$$

For a given combination of loads (i.e. a unit stress vector), the elastic buckling strength of the plate is compared to its material yield strength (i.e. defined by $\chi_x = \chi_y = 0$). In case the plate buckles elastically before yielding, the stress coefficients χ_x and χ_y take on non-zero values. In case of a square plate without shear, the equations to determine the post-buckling stress coefficients reduce to

$$\chi_{x,max} = 1 + \frac{R_y - R_{x,cr}}{R_x} \tag{3.18a}$$

$$\chi_{x,min} = -\chi_{x,max} \tag{3.18b}$$

$$\chi_{y,max} = 1 + \frac{R_x - R_{y,cr}}{R_y} \tag{3.18c}$$

$$\chi_{y,min} = -\chi_{y,max} \tag{3.18d}$$

These maximum and minimum values of χ_x and χ_y are introduced into Equation (3.17) according to the locations of initial yield

(a) in the case of yielding at mid-length edges of plate buckles; $\chi_{x,max}$, $\chi_{y,min}$,

(b) in the case of yielding in the corners of plate; $\chi_{x,max}$, $\chi_{y,max}$,

(c) in the case of yielding at mid-breadth edges of plate buckle; $\chi_{x,min}$, $\chi_{y,max}$.

These locations of initial yield are shown in Figure 3.9. In Figure 3.10, results obtained with the above stress coefficients are compared to the numerical results presented in §2.2.3 ($\alpha = 1$, $\beta = 3$). As shown in §2.2.3, it is in fact the value of $c = \sigma_y/\sigma_x$ which determines the location of initial yield and not simply whether R_x and R_y are compressive or tensile. Accordingly, the ultimate strength of the plating is determined by gradually increasing the applied stresses R_x and R_y until the equivalent stresses in one or more location sets, i.e. (a), (b) or (c), reach yield.

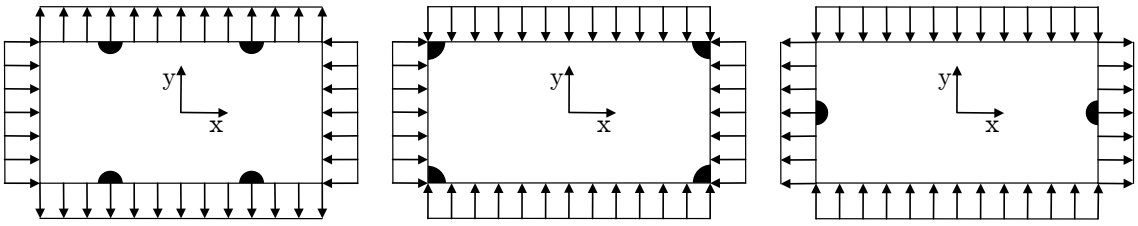

(a) mid-length edges (b) corners (c) mid-breadth edges

Figure 3.9.: Locations of initial yield in buckled plate (shown for $\alpha = 2$)

Bias and Precision

In accordance with the evaluation scheme described in §3.1, the proof of Ueda et al. has been used to calculate the capacity of plating for the 360 evaluation points. The resulting scatter plots for both the design space and design subspace are shown in Figure 3.11. The five key performance indicators used to measure precision and bias are shown in Table 3.2. Regarding the overall measure of error (KPI_1), the average of the squares of the residuals S_r/n_s is high for the design space ($S_r/n_s = 0.018$) and very high for the design subspace ($S_r/n_s = 0.038$). With respect to the measure of bias (KPI_2), the least-squares fit of a straight line through the R_{FEA} - R_{proof} data points gives a moderately/significantly non-conservative slope for the design space ($m_{lsr} = 1.11$) and an extremely non-conservative slope for the design subspace ($m_{lsr} = 1.35$). Concerning the measure of precision (KPI_3), the coefficients of determination reflect a very high degree of scatter for both the design space ($R_D{}^2 = 0.62$) and the design subspace ($R_D{}^2 = 0.57$). Regarding the extent of non-conservatism (KPI_4), a straight line through the 95^{th} percentile gives an extremely non-conservative slope for both the design space ($m_{95} = 1.61$) and design subspace ($m_{95} = 1.91$). With respect to the extent of conservatism (KPI_5), a straight line through the 5^{th} percentile gives a slope without bias for the design space ($m_5 = 1.00$) and a significantly non-conservative slope for the design subspace ($m_5 = 1.18$).

KPI		Design space	Design subspace	Target
1	S_r/n_s	0.018	0.038	0.000
2	m_{lsr}	1.11	1.35	1.00
3	$R_D{}^2$	0.62	0.57	1.00
4	m_{95}	1.61	1.91	1.00
5	m_5	1.00	1.18	1.00

Table 3.2.: Key performance indicators (Ueda et al.).

In order to identify any inherent problems within the proof of Ueda et al. for specific parameters, the mean and extreme values of the ratio of stress vector magnitudes, $\Gamma = R_{proof}/R_{FEA}$, are shown in Figure 3.12 for each value of plate aspect ratio (α), plate slenderness parameter (β), quadrants of compressive/tensile load combinations (Q1, Q2 and Q4) and levels of shear (R_τ). In case of the plate aspect ratios, the mean values of Γ indicate a moderately/significantly non-conservative bias for $\alpha = 1$, a significantly/extremely non-conservative bias for $\alpha = 3$ and an extremely non-conservative bias for $\alpha = 5$, i.e. in-

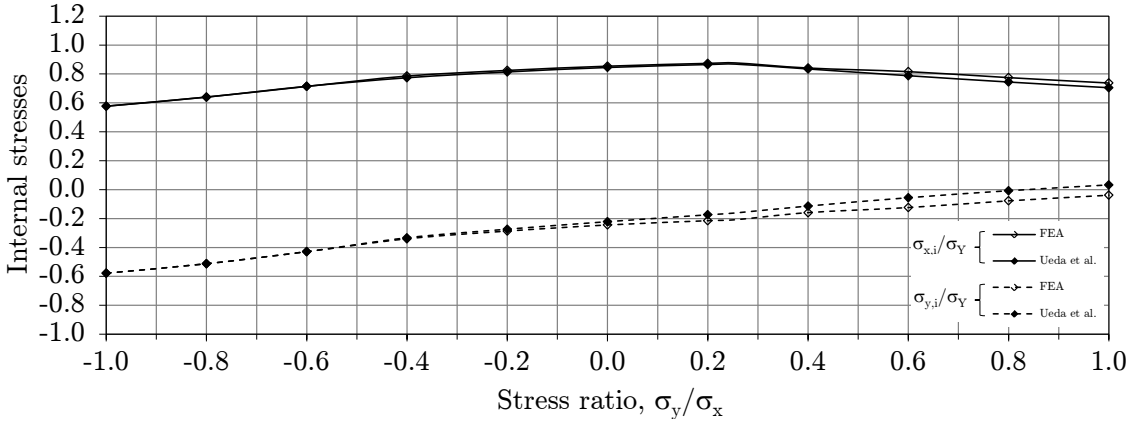

(a) Normalised internal stresses, $\sigma_{x,i}/\sigma_Y$, $\sigma_{y,i}/\sigma_Y$ - mid-length edges

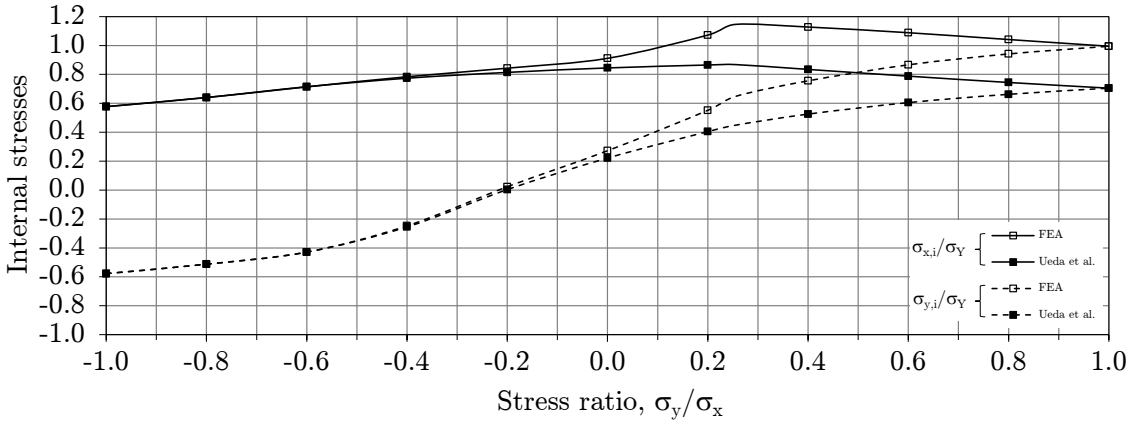

(b) Normalised internal stresses, $\sigma_{x,i}/\sigma_Y$, $\sigma_{y,i}/\sigma_Y$ - corners

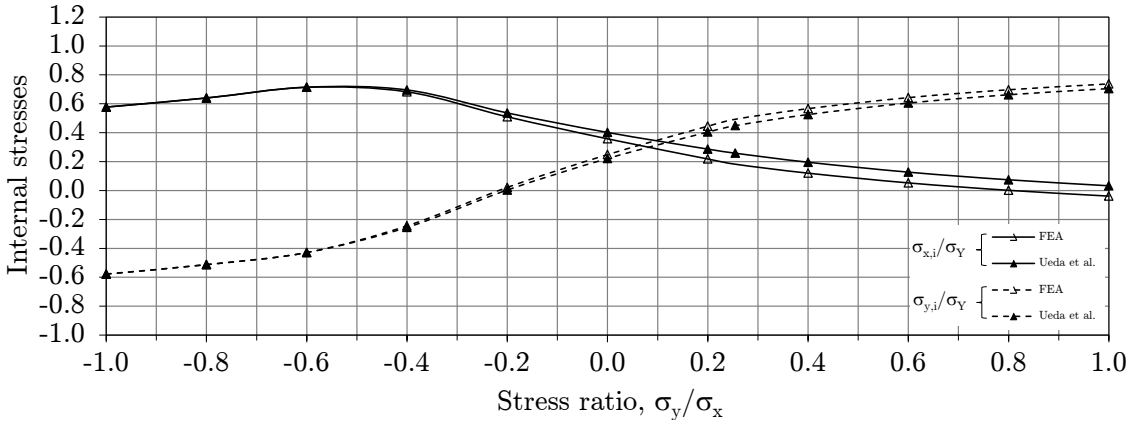

(c) Normalised internal stresses, $\sigma_{x,i}/\sigma_Y$, $\sigma_{y,i}/\sigma_Y$ - mid-breadth edges

Figure 3.10.: Comparisons of stress distributions in buckled plate at initial yield.

creasing non-conservatism with increasing aspect ratios. The ranges of extreme values indicate good precision for $\alpha = 1$ to very poor precision for $\alpha = 5$, i.e. decreasing precision with increasing plate aspect ratios. In case of the plate slenderness parameters, the mean values of Γ indicate a moderately/significantly non-conservative bias for $\beta = 1$ to an ex-

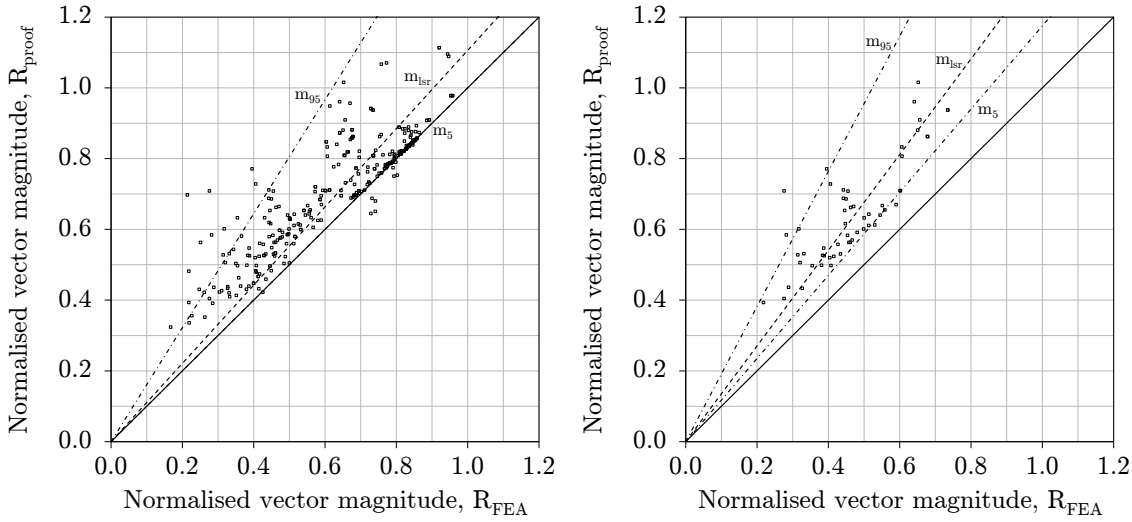

(a) Design space (360 evaluation points) (b) Design subspace (56 evaluation points)

Figure 3.11.: Scatter plots of R_{FEA} - R_{proof} (Ueda et al.).

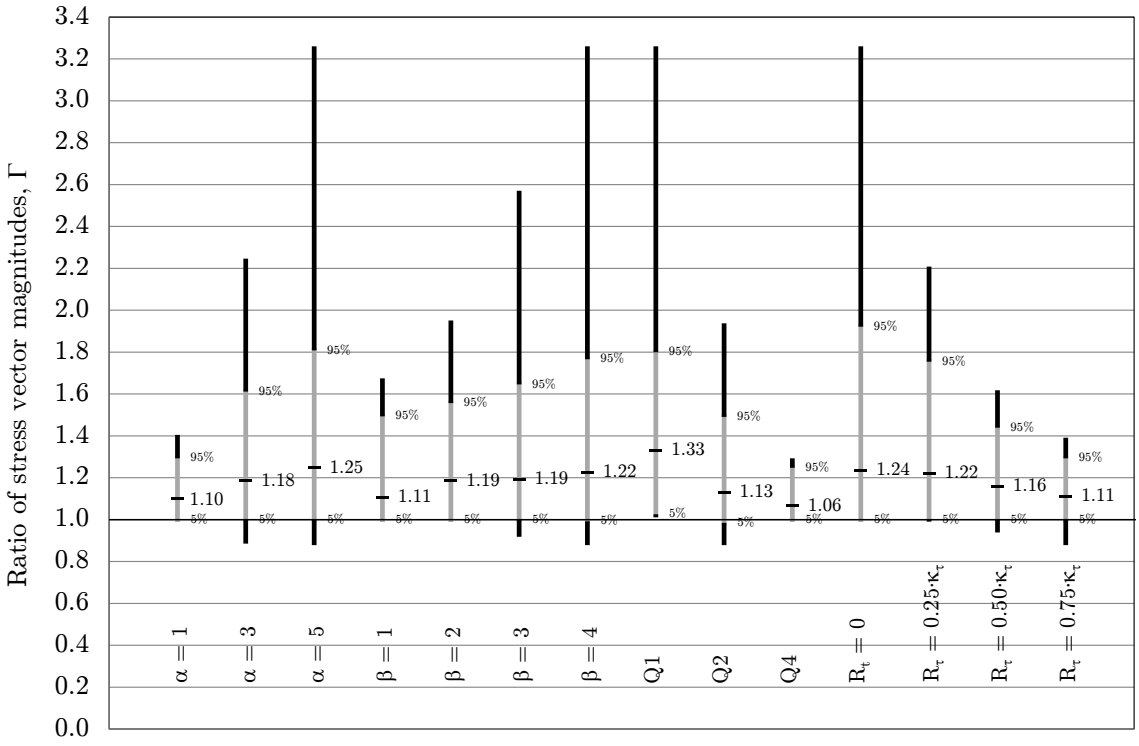

Figure 3.12.: Evaluation of data subsets (Ueda et al.).

tremely non-conservative bias for $\beta = 4$, i.e. increasing non-conservatism with increasing plate slenderness. The ranges of extreme values indicate poor precision for $\beta = 1$ to very poor precision for $\beta = 4$, i.e. decreasing precision with increasing plate slenderness. In case of the compressive/tensile load combinations, the mean values of Γ indicate an extremely non-conservative bias in Q1, a significantly non-conservative bias in Q2 and a moderately

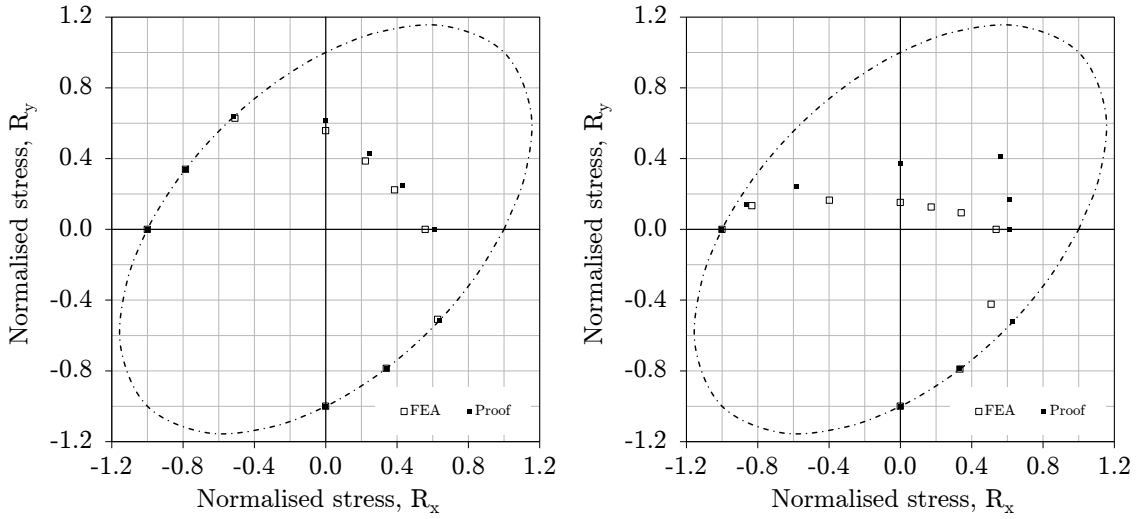

(a) $\alpha = 1$, $\beta = 4$, $R_\tau = 0$ (b) $\alpha = 5$, $\beta = 4$, $R_\tau = 0$

Figure 3.13.: Comparison plots (Ueda et al.).

non-conservative bias in Q4. The ranges of extreme values indicate very poor precision in Q1, poor precision in Q2, but good precision in Q4. In case of shear, the mean values of Γ reveal an extremely non-conservative bias for $R_\tau = 0$ to a significantly non-conservative bias for $R_\tau = 0.75 \cdot \kappa_\tau$, i.e. decreasing non-conservatism with increasing shear. The ranges of extreme values indicate very poor precision in the absence of shear to good precision for $R_\tau = 0.75 \cdot \kappa_\tau$, i.e. increasing precision with increasing shear.

In order to obtain an impression of the strengths and weaknesses of the proof of Ueda et al., the lowest and highest values of the squares of the residuals (S_r/n_s) for each combination of plate aspect ratio (α), plate slenderness parameter (β) and level of shear (R_τ) have been calculated. The lowest value of S_r/n_s is for the combination $\alpha = 1$, $\beta = 4$ and $R_\tau = 0$, the capacity curve of which is plotted in Figure 3.13(a). Conversely, the highest value of S_r/n_s is for the combination $\alpha = 5$, $\beta = 4$ and $R_\tau = 0$, the capacity curve of which is plotted in Figure 3.13(b).

3.3. Proofs from shipbuilding practice

Almost all ships in the world's commercial fleet are built according to the construction standards of classification societies. Even many non-commercial ships (e.g. navy and other government vessels) are built according to standards developed specially by classification societies. When a ship complies with the construction standards of a classification society it is assigned a class designation. Regular surveys are carried out to verify that ships in service remain in compliance with these standards. In principle, classification societies are independent, self-regulating, externally-audited bodies. To ensure their construction standards keep up with the state-of-the-art, classification societies incorporate the results of ongoing, relevant research, tempered by in-service experience gained from the classification of many types of ships over many years.

Following the International Load Line Convention of 1930 and its recommendation

that classification societies ensure "as much uniformity as possible in the application of the standards of strength upon which freeboard is based", the first conference of the seven major classification societies was hosted by Registro Italiano Navale (RINA) in 1939 [52]. The other societies in attendance were the American Bureau of Shipping (ABS), Bureau Veritas (BV), Det norske Veritas (DnV), Germanischer Lloyd (GL), Lloyd's Register (LR) and Nippon Kaiji Kyokai (ClassNK). In 1955 a second major conference was held which led to the creation of working parties on specific topics and in 1968 the International Association of Classification Societies (IACS) was formed. Today more than 90% of the world's cargo carrying tonnage is covered by the classification rules of IACS member societies [52]. Accordingly, the most important proofs of plate capacity in shipbuilding practice can be found in the classification rules of IACS member societies. In 1989 the IACS Working Party on Strength (WP/S) delivered the first Unified Requirement (UR) concerning the strength of ships which contained explicit buckling strength criteria. The *IACS Longitudinal Strength Standard* (UR S11) contains buckling strength requirements for plate panels and longitudinals subject to hull girder bending and shear stresses based on the Johnson-Ostenfeld plasticity correction discussed in §2.1.4. However, the UR addresses axial and shear loads in isolation and does not include a capacity equation for plates under combined in-plane loads.

Nevertheless, although IACS Unified Requirements (UR) are minimum requirements to be incorporated into the rules of all member societies, several members declared "reservations" against the UR S11 proof of buckling strength, opting instead for their own criteria. This led initially to extensive efforts within the WP/S to agree on a harmonised proof of buckling strength which carried on into the development of the IACS common structural rules. Common structural rules are construction standards which are used by all IACS member societies without the possibility of reservations. In 2006 the *IACS Common Structural Rules for Bulk Carriers* (CSR-BC) and *IACS Common Structural Rules for Double Hull Oil Tankers* (CSR-OT) came into force. Unfortunately, these two rule sets were developed independently by two different groups of IACS member societies such that the buckling strength rules in CSR-OT were (for all intents and purposes) based on DnV's computerised buckling code PULS (Panel Ultimate Limit State) while in CSR-BC they were based on the buckling strength rules of GL (in turn based on the German construction standard DIN 18800). Despite extensive efforts to harmonise the proofs of buckling strength in CSR-BC and CSR-OT, an agreement on a single proof could not be reached.

Therefore, in 2008 efforts were renewed to harmonise the CSR buckling strength criteria within the framework of the *IACS Common Structural Rules for Bulk Carriers and Oil Tankers* (CSR BC & OT). The purpose of CSR BC & OT was to harmonise load and strength criteria common to both bulk carriers and oil tankers (Part One) and to provide additional requirements unique to each ship type (Part Two). Included in the former were the buckling strength criteria for which a dedicated project team (HPT02) was established[4]. Following six years of discussion and analyses, it was concluded that the CSR BC & OT buckling strength criteria would be based on those in the GL rules for classification and construction. This decision was not based on accuracy and precision alone (in this regard PULS would have been an equally acceptable choice), but also because the GL proof of buckling strength possessed qualities suitable for both the printed and programmed versions of CSR BC & OT (i.e. robust, concise, transparent, physically-

[4] For the sake of full disclosure, the author represented GL in WP/S, CSR-BC/CSR-OT and CSR BC & OT efforts to harmonise the IACS buckling strength criteria.

based, meaningful and dimensionally consistent quantities, easily programmable, efficient solutions etc.). However, some changes were made to the GL proof of buckling strength within the development of CSR BC & OT. In particular, in order to improve its accuracy and precision, as well as to remove the need for a Poisson correction (discussed below), the GL proof of plate capacity under combined in-plane loads was revised on the basis of Chapter 4. This revised proof has also been used in the new *IACS Longitudinal Strength Standard for Container Ships* (UR S11A) as well as the new *DNVGL Rules for Classification* (applicable to all ship types) which were developed after the 2013 merger of DnV and GL.

Accordingly, in this section the proofs of plate capacity prior to CSR BC & OT are examined. In particular, because they formed the basis of the CSR-OT and CSR-BC buckling strength criteria, the historical development of the DnV and GL proofs of plate capacity are discussed. Firstly, the plate capacity proof within DnV Classification Note 30.1 (CN 30.1) will be examined followed by the plate capacity proof of GL based on DIN 4114. Both proofs are based on elastic buckling strength analyses with a plasticity correction and are the predecessors to the CSR proofs. Next the CSR proofs themselves will be examined beginning with DnV's PULS (CSR-OT) and followed by the GL proof based on DIN 18800 (CSR-BC). Finally, because the latter GL proof is based on beam stresses, modified stress values are needed if σ_x and σ_y contain Poisson effects (i.e. from finite element calculations). Accordingly, in an attempt to simplify its use, BV developed a modified version of the GL proof to eliminate the need for this Poisson correction. This modified proof was used provisionally in CSR BC & OT development and so is also examined.

3.3.1. Elastic analyses with plasticity correction (DnV and GL)

In §2.1.4 it was shown how an ultimate value of stress can be calculated using Johnson-Ostenfeld formulae to correct the elastic buckling stress of a plate for plasticity, i.e. material non-linearity, not geometric non-linearity. There the plate was subjected to a uniaxial stress σ_x. However, for a plate subjected to combined in-plane stresses (i.e. σ_x, σ_y and τ_{xy}), it is possible to describe an equivalent stress based on the von Mises equation[5]

$$\sigma_{eq} = \sqrt{{\sigma_x}^2 - \sigma_x \cdot \sigma_y + {\sigma_y}^2 + 3 \cdot {\tau_{xy}}^2} \tag{3.19}$$

and compare this to an ultimate value of equivalent stress $\sigma_{eq,ult}$ which is equal to an equivalent elastic stress $\sigma_{eq,cr}$ corrected for plasticity.

CN 30.1

In the earlier editions of DnV's Classification Note 30.1 (1982 and 1984), this comparison was made in two steps in case of combined biaxial and shear stresses. A utilisation factor η_{cs} was first calculated for a combination of uniaxial compression and shear and then a separate utilisation factor η_c for the remaining uniaxial stress component. On the basis of these two utilisation factors, a final utilisation factor for combined biaxial and shear stresses was then calculated

[5] This equation is the same as Equation (2.1) except that it is here intended for externally applied stresses (i.e. not internal stresses) and expanded to include shear.

$$\eta = \sqrt{{\eta_{cs}}^2 + 2/\alpha^2 \cdot \eta_{cs} \cdot \eta_c + {\eta_c}^2} \tag{3.20}$$

However, the procedure was amended in the 1987 edition of CN 30.1 [53] such that this comparison was performed in a single step based on an equivalent reference degree of slenderness

$${\lambda_{eq}}^2 = \frac{\sigma_Y}{\sigma_{eq}} \left[\left(\frac{\sigma_x}{\sigma_{x,cr}} \right)^{c_\alpha} + \left(\frac{\sigma_y}{\sigma_{y,cr}} \right)^{c_\alpha} + \left(\frac{\tau_{xy}}{\tau_{xy,cr}} \right)^{c_\alpha} \right]^{1/c_\alpha} \tag{3.21}$$

where $c_\alpha = 2 - 1/\alpha$. On the basis of λ_{eq}, the (normalised) ultimate value of the equivalent stress is then calculated using the Johnson-Ostenfeld correction as

$$\frac{\sigma_{eq,ult}}{\sigma_Y} = \begin{cases} \dfrac{1}{\sqrt{1 + {\lambda_{eq}}^4}} & \lambda_{eq} \leqslant 1.0 \\ \dfrac{1}{\sqrt{2} \cdot \lambda_{eq}} & 1.0 < \lambda_{eq} \leqslant 5.0 \end{cases} \tag{3.22}$$

DIN 4114

The German construction standard DIN 4114 (Steel Structures; Stability) was first published in July 1952 and provides buckling strength criteria in case of combined uniaxial compression and shear [54]. These criteria were first introduced into the GL rules for the classification and construction of ships in 1973. In January 1989 GL issued Supplement No. 2 to its 1986 hull rules in which these criteria were revised to account for biaxial compression combined with shear and where the equivalent elastic buckling stress $\sigma_{eq,cr}$ is calculated using some rather cumbersome equations, but which allow the equivalent reference degree of slenderness to be calculated simply as

$$\lambda_{eq} = \sqrt{\frac{\sigma_Y}{\sigma_{eq,cr}}} \tag{3.23}$$

On the basis of λ_{eq}, the (normalised) ultimate value of the equivalent stress is then calculated as

$$\frac{\sigma_{eq,ult}}{\sigma_Y} = \begin{cases} 1.0 & \lambda_{eq} < \dfrac{1}{\sqrt{2.04}} \\ 1.474 - 0.677 \cdot \lambda_{eq} & \dfrac{1}{\sqrt{2.04}} \leqslant \lambda_{eq} < \dfrac{1}{\sqrt{0.6}} \\ \dfrac{1}{{\lambda_{eq}}^2} & \dfrac{1}{\sqrt{0.6}} \leqslant \lambda_{eq} \end{cases} \tag{3.24}$$

A comparison of the CN 30.1 and the amended DIN 4114 equivalent reference degrees of slenderness are shown in Figure 3.14 for the 360 evaluation points described in §3.1.2 with a comparison of the plasticity corrections shown in Figure 3.15.

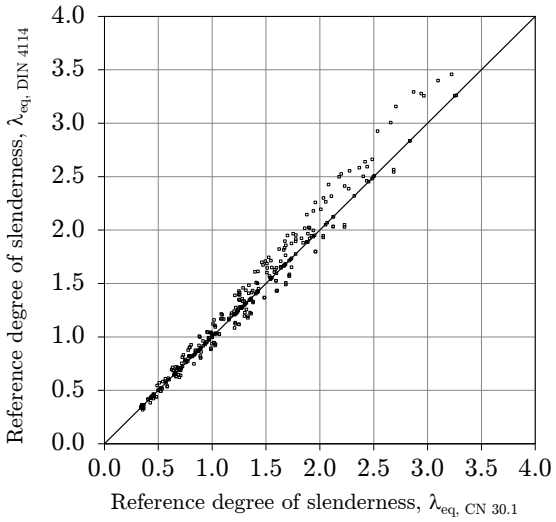

Figure 3.14.: Comparison of equivalent reference degrees of slenderness, λ_{eq}.

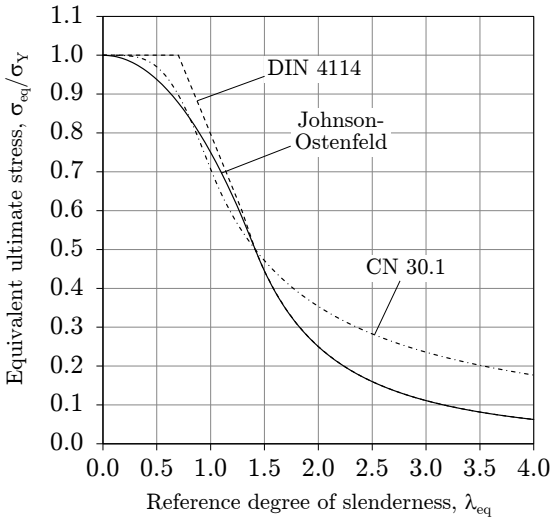

Figure 3.15.: Comparison of plasticity corrections.

Bias and Precision - CN 30.1

In accordance with the evaluation scheme described in §3.1, the CN 30.1 proof has been used to calculate the capacity of plating for the 360 evaluation points. The resulting scatter plots for both the design space and design subspace are shown in Figure 3.16. The five key performance indicators used to measure precision and bias are shown in Table 3.3. Regarding the overall measure of error (KPI_1), the average of the squares of the residuals S_r/n_s is very high for the design space ($S_r/n_s = 0.032$), but quite low for the design subspace ($S_r/n_s = 0.005$). With respect to the measure of bias (KPI_2), the least-squares fit of a straight line through the R_{FEA} - R_{proof} data points gives a significantly conservative slope for both the design space ($m_{lsr} = 0.82$) and design subspace ($m_{lsr} = 0.88$). Concerning the measure of precision (KPI_3), the coefficients of determination reflect a very high degree of scatter for the design space (${R_D}^2 = 0.63$), but a low degree of scatter for the design subspace (${R_D}^2 = 0.85$). Regarding the extent of non-conservatism (KPI_4), a straight line through the 95^{th} percentile gives a moderately non-conservative slope for the design space ($m_{95} = 1.08$) and a moderately/significantly non-conservative slope for the design subspace ($m_{95} = 1.10$). With respect to the extent of conservatism (KPI_5), a straight line through the 5^{th} percentile gives an extremely conservative slope for both the design space ($m_5 = 0.52$) and design subspace ($m_5 = 0.75$).

KPI		Design space	Design subspace	Target
1	S_r/n_s	0.032	0.005	0.000
2	m_{lsr}	0.82	0.88	1.00
3	${R_D}^2$	0.63	0.85	1.00
4	m_{95}	1.08	1.10	1.00
5	m_5	0.52	0.75	1.00

Table 3.3.: Key performance indicators (CN 30.1).

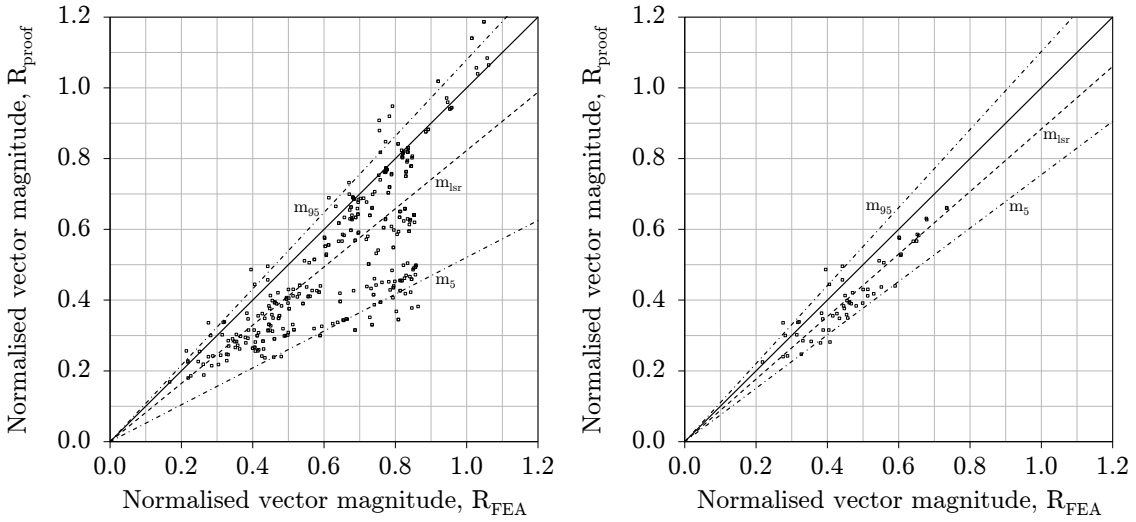

(a) Design space (360 evaluation points)

(b) Design subspace (56 evaluation points)

Figure 3.16.: Scatter plots of R_{FEA} - R_{proof} (CN 30.1).

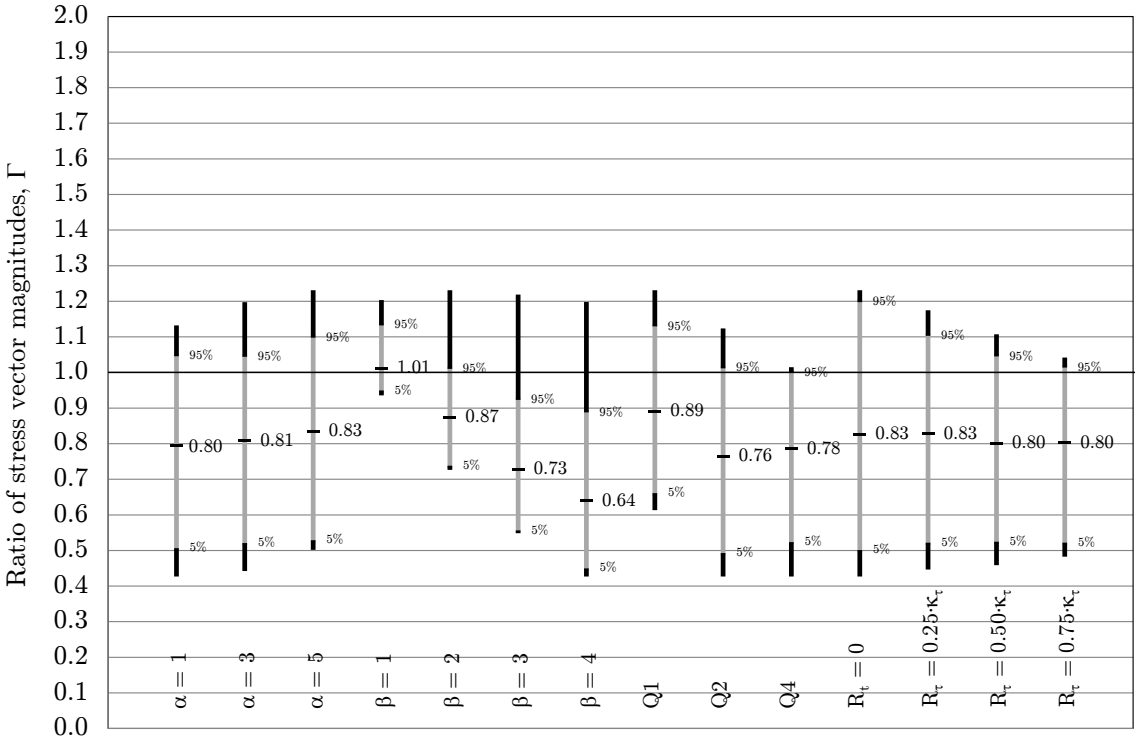

Figure 3.17.: Evaluation of data subsets (CN 30.1).

In order to identify any inherent problems within the CN 30.1 proof for specific parameters, the mean and extreme values of the ratio of stress vector magnitudes, $\Gamma = R_{proof}/R_{FEA}$, are shown in Figure 3.17 for each value of plate aspect ratio (α), plate slenderness parameter (β), quadrants of compressive/tensile load combinations (Q1, Q2 and Q4) and levels of shear (R_τ). In case of the plate aspect ratios, the mean values

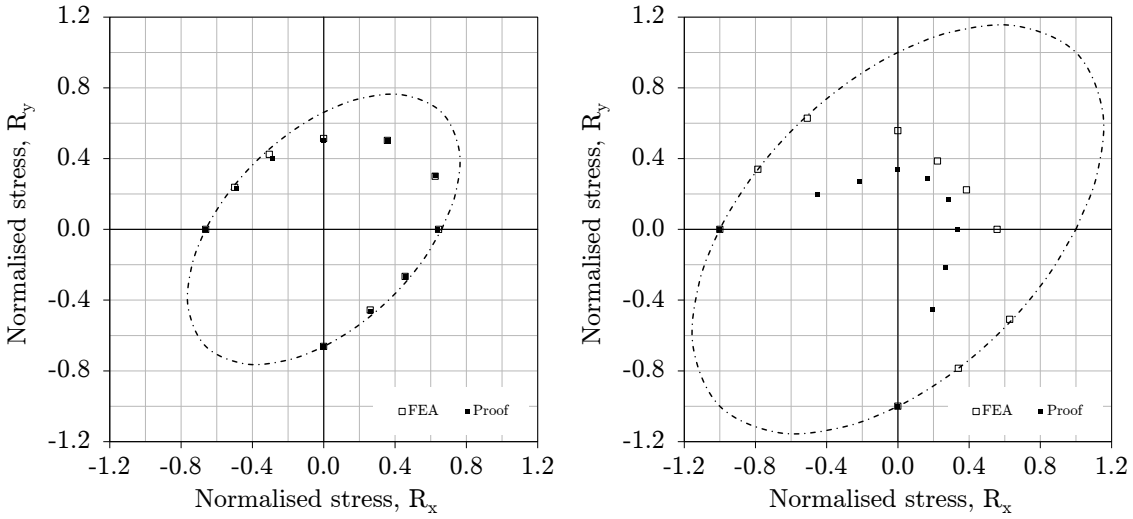

(a) $\alpha = 3,\ \beta = 1,\ R_\tau = 0.75 \cdot \kappa_\tau$ (b) $\alpha = 1,\ \beta = 4,\ R_\tau = 0$

Figure 3.18.: Comparison plots (CN 30.1).

of Γ indicate a significantly to significantly/extremely conservative bias for all values of α. The ranges of extreme values indicate poor to quite poor precision for all plate aspect ratios. In case of the plate slenderness parameters, the mean values of Γ indicate a slightly non-conservative bias for $\beta = 1$ to an extremely conservative bias for $\beta = 4$, i.e. increasing conservatism with increasing plate slenderness. The ranges of extreme values indicate quite good precision for $\beta = 1$ to somewhat poor precision for $\beta = 4$, i.e. decreasing precision with increasing plate slenderness. In case of the compressive/tensile load combinations, the mean values of Γ indicate a moderately/significantly conservative bias in Q1, an extremely conservative bias in Q2 and a significantly/extremely conservative bias in Q4. The ranges of extreme values indicate poor precision in all quadrants. In case of shear, the mean values of Γ reveal a significantly to significantly/extremely conservative bias for all levels of shear. The ranges of extreme values indicate very poor precision in the absence of shear to poor precision for $R_\tau = 0.75 \cdot \kappa_\tau$, i.e. increasing precision with increasing shear.

In order to obtain an impression of the strengths and weaknesses of the CN 30.1 proof, the lowest and highest values of the squares of the residuals (S_r/n_s) for each combination of plate aspect ratio (α), plate slenderness parameter (β) and level of shear (R_τ) have been calculated. The lowest value of S_r/n_s is for the combination $\alpha = 3$, $\beta = 1$ and $R_\tau = 0.75 \cdot \kappa_\tau$, the capacity curve of which is plotted in Figure 3.18(a). Conversely, the highest value of S_r/n_s is for the combination $\alpha = 1$, $\beta = 4$ and $R_\tau = 0$, the capacity curve of which is plotted in Figure 3.18(b).

Bias and Precision - Amended DIN 4114

In accordance with the evaluation scheme described in §3.1, the amended DIN 4114 proof has been used to calculate the capacity of plating for the 360 evaluation points. The resulting scatter plots for both the design space and design subspace are shown in Figure 3.19. The five key performance indicators used to measure precision and bias are shown in

Table 3.4. Regarding the overall measure of error (KPI_1), the average of the squares of the residuals S_r/n_s is very high for the design space ($S_r/n_s = 0.039$) and quite high for the design subspace ($S_r/n_s = 0.020$). With respect to the measure of bias (KPI_2), the least-squares fit of a straight line through the R_{FEA} - R_{proof} data points gives a significantly conservative slope for the design space ($m_{lsr} = 0.84$) and an extremely conservative slope for the design subspace ($m_{lsr} = 0.78$). Concerning the measure of precision (KPI_3), the coefficients of determination reflect a very high degree of scatter for the design space ($R_D{}^2 = 0.63$) and a quite high degree of scatter for the design subspace ($R_D{}^2 = 0.69$). Regarding the extent of non-conservatism (KPI_4), a straight line through the 95^{th} percentile gives a moderately/significantly non-conservative slope for the design space ($m_{95} = 1.10$) and a slightly non-conservative slope for the design subspace ($m_{95} = 1.03$). With respect to the extent of conservatism (KPI_5), a straight line through the 5^{th} percentile gives an extremely conservative slope for both the design space ($m_5 = 0.36$) and design subspace ($m_5 = 0.45$).

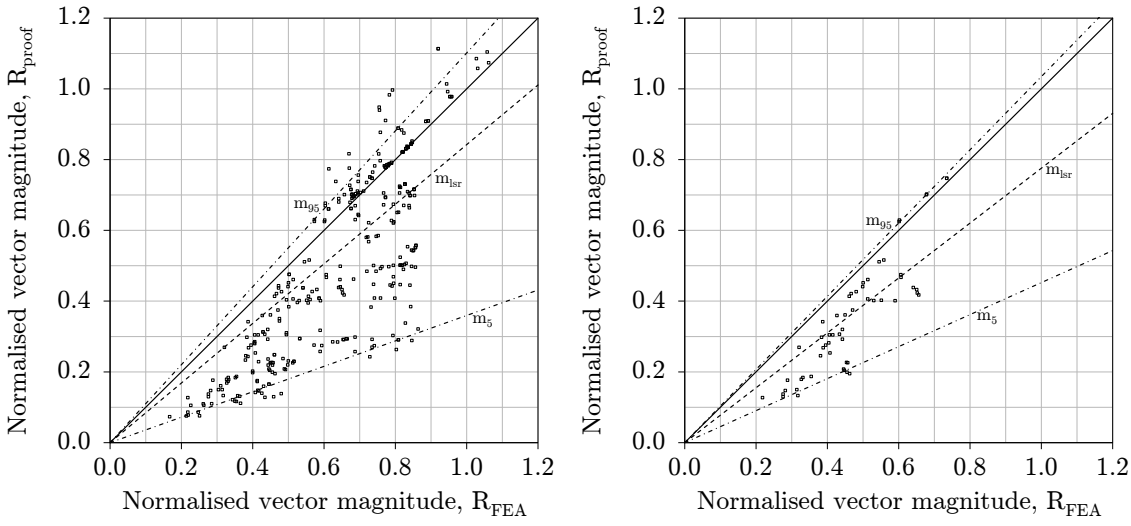

(a) Design space (360 evaluation points) (b) Design subspace (56 evaluation points)

Figure 3.19.: Scatter plots of R_{FEA} - R_{proof} (Amended DIN 4114).

KPI		Design space	Design subspace	Target
1	S_r/n_s	0.039	0.020	0.000
2	m_{lsr}	0.84	0.78	1.00
3	$R_D{}^2$	0.63	0.69	1.00
4	m_{95}	1.10	1.03	1.00
5	m_5	0.36	0.45	1.00

Table 3.4.: Key performance indicators (Amended DIN 4114).

In order to identify any inherent problems within the amended DIN 4114 proof for specific parameters, the mean and extreme values of the ratio of stress vector magnitudes, $\Gamma = R_{proof}/R_{FEA}$, are shown in Figure 3.20 for each value of plate aspect ratio (α), plate

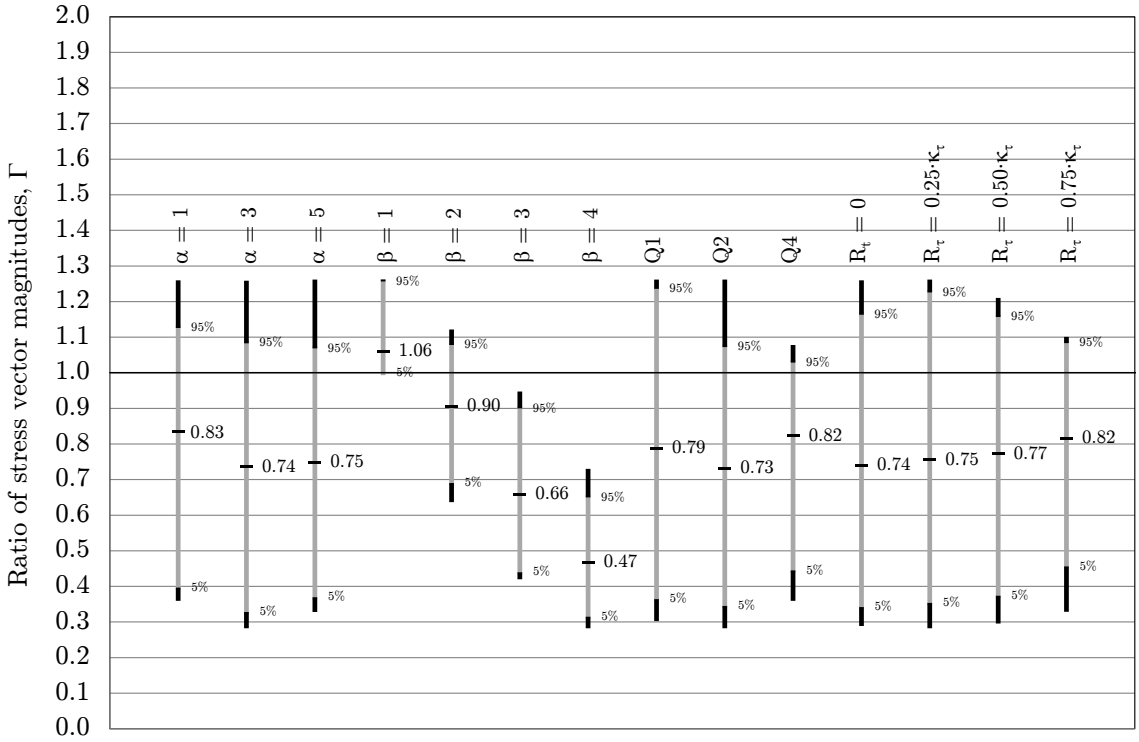

Figure 3.20.: Evaluation of data subsets (Amended DIN 4114).

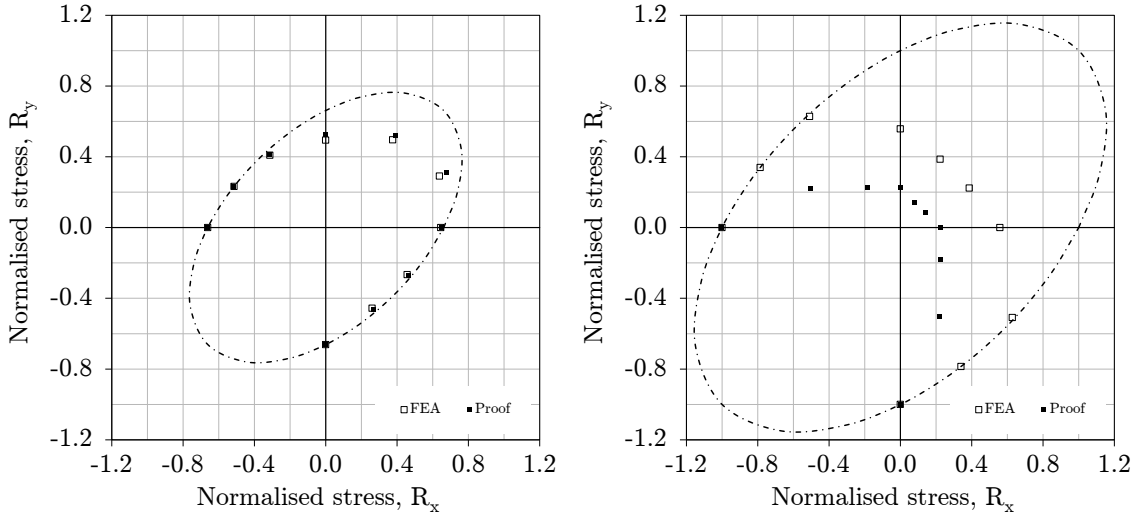

(a) $\alpha = 5,\ \beta = 1,\ R_\tau = 0.75 \cdot \kappa_\tau$ (b) $\alpha = 1,\ \beta = 4,\ R_\tau = 0$

Figure 3.21.: Comparison plots (Amended DIN 4114).

slenderness parameter (β), quadrants of compressive/tensile load combinations (Q1, Q2 and Q4) and levels of shear (R_τ). In case of the plate aspect ratios, the mean values of Γ indicate a significantly conservative bias for $\alpha = 1$ and an extremely conservative bias for $\alpha = 3$ and $\alpha = 5$. The ranges of extreme values indicate very poor precision for all plate aspect ratios. In case of the plate slenderness parameters, the mean values of Γ

indicate a moderately non-conservative bias for $\beta = 1$ to an extremely conservative bias for $\beta = 4$, i.e. increasing conservatism with increasing plate slenderness. The ranges of extreme values indicate good precision for $\beta = 1$ and $\beta = 4$, somewhat good precision for $\beta = 2$ and poor precision for $\beta = 3$. In case of the compressive/tensile load combinations, the mean values of Γ indicate a significantly/extremely conservative bias in Q1, an extremely conservative bias in Q2 and a significantly conservative bias in Q4. The ranges of extreme values indicate quite poor to very poor precision in all quadrants. In case of shear, the mean values of Γ reveal an extremely conservative bias in the absence of shear and an extremely to significantly/extremely conservative bias in the presence of shear, i.e. decreasing conservatism with increasing shear. The ranges of extreme values indicate quite poor to very poor precision.

In order to obtain an impression of the strengths and weaknesses of the amended DIN 4114 proof, the lowest and highest values of the squares of the residuals (S_r/n_s) for each combination of plate aspect ratio (α), plate slenderness parameter (β) and level of shear (R_τ) have been calculated. The lowest value of S_r/n_s is for the combination $\alpha = 5$, $\beta = 1$ and $R_\tau = 0.75 \cdot \kappa_\tau$, the capacity curve of which is plotted in Figure 3.21(a). Conversely, the highest value of S_r/n_s is for the combination $\alpha = 1$, $\beta = 4$ and $R_\tau = 0$, the capacity curve of which is plotted in Figure 3.21(b).

3.3.2. PULS (DnV)

In October 2002 DnV replaced CN 30.1 with its *Recommended Practice DNV-RP-201 (Buckling Strength of Plated Structures)*. As noted in its introduction, DNV-RP-201 describes two different, but equally acceptable, methods for buckling and ultimate strength assessment of plated structures. The first method is a "conventional" buckling code for plates and stiffeners based on an updated version of CN 30.1 where the proof of plate capacity is based on the BV amendment of the DIN 18800 proof (presented in §3.3.4). The second method is a "computerised, semi-analytical" buckling code called PULS (Panel Ultimate Limit State). By means of a description of the *advanced buckling assessment method* required for the check of plates and stiffened panels subjected to combined stress fields, PULS was ostensibly included in CSR-OT.

Although its (energy) formulations are derived analytically using a variational method, PULS is characterised as *semi-analytical* because the resulting set of equations are solved with a numerical method that is also used for incrementally advancing the solution along the load-displacement curve. Variational methods are important techniques of mathematical approximation and are used in the mechanics of materials to solve otherwise intractable boundary value problems. The objective of variational methods is to identify from a set of admissible functions that which represents the deflected shape of an elastic body in stable equilibrium [55].

In this regard, the Ritz method[6] applies the *principle of minimum potential energy* to identify the deflected shape (of all shapes that satisfy the boundary conditions) which minimises the change in the total potential energy Π of the system. When there is no change in the total potential energy of the system, reference is alternatively made to the

[6] Often called the *Rayleigh-Ritz* method since the methods of Rayleigh and Ritz are the same when only one-term expressions are used to describe buckling deflections. An alternative energy formulation can be obtained by Galerkin's method wherein the governing differential equation of the plate is used to define the total potential energy of the system [55].

principle of stationary potential energy

$$\delta\Pi = \delta U + \delta V = 0 \tag{3.25}$$

where δU is the change in internal strain energy and δV the change in the potential of external loads. The strain energy U stored in the plate during deformation is found by integrating the work of internal forces, where the strain energy calculated in PULS has both a membrane component U_m and a bending component U_b, i.e. $U = U_m + U_b$ (the latter based on the Love-Kirchoff approximation). In calculating the potential of *in-plane* external loads, the displacements at the edges of the plate are calculated using the non-linear plate theory of Marguerre [56] who extended the membrane strain-displacement relations of von Kármán to plates with geometric imperfections

$$\epsilon_x = u_x + \frac{1}{2}w_x^2 + w_{0,x} \cdot w_x \tag{3.26a}$$

$$\epsilon_y = v_y + \frac{1}{2}w_y^2 + w_{0,y} \cdot w_y \tag{3.26b}$$

$$\gamma_{xy} = u_y + v_x + w_x \cdot w_y + w_{0,x} \cdot w_y + w_{0,y} \cdot w_x \tag{3.26c}$$

where w and w_0 are the additional and initial out-of-plane deflections of the plate, respectively.

Because the lateral buckling deflections are discretised in PULS using a double Fourier series

$$w(x,y) = \sum_{m=1}^{M}\sum_{n=1}^{N} A_{mn} \cdot \sin\left(\frac{m\pi}{a}x\right)\sin\left(\frac{n\pi}{b}y\right) \tag{3.27}$$

the principle of stationary potential energy can be alternatively expressed using the Ritz method as

$$\frac{\partial\Pi}{\partial A_{mn}} = 0 \tag{3.28}$$

which reduces the problem of finding the deflected shape of the plate in stable equilibrium to finding the unknown displacement amplitudes A_{mn} in Equation (3.27).

As shown by Byklum and Amdahl [57], in case of large deflections the potential energy Π of a plate is of the fourth order in the deflection. Therefore, the equations resulting from Equation (3.28) are of the third order in the displacement amplitudes A_{mn}. In order to avoid solving a set of third order equations, an incremental solution using a numerical perturbation scheme with arc length control is used in PULS to obtain a linear equation system. Details pertaining to the application of the perturbation method to plate buckling problems are reported by Steen [58].

For each incremental step along the load-displacement curve, stresses are calculated at the "hot spot" locations (see Figure 3.9), whereby it is normal to assume plane stress

conditions for thin plates (i.e. $\sigma_z = \tau_{yz} = \tau_{zx} = 0$)

$$\sigma_x = \frac{E}{1+\nu^2}(\epsilon_x + \nu \cdot \epsilon_y) \tag{3.29a}$$

$$\sigma_y = \frac{E}{1+\nu^2}(\epsilon_y + \nu \cdot \epsilon_x) \tag{3.29b}$$

$$\tau_{xy} = G \cdot \gamma_{xy} \tag{3.29c}$$

from which the equivalent von Mises stress is calculated

$$\sigma_{eq} = \sqrt{\sigma_x^2 + \sigma_y^2 - \sigma_x \cdot \sigma_y + 3 \cdot \tau_{xy}^2} \tag{3.30}$$

and compared to the yield stress, i.e. $\sigma_{eq} \leqslant \sigma_Y$. As shown in Chapter 2, yielding within the middle plane of the plate is a precursor to collapse.

Bias and Precision

In accordance with the evaluation scheme described in §3.1, PULS has been used to calculate the capacity of plating for the 360 evaluation points. Like the proof of Ueda et al. as well as the CN 30.1 and DIN 4114 proofs, it is important to recognise that the plate reduction factors κ_x, κ_y and κ_τ are inherently calculated within PULS (unlike the remaining proofs of this chapter where these factors are obtained from the finite element analyses and used as input). Accordingly, the bias and precision in this section not only reflect any errors in the shape of the capacity curves, but their endpoints as well, i.e. PULS is measured against relatively higher standards of bias and precision together with the above-mentioned proofs. With this in mind, the resulting scatter plots for both the design space and design subspace are shown in Figure 3.22. The five key performance indicators used to measure precision and bias are shown in Table 3.5. Regarding the overall measure of error (KPI_1), the average of the squares of the residuals S_r/n_s is very low for both the design space ($S_r/n_s = 0.004$) and design subspace ($S_r/n_s = 0.004$). With respect to the measure of bias (KPI_2), the least-squares fit of a straight line through the R_{FEA} - R_{proof} data points gives a slightly non-conservative slope for the design space ($m_{lsr} = 1.04$) and a moderately/significantly non-conservative slope for the design subspace ($m_{lsr} = 1.11$). Concerning the measure of precision (KPI_3), the coefficients of determination reflect a very low degree of scatter for both the design space (${R_D}^2 = 0.92$) and design subspace (${R_D}^2 = 0.94$). Regarding the extent of non-conservatism (KPI_4), a straight line through the 95^{th} percentile gives a significantly/extremely non-conservative slope for both the design space ($m_{95} = 1.20$) and design subspace ($m_{95} = 1.21$). With respect to the extent of conservatism (KPI_5), a straight line through the 5^{th} percentile gives a slightly conservative slope for the design space ($m_5 = 0.96$) and a slope without bias for the design subspace ($m_5 = 1.00$).

In order to identify any inherent problems within PULS for specific parameters, the mean and extreme values of the ratio of stress vector magnitudes, $\Gamma = R_{proof}/R_{FEA}$, are shown in Figure 3.23 for each value of plate aspect ratio (α), plate slenderness parameter (β), quadrants of compressive/tensile load combinations (Q1, Q2 and Q4) and levels of shear (R_τ). In case of the plate aspect ratios, the mean values of Γ indicate a slightly/moderately non-conservative bias for all values of α. The ranges of extreme values

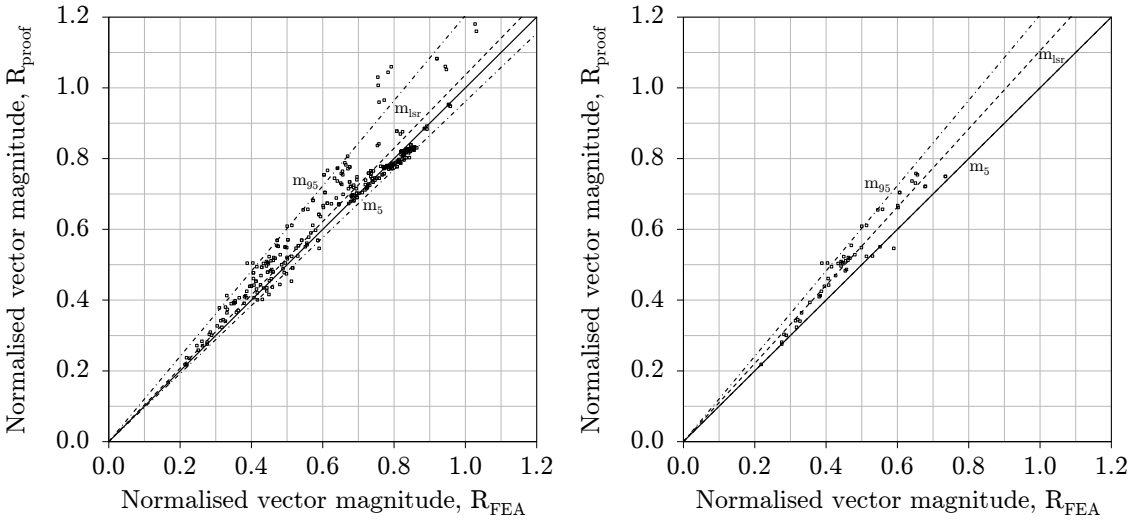

(a) Design space (360 evaluation points)

(b) Design subspace (56 evaluation points)

Figure 3.22.: Scatter plots of R_{FEA} - R_{proof} (PULS).

KPI		Design space	Design subspace	Target
1	S_r/n_s	0.004	0.004	0.000
2	m_{lsr}	1.04	1.11	1.00
3	$R_D{}^2$	0.92	0.94	1.00
4	m_{95}	1.20	1.21	1.00
5	m_5	0.96	1.00	1.00

Table 3.5.: Key performance indicators (PULS).

indicate good precision for all values of α. In case of the plate slenderness parameters, the mean values of Γ indicate a moderately to slightly non-conservative bias for all values of β. The ranges of extreme values indicate good to quite good precision for all plate slenderness parameters. In case of the compressive/tensile load combinations, the mean values of Γ indicate a moderately/significantly non-conservative bias in Q1 and a slightly non-conservative bias in Q2 and Q4. The ranges of extreme values indicate good precision (Q1) to very good precision (Q2 and Q4). In case of shear, the mean values of Γ reveal a slightly non-conservative bias in the absence of shear to a moderately non-conservative bias for $R_\tau = 0.75 \cdot \kappa_\tau$, i.e. increasing non-conservatism with increasing levels of shear. The ranges of extreme values indicate good to quite good precision for all values of shear.

In order to obtain an impression of the strengths and weaknesses of PULS, the lowest and highest values of the squares of the residuals (S_r/n_s) for each combination of plate aspect ratio (α), plate slenderness parameter (β) and level of shear (R_τ) have been calculated. The lowest value of S_r/n_s is for the combination $\alpha = 5$, $\beta = 3$ and $R_\tau = 0.5 \cdot \kappa_\tau$, the capacity curve of which is plotted in Figure 3.24(a). Conversely, the highest value of S_r/n_s is for the combination $\alpha = 5$, $\beta = 1$ and $R_\tau = 0$, the capacity curve of which is plotted in Figure 3.24(b).

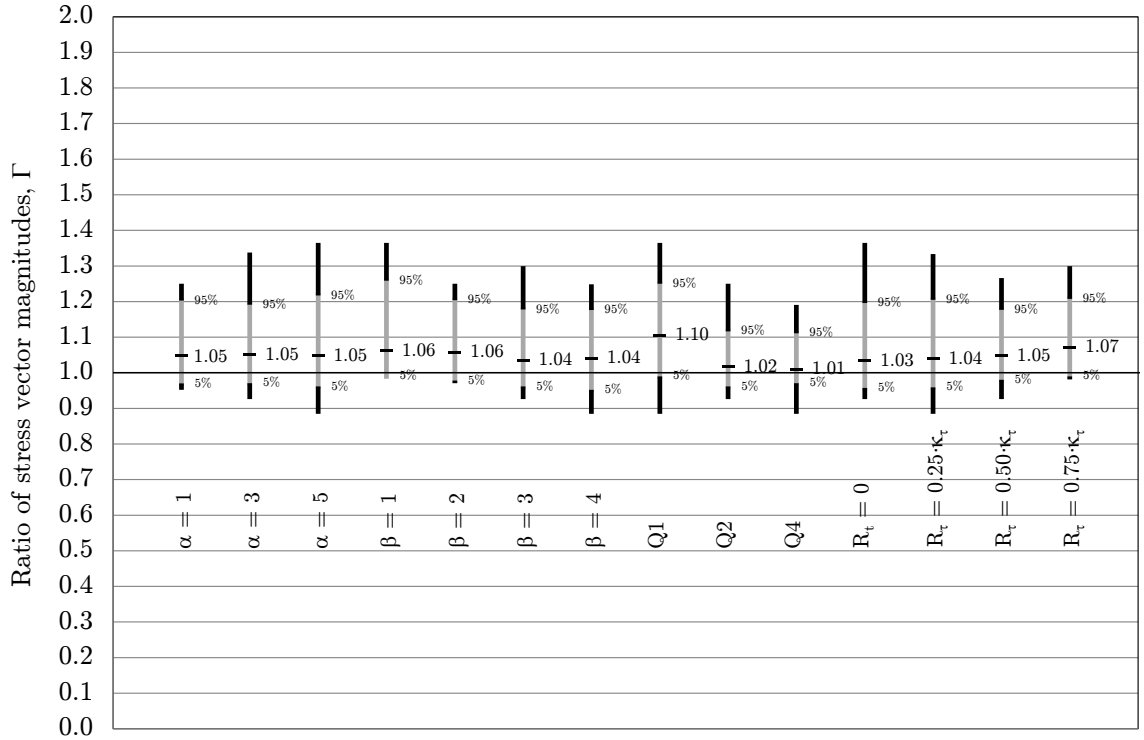

Figure 3.23.: Evaluation of data subsets (PULS).

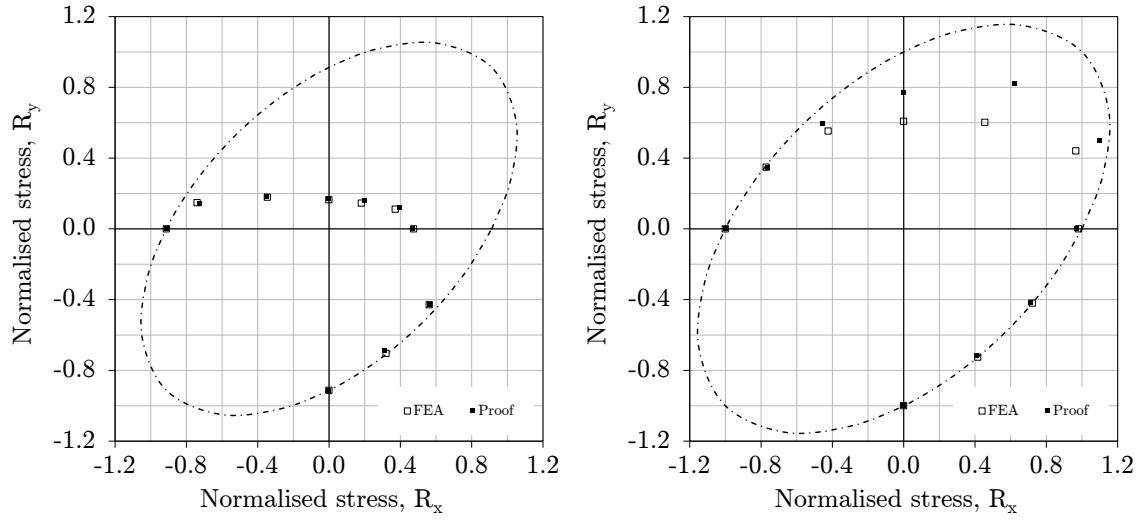

(a) $\alpha = 5,\ \beta = 3,\ R_\tau = 0.5 \cdot \kappa_\tau$ (b) $\alpha = 5,\ \beta = 1,\ R_\tau = 0$

Figure 3.24.: Comparison plots (PULS).

3.3.3. Amended DIN 18800 (GL)

In November 1990 an updated series of the German construction standard DIN 18800 (Structural Steelwork) set out practical rules for engineers based on the philosophy of design and safety formulated in *Principles for the Specification of Requirements Relating*

to the Safety of Structures [59] (as referenced in [26] and [47]). The updated DIN 18800 was developed jointly by the *Building and Civil Engineering Standards Committee* and the *German Committee for Structural Steelwork* (as noted in §2.1.4). The new series of standards are based on the ultimate strength concept and replace DIN 4114 from July 1952 as well as DASt-Guidelines 012 (Proof of Safety against Buckling of Plates) from 1979 which are based on elastic theory (with plasticity corrections). Part 3 of DIN 18800 (Analysis of Safety against Buckling of Plates) contains a proof of plate capacity under combined in-plane loads (Item 504 - Analysis for coexistent edges stresses σ_x, σ_y and τ_{xy}) [26]

$$\left(\frac{R_x}{\kappa_x}\right)^{e_1} + \left(\frac{R_y}{\kappa_y}\right)^{e_2} - B \cdot \left(\frac{R_x}{\kappa_x}\right) \cdot \left(\frac{R_y}{\kappa_y}\right) + \left(\frac{R_\tau}{\kappa_\tau}\right)^{e_3} = 1.0 \tag{3.31}$$

where

$$e_1 = 1 + \kappa_x^4 \tag{3.32a}$$

$$e_2 = 1 + \kappa_y^4 \tag{3.32b}$$

$$e_3 = 1 + \kappa_x \cdot \kappa_y \cdot \kappa_\tau^2 \tag{3.32c}$$

and

$$B = \begin{cases} (\kappa_x \cdot \kappa_y)^6 & \text{if } \sigma_x > 0 \text{ and } \sigma_y > 0 \\ \dfrac{\sigma_x \cdot \sigma_y}{|\sigma_x \cdot \sigma_y|} & \text{if } \sigma_x \leqslant 0 \quad \text{or} \quad \sigma_y \leqslant 0 \end{cases} \tag{3.33}$$

Each term in Equation (3.32) is not to exceed 1.0.

As with Paik's proof, Equation (3.31) is a generalised form of the von Mises failure criteria as shown in Equation (3.11). In addition to being based on the ultimate strength concept, the two most important points of departure for this proof compared to earlier DIN proofs is its relative ease of use and its (normally) conservative results compared to theoretical and experimental investigations [60]. Because DIN 18800 was developed principally for civil engineering applications (e.g. plate girder bridges) these investigations focussed primarily on combinations of uniaxial and shear stresses.

In 1997 GL revised its proof of buckling strength on the basis of the ultimate strength concept embodied in DIN 18800. However, in order to improve its *practical application*, the calculation methodology of DIN 18800 was simplified in some areas and otherwise adapted to the hull structures of ships [61]. Moreover, results of its own research were incorporated into GL's new buckling strength requirements. For instance, large-scale tests were performed for typical ship structure panels under combined biaxial in-plane compression and lateral loads [10]. On the basis of such research, three changes were incorporated into the GL proof of plate capacity.

1. Removal of reduction factors from denominators of interaction terms

Equation (3.31) was redefined to normalise stresses in the interaction term on the basis of yield stress rather than ultimate (uniaxial) stresses

$$\left(\frac{R_x}{\kappa_x}\right)^{e_1} + \left(\frac{R_y}{\kappa_y}\right)^{e_2} - B \cdot R_x \cdot R_y + \left(\frac{R_\tau}{\kappa_\tau}\right)^{e_3} = 1.0 \tag{3.34}$$

2. Redefinition of interaction coefficient B

In case $\sigma_x > 0$ and $\sigma_y > 0$, the exponent on the product $(\kappa_x \cdot \kappa_y)$ is reduced from six to five. In case $\sigma_x \leqslant 0$ or $\sigma_y \leqslant 0$, B is set equal to unity.

$$B = \begin{cases} (\kappa_x \cdot \kappa_y)^5 & \text{if } \sigma_x > 0 \text{ and } \sigma_y > 0 \\ 1.0 & \text{if } \sigma_x \leqslant 0 \text{ or } \sigma_y \leqslant 0 \end{cases} \tag{3.35}$$

3. Introduction of corrected stresses to account for Poisson effects

In general finite element analyses are required to directly assess the strength of ship hull structures. In some cases a *global direct strength analysis* is required to assess the overall hull girder response while in other cases a *partial ship structural analysis* to assess the strength of hull girder structural members, primary supporting structural members and bulkheads is sufficient, e.g. a cargo hold analysis [62]. In such cases linear elastic analyses are usually performed with a b x b mesh size to carry out a yield assessment. Buckling strength assessments are carried out separately on a plate-by-plate basis. In order to do so, linearised *reference stresses* are calculated over the edges of each plate as a function of the finite element stresses[7]. Of course, the stresses from finite element analyses contain a Poisson effect which is not present in the beam stresses upon which the exponents and interaction coefficient in Equation (3.32) and Equation (3.35), respectively, are based. Accordingly, as shown in Figure 3.25, the plates stresses σ_x^* and σ_y^* obtained from finite element analyses need to be converted into beam stresses σ_x and σ_y, respectively, for use in Equation (3.34)

$$\sigma_x = \frac{(\sigma_x^* - 0.3 \cdot \sigma_y^*)}{0.91} \tag{3.36a}$$

$$\sigma_y = \frac{(\sigma_y^* - 0.3 \cdot \sigma_x^*)}{0.91} \tag{3.36b}$$

where Poisson's ratio is taken as $\nu = 0.3$.

When the compressive stresses fulfil the condition $\sigma_y^* < 0.3 \cdot \sigma_x^*$, then $\sigma_y = 0$ and $\sigma_x = \sigma_x^*$. Similarly, when the compressive stresses fulfil the condition $\sigma_x^* < 0.3 \cdot \sigma_y^*$, then $\sigma_x = 0$ and $\sigma_y = \sigma_y^*$. No Poisson correction is applied when either σ_x^* or σ_y^* are tensile stresses. However, from the mechanics of materials, these Poisson corrections should in fact be

$$\sigma_x = \sigma_x^* - 0.3 \cdot \sigma_y^* \tag{3.37a}$$

$$\sigma_y = \sigma_y^* - 0.3 \cdot \sigma_x^* \tag{3.37b}$$

Accordingly, Equation (3.37) ensures that the plate and beam stresses have the same corresponding strains, but Equation (3.36) introduces some conservatism (about 10 %) into the conversion.

[7] When necessary, plates with an irregular geometry are idealised as equivalent rectangular plates. In §5.1.1 the idealisation of plate geometries and determination of reference stresses are discussed in detail.

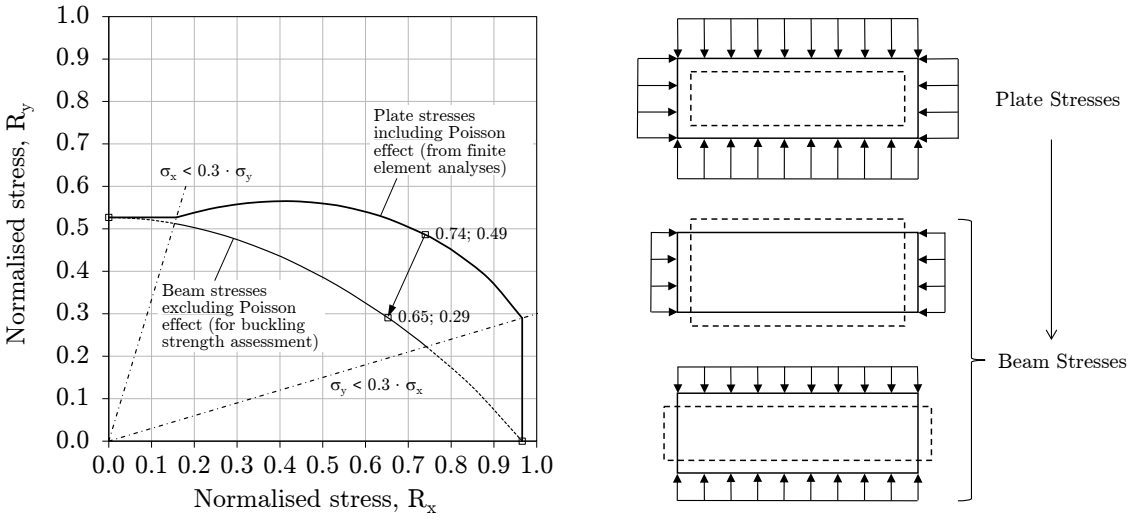

Figure 3.25.: Poisson correction.

Bias and Precision

In accordance with the evaluation scheme described in §3.1, the amended DIN 18800 proof (with Poisson correction) has been used to calculate the capacity of plating for the 360 evaluation points. The resulting scatter plots for both the design space and design subspace are shown in Figure 3.26. The five key performance indicators used to measure precision and bias are shown in Table 3.6. Regarding the overall measure of error (KPI_1), the average of the squares of the residuals S_r/n_s is high for the design space ($S_r/n_s = 0.018$), but quite low for the design subspace ($S_r/n_s = 0.005$). With respect to the measure of bias (KPI_2), the least-squares fit of a straight line through the R_{FEA} - R_{proof} data points gives a significantly conservative slope for the design space ($m_{lsr} = 0.87$) and a moderately conservative slope for the design subspace ($m_{lsr} = 0.93$). Concerning the measure of precision (KPI_3), the coefficients of determination reflect a high degree of scatter for the design space ($R_D{}^2 = 0.73$), but somewhat low degree of scatter for the design subspace ($R_D{}^2 = 0.80$). Regarding the extent of non-conservatism (KPI_4), a straight line through the 95^{th} percentile gives a significantly non-conservative slope for both the design space ($m_{95} = 1.14$) and design subspace ($m_{95} = 1.13$). With respect to the extent of conservatism (KPI_5), a straight line through the 5^{th} percentile gives an extremely conservative slope for both the design space ($m_5 = 0.67$) and design subspace ($m_5 = 0.75$).

KPI		Design space	Design subspace	Target
1	S_r/n_s	0.018	0.005	0.000
2	m_{lsr}	0.87	0.93	1.00
3	$R_D{}^2$	0.73	0.80	1.00
4	m_{95}	1.14	1.13	1.00
5	m_5	0.67	0.75	1.00

Table 3.6.: Key performance indicators (Amended DIN 18800).

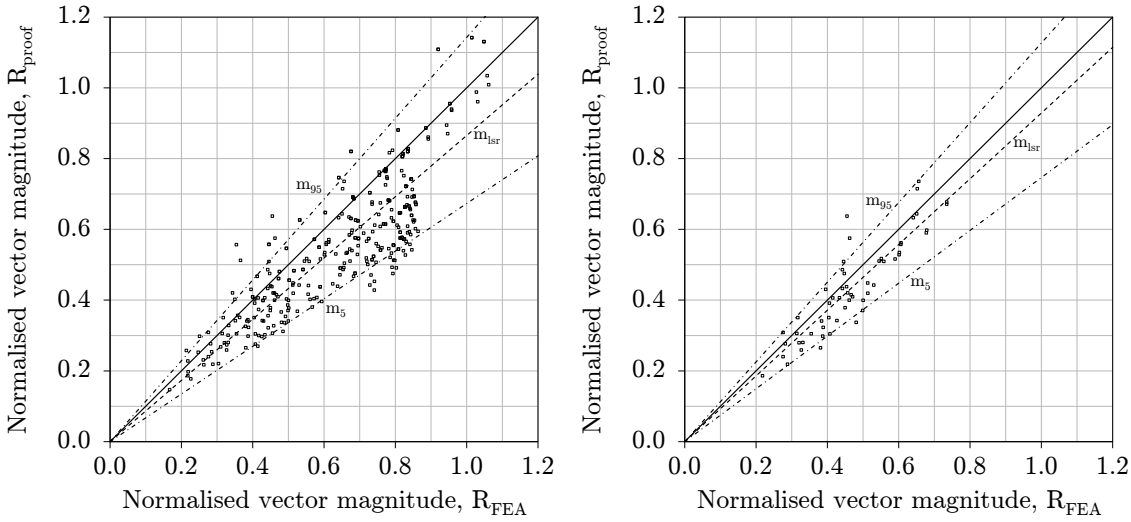

(a) Design space (360 evaluation points) (b) Design subspace (56 evaluation points)

Figure 3.26.: Scatter plots of R_{FEA} - R_{proof} (Amended DIN 18800).

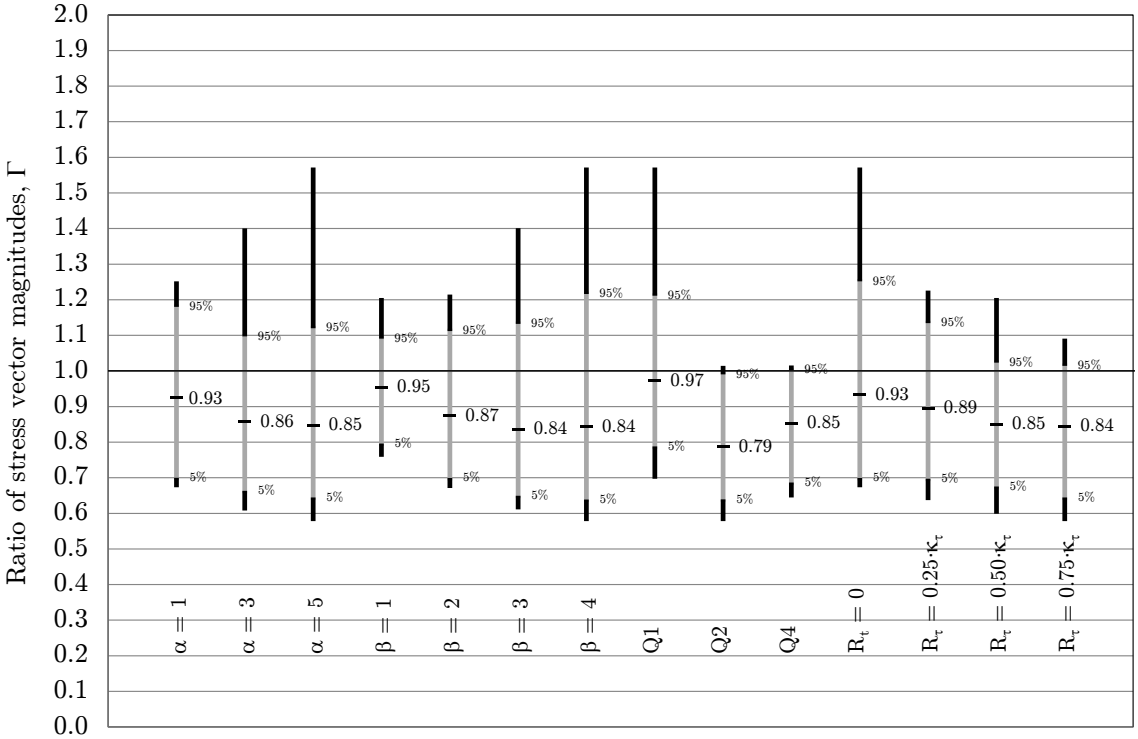

Figure 3.27.: Evaluation of data subsets (Amended DIN 18800).

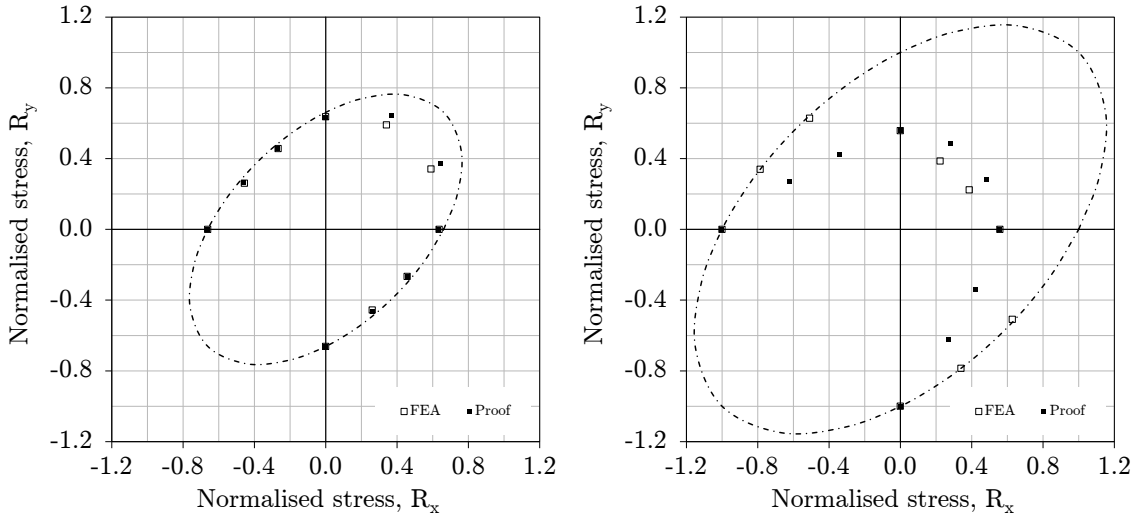

(a) $\alpha = 1$, $\beta = 1$, $R_\tau = 0.75 \cdot \kappa_\tau$ (b) $\alpha = 1$, $\beta = 4$, $R_\tau = 0$

Figure 3.28.: Comparison plots (Amended DIN 18800).

In order to identify any inherent problems within the amended DIN 18800 proof (with Poisson correction) for specific parameters, the mean and extreme values of the ratio of stress vector magnitudes, $\Gamma = R_{proof}/R_{FEA}$, are shown in Figure 3.27 for each value of plate aspect ratio (α), plate slenderness parameter (β), quadrants of compressive/tensile load combinations (Q1, Q2 and Q4) and levels of shear (R_τ). In case of the plate aspect ratios, the mean values of Γ indicate a moderately conservative bias for $\alpha = 1$ to a significantly conservative bias for $\alpha = 5$, i.e. increasing conservatism with increasing aspect ratios. The ranges of extreme values indicate poor to somewhat poor precision for all plate aspect ratios. In case of the plate slenderness parameters, the mean values of Γ indicate a slightly/moderately conservative bias for $\beta = 1$ to a significantly conservative bias for $\beta = 4$, i.e. a general increase in conservatism with increasing plate slenderness. The ranges of extreme values indicate good precision for $\beta = 1$ to quite poor precision for $\beta = 4$, i.e. decreasing precision with increasing plate slenderness. In case of the compressive/tensile load combinations, the mean values of Γ indicate a slightly conservative bias in Q1, a significantly/extremely conservative bias in Q2 and a significantly conservative bias in Q4. The ranges of extreme values indicate somewhat poor precision in Q1 but good precision in Q2 and Q4. In case of shear, the mean values of Γ reveal a moderately conservative bias in the absence of shear to a significantly conservative bias for $R_\tau = 0.75 \cdot \kappa_\tau$, i.e. increasing conservatism with increasing levels of shear. The ranges of extreme values indicate quite poor precision in the absence of shear to somewhat good precision for $R_\tau = 0.75 \cdot \kappa_\tau$, i.e. increasing precision with increasing levels of shear.

In order to obtain an impression of the strengths and weaknesses of the amended DIN 18800 proof (with Poisson correction), the lowest and highest values of the squares of the residuals (S_r/n_s) for each combination of plate aspect ratio (α), plate slenderness parameter (β) and level of shear (R_τ) have been calculated. The lowest value of S_r/n_s is for the combination $\alpha = 1$, $\beta = 1$ and $R_\tau = 0.75 \cdot \kappa_\tau$, the capacity curve of which is plotted in Figure 3.28(a). Conversely, the highest value of S_r/n_s is for the combination $\alpha = 1$, $\beta = 4$ and $R_\tau = 0$, the capacity curve of which is plotted in Figure 3.28(b).

3.3.4. Provisional CSR BC & OT (BV)

When CSR-OT was introduced in 2008, it was required that plate buckling under combined in-plane stresses be assessed with a so-called *advanced buckling assessment method*. The method was required to consider the following effects [32]

1. non-linear geometrical behaviour,
2. inelastic material behaviour,
3. initial deflections - geometrical imperfections/out-of-flatness,
4. welding residual stresses,
5. interactions between buckling modes and structural elements; plates, stiffeners, girders etc.,
6. simultaneous acting loads; biaxial compression/tension, shear and lateral pressure,
7. boundary conditions.

As noted in §3.3.2, this *advanced buckling assessment method* referred to PULS in all but name (despite the fact that PULS does not consider inelastic material behaviour). However, alternative advanced buckling analysis methods were permitted provided they considered the foregoing effects and compared well with benchmark results obtained with PULS. Towards this end Bureau Veritas introduced the *BV Advanced Buckling Assessment Method*. In fact, this method was based on the GL proof of buckling strength (in turn based on DIN 18800 and included in CSR-BC), but with a change to the exponents and coefficients of the plate capacity equation insofar that they implicitly account for Poisson effects

$$\left(\frac{R_x}{\kappa_x}\right)^{e_1} + \left(\frac{R_y}{\kappa_y}\right)^{e_2} - B \cdot \left(\frac{R_x}{\kappa_x}\right) \cdot \left(\frac{R_y}{\kappa_y}\right) + \left(\frac{R_\tau}{\kappa_\tau}\right)^{e_3} = 1.0 \tag{3.38}$$

where

$$e_1 = e_2 = e_3 = 2 \tag{3.39}$$

and

$$B = \begin{cases} 1 - \dfrac{b}{120 \cdot t} & \text{if } \dfrac{b}{t} \leqslant 120 \\ 0 & \text{if } \dfrac{b}{t} > 120 \end{cases} \tag{3.40}$$

in case $\sigma_x \geqslant 0$ and $\sigma_y \geqslant 0$, otherwise $B = 1$ (i.e. in Quadrants 2, 3 and 4). The BV *Advanced Buckling Assessment Method* was used provisionally as the proof of plate capacity under combined in-plane loads in initial harmonisation efforts and was included in the first external release of CSR BC & OT in April 2013. However, as shown below, the proof tends to overestimate plate capacity in Quadrant 1 and underestimate capacity in Quadrants 2

and 4 such that an improved proof was needed for inclusion in CSR BC & OT (i.e. the proof developed in Chapter 4).

Bias and Precision

In accordance with the evaluation scheme described in §3.1, the provisional CSR BC & OT proof has been used to calculate the capacity of plating for the 360 evaluation points. The resulting scatter plots for both the design space and design subspace are shown in Figure 3.29. The five key performance indicators used to measure precision and bias are shown in Table 3.7. Regarding the overall measure of error (KPI_1), the average of the squares of the residuals S_r/n_s is high for the design space ($S_r/n_s = 0.012$), but very low for the design subspace ($S_r/n_s = 0.003$). With respect to the measure of bias (KPI_2), the least-squares fit of a straight line through the R_{FEA} - R_{proof} data points gives a moderately conservative slope for the design space ($m_{lsr} = 0.94$) and a moderately non-conservative slope for the design subspace ($m_{lsr} = 1.08$). Concerning the measure of precision (KPI_3), the coefficients of determination reflect a very high degree of scatter for the design space (${R_D}^2 = 0.68$), but a very low degree of scatter for the design subspace (${R_D}^2 = 0.95$). Regarding the extent of non-conservatism (KPI_4), a straight line through the 95^{th} percentile gives an extremely non-conservative slope for the design space ($m_{95} = 1.26$) and a significantly non-conservative slope for the design subspace ($m_{95} = 1.17$). With respect to the extent of conservatism (KPI_5), a straight line through the 5^{th} percentile gives an extremely conservative slope for the design space ($m_5 = 0.73$), but only a slightly conservative slope for the design subspace ($m_5 = 0.97$).

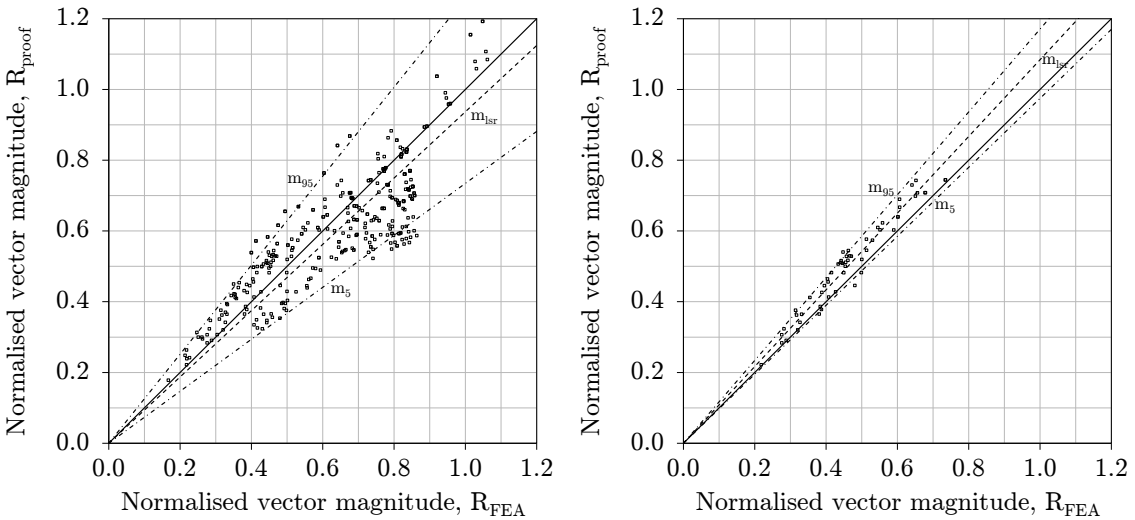

(a) Design space (360 evaluation points) (b) Design subspace (56 evaluation points)

Figure 3.29.: Scatter plots of R_{FEA} - R_{proof} (Provisional CSR BC & OT).

In order to identify any inherent problems within the provisional CSR BC & OT proof for specific parameters, the mean and extreme values of the ratio of stress vector magnitudes, $\Gamma = R_{proof}/R_{FEA}$, are shown in Figure 3.30 for each value of plate aspect ratio (α), plate slenderness parameter (β), quadrants of compressive/tensile load combinations

KPI		Design space	Design subspace	Target
1	S_r/n_s	0.012	0.003	0.000
2	m_{lsr}	0.94	1.08	1.00
3	$R_D{}^2$	0.68	0.95	1.00
4	m_{95}	1.26	1.17	1.00
5	m_5	0.73	0.97	1.00

Table 3.7.: Key performance indicators (Provisional CSR BC & OT).

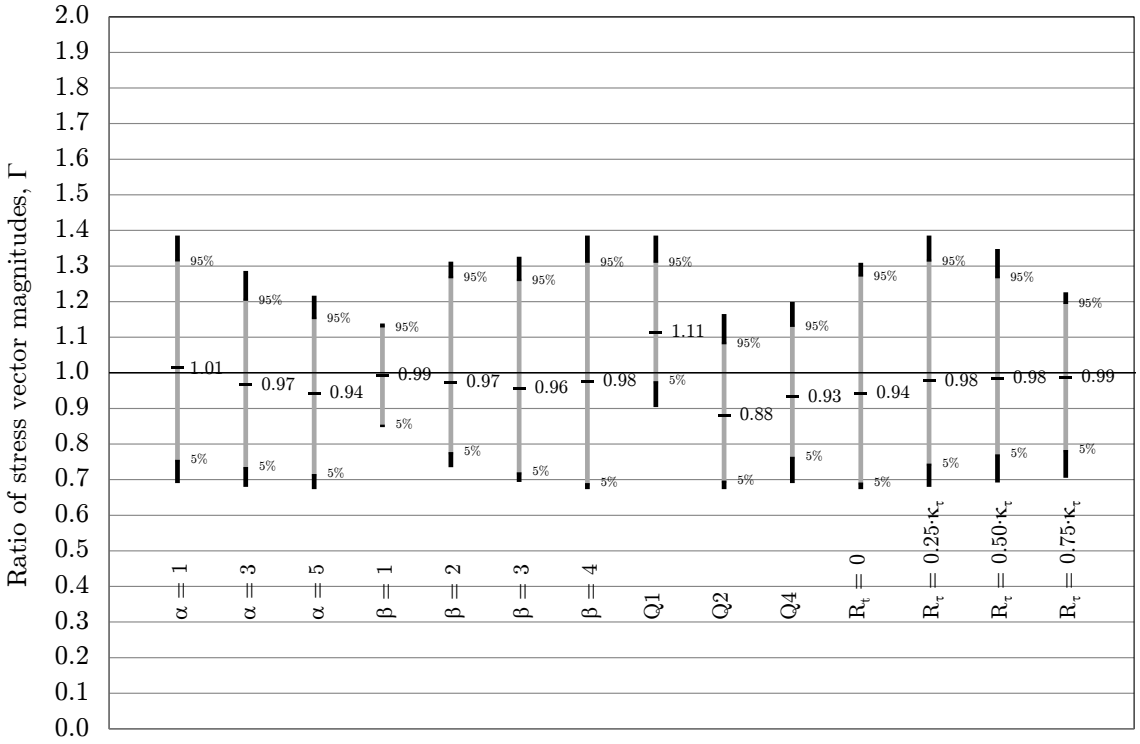

Figure 3.30.: Evaluation of data subsets (Provisional CSR BC & OT).

(Q1, Q2 and Q4) and levels of shear (R_τ). In case of the plate aspect ratios, the mean values of Γ indicate a slightly non-conservative bias for $\alpha = 1$, a slightly conservative bias for $\alpha = 3$ and a moderately conservative bias for $\alpha = 5$, i.e. increasing conservatism with increasing aspect ratios. The ranges of extreme values indicate quite poor precision for $\alpha = 1$ to somewhat poor precision for $\alpha = 5$, i.e. increasing precision with increasing plate aspect ratios. In case of the plate slenderness parameters, the mean values of Γ indicate a slightly conservative bias for all values of β. The ranges of extreme values indicate good precision for $\beta = 1$ to quite poor precision for $\beta = 4$, i.e. decreasing precision with increasing plate slenderness. In case of the compressive/tensile load combinations, the mean values of Γ indicate a significantly non-conservative bias in Q1, a significantly conservative bias in Q2 and a moderately conservative bias in Q4. The ranges of extreme values indicate good to somewhat good precision in all quadrants. In case of shear, the mean values of Γ reveal a moderately conservative bias in the absence of shear and a slightly conservative bias when

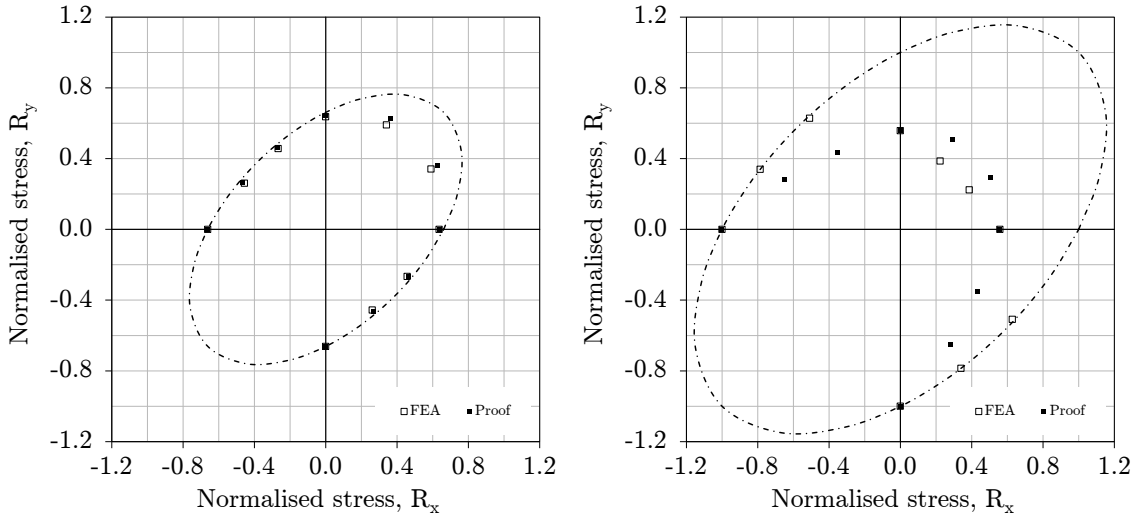

(a) $\alpha = 1,\ \beta = 1,\ R_\tau = 0.75 \cdot \kappa_\tau$ (b) $\alpha = 1,\ \beta = 4,\ R_\tau = 0$

Figure 3.31.: Comparison plots (Provisional CSR BC & OT).

shear is present. The ranges of extreme values indicate quite poor precision in the absence of shear and quite poor to somewhat poor precision when shear is present, i.e. increasing precision with increasing levels of shear.

In order to obtain an impression of the strengths and weaknesses of the provisional CSR BC & OT proof, the lowest and highest values of the squares of the residuals (S_r/n_s) for each combination of plate aspect ratio (α), plate slenderness parameter (β) and level of shear (R_τ) have been calculated. The lowest value of S_r/n_s is for the combination $\alpha = 1$, $\beta = 1$ and $R_\tau = 0.75 \cdot \kappa_\tau$, the capacity curve of which is plotted in Figure 3.31(a). Conversely, the highest value of S_r/n_s is for the combination $\alpha = 1$, $\beta = 4$ and $R_\tau = 0$, the capacity curve of which is plotted in Figure 3.31(b).

4. New Proof

The purpose of this chapter is to develop a new proof of plate capacity under combined in-plane loads. Towards this end, the problem to be solved is stated quite precisely in §4.1 using quantitative and qualitative criteria which define an *acceptable* proof of plate capacity. This is followed in §4.2 by an evaluation of the existing proofs presented in Chapter 3 which shows that each of these proofs fails to satisfy the defined acceptability criteria. Accordingly, in §4.3 a *hypothetical* proof of plate capacity under combined in-plane loads is postulated using a generalised form of the von Mises equation where the exponent e_0 and the interaction coefficient B are derived on the basis of observations made in the investigation of plating collapse mechanisms. Because the hypothetical proof falls just short of satisfying all quantitative acceptance criteria, the exponent e_0 and the interaction coefficient B are redefined on the basis of additional numerical studies (in case of biaxial compression only). The new proof is then evaluated using the same scheme applied to existing proofs. The chapter ends with a description and evaluation in §4.4 of the proof used in the newly harmonised *IACS Common Structural Rules for Bulk Carriers and Oil Tankers* which is based on the present work.

4.1. Problem statement

As noted in Chapter 1, a proof of plate capacity is needed with which to reliably and efficiently design ship plating. As this proof is intended for use in the design and classification of ships, it needs not only to be based on the ultimate strength concept, but needs as well to satisfy certain qualitative and quantitative criteria. In qualitative terms, the proof needs to be (1) concise, (2) physically-based and (3) directly solvable. In quantitative terms, the proof needs to be (1) precise, (2) accurate and (3) robust. Certainly some existing proofs in both literature and the shipbuilding industry meet many of these criteria (primarily the qualitative criteria), only to fail in some important respect, e.g. lack of robustness or direct solution capability. Without an acceptable proof of plate capacity, ships will either be over-designed with weight penalties which must be borne throughout their service lives or be at risk of serious, sometimes catastrophic, structural failure. As discussed in Chapter 1, the ultimate hull girder collapse of MOL Comfort (which reportedly initiated in the bottom shell plating under biaxial loading) is one of the more recent and high profile examples which illustrates the need for such a proof. Accordingly, the problem to be solved in the present work is to develop a proof of plate capacity under combined in-plane loads which meet all of the quantitative and qualitative criteria listed above and which are now defined in detail.

4.1.1. Quantitative Criteria

As noted above, an acceptable proof of plate capacity needs to be (1) precise, (2) accurate and (3) robust, where the latter criterion of robustness requires that the results of a proof be precise and accurate over the full range of load combinations and plating configurations relevant for the shipbuilding industry. In other words, the criterion of robustness is met when the criteria for precision and accuracy are satisfied over the whole of the *design space* (i.e. as defined in §3.1.2).

Precision and accuracy

In §3.1.1 the concepts of precision and accuracy (or bias) were presented together with five key performance indicators (KPI's) for their measurement. Existing proofs were subsequently presented together with their associated KPI's. In Table 4.1 the best values of KPI_1, KPI_2 and KPI_3 obtained with these proofs are shown for both the design space and subspace. As can be seen, the most precise and accurate results are obtained with Paik's proof, but only for the design subspace. When considering the whole of the design space (i.e. including tensile stresses as well as plates with slenderness parameters of $\beta = 1$ or $\beta = 4$ or an aspect ratio of $\alpha = 1$), the most precise and accurate results are obtained with the computerised buckling code PULS. This result is not surprising. The proof of Paik is based on a limited set of non-linear finite element results, whereas PULS is based on analytically derived energy formulations in combination with a numerical method for their solution. For this reason, it is to be expected that the results of PULS are more robust.

KPI		Design Space		Design Subspace		Target
1	S_r/n_s	0.011	0.004	**0.001**	0.004	0.000
2	m_{lsr}	0.91	1.04	**1.03**	1.11	1.00
3	$R_D{}^2$	0.72	0.92	**0.95**	0.94	1.00
		Paik	PULS	Paik	PULS	

Table 4.1.: Key performance indicators KPI_1 to KPI_3 for proofs of Paik and PULS.

In terms of precision and accuracy, the goal of the present work is to develop a proof of plate capacity which has at least the same degrees of precision and accuracy for *both* the design space *and* subspace as the highest degrees obtained with existing proofs for *either* the design space *or* subspace. Therefore, based on Paik's proof in the design subspace, the following acceptance criteria are defined for the KPI's related to precision and accuracy:

KPI_1: $\quad S_r/n_s \leqslant 0.001$

KPI_2: $\quad 0.97 \leqslant m_{lsr} \leqslant 1.00$

KPI_3: $\quad R_D^2 \geqslant 0.95$

As can be seen, a 3% deviation from the target slope $m_{lsr} = 1.00$ is accepted for KPI_2 based on Paik's proof. However, contrary to this existing proof, any bias in an acceptable proof must be conservative.

Measures of conservatism and non-conservatism

Further to the foregoing, results for the remaining two KPI's are shown for the proofs of Paik and PULS in Table 4.2. As explained previously, the fourth KPI $\mathfrak{m}_{95}$ measures the inherent non-conservatism in a proof while the fifth KPI $\mathfrak{m}_5$ measures conservatism. As can be seen, the amount of non-conservatism in PULS and the proof of Paik is rather high, i.e. 5% of the stress vector magnitudes according to these proofs are at least 13% to 21% higher than those obtained with finite element analyses. Conversely, the amount of conservatism of the 5^{th} percentile is at most 5% (except in case of the design space results for Paik's proof).

KPI		Design Space		Design Subspace		Target
4	m_{95}	1.18	1.20	1.13	1.21	1.00
5	m_5	0.73	0.96	0.95	1.00	1.00
	m_{95} - m_5	0.45	0.24	**0.18**	0.21	0.00
		Paik	PULS	Paik	PULS	

Table 4.2.: Key performance indicators KPI_4 and KPI_5 for proofs of Paik and PULS.

Accordingly, because the degrees of conservatism and non-conservatism for these existing proofs are excessively biased towards non-conservatism, the acceptance criteria for the KPI's related to measures of conservatism and non-conservatism are instead based on the smallest spread between KPI_4 and KPI_5, i.e. Paik's proof for the design subspace where $\mathfrak{m}_{95} - \mathfrak{m}_5 = 0.18$. Using the above maximum *conservatism* of 5% instead for the maximum *non-conservatism*, the following acceptance criteria are defined for the KPI's related to measures of conservatism and non-conservatism:

KPI_4: $\quad \mathfrak{m}_{95} \leqslant 1.05$

KPI_5: $\quad \mathfrak{m}_5 \geqslant 0.87$

That is, the acceptable degree of conservatism is calculated as $\mathfrak{m}_5 \geqslant \mathfrak{m}_{95} - 0.18 = 0.87$. Accordingly, similar to the measures of precision and accuracy, the goal of the present work is to develop a proof of plate capacity which has at most the same spread between measures of conservatism and non-conservatism for *both* the design space *and* subspace as the smallest amount of spread obtained with existing proofs for *either* the design space *or* subspace, but with a rather significant shift of 8% in bias towards more conservative results.

4.1.2. Qualitative Criteria

As noted above, an acceptable proof of plate capacity needs to be (1) concise, (2) physically-based and (3) directly solvable. Although it is sometimes difficult to precisely define and differentiate these criteria, each will now be discussed.

Concise

The main reason for a proof of plate capacity to be concise is so that ship designers and plan approval engineers are able to independently verify results obtained with the software rule packages which are today normally provided by classification societies. These software rule packages are provided as an *aid* for designers and plan approval engineers, but are not intended to be "black box" substitutes for their engineering responsibilities. For this reason, designers and plan approval engineers need concise (and transparent) buckling strength proofs. A beneficial corollary of this is that almost all "bugs" in software rule packages are discovered by designers and plan approval engineers through comparison with the printed rules, where hand calculations are often times involved. Of course, the number of software "bugs" for a given proof is reduced with increasing conciseness. In addition to the engineering aspect of the need for a concise proof, there is also a legal aspect insofar that the (legally binding) rules of classification need to be documented in printed format.

Physically-based

Related to the foregoing, a proof of plate capacity must be physically-based. Designers and plan approval engineers must be able to clearly and immediately understand how the various load and plate parameters affect capacity so that ship plating may be reliably and efficiently designed. For example, a designer needs to be able to understand why and when buckling stiffeners are a preferred design solution compared to increased plate thickness. This is not possible with proofs riddled with coefficients and devoid of physics. Moreover, a physically-based proof is also important for rule developers. Whenever improvements are required, e.g. due to in-service experience, the physics of the existing proof must be readily apparent.

Directly solvable

For the plan approval of a ship, there are normally several dynamic load cases required for the assessment of strength. For instance, in the IACS CSR BC & OT [23] there are 22 dynamic load cases related to head, following, beam and oblique seas. These dynamic load cases are in addition to still water load cases corresponding to various departure, arrival, seagoing, sheltered/harbour, ballast loading/unloading and cargo loading/unloading conditions. Accordingly, because most ships usually have thousands of plate fields, the number of buckling strength checks which must be performed will generally be immense (for both so-called prescriptive checks and direct strength analyses). For this reason, a proof of plate capacity needs not only to be concise, but must also be solvable without the need for iterations if several hours of calculations are to be avoided for checking each design variation.

In particular, because many rule sets do not always allow the capacity of plating to be fully utilised, it must be possible to isolate the *stress multiplier factor at failure* μ in the proof of capacity. This factor is similar to the ratio of proof and FEA stress vector magnitudes $\Gamma = \mathsf{R}_{\mathtt{proof}}/\mathsf{R}_{\mathtt{FEA}}$ used in the quantitative evaluation of proofs except that the *stress multiplier factor at failure* is defined as the ratio of ultimate and applied stress vector magnitudes $\mu = \mathsf{R}_{\mathtt{ult}}/\mathsf{R}_{\mathtt{applied}}$, where $\mathsf{R}_{\mathtt{ult}}$ is defined by the proof of plate capacity. For

instance, in IACS CSR BC & OT [23] only 80% of plate capacity may be utilised under purely static loads (e.g. in harbours or sheltered waters), where the degree of utilisation is reflected in a so-called utilisation factor $\eta = 1/\mu$. Accordingly, in terms of a proof based on the generalised form of the von Mises failure criterion

$$\left(\frac{\mu \cdot \sigma_x}{\kappa_x \cdot \sigma_Y}\right)^{e_1} + \left(\frac{\mu \cdot \sigma_y}{\kappa_y \cdot \sigma_Y}\right)^{e_2} - B \cdot \left(\frac{\mu \cdot \sigma_x}{\kappa_x \cdot \sigma_Y}\right) \cdot \left(\frac{\mu \cdot \sigma_y}{\kappa_y \cdot \sigma_Y}\right) + \left(\frac{\mu \cdot \tau_{xy}}{\kappa_\tau \cdot \tau_Y}\right)^{e_3} = 1.0 \quad (4.1)$$

a direct solution is only possible if the stress multiplier factor at failure μ can be isolated. This requires that all terms in Equation (4.1) have the same exponent, i.e.

$$\left(\frac{\mu \cdot \sigma_x}{\kappa_x \cdot \sigma_Y}\right)^{e_0} + \left(\frac{\mu \cdot \sigma_y}{\kappa_y \cdot \sigma_Y}\right)^{e_0} - B \cdot \left(\frac{\mu \cdot \sigma_x}{\kappa_x \cdot \sigma_Y}\right)^{e_0/2} \cdot \left(\frac{\mu \cdot \sigma_y}{\kappa_y \cdot \sigma_Y}\right)^{e_0/2} + \left(\frac{\mu \cdot \tau_{xy}}{\kappa_\tau \cdot \tau_Y}\right)^{e_0} = 1.0 \quad (4.2)$$

or

$$\left(\frac{\mu \cdot R_x}{\kappa_x}\right)^{e_0} + \left(\frac{\mu \cdot R_y}{\kappa_y}\right)^{e_0} - B \cdot \left(\frac{\mu \cdot R_x}{\kappa_x}\right)^{e_0/2} \cdot \left(\frac{\mu \cdot R_y}{\kappa_y}\right)^{e_0/2} + \left(\frac{\mu \cdot R_\tau}{\kappa_\tau}\right)^{e_0} = 1.0 \quad (4.3)$$

such that

$$\mu^{e_0} \cdot \left[\left(\frac{R_x}{\kappa_x}\right)^{e_0} + \left(\frac{R_y}{\kappa_y}\right)^{e_0} - B \cdot \left(\frac{R_x}{\kappa_x}\right)^{e_0/2} \cdot \left(\frac{R_y}{\kappa_y}\right)^{e_0/2} + \left(\frac{R_\tau}{\kappa_\tau}\right)^{e_0}\right] = 1.0 \quad (4.4)$$

and

$$\mu = \left[\left(\frac{R_x}{\kappa_x}\right)^{e_0} + \left(\frac{R_y}{\kappa_y}\right)^{e_0} - B \cdot \left(\frac{R_x}{\kappa_x}\right)^{e_0/2} \cdot \left(\frac{R_y}{\kappa_y}\right)^{e_0/2} + \left(\frac{R_\tau}{\kappa_\tau}\right)^{e_0}\right]^{1/e_0} \quad (4.5)$$

or

$$\eta = 1/\mu = \left[\left(\frac{R_x}{\kappa_x}\right)^{e_0} + \left(\frac{R_y}{\kappa_y}\right)^{e_0} - B \cdot \left(\frac{R_x}{\kappa_x}\right)^{e_0/2} \cdot \left(\frac{R_y}{\kappa_y}\right)^{e_0/2} + \left(\frac{R_\tau}{\kappa_\tau}\right)^{e_0}\right]^{e_0} \quad (4.6)$$

where η must less than or equal to the allowable utilisation factor η_{all}, e.g. $\eta \leqslant \eta_{all} = 0.80$ under purely static loads.

4.2. Evaluation of existing proofs

As noted in the introduction to this chapter, none of the existing proofs of plate capacity presented in Chapter 3 satisfy all of the quantitative and qualitative acceptance criteria delineated in §4.1.1 and §4.1.2, respectively (in particular the former). With direct reference to Chapter 3, this will now be explained.

Quantitative criteria

In Table 4.3 and Table 4.4 all of the key performance indicators obtained in Chapter 3 for the design space and subspace, respectively, are summarised and compared to the quantitative acceptance criteria delineated in §4.1.1. Those measurements which meet the acceptance criteria are highlighted.

KPI	Criteria	Paik	Ueda et al.	CN 30.1	DIN 4114	PULS	DIN 18800	Prov. CSR BC & OT
1	$S_r/n_s \leq 0.001$	0.011	0.018	0.032	0.039	0.004	0.018	0.012
2	$0.97 \leq m_{lsr} \leq 1.00$	0.91	1.11	0.82	0.84	1.04	0.87	0.94
3	$R_D^2 \geq 0.95$	0.72	0.62	0.63	0.63	0.92	0.73	0.68
4	$m_{95} \leq 1.05$	1.18	1.61	1.08	1.10	1.20	1.14	1.26
5	$m_5 \geq 0.87$	0.73	1.00	0.52	0.36	0.96	0.67	0.73

Table 4.3.: Summary of quantitative results for existing proofs in design space.

KPI	Criteria	Paik	Ueda et al.	CN 30.1	DIN 4114	PULS	DIN 18800	Prov. CSR BC & OT
1	$S_r/n_s \leq 0.001$	0.001	0.038	0.005	0.020	0.004	0.005	0.003
2	$0.97 \leq m_{lsr} \leq 1.00$	1.03	1.35	0.88	0.78	1.11	0.93	1.08
3	$R_D^2 \geq 0.95$	0.95	0.57	0.85	0.69	0.94	0.80	0.95
4	$m_{95} \leq 1.05$	1.13	1.91	1.10	1.03	1.21	1.13	1.17
5	$m_5 \geq 0.87$	0.95	1.18	0.75	0.45	1.00	0.75	0.97

Table 4.4.: Summary of quantitative results for existing proofs in design subspace.

As can be seen, only two of the existing proofs (Ueda et al. and PULS) meet even a single acceptance criterion in the design space. This is an unsurprising result since the acceptance criteria are based on the best KPI's obtained with Paik's proof in the design subspace. However, as noted above, *all* of the precision and accuracy criteria need to be met in the design space if a proof is to be considered precise, accurate *and robust*.

With respect to the design subspace, two of the existing proofs meet more than one of the acceptance criterion (Paik and the provisional CSR BC & OT proofs). Both of these proofs (as well as PULS) would probably meet all of the performance criteria (i.e. for the design subspace) if the results obtained with each were more conservatively biased. This is rather instructive since both the Paik and the provisional CSR BC & OT proofs are based on a generalised form of the von Mises failure criterion shown in Equation (4.3).

Qualitative criteria

With few exceptions, all of the existing proofs presented in Chapter 3 meet the qualitative criteria delineated in §4.1.2. The corresponding qualities of these proofs are summarised in Table 4.5 and discussed below.

Criteria	Paik	Ueda et al.	CN 30.1	DIN 4114	PULS	DIN 18800	Prov. CSR BC & OT
Concise	✓	✓	✓	✓	✗	✓	✓
Physically-based	✓	✓	✓	✓	✓	✓	✓
Directly solvable	✓	✗	✓	✓	✗	✗	✓

Table 4.5.: Summary of qualitative results for existing proofs.

Concise

Regarding the criterion of conciseness, all of the proofs presented in Chapter 3, except the computerised semi-analytical buckling code PULS, are sufficiently concise to be documented in rules for the classification of ships. Certainly this is true of the proofs from shipbuilding practice since they have been directly obtained from various rule sets (again except for PULS). However, Paik's proof, consisting of two simple equations, is the best in terms of conciseness with the provisional CSR BC & OT proof of comparable simplicity.

Conversely, the proof of Ueda et al. is somewhat difficult to document, firstly because the equations for the elastic buckling strength of plating under combined loads need to be included and secondly because the equations for the stress coefficients are rather cumbersome, especially when the effects of shear are taken into account. Nevertheless, the proof is sufficiently concise to be included in a rule set.

Lastly, because it is obviously not suitable for inclusion in printed rules, PULS has been implemented into a stand-alone software with an "easy and intuitive" interface. The buckling code is also available in Microsoft Excel format and for automatic rule checks in the NAUTICUS Hull software. However, in order to offer it as a tool for plan approval, the parameters governing the discretisation of buckling deflections and solution of the equilibrium equations are pre-determined and fixed. Furthermore, these parameters are not disclosed to the user. For this reason, some consider PULS to be something of a "black-box". Even if the fundamental theory behind it is transparent, the calculation itself is not because the user has no knowledge or control of the pre-processing, solution and post-processing options. In this regard, PULS differs from most commercially-available finite element analysis packages.

Physically-based

All of the proofs presented in Chapter 3 are physically-based using the von Mises failure criterion directly (i.e. PULS and the proof of Ueda et al.) or using some generalised form of the von Mises equation (i.e. the remaining proofs). However, in case of the amended DIN 18800 proof, some designers and approval engineers find the transformation from plate to beam stresses (in case of finite element analyses), i.e. the so-called *Poisson correction*, difficult to understand and/or apply.

Notably, in case of the computerised buckling code PULS, the available software offers colour plots showing capacity curves, eigenmodes, model imperfections, out-of-plane deflections as well as in-plane normal, shear and von Mises stresses at initial yield (i.e. in addition to utilisation factors for buckling strength and ultimate capacity). These features provide ship designers and plan approval engineers with some insight into the failure mechanism of plates and also makes PULS particularly useful for rule developers.

Directly solvable

With respect to the direct solution criterion, those proofs based on a generalised form of the von Mises equation can be solved directly. The exception to this is the amended DIN 18800 proof where the *stress multiplier factor at failure* μ cannot be isolated in the interaction equation. This is because the exponents e_1, e_2 and e_3 generally take on different values

(the Poisson correction is not a problem in this concern since it depends only on the ratio of σ_x and σ_y and not on the magnitude of μ).

Regarding the proof of Ueda et al., obtaining efficient solutions is also not possible since the applied loads need to be gradually incremented in order to determine the capacity of the plating. Furthermore, in some cases Equation (3.17) has no *real* solutions or solutions which are not unique (i.e. two possible solutions). This could be due to misprints in reference [51] or the author's own programming errors although the calculation method used has been validated against examples provided in reference [51] for the ultimate strength of square plates under biaxial loading. Moreover, as a co-author of the Ueda et al. paper [51], it is perhaps telling that Paik focussed his subsequent efforts on a generalised form of the von Mises equation as presented in §3.2.1.

Finally, although PULS is a fundamentally sound proof of plate capacity, calculation times are considerably longer compared to closed form solutions. Like the proof of Ueda et al., this is because the applied loads in PULS need to be gradually incremented in order to determine the capacity of the plating. Increased calculation times are particularly noticeable when many buckling strength checks need to performed, e.g. for cargo hold models. This drawback combined with those described above have made some classification societies reluctant to reference PULS in their rules for the classification of ships.

4.3. Development and evaluation of new proof

On the basis of the foregoing evaluations, a proof based on a generalised form of the von Mises equation appears to hold the most promise for satisfying all of the quantitative and qualitative acceptance criteria outlined in §4.1. In terms of the qualitative criteria, in can be seen in Table 4.5 that only four of the existing proofs presented in Chapter 3 (i.e. Paik, CN 30.1, DIN 4114 and provisional CSR BC & OT) are concise, physically-based and directly solvable. Of these proofs, it can be seen from the results presented in Tables 4.3 and 4.4 that proofs based on a generalised form of the von Mises equation (i.e. Paik and provisional CSR BC & OT) are appreciably more precise and accurate than the proofs based on elastic analyses with plasticity corrections (i.e. CN 30.1 and DIN 4114). This is shown in Table 4.6 where the rankings for each of the five KPI's are summarised.

	Design Space				Design Subspace			
KPI	Paik	CN 30.1	DIN 4114	Prov. CSR BC & OT	Paik	CN 30.1	DIN 4114	Prov. CSR BC & OT
1	1	3	4	2	1	3	4	2
2	1	4	3	2	1	3	4	2
3	1	3	3	2	1	3	4	1
4	3	1	2	4	3	2	1	4
5	1	3	4	1	2	3	4	1

Table 4.6.: Ranking of proofs.

Here the proofs of Paik and provisional CSR BC & OT are ranked 1 and 2 for all KPI's except KPI 4. This exception is in general the case because the proofs based on elastic analyses with plasticity corrections are comparably conservative while the proofs of Paik and provisional CSR BC & OT are either imprecise with a conservative bias (i.e. for the design space) or precise with a non-conservative bias (i.e. for the design sub-

space). Accordingly, a solution is sought in a more precise and accurate proof based on a generalised form of the von Mises equation. Again, as noted in §4.1.2, the same exponents are needed for each term of the equation in order that the stress multiplier at failure μ can be isolated. Accordingly, the new proof of plate capacity is to be formulated as

$$\left(\frac{\mu\cdot\sigma_x}{\kappa_x\cdot\sigma_Y}\right)^{e_0}+\left(\frac{\mu\cdot\sigma_y}{\kappa_y\cdot\sigma_Y}\right)^{e_0}-B\cdot\left(\frac{\mu\cdot\sigma_x}{\kappa_x\cdot\sigma_Y}\right)^{e_0/2}\cdot\left(\frac{\mu\cdot\sigma_y}{\kappa_y\cdot\sigma_Y}\right)^{e_0/2}+\left(\frac{\mu\cdot\tau_{xy}}{\kappa_\tau\cdot\tau_Y}\right)^{e_0}=1.0 \quad (4.7)$$

or

$$\left(\frac{\mu\cdot R_x}{\kappa_x}\right)^{e_0}+\left(\frac{\mu\cdot R_y}{\kappa_y}\right)^{e_0}-B\cdot\left(\frac{\mu\cdot R_x}{\kappa_x}\right)^{e_0/2}\cdot\left(\frac{\mu\cdot R_y}{\kappa_y}\right)^{e_0/2}+\left(\frac{\mu\cdot R_\tau}{\kappa_\tau}\right)^{e_0}=1.0 \quad (4.8)$$

in terms of normalised stresses (i.e. Equation (4.3)).

4.3.1. Framework of new proof

With the aim of developing a new proof of plate capacity based on Equation (4.8), the framework of the proof will now be built up quadrant by quadrant. Based on the mechanics of plating collapse investigated in Chapter 2, this framework is intended to facilitate a more physically-based proof.

Yielding in Quadrant 3

Whenever gross yielding occurs throughout the plate, the capacity equation should of course be that of the von Mises ellipse, as shown in Figure 4.1 (where $R_\tau = 0$). In terms of Equation (4.8), this means that $B = 1$, $e_0 = 2$ and the plate reduction factors are equal to unity (i.e. $\kappa_x = \kappa_y = \kappa_\tau = 1.0$) such that Equation (4.8) is reduced to

$$R_x^2 + R_y^2 - R_x\cdot R_y + R_\tau^2 = 1.0 \quad (4.9)$$

Here the stress multiplier factor at failure μ is set to unity in order to obtain ultimate plate strength. As shown in Figure 4.2 (again where $R_\tau = 0$), Equation (4.9) defines plate capacity in Quadrant 3 where it is generally assumed that the magnitude of shear stress is either insufficient to induce buckling (i.e. $R_\tau < R_{\tau,cr}$) or that the magnitude of tensile stresses in the x- and/or y-directions is sufficient to prevent shear buckling. Even if shear buckling were to occur, it is assumed that the presence of tensile stresses R_x and R_y mitigate the out-of-plane shear deflections to the point where any post-buckling redistribution of internal stresses is negligible. Moreover, as discussed in §2.3, post-buckling effects under shear are not as significant as those under uniaxial loads.

Yielding/buckling in Quadrants 2 and 4

Collapse due to gross yielding

The foregoing absence of post-buckling effects in Quadrant 3 is assumed to continue into Quadrant 2 for those combinations of normalised stress where $R_y \leqslant \kappa_y'$. Here the

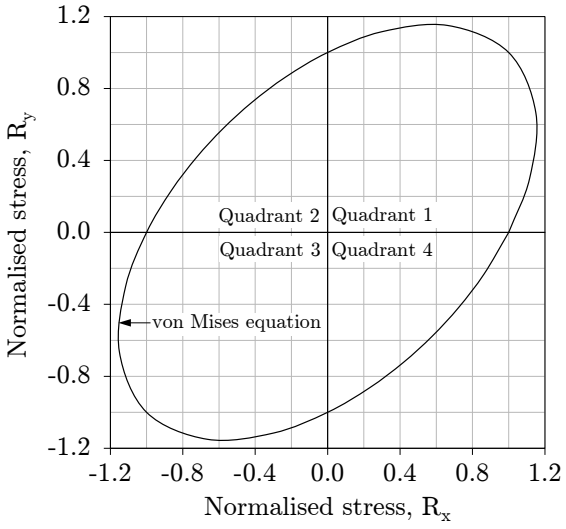

Figure 4.1.: Von Mises ellipse.

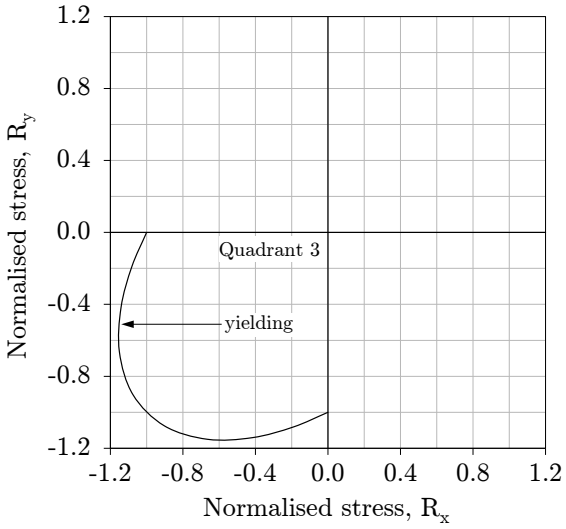

Figure 4.2.: Yielding in Quadrant 3.

quantity κ'_y is equal to the *reduced* uniaxial strength of the plate (in the y-direction) considering shear (i.e. $R_x = 0$, $R_\tau \geqslant 0$). In other words, the quantity κ'_y is a plate reduction factor which takes into account the effects of any shear loads which may be present (i.e. $\kappa'_y = \kappa_y$ in the absence of shear). In particular, when $R_x = 0$ (and again setting the stress multiplier factor at failure μ to unity), Equation (4.8) is reduced to

$$\left(\frac{R_y}{\kappa_y}\right)^{e_0} + \left(\frac{R_\tau}{\kappa_\tau}\right)^{e_0} = 1.0 \tag{4.10}$$

which defines plate capacity in the $R_y - R_\tau$ plane. When rearranging this equation in terms of R_y, the quantity κ'_y is obtained

$$\kappa'_y = R_y = \kappa_y \cdot \left[1 - \left(\frac{R_\tau}{\kappa_\tau}\right)^{e_0}\right]^{1/e_0} \tag{4.11}$$

As shown in Figure 4.3, this means that the von Mises ellipse describes collapse in Quadrant 2 up to the point $(R_{x,Y}, \kappa'_y)$ where $R_{x,Y}$ refers to the value of R_x which when combined with $R_y = \kappa'_y$ and R_τ satisfies Equation (4.9), i.e. the von Mises failure criterion. Of course, the assumption of gross yielding in Quadrant 2 is more tenuous than in Quadrant 3 due to the presence of compressive stresses in the y-direction. Nevertheless, these compressive stresses are normally secondary stresses (i.e. $|R_y| < |R_x|$ in Quadrant 2) such that the tensile stresses in the x-direction are assumed to be of sufficient magnitude to inhibit buckling. As shown in Figure 4.3, the same assumptions and treatment apply analogously in Quadrant 4.

Collapse due to buckling

For those combinations of normalised stress in Quadrant 2 where $R_x > R_{x,Y}$, buckling is assumed to take place. However, as shown in Figure 4.4, for all such values of R_x it is assumed that plate capacity in the y-direction is defined by $R_y = \kappa'_y$, i.e. this is the equivalent of setting $R_x = 0$ whenever $R_x > R_{x,Y}$. This is normally a conservative assumption

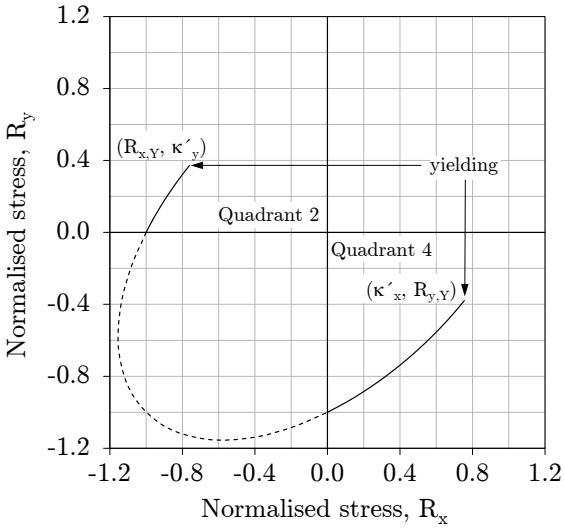

Figure 4.3.: Yielding in Quadrants 2 and 4.

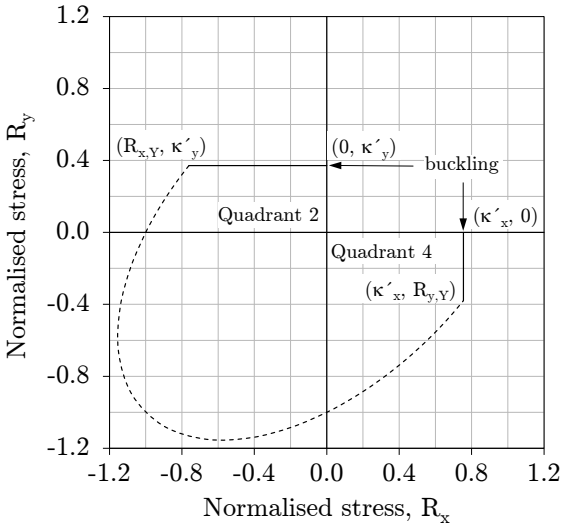

Figure 4.4.: Buckling in Quadrants 2 and 4.

since, as explained in §2.2, tensile stresses in the x-direction will tend to increase plate capacity in the y-direction by restraining the out-of-plane deflections (thereby mitigating the redistribution of stresses towards the edges and corners of the plate).

One reason for this conservatism is that the new proof incorporates a design principle which limits the magnitudes of applied stresses in the x- and y-directions to those stresses which define the capacity of the plate when applied in the absence of each other, i.e. $R_x \leqslant \kappa'_x$ and $R_y \leqslant \kappa'_y$. This design principle was first included in the buckling strength rules of Germanischer Lloyd, but is there only relevant in Quadrant 1. The reasoning behind this principle is that the presence of a secondary stress component cannot be a *necessary condition* for allowing another stress component to exceed its ultimate stress, e.g. $R_y > \kappa'_y$. In other words, because the presence of a secondary stress cannot generally be guaranteed (particularly in the case of independent stresses), stress limits are applied.

Finally, although the capacity of the plate is defined throughout Quadrant 2 by Equation (4.8), i.e. a generalised form of the von Mises equation, it should be noted that the plate reduction factors κ_x, κ_y and κ_τ, as well as the exponent e_0 and interaction coefficient B of the von Mises equation, do not remain constant throughout. In particular, for the segment of the plate capacity curve defined by $R_y = \kappa'_y$, the beneficial effects of tensile stresses in mitigating post-buckling effects are reflected in changing values of the plate reduction factors, i.e. $\kappa_x \to 1.0$, $\kappa_y \to 1.0$ and $\kappa_\tau \to 1.0$, as well as in changing values of the exponent and interaction coefficient of the von Mises equation, i.e. $e_0 \to 2.0$ and $B \to 1.0$, with increasing magnitudes of tensile stresses. Nevertheless, it is far simpler when the segment of the plate capacity curve between $R_x = 0$ and $R_x = R_{x,Y}$ is defined by Equation (4.10), rather than explicitly defining (transitioning) values of κ_x, κ_y, κ_τ, e_0 and B for use in Equation (4.8). As shown in Figure 4.4, the same assumptions and treatment apply analogously in Quadrant 4.

Error analysis

Ignoring the beneficial effects of tensile stresses on the capacity of the plate is a

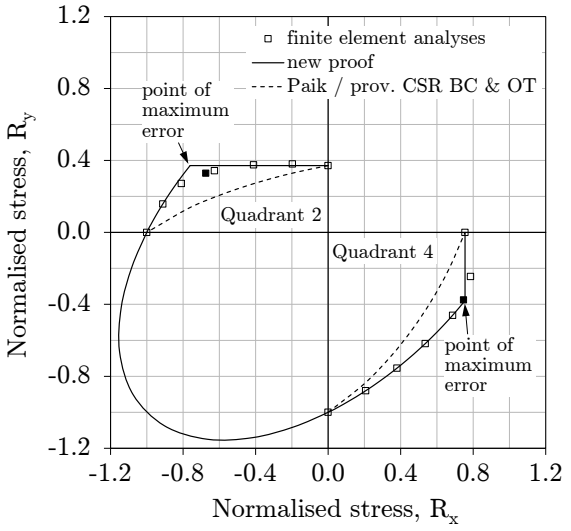

Figure 4.5.: Comparison of results.

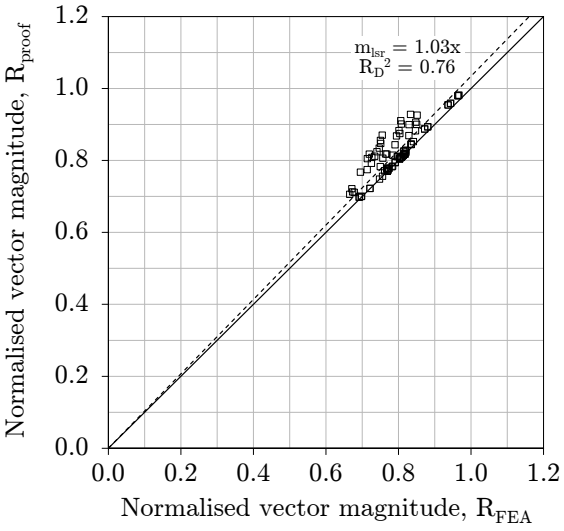

Figure 4.6.: Maximum errors (96 data points).

source of significant error in the Paik and provisional CSR BC & OT proofs (albeit on the conservative side of results in Quadrants 2 and 4, e.g. see Figures 3.8 (b) and 3.31 (b)). In Quadrants 2 and 4 these proofs describe the capacity of the plate using the von Mises equation, but with the components of applied stresses normalised by *ultimate* stress rather than *yield* stress (recalling that $\kappa_x = \kappa_y = \kappa_\tau = 1.0$ in case of gross yielding), i.e.

$$\left(\frac{R_x}{\kappa_x}\right)^2 + \left(\frac{R_y}{\kappa_y}\right)^2 - \left(\frac{R_x}{\kappa_x}\right) \cdot \left(\frac{R_y}{\kappa_y}\right) + \left(\frac{R_\tau}{\kappa_\tau}\right)^2 = 1.0 \tag{4.12}$$

In Figure 4.5 the capacity of plating with an aspect ratio $\alpha = 3$ and plate slenderness parameter $\beta = 2$ is shown for Quadrants 2 and 4. Here the results obtained with finite element analyses are compared to results obtained with the Paik and provisional CSR BC & OT proofs. As can be seen, these proofs significantly underestimate the capacity of plating in Quadrants 2 and 4. Conversely, plate capacities obtained with the yielding/buckling approach described above is seen to agree well with the results of finite element analyses. This latter approach was intuitively presumed by Smith et al. [63] to be plausible on the basis of elastic buckling strength in Quadrants 2 and 4[1], but who cautioned that "buckling stresses provide useful indicators of behaviour but cannot be used to determine (ultimate) strength (or strength interaction). This is because initial buckling theory takes no account of the complex redistribution of mid-thickness and surface stresses which occur during loading. In fact, the limited numerical data available show that tensile stress can result in some reduction of strength before the yield surface is reached". Indeed, numerical studies in the present work confirm that there is the potential for some non-conservatism associated with those stress combinations near the transitions from (inelastic) buckling to gross yielding, i.e. where $R_x \rightarrow R_{x,Y}$ and $R_y \rightarrow R_{y,Y}$.

In fact, as shown in Figure 4.5, the potential for this non-conservatism is greatest precisely where the stress limits and the von Mises ellipse intersect in Quadrants 2 and 4 (i.e. at $R_{x,Y}, \kappa'_y$ and $\kappa'_x, R_{y,Y}$). To investigate the significance of this potential error,

[1] The validity of this approach is also supported by the distribution of internal stresses described by Ueda et al. [51].

additional finite element analyses were performed along the stress vector of this intersection for 96 combinations of plate aspect ratio α, plate slenderness parameter β and all four levels of shear R_τ in Quadrants 2 and 4, i.e. 3 x 4 x 4 x 2 = 96 evaluation points. The results are shown in Figure 4.6 where a straight line through the R_{FEA} - R_{proof} evaluation points has a slightly non-conservative slope of 1.03 (least square regression without an intercept term, $R^2_D = 0.76$). In Quadrant 2 the average of maximum errors is about 5.7% (maximum 13.2%). However, because transverse tensile stresses are acting over the entire length of the plate and therefore more effective in limiting out-of-plane deflections, in Quadrant 4 the average of maximum errors is only about 1.0% (maximum 6.5%).

In cases where the design load is realised and the capacity of a plate is slightly exceeded, the additional load will be taken over by the supporting structure and/or strain hardening (which has not been included in the finite element analyses). In practice the scantlings of plates are normally driven by their capacity under biaxial compression (i.e. Quadrant 1). However, if a proof of plate capacity is so conservative in Quadrants 2 and 4 that they govern plate thickness (i.e. even when the critical load combination is truly not in these quadrants), a more precise and accurate proof is needed, if for no other reason then to allow the thickness of plating to be governed by its capacity under biaxial compression in Quadrant 1 (i.e. when the critical load combination is truly in this quadrant).

Buckling in Quadrant 1

The stress limits in Quadrants 2 and 4 which prevent components of applied stress R_x and R_y from exceeding (normalised) ultimate stresses κ'_x and κ'_y, respectively, continue into Quadrant 1. These limits are shown in Figure 4.7 and govern whenever collapse initiates in the corners of the plate, i.e. in case of sturdy plates[2]. Unlike yielding along the sides of the plate, here the biaxial compressive stresses are working "against each other" to delay yielding as reflected in the interaction term of the von Mises equation. However, when collapse does not initiate in the corners of the plate, its (inelastic) buckling capacity in Quadrant 1 is described by Equation (4.8) where the values of the exponent e_0 and interaction coefficient B are functions of the plate aspect ratio α and slenderness parameter β. As shown in Figure 4.8, this portion of the capacity curve completes the proof.

4.3.2. Hypothetical Proof of Plate Capacity

Based solely on the mechanics of plating collapse presented in Chapter 2, a hypothetical proof *without any numerical calibration* can now be developed. As reflected in the framework described above, the capacity of plates in Quadrants 2, 3 and 4 can be determined on the basis of ultimate plate strength under single load components (i.e. κ_x, κ_y and κ_τ) and the von Mises failure criterion. For this reason, the task of developing a hypothetical proof of plate capacity is reduced to determining values of the exponent e_0

[2] As shown in Appendix D, the presence of a secondary (compressive) stress R_y may increase the capacity of the plate under a primary (compressive) stress R_x (and vice versa). This is not the case with combined axial and shear stresses (as also shown in Appendix D) and explains why no shear stress limit is required.

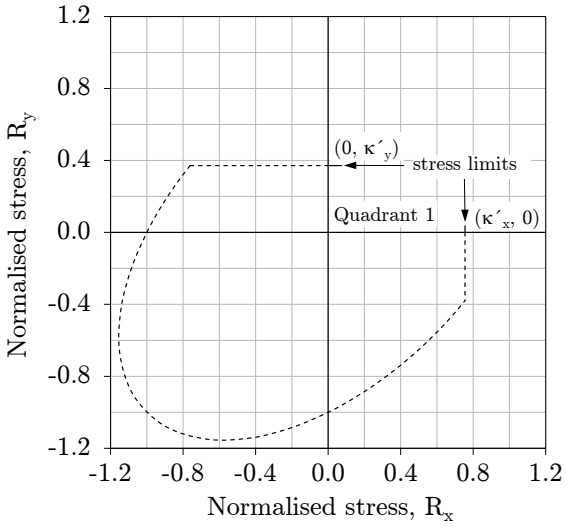

Figure 4.7.: Stress limits in Quadrant 1.

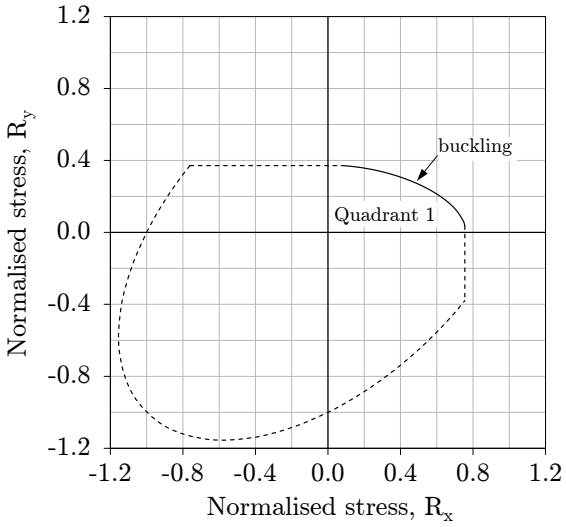

Figure 4.8.: Buckling in Quadrant 1.

and interaction coefficient B (in Quadrant 1) for Equation (4.8) with the stress multiplier factor at failure μ set to unity, i.e.

$$\left(\frac{R_x}{\kappa_x}\right)^{e_0} + \left(\frac{R_y}{\kappa_y}\right)^{e_0} - B \cdot \left(\frac{R_x}{\kappa_x}\right)^{e_0/2} \cdot \left(\frac{R_y}{\kappa_y}\right)^{e_0/2} + \left(\frac{R_\tau}{\kappa_\tau}\right)^{e_0} = 1.0 \qquad (4.13)$$

As discussed in §2.2.4, it is to be expected that the collapse of *slender* plates in Quadrant 1 is dominated by elastic buckling such that the shape of their capacity curves approaches the shape of the elastic buckling strength interaction curve (i.e. in the R_x-R_y plane for a given level of shear). Conversely, it is to be expected that the collapse of *sturdy* plates includes significant yielding such that the shape of their capacity curves approaches that of the von Mises ellipse (i.e. again in the R_x-R_y plane for a given level of shear).

Accordingly, if it is *hypothesised* that the effects of plate aspect ratio are *secondary* compared to those of plate slenderness and that the *shape* of the plate capacity curve in the R_x-R_y plane is unaffected by shear, then the (linear) elastic buckling interaction equation of a square plate may be used for *slender* plates. Conversely, in case of *sturdy* plates, the (quadratic) von Mises equation may be used (where plate aspect ratio already has no role). Accordingly, what remains is to define the limiting values of slenderness for which the behaviour of plates is perfectly elastic and perfectly plastic, i.e. nominal definitions of *slender* and *sturdy* plates, respectively. On the basis of the right-hand side of Figure 2.20, these limits are defined as $\beta \geqslant 4$ for perfectly elastic behaviour and $\beta \leqslant 0.5$ for perfectly plastic behaviour. With reference to Equation (4.13), this means that $e_0 = 1$ and $B = 0$ when $\beta \geqslant 4$ and that $e_0 = 2$ and $B = 1$ when $\beta \leqslant 0.5$. Linear interpolation will be used to define the exponent e_0 and interaction coefficient B for plate behaviour between these two extremes, resulting in the following equations

$$e_0 = (7.5 - \beta)/3.5, \quad \text{where } 1 \leqslant e_0 \leqslant 2 \qquad (4.14)$$

$$B = (4.0 - \beta)/3.5, \quad \text{where } 0 \leqslant B \leqslant 1 \qquad (4.15)$$

which are plotted in Figure 4.9. These equations (for use in Quadrant 1), together with the framework described above, comprise the *hypothetical proof* based on the mechanics of plating collapse presented in Chapter 2, i.e. a physically-based proof without any numerical calibration. Because the proof is based on a generalised form of the von Mises equation (with the same value of e_0 for all terms), the qualitative acceptance criteria defined in §4.1.2 are fulfilled. Accordingly, only an evaluation of the hypothetical proof against the quantitative acceptance criteria delineated in §4.1.1 remains.

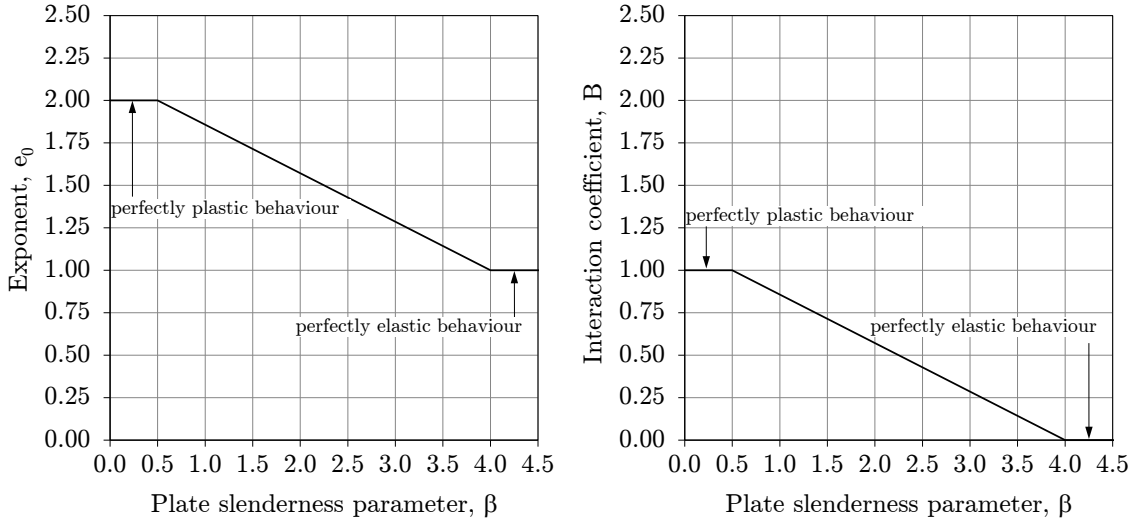

(a) Exponent e_0 (b) Interaction coefficient B

Figure 4.9.: Plots of exponent e_0 and interaction coefficient B.

Therefore, in accordance with the evaluation scheme described in §3.1, the hypothetical proof has been used to calculate the capacity of plating for the 360 evaluation points. The resulting scatter plots for both the design space and design subspace are shown in Figure 4.10. The five key performance indicators used to measure precision and bias are shown in Table 4.7 together with the acceptance criteria. On the basis of these indicators, it can be seen that the hypothetical proof generally performs better than any of the existing proofs. Regarding the overall measure of error (KPI_1), the average of the squares of the residuals S_r/n_s is very low for both the design space ($S_r/n_s = 0.002$) and design subspace ($S_r/n_s = 0.001$). With respect to the measure of bias (KPI_2), the least-squares fit of a straight line through the R_{FEA} - R_{proof} data points gives a slightly conservative slope for both the design space ($m_{lsr} = 0.99$) and design subspace ($m_{lsr} = 0.97$). Concerning the measure of precision (KPI_3), the coefficients of determination reflect a very low degree of scatter for both the design space (${R_D}^2 = 0.95$) and design subspace (${R_D}^2 = 0.94$). Regarding the extent of non-conservatism (KPI_4), a straight line through the 95^{th} percentile gives a moderately non-conservative slope for both the design space ($m_{95} = 1.09$) and design subspace ($m_{95} = 1.09$). With respect to the extent of conservatism (KPI_5), a straight line through the 5^{th} percentile gives a significantly/extremely conservative slope for the design space ($m_5 = 0.80$) and a significantly conservative slope for the design subspace ($m_5 = 0.84$).

In order to identify any inherent problems within the hypothetical proof for specific parameters, the mean and extreme values of the ratio of stress vector magnitudes,

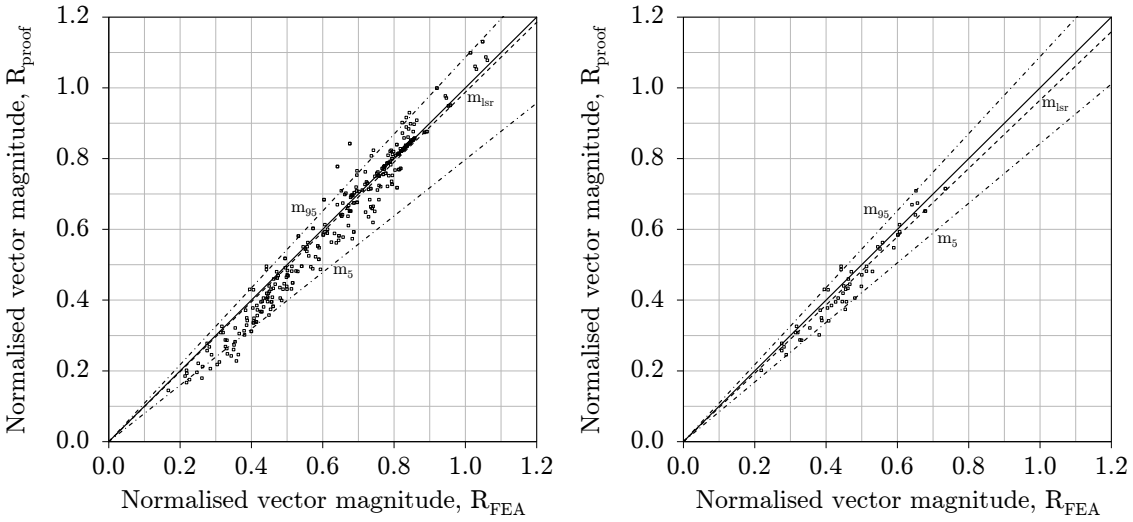

(a) Design space (360 evaluation points) (b) Design subspace (56 evaluation points)

Figure 4.10.: Scatter plots of R_{FEA} - R_{proof} (hypothetical proof).

KPI		Target	Design space	Design subspace	Criteria
1	S_r/n_s	0.000	0.002	0.001	$S_r/n_s \leq 0.001$
2	m_{lsr}	1.00	0.99	0.97	$0.97 \leq m_{lsr} \leq 1.00$
3	R_D^2	1.00	0.95	0.94	$R_D^2 \geq 0.95$
4	m_{95}	1.00	1.09	1.09	$m_{95} \leq 1.05$
5	m_5	1.00	0.80	0.84	$m_5 \geq 0.87$

Table 4.7.: Key performance indicators (hypothetical proof).

$\Gamma = R_{proof}/R_{FEA}$, are shown in Figure 4.11 for each value of plate aspect ratio (α), plate slenderness parameter (β), quadrants of compressive/tensile load combinations (Q1, Q2 and Q4) and levels of shear (R_τ). In case of the plate aspect ratios, the mean values of Γ indicate a slightly to moderately conservative bias for all values of α. The ranges of extreme values indicate good precision for all plate aspect ratios. In case of the plate slenderness parameters, the mean values of Γ indicate a slightly non-conservative bias for $\beta = 1$ and $\beta = 2$, but a slightly/moderately conservative bias for $\beta = 3$ and a significantly conservative bias for $\beta = 4$. The ranges of extreme values indicate good precision for $\beta = 2$ and $\beta = 4$, but quite good precision for $\beta = 3$ and very good precision for $\beta = 1$. In case of the compressive/tensile load combinations, the mean values of Γ indicate a moderately to slightly conservative bias for all quadrants. The ranges of extreme values indicate good precision in Quadrants 1 and 2 with very good precision in Quadrant 4. In case of shear, the mean values of Γ reveal a slightly non-conservative bias in the absence of shear and a slightly to moderately conservative bias in the presence of shear. The ranges of extreme values indicate good precision for all levels of shear.

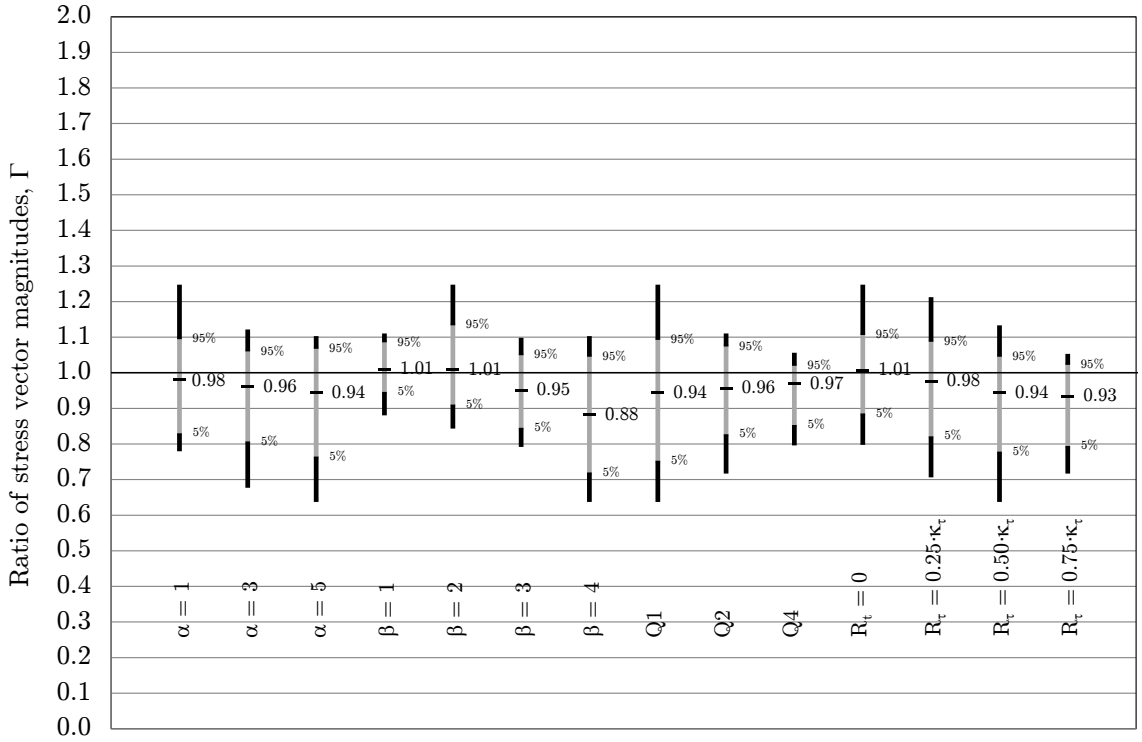

Figure 4.11.: Evaluation of data subsets (hypothetical proof).

4.3.3. Exponent e_0 (Quadrant 1)

As seen in Table 4.7, the hypothetical proof satisfies or nearly satisfies KPI's 1, 2 and 3 in both the design space and subspace. However, as reflected in KPI's 4 and 5, the main problem with the hypothetical proof is the significant scatter between the 5^{th} and 95^{th} percentiles, particularly in Quadrant 1. Although the degree of precision in Quadrant 1 is "good" relative to existing proofs, it can be seen in Figure 4.11 that the scatter of results in absolute terms is rather high (this can also be seen in comparison to other data subsets within Figure 4.11). Accordingly, in an effort to satisfy all of the quantitative acceptance criteria established in §4.1.1, the next task in developing a new proof of plate capacity is to better capture the effects of plate aspect ratio α and shear R_τ in Quadrant 1 (effects which were excluded from the hypothetical proof). Towards this end, equations will now be developed numerically with which to calculate more precise values of the exponent e_0 and interaction coefficient B (i.e. in case of biaxial compression) according to Equation (4.8), i.e.

$$\left(\frac{R_x}{\kappa_x}\right)^{e_0} + \left(\frac{R_y}{\kappa_y}\right)^{e_0} - B \cdot \left(\frac{R_x}{\kappa_x}\right)^{e_0/2} \cdot \left(\frac{R_y}{\kappa_y}\right)^{e_0/2} + \left(\frac{R_\tau}{\kappa_\tau}\right)^{e_0} = 1.0 \qquad (4.16)$$

where the stress multiplier factor at failure μ is again set to unity. Of course, it is not possible to simultaneously derive unique values of e_0 and B (i.e. one equation, two unknowns). For this reason, it is necessary in the first step to separate these two quantities. Since the value of e_0 must remain valid in case $R_y = 0$ and in case $R_x = 0$, unique values of e_0 can be derived using either of the following equations

$$\left(\frac{R_x}{\kappa_x}\right)^{e_0} + \left(\frac{R_\tau}{\kappa_\tau}\right)^{e_0} = 1.0 \tag{4.17}$$

in case $R_y = 0$ or

$$\left(\frac{R_y}{\kappa_y}\right)^{e_0} + \left(\frac{R_\tau}{\kappa_\tau}\right)^{e_0} = 1.0 \tag{4.18}$$

in case $R_x = 0$.

Accordingly, in addition to the 360 evaluation points tabulated and plotted in Appendix C (i.e. R_x-R_y-R_τ stress combinations in Quadrants 1, 2 and 4), additional finite element analyses were performed for stress combinations R_x-R_τ, R_y-R_τ and R_x-R_y in Quadrant 1 (the latter combinations for use in the following subsection to determine an equation for the interaction coefficient B). A typical capacity curve from these analyses is shown in Figure 4.12 for plating with an aspect ratio $\alpha = 3$ and plate slenderness parameter $\beta = 2$. In addition to the plate aspect ratios $\alpha = 1$, $\alpha = 3$ and $\alpha = 5$, analyses were also performed for the plate aspect ratio $\alpha = 10$. Since plates with aspect ratios greater than $\alpha = 5$ are sometimes used, e.g. the side shell plating of single side skin bulk carriers, these additional analyses were performed to ensure that the resulting equations for e_0 and B would also be valid for these plates (even if the equations are not optimised for such large aspect ratios). Furthermore, additional finite element analyses were performed for plating with a plate slenderness parameter $\beta = 0.5$. As will be seen, this was necessary in order to accurately characterise (and limit) the resulting equations to take into account gross yielding. A summary of the 19 combinations of plate aspect ratio α and plate slenderness parameter β are shown in Figure 4.13. Because each of these combinations is comprised of seven stress combinations in terms of R_x-R_τ, R_y-R_τ and R_x-R_y (as shown in Figure 4.12), in total 19 x 7 x 3 = 399 data points are used to determine the exponent e_0 and interaction coefficient B. Some of the R_x-R_y data points overlap with the 360 evaluation points, i.e. in case $R_\tau = 0$. All results are tabulated and plotted in Appendix D.

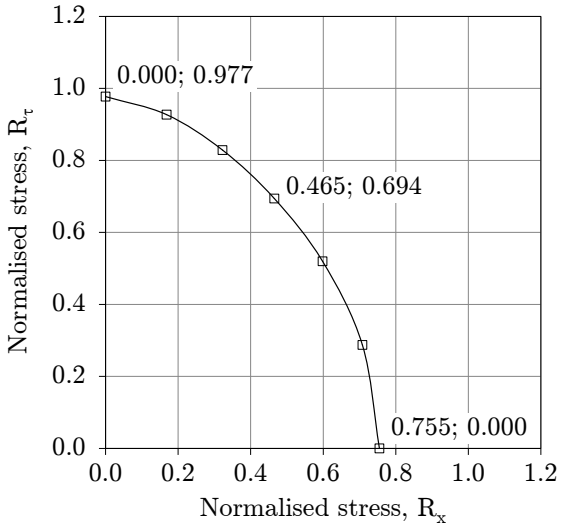

Figure 4.12.: Capacity curve ($\alpha = 3$, $\beta = 2$).

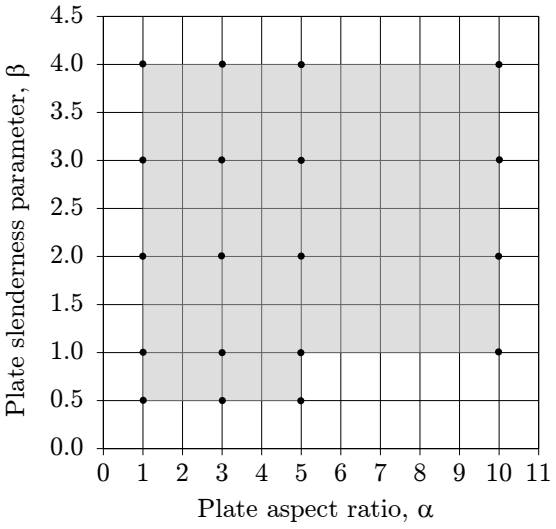

Figure 4.13.: Plating configurations.

In order to derive an equation with which to determine the values of e_0, corresponding

quantities from the capacity curves are substituted into Equations (4.17) and (4.18) which are then solved for e_0. For example, in case of the capacity curve shown in Figure 4.12 ($\alpha = 3$, $\beta = 2$), the plate reduction factors κ_x and κ_τ are equal, respectively, to $R_{x,ult}$ when $R_\tau = 0$ (i.e. $\kappa_x = R_{x,ult} = 0.755$) and $R_{\tau,ult}$ when $R_x = 0$ (i.e. $\kappa_\tau = R_{\tau,ult} = 0.977$). Accordingly, for the data point $R_x = 0.465$, $R_\tau = 0.694$, Equation (4.17) becomes

$$\left(\frac{0.465}{0.755}\right)^{e_0} + \left(\frac{0.694}{0.977}\right)^{e_0} = 1.0 \tag{4.19}$$

for which $e_0 = 1.70$. This result is plotted in Figure 4.14(b) where arctangent $(R_\tau/R_x) = 56°$. This calculation is repeated for each of the five stress combinations comprising the R_x-R_τ and R_y-R_τ capacity curves which have non-zero components, i.e. the endpoints of the capacity curves are not included since they involve no interaction of stresses. All results for $\beta = 1$, $\beta = 2$, $\beta = 3$ and $\beta = 4$ are shown in Figure 4.14 for all R_x-R_τ capacity curves and in Figure 4.15 for all R_y-R_τ capacity curves. The results for $\beta = 0.5$ are shown separately in Figure 4.16.

As can be seen, for each combination of α and β, the derived values of e_0 remain fairly constant for the R_x-R_τ stress combinations, but not so for the R_y-R_τ stress combinations. Moreover, for each value of β, the average derived values of e_0 remain fairly constant for all values of α in case of R_x-R_τ stress combinations, but increase with α in case of R_y-R_τ stress combinations. These average values are plotted separately for R_x-R_τ and R_y-R_τ in Figure 4.17 as a function of β (i.e. the average for all values of α). These results show clearly that the average (derived) values of e_0 are higher for R_y-R_τ stress combinations compared to R_x-R_τ stress combinations (due to the presence of higher tensile stresses under shear where yielding initiates under longitudinal loads, i.e. compared to where yielding initiates under transverse loads). Nevertheless, in order to isolate the stress multiplier factor at failure μ in Equation (4.8), a single value of the exponent e_0 is required for each term in the capacity equation. The possibilities in this regard are to optimise the values of e_0 on the basis of R_x-R_τ stress combinations, R_y-R_τ stress combinations or some combination thereof. However, the decision in this regard is rather straightforward. Firstly, because the base of each term in the interaction equation is less than or equal to unity, the lower values of e_o should be taken to limit non-conservative results, e.g. $(0.694)^{2.0} > (0.694)^{2.1}$. Secondly, because the capacity of plating under longitudinal stresses R_x is generally greater than under transverse stresses R_y, ships are normally longitudinally-framed in order to increase their strength under global longitudinal bending moments (combined with global shear forces). For both these reasons, the design equation for e_0 is derived on the basis of R_x-R_τ stress combinations.

Accordingly, in Figure 4.17 the following *power* equation of best fit to the derived values of e_0 is plotted (i.e. on the basis of R_x-R_τ stress combinations)

$$e_0 = 2.01/\beta^{0.275} \tag{4.20}$$

Therefore, two simplified equations are considered for the proof of capacity

$$e_0 = 2/\beta^{0.25} \tag{4.21}$$

and

$$e_0 = 2/\beta^{0.30} \tag{4.22}$$

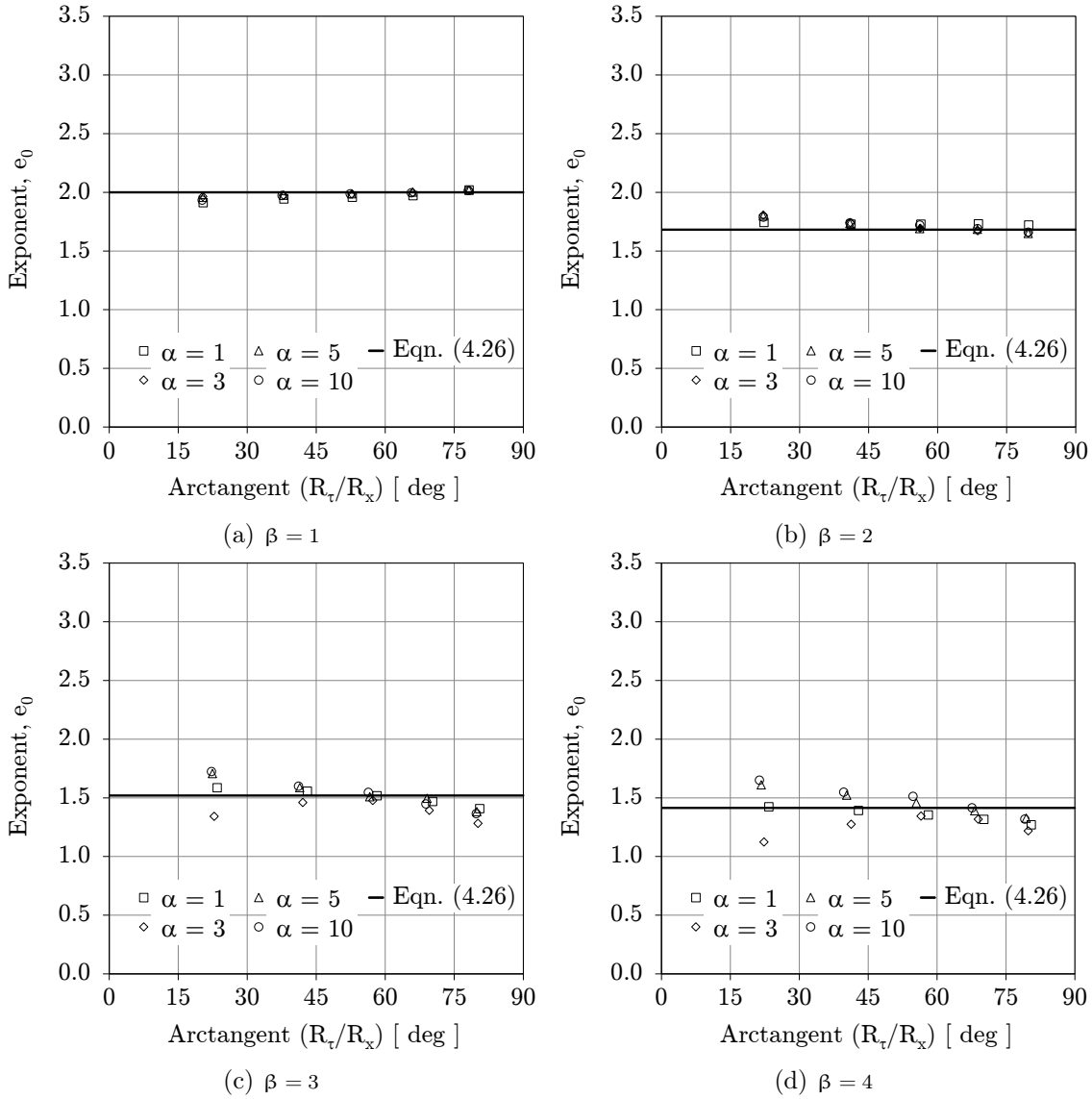

Figure 4.14.: Derived values of e_0 (R_x-R_τ).

with the former resulting in a slightly higher coefficient of determination (as shown below). As can be seen in Figure 4.17, the values of e_0 approach a limiting value of 2 when $\beta = 1$ (this limit is verified by the results for $\beta = 0.5$). This is an unsurprising result since the plate reduction factors κ and interaction coefficient B all approach unity as the plate slenderness parameters become lower such that the plate capacity equation approaches that of the von Mises yield equation

$$R_x^2 + R_y^2 - R_x \cdot R_y + R_\tau^2 = 1.0 \tag{4.23}$$

or

$$R_x^2 + R_\tau^2 = 1.0 \tag{4.24}$$

when $R_y = 0$, and

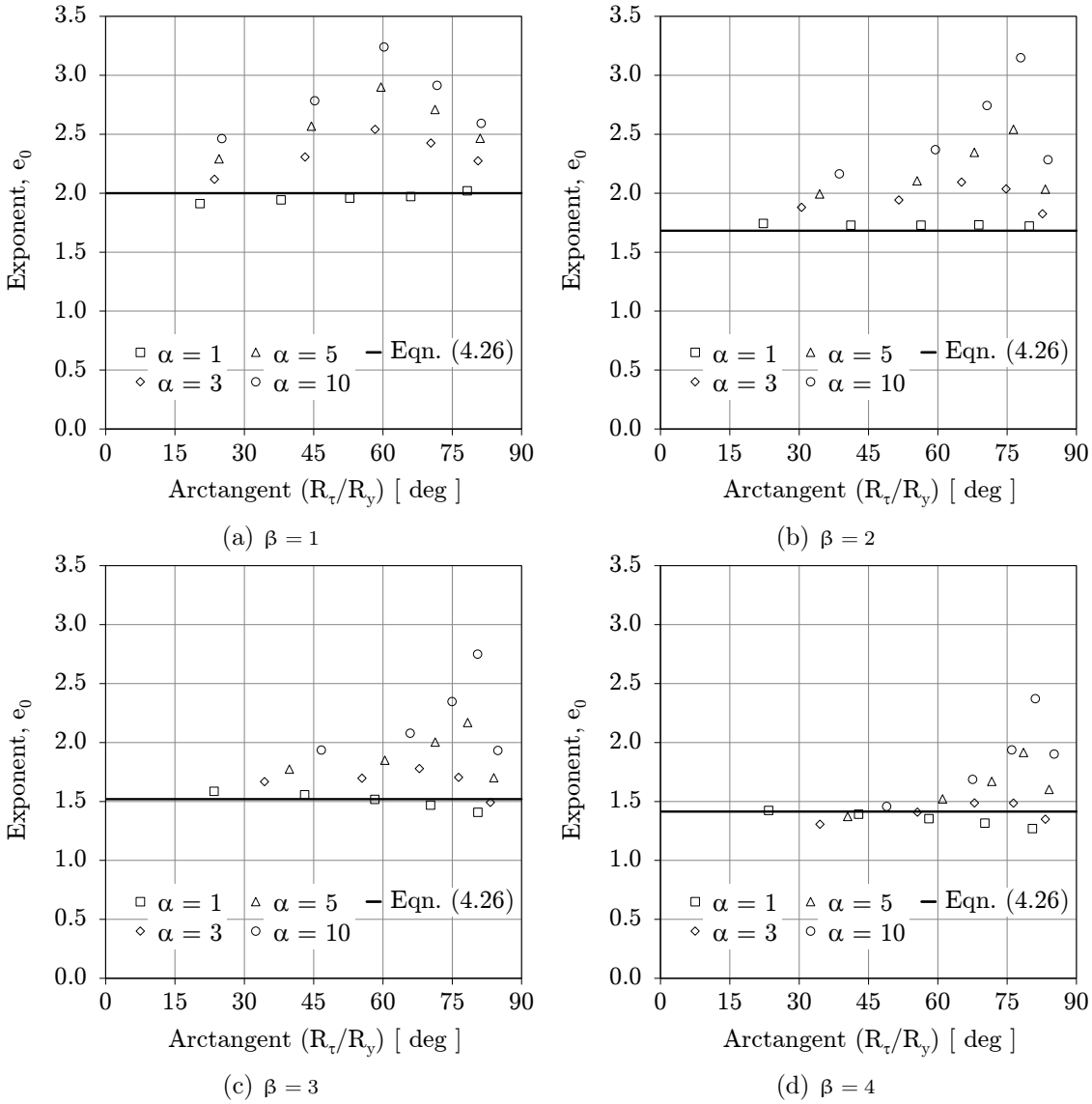

(a) $\beta = 1$ (b) $\beta = 2$

(c) $\beta = 3$ (d) $\beta = 4$

Figure 4.15.: Derived values of e_0 (R_y-R_τ).

$$R_y^2 + R_\tau^2 = 1.0 \tag{4.25}$$

when $R_x = 0$. Accordingly, the value of e_0 is limited to a maximum value of $e_{0,max} = 2$, i.e.

$$e_0 = 2/\beta^{0.25} \leqslant 2 \tag{4.26}$$

The values for e_0 resulting from this equation are also plotted in Figures 4.14 to 4.16. As expected, these values agree best with R_y-R_τ stress combinations in case $\alpha = 1$. Using Equation (4.26) for the exponent e_0, the magnitudes of stress vectors are calculated using Equations (4.17) and (4.18), respectively, for all combinations of R_x-R_τ and R_y-R_τ (i.e. 2 x 19 x 5 = 190 vectors) and compared in Figure 4.18 to the magnitudes of stress

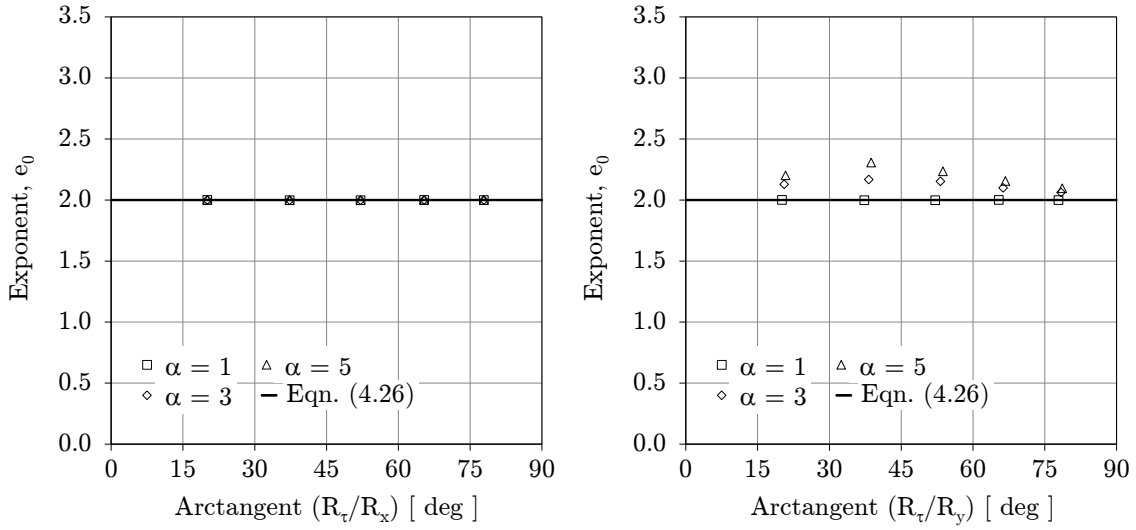

(a) R_x-R_τ (b) R_y-R_τ

Figure 4.16.: Derived values of e_0 ($\beta = 0.5$).

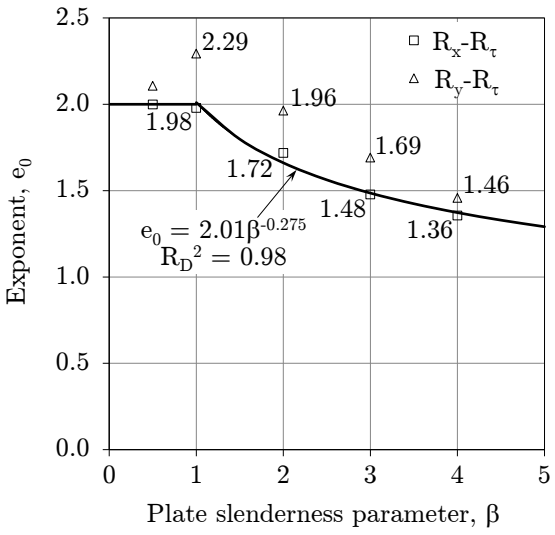

Figure 4.17.: Design equation for e_0.

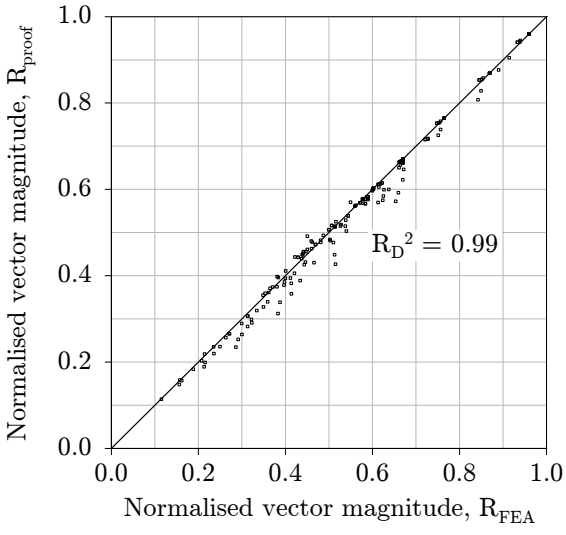

Figure 4.18.: Evaluation of equation for e_0.

vectors calculated on the basis of finite element analyses. As can be seen, the coefficient of determination is equal to $R_D^2 = 0.99$ ($m_{lsr} = 1$) with most of the scatter on the conservative side of results (an ever so slightly higher coefficient of determination $R_D^2 = 0.9902$ is obtained for the equation $e_0 = 2/\beta^{0.25} \leqslant 2$ compared to $R_D^2 = 0.9897$ for the equation $e_0 = 2/\beta^{0.30} \leqslant 2$).

4.3.4. Interaction Coefficient B (Quadrant 1)

Similar to above, an equation with which to determine the value of the interaction coefficient B may be determined numerically by substituting the values of (R_x/κ_x) and (R_y/κ_y) obtained by finite element analyses, together with the values of e_0 determined by Equation

(4.26), into Equation (4.8) where $R_\tau = 0$ and the stress multiplier factor at failure μ is set to unity, i.e.

$$\left(\frac{R_x}{\kappa_x}\right)^{e_0} + \left(\frac{R_y}{\kappa_y}\right)^{e_0} - B \cdot \left(\frac{R_x}{\kappa_x}\right)^{e_0/2} \cdot \left(\frac{R_y}{\kappa_y}\right)^{e_0/2} = 1.0 \tag{4.27}$$

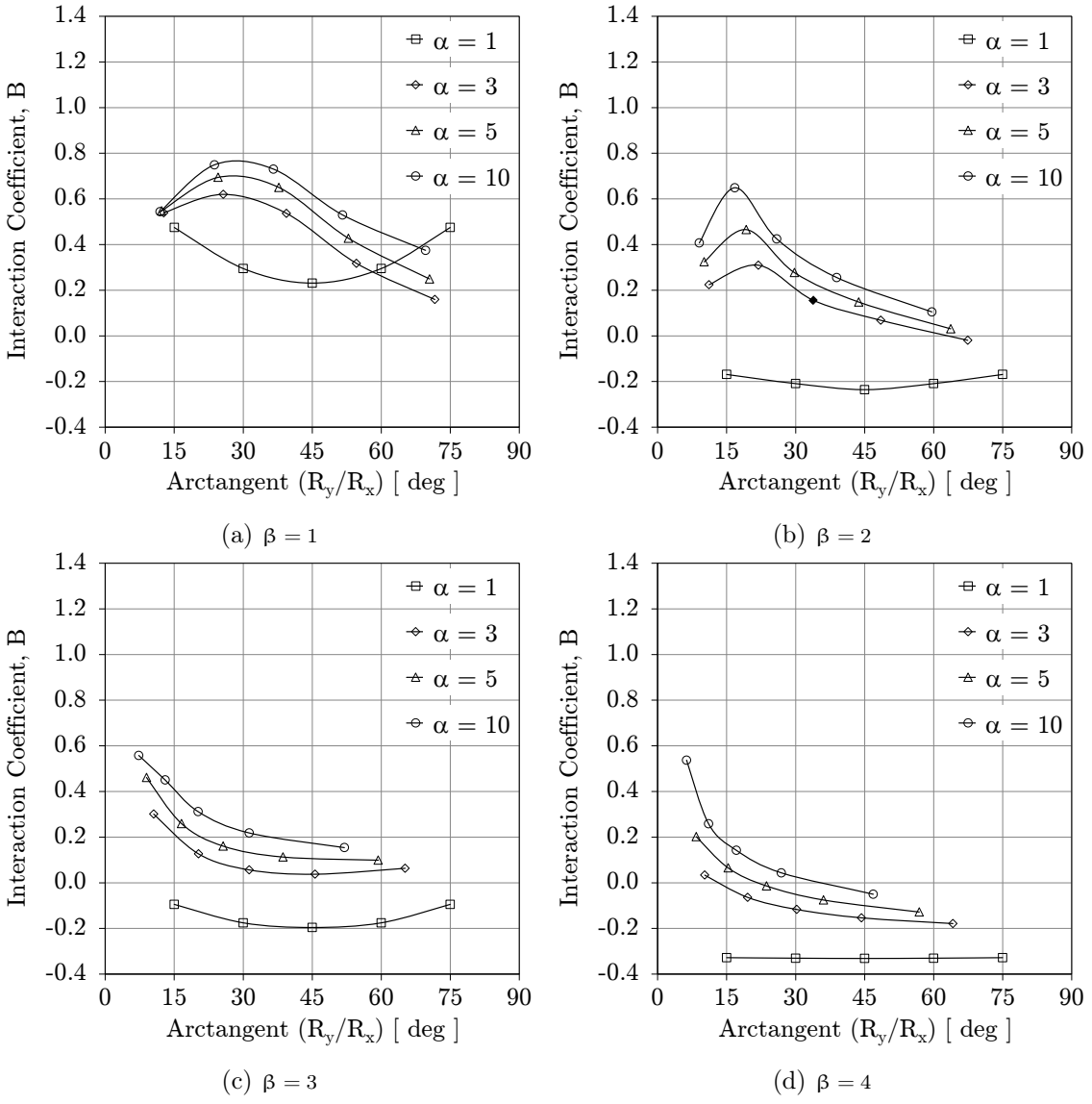

Figure 4.19.: Derived values of B.

which can then be solved for B (the assumption that B is not highly dependent on R_τ will be confirmed in the following subsection). For example, in case of the R_x-R_y capacity curve for plating with an aspect ratio $\alpha = 3$ and slenderness parameter $\beta = 2$ (i.e. $R_\tau = 0$, see Table D.2 and Figure D.2 in Appendix D), the plate reduction factors κ_x and κ_y are equal, respectively, to $R_{x,ult}$ when $R_y = 0$ (i.e. $\kappa_x = 0.755$) and $R_{y,ult}$ when $R_x = 0$ (i.e. $\kappa_y = 0.371$). According to Equation (4.26), $e_0 = 2/2^{0.25} = 1.68$ for a plate of slenderness $\beta = 2$. Therefore, for the data point $R_x = 0.441$ and $R_y = 0.295$, Equation

(4.27) becomes

$$\left(\frac{0.441}{0.755}\right)^{1.68} + \left(\frac{0.295}{0.371}\right)^{1.68} - \mathrm{B} \cdot \left(\frac{0.441}{0.755}\right)^{0.84} \cdot \left(\frac{0.295}{0.371}\right)^{0.84} = 1.0 \qquad (4.28)$$

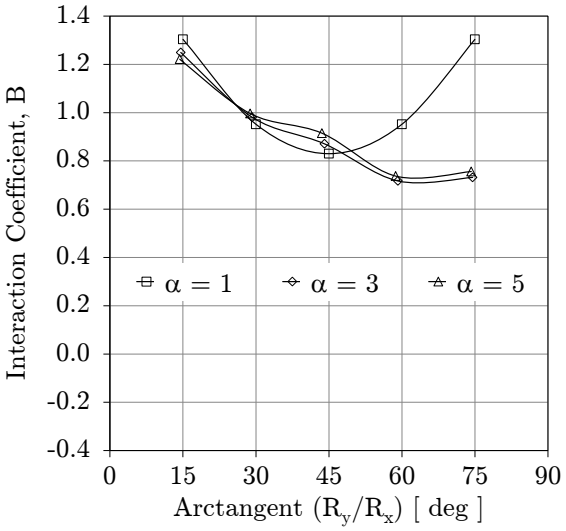

Figure 4.20.: Derived values of B($\beta = 0.5$).

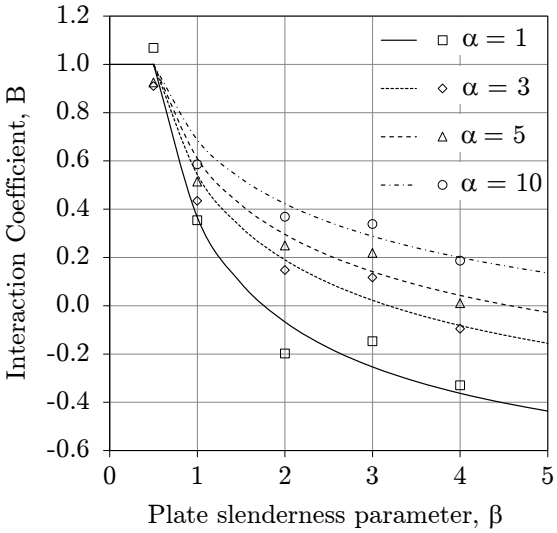

Figure 4.21.: Curves of best fit for B.

for which B = 0.156. This result is indicated in Figure 4.19(b) where arctangent $(R_y/R_x) = 34°$. This calculation is repeated for each of the five stress combinations comprising the R_x-R_y capacity curves which have non-zero components, i.e. the endpoints of the capacity curves are again not included since they involve no interaction of stresses. All results for $\beta = 1$, $\beta = 2$, $\beta = 3$ and $\beta = 4$ are shown in Figure 4.19. The results for $\beta = 0.5$ are shown separately in Figure 4.20.

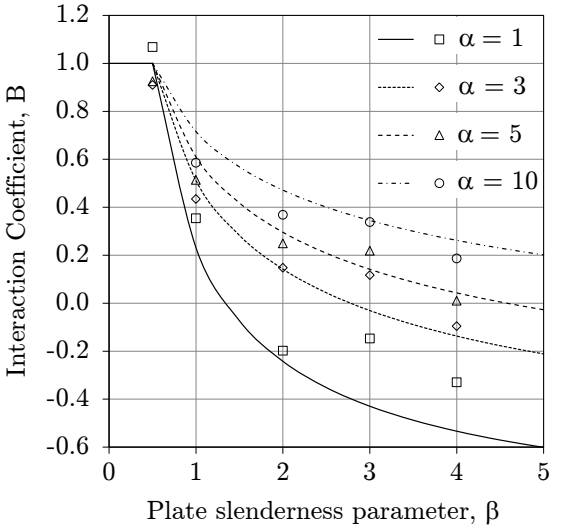

Figure 4.22.: Design curves for B.

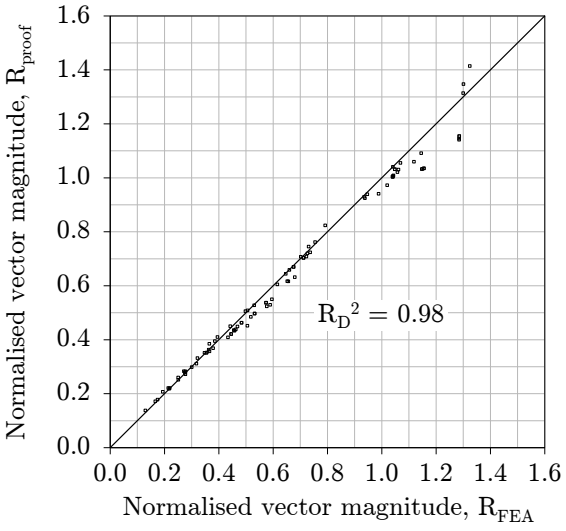

Figure 4.23.: Evaluation of design equation for B.

As can be seen, for each value of β the derived values of B generally decrease with

decreasing values of α and increasing values of R_y/R_x (except in case of the plate aspect ratio $\alpha = 1$ for which the derived values of B remain relatively constant). Furthermore, the derived values of B generally decrease with increasing values of β. For this reason, the equation defining the interaction coefficient B should be a function of α and β (as will be seen below, B need not be defined as a function of R_y/R_x). Accordingly, to derive an equation for the interaction coefficient B, the average values are plotted in Figure 4.21 as a function of β for each value of α. This plot reflects that the average derived values of B decrease with decreasing values of α and increasing values of β. On the basis of these results, curves of best fit to the derived values of B are also shown in Figure 4.21 based on the following *power* equation

$$B = 2/(2 \cdot \beta)^{0.55/\alpha^{0.35}} - 1 \tag{4.29}$$

However, for the purpose of design, Equation (4.29) is slightly amended

$$B = 2/(2 \cdot \beta)^{0.7/\sqrt{\alpha}} - 1 \leqslant 1 \tag{4.30}$$

to obtain moderately more conservative results, especially for $\alpha = 1$ and $\alpha = 3$. A maximum value of $B_{max} = 1$ is added so that Equation (4.27) (and ultimately Equation (4.8)) agrees with the von Mises (yield) equation for sturdy plating, i.e. small plate slenderness parameters. Design curves based on Equation (4.30) are shown in Figure 4.22.

Using Equation (4.30) for the interaction coefficient B (together with Equation (4.26) for e_0), the magnitudes of stress vectors are calculated using Equation (4.27) for all combinations of R_x-R_y, i.e. 19 x 5 = 95 vectors, and compared in Figure 4.23 to the magnitudes of stress vectors calculated on the basis of finite element analyses. As can be seen, the coefficient of determination is equal to $R_D^2 = 0.98$ ($m_{lsr} = 1$) with most of the scatter again on the conservative side of results.

Finally, in order to obtain an impression of the importance of accurately calculating the interaction coefficient B, the magnitude of the interaction term $B \cdot (R_x/\kappa_x)^{e_0/2} \cdot (R_y/\kappa_y)^{e_0/2}$ has been calculated for all 95 R_x-R_y data points, i.e. the *absolute* value of the interaction term as a fraction of the plate capacity 1.0. These results show that the contribution of the interaction term is highly dependent on the plate slenderness parameter β. In case $\beta = 0.5$, the average magnitude of the interaction term is about 0.53. For a plate slenderness parameter $\beta = 1$, the average magnitude drops to 0.25 and to 0.13 for $\beta = 2$. For the remaining plate slenderness parameters $\beta = 3$ and $\beta = 4$, the average magnitude of the interaction term is about 0.10. These average values have been obtained with shear $R_\tau = 0$ and decrease with increasing values of shear.

4.3.5. Quantitative evaluation

On the basis of the foregoing, the formulation of the new proof is shown in Box 4.1. As can be seen, a third stress limit has been added to prevent the shear capacity of the plate from being exceeded. As noted previously, because the proof is based on a generalised form of the von Mises equation (with the same value of e_0 for all terms), the qualitative acceptance criteria defined in §4.1.2 are fulfilled. Accordingly, only an evaluation of the new proof against the quantitative acceptance criteria delineated in §4.1.1 remains.

Therefore, in accordance with the evaluation scheme described in §3.1, the new proof has been used to calculate the capacity of plating for the 360 evaluation points. The resulting scatter plots for both the design space and design subspace are shown in Figure

4.24. The five key performance indicators used to measure precision and bias are shown in Table 4.8. Regarding the overall measure of error (KPI_1), the average of the squares of the residuals S_r/n_s is very low for both the design space ($S_r/n_s = 0.001$) and design subspace ($S_r/n_s = 0.001$). With respect to the measure of bias (KPI_2), the least-squares fit of a straight line through the R_{FEA} - R_{proof} data points gives a slightly conservative slope for both the design space ($m_{lsr} = 0.99$) and design subspace ($m_{lsr} = 0.97$). Concerning the measure of precision (KPI_3), the coefficients of determination reflect a very low degree of scatter for both the design space (${R_D}^2 = 0.97$) and design subspace (${R_D}^2 = 0.98$). Regarding the extent of non-conservatism (KPI_4), a straight line through the 95^{th} percentile gives a slightly non-conservative slope for both the design space ($m_{95} = 1.04$) and design subspace ($m_{95} = 1.02$). With respect to the extent of conservatism (KPI_5), a straight line through the 5^{th} percentile gives a significantly conservative slope for the design space ($m_5 = 0.87$) and a moderately/significantly conservative slope for the design subspace ($m_5 = 0.90$). Nevertheless, all key performance indicators associated with the new proof meet the quantitative acceptance criteria defined in §4.1.1, as highlighted in Table 4.8.

The capacity of plates under combined in-plane loads is defined by the following equation

$$\left(\frac{R_x}{\kappa_x}\right)^{e_0} + \left(\frac{R_y}{\kappa_y}\right)^{e_0} - B \cdot \left(\frac{R_x}{\kappa_x}\right)^{e_0/2} \cdot \left(\frac{R_y}{\kappa_y}\right)^{e_0/2} + \left(\frac{R_\tau}{\kappa_\tau}\right)^{e_0} = 1.0$$

where $e_0 = 2 \;/\; \beta^{0.25} \leqslant 2$ $\quad B = 2 \;/\; (2 \cdot \beta)^{0.7/\sqrt{\alpha}} - 1 \leqslant 1$ $\quad$ for $R_x \geqslant 0$ and $R_y \geqslant 0$

$e_0 = 2$ $\quad B = \kappa_x = \kappa_y = \kappa_\tau = 1$ $\quad$ for $R_x < 0$ or $R_y < 0$

and where the following stress limits are to be observed

$$\left(\frac{R_x}{\kappa_x}\right)^{2/\beta^{0.25}} + \left(\frac{R_\tau}{\kappa_\tau}\right)^{2/\beta^{0.25}} \leqslant 1.0 \quad \text{for } R_x \geqslant 0 \qquad \text{(i)}$$

$$\left(\frac{R_y}{\kappa_y}\right)^{2/\beta^{0.25}} + \left(\frac{R_\tau}{\kappa_\tau}\right)^{2/\beta^{0.25}} \leqslant 1.0 \quad \text{for } R_y \geqslant 0 \qquad \text{(ii)}$$

$$\left(\frac{R_\tau}{\kappa_\tau}\right) \leqslant 1.0 \qquad \text{(iii)}$$

Box 4.1.: Formulation of new proof

KPI		Target	Design space	Design subspace	Criteria
1	S_r/n_s	0.000	0.001	0.001	$S_r/n_s \leq 0.001$
2	m_{lsr}	1.00	0.99	0.97	$0.97 \leq m_{lsr} \leq 1.00$
3	${R_D}^2$	1.00	0.97	0.98	${R_D}^2 \geq 0.95$
4	m_{95}	1.00	1.04	1.02	$m_{95} \leq 1.05$
5	m_5	1.00	0.87	0.90	$m_5 \geq 0.87$

Table 4.8.: Key performance indicators (new proof).

Even so, in order to identify any inherent problems within the new proof for spe-

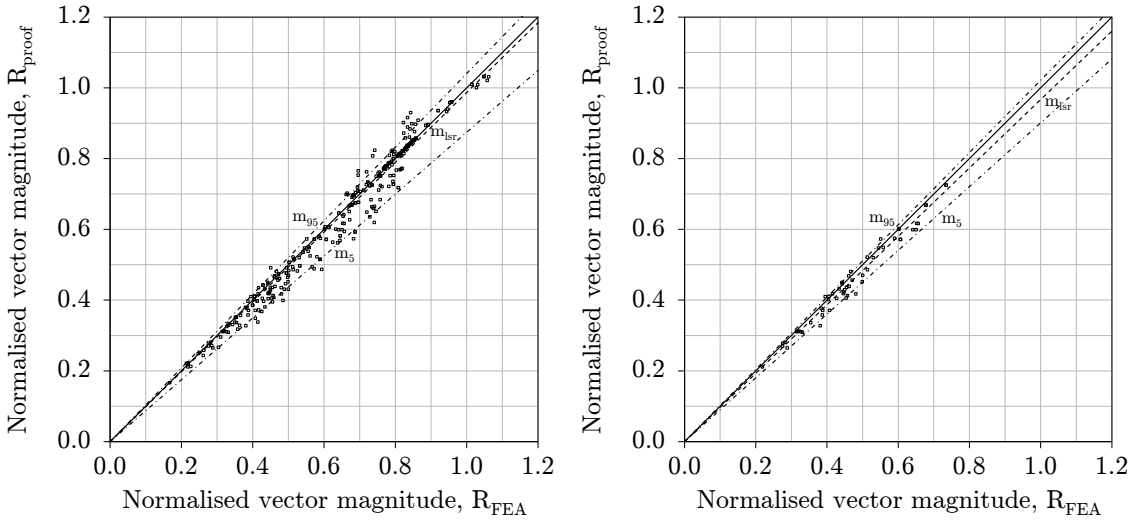

(a) Design space (360 evaluation points) (b) Design subspace (56 evaluation points)

Figure 4.24.: Scatter plots of R_{FEA} - R_{proof} (new proof).

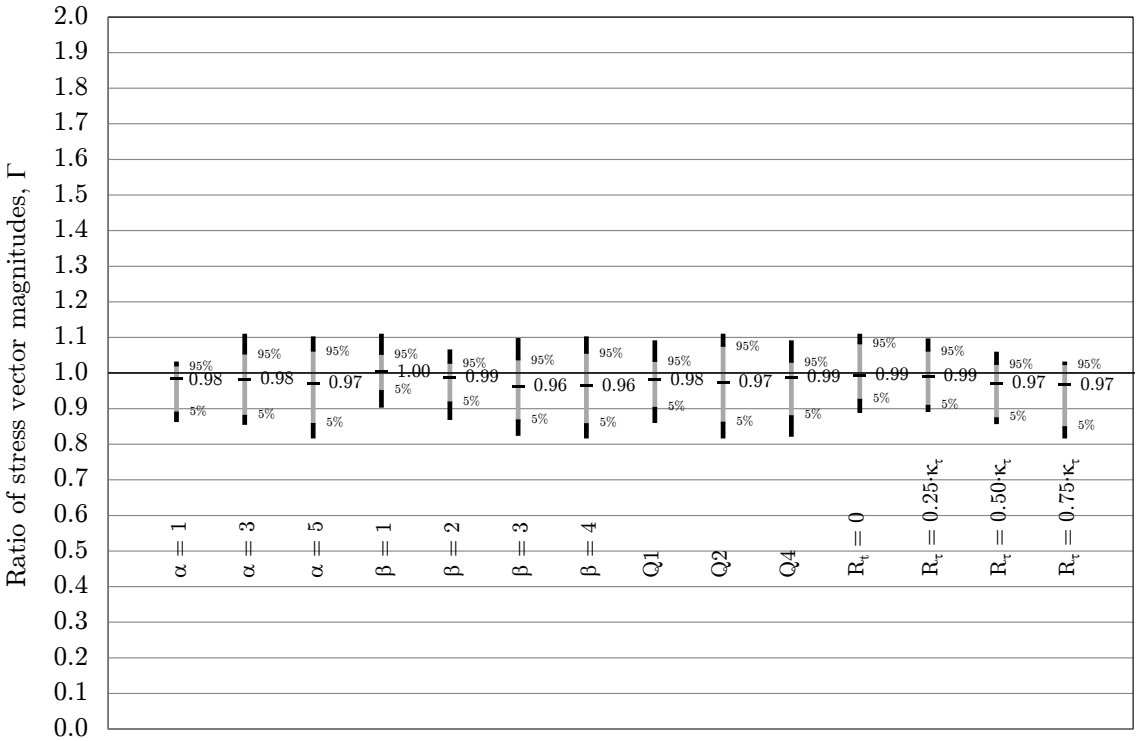

Figure 4.25.: Evaluation of data subsets (new proof).

cific parameters, the mean and extreme values of the ratio of stress vector magnitudes, $\Gamma = R_{proof}/R_{FEA}$, are shown in Figure 4.25 for each value of plate aspect ratio (α), plate slenderness parameter (β), quadrants of compressive/tensile load combinations (Q1, Q2 and Q4) and levels of shear (R_τ). In case of the plate aspect ratios, the mean values of Γ indicate a slightly conservative bias for all values of α. The ranges of extreme values

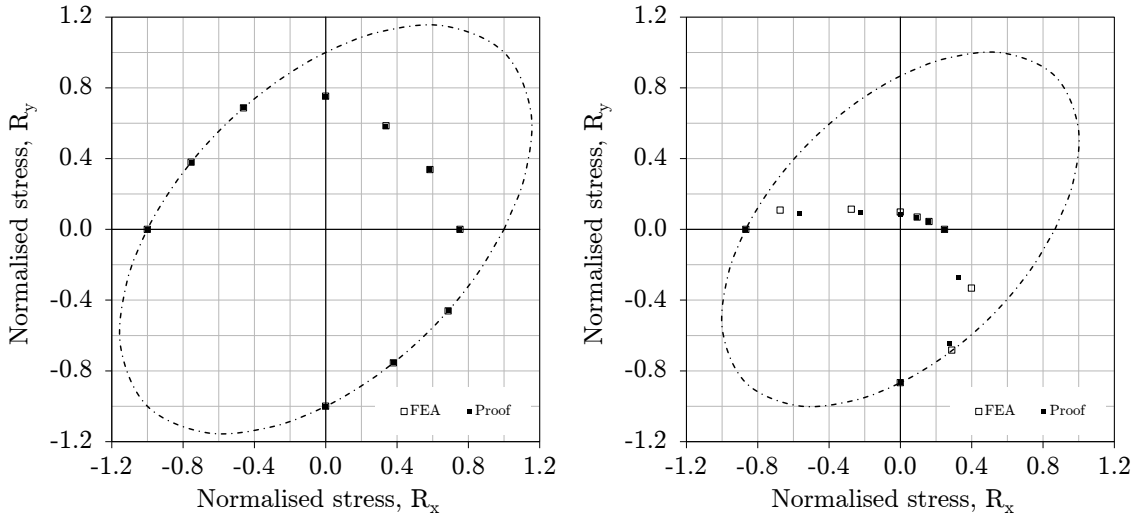

(a) $\alpha = 1,\ \beta = 2,\ R_\tau = 0$ (b) $\alpha = 5,\ \beta = 4,\ R_\tau = 0.75 \cdot \kappa_\tau$

Figure 4.26.: Comparison plots (new proof).

indicate quite good to very good precision for all plate aspect ratios. Similarly, in case of the plate slenderness parameters, the mean values of Γ indicate no bias for $\beta = 1$ and a slightly conservative bias for all remaining values of β. The ranges of extreme values indicate quite good precision for $\beta = 4$ and very good precision for all remaining values of β. In case of the compressive/tensile load combinations, the mean values of Γ indicate a slightly conservative bias for all quadrants. The ranges of extreme values indicate quite good precision in Quadrant 2 and very good precision in Quadrants 1 and 4. In case of shear, the mean values of Γ reveal a slightly conservative bias for all values of R_τ. The ranges of extreme values indicate very good precision for all levels of shear.

In order to obtain an impression of the strengths and weaknesses of the new proof, the lowest and highest values of the squares of the residuals (S_r/n_s) for each combination of plate aspect ratio (α), plate slenderness parameter (β) and level of shear (R_τ) have been calculated. The lowest value of S_r/n_s is for the combination $\alpha = 1$, $\beta = 2$ and $R_\tau = 0$, the capacity curve of which is plotted in Figure 4.26(a). Conversely, the highest value of S_r/n_s is for the combination $\alpha = 5$, $\beta = 4$ and $R_\tau = 0.75 \cdot \kappa_\tau$, the capacity curve of which is plotted in Figure 4.26(b). As can be seen, even though this latter combination is "in the corner" of the design space (see Figure 3.5), quite good accuracy is still achieved with the new proof. Results obtained using the new proof are tabulated and plotted for all load combinations and plating configurations in Appendices C and D.

4.4. CSR BC & OT proof

In 2006 the *IACS Common Structural Rules for Double Hull Oil Tankers* (CSR-OT) and *IACS Common Structural Rules for Bulk Carriers* (CSR-BC) came into force with the goal of achieving more robust and safer ships. However, because these two rule sets were independently developed by two different groups of IACS member societies, there existed some inconsistencies in requirements common to both ship types. For instance, as mentioned in

§3.3, the buckling strength rules in CSR-OT were (for all intents and purposes) based on DnV's computerised buckling code PULS (see §3.3.2) while in CSR-BC they were based on GL's amended DIN 18800 buckling strength rules (see §3.3.3). Accordingly, in order to remove these inconsistencies, IACS initiated a project in 2008 to harmonise those aspects of the rules common to both ship types. This resulted in the new *IACS Common Structural Rules for Bulk Carriers and Oil Tankers* (CSR BC & OT) comprising harmonised load and strength criteria common to both bulk carriers and oil tankers (Part One) as well as additional requirements unique to each ship type (Part Two).

In this regard, an IACS project team designated HPT02 was tasked with harmonising the buckling strength requirements for CSR BC & OT. In initial harmonisation efforts the *BV Advanced Buckling Assessment Method* was used provisionally for the proof of plate capacity under combined in-plane loads and was included in the first external release of CSR BC & OT in April 2013. As noted in §3.3.4, this method was based on the GL proof of buckling strength (in turn based on DIN 18800 and included in CSR-BC), but with a change to the exponents and interaction coefficient of the plate capacity equation in order to avoid the need for the Poisson correction. However, as shown (extremely) in Figure 3.31(b), the proof tends to overestimate plate capacity in Quadrant 1 and underestimate capacity in Quadrants 2 and 4 such that an improved proof was needed for inclusion in CSR BC & OT.

The proof of plate capacity ultimately included in CSR BC & OT is a slight variant of the new proof developed in the previous section. The single difference in the CSR BC & OT plate capacity formulation compared to the proof shown in Box 4.1 is the definition of the interaction coefficient B under biaxial compression (i.e. Quadrant 1). One of the great strengths of classification societies is their reservoir of successful (and unsuccessful) in-service experience. However, this experience has two inseparable components; capacity and demand. When the new proof of plate capacity was used together with the newly harmonised load definitions, consequence studies showed that the thickness required for plates under biaxial compression were too conservative compared to that of successful in-service experience. Accordingly, instead of recalibrating the load formulations, it was decided that the easiest solution to this problem would be to increase the values of the interaction coefficient B, thereby relaxing the required thickness of plates in Quadrant 1

$$B = 0.7 - 0.3 \cdot \beta/\alpha^2 \tag{4.31}$$

It is hoped that this is a short-term solution. In any case, Figure 4.27 shows the resulting design curves for the interaction coefficient B using Equation (4.31) overlaid on those previously shown in Figure 4.22 based on Equation (4.30). As explained, Equation (4.31) results in higher values of B for almost all combinations of plate aspect ratio α and plate slenderness parameter β (reference is here made to the above analysis regarding the contribution of the interaction term to the capacity of the plate, which reduces with increasing plate slenderness).

Using Equation (4.31) for the interaction coefficient B (together with Equation (4.26) for e_0), the magnitudes of stress vectors are calculated using Equation (4.27) for all combinations of R_x-R_y, i.e. 19 x 5 = 95 vectors, and compared in Figure 4.28 to the magnitudes of stress vectors calculated on the basis of finite element analyses. As can be seen, the coefficient of determination is equal to $R_D^2 = 0.95$ ($m_{lsr} = 1$) with most of the scatter on the non-conservative side of results. However, although Equation (4.31) leads to a mean non-conservative bias of 1.03 in Quadrant 1 (as shown below), this remains substantially

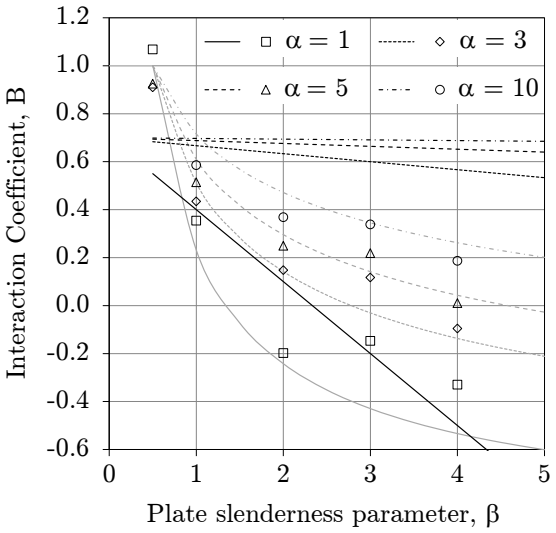

Figure 4.27.: Design curves for B (CSR BC & OT proof).

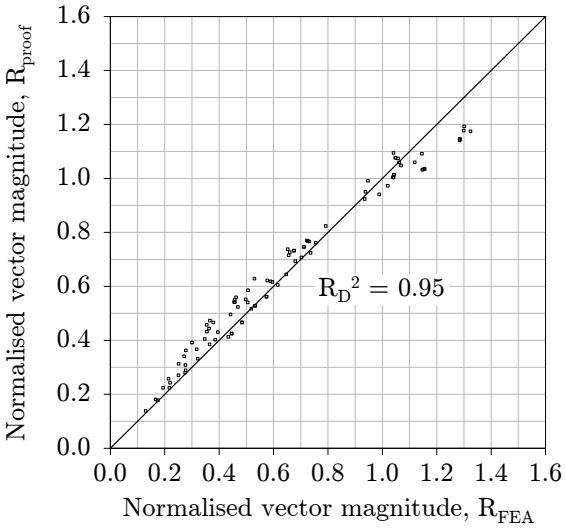

Figure 4.28.: Evaluation of design equation for B (CSR BC & OT proof).

below the mean non-conservative bias of 1.11 obtained with the provisional CSR BC & OT proof (see Figure 3.30).

4.4.1. Quantitative evaluation

On the basis of the foregoing, the formulation of the CSR BC & OT proof is the same as that shown in Box 4.1, but using the alternative definition of the interaction coefficient B according to Equation (4.31). Because the proof is based on a generalised form of the von Mises equation (with the same value of e_0 for all terms), the qualitative acceptance criteria defined in §4.1.2 are fulfilled. Accordingly, only an evaluation of the CSR BC & OT proof against the quantitative acceptance criteria delineated in §4.1.1 remains.

Therefore, in accordance with the evaluation scheme described in §3.1, the CSR BC & OT proof has been used to calculate the capacity of plating for the 360 evaluation points. The resulting scatter plots for both the design space and design subspace are shown in Figure 4.29. The five key performance indicators used to measure precision and bias are shown in Table 4.9. Regarding the overall measure of error (KPI_1), the average of the squares of the residuals S_r/n_s is very low for both the design space ($S_r/n_s = 0.001$) and design subspace ($S_r/n_s = 0.001$). With respect to the measure of bias (KPI_2), the least-squares fit of a straight line through the R_{FEA} - R_{proof} data points gives no bias for the design space ($m_{lsr} = 1.00$) and a slightly non-conservative bias for the design subspace ($m_{lsr} = 1.03$). Concerning the measure of precision (KPI_3), the coefficients of determination reflect a very low degree of scatter for both the design space ($R_D{}^2 = 0.96$) and design subspace ($R_D{}^2 = 0.93$). Regarding the extent of non-conservatism (KPI_4), a straight line through the 95th percentile gives a moderately/significantly non-conservative slope for the design space ($m_{95} = 1.10$) and a significantly non-conservative slope for the design subspace ($m_{95} = 1.16$). With respect to the extent of conservatism (KPI_5), a straight line through the 5th percentile gives a significantly conservative slope for the design space ($m_5 = 0.87$) and a moderately/significantly conservative slope for the design subspace ($m_5 = 0.91$).

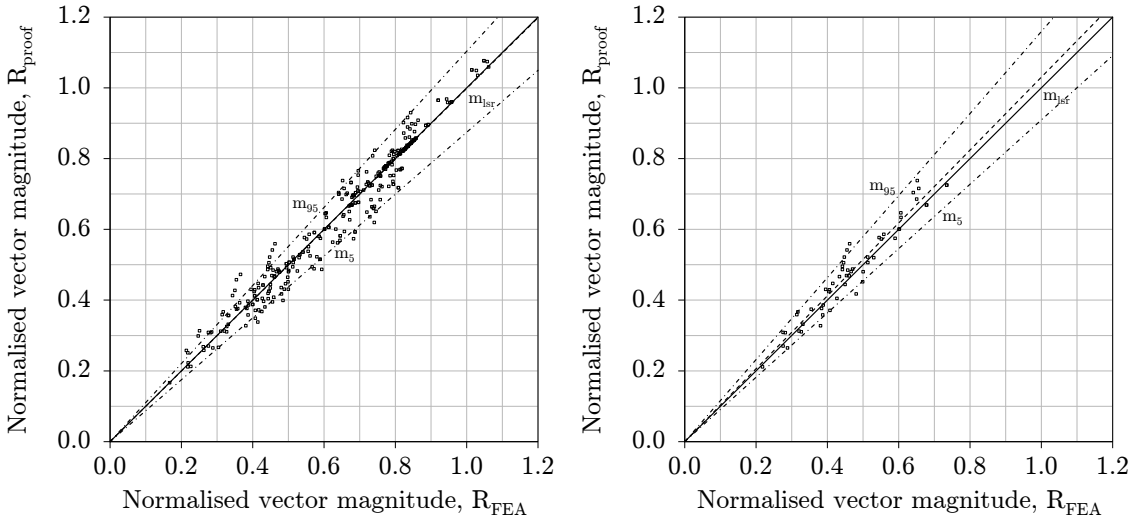

(a) Design space (360 evaluation points) (b) Design subspace (56 evaluation points)

Figure 4.29.: Scatter plots of R_{FEA} - R_{proof} (CSR BC & OT proof).

KPI		Target	Design space	Design subspace	Criteria
1	S_r/n_s	0.000	0.001	0.001	$S_r/n_s \leq 0.001$
2	m_{lsr}	1.00	1.00	1.03	$0.97 \leq m_{lsr} \leq 1.00$
3	R_D^2	1.00	0.96	0.93	$R_D^2 \geq 0.95$
4	m_{95}	1.00	1.10	1.16	$m_{95} \leq 1.05$
5	m_5	1.00	0.87	0.91	$m_5 \geq 0.87$

Table 4.9.: Key performance indicators (CSR BC & OT proof).

Accordingly, the CSR BC & OT proof meets the acceptance criteria in four of five KPI's for the design space and two of five KPI's for the design subspace, as highlighted in Table 4.9.

In order to identify any inherent problems within the CSR BC & OT proof for specific parameters, the mean and extreme values of the ratio of stress vector magnitudes, $\Gamma = R_{proof}/R_{FEA}$, are shown in Figure 4.30 for each value of plate aspect ratio (α), plate slenderness parameter (β), quadrants of compressive/tensile load combinations (Q1, Q2 and Q4) and levels of shear (R_τ). In case of the plate aspect ratios, the mean values of Γ indicate a slightly conservative bias for $\alpha = 1$, a slightly non-conservative bias for $\alpha = 3$ and no bias for $\alpha = 5$. The ranges of extreme values indicate very good precision for $\alpha = 1$ and good precision for the remaining two plate aspect ratios. Similarly, in case of the plate slenderness parameters, the mean values of Γ indicate slightly non-conservative biases for $\beta = 1$ and $\beta = 2$ with slightly conservative biases for $\beta = 3$ and $\beta = 4$. The ranges of extreme values indicate very good precision for $\beta = 1$ and $\beta = 2$ with good precision for the remaining two values of β. In case of the compressive/tensile load combinations, the mean values of Γ indicate a slightly non-conservative bias for Quadrant 1 (due to the revised equation for B) and slightly conservative biases in the remaining two quadrants. The ranges of extreme values indicate good precision in Quadrant 1, quite good precision

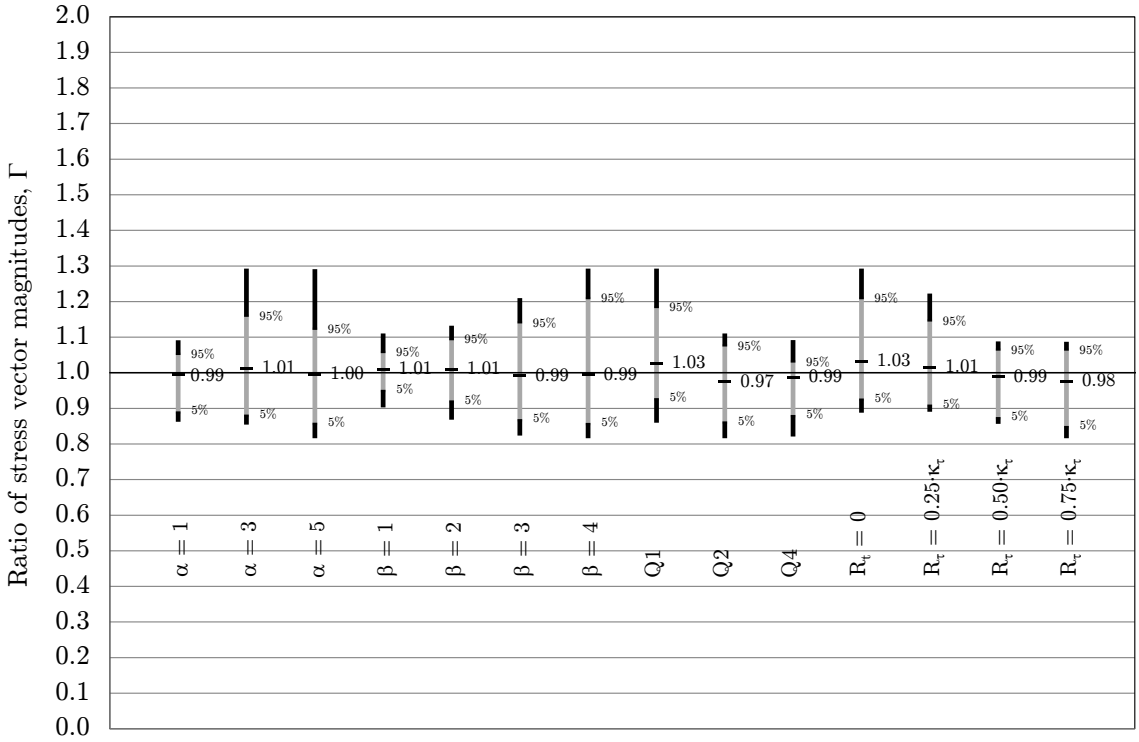

Figure 4.30.: Evaluation of data subsets (CSR BC & OT proof).

in Quadrant 2 and very good precision in Quadrant 4. In case of shear, the mean values of Γ reveal a slightly non-conservative bias in the absence of shear which transitions to a slightly conservative bias for $R_\tau = 0.75 \cdot \kappa_\tau$. The ranges of extreme values indicate good precision for $R_\tau = 0$ and $R_\tau = 0.25 \cdot \kappa_\tau$ with quite good precision for $R_\tau = 0.5 \cdot \kappa_\tau$ and $R_\tau = 0.75 \cdot \kappa_\tau$.

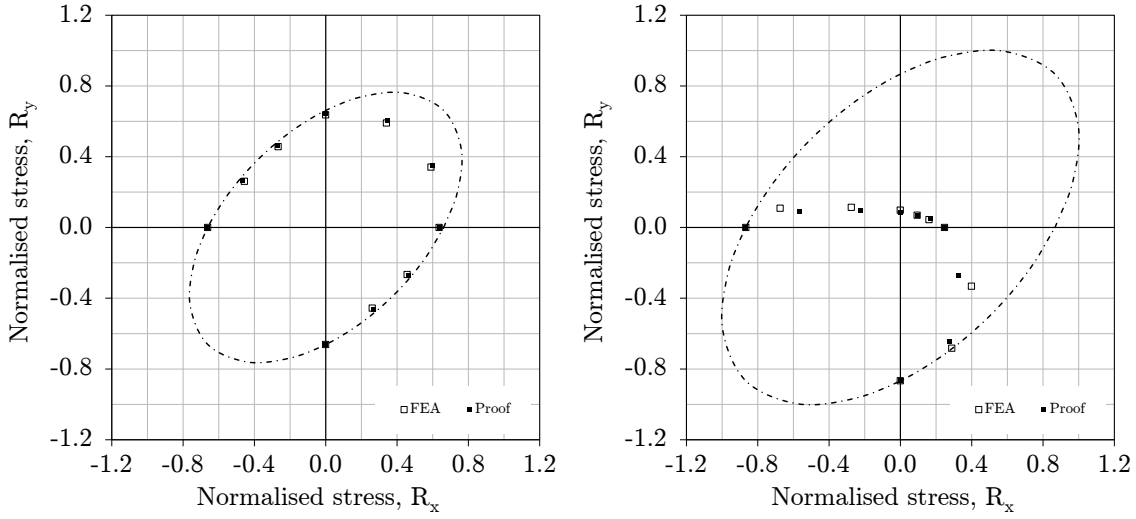

(a) $\alpha = 1$, $\beta = 1$, $R_\tau = 0.75 \cdot \kappa_\tau$ (b) $\alpha = 5$, $\beta = 4$, $R_\tau = 0.75 \cdot \kappa_\tau$

Figure 4.31.: Comparison plots (CSR BC & OT proof).

In order to obtain an impression of the strengths and weaknesses of the CSR BC & OT proof, the lowest and highest values of the squares of the residuals (S_r/n_s) for each combination of plate aspect ratio (α), plate slenderness parameter (β) and level of shear (R_τ) have been calculated. The lowest value of S_r/n_s is for the combination $\alpha = 1$, $\beta = 1$ and $R_\tau = 0.75 \cdot \kappa_\tau$, the capacity curve of which is plotted in Figure 4.31(a). Conversely, the highest value of S_r/n_s is for the combination $\alpha = 5$, $\beta = 4$ and $R_\tau = 0.75 \cdot \kappa_\tau$, the capacity curve of which is plotted in Figure 4.31(b). Like the new proof shown in Box 4.1, it can be seen that quite good accuracy is still achieved with the CSR BC & OT proof "in the corners" of the design space.

5. Design Application

In the previous chapter a proof of plate capacity under combined in-plane loads was developed where the edges of the plate were simply-supported and forced to remain straight. Neither the effects of in-plane bending nor lateral loads were considered. Moreover, the plate was free of residual stresses, but had an initial deflection shape defined by its eigenmodes and an initial deflection magnitude defined by $\delta_0 = \mathfrak{b}/200$. From a theoretical point of view, the proof is in and of itself informative insofar as it quantifies the influence of the plate aspect ratio α and plate slenderness parameter β on the collapse strength of plates under biaxial compression (with and without shear). In addition, the proof provides a more physical treatment of the collapse behaviour of plates under tensile loads. However, as noted previously, the motivation underlying this development is ultimately to obtain a proof of plate capacity for use in the shipbuilding industry. Towards this end, the present chapter illustrates in some detail how the proof developed in Chapter 4 may be applied in practice. In §5.1 an overview of the proof of stiffened panel capacity is presented, explaining how the strengths of plates and stiffeners are decoupled and separately calculated. Regarding the former, it is demonstrated that the proof of plate capacity developed in Chapter 4 remains valid in case of boundary conditions, load components and initial imperfections relevant for the shipbuilding industry, provided the influences of each are accurately captured in the plate reduction factors. In §5.2 two examples of design application are presented where the capacity of stiffened panels in the bottom shell and side shell of a double hull VLCC are calculated both numerically and according to the new proof, the former stiffened panel being particularly relevant to hull girder ultimate strength.

5.1. Proof of stiffened panel strength

As shown in Figure 5.1, modern day ship structures are essentially assemblages of stiffened panels. In a double bottom construction, for example, the bottom shell and inner bottom are comprised of stiffened panels which are supported by floors in the transverse direction and girders in the longitudinal direction, each of which are also stiffened panels. Plating which contributes to the longitudinal bending strength of the ship is almost always stiffened in the longitudinal direction, although it may sometimes be vertically-framed near the (vertical) neutral axis of the ship's cross-section where longitudinal bending stresses are smallest, e.g. in order to provide strengthening against ice loads. Conversely, plating which contributes to the transverse strength of the ship is normally stiffened in the transverse direction, although here again some transverse structures may be vertically-framed, e.g. the corrugated transverse bulkheads of bulk carriers where sufficient transverse strength may be provided by the upper/lower stools and adjacent structure (see Figure 5.1).

In general, all of these stiffened panels are subject to complex combinations of in-plane and lateral loads arising not only from routine service conditions, but as well from extreme conditions and/or accidents. In the language of probabilistic design, it is the responsibility of structural designers and classification societies to ensure that the design

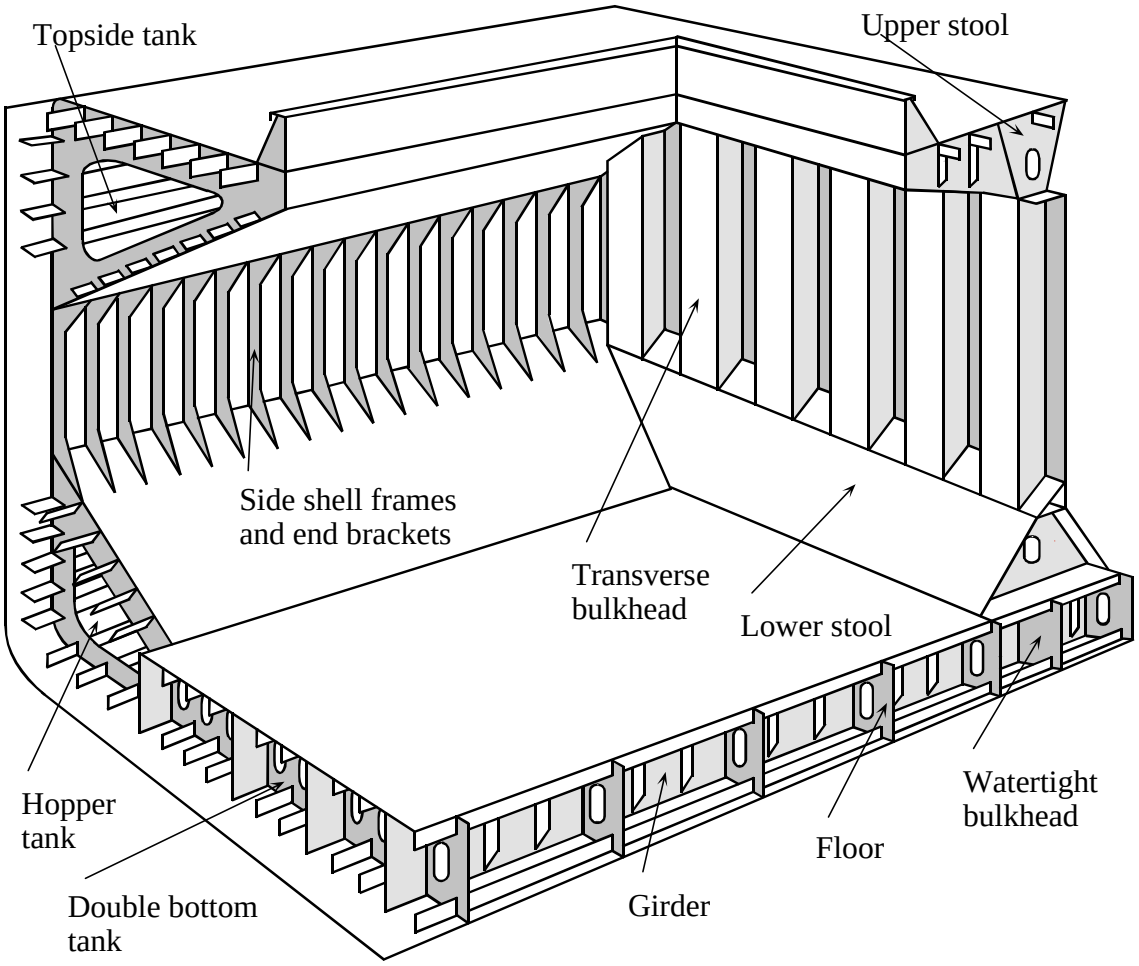

Figure 5.1.: Typical cargo hold configuration for a single side skin bulk carrier (reproduced from reference [64] with permission of the International Association of Classification Societies).

capacity (or *characteristic strength*) of these stiffened panels is greater than or equal to the design demand (or *characteristic load*) throughout the design service life of the ship (with adequate margins of safety against various uncertainties). Of course, *capacity* may be defined in a number of ways. Within the approach known as *limit state design*, four types of limit states are widely recognised [23, 35]:

1. serviceability limit state (SLS)
2. ultimate limit state (ULS)
3. fatigue limit state (FLS)
4. accidental limit state (ALS)

In terms of ship plating, the serviceability limit state (SLS) normally refers to limits in terms of deflection and vibration behaviour during normal operations. In this regard,

for example, it was already mentioned in §3.1.2 that most shipbuilding rules provide minimum plate slenderness values to 1) avoid excessive welding distortions, 2) avoid excessive elastic deflections and 3) promote good vibration behaviour. The ultimate limit state (ULS), however, refers to a limit where the structure collapses due to loss of stiffness when its ultimate strength is reached (as defined by the peak of the load-displacement curve). Today the strength requirements of classification societies are increasingly based on the ultimate limit state, despite the widespread misconception that they are based solely on allowable stress as some fraction of the yield stress. Of course, a necessary condition for attaining its ultimate strength is that plating remain ductile throughout loading. Brittle fracture is a particularly dangerous and sudden form of collapse against which steel grade requirements have been established as a function of plate thickness, tensile strength, temperature (if below -20°C) as well as severity of consequences associated with structural failure. As noted in §1.2, ductile plating is an assumption of the present work. In addition to brittle fracture, fatigue fracture of structural members refers to the unstable growth of a crack under the combined effects of stress concentration and cyclic loading, i.e. the fatigue limit state (FLS). Classification societies generally invest substantially in the development of their fatigue strength requirements in order that the fatigue life of ship structures (i.e. their capacity for accumulated damage) is greater than their design life. Finally, the accidental limit state (ALS) refers to the capacity of ship structures to prevent/limit loss of life, environmental pollution and loss of property (i.e. ship and cargo) in the aftermath of accidents or abnormal events (e.g. collision, grounding, flooding, explosion and/or fire). In this regard, shipbuilding rules typically define loads based on accidental design scenarios and then check to ensure that critical ship structures have adequate redundancy to survive the event.

In terms of the capacity of stiffened panels, today most shipbuilding rules define a proof based on ultimate strength (i.e. ULS design) rather than allowable stress, whereby proof of sufficient capacity is typically separated into distinct proofs for single plate fields and panel stiffeners with the capacity of the panel defined by the lesser of the two. Such decoupling is based on the assumption that plating and attached framing have similar in-plane, post-buckled stiffness (any differences in pre-buckled stiffness will be accounted for in *direct strength analyses*), otherwise the stiffer of the two would take a disproportionate share of the load. Nevertheless, the capacities of plating and stiffeners remain interdependent whereby stiffeners provide boundary conditions for plating which in turn constitutes (in most cases) the larger of stiffener flanges.

5.1.1. Proof of sufficient plate capacity

As noted in §4.4, the proof of plate capacity developed in Chapter 4 has been implemented in the newly harmonised *IACS Common Structural Rules for Bulk Carriers and Oil Tankers* (CSR BC & OT), although its use is generally valid for any such application. Because the capacity of plating is defined by its ultimate strength, the proof belongs to the *ultimate limit state* (ULS) design method. As can be seen in Box 5.1, the ratios of *characteristic strength* and *characteristic load* under single stress components are critical elements in the proof of plate capacity. These characteristic values are calculated from idealisations of plates and loads and their ratios comprise the base components of the exponential terms, i.e. $\mu \cdot R_x/\kappa_x$, $\mu \cdot R_y/\kappa_y$ and $\mu \cdot R_\tau/\kappa_\tau$, where μ is the *stress multiplier at factor at failure* which is included to limit utilisation of ultimate plate strength. As shown

below, the use of plate reduction factors κ_x, κ_y and κ_τ are a particularly convenient aspect of the proof since it permits a single proof of plate capacity to be used for any combination of boundary conditions, loads and initial imperfections. This is made possible by assuming that any changes in boundary conditions, loads and initial imperfections are reflected in the *endpoints* of the capacity curve, i.e. the plate reduction factors κ_x, κ_y and κ_τ, while the *shape* of the capacity (or interaction) curve is maintained. However, the proof shown in Box 5.1 is only intended for plane plates. A revised proof of capacity for curved plates under the combined effects of in-plane and lateral loads is presented in Appendix A (curved plates are defined as plates having a radius of curvature $R \leqslant 2500 \cdot t$).

The capacity of plates under combined in-plane loads is defined by the following equation

$$\left(\frac{\mu \cdot R_x}{\kappa_x}\right)^{e_0} + \left(\frac{\mu \cdot R_y}{\kappa_y}\right)^{e_0} - B \cdot \left(\frac{\mu \cdot R_x}{\kappa_x}\right)^{e_0/2} \cdot \left(\frac{\mu \cdot R_y}{\kappa_y}\right)^{e_0/2} + \left(\frac{\mu \cdot R_\tau}{\kappa_\tau}\right)^{e_0} = 1.0$$

where
$e_0 = 2 \;/\; \beta^{0.25} \leqslant 2$ $\quad B = 2 \;/\; (2 \cdot \beta)^{0.7/\sqrt{\alpha}} - 1 \leqslant 1$ $\quad$ for $R_x \geqslant 0$ and $R_y \geqslant 0$
$e_0 = 2$ $\quad B = \kappa_x = \kappa_y = \kappa_\tau = 1$ $\quad$ for $R_x < 0$ or $R_y < 0$

and where the following stress limits are to be observed

$$\left(\frac{\mu \cdot R_x}{\kappa_x}\right)^{2/\beta^{0.25}} + \left(\frac{\mu \cdot R_\tau}{\kappa_\tau}\right)^{2/\beta^{0.25}} \leqslant 1.0 \quad \text{for } R_x \geqslant 0 \qquad \text{(i)}$$

$$\left(\frac{\mu \cdot R_y}{\kappa_y}\right)^{2/\beta^{0.25}} + \left(\frac{\mu \cdot R_\tau}{\kappa_\tau}\right)^{2/\beta^{0.25}} \leqslant 1.0 \quad \text{for } R_y \geqslant 0 \qquad \text{(ii)}$$

$$\left(\frac{\mu \cdot R_\tau}{\kappa_\tau}\right) \leqslant 1.0 \qquad \text{(iii)}$$

Box 5.1.: New proof (from Chapter 4) incorporating the *stress multiplier factor at failure*, μ

Plate idealisation

In some cases the geometry and/or thickness of plates may need to be idealised before the plate reduction factors can be calculated. In case of *direct strength analyses*, plates with irregular or triangular geometries (e.g. in way of transverse web frames) need to be converted into an equivalent rectangular plate (also referred to as an *elementary plate panel* or EPP). In case of plates with irregular geometries, the procedure within CSR BC & OT is to identify the four corners of the bounding polygon closest to right angles [23]. The distances along the bounding polygon between the corners are calculated and the pair of opposite edges with the smallest total length is identified. The distance between the midpoints of these edges defines the length of the equivalent plate a_{eq} with the breadth of the equivalent plate defined as $b_{eq} = A/a_{eq}$, where A is the area of the original plate. In case of plates with triangular geometries, the longest median defines the nominal length $a_{eq,nom}$ of the equivalent rectangular plate with the nominal breadth defined as $b_{eq,nom} = A/a_{eq,nom}$, where A is again the area of the original plate. The breadth of the equivalent rectangular plate is then defined as $b_{eq} = b_{eq,nom}/C_{tri}$ and the length as $a_{eq} = C_{tri} \cdot a_{eq,nom}$, where the coefficient $C_{tri} = 0.4 \cdot b_{eq,nom}/a_{eq,nom} + 0.6$ has been

derived from the eigenvalue analyses of plates with right-angled triangular and isosceles triangular shapes. Where the thickness of finite elements is not constant over the plate field, a weighted average thickness is to be used in the buckling strength analyses[1]

$$t = \frac{\sum_1^n A_i \cdot t_i}{\sum_1^n A_i} \tag{5.1}$$

where n is the number of finite elements defining the plate.

In the case of *prescriptive analyses* where the thickness changes over the breadth b of a plate field, the plate reduction factor κ_x is calculated in CSR BC & OT using an equivalent plate defined by the smaller plate thickness t_1 and a reduced breadth b_{eq} of the plate field

$$b_{eq} = b_1 + b_2 \left(\frac{t_1}{t_2}\right)^{1.5} \tag{5.2}$$

where b_1 and b_2 are the breadths associated with the smaller plate thickness t_1 and larger plate thickness t_2, respectively. In case the thickness changes over the length a of a plate field, the smaller plate thickness is to be used for the entire field. Here it may be noted that the plate thickness upon which ultimate strength calculations are based is generally the net thickness of the plate, i.e. without corrosion additions or any additional thickness required by the owner (i.e. so-called *owner's extras*). In the context of IACS rules and requirements, this is referred to as the *net scantling approach*.

Lastly, in case the yield strength changes within a plate field, the lesser of the yield strengths is to be used when calculating plate capacity. Although this has no effect on the plate reduction factor, it is the product of the yield stress and the plate reduction factor which defines the ultimate strength of the plate under a single stress component, e.g. $\sigma_{x,ult} = \kappa_x \cdot \sigma_Y$.

Load idealisation

When performing *prescriptive analyses* of scantlings, stresses are defined on the basis of simple beam theory such that their definition is rather straightforward. Conversely, in case of *direct strength analyses* using the finite element method, the distribution of stresses acting on the plate are rarely uniform. Accordingly, procedures are required for determining the so-called reference stresses to be used in the proof of plate capacity. These reference stresses are based on the finite element stresses transformed into the local coordinate system of an equivalent rectangular plate, i.e. the EPP.

In case of plates with irregular or triangular geometries, the longitudinal, transverse and shear stresses are calculated in CSR BC & OT using a weighted average approach. In this case the edge stress ratios are to be taken as $\psi_x = \sigma_{x,max}/\sigma_{x,min} = 1$ and $\psi_y = \sigma_{y,max}/\sigma_{y,min} = 1$, i.e. no in-plane bending along either edge. In case of regular geometries, the following procedures are included in CSR BC & OT for calculating *stress-based* reference stresses along the edges of the plate (an alternative procedure for calculating *displacement-based* reference stresses is included in the *IACS Common Structural Rules for Bulk Carriers* (CSR BC) [31]).

[1] Throughout the following discussion of plate and load idealisation, the subscript i is used as a counter of finite elements rather than an indication of internal stress.

Longitudinal stress σ_x

In case of longitudinal stress, the distribution of $\sigma_x(x)$ over the length of the plate is represented by a second order polynomial curve (to take into account in-plane bending stresses in the plate due to out-of-plane stiffener deflection)

$$\sigma_x(x) = C_1 \cdot x^2 + C_2 \cdot x + C_3 \tag{5.3}$$

The curve of best fit is obtained by minimising the square error Π using the area of each element A_i as a weighting factor

$$\Pi = \sum_{i=1}^{n_e} A_i \left[\sigma_{x,i} - \left(C_1 \cdot x_i^2 + C_2 \cdot x_i + C_3\right)\right]^2 \tag{5.4}$$

where n_e is the number of finite elements and $\sigma_{x,i}$ is the stress at the centroid of each finite element. The unknown coefficients C_1, C_2 and C_3 are obtained by setting to zero the first derivatives of the square error Π with respect to each, e.g. $\partial\Pi/\partial C_1 = 0$, and solving the resulting set of equations, i.e. a 3 x 3 matrix.

The average longitudinal stresses σ_{x1} and σ_{x2} over b x b areas at each end of the plate as well as the average longitudinal stress σ_{x3} over a b x b area centred at the peak of the computed 2nd order polynomial curve are then calculated and the maximum taken to be the magnitude of reference stress in the longitudinal direction

$$\sigma_x = max.(\sigma_{x1}; \sigma_{x2}; \sigma_{x3}) \tag{5.5}$$

Here the average stress σ_{x3} is only considered if the peak of the computed 2nd order polynomial curve is at least $b/2$ away from the ends of the plate. The edge stress ratio for longitudinal stresses is taken as $\psi_x = \sigma_{x,min}/\sigma_{x,max} = 1$, i.e. no in-plane bending.

Transverse stress σ_y

In case of transverse stress, the distribution of $\sigma_y(x)$ over the length of the plate is assumed to be linear

$$\sigma_y(x) = A + B \cdot x \tag{5.6}$$

Once again, the curve of best fit is obtained by minimising the square error Π using the area of each element as a weighting factor

$$\Pi = \sum_{i=1}^{n_e} A_i \left[\sigma_{y,i} - (A + B \cdot x_i)\right]^2 \tag{5.7}$$

where $\sigma_{y,i}$ is again the stress at the centroid of each finite element. Similar to that for longitudinal stresses, the unknown coefficients A and B are obtained by setting to zero the first derivatives of the square error Π with respect to each, e.g. $\partial\Pi/\partial A = 0$, and solving the resulting set of equations, i.e. a 2 x 2 matrix.

The magnitude of transverse stress is then taken as

$$\sigma_y = max.[A, A + B \cdot a) \tag{5.8}$$

and the edge stress ratio as

$$\psi_y = \frac{\min.[A, A + B \cdot a)}{\max.[A, A + B \cdot a)} \quad \text{for} \quad \sigma_y \geqslant 0 \tag{5.9a}$$

$$\psi_y = 1 \quad \text{for} \quad \sigma_y < 0 \tag{5.9b}$$

Shear stress τ_{xy}

In case of shear stress τ_{xy}, a weighted average approach is used such that

$$\tau_{xy} = \frac{\sum_1^{n_e} A_i \cdot \tau_{xy,i}}{\sum_1^{n_e} A_i} \tag{5.10}$$

Here again, $\tau_{xy,i}$ is the shear stress at the centroid of each finite element.

Poisson correction

Finally, in case of grillage analyses where the stresses are based on beam theory (e.g. scantling check of hatch covers), stresses in the x- and y-directions need first to be corrected before a capacity check can be performed. This is because stresses which include the Poisson effect are greater than those according to beam theory for a given level of strain in the structure. Therefore, because stresses used in the proof of plate capacity include Poisson effects, stresses based on beam theory are to be corrected as follows

$$\sigma_x = \frac{\sigma_{xb} + \nu \cdot \sigma_{yb}}{1 - \nu^2} \tag{5.11a}$$

$$\sigma_y = \frac{\sigma_{yb} + \nu \cdot \sigma_{xb}}{1 - \nu^2} \tag{5.11b}$$

where σ_{xb} and σ_{yb} are the longitudinal and transverse stresses, respectively, based on beam theory.

Plate reduction factors

In Chapter 2 the plate reduction factors for rectangular plates under single stress components (i.e. κ_x, κ_y and κ_τ) were numerically calculated and compared to various formulations from both literature and the shipbuilding industry. Here the plates were simply-supported on all edges with uniform axial and shear stresses over the length/breadth of the plate. Although these idealised conditions are largely valid for most of the structure contributing to the longitudinal strength of a ship (i.e. the most critical aspect of ship strength), there is much structure throughout the ship for which these conditions are clearly invalid. For this reason, shipbuilding rules normally provide plate reduction factors for several combinations of other idealised boundary conditions (i.e. free, simply-supported or clamped edges) and applied stresses (including in-plane bending). In CSR BC & OT, 25 such cases are provided for plane plates alone (including the variations due to in-plane bending). It is then the responsibility of designers and plan approval engineers to determine which idealised case is most appropriate for a given structure and load. For instance, in case of floors or girders with lightening holes or access openings, the plating between stiffeners is

decomposed into smaller plate elements which may then be evaluated with the proof of capacity taking into account the revised dimensions and relevant boundary conditions, e.g. free edge in case the edge adjacent to an opening is not stiffened. The strength of webs and flanges of corrugated bulkheads may also be evaluated using a nominal plate aspect ratio ($\alpha = 2$ in case of CSR BC & OT) and assuming simply-supported edges.

As noted above, plate reduction factors (explicitly) capture the effects of boundary conditions and stresses over the length/breadth of the plate. In this regard, various definitions of plate reduction factors are used for different combinations of boundary conditions and loads. Moreover, for each of these combinations, plate reduction factors are assumed to (implicitly) capture the effects of lateral pressure and initial imperfections (i.e. residual stresses and deflections) even though, in case of the former, out-of-plane loads are assumed to have a negligible effect on the in-plane capacity of the plate (in accordance with DIN 18800 [26]). As mentioned previously, these assumptions conveniently allow a single proof of plate capacity to be used for any combination of boundary conditions, loads and initial imperfections, provided the influences of each are accurately reflected in the plate reduction factors. Accordingly, although the determination of plate reduction factors is beyond the scope of the present work, some examples are in order to demonstrate that the proof of plate capacity under combined loads (as shown in Box 5.1) remains valid in case of other boundary conditions, loads and initial imperfections relevant for the shipbuilding industry.

Other boundary conditions

Upon first glance of the buckling cases in CSR BC & OT, one of the more obvious variations in boundary conditions for investigation would seem to be plates with all four edges clamped against rotation (Case Nos. 13 and 14). Indeed, such boundary conditions do result in an interaction curve which is more rectangular in shape (i.e. less interaction between the axial stress components) such that the proof shown in Box 5.1 would be relatively conservative. However, in practice such boundary conditions are quite difficult to achieve and have been included in CSR BC & OT more so for the sake of completeness. Under in-plane axial stresses, the internal energy of continuous plating is minimised when it buckles out-of-plane in opposite directions on each side of its supports (in both the x- and y-directions), a deflection pattern which closely resembles simply-supported edges. Any effect of the rotational restraint provided by stiffeners is taken into account by increasing the elastic buckling factor K which in turn increases the value of the plate reduction factor κ, but essentially the edge conditions of the plating remain simply-supported. Even when a plate is preloaded by an extreme lateral pressure, it has been shown in finite element analyses (see below) and observed in tests [10] that the plating snaps out of the deflection pattern due to the lateral load and into a deflection pattern which minimises the internal energy under in-plane axial loads (i.e. its eigenmode). However, in a very few cases, it may be appropriate to consider *some* edges of the plate clamped against rotation. For instance, in CSR BC & OT the short edges of the shell plating of single side skin bulk carriers may be considered clamped against rotation due to the substantial restraint provided by the adjacent wing and hopper tank structures, although the strengthening effects of these boundary conditions are quite local.

One of the more common variations in boundary conditions found in shipbuilding is three edges simply-supported with the fourth edge free from any support. As suggested

above and shown in Figure 5.2, this is the case for plating adjacent to lightening holes and access openings (without edge reinforcements) in the floors and girders of the double bottom structure. Here the plate is subject to axial stresses in the local x-direction (e.g. due to longitudinal bending or transverse compression of the hull girder) combined with shear stresses (e.g. near the ends of floors and girders due to lateral loading of the double bottom). In Figure 5.3 the capacity curve of a plate with a free edge ($\alpha = 1$, $\beta = 2$) is compared to that with all four edges simply-supported. As can be seen, the capacity curve for the plate with one free edge takes on the same shape as that for the plate simply-supported on all edges (i.e. a function of the exponent e_0, as defined by the plate slenderness parameter β, since $R_y = 0$). Here a standard access opening of 600 x 800 mm in accordance with SOLAS [65] requirements has been centred in a 2400 x 800 mm plate field in the double bottom[2]. In practice, the vertical extension of such openings should not exceed one half of the height of the floor/girder. Accordingly, for the standard access opening 600 x 800 mm in a plate field of 800 mm spacing, it is possible that the remaining plating above/below the opening has an aspect ratio $\alpha = 2$ (i.e. a double bottom height of 1600 mm and vertically-centred opening). This of course increases the effect of the free edge on the capacity of the plate leading to an error which may approach 10%. However, this is something of an upper bound on the error and is at the boundary of practical ship design. Moreover, for plating adjacent to lightening holes and access openings, the ends of the "free" edge are not truly free, i.e. they are supported by the plating and sniped stiffeners in line with the longitudinal axis of the opening.

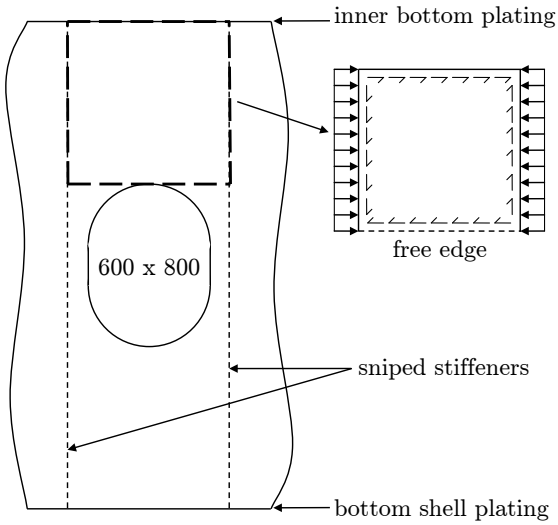

Figure 5.2.: Idealisation of plating adjacent to access opening.

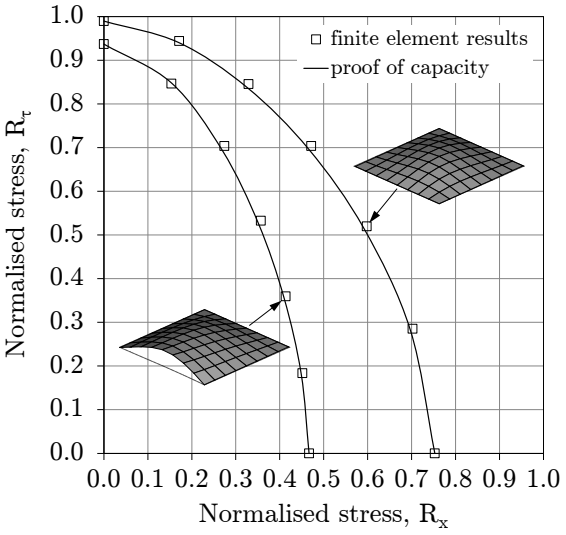

Figure 5.3.: Capacity curve of plate with free edge ($\alpha = 1$, $\beta = 2$).

Yet another common variation in boundary conditions found in shipbuilding is when one edge is allowed to pull in, i.e. no edge restraint. In fact, preventing the in-plane deflection of plating at the edges of stiffened panels is rarely possible in ship structures since the restraint would need to come from perpendicular supporting structure which in

[2] According to Chapter II-1, Part A-1, Regulation 3-6, Paragraph 5.2 of SOLAS, such a configuration requires the provision of gratings or other foot holds since the distance of the opening from the bottom shell plating is otherwise not to exceed 600 mm (i.e. to facilitate access).

general is only able to prevent deflections in its own plane. Conversely, within the extent of stiffened panels, perfect in-plane restraint occurs naturally due to the reciprocal action in adjacent plate fields, i.e. in-plane force balance. Accordingly, within CSR BC & OT there are two different methods for assessing the capacity of plating depending on whether or not the plating has in-plane restraint. For structures *with* in-plane restraint, such as continuous shell and deck plating, capacity is calculated using *Method A*. For structures *without* in-plane restraint, such as side and bottom girders that are not in line with decks and bulkheads, respectively, capacity is calculated using *Method B*. In fact, Method A and Method B are identical except for the value of a factor ($c_1 = 1 - 1/\alpha$) used in the calculation of the plate reduction factor κ_y defining the characteristic (transverse) strength of the plate (pull-in on the short edges of the plate is assumed to have a negligible effect on its capacity). In case of Method B, a plate aspect ratio of $\alpha = \infty$ is taken such that $c_1 = 1$, resulting in a smaller ultimate (transverse) strength of the plating compared to those plates with in-plane restraint (to an extent dependent on α).

The mechanics underlying the foregoing treatment of edge restraint within CSR BC & OT is actually based on the buckling strength rules of Germanischer Lloyd [30]. In these rules transverse loads are differentiated between *strain-based* loads and *stress-based* loads. As illustrated in Figure 5.4, the former refers to non-uniform stresses arising from uniformly-applied strains (e.g. hull girder bending) and the latter to non-uniform strains arising from uniformly-applied stresses (e.g. side girders under ice loading). Of course, due to the reciprocal action of neighbouring plates, only one edge of the plate is normally free to pull in. The resulting change in plate capacity when one (long) edge of a plate ($\alpha = 3$, $\beta = 3$) has no edge restraint is shown in Figure 5.5. As can be seen, in such cases the proof of plate capacity performs as well as for the case where all edges are restrained against pull-in.

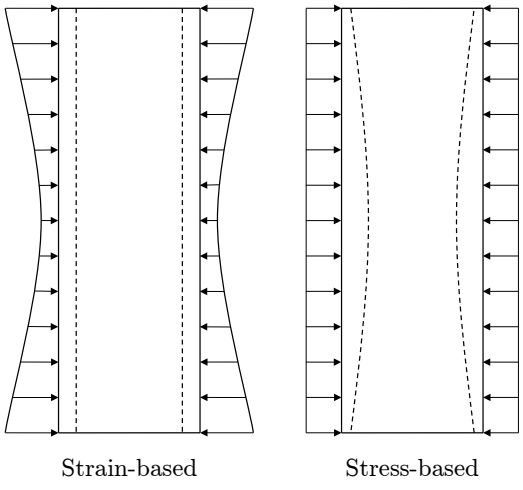

Figure 5.4.: Strain-based and stress-based loads.

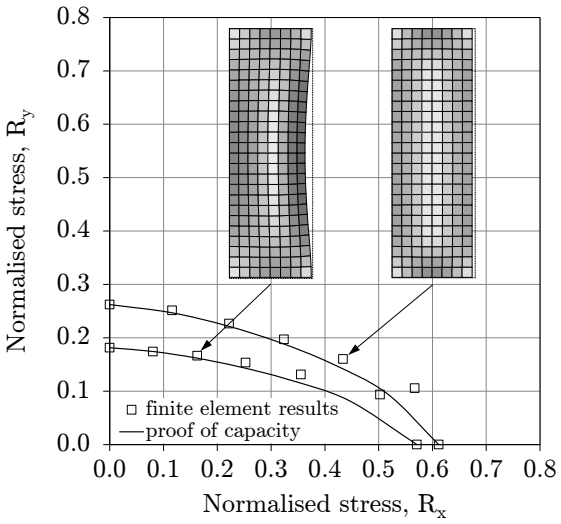

Figure 5.5.: Capacity curve of plates without edge restraint ($\alpha = 3$, $\beta = 3$).

Additional load components

As noted above, plate reduction factors also capture the effect of other load com-

ponents such as in-plane bending. Because individual plate fields are relatively small compared to the ship as a whole, the in-plane bending due to global bending of the hull girder (vertical and horizontal) is normally assumed to result in uniform stress distribution over the length and breadth of plates (one notable exception here is the in-plane bending of vertical stiffened side shell plating of single side skin bulk carriers which generally have rather large aspect ratios). Accordingly, it is usually local loads such as double bottom bending which subject plates to in-plane bending (e.g. floors and girders). In such cases, the effects of in-plane bending are reflected in the elastic buckling factor K which in turn are reflected in the plate reduction factor κ that is used in the proof of capacity. As an example, a capacity curve is shown in Figure 5.6 for a plate ($\alpha = 3$, $\beta = 3$) subjected simultaneously to shear stresses and transverse in-plane bending. Here the in-plane bending is described by the edge stress ratio $\psi = \sigma_{y,min}/\sigma_{y,max} = 0$, where $\sigma_{y,min}$ is the minimum stress along the side and $\sigma_{y,max}$ is the maximum. Such a stress state occurs, for instance, in case of a vertically stiffened plate field at the end of a bottom longitudinal girder, i.e. under lateral loads the girder is effectively clamped against rotation by the supporting structure of the transverse bulkhead such that pure in-plane bending is superimposed on compressive stresses (of comparable magnitude) due to hull girder bending. As can be seen, the shape of the capacity curve for in-plane bending ($\psi = 0$) is similar to the shape of the capacity curve for the (standard) case of no in-plane bending ($\psi = 1$), upon which the proof of plate capacity is based.

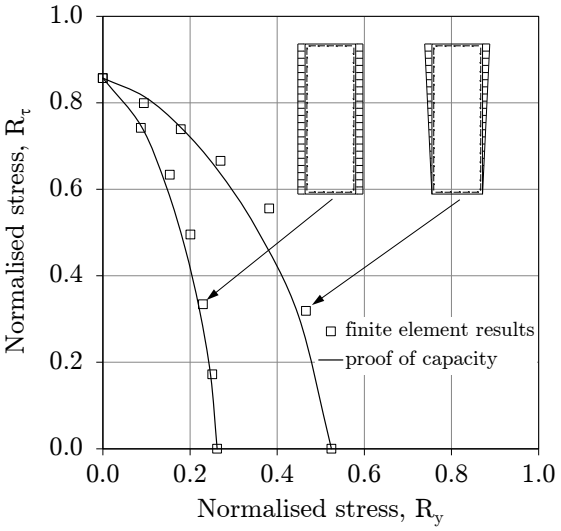

Figure 5.6.: Capacity curve of plate under in-plane bending ($\alpha = 3$, $\beta = 3$).

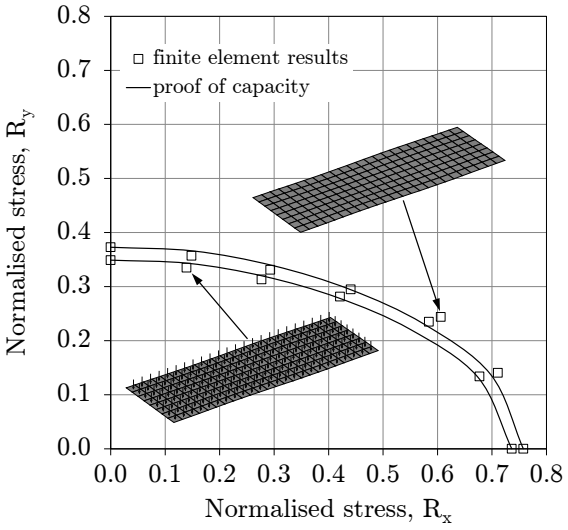

Figure 5.7.: Capacity curve of plate under lateral load ($\alpha = 3$, $\beta = 2$).

Another load component not explicitly considered in the development of the plate capacity proof is lateral pressure. As noted above, out-of-plane loads are assumed to have a negligible effect on the in-plane capacity of the plate in accordance with DIN 18800 [26]. In this regard, Figure 5.7 compares the capacity curves for typical bottom shell plating ($\alpha = 3$, $\beta = 2$) under biaxial compression with and without lateral pressure. Here the plate was pre-loaded with a lateral pressure of $p = 271.0$ kN/m^2 which is the pressure required to initial yield according to the following equation

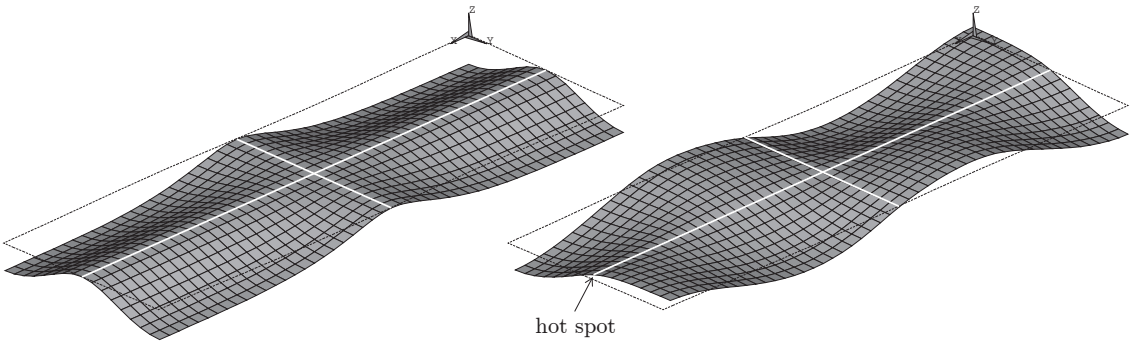

(a) Deflection under lateral load (b) Deflection under lateral and in-plane loads

Figure 5.8.: Deflection patterns under lateral load ($p = 271.0\ kN/m^2$, $\alpha = 3$, $\beta = 2$).

$$p = \frac{2 \cdot \sigma_Y}{\sqrt{1 - \nu + \nu^2}} \cdot \left(\frac{t}{b}\right)^2 \tag{5.12}$$

In this case the average loss of capacities (i.e. reduction in magnitude of the ultimate load vectors) due to the lateral pressure is about 4.8%. Moreover, as shown in Figure 5.7, the shape of capacity curves with and without pressure are the same. Accordingly, the proof of capacity remains valid where any loss in capacity due to the presence of lateral pressure need only be reflected in the plate reduction factors κ_x and κ_y. In case of square plates, Søreide and Czujko [66] alternatively suggest an interactive relationship between biaxial compression and lateral load of the form

$$(R_x)^{e_1} - B \cdot R_x \cdot R_y + (R_y)^{e_2} = (1 + \xi \cdot R_p)^{e_4} \tag{5.13}$$

where the quantity $R_p = p/p_{ult}$ is the lateral load normalised against its defined ultimate value (e.g. first yield).

To better understand why lateral pressure has such a small effect on the capacity of plates under in-plane loads, some insight into the collapse mechanism is required. Towards this end, it is noteworthy that the presence of lateral pressure does not prevent deflection of the plate into a shape which minimises internal energy under compressive loads. This is illustrated in Figure 5.8 which shows the deflection under lateral load alone (Figure 5.8(a)) and the deflection at collapse after an in-plane longitudinal load was applied in a second load step (Figure 5.8(b)). The same is true when transverse loads are applied. Here the finite element analyses are performed with a symmetric model to correctly capture the effect of the lateral pressure with the location of stiffeners indicated in Figure 5.8 (a finer mesh is also used to better illustrate the patterns of deflection).

Moreover, the locations of collapse initiation are the same with or without lateral pressure. Therefore, in order to study the development of plate collapse, the internal stresses at the mid-length edge "hotspot" identified in Figure 5.8(b) are shown in Figure 5.9. Here the tracking of internal stress development begins following application of the lateral pressure, i.e. longitudinal load $R_x = 0$. Accordingly, as shown in Figures 5.9(a) and 5.9(b), edge hinges develop under the lateral pressure as evidenced by yielding in the top and bottom fibres of the plate for $R_x = 0$ (i.e. $R_{e,i} \simeq 1$) due to large tensile and compressive stresses $R_{y,i}$, respectively, in the transverse direction. With the application of

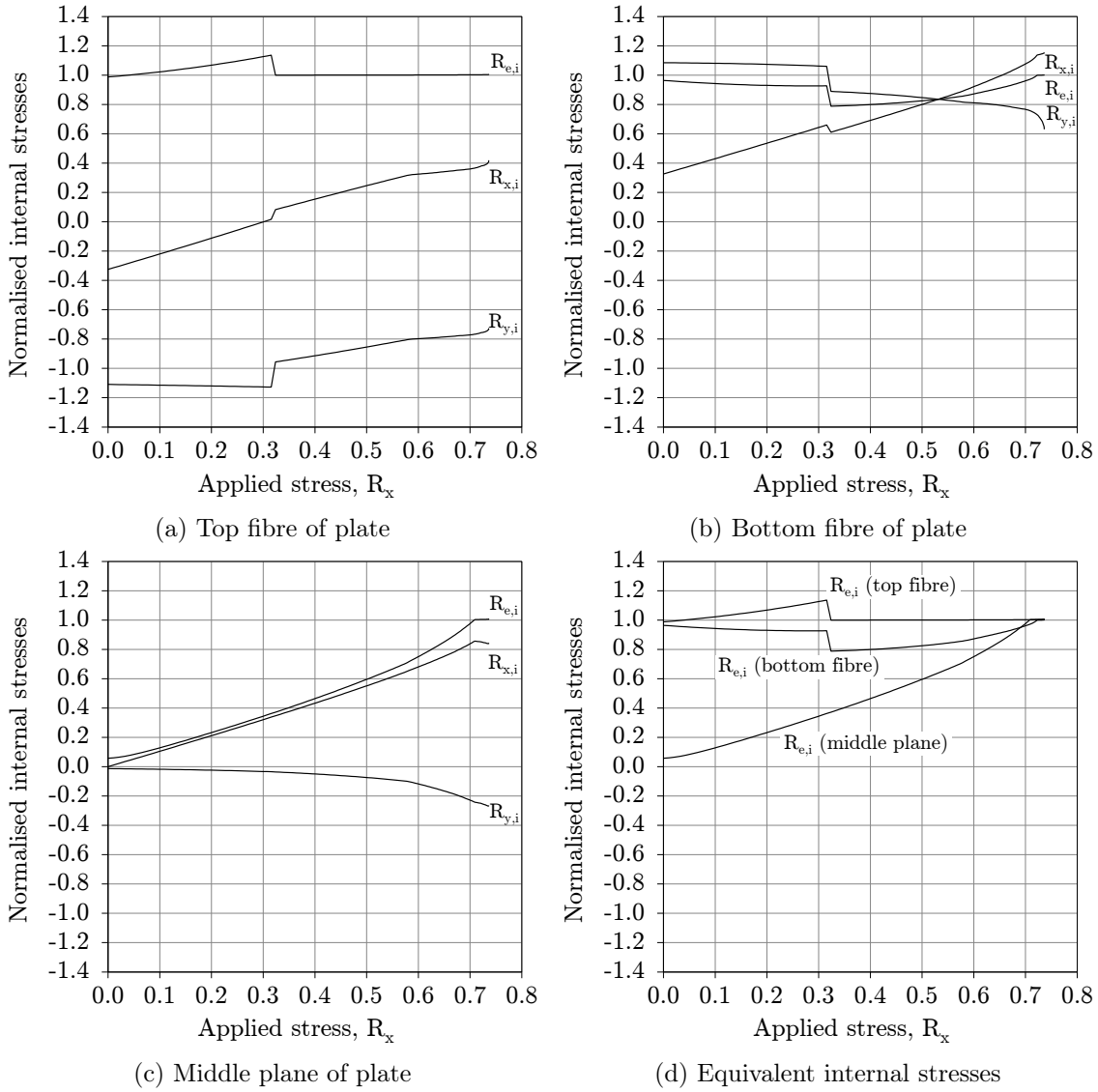

(a) Top fibre of plate

(b) Bottom fibre of plate

(c) Middle plane of plate

(d) Equivalent internal stresses

Figure 5.9.: Internal stresses in plate under lateral pressure and longitudinal in-plane compression.

the longitudinal load R_x (i.e. $R_y = 0$), the internal stress $R_{x,i}$ in the x-direction directly increases. However, because of changes in $R_{y,i}$ due to changes in the deflection pattern of the plate, the equivalent internal stresses in both the top and fibres remain close to $R_{e,i} = 1.0$ throughout the application of the longitudinal load.

Conversely, as shown in Figure 5.9(c), the stress levels in the middle plane of the plate under lateral pressure alone are quite small, i.e for $R_x = 0$. This is because lateral loads are primarily resisted by pure bending in the absence of significant membrane action (i.e. there is little strain in the middle plane of the plate since its edges, although straight, are otherwise able to freely move in-plane). Accordingly, the equivalent stress $R_{e,i}$ in the middle plane of the plate under lateral pressure alone is only about 6.5% of yield. As the magnitude of the longitudinal load R_x increases, so too does the magnitude of internal stresses $R_{x,i}$ and $R_{y,i}$ in the middle plane of the plate, the latter due to the magnifica-

tion of out-of-plane deflections as shown in Figure 5.8(b).[3] This growth of longitudinal and transverse stresses in the middle plane of the plate leads directly to larger equivalent stresses $R_{e,i}$ in this plane. As noted in Chapter 2, through thickness plasticity (along the plate edges) is a precursor to collapse under in-plane axial loads. This means that plate collapse only occurs once the equivalent stresses in all fibres of the plate reach yield, i.e. $R_{e,i} = 1$ in the top, bottom and middle fibres of the plate. However, as shown in Figure 5.9(d), here yielding in the middle fibres of the plate depends almost exclusively on the magnitude of applied in-plane loads, although membrane action would be expected to increase together with plate slenderness (as evident in test results reported by Becker [49]).

Initial imperfections

Within modern day shipbuilding, most steel structures are subjected to *time-dependent temperature gradients* during welding and to a lesser extent thermal cutting. As noted by Paik and Thayamballi [35], when steel is heated during welding the molten portion expands and is compressed by the surrounding steel which remains relatively cool. Once the temperature drops in the heated portion, it is subjected to locked in tensile stresses and distortions which may be minimised by proper welding procedures and fabrication methods, but never eliminated. Accordingly, in addition to boundary conditions and other load components, plate reduction factors need also to account for the effects of these initial imperfections.

In terms of distortions due to welding, a double Fourier series imperfection shape is widely used to characterise residual deflections in plating

$$\frac{\delta}{\delta_0} = \sum_{i=1}^{m} \sum_{j=1}^{n} \sin\frac{i\pi}{a}x \cdot \sin\frac{j\pi}{b}y \tag{5.14}$$

where δ_0 is the magnitude of initial (out-of-plane) deflection. However, initial imperfection shapes are normally such that they predominantly have one half-wave in the shorter direction, allowing them to be adequately described by out-of-plane deflection along the centreline $y = b/2$ of the plate

$$\frac{\delta}{\delta_0} = \sum_{i=1}^{m} \sin\frac{i\pi x}{a} \tag{5.15}$$

The magnitude of initial deflection δ_0 is of particular importance since the capacity of plating is inversely related to this quantity. For this reason, several empirical formulations are available in the literature for calculating design magnitudes, with one of the more well known formulations provided by Smith et al. [63] for three different levels of imperfections

$$\frac{\delta_0}{t} = \begin{cases} 0.025 \cdot \beta^2 & \text{slight} \\ 0.100 \cdot \beta^2 & \text{average} \\ 0.300 \cdot \beta^2 & \text{severe} \end{cases} \tag{5.16}$$

[3] The magnification of deflections used in Figure 5.8 are optimised for better illustration. The magnitude of out-of-plane deflections at collapse under combined lateral and longitudinal loads are about 3.5 times greater than under lateral pressure alone.

However, in shipbuilding the magnitudes of initial deflection are unknown beforehand and so are not an explicit parameter in plating design. For instance, the plate reduction factors used in CSR BC & OT are empirically derived on the basis of experimental and numerical results. Accordingly, post-construction surveys are carried out to ensure that plating complies with deflection tolerances. For instance, ships built according to the rules of IACS member societies need to comply with tolerances delineated in the *IACS Shipbuilding and Repair Quality Standard* [67] for the hull structure during the newbuilding stage and repair standard when the quality standard is not satisfied.

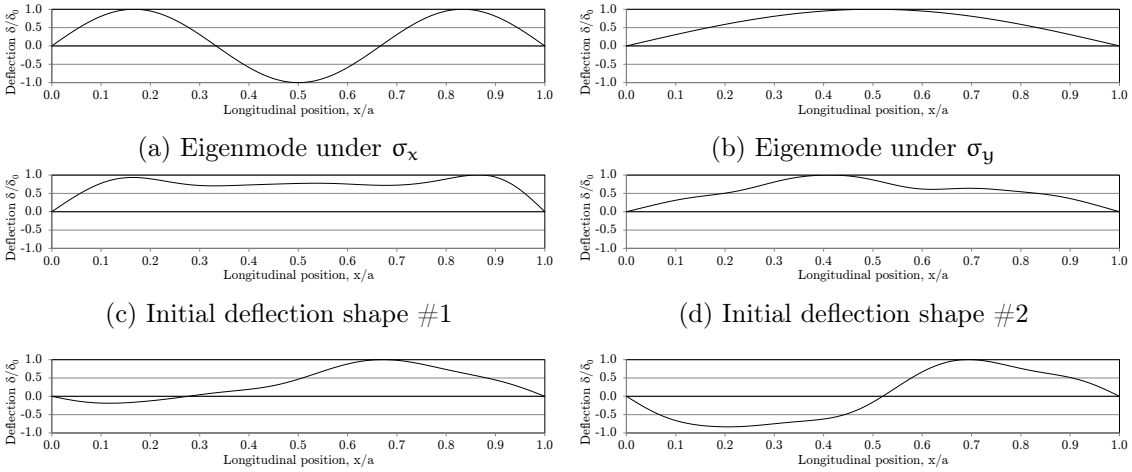

(a) Eigenmode under σ_x

(b) Eigenmode under σ_y

(c) Initial deflection shape #1

(d) Initial deflection shape #2

(e) Initial deflection shape #3

(f) Initial deflection shape #4

Figure 5.10.: Initial deflection shapes.

With respect to the shape of imperfections, the proof of plate capacity developed in Chapter 4 is based on results using the critical eigenmodes of plates for the initial deflection shapes (as described in Appendix B). In order to investigate whether the resulting proof remains valid for other types of imperfection shapes, capacities for a plate ($\alpha = 3$, $\beta = 2$) under biaxial compression have been numerically calculated using four typical initial deflection patterns reported by Paik and Thayamballi [35] (see also Paik and Pedersen [68]). These shapes have been chosen amongst several deflection measurements obtained by Ueda and Yao [69] from 21 bulk carriers and 12 car carriers and are shown in Figure 5.10 together with the critical eigenmodes under longitudinal and transverse compression. A deflection magnitude of $\delta_0 = b/200$ was used in all analyses which was sufficient to prevent the plate from snapping into any of its eigenmodes upon load application (i.e. in case of imperfection shapes #1 to #4). Capacities of the plate based on all imperfection shapes are compared in Figure 5.11. As can be seen, the shape of the capacity curves delineated by numerical results may not be the same, but those based on eigenmode deflections provide a good representation of the critical imperfections.

In addition to initial deflections, plate reduction factors need also to account for residual stresses due primarily to welding. Similar to initial deflections, some authors have developed formulations for plate reduction factors which explicitly account for the level of residual welding stresses. For instance, Frieze et al. [70] have developed plate reduction curves for "unwelded", "lightly welded" and "heavily welded" plates. However, within the shipbuilding industry, plate reduction factors implicitly account for welding residual

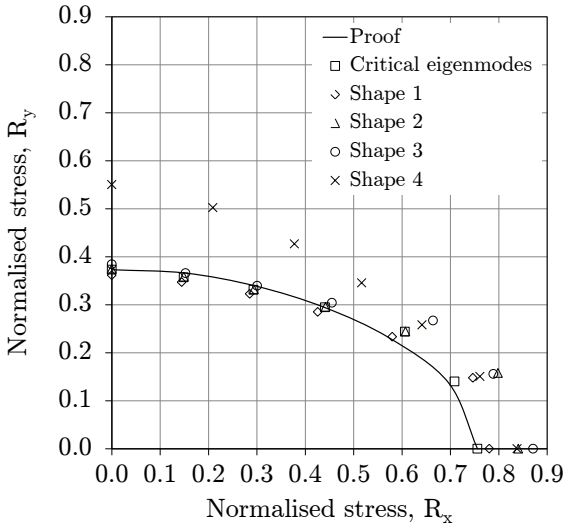

Figure 5.11.: Capacity curve of plates with various initial deflection shapes.

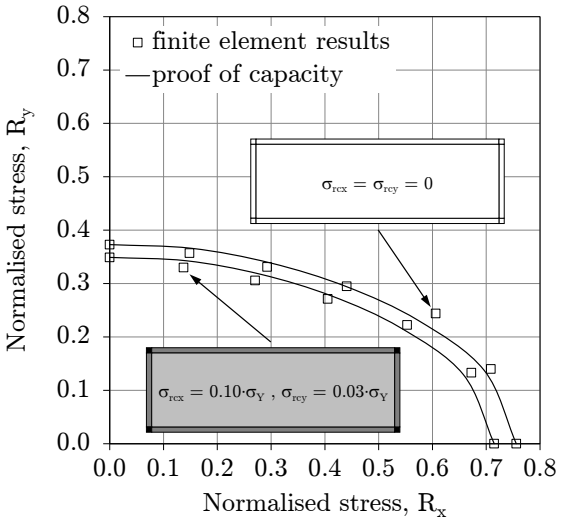

Figure 5.12.: Capacity curve of plate with residual stresses.

stresses and where the quality of welds are controlled through classification society rules, welding procedure qualification, welder certification as well as weld monitoring and control [71].

With respect to residual stresses, the proof of plate capacity developed in Chapter 4 is based on results for *unwelded* plates (i.e. without residual stresses) such that some additional numerical calculations are needed to validate the proof for welded plates (i.e. with residual stresses). As noted above, residual tensile stresses develop due to welding in the so-called *heat-affected zone* (HAZ) along the edges of the plate, between which compressive stresses develop in order to maintain force equilibrium. Accordingly, the internal stresses in the body of the plate reach yield under the application of a smaller compressive in-plane stress compared to stress-free plates, i.e. residual stresses generally reduce the capacity of plates. Because the tensile zones are adjacent to the edges of the plate, Hughes notes that they have a negligible effect on the stability of the plate [9]. Moreover, as further noted by Hughes, the breadth of these zones are relatively small such that the effective aspect ratio α' of the plate is only slightly reduced. In general, residual stresses due to welding develop in both the x- and y-directions of the plate and are normally idealised as tensile and compressive blocks as shown in the inset of Figure 5.12. Based on equilibrium considerations, the breadth of the tensile block b_t in the x-direction is equal to

$$b_t = \frac{\sigma_{rcx}}{2 \cdot (\sigma_{rcx} - \sigma_{rtx})} \cdot b \tag{5.17}$$

where σ_{rcx} and σ_{rtx} are the residual compression and tension stresses, respectively. As noted by Hughes [9], the compressive residual stresses in welded plates rarely exceed $0.1 \cdot \sigma_Y$ and, although tensile residual stresses may well reach yield, stress-relief normally occurs due to the alternating tension and compression of the plate under hull girder bending (referred to as "shakedown") resulting locally in small plastic strains. Accordingly, based on measurements reported by Cheng et al. in Appendix B of reference [72] (also reported in reference [35]), $-0.7 \cdot \sigma_Y$ is considered to be an appropriate value of tensile compressive stresses due to welding.

Accordingly, for residual stresses of $\sigma_{rcx} = 0.1 \cdot \sigma_Y$ and $\sigma_{rtx} = -0.7 \cdot \sigma_Y$, the resulting breadth of the tensile zones in the x-direction according to Equation (5.17) is equal to

$$b_t = \frac{\sigma_{rcx}}{2 \cdot (\sigma_{rcx} - \sigma_{rtx})} \cdot b = \frac{0.1 \cdot \sigma_Y}{2 \cdot (0.1 \cdot \sigma_Y + 0.7 \cdot \sigma_Y)} \cdot b = \frac{b}{16} \tag{5.18}$$

For a finite element model of a plate with 16 square elements of equal size across its breadth, tensile zones in the x-direction would therefore have the breadth of a single element. Using the same breadth $a_t = b_t = b/16$ and magnitude $\sigma_{rty} = \sigma_{rtx} = -0.7 \cdot \sigma_Y$ of tensile zones along the short edges of a plate, the magnitude of compressive residual stress in the y-direction is calculated as $\sigma_{rcy} = 0.03 \cdot \sigma_Y$ (it is for this reason that residual stresses in the transverse direction are often neglected). Accordingly, with reference to the inset in Figure 5.12, the following residual stresses are used in the numerical analyses of a welded plate

$$\sigma_{rx} = \begin{cases} \sigma_{rtx} & \text{for } 0 \leqslant y \leqslant b_t \\ \sigma_{rcx} & \text{for } b_t \leqslant y \leqslant b - b_t \\ \sigma_{rtx} & \text{for } b - b_t \leqslant y \leqslant b \end{cases} \tag{5.19}$$

in the x-direction, and

$$\sigma_{ry} = \begin{cases} \sigma_{rty} & \text{for } 0 \leqslant x \leqslant a_t \\ \sigma_{rcy} & \text{for } a_t \leqslant x \leqslant a - a_t \\ \sigma_{rty} & \text{for } a - a_t \leqslant x \leqslant a \end{cases} \tag{5.20}$$

in the y-direction. Using this residual stress state, the capacities of a welded plate under biaxial compression are compared in Figure 5.12 to that for an unwelded plate ($\alpha = 3$, $\beta = 2$). As can be seen, the loss of capacity due to residual stresses is about 7.0%. However, the shape of both capacity curves is the same such that the results obtained with the proof of plate capacity compare well with both sets of numerical results.

Evaluation

Following the calculation of plate reduction factors (κ_x, κ_y and κ_τ) and reference stresses (R_x, R_y and R_τ), the capacity of the plate can then be evaluated. By substituting these factors and stresses into the capacity equation shown in Box 5.1, the equation can then be solved in terms of the stress multiplier factor at failure μ. Within CSR BC & OT, a utilisation factor is then defined as the reciprocal of the minimum value of μ

$$\eta = \frac{1}{\mu_{min}} \tag{5.21}$$

and then compared to an allowable value of the utilisation factor η_{all} which is defined as a function of the type of structure and load combination, i.e. whether the applied stresses are due to a static load or combined static and dynamic loads

$$\eta \leqslant \eta_{all} \tag{5.22}$$

The utilisation factor is best understood as the ratio of applied loads and the ultimate capacity of the plate, i.e. the ratio of stress vector magnitudes.

5.1.2. Proof of sufficient stiffener capacity

As noted above, the ultimate strength of a stiffened panel is defined as the minimum of the ultimate strength of the plating and the ultimate strength of the stiffeners. In terms of the latter, CSR BC & OT includes checks for two separate collapse modes

1. overall panel buckling (elastic),
2. lateral buckling (inelastic).

In CSR BC (and legacy GL rules), three additional collapse modes are considered

3. torsional buckling (inelastic),
4. web buckling (inelastic),
5. flange buckling (inelastic).

Analogous to the analysis of plating strength, the mode of collapse associated with the minimum stress multiplier at failure μ is the critical mode which defines stiffener strength.

Overall panel buckling

Regarding the first mode of collapse, overall panel buckling is synonymous with elastic stiffener buckling, i.e. lateral or out-of-plane buckling. In this mode of collapse the panel buckles elastically as if it were a plate. For this reason, the computerised buckling code PULS uses orthotropic plate theory to check for overall panel buckling (orthotropic plate theory was also used in the GL buckling strength rules prior to 1997). As noted by Hughes [9], overall panel buckling is a sudden mode of collapse requiring adjacent structure to take over a considerable amount of load. However, the lateral loads carried by most ship panels lead to stiffener scantlings which are normally sufficient to prevent this mode of collapse.

Lateral buckling

Contrary to overall panel buckling, collapse under lateral buckling is a relatively gradual process whereby the initial out-of-plane deflection of the stiffener is magnified under in-plane loads until the yield stress is reached either in the flange of the stiffener (i.e. *stiffener induced* failure) or in the attached plating (i.e. *plating induced* failure). In addition to these second order effects, bending stresses due to lateral pressure will either retard or hasten yielding depending on the sign of the resulting bending moment, i.e. whether the pressure is on the plate side or the stiffener side. Although yielding at mid-span of the stiffener may be considered a precursor to stiffener collapse, there is generally some margin before the ultimate strength of the stiffener is reached. The magnitude of this margin depends largely on the relative magnitude (and sign) of the longitudinal stress which directly increases (or decreases) internal stress over the entire cross-section of the plate-stiffener combination.

2^{nd} order theory

In CSR BC & OT, capacity checks associated with overall panel buckling and lateral buckling are performed using 2^{nd} order theory. Provision for the use of 2^{nd} order theory was initially included in DIN 18800, but the procedure was first implemented in shipbuilding through the 1997 GL buckling strength rules and subsequently in CSR BC. The procedure considers the following loads

a. compressive stresses parallel to the stiffener,

b. compressive stresses perpendicular to the stiffener,

c. shear stresses in the plate,

d. lateral loads (e.g. external sea pressure)

and is described in detail in reference [73]. However, the following description is based closely on reference [61].

As shown in Figure 5.13, when a stiffener with initial deflection δ_0 (at midspan) is subjected to a compressive (axial) force F_x, this initial deflection is magnified such that the total deflection δ (at midspan) becomes

$$\delta = \delta_0 \cdot \frac{F_{x,cr}}{F_{x,cr} - F_x} \tag{5.23}$$

where

$$F_{x,cr} = \frac{\pi^2}{a^2} \cdot E \cdot I_{zz} \tag{5.24}$$

is the critical buckling force and $F_x = \mu \cdot \sigma_x \cdot A_x$, where A_x is the cross-sectional area of the plate-stiffener combination. Moreover, the quantity I_{zz} is the moment of inertia of the stiffener with attached plating, the extent of which is equal to the lesser of the effective *width* considering plate buckling (i.e. $\kappa_x \cdot b$) and the effective *breadth* considering shear lag effects under bending (i.e. $\chi \cdot b$, where χ is the effective breadth coefficient)[4]. Accordingly, the bending moment $M_{zz,0}(x)$ caused by the compressive force F_x is

$$M_{zz,0}(x) = \delta(x) \cdot F_x \tag{5.25}$$

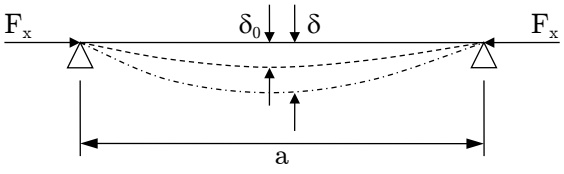

Figure 5.13.: Magnification of initial deflection.

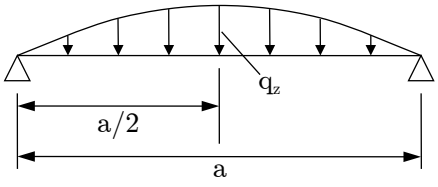

Figure 5.14.: Equivalent sinusoidal line load.

According to DIN 18800, Part 2, Section 2, this bending moment may be alternatively defined in terms of an equivalent sinusoidal lateral line load

[4] Admittedly, as noted by Faulkner [29], "in many practical structures the two effects occur together and are not separable or additive".

$$q_z(x) = q_z \cdot \sin\left(\frac{\pi \cdot x}{a}\right) \tag{5.26}$$

as shown in Figure 5.14. Through integration, this results in the following bending moment at midspan

$$M_{zz,0} = \delta \cdot F_x = \frac{q_z \cdot a^2}{\pi^2} \tag{5.27}$$

By substituting the total deflection δ defined by Equation (5.23) into Equation (5.27), the line load at midspan q_z becomes

$$q_z = \delta \cdot F_x \cdot \frac{\pi^2}{a^2} = F_{x,cr} \cdot \frac{\frac{\pi^2}{a^2} \cdot F_x \cdot \delta_0}{F_{x,cr} - F_x} \tag{5.28}$$

Accordingly, the bending moment of the stiffener (at midspan) becomes

$$M_{zz,0} = \frac{q_z \cdot a^2}{\pi^2} = F_{x,cr} \cdot \frac{\frac{\pi^2}{a^2} \cdot F_x \cdot \delta_0}{\frac{\pi^2}{a^2} \cdot F_{x,cr} - \frac{\pi^2}{a^2} \cdot F_x} = F_{x,cr} \cdot \frac{p_{z,x} \cdot \delta_0}{c_f - p_{z,x}} \tag{5.29}$$

where $p_{z,x} = \frac{\pi^2}{a^2} \cdot F_x$ is the equivalent lateral pressure caused by the longitudinal force F_x and $c_f = \frac{\pi^2}{a^2} \cdot F_{x,cr}$ is the elastic capacity of the stiffener.

Analogously, equations for equivalent lateral pressures can also be derived for transverse stresses $\mu \cdot \sigma_y$, i.e. $p_{z,y}$, and shear stresses $\mu \cdot \tau_{xy}$, i.e. $p_{z,\tau}$. In case of the latter, shear stresses are transformed into principal stresses and the supporting effect of the tension stresses are neglected. Accordingly, the *total* equivalent lateral pressure can be expressed as

$$p_z = p_{z,x} + p_{z,y} + p_{z,\tau} \tag{5.30}$$

such that the *total* bending moment of the stiffener at midspan due to in-plane forces becomes

$$M_{zz,0} = F_{x,cr} \cdot \frac{p_z \cdot \delta_0}{c_f - p_z} \tag{5.31}$$

Upon inspection of Equation (5.31), it can be seen that the quantity $\frac{p_z}{c_f - p_z}$ is a deflection magnification factor. Accordingly, once the total equivalent lateral pressure p_z equals the elastic capacity of the stiffener c_f, the elastic deflection of the stiffener becomes infinite, i.e. overall panel buckling. Accordingly, the capacity of the panel corresponding to collapse mode 1 (overall panel buckling) may be expressed as

$$p_z / c_f = 1 \tag{5.32}$$

Regarding the second mode of collapse (lateral buckling), the bending moment of the stiffener at midspan due to in-plane stresses $M_{zz,0}$ is combined with the bending moment of the stiffener at midspan due to the lateral load $M_{zz,1}$ in order to obtain the total bending stress in the stiffener

$$\sigma_b = \frac{M_{zz,0} + M_{zz,1}}{Z} \tag{5.33}$$

where Z is the section modulus of the stiffener with attached plating as defined above[5]. This bending stress is in turn combined with the longitudinal stress σ'_x (corrected to take into account the reduced effective width of plating due to buckling) and compared to the yield stress of the plate, resulting in the following capacity equation for lateral stiffener buckling (collapse mode 2)

$$\frac{\sigma'_x + \sigma_b}{\sigma_Y} = 1 \tag{5.34}$$

or

$$\frac{\mu \cdot \sigma'_x + \sigma_b}{\sigma_Y} = 1 \tag{5.35}$$

when the stress multiplier factor at failure μ is included. Here the quantity σ_b implicitly contains the effects of μ applied to each single component of in-plane stress.

Torsional, web and flange buckling

In CSR BC & OT, slenderness requirements (including tripping brackets) are used to control torsional stiffener buckling, as well as buckling of the stiffener web and flange. However, in case of bulb, angle and tee profiles under a compressive longitudinal load, a warping stress σ_w is also included in the lateral buckling check such that Equation (5.35) becomes

$$\frac{\mu \cdot \sigma'_x + \sigma_b + \sigma_w}{\sigma_Y} = 1 \tag{5.36}$$

In case of flat bars, the effective web thickness is decreased to account for local lateral deformation.

5.2. Examples of design application

As noted above, proof that a stiffened panel has sufficient capacity is typically separated into distinct proofs for single plate fields and for stiffeners. In the proof of single plates, the plate is idealised as rectangular with the effects of boundary conditions and applied loads reflected in the plate reduction factors. In CSR BC & OT these conditions and loads are assumed to be perfect where rotational, out-of-plane and in-plane restraints along the edges of the plate are assumed to be either infinite or zero and applied loads are assumed to be linearly distributed over the edges of the plate. However, even in finite element analyses, these assumptions are never completely correct when a stiffened panel rather than a single plate is modelled.

Accordingly, to give some indication of the error inherent in an approach with the above-mentioned assumptions, this section includes two sample calculations where the plate capacity according to the procedure prescribed in CSR BC & OT is compared to that of a stiffened panel based on finite element analyses. The first capacity calculation is based on stiffened bottom plating under biaxial compression together with lateral pressure

[5] The section modulus calculated at the stiffener flange is used to check for *stiffener-induced* failure and the section modulus calculated at the attached plating is used to check for *plate-induced* failure.

(i.e. typical double bottom loading). The second calculation is based on stiffened side shell plating under combined axial and shear stresses together with lateral pressure (typical loading at/near the lower flange of the hull girder). In both calculations a panel with five stiffeners is modelled with scantlings as shown in Table 5.1. These scantlings are from a 315 metre double hull VLCC (very large crude carrier) as published in the report of the Special Task Committee VI.2 of ISSC 2000 [74][6].

frame spacing, b [mm]	830
frame span, a [mm]	4980
nominal plate thickness, t [mm]	20.5
minimum yield stress, σ_Y [N/mm^2]	315
stiffener	T 550 x 12 + 150 x 25

Table 5.1.: Scantlings of double hull VLCC stiffened panel.

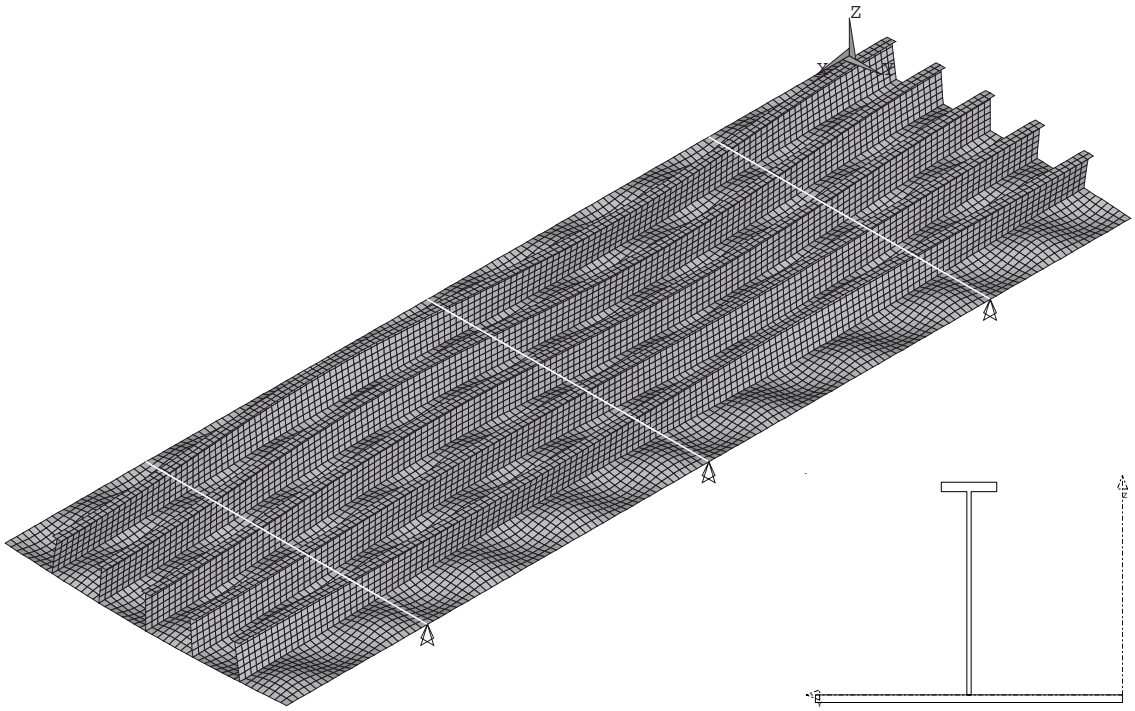

Figure 5.15.: Finite element model and section of stiffened panel in double hull VLCC.

Therefore, the plating in this model has an aspect ratio $\alpha = 4980/830 = 6.0$ and a slenderness parameter $\beta = 830/20.5 \cdot \sqrt{315/206000} = 1.58$. In both calculations, the plate is pre-loaded with a (constant) lateral pressure before the in-plane loads are applied. Because a VLCC is generally able to pass through the Suez Canal, a static pressure head corresponding to a draught of 20 metres is used plus a nominal dynamic (head sea) com-

[6] The original frame span of $a = 4950$mm was omitted from the report of the Special Task Committee, but obtained previously from its Chairman (T. Yao, personal communication, 20 January 2003). However, a span of $a = 4980$mm was used in the present calculations to round off the aspect ratio of the plate to $\alpha = 4980/830 = 6.0$.

ponent of 10%, i.e. $p = (20 + 2) \cdot 9.807 = 215.8\ kN/m^2$. The analyses are carried out in accordance with the procedure developed and agreed within the IACS harmonisation project team HPT02 for performing non-linear finite element analyses of stiffened panels [75]. In accordance with this procedure, a 3-span finite element model ($\frac{1}{2} + 1 + 1 + \frac{1}{2}$) is used as shown in Figure 5.15 (with initial deflections magnified 20 times).

5.2.1. Bottom shell plating (σ_x-σ_y)

In Figure 5.16 separate capacity curves for plating and stiffeners are compared to finite element results for the panel under biaxial compression combined with lateral pressure. Here the capacity curve for stiffeners is based on the proof of lateral buckling strength included in CSR BC & OT. Normally the capacity of the stiffeners is critical when the longitudinal stress R_x is dominant, but this is not the case for the panel described in Table 5.1, which is indicative of relatively strong stiffeners (i.e. compared to the strength of plating). In terms of the two plate capacity curves, these have been developed using the proof of plate capacity shown in Box 5.1 ($\mu = 1$) with the plate reduction factors κ_x and κ_y obtained from finite element analyses of a single plate. However, of the two plate capacity curves, one curve is based on the stresses R_x and R_y applied directly to the panel (applied stresses), while the other is based on the resulting stresses acting on the plating at mid-span as determined by elastic finite element analyses (reference stresses). The plating capacity curves calculated on the basis of applied stresses are generally non-conservative as they do not account for the redistribution of stresses which take place within the stiffened panel, the most important of which are the additional bending stresses in the attached plating due to the deflection of the stiffeners under a lateral load (stress redistribution may take place for other reasons, e.g. due to stiffeners which have a higher/lower in-plane stiffness compared to the plating).

For example, the collapse stress of the plating under an applied longitudinal stress (i.e. $R_y = 0$) is $R_{x,ult} = 0.864$. However, this is the collapse stress when the lateral and in-plane loads are applied to the plate in isolation. When the lateral and in-plane loads are instead applied to a stiffened panel, the former induces mid-span bending stresses of approximately $R_x = 0.073$ in the plating such that collapse stress of the plate under an applied longitudinal stress is $R_{x,ult} = 0.864 - 0.073 = 0.791$, i.e. panel collapse due to plate failure. As can be seen in Figure 5.16, this collapse stress agrees well with the result of finite element analysis for the panel, i.e. for $R_y = 0$. Moreover, the ultimate transverse stress $R_{y,ult} = 0.369$ of the plate also agrees well with the result of finite element analyses for the panel, i.e. for $R_x = 0$. As the relative magnitude of transverse stresses increases, the differences between the plate capacity curves based on applied and reference stresses are reduced, eventually converging under a purely transverse stress. As can be seen in Figure 5.16, although the endpoints of the capacity curve based on (plate) reference stresses agree well with finite element analyses of the panel, its shape leads to some conservatism within the range of biaxial compressive stresses $0.2 < c = \sigma_y/\sigma_x < 0.7$. In other words, the capacity curve of the panel is more rectangular than that for the plating, suggesting that the presence of stiffeners may not be fully accounted for in a proof where the strength of plates and stiffeners are decoupled. However, given that the balance of strength between plating and stiffener is biased towards the latter (i.e. for the panel in question), further analyses are required before any general conclusions can be reached.

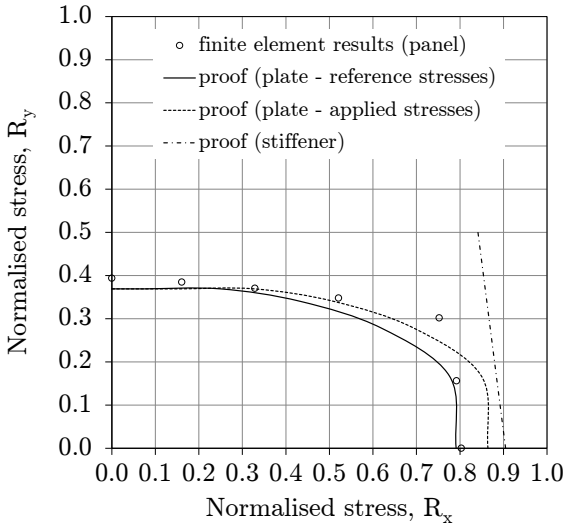

Figure 5.16.: Capacity of bottom shell panel.

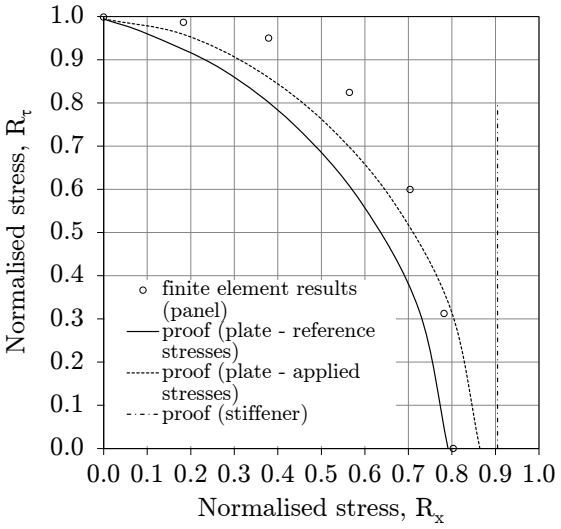

Figure 5.17.: Capacity of side shell panel.

5.2.2. Side shell plating (σ_x-τ_{xy})

In Figure 5.17 separate capacity curves for plating and stiffeners are compared to finite element results for the panel under longitudinal compression in the presence of shear (again combined with lateral pressure). As in §5.2.1 the capacity curve for stiffeners is based on the proof of lateral buckling strength included in CSR BC & OT and the two plate capacity curves have been developed using the proof of plate capacity shown in Box 5.1 ($\mu = 1$) with the plate reduction factors κ_x and κ_τ obtained from finite element analyses of a single plate. Once again, only the capacity of the plating is critical. As in the case of biaxial compression, the plating capacity curves calculated on the basis of applied stresses are generally non-conservative as they do not account for the additional mid-span bending stresses in the attached plating due to the deflection of the stiffeners under a lateral load.

As calculated previously, the collapse stress of the *unstiffened* plating (*with* infinite out-of-plane support) under an applied longitudinal stress (i.e. $R_\tau = 0$) is $R_{x,ult} = 0.864$. The collapse stress of the *stiffened* plate (*without* infinite out-of-plane support) under an applied longitudinal stress is $R_{x,ult} = 0.864 - 0.073 = 0.791$, which again agrees well with the result of finite element analysis for the panel, i.e. in the absence of shear. Moreover, the ultimate shear stress $R_{\tau,ult} = 0.994$ of the plate also agrees well with the result of finite element analyses for the panel, i.e. for $R_x = 0$. As the relative magnitude of shear stresses increases, the differences between the plate capacity curves based on applied and reference stresses are again reduced, eventually converging under a pure shear stress. As can be seen in Figure 5.17, the endpoints of the capacity curve based on (plate) reference stresses agree well with finite element analyses of the panel, but its shape again leads to some conservatism in the range of shear stresses $0.5 < R_\tau < 0.9$. In other words, the capacity curve of the panel is again more rectangular than that for the plating, suggesting that the proof of panel strength may not be fully accounting for the interaction between plating and stiffeners. However, because the stiffeners of the panel in question are relatively strong compared to the plating, once again no overall conclusions can be drawn in the absence of further analyses.

6. Conclusions

In this chapter the main results, conclusions and contributions to knowledge are summarised. A direction for future research is also proposed. In §6.1 results directly related to the problem stated in Chapter 4 are outlined and conclusions drawn. In §6.2 contributions to knowledge made in the course of solving the stated problem are delineated. Finally, regarding introduction of the new proof of plate capacity into the rules of classification societies, future research related to the capacity of unstiffened plates and stiffened panels is proposed in §6.3.

6.1. Summary of results and conclusions

As noted in Chapter 1, a proof of plate capacity under combined in-plane loads is needed with which to reliably and efficiently design ship plating, i.e. so that the demands on structure are met over the service life of a ship without incurring a needless weight penalty. In quantitative terms, this proof needs to be (1) precise, (2) accurate and (3) robust. In qualitative terms, this proof needs to be (1) concise, (2) physically-based and (3) directly solvable. In Chapter 3 existing proofs were described and subsequently evaluated against quantitative and qualitative acceptance criteria delineated in Chapter 4. In terms of the latter, it may be *concluded* that several of the existing proofs are deemed to be concise, physically-based and directly solvable as summarised in Table 6.1.

Criteria	Paik	Ueda et al.	CN 30.1	DIN 4114	PULS	DIN 18800	Prov. CSR BC & OT
Concise	✓	✓	✓	✓	✗	✓	✓
Physically-based	✓	✓	✓	✓	✓	✓	✓
Directly solvable	✓	✗	✓	✓	✗	✗	✓

Table 6.1.: Summary of qualitative results (existing proofs).

In terms of quantitative criteria, results of plate capacities obtained with each proof were compared against results obtained from an extensive series of numerical studies based on the finite element method covering all load combinations and plating configurations relevant for the shipbuilding industry. As summarised in Table 6.2 and Table 6.3, respectively, it may be *concluded* from these comparisons that none of the existing proofs satisfy all quantitative acceptance criteria in either the design space or subspace.

Because no existing proof was found to satisfy all quantitative and qualitative acceptance criteria, a *hypothetical* proof of plate capacity under combined in-plane loads was postulated which well reflected the mechanics of plating collapse described in Chapter 2 as well as the strengths of existing proofs investigated in Chapter 3. In order to satisfy qualitative acceptance criteria, this proof was based on a generalised form of the von Mises equation

KPI	Criteria	Paik	Ueda et al.	CN 30.1	DIN 4114	PULS	DIN 18800	Prov. CSR BC & OT
1	$S_r/n_s \leq 0.001$	0.011	0.018	0.032	0.039	0.004	0.018	0.012
2	$0.97 \leq m_{lsr} \leq 1.00$	0.91	1.11	0.82	0.84	1.04	0.87	0.94
3	$R_D{}^2 \geq 0.95$	0.72	0.62	0.63	0.63	0.92	0.73	0.68
4	$m_{95} \leq 1.05$	1.18	1.61	1.08	1.10	1.20	1.14	1.26
5	$m_5 \geq 0.87$	0.73	1.00	0.52	0.36	0.96	0.67	0.73

Table 6.2.: Summary of quantitative results for existing proofs (design space).

KPI	Criteria	Paik	Ueda et al.	CN 30.1	DIN 4114	PULS	DIN 18800	Prov. CSR BC & OT
1	$S_r/n_s \leq 0.001$	0.001	0.038	0.005	0.020	0.004	0.005	0.003
2	$0.97 \leq m_{lsr} \leq 1.00$	1.03	1.35	0.88	0.78	1.11	0.93	1.08
3	$R_D{}^2 \geq 0.95$	0.95	0.57	0.85	0.69	0.94	0.80	0.95
4	$m_{95} \leq 1.05$	1.13	1.91	1.10	1.03	1.21	1.13	1.17
5	$m_5 \geq 0.87$	0.95	1.18	0.75	0.45	1.00	0.75	0.97

Table 6.3.: Summary of quantitative results for existing proofs (design subspace).

$$\left(\frac{R_x}{\kappa_x}\right)^{e_0} + \left(\frac{R_y}{\kappa_y}\right)^{e_0} - B \cdot \left(\frac{R_x}{\kappa_x}\right)^{e_0/2} \cdot \left(\frac{R_y}{\kappa_y}\right)^{e_0/2} + \left(\frac{R_\tau}{\kappa_\tau}\right)^{e_0} = 1.0 \tag{6.1}$$

where the exponent e_0 and interaction coefficient B were hypothesised on the basis of observations made in the investigation of plating collapse mechanisms. Here the influence of plate slenderness on the capacity of plates under biaxial compression as well as the behaviour of plates under secondary tensile loads were particularly important. As shown in Table 6.4, it may be *concluded* that only some slight deficiencies in precision prevent the hypothetical proof from satisfying all quantitative acceptance criteria in both the design space and subspace. It is perhaps worth reiterating that this proof is based solely on the mechanics of plating collapse presented in Chapter 2, i.e. without any numerically-based definitions of the exponent e_0 and interaction coefficient B.

KPI		Target	Design space	Design subspace	Criteria
1	S_r/n_s	0.000	0.002	0.001	$S_r/n_s \leq 0.001$
2	m_{lsr}	1.00	0.99	0.97	$0.97 \leq m_{lsr} \leq 1.00$
3	$R_D{}^2$	1.00	0.95	0.94	$R_D{}^2 \geq 0.95$
4	m_{95}	1.00	1.09	1.09	$m_{95} \leq 1.05$
5	m_5	1.00	0.80	0.84	$m_5 \geq 0.87$

Table 6.4.: Key performance indicators for hypothetical proof.

Nevertheless, in order to obtain more precise results, the exponent e_0 and interaction coefficient B were subsequently redefined on the basis of 399 additional finite element analyses to reflect more closely the influences of aspect ratio α and slenderness parameter β on the capacity of plates in Quadrant 1 (also in the presence of shear). The resulting proof is shown in Box 6.1 and satisfies all quantitative acceptance criteria in both the design space and subspace as shown in Table 6.5. Having fulfilled all quantitative and qualitative acceptance criteria for a proof of plate capacity under combined in-plane

loads, it may therefore be *concluded* that this proof solves the problem stated in Chapter 4.

The capacity of plates under combined in-plane loads is defined by the following equation

$$\left(\frac{\mu \cdot R_x}{\kappa_x}\right)^{e_0} + \left(\frac{\mu \cdot R_y}{\kappa_y}\right)^{e_0} - B \cdot \left(\frac{\mu \cdot R_x}{\kappa_x}\right)^{e_0/2} \cdot \left(\frac{\mu \cdot R_y}{\kappa_y}\right)^{e_0/2} + \left(\frac{\mu \cdot R_\tau}{\kappa_\tau}\right)^{e_0} = 1.0$$

where $e_0 = 2 \,/\, \beta^{0.25} \leqslant 2$ $\quad B = 2 \,/\, (2 \cdot \beta)^{0.7/\sqrt{\alpha}} - 1 \leqslant 1$ $\quad$ for $R_x \geqslant 0$ and $R_y \geqslant 0$

$e_0 = 2$ $\quad B = \kappa_x = \kappa_y = \kappa_\tau = 1$ $\quad$ for $R_x < 0$ or $R_y < 0$

and where the following stress limits are to be observed

$$\left(\frac{\mu \cdot R_x}{\kappa_x}\right)^{2/\beta^{0.25}} + \left(\frac{\mu \cdot R_\tau}{\kappa_\tau}\right)^{2/\beta^{0.25}} \leqslant 1.0 \quad \text{for } R_x \geqslant 0 \qquad \text{(i)}$$

$$\left(\frac{\mu \cdot R_y}{\kappa_y}\right)^{2/\beta^{0.25}} + \left(\frac{\mu \cdot R_\tau}{\kappa_\tau}\right)^{2/\beta^{0.25}} \leqslant 1.0 \quad \text{for } R_y \geqslant 0 \qquad \text{(ii)}$$

$$\left(\frac{\mu \cdot R_\tau}{\kappa_\tau}\right) \leqslant 1.0 \qquad \text{(iii)}$$

Box 6.1.: Formulation of new proof

KPI		Target	Design space	Design subspace	Criteria
1	S_r/n_s	0.000	0.001	0.001	$S_r/n_s \leq 0.001$
2	m_{lsr}	1.00	0.99	0.97	$0.97 \leq m_{lsr} \leq 1.00$
3	$R_D{}^2$	1.00	0.97	0.98	$R_D{}^2 \geq 0.95$
4	m_{95}	1.00	1.04	1.02	$m_{95} \leq 1.05$
5	m_5	1.00	0.87	0.90	$m_5 \geq 0.87$

Table 6.5.: Key performance indicators (new proof).

For this reason, the proof of plate capacity included in the newly harmonised *IACS Common Structural Rules for Bulk Carriers and Oil Tankers* has been based on the proof shown in Box 6.1. However, when used together with newly harmonised load models, the interaction coefficient B was recalibrated so that the scantlings of ships from successful in-service experience remained largely unchanged (i.e. under biaxial compression). The quantitative evaluation of this recalibrated proof is shown in Table 6.6. Here it may be *concluded* that the proof included in the newly harmonised *IACS Common Structural Rules for Bulk Carriers and Oil Tankers*, although not fulfilling all of the quantitative acceptance criteria, still performs far better than any of the existing proofs presented in Chapter 3.

Finally, the design application of the newly developed proof as used in the *IACS Common Structural Rules for Bulk Carriers and Oil Tankers* was subsequently presented. Here it was shown that the effects on plating capacity of other boundary conditions (i.e. free edges and edge pull-in), additional load components (i.e. in-plane bending and lateral pressure) and more realistic initial imperfections (i.e. residual deflections and stresses based on measurements) can be adequately captured in the plate reduction factors κ_x,

KPI		Target	Design space	Design subspace	Criteria
1	S_r/n_s	0.000	0.001	0.001	$S_r/n_s \leq 0.001$
2	m_{lsr}	1.00	1.00	1.03	$0.97 \leq m_{lsr} \leq 1.00$
3	$R_D{}^2$	1.00	0.96	0.93	$R_D{}^2 \geq 0.95$
4	m_{95}	1.00	1.10	1.16	$m_{95} \leq 1.05$
5	m_5	1.00	0.87	0.91	$m_5 \geq 0.87$

Table 6.6.: Key performance indicators (CSR BC & OT proof).

κ_y and κ_τ, i.e. the *endpoints* of capacity curves. On the basis of these results, it may be *concluded* that the newly developed proof remains valid in case of boundary conditions, loads and initial imperfections relevant for the shipbuilding industry, i.e. these variations have little effect on the *shape* of capacity curves. Moreover, on the basis of numerical calculations performed for the bottom and side shell structures of a double hull VLCC, it may be *concluded* that the proof of stiffened panel capacity can be made using decoupled proofs of plate capacity and stiffener capacity (albeit somewhat conservatively in case of the panel and load combinations analysed in §5.2).

6.2. Summary of contributions

An extensive series of numerical studies based on the finite element method have been performed covering all load combinations and plating configurations relevant for the shipbuilding industry. Analyses of the results have led to the following contributions to knowledge:

1. the mechanics of plating collapse under single and combined in-plane loads have been thoroughly investigated resulting in an improved understanding of collapse mechanisms as well as stress redistributions in the post-buckling, post-yield and post-collapse phases of response. Moreover, because the ultimate strengths of plating under single stress components define the reference stresses used in most proofs of plate capacity, formulations found in literature and the shipbuilding industry for defining the characteristic strength of plating under single stress components have been thoroughly discussed and compared to numerical results.

2. in the presence of primary tensile stresses, it has been shown numerically that gross yielding occurs in plates even under the application of a secondary compressive stress. This contradicts closed-form proofs used heretofore in the shipbuilding industry which assume that plate buckling ensues under any level of compressive stress. Moreover, it has been shown numerically that the ultimate compressive strength of plating is often higher in the presence of a secondary tensile stress. This is contrary to results obtained with closed-form proofs used heretofore in the shipbuilding industry which generally show a steadily decreasing capacity of plating with increasing tensile stresses.

3. in case of biaxial compressive stresses, it has been shown numerically that the shape of the interaction curve is highly dependent on the slenderness of the plating, ap-

proaching a linear elastic curve for slender plating and a quadratic yield ellipse for sturdy plating. Moreover, it has also been shown that the shape of the interaction curve is dependent on the aspect ratio of the plate, with the capacity of plating generally increasing with decreasing aspect ratio. In this regard, equations have been developed for the exponent e_0 and interaction coefficient B of a generalised form of the von Mises equation with which the buckling capacity of plating can be determined under biaxial compression.

4. for all load combinations and plating configurations relevant for the shipbuilding industry, a proof of plane plate capacity has been developed and shown to be more precise, accurate and robust than any existing proof. Moreover, the proof is concise, based on the mechanics of plating collapse and solvable without the need for iterations.

5. because the newly developed proof of plate capacity is based on numerical studies of simply-supported plates, uniform in-plane loads and idealised initial imperfections, the validity of its application in case of other boundary conditions (i.e. free edges and edge pull-in), additional load components (i.e. in-plane bending and lateral pressure) and more realistic initial imperfections (i.e. residual deflections and stresses based on measurements) has been demonstrated. In this regard, it has been shown that these effects can be adequately captured in the plate reduction factors κ_x, κ_y and κ_τ, thereby validating use of the newly developed proof in case of those boundary conditions, loads and initial imperfections relevant for the shipbuilding industry. Moreover, the marginal effect of out-of-plane loads (i.e. lateral pressure) on the in-plane strength of plating has been investigated.

6. on the basis of numerical calculations performed for the bottom and side shell structures of a double hull VLCC, it has been shown that the proof of stiffened panel capacity can be made using decoupled proofs of plate capacity and stiffener capacity.

7. regarding curved plate capacity under combined in-plane and lateral loads, a revision to the DIN 18800 proof (already used extensively in the shipbuilding industry) has been explained and evaluated. The revised proof of curved plate capacity is seen to be more accurate and precise than the DIN 18800 proof, particularly in case of combined axial and hoop stresses.

In terms of practical contributions to the shipbuilding industry, the proofs of plane plate capacity and curved plate capacity developed/presented in the present work have both been included in the newly harmonised *IACS Common Structural Rules for Bulk Carriers and Oil Tankers*, the new *IACS Longitudinal Strength Standard for Container Ships* (UR S11A) as well as the new *DNVGL Rules for Classification* which are applicable to all ship types. In future, more extensive use of the proofs can be reasonably expected as classification societies seek to harmonise their own buckling strength rules with those included in the aforementioned IACS rules and requirements (as noted in §3.3, more than 90% of the world's cargo carrying tonnage is covered by IACS rules and requirements for the classification of seagoing ships).

6.3. Future research

In terms of future research, two suggestions are offered regarding introduction of the new proof of plate capacity into the rules of classification societies:

1. As can be seen in Box 6.1, $e_0 = 2$ for $\beta \leqslant 1$ and $B = 1$ for $\beta \leqslant 0.5$ in case of square plates under biaxial compression. Accordingly, on the basis of the numerical calibration, the design capacity equation transitions into the von Mises equation between $0.5 \leqslant \beta \leqslant 1.0$ (provided $\kappa_x = \kappa_y = \kappa_\tau = 1$). This agrees well, for instance, with Hughes [9] whose numerical solution for square plates under biaxial compression shows that gross yielding takes place for plates of slenderness $\beta \leqslant 0.67$ (see Equations (2.43) and (2.44)). As shown in Figure 2.9, this transition range also agrees well with that for square plates under uniaxial compression (according to finite element analyses). However, in the rules of classification societies, it is intended that the plate reduction factors (κ_x, κ_y and κ_τ) be obtained using the DIN 18800 formulae. Although it was shown in Chapter 2 that these formulae agree reasonably well with the finite element analyses upon which the derivation of the exponent e_0 and interaction coefficient B are based, the transitions to gross yielding differ slightly. For instance, it can be seen in Figure 2.9, that the DIN 18800 formulae predict yielding behaviour under uniaxial compression to take place for square plates of slenderness $\beta \leqslant 1.58$. Accordingly, using the new proof of plate capacity together with the DIN 18800 formulae for plate reduction factors (in general) could benefit from a parametric study to evaluate the significance of any anomalies which may arise (e.g. if $\kappa_x = \kappa_y = \kappa_\tau = 1$, but $e_0 \neq 2$ and/or $B \neq 1$, due to slight discrepancies concerning the onset of yielding behaviour).

2. As discussed in §5.1, proof that a stiffened panel has sufficient capacity is typically separated into distinct proofs for single plate fields and stiffeners with the capacity of the panel defined by the lesser of the two. However, as evidenced by the conservative results presented in §5.2 for some combinations of stresses applied to the panel of a double hull VLCC, there is most likely some interaction between plating and stiffeners which is not fully accounted for in the current procedure for decoupling of capacity proofs. Moreover, the ratios of load carried by plating and stiffeners are themselves a function of relative in-plane stiffness, which in turn depends on scantlings, initial imperfections and load types (e.g. the in-plane stiffness of a stiffener is a function of lateral load). Accordingly, it is suggested that the current method of decoupling plate and stiffener strength used by classification societies could benefit from future research. When necessary, better procedures to account for the interaction of plating, stiffeners and loads should be developed.

7. References

[1] Mitsui O.S.K. Lines Press Release. Incident with Containership MOL Comfort. 17 June 2013, Tokyo, Japan.

[2] Mitsui O.S.K. Lines Press Release. Incident Involving the Containership MOL Comfort - Urgent Update No. 12. 27 June 2013, Tokyo, Japan.

[3] Mitsui O.S.K. Lines Press Release. Incident Involving the Containership MOL Comfort - Update No. 19. 06 July 2013, Tokyo, Japan.

[4] Mitsui O.S.K. Lines Press Release. Incident Involving the Containership MOL Comfort - Update No. 25. 11 July 2013, Tokyo, Japan.

[5] M. Mitev."MOL Comfort demands as much as $500m against Mitsubishi". Vessel Finder Maritime News, 15 December 2014.

[6] Committee on Large Container Ship Safety (Japan's Ministry of Land, Infrastructure, Transport and Tourism). Interim Report of Committee on Large Container Ship Safety. 2013, Tokyo, Japan.

[7] The Investigative Panel on Large Container Ship Safety (ClassNK). Investigation Report on Structural Safety of Large Container Ships. 2014, Tokyo, Japan.

[8] International Association of Classification Societies. Requirements concerning strength of ships. Unified Requirement S11A; Longitudinal strength standard for container ships, 2015.

[9] O.F. Hughes. *Ship Structural Design: A Rationally-Based, Computer-Aided Optimization Approach*. Society of Naval Architects and Marine Engineers, Jersey City, U.S.A., 1988.

[10] E.D. Egge. Untersuchungen zum Festigkeitsverhalten von ebenen versteiften Plattenfeldern mit zunehmender Auslastung der Struktur (in German). Technical report, Germanischer Lloyd, Hamburg, Germany, 1995. Abschlußbericht zum Vorhaben MTK 0443 A.

[11] D. Faulkner. Compression tests on welded eccentrically stiffened plate panels (paper 25, 581-617). In P.J. Dowling J.E. Harding and P.A. Frieze, editors, *Steel Plated Structures: An International Symposium*, Crosby Lockwood Staples, London, England, 1977.

[12] L. Schuman and G. Back. Strength of rectangular flat plates under edge compression. Technical report, National Advisory Committee for Aeronautics, Washington, U.S.A., 1930. Report No. 356.

[13] T. von Kármán, E.E. Sechler and L.H. Donnell. The strength of thin plates in compression. *ASME Transactions*, 54:53, 1932.

[14] S. Chatterjee and P.J. Dowling. The design of box girder compression flanges (paper 8, 196-228). In P.J. Dowling J.E. Harding and P.A. Frieze, editors, *Steel Plated Structures: An International Symposium*, Crosby Lockwood Staples, London, England, 1977.

[15] E.E. Sechler. The ultimate compressive strength of thin sheet metal panels. In partial fulfillment of the requirements for the degree of Doctor of Philosophy. California Institute of Technology, Pasadena, U.S.A., 1934.

[16] S. Timoshenko. *Theory of Elastic Stability.* McGraw-Hill Book Company, New York, U.S.A., 1936.

[17] G. Winter. Strength of thin steel compression flanges. *ASCE Transactions*, 112:527, 1947.

[18] American Iron and Steel Institute. Specification for the design of light gage steel structural members, New York, U.S.A., 1946.

[19] Eurocode 3; Design of steel structures. Part 1-5: Plated structural elements. EN 1993-1-5, 2006.

[20] International Association of Classification Societies. Requirements concerning strength of ships. Unified Requirement S11; Longitudinal strength standard (Rev. 7), 2010.

[21] F. Bleich. *Buckling Strength of Metal Structures.* McGraw-Hill Book Company, New York, U.S.A., 1952.

[22] J.M. Frankland. The strength of ship plating under edge compression. Technical report, United States Experimental Model Basin, Washington, U.S.A., 1940. Report No. 469.

[23] International Association of Classification Societies. Common Structural Rules for Bulk Carriers and Oil Tankers (Rev. 1), 2014.

[24] International Association of Classification Societies. Requirements concerning strength of ships. Unified Requirement S18; Evaluation of scantlings of corrugated transverse watertight bulkheads in non-CSR bulk carriers considering hold flooding (Rev. 9), 2014.

[25] International Association of Classification Societies. Requirements concerning strength of ships. Unified Requirement S19; Evaluation of scantlings of the transverse watertight corrugated bulkhead between cargo holds nos. 1 and 2, with cargo hold no. 1 flooded, for existing bulk carriers (Rev. 5), 2004.

[26] Deutsches Institut für Normung e.V. DIN 18800; Structural steelwork. Part 3: Analysis of safety against buckling of plates. Beuth Verlag, Berlin, Germany, 1990.

[27] J. Scheer U. Peil and G. Fuchs. Auswertung von internationalen Veröffentlichungen, Versuchsberichten, Kommissionspapieren u.ä. auf dem Gebiet des Beulens von Platten aus Stahl (in German). Technical report, Institutes für Stahlbau, Technische Universität Braunschweig, Braunschweig, Germany, 1987. Report No. 6095.

[28] J.B. Caldwell. Ultimate longitudinal strength (written discussion). *RINA Transactions*, 107:411, 1965.

[29] D. Faulkner. A review of effective plating for use in the analysis of stiffened plating in bending and compression. *Journal of Ship Research*, 19(1):1–17, March 1975.

[30] Germanischer Lloyd GmbH. Rules for Classification and Construction. I - Ship Technology; Part 1 - Seagoing Ships; Chapter 1 - Hull Structures; Section 3 - Design Principles, 1997.

[31] International Association of Classification Societies. Common Structural Rules for Bulk Carriers, 2006.

[32] International Association of Classification Societies. Common Structural Rules for Double Hull Oil Tankers, 2006.

[33] DNV GL. Class Guideline - Buckling, DNVGL-CG-0128, 2015.

[34] S. Valsgård. Numerical design prediction of the capcity of plates in biaxial in-plane compression. *Computers & Structures*, 12:729–739, 1980.

[35] J.K. Paik and A.K. Thayamballi. *Ultimate Limit State Design of Steel-Plated Structures*. John Wiley and Sons Ltd., Chicester, England, 2003.

[36] K.C. Rockey H.R. Evans and D.M. Porter. Ultimate load capacity of stiffened webs subjected to shear and bending (Paper 4, Session B, 45-61). In *Proceedings of an international conference on steel box girder bridges*, Institution of Civil Engineers, London, England, 1973.

[37] H. Wagner. Flat sheet metal girders with very thin metal web. Technical report, National Advisory Committee for Aeronautics, Washington, U.S.A., 1931. Technical Memorandum Nos. 604/605/606.

[38] H. Wagner and W. Ballerstedt. Tension fields in originally curved, thin sheets during shearing stresses. Technical report, National Advisory Committee for Aeronautics, Washington, U.S.A., 1935. Technical Memorandum No. 774.

[39] P. Kuhn J.P. Peterson and L.R. Levin. A summary of diagonal tension, Parts I and II. Technical report, National Advisory Committee for Aeronautics, Washington, U.S.A., 1952. Technical Note Nos. 2661/2662.

[40] P. Dubas and E. Gehri. Behaviour and design of steel plated structures. Technical report, ECCS-CECM-EKS, Zürich, Switzerland, 1986. No. 44.

[41] K.C. Rockey. The design of web plates for plate and box girders - a state of the art report (paper 19, 459-485). In P.J. Dowling J.E. Harding and P.A. Frieze, editors, *Steel Plated Structures: An International Symposium*, Crosby Lockwood Staples, London, England, 1977.

[42] J.K. Paik. A new concept of the effective shear modulus for a plate buckled in shear. *Journal of Ship Research*, 39(1):70–75, 1995.

[43] J.K. Paik. Ultimate strength design equations of plates and stiffened panels under combined loads. Final Report to the American Bureau of Shipping, Ship Structural Mechanics Lab, Pusan National University, July 1999.

[44] J.K. Paik A.K. Thayamballi and B.J. Kim. Advanced ultimate strength formulations for ship plating under combined biaxial compression/tension, edge shear, and lateral pressure loads. *Marine Technology*, 38(1):9–25, 2001.

[45] S. Zhang P. Kumar and S.E. Rutherford. Ultimate shear strength of plates and stiffened panels. *Ships and Offshore Structures*, 3(2):105–112, 2008.

[46] D. Faulkner J.C. Adamchak G.J. Snyder and M.F. Vetter. Synthesis of welded grillages to withstand compression and normal loads. *Computers & Structures*, 3:221–246, 1973.

[47] Deutsches Institut für Normung e.V. DIN 18800; Structural steelwork. Part 2: Analysis of safety against buckling of linear members and frames. Beuth Verlag, Berlin, Germany, 1990.

[48] H. Becker. Feasibility study of model tests on ship hull girders. Technical report, Ship Structure Committee, Washington, U.S.A., 1969. SSC-194.

[49] H. Becker R. Goldman and J. Pazerycki. Compressive strength of ship hull girders, Part I - Unstiffened plates. Technical report, Ship Structure Committee, Washington, U.S.A., 1970. SSC-217.

[50] Det norske Veritas. Rules for the Design, Construction and Inspection of Offshore Structures. Appendix C - Steel Structures, 1977.

[51] Y. Ueda S.M.H. Rashed and J.K. Paik. Buckling and ultimate strength interaction in plates and stiffened panels under combined inplane biaxial and shearing forces. *Marine Structures*, 8:1–36, 1995.

[52] International Association of Classification Societies. Classification societies - what, how and why? London, England, 2015.

[53] Det norske Veritas. Buckling Strength Analysis. Classification Notes No. 30.1, 1987.

[54] Deutsches Institut für Normung e.V. DIN 4114; Steel structures; Stability. Beuth Verlag, Berlin, Germany, 1952.

[55] R. Szilard. *Theory and Analysis of Plates: Classical and Numerical Methods*. Prentice-Hall Inc., New Jersey, U.S.A., 1974.

[56] K. Marguerre. The apparent width of the plate in compression. Technical report, National Advisory Committee for Aeronautics, Washington, U.S.A., 1937. Report No. 833.

[57] E. Byklum and J. Amdahl. A simplified method for elastic large deflection analysis of plates and stiffened panels due to local buckling. *Thin-Walled Structures*, 40:925–953, 2002.

[58] E. Steen. Application of the perturbation method to plate buckling problems. Technical report, Mechanics Division, Department of Mathematics, University of Oslo, Oslo, Norway, 1998. Research Report in Mechanics No. 98-1.

[59] Deutsches Institut für Normung e.V. Principles for the specification of requirements relating to the safety of structures. Beuth Verlag, Berlin, Germany, 1981.

[60] J. Lindner and W. Habermann. Zur Weiterentwicklung des Beulnachweises für Platten bei mehrachsiger Beanspruchung (in German). *Stahlbau*, 57:333–339, 1988.

[61] M. Böckenhauer and H.-J. Schulte. An introduction to the new requirements of Germanischer Lloyd for proof of buckling strength. Technical report, Germanischer Lloyd, Hamburg, Germany, 1997.

[62] DNV GL. Class Guideline - Finite element analysis, DNVGL-CG-0127, 2015.

[63] C.S. Smith P.C. Davidson J.C. Chapman and P.J. Dowling. Strength and stiffness of ships' plating under in-plane compression and tension (written discussion). *RINA Transactions*, 130:277–296, 1987.

[64] International Association of Classification Societies. Recommendation No. 76; IACS Guidelines for Surveys, Assessment and Repair of Hull Structure - Bulk Carriers (Corr. 1), 2007.

[65] International Maritime Organisation. Consolidated text of the International Convention for the Safety of Life at Sea, 1974, and its Protocol of 1988: articles, annexes and certificates, London, England, 2016.

[66] T. Søreide and J. Czujko. Load carrying capacities of plates under combined lateral load and axial/biaxial compression. *The 2nd International Symposiuim on Practical Design in Shipbuilding*, pages 493–500, 1983.

[67] International Association of Classification Societies. Recommendation No. 47; Shipbuilding and Repair Quality Standard (Rev. 7), 2013.

[68] J.K. Paik and P.T. Pedersen. A simplified method for predicting ultimate compressive strength of ship panels. *International Shipbuilding Progress*, 43(434):139–157, 1996.

[69] Y. Ueda and T. Yao. The influence of complex initial deflection modes on the behaviour and ultimate strength of rectangular plates in compression. *Journal of Constructional Steel Research*, 5(4):265–302, 1985.

[70] P.A. Frieze P.J. Dowling and R.E. Hobbs. Ultimate load behaviour of plates in compression (paper 2, 24-50). In P.J. Dowling J.E. Harding and P.A. Frieze, editors, *Steel Plated Structures: An International Symposium*, Crosby Lockwood Staples, London, England, 1977.

[71] P.L. Moore. The importance of welding quality in ship construction (paper 40, 357-363). In *Analysis and design of marine structures: An international symposium.* 2nd International Conference on Marine Structures (MARSTRUCT 2009) March 16 - 18, 2009 Lisbon, Portugal.

[72] Q. Chen T.J.E. Zimmerman D.D. DeGeer and B.W. Kennedy. Strength and stability testing of stiffened plate components. Technical report, Ship Structure Committee, Washington, U.S.A., 1997. SSC-399.

[73] J. Lindner J. Sheer and H. Schmidt. *Stahlbauten - Erläuterungen zu DIN 18 800 Teil 1 bis Teil 4 (in German).* Beuth Verlag, Berlin, Germany, 1993.

[74] T. Yao O.C. Astrup P. Caridis Y.N. Chen S.-R. Cho R.S. Dow O. Niho and P. Rigo. Ultimate hull girder strength. Special Task Committee VI.2, 14th International Ship and Offshore Structurees Committee, 2-6 October 2000, Nagasaki, Japan.

[75] International Association of Classification Societies. Validation of non-linear buckling procedure. CSR BC & OT - Technical Background Report (Pt. 1, Ch 8, Sec 5), Rev. 2, 2014.

[76] International Association of Classification Societies. Curved plate capacity under combined loads. CSR BC & OT - Technical Background Report (Pt. 1, Ch 8, Sec 5), Rev. 1, 2015.

[77] ANSYS, Element Reference, Release 13.0, I. Element Library.

[78] ANSYS, Theory Reference, Release 13.0, 4. Structures with Material Nonlinearities, 4.2. Rate-Independent Plasticity.

Appendices

Appendix A. Proof of Curved Plate Capacity

Although the majority of plating used in the construction of ships is plane, curved shell plating is used extensively in the fore and aft regions of the ship as well as the bilge area within the parallel midbody. The latter is particularly relevant in terms of hull girder ultimate strength. Because the collapse behaviour of curved plating is generally different from that of plane plating (depending on the degree of curvature), an alternate proof of capacity is needed. In this regard, the purpose of this Appendix is to evaluate the DIN 18800 proof of curved plate capacity (based on a generalised form of the von Mises equation) and to show how both accuracy and precision can be improved with the addition of a non-zero interaction term. This evaluation is performed under two stress components in the first section of this appendix (§A.1) and under three stress components in the second section (§A.2). The resulting correction has been included in the newly harmonised *IACS Common Structural Rules for Bulk Carriers and Oil Tankers*, the new *IACS Longitudinal Strength Standard for Container Ships* (UR S11A)[1] as well as the new *DNV GL Rules for Classification* which are applicable to all ship types.

A.1. Evaluation of proof under two stress components

Within the shipbuilding industry, the DIN 18800 proof was initially implemented in the buckling strength rules of Germanischer Lloyd and subsequently in the *IACS Common Structural Rules for Bulk Carriers*. As mentioned above, the proof is based on a generalised form of the von Mises equation

$$\left(\frac{\sigma_x}{\sigma_{x,ult}}\right)^{e_1} + \left(\frac{\sigma_\theta}{\sigma_{\theta,ult}}\right)^{e_2} - B \cdot \left(\frac{\sigma_x}{\sigma_{x,ult}}\right) \cdot \left(\frac{\sigma_\theta}{\sigma_{\theta,ult}}\right) + \left(\frac{\tau_{x\theta}}{\tau_{x\theta,ult}}\right)^{e_3} = 1.0 \qquad \text{(A.1)}$$

where $e_1 = e_2 = 1.25$, $e_3 = 2$ and $B = 0$, i.e. no interaction term. In Equation (A.1), the axial, hoop and shear stresses are denoted by σ_x, σ_θ and $\tau_{x\theta}$, respectively. Here it should be noted that lateral pressure p on a curved plate induces hoop stresses in the plating according to the equation

$$\sigma_\theta = \frac{p \cdot R}{t} \qquad \text{(A.2)}$$

where R is the radius of curvature. As in the case of plane plates, Equation (A.1) may be expressed in terms of normalised stresses

[1] In case of (global) axial and shear stresses, the existing and revised proofs are the same. Only when hoop stresses are considered, e.g. due to local lateral loads, does the correction have any influence on calculated capacity (see S11A.6.2).

$$\left(\frac{R_x}{\kappa_x}\right)^{1.25} + \left(\frac{R_\theta}{\kappa_\theta}\right)^{1.25} + \left(\frac{R_\tau}{\kappa_\tau}\right)^{2} = 1.0 \tag{A.3}$$

where $R_x = \sigma_x/\sigma_Y$, $R_\theta = \sigma_\theta/\sigma_Y$ and $R_\tau = \sqrt{3}\cdot\tau_{x\theta}/\sigma_Y$, respectively, and κ_x, κ_θ and κ_τ are the corresponding plate reduction factors. In case of tensile stresses, the corresponding axial or hoop stress is set to zero, i.e. $R_x \geqslant 0$, $R_\theta \geqslant 0$. This is consistent with the treatment of tensile stresses in the proof of capacity for plane plates.

Plate	d/t	Axial length, d [mm]	Thickness, t [mm]	Radius, R [mm]	Yield stress, σ_Y [N/mm^2]
1	75	1200	16.0	2300	315
2	60	1200	20.0		
3	50	1200	24.0		
4	150	2400	16.0		
5	120	2400	20.0		
6	100	2400	24.0		
7	300	4800	16.0		
8	240	4800	20.0		
9	200	4800	24.0		

Table A.1.: Description of plates used in finite element analyses.

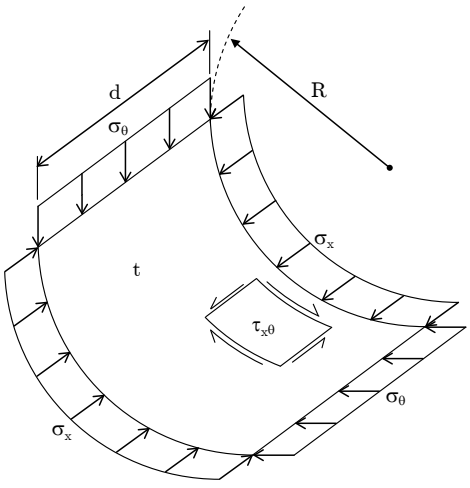

Figure A.1.: Cylinder nomenclature.

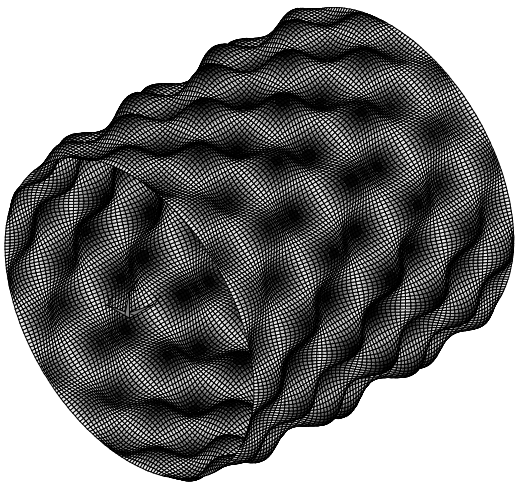

Figure A.2.: Finite element model of cylinder.

In order to evaluate the proof of curved plate capacity, a series of numerical studies based on the finite element method were performed for nine plates with a constant radius of curvature $R = 2300$ mm, but different axial length d to thickness t ratios as defined in Table A.1. The nomenclature used in this table is illustrated in Figure A.1 where curved plating is defined as plating with a radius of curvature $R \leqslant 2500\cdot t$. The scantlings shown in Table A.1 are representative of those for shell plating in the bilge area of ships. A description

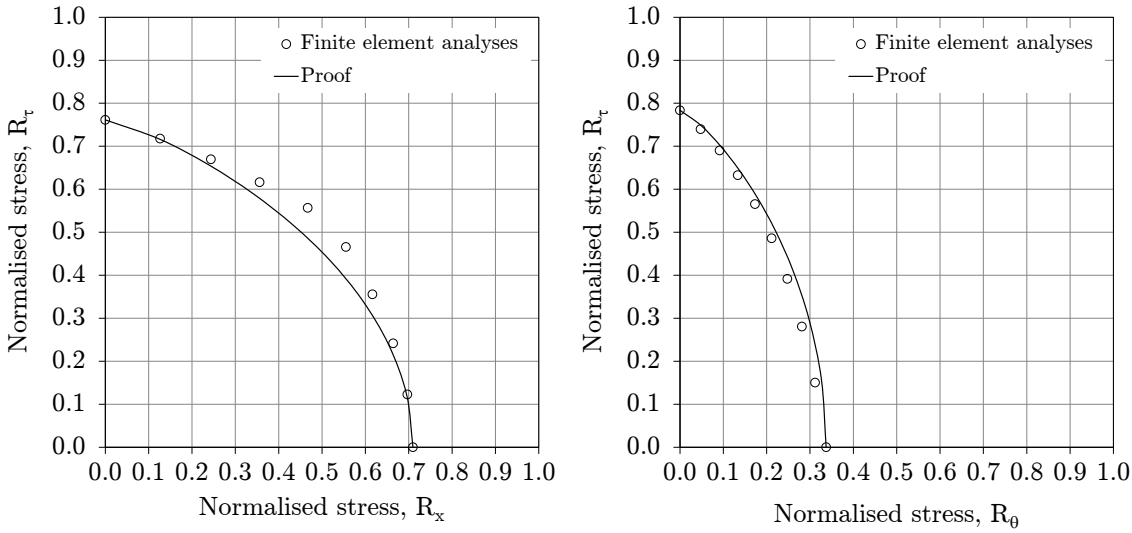

(a) R_x-R_τ (b) R_θ-R_τ

Figure A.3.: Comparison plots for existing proof (Plate 5, $d/t = 120$).

of the finite element analyses is included in Appendix 1 of reference [76][2]. Because the circumferential length of a curved plate has no effect on its buckling or ultimate strength, cylindrical shells (without stiffening) were modelled in all finite element analyses. A typical deformation plot of a cylinder under pure axial stress is shown in Figure A.2.

For each of the nine plates described in Table A.1, the ultimate capacity was determined under ten combinations each of two stress components R_x - R_θ (axial and hoop stresses), R_x - R_τ (axial and shear stresses) and R_θ - R_τ (hoop and shear stresses). These results were then compared to those obtained using Equation (A.3). For stress combinations involving shear, i.e. R_x - R_τ and R_θ - R_τ, results of the comparison for *Plate 5* (d/t = 120) are shown in Figure A.3[3]. Comparison results for all plates are plotted in Appendix 2 of reference [76]. Using the quantitative evaluation scheme presented in §3.1 for capacity proofs of plane plates, the results for these two stress combinations are tabulated in Table A.2 and plotted in Figure A.4. These results are based on 9 x 8 = 72 evaluation points (data points where $R_x = 0$, $R_\theta = 0$ or $R_\tau = 0$ are omitted since they can be directly calculated from plate reduction factors) and show that the existing proof based on DIN 18800 is reasonably accurate and precise for stress combinations R_x - R_τ (axial and shear stresses) and R_θ - R_τ (hoop and shear stresses).

For the stress combination excluding shear, i.e. R_x - R_θ, results of the comparison for *Plate 5* (d/t = 120) are shown in Figure A.5(a). As noted above, comparison results for all plates are plotted in Appendix 2 of reference [76]. Using again the quantitative evaluation scheme presented in §3.1 for capacity proofs of plane plates, the results for this

[2] Although the author is responsible for the subsequent analyses, the finite element analyses were performed by Det norske Veritas (DnV) using the Abaqus finite element code. In this regard, the author performed similar analyses using the ANSYS finite element code, but only to establish the boundary conditions to be used in the models and to verify selected DnV results.

[3] As shown in Figures A.3(a) and A.3(b), the ultimate shear stresses for Plate 5 are $R_{\tau,ult} = 0.761$ and $R_{\tau,ult} = 0.784$, respectively. This discrepancy arises due to differences in the initial imperfection shapes used in the finite element models for each calculation set (as noted in Appendix 1 of reference [76]).

KPI		Target	R_x - R_τ	R_θ - R_τ	Criteria
1	S_r/n_s	0.000	0.003	0.000	$S_r/n_s \leq 0.001$
2	m_{lsr}	1.00	0.99	1.00	$0.97 \leq m_{lsr} \leq 1.00$
3	R_D^2	1.00	0.80	0.98	$R_D^2 \geq 0.95$
4	m_{95}	1.00	1.13	1.08	$m_{95} \leq 1.05$
5	m_5	1.00	0.86	0.94	$m_5 \geq 0.87$

Table A.2.: Key performance indicators for existing proof (R_x - R_τ and R_θ - R_τ).

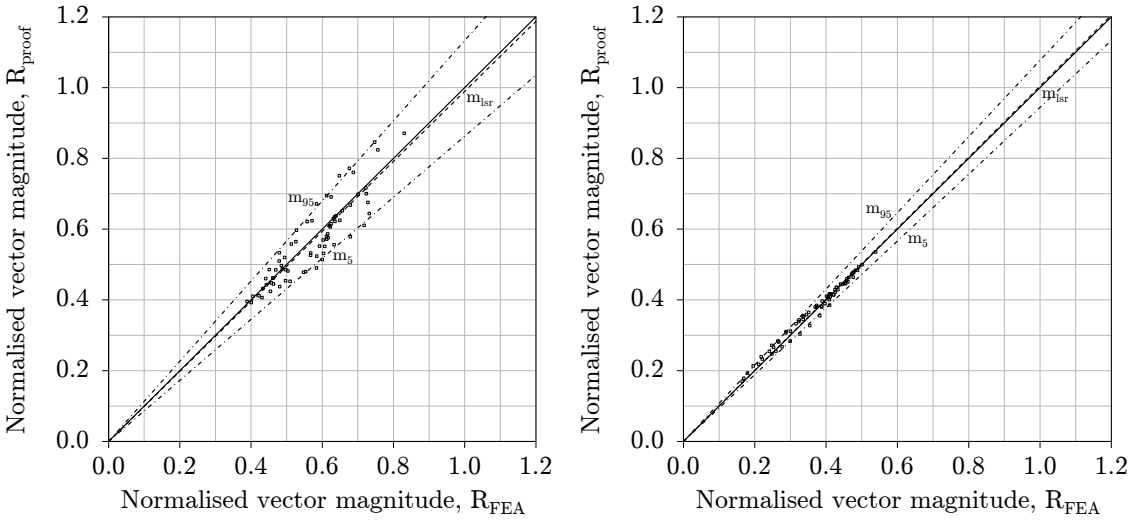

(a) R_x-R_τ (b) R_θ-R_τ

Figure A.4.: Scatter plots for existing proof (R_x - R_τ and R_θ - R_τ).

stress combination are tabulated in Table A.3 and plotted in Figure A.6(a). Contrary, to the stress combinations including shear, these results show that the existing proof based on DIN 18800 is rather conservative for the stress combination R_x - R_θ (axial and hoop stresses), i.e. due to the quasi-rectangular shape of the capacity curve delineated by the results of finite element analyses.

KPI		Target	Existing proof	Revised proof	Criteria
1	S_r/n_s	0.000	0.009	0.002	$S_r/n_s \leq 0.001$
2	m_{lsr}	1.00	0.87	0.98	$0.97 \leq m_{lsr} \leq 1.00$
3	R_D^2	1.00	0.92	0.95	$R_D^2 \geq 0.95$
4	m_{95}	1.00	0.97	1.08	$m_{95} \leq 1.05$
5	m_5	1.00	0.72	0.85	$m_5 \geq 0.87$

Table A.3.: Key performance indicators for existing and revised proofs (R_x - R_θ).

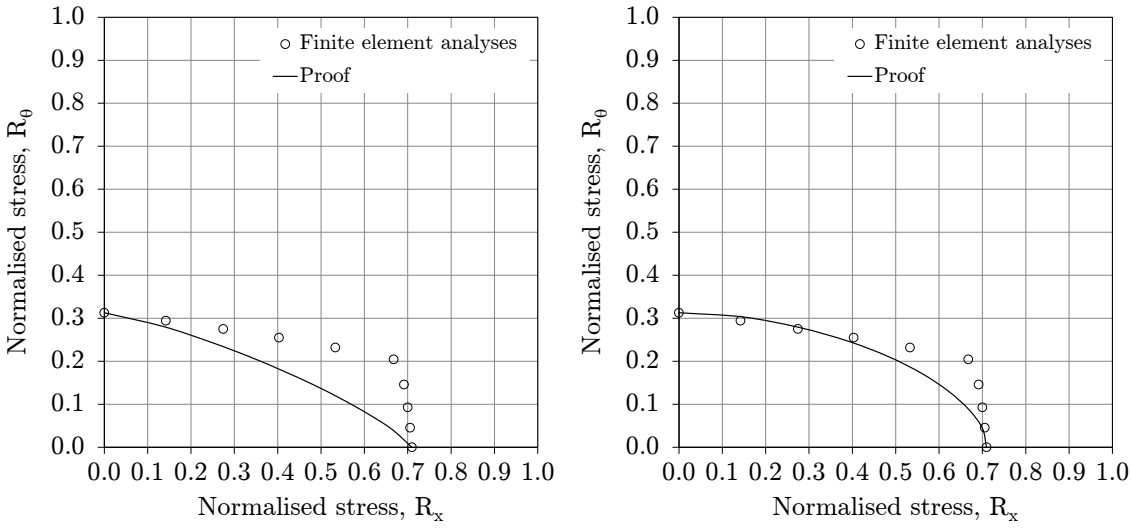

(a) R_x - R_θ - Existing proof (b) R_x - R_θ - Revised proof

Figure A.5.: Comparison plots for existing and revised proofs (Plate 5, $d/t = 120$).

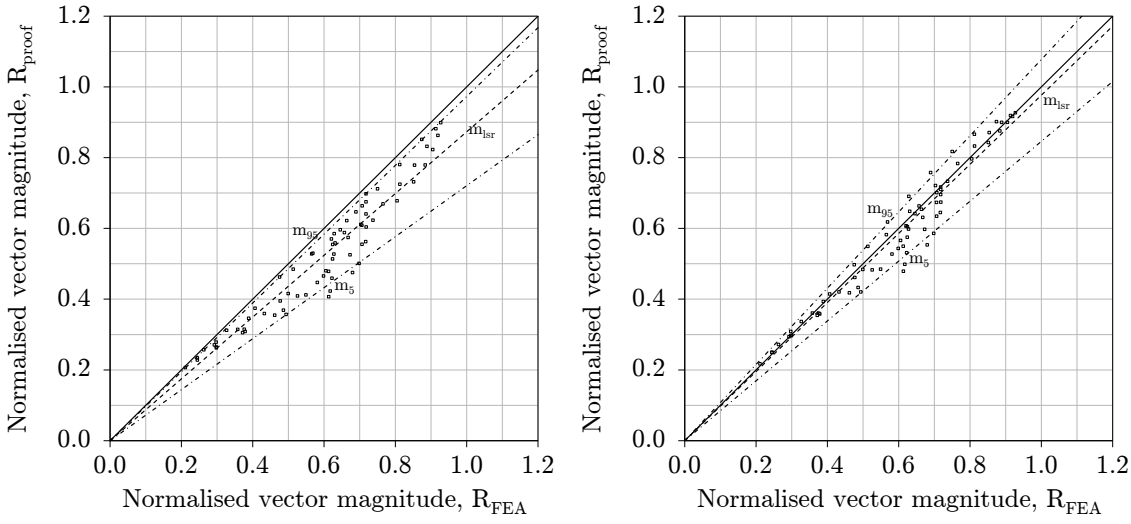

(a) R_x - R_θ - Existing proof (b) R_x - R_θ - Revised proof

Figure A.6.: Scatter plots for existing and revised proofs (R_x - R_θ).

In an effort to correct this conservatism, additional comparisons were made using a revised proof in which an R_x - R_θ interaction term is added to the existing proof. Here an interaction coefficient equal to $B = 0.5$ was used

$$\left(\frac{R_x}{\kappa_x}\right)^{1.25} + \left(\frac{R_\theta}{\kappa_\theta}\right)^{1.25} - 0.5 \cdot \left(\frac{R_x}{\kappa_x}\right) \cdot \left(\frac{R_\theta}{\kappa_\theta}\right) + \left(\frac{R_\tau}{\kappa_\tau}\right)^2 = 1.0 \tag{A.4}$$

The rationale behind using an interaction term is to avoid any degradation in the existing levels of accuracy and precision for stress combinations R_x - R_τ and R_θ - R_τ which might occur if the exponents in the capacity equation were changed. For the stress combination

R_x - R_θ, revised results of the comparison for *Plate 5* (d/t = 120) are shown in Figure A.5(b).

Again using the quantitative evaluation scheme presented in §3.1 for capacity proofs of plane plates, the results using Equation (A.4) for the stress combination R_x - R_θ are tabulated in Table A.3 and plotted in Figure A.6(b). Although not all key performance indicators fall within the ranges of acceptable values, a marked improvement in the accuracy can be seen (i.e. $m_{lsr} = 0.87 \rightarrow m_{lsr} = 0.98$) as well as a moderate improvement in precision (i.e. $R^2_D = 0.92 \rightarrow R^2_D = 0.95$).

A.2. Evaluation of proof under three stress components

For each of the nine plates described in Table A.1, the ultimate capacity was also determined under three stress components R_x - R_θ - R_τ for three different levels of shear. These results were then compared to those obtained using Equation (A.3), i.e. the existing proof, and those obtained using Equation (A.4), i.e. the revised proof. Results of the comparison for *Plate 5* (d/t = 120) are shown in Figure A.7(a) for the existing proof and Figure A.7(b) for the revised proof. Comparison results for all plates are plotted in Appendix 3 of reference [76].

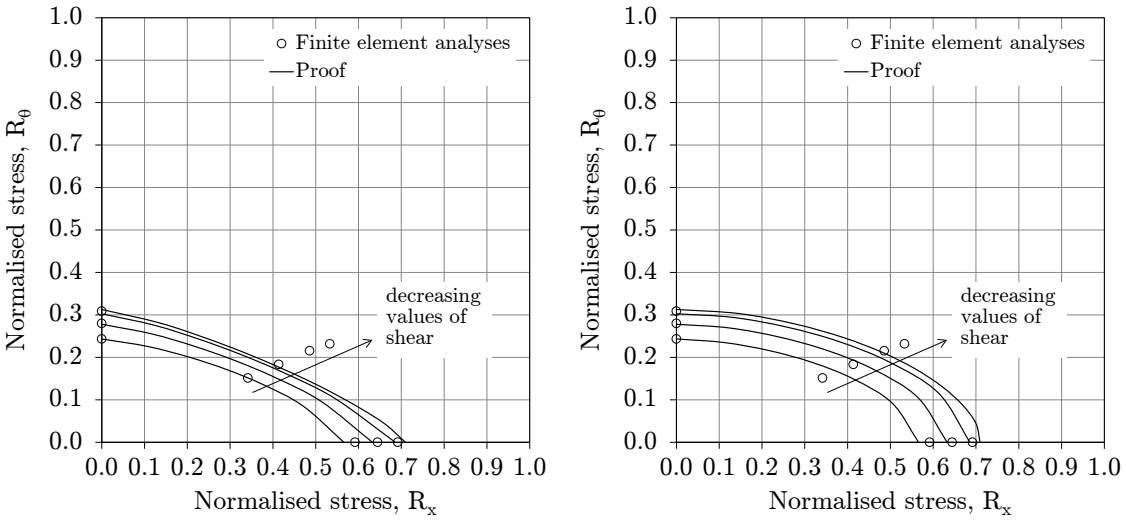

(a) R_x - R_θ - R_τ - Existing proof

(b) R_x - R_θ - R_τ - Revised proof

Figure A.7.: Comparison plots for existing and revised proofs (Plate 5, $d/t = 120$).

Again using the quantitative evaluation scheme presented in §3.1 for capacity proofs of plane plates, the results for three stress components are tabulated in Table A.4 and plotted in Figure A.8. These results are based on ((3 x 3) + 1) x 9 = 90 evaluation points (here only a single evaluation point is used in case $R_\tau = 0$ since the capacity of plating where $R_x = R_\tau = 0$ and $R_\theta = R_\tau = 0$ can be directly calculated from the plate reduction factors κ_θ and κ_x, respectively). As can be seen, these results reflect a slight increase (albeit non-conservative) in the accuracy ($m_{lsr} = 0.97 \rightarrow m_{lsr} = 1.02$) and a marked improvement in precision ($R^2_D = 0.84 \rightarrow R^2_D = 0.91$) when using the revised proof.

It can be concluded from the foregoing that the improvements in accuracy and precision using Equation (A.4) compared to Equation (A.3) are more significant under com-

KPI		Target	Existing proof	Revised proof	Criteria
1	S_r/n_s	0.000	0.004	0.002	$S_r/n_s \leq 0.001$
2	m_{lsr}	1.00	0.97	1.02	$0.97 \leq m_{lsr} \leq 1.00$
3	$R_D{}^2$	1.00	0.84	0.91	$R_D{}^2 \geq 0.95$
4	m_{95}	1.00	1.15	1.16	$m_{95} \leq 1.05$
5	m_5	1.00	0.78	0.90	$m_5 \geq 0.87$

Table A.4.: Key performance indicators for existing and revised plots (R_χ - R_θ - R_τ).

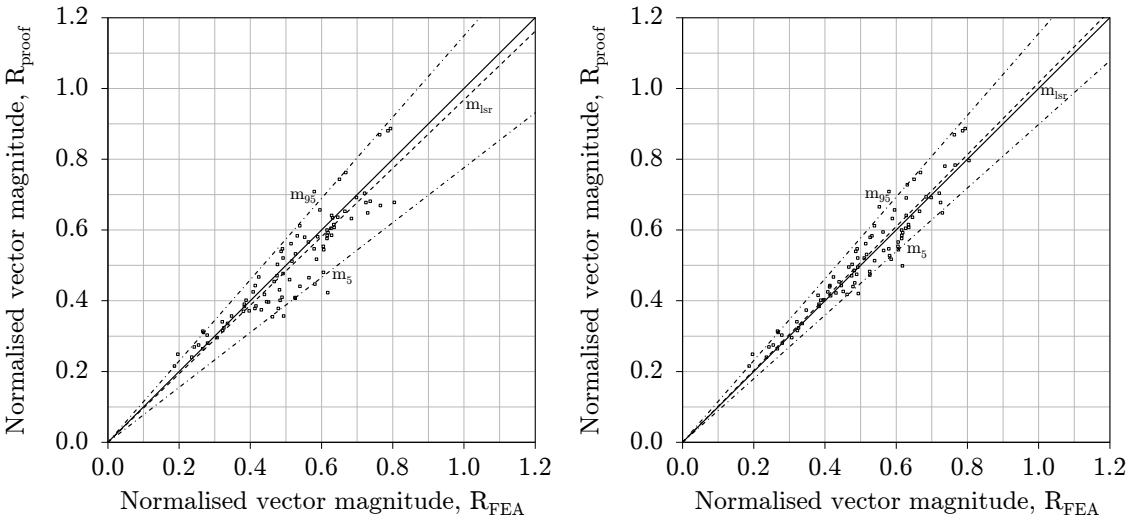

(a) R_χ - R_θ - R_τ - Existing proof

(b) R_χ - R_θ - R_τ - Revised proof

Figure A.8.: Scatter plots for existing and revised proofs (R_χ - R_θ - R_τ).

bined axial and hoop stresses, i.e. R_χ - R_θ, than under combined axial, hoop and stresses, i.e. R_χ - R_θ - R_τ. However, because the former is relevant for shell plating in the bilge area (i.e. due to dominant axial stresses under hull girder bending and hoop stresses under external sea pressure), the IACS harmonisation project team HPT02 decided to include the interaction term in the *IACS Common Structural Rules for Bulk Carriers and Oil Tankers*. As noted above, the revised proof expressed in Equation (A.4) is also included (at least implicitly) in the new *IACS Longitudinal Strength Standard for Container Ships* (UR S11A) as well as the new *DNV GL Rules for Classification* which are applicable to all ship types.

Appendix B. Numerical Studies

Numerical studies based on the finite element method have been used extensively throughout the present work using the ANSYS software package (Release 13.0). These studies have been used to better understand the mechanics of plating collapse (Chapter 2), quantitatively evaluate existing proofs of plate capacity (Chapter 3), develop a new proof of plate capacity (Chapter 4) and demonstrate the practical application of this proof within the shipbuilding industry (Chapter 5). In case of the stiffened panels analysed in Chapter 5, the numerical study of bottom shell and side shell structures of a double hull VLCC have been performed in strict adherence to a procedure developed and agreed within the IACS harmonisation project team HPT02 for performing non-linear finite element analyses of stiffened panels [75]. This procedure has been validated against tests of four stiffened panels carried out by Germanischer Lloyd [10]. In the present work, this procedure is also used for the analyses of single plates where stiffeners are modelled by simple supports (in fact, a single batch file has been used with options for switching between the analysis of stiffened panels and the analysis of single plates). Because the IACS procedure for analysing stiffened panels is already in the public domain, only its application to single plates is here described. In the first section of this appendix (§B.1), the procedure used for performing finite element analyses is described. In the second section of this appendix (§B.2), comparisons with test results are used to validate this procedure.

B.1. Description of finite element analyses

B.1.1. General

Non-linear buckling analyses are essentially performed in two steps. When perfectly in-plane loads are applied to a plane plate in the absence of any out-of-plane loads (e.g. lateral pressure), the out-of-plane deflections which are needed to initiate buckling will not develop. Accordingly, the first step is to perform a linear eigenvalue analysis in order to generate an initial deflection shape for the plate. Alternatively, initial deflection shapes (theoretical or measured) may be modelled directly. In the second step, a non-linear analysis is performed, the aim being to obtain a stable load-deflection curve, the peak of which defines the ultimate capacity of the plate.

B.1.2. Model extent

The extent of model used in all analyses is a single a x b plate. As noted below, the model is simply supported on all edges. In case of symmetric deflection patterns, a model with out-of-plane support along its centrelines $x = a/2$ and $y = b/2$ together with rotational restraint along the edges may also be used to represent continuous plating. However, such a model is precluded in the present study by the asymmetric deflection patterns associated with shear loads. As shown in Figure B.1(a), the differences in ultimate plate strength

($\alpha = 3$, $\beta = 3$) under axial loads using these two models is negligible (although some differences in unloading are evident under longitudinal stress σ_x). In Figure B.1(b), the stress strain-curve under shear for a single plate supported simply on all edges ($\alpha = 3$, $\beta = 3$) is compared to that for continuous plating comprised of nine plate fields (i.e. three frame spacings by three frame spans). As can be seen, there is only a slight increase (2.16%) in the ultimate strength of continuous plating due to the strengthening effect of the asymmetric deflection.

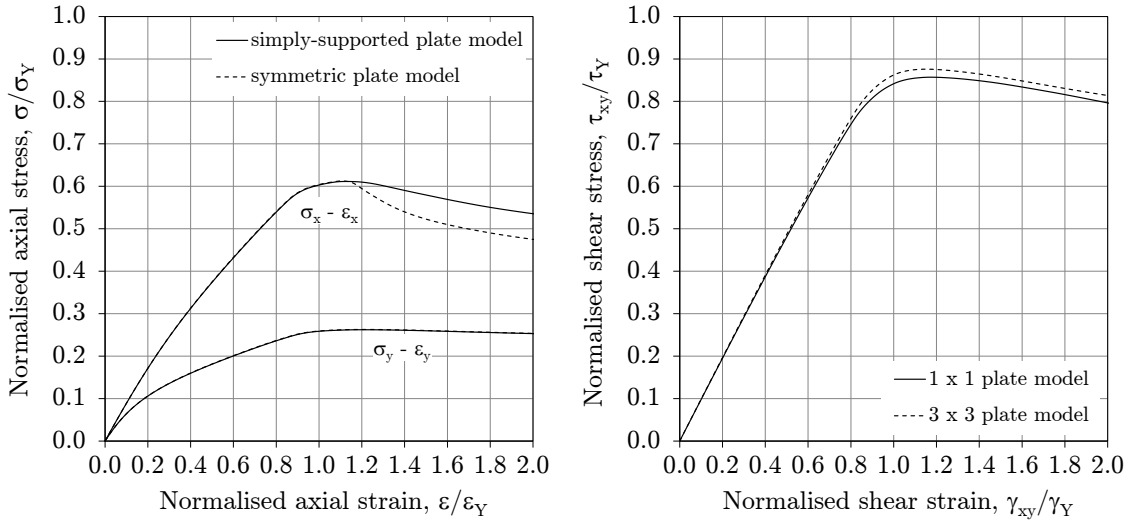

(a) Axial loads (b) Shear load

Figure B.1.: Model comparisons ($\alpha = 3$, $\beta = 3$).

B.1.3. Element type and meshing

In the HPT02 agreed procedure for stiffened panels, 4-node shell elements may be used with six elements across the breadth b of the plate. However, in case of a single plate model, the drastically reduced degrees of freedom allow an 8-node element to be used with eight elements across the breadth b of the plate. Because the length a of a single plate used in the present work is always an exact multiple of the frame spacing b, the edge length of elements in the x-direction are exactly equal to those in the y-direction (i.e. $b/8$ x $b/8$ elements). Plates are modelled using the ANSYS element *Shell281* which is an 8-node element with six degrees of freedom at each node. The element is suitable for analysing thin to moderately-thick shell structures [77].

The single exception to the foregoing, is the analysis of plates with residual stresses (§5.1.1). Due to the small width of the tensile zone along plate edges, the size of elements are here reduced to $b/16$ x $b/16$ and the 4-node shell element *Shell181* is used (with the full integration option). Like its 8-node counterpart, *Shell181* is also suitable for analysing thin to moderately-thick shell structures [77].

B.1.4. Material properties and real constants

A bi-linear material model including strain-hardening effect is used in all analyses. In this regard, the ANSYS option *TB, BISO* is used for which the von Mises yield criteria

is coupled with an isotropic work hardening assumption (i.e. under progressive yielding the yield surface remains centred about its initial centreline and expands in size as the plastic strains develop [78]). The bilinear stress-strain curve is initially defined by the elastic modulus of the material $E = 206,000\,N/mm^2$. Once the specified yield stress σ_Y is reached, the curve continues along a slope defined by the strain hardening parameter $E_T = 1000\,N/mm^2$. A Poisson's ratio $\nu = 0.3$ is used in all analyses.

For the analysis of the stiffened panel in Chapter 5, the scantlings and yield stresses are directly provided. However, in all analyses of single plates, the thickness, breadth (i.e. frame spacing) and yield stress is always given in terms of the (non-dimensional) plate slenderness parameter $\beta = b/t \cdot \sqrt{\sigma_Y/E}$. For this reason, the corresponding combinations of plate thickness t and yield stress σ_Y used in the finite element analyses for each value of β are shown in Table B.1. The frame spacing remains constant at $b = 850\,mm$.

		Set 1		Set 2	
β	b [mm]	t [mm]	σ_Y [N/mm^2]	t [mm]	σ_Y [N/mm^2]
0.5	850	57.40	235	57.40	235
1.0	850	28.71	235	28.71	235
1.5	850	-	-	19.14	235
2.0	850	16.62	315	14.35	235
2.5	850	-	-	11.48	235
3.0	850	11.08	315	9.57	235
3.5	850	-	-	8.20	235
4.0	850	8.82	355	7.18	235
5.0	850	-	-	5.74	235

Table B.1.: Combinations of plate thickness t and yield stress σ_Y used in finite element analyses.

All evaluation and calibration data used in Chapters 3 and 4, as well as single plate analyses performed in Chapter 5 (Design Application), are based on *Set 1* combinations. Analyses performed in Chapter 2 (Mechanics of Plating Collapse), where the effects of plate slenderness are often compared, are based primarily on *Set 2* combinations such that these effects are studied by changing only the b/t ratios. Differences in the results using either of these two sets (i.e. in case of $\beta = 2$, $\beta = 3$ and $\beta = 4$) are negligible.

B.1.5. Boundary conditions and load application

In all analyses, constraint equations are used to force the edges of the model to remain straight in the plane of the plate. As noted in the HPT02 agreed procedure [75], this is done to reflect the force balance which exists between adjacent plate fields. As shown in Figure B.2(a), this is achieved in the longitudinal direction by restraining all nodal displacements in the x-direction at $x = 0$ and using the ANSYS *CP* command to couple all nodal displacements in the x-direction at $x = a$. In the transverse y-direction, the ANSYS command *CE* is used to establish constraint equations which force the edges at $y = 0$ and $y = b$ to remain parallel to each other, the resulting constraints of which can be seen in Figure B.2(b). For the sake of numerical stability, a single node at $x = y = 0$ is restrained against displacements in the y-direction. No restraints against rotation about the z-axis

are applied. The effects of all in-plane constraints can be seen in the magnified deflections of a plate under pure shear as shown in Figure B.2(c). For the analyses performed in §5.1.1 of a plate with a single free edge (i.e. no in-plane or out-of-plane restraint) as well as a plate with free pull-in on a single edge (i.e. no in-plane restraint), analyses are performed without the constraint equations at $y = b$.

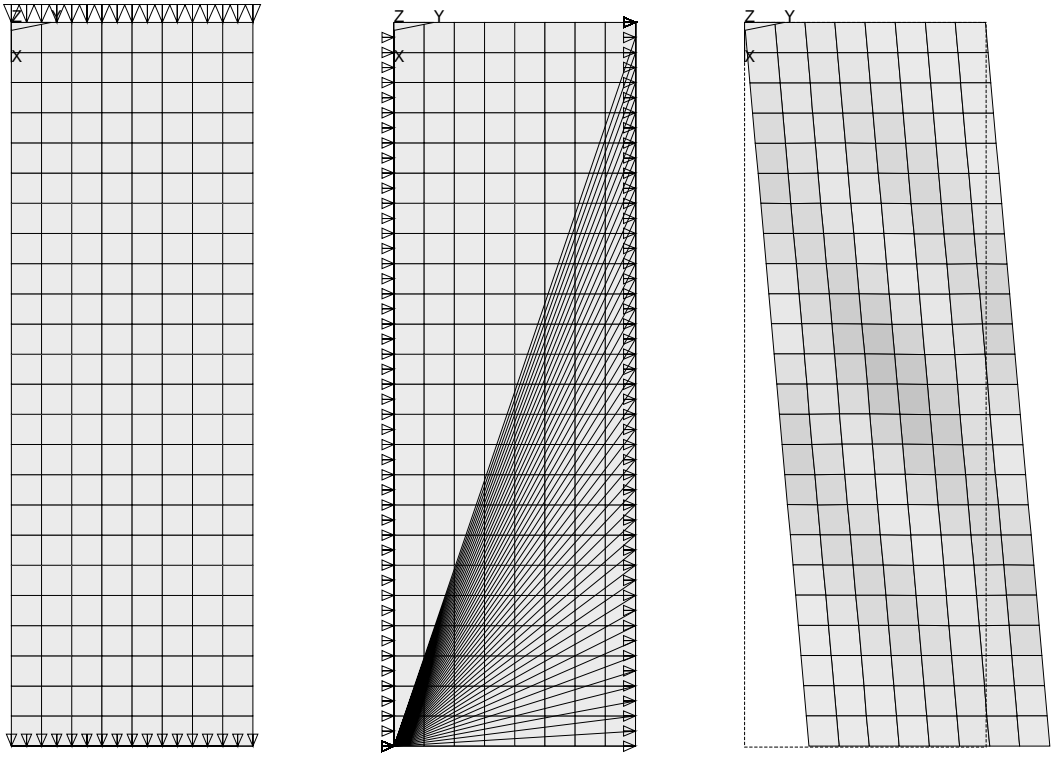

(a) Coupled displacements in x-direction (b) Coupled displacements in y-direction (c) In-plane displacement under pure shear

Figure B.2.: In-plane constraints.

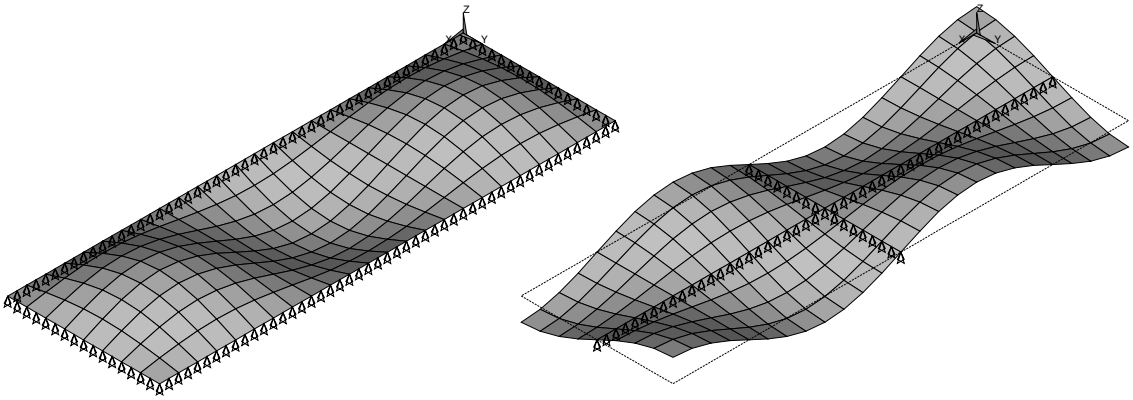

(a) Simply-supported plate model (b) Symmetric plate model

Figure B.3.: Single plate models.

In addition to the foregoing, all edges of the model are restrained against out-of-plane deflections, but are allowed to rotate freely. The exceptions to this are the analyses in §5.1.1 of a plate with a single free edge and of a plate under lateral pressure. In case of the latter, the edges of the model are restrained against rotation and out-of-plane deflections are instead restrained along the centrelines of the model (i.e. $x = a/2$ and $y = b/2$). Both models are shown in Figure B.3.

Regarding the application of in-plane loads, this is performed in all cases by applying forces directly to nodes using the ANSYS *F* command. For the analysis of lateral pressure in §5.1.1, the pressure is firstly applied directly to elements using the ANSYS *SFE* command. In a second load step, the pressure is kept constant while the in-plane loads are incrementally applied.

B.1.6. Initial imperfections

In order to account for any residual stresses and deflections due to welding and cutting, initial out-of-plane deflections with a magnitude of $\delta_0 = b/200$ are applied to all plate models. In accordance with the agreed HPT02 procedure, initial deflection shapes are based on eigenmodes resulting from linear elastic buckling analyses. Because a plate model may not snap into the eigenmode associated with minimum internal (strain) energy, all relevant eigenmodes need to be checked. In accordance with the agreed HPT02 procedure, this means that analyses are performed with initial deflection shapes based on eigenmodes for each load component in isolation as well as the eigenmode associated with the actual load combination.

For instance, the eigenmodes used in the analyses of a plate under biaxial compression combined with shear are shown in Figure B.4. Here the load combination has been chosen to illustrate that its associated eigenmode may differ from eigenmodes associated with either load component in isolation. The critical eigenmode is that resulting in the lowest capacity of the plate.

The only exceptions to the foregoing are the analyses in Chapter 2 pertaining to *ideal* plates and the analyses in Chapter 5 pertaining to the study of initial imperfections. In case of the former, initial out-of-plane deflections with an amplitude of 0.0005 mm have been used (i.e. $b/1700000$). In case of the latter, deflection shapes shown in Figure 5.10(c) to 5.10(f) are directly applied to the plate model using the ANSYS *D* command which defines the degree of freedom constraints at nodes (the model geometry is then updated on the basis of the resulting deflection shape). For the subsequent investigation of residual stresses, elements are pre-stressed using the ANSYS *INISTATE* command.

B.1.7. Solution algorithm

All analyses have been performed using an arc length solution algorithm in order to capture the unloading portion of the stress-strain curve, thereby clearly defining its peak. The reference arc length radius (which defines the initial arc length) has been defined as 1/100 of the total load. During solution iteration, any subsequent modification of arc length is limited by the default minimum and maximum arc lengths included in the ANSYS code. Non-linear geometric effects are included using the ANSYS *NLGEOM* command. Following solution, average stress and strain values for the model are calculated and plotted to ensure that plate response is stable and without convergence problems.

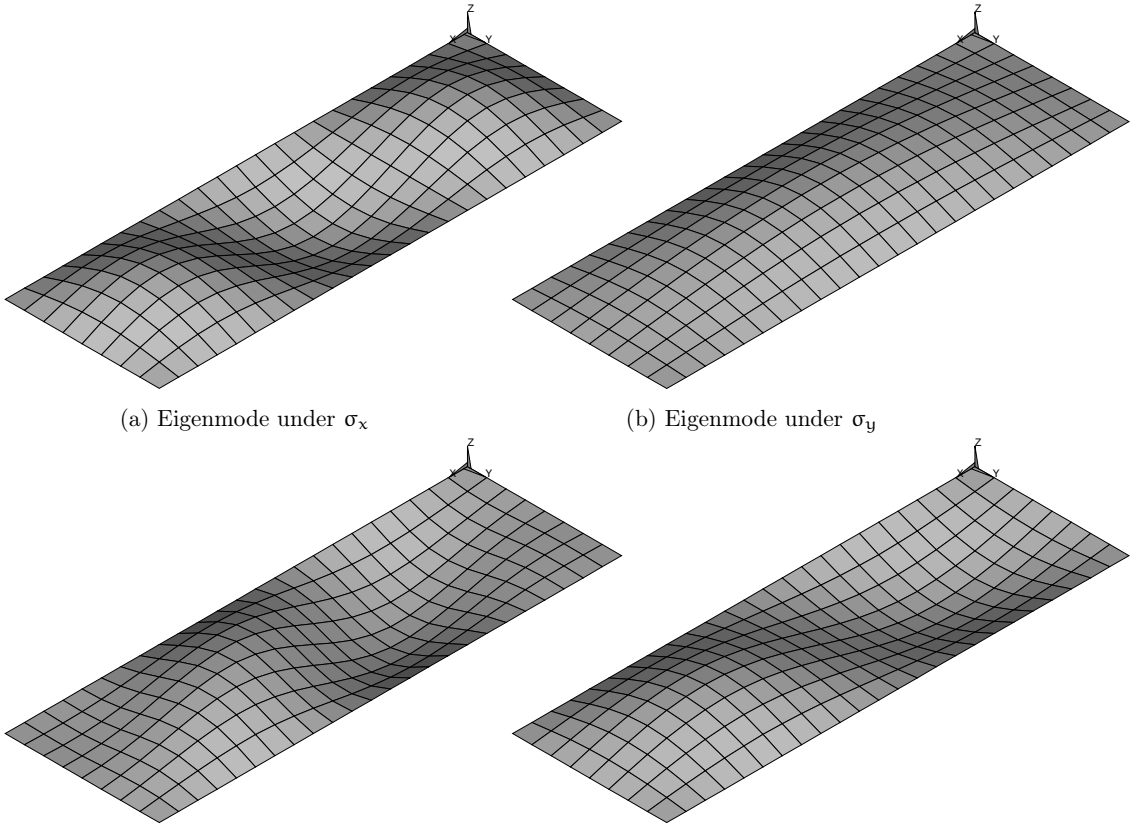

(a) Eigenmode under σ_x

(b) Eigenmode under σ_y

(c) Eigenmode under τ_{xy}

(d) Eigenmode under σ_x-σ_y-τ_{xy} ($c = 0.3$)

Figure B.4.: Eigenmode shapes.

In this regard, the evaluation data used in the present work is based on four uniform levels of shear *at collapse*; 0, $0.25 \cdot \tau_{xy,ult}$, $0.50 \cdot \tau_{xy,ult}$ and $0.75 \cdot \tau_{xy,ult}$. Accordingly, except in cases of $\tau_{xy} = 0$, iterations are required to find the value of *applied* shear stress $\tau_{xy,applied}$ which results in the specified magnitude of shear stress $\tau_{xy,ult}$ at *collapse*. To explain, the magnitude of collapse loads are defined by the product of the applied loads and the time corresponding to the peak of the load-displacement curve (i.e. where time = 1.0 at the end of the load step during which the in-plane loads are incrementally applied). Since the time of collapse is not known beforehand, the magnitude of applied shear needs to be iteratively adjusted until the product of applied shear and the time at collapse equals the specified magnitude of shear at collapse. This occurs whenever the magnitude of applied shear stress $\tau_{xy,applied}$ is equal to the specified magnitude of shear stress at collapse divided by the time at collapse, e.g. $(\tau_{xy,ult}/0.84) \cdot 0.84 = \tau_{xy,ult}$, where time = 0.84 at collapse and $\tau_{xy,applied} = \tau_{xy,ult}/0.84$.

B.2. Validation of procedure

B.2.1. Comparison with stiffened panel tests

As noted above, all finite element analyses in the present work have been performed in strict adherence to a procedure developed and agreed within the IACS harmonisation project

team HPT02 for performing non-linear finite element analyses of stiffened panels [75]. To ensure that each classification society had correctly implemented the procedure, all eight members analysed a benchmark panel under four load combinations; (1) σ_x, (2) σ_y, (3) $\sigma_x + \sigma_y + \tau_{xy}$ and (4) $\sigma_x + \sigma_y + \tau_{xy} + p$. The capacities obtained by members under the four combinations were compared to ensure that they were within $\pm$ 5% of the average magnitudes of capacity. Here it is important to note that three different finite element codes were used (i.e. ANSYS, ABAQUS and MSC MARC).

The HPT02 procedure has also been validated against laboratory tests of four stiffened panels carried out by Egge of Germanischer Lloyd [10]. These panels were comprised of three frame bays and five frame spacings. Each of the four panels were firstly preloaded by a lateral pressure and secondly by a transverse compression load. Each panel was then loaded under longitudinal compression to the point of collapse. Accordingly, the batch file used in the present work has also been validated against these four panel collapse tests. The measured scantlings and material properties of each panel are listed in Table B.2 (each panel was stiffened with HP 80 x 6 profiles).

Panel	a [mm]	b [mm]	t [mm]	σ_Y [N/mm^2]	β	t_{web} [mm]	$\sigma_{Y,web}$ [N/mm^2]
I	1320	440	6.05	314	2.84	6.02	292
II			6.07	352	3.00	6.00	299
III			6.05	338	2.95	6.00	297
IV			4.05	349	4.47	6.02	298

Table B.2.: Scantlings and material properties of test panels.

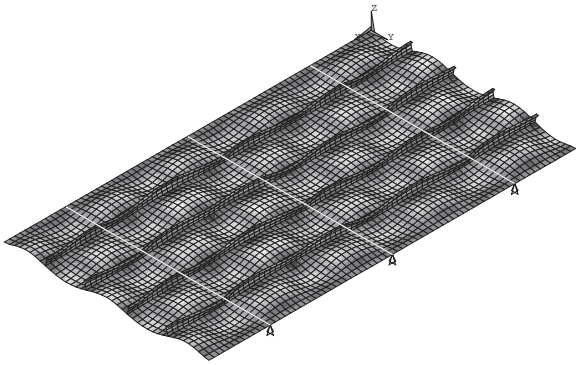

Figure B.5.: Finite element model of test panels.

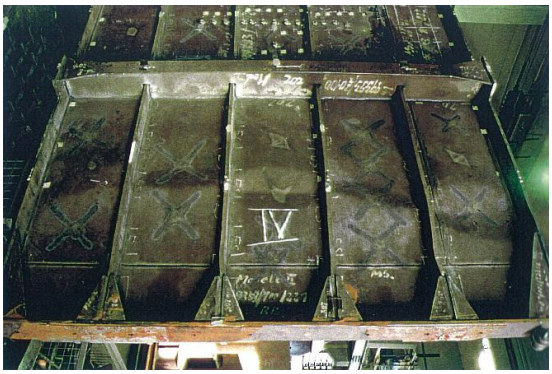

Figure B.6.: Fairing of Panel IV (reproduced from reference [10] with permission of E.D. Egge and Germanischer Lloyd).

The model used in the validation finite element analyses is shown in Figure B.5. The magnitude of load components and results obtained with finite element analyses are shown in Table B.3 (here the lateral load p is measured in metres of static pressure head). As can be seen in the calculated errors, the agreement is quite good. Although the error in case of Panel IV is -6.9%, the results of this panel test are not as reliable as those of the other three panels. Unfortunately, as shown in Figure B.6, Panel IV was heavily *faired* using

Panel	p [m]	σ_y [N/mm^2]	$\sigma_{x,test}$ [N/mm^2]	$\sigma_{x,FEA}$ [N/mm^2]	Error
I	2.65	43.0	187.6	189.9	1.2%
II	5.30	43.0	194.0	199.2	2.7%
III	5.30	69.0	190.0	183.8	-3.3%
IV	2.40	47.0	185.0	172.2	-6.9%

Table B.3.: Applied loads and results.

heat treatment in an effort by the shipyard to reduce the magnitude of large post-welding deflections. According to Egge, this resulted in an indeterminate state of initial conditions (i.e. uncontrolled residual stresses and very short-waved pre-deformations).

B.2.2. Comparison with unstiffened plate tests

In addition to the foregoing, an effort has been made to validate the finite element analyses used in the present work against full-scale tests of unstiffened plates under combined loading. Unfortunately, the only publicly-available data which the author could find is of small-scale tests of plates under biaxial compression and lateral pressure [49]. As noted in the introduction to the corresponding test report, experimental data on biaxial compression strength was reported there for the first time. The tests were carried out in 1970 during a research project sponsored by the Ship Structure Committee [48] and the author could find no results from subsequently performed tests.

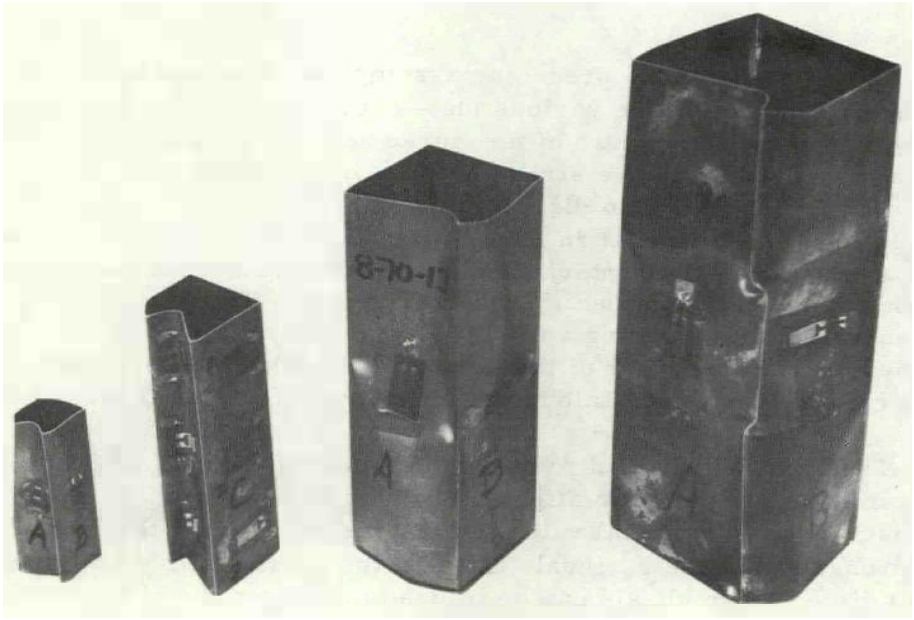

Figure B.7.: Post-collapse test specimens (reproduced from reference [49] with permission of the Ship Structure Committee).

As mentioned, the scale of the above-mentioned tests were small. All test specimens were square cross-sectional tubes fabricated from flat rectangular plates having a nominal

b/t	b [mm]	a [mm]	t [mm]	σ_Y [N/mm^2]	E [N/mm^2]	ν	β
30	22.86	68.58	0.762	270.3	199948	0.28	1.10
50	38.10	114.3					1.84
70	53.34	160.0					2.57
90	68.58	205.7					3.31

Table B.4.: Scantlings and material properties of test specimens.

thickness of 0.726 mm (0.03 in.) and an aspect ratio $\alpha = 3$. Four basic specimens were tested as shown in Figure B.7. The scantlings and material properties of all four specimens

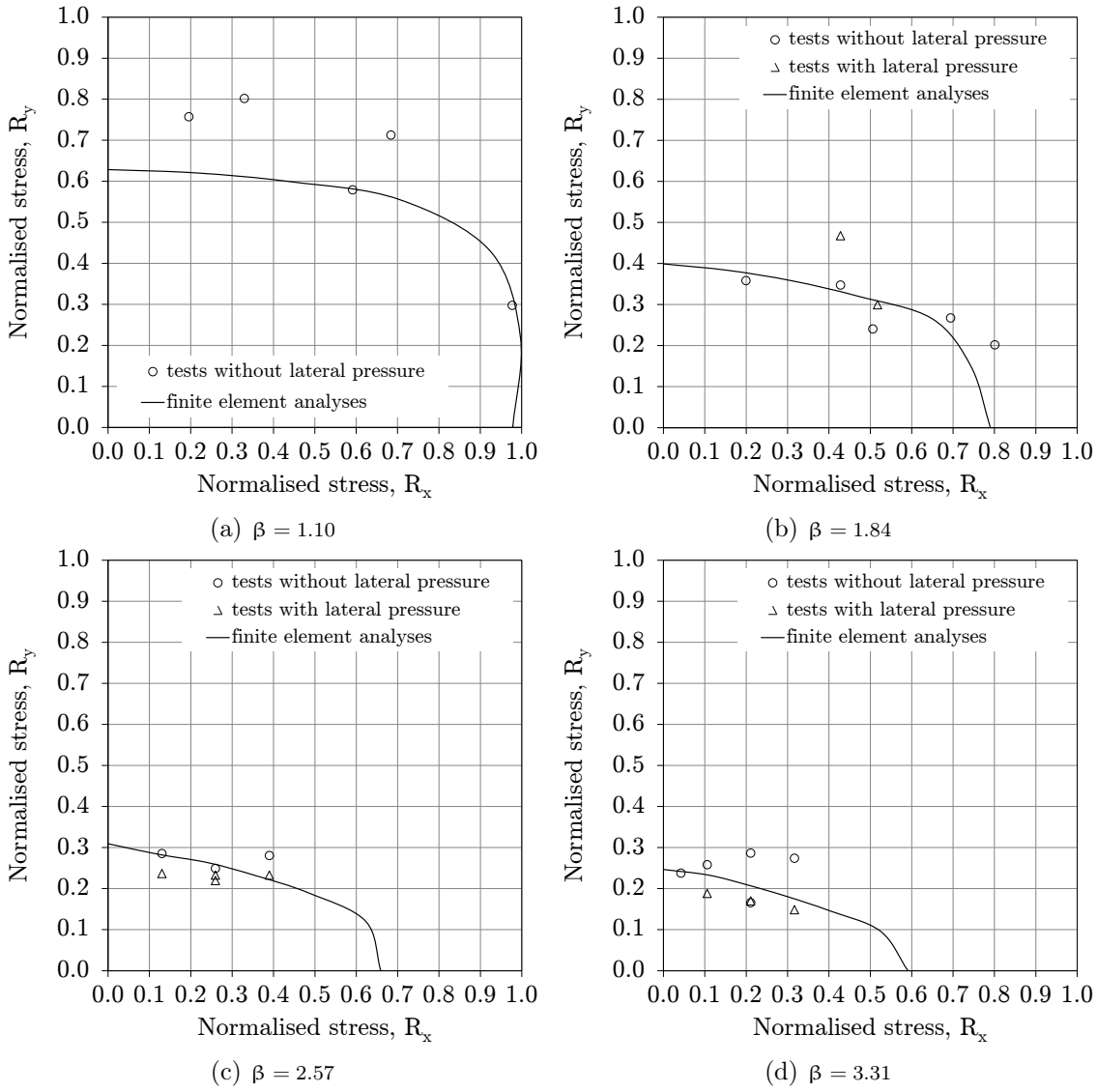

(a) β = 1.10 (b) β = 1.84

(c) β = 2.57 (d) β = 3.31

Figure B.8.: Comparisons between tests and finite element analyses.

are summarised in Table B.4. Theoretically, the small scale of the tests should have no effect on the results, but in practice provided several challenges with respect to fabrication (e.g. fairness, residual stresses) as well as testing (e.g. boundary conditions and load application).

Nevertheless, plate capacity curves based on finite element analyses are compared in Figure B.8 to all test results of plates under biaxial compression (results from uniaxial compression tests were often incompatible with biaxial compression test results and so have been omitted). In general, it can be concluded that the agreement between the test results and finite element analyses are as good as could be reasonably expected given the relatively high degree of scatter in the test results ("a feature common to all compression tests on thin plates", according to Winter [17]).

Appendix C. Evaluation Data

C.1. Tabular Results

In this section the results of finite element analyses used in the evaluation of proofs are tabulated. Results obtained with the new proof are also included.

		Finite Element Analyses					New Proof			
	data point	run id	$R_{x,ult}$	$R_{y,ult}$	$R_{\tau,\ ult}$	Magnitude	$R_{x,ult}$	$R_{y,ult}$	$R_{\tau,\ ult}$	Magnitude
$\tau_{xy} = 0$	1	11103	0.908	0.524	0.000	1.048	0.894	0.516	0.000	1.032
	2	11105	0.524	0.908	0.000	1.048	0.516	0.894	0.000	1.032
	3	11109	-0.421	0.721	0.000	0.835	-0.421	0.721	0.000	0.835
	4	11111	-0.726	0.415	0.000	0.836	-0.726	0.415	0.000	0.836
	5	11121	0.415	-0.726	0.000	0.836	0.415	-0.726	0.000	0.836
	6	11123	0.721	-0.421	0.000	0.835	0.721	-0.421	0.000	0.835
$\tau_{xy} = 0.25 \cdot \tau_{xy,ult}$	7	41101	0.942	0.000	0.250	0.953	0.947	0.000	0.252	0.959
	8	41103	0.869	0.502	0.250	1.014	0.865	0.500	0.249	1.010
	9	41105	0.502	0.869	0.250	1.014	0.500	0.865	0.249	1.010
	10	41107	0.000	0.942	0.250	0.953	0.000	0.947	0.252	0.959
	11	41109	-0.407	0.697	0.250	0.820	-0.407	0.698	0.250	0.821
	12	41111	-0.702	0.401	0.250	0.821	-0.703	0.402	0.250	0.822
	13	41121	0.401	-0.702	0.250	0.821	0.402	-0.703	0.250	0.822
	14	41123	0.697	-0.407	0.250	0.820	0.698	-0.407	0.250	0.821
$\tau_{xy} = 0.50 \cdot \tau_{xy,ult}$	15	51101	0.837	0.000	0.500	0.885	0.845	0.000	0.505	0.894
	16	51103	0.756	0.437	0.500	0.920	0.769	0.444	0.509	0.936
	17	51105	0.437	0.756	0.500	0.920	0.444	0.769	0.509	0.936
	18	51107	0.000	0.837	0.500	0.885	0.000	0.845	0.505	0.894
	19	51109	-0.361	0.619	0.500	0.772	-0.363	0.623	0.503	0.778
	20	51111	-0.623	0.356	0.500	0.773	-0.627	0.358	0.503	0.779
	21	51121	0.356	-0.623	0.500	0.773	0.358	-0.627	0.503	0.779
	22	51123	0.619	-0.361	0.500	0.772	0.623	-0.363	0.503	0.778
$\tau_{xy} = 0.75 \cdot \tau_{xy,ult}$	23	61101	0.636	0.000	0.750	0.770	0.641	0.000	0.756	0.775
	24	61103	0.590	0.341	0.749	0.808	0.591	0.341	0.750	0.808
	25	61105	0.341	0.590	0.749	0.808	0.341	0.591	0.750	0.808
	26	61107	0.000	0.636	0.750	0.770	0.000	0.641	0.756	0.775
	27	61109	-0.267	0.457	0.750	0.683	-0.271	0.465	0.764	0.696
	28	61111	-0.456	0.261	0.750	0.681	-0.466	0.266	0.767	0.696
	29	61121	0.261	-0.456	0.750	0.681	0.266	-0.466	0.767	0.696
	30	61123	0.457	-0.267	0.750	0.683	0.465	-0.271	0.764	0.696

Table C.1.: $\alpha = 1$, $\beta = 1$.

		Finite Element Analyses					New Proof			
	data point	run id	$R_{x,ult}$	$R_{y,ult}$	$R_{\tau,\ ult}$	Magnitude	$R_{x,ult}$	$R_{y,ult}$	$R_{\tau,\ ult}$	Magnitude
$\tau_{xy} = 0$	31	12103	0.585	0.338	0.000	0.676	0.580	0.335	0.000	0.670
	32	12105	0.338	0.585	0.000	0.676	0.335	0.580	0.000	0.670
	33	12109	-0.461	0.686	0.000	0.827	-0.461	0.686	0.000	0.827
	34	12111	-0.755	0.380	0.000	0.845	-0.755	0.380	0.000	0.845
	35	12121	0.380	-0.755	0.000	0.845	0.380	-0.755	0.000	0.845
	36	12123	0.686	-0.461	0.000	0.827	0.686	-0.461	0.000	0.827
$\tau_{xy} = 0.25 \cdot \tau_{xy,ult}$	37	42101	0.714	0.000	0.247	0.728	0.709	0.000	0.246	0.723
	38	42103	0.542	0.313	0.247	0.641	0.546	0.315	0.249	0.646
	39	42105	0.313	0.542	0.247	0.641	0.315	0.546	0.249	0.646
	40	42107	0.000	0.714	0.247	0.728	0.000	0.709	0.246	0.723
	41	42109	-0.446	0.663	0.247	0.812	-0.447	0.665	0.248	0.814
	42	42111	-0.730	0.367	0.247	0.829	-0.731	0.368	0.248	0.831
	43	42121	0.367	-0.730	0.247	0.829	0.368	-0.731	0.248	0.831
	44	42123	0.663	-0.446	0.247	0.812	0.665	-0.447	0.248	0.814
$\tau_{xy} = 0.50 \cdot \tau_{xy,ult}$	45	52101	0.612	0.000	0.495	0.675	0.606	0.000	0.490	0.669
	46	52103	0.460	0.266	0.495	0.603	0.463	0.268	0.498	0.607
	47	52105	0.266	0.460	0.495	0.603	0.268	0.463	0.498	0.607
	48	52107	0.000	0.612	0.495	0.675	0.000	0.606	0.490	0.669
	49	52109	-0.397	0.591	0.495	0.767	-0.400	0.595	0.498	0.772
	50	52111	-0.648	0.326	0.495	0.780	-0.654	0.329	0.499	0.787
	51	52121	0.326	-0.648	0.495	0.780	0.329	-0.654	0.499	0.787
	52	52123	0.591	-0.397	0.495	0.767	0.595	-0.400	0.498	0.772
$\tau_{xy} = 0.75 \cdot \tau_{xy,ult}$	53	62101	0.438	0.000	0.742	0.613	0.433	0.000	0.734	0.606
	54	62103	0.329	0.190	0.742	0.573	0.329	0.190	0.741	0.572
	55	62105	0.190	0.329	0.742	0.573	0.190	0.329	0.741	0.572
	56	62107	0.000	0.438	0.742	0.613	0.000	0.433	0.734	0.606
	57	62109	-0.300	0.446	0.742	0.687	-0.294	0.438	0.729	0.675
	58	62111	-0.482	0.242	0.742	0.689	-0.492	0.247	0.758	0.704
	59	62121	0.242	-0.482	0.742	0.689	0.247	-0.492	0.758	0.704
	60	62123	0.446	-0.300	0.742	0.687	0.438	-0.294	0.729	0.675

Table C.2.: $\alpha = 1$, $\beta = 2$.

		Finite Element Analyses					New Proof			
	data point	run id	$R_{x,ult}$	$R_{y,ult}$	$R_{\tau,\ ult}$	Magnitude	$R_{x,ult}$	$R_{y,ult}$	$R_{\tau,\ ult}$	Magnitude
$\tau_{xy} = 0$	61	13103	0.461	0.266	0.000	0.532	0.431	0.249	0.000	0.497
	62	13105	0.266	0.461	0.000	0.532	0.249	0.431	0.000	0.497
	63	13109	-0.495	0.652	0.000	0.819	-0.467	0.614	0.000	0.772
	64	13111	-0.776	0.353	0.000	0.852	-0.776	0.353	0.000	0.852
	65	13121	0.353	-0.776	0.000	0.852	0.353	-0.776	0.000	0.852
	66	13123	0.652	-0.495	0.000	0.819	0.614	-0.467	0.000	0.772
$\tau_{xy} = 0.25 \cdot \tau_{xy,ult}$	67	43101	0.571	0.000	0.232	0.586	0.565	0.000	0.229	0.580
	68	43103	0.412	0.238	0.232	0.494	0.397	0.229	0.223	0.477
	69	43105	0.238	0.412	0.232	0.494	0.229	0.397	0.223	0.477
	70	43107	0.000	0.571	0.232	0.586	0.000	0.565	0.229	0.580
	71	43109	-0.474	0.623	0.232	0.794	-0.434	0.571	0.212	0.727
	72	43111	-0.754	0.343	0.232	0.838	-0.755	0.343	0.232	0.840
	73	43121	0.343	-0.754	0.232	0.838	0.343	-0.755	0.232	0.840
	74	43123	0.623	-0.474	0.232	0.794	0.571	-0.434	0.212	0.727
$\tau_{xy} = 0.50 \cdot \tau_{xy,ult}$	75	53101	0.470	0.000	0.464	0.541	0.466	0.000	0.459	0.536
	76	53103	0.340	0.196	0.463	0.475	0.330	0.190	0.450	0.461
	77	53105	0.196	0.340	0.463	0.475	0.190	0.330	0.450	0.461
	78	53107	0.000	0.470	0.464	0.541	0.000	0.466	0.459	0.536
	79	53109	-0.417	0.548	0.464	0.739	-0.372	0.489	0.414	0.659
	80	53111	-0.681	0.310	0.463	0.794	-0.686	0.312	0.467	0.800
	81	53121	0.310	-0.681	0.463	0.794	0.312	-0.686	0.467	0.800
	82	53123	0.548	-0.417	0.464	0.739	0.489	-0.372	0.414	0.659
$\tau_{xy} = 0.75 \cdot \tau_{xy,ult}$	83	63101	0.303	0.000	0.694	0.502	0.306	0.000	0.701	0.507
	84	63103	0.216	0.125	0.695	0.472	0.217	0.125	0.697	0.474
	85	63105	0.125	0.216	0.695	0.472	0.125	0.217	0.697	0.474
	86	63107	0.000	0.303	0.694	0.502	0.000	0.306	0.701	0.507
	87	63109	-0.306	0.403	0.695	0.646	-0.276	0.363	0.626	0.582
	88	63111	-0.550	0.250	0.695	0.725	-0.554	0.252	0.700	0.731
	89	63121	0.250	-0.550	0.695	0.725	0.252	-0.554	0.700	0.731
	90	63123	0.403	-0.306	0.695	0.646	0.363	-0.276	0.626	0.582

Table C.3.: $\alpha = 1,\ \beta = 3$.

		Finite Element Analyses					New Proof			
	data point	run id	$R_{x,ult}$	$R_{y,ult}$	$R_{\tau,\ ult}$	Magnitude	$R_{x,ult}$	$R_{y,ult}$	$R_{\tau,\ ult}$	Magnitude
$\tau_{xy} = 0$	91	14103	0.386	0.223	0.000	0.446	0.365	0.211	0.000	0.421
	92	14105	0.223	0.386	0.000	0.446	0.211	0.365	0.000	0.421
	93	14109	-0.509	0.628	0.000	0.808	-0.452	0.558	0.000	0.718
	94	14111	-0.786	0.340	0.000	0.856	-0.786	0.340	0.000	0.856
	95	14121	0.340	-0.786	0.000	0.856	0.340	-0.786	0.000	0.856
	96	14123	0.628	-0.509	0.000	0.808	0.558	-0.452	0.000	0.718
$\tau_{xy} = 0.25{\cdot}\tau_{xy,ult}$	97	44101	0.502	0.000	0.208	0.516	0.501	0.000	0.208	0.515
	98	44103	0.342	0.197	0.208	0.413	0.330	0.190	0.201	0.398
	99	44105	0.197	0.342	0.208	0.413	0.190	0.330	0.201	0.398
	100	44107	0.000	0.502	0.208	0.516	0.000	0.501	0.208	0.515
	101	44109	-0.456	0.563	0.208	0.734	-0.412	0.509	0.188	0.664
	102	44111	-0.768	0.332	0.208	0.845	-0.769	0.332	0.208	0.846
	103	44121	0.332	-0.768	0.208	0.845	0.332	-0.769	0.208	0.846
	104	44123	0.563	-0.456	0.208	0.734	0.509	-0.412	0.188	0.664
$\tau_{xy} = 0.50{\cdot}\tau_{xy,ult}$	105	54101	0.393	0.000	0.416	0.461	0.397	0.000	0.420	0.466
	106	54103	0.277	0.160	0.416	0.400	0.267	0.154	0.401	0.386
	107	54105	0.160	0.277	0.416	0.400	0.154	0.267	0.401	0.386
	108	54107	0.000	0.393	0.416	0.461	0.000	0.397	0.420	0.466
	109	54109	-0.405	0.500	0.416	0.687	-0.350	0.431	0.359	0.593
	110	54111	-0.713	0.308	0.416	0.813	-0.715	0.309	0.417	0.815
	111	54121	0.308	-0.713	0.416	0.813	0.309	-0.715	0.417	0.815
	112	54123	0.500	-0.405	0.416	0.687	0.431	-0.350	0.359	0.593
$\tau_{xy} = 0.75{\cdot}\tau_{xy,ult}$	113	64101	0.232	0.000	0.624	0.429	0.240	0.000	0.644	0.443
	114	64103	0.162	0.094	0.624	0.406	0.164	0.095	0.631	0.411
	115	64105	0.094	0.162	0.624	0.406	0.095	0.164	0.631	0.411
	116	64107	0.000	0.232	0.624	0.429	0.000	0.240	0.644	0.443
	117	64109	-0.294	0.362	0.624	0.589	-0.257	0.317	0.545	0.515
	118	64111	-0.613	0.265	0.623	0.758	-0.607	0.262	0.617	0.751
	119	64121	0.265	-0.613	0.623	0.758	0.262	-0.607	0.617	0.751
	120	64123	0.362	-0.294	0.624	0.589	0.317	-0.257	0.545	0.515

Table C.4.: $\alpha = 1$, $\beta = 4$.

		Finite Element Analyses					New Proof			
	data point	run id	$R_{x,ult}$	$R_{y,ult}$	$R_{\tau,\ ult}$	Magnitude	$R_{x,ult}$	$R_{y,ult}$	$R_{\tau,\ ult}$	Magnitude
$\tau_{xy} = 0$	121	11303	0.953	0.458	0.000	1.057	0.920	0.442	0.000	1.021
	122	11305	0.459	0.646	0.000	0.792	0.477	0.672	0.000	0.824
	123	11309	-0.433	0.602	0.000	0.742	-0.481	0.669	0.000	0.824
	124	11311	-0.765	0.364	0.000	0.848	-0.767	0.365	0.000	0.849
	125	11321	0.415	-0.726	0.000	0.836	0.415	-0.726	0.000	0.836
	126	11323	0.721	-0.421	0.000	0.835	0.721	-0.421	0.000	0.835
$\tau_{xy} = 0.25 \cdot \tau_{xy,ult}$	127	41301	0.946	0.000	0.250	0.957	0.948	0.000	0.251	0.959
	128	41303	0.916	0.440	0.250	1.027	0.893	0.429	0.244	1.000
	129	41305	0.446	0.627	0.250	0.783	0.461	0.649	0.258	0.810
	130	41307	0.000	0.654	0.250	0.670	0.000	0.650	0.249	0.666
	131	41309	-0.421	0.586	0.250	0.736	-0.462	0.643	0.274	0.808
	132	41311	-0.742	0.353	0.250	0.834	-0.742	0.353	0.250	0.834
	133	41321	0.401	-0.702	0.250	0.821	0.402	-0.703	0.250	0.822
	134	41323	0.697	-0.407	0.250	0.820	0.698	-0.407	0.250	0.821
$\tau_{xy} = 0.50 \cdot \tau_{xy,ult}$	135	51301	0.844	0.000	0.500	0.892	0.847	0.000	0.502	0.896
	136	51303	0.810	0.389	0.500	0.944	0.800	0.385	0.494	0.933
	137	51305	0.415	0.584	0.500	0.772	0.414	0.582	0.498	0.770
	138	51307	0.000	0.606	0.500	0.671	0.000	0.587	0.485	0.651
	139	51309	-0.385	0.535	0.500	0.719	-0.408	0.567	0.530	0.763
	140	51311	-0.663	0.315	0.500	0.789	-0.664	0.316	0.500	0.790
	141	51321	0.356	-0.623	0.500	0.773	0.358	-0.627	0.503	0.779
	142	51323	0.619	-0.361	0.500	0.772	0.623	-0.363	0.503	0.778
$\tau_{xy} = 0.75 \cdot \tau_{xy,ult}$	143	61301	0.644	0.000	0.750	0.776	0.646	0.000	0.752	0.778
	144	61303	0.625	0.300	0.750	0.818	0.618	0.297	0.741	0.808
	145	61305	0.357	0.502	0.750	0.753	0.337	0.474	0.708	0.711
	146	61307	0.000	0.514	0.750	0.672	0.000	0.480	0.700	0.627
	147	61309	-0.305	0.424	0.750	0.678	-0.310	0.432	0.764	0.691
	148	61311	-0.499	0.237	0.750	0.702	-0.502	0.239	0.755	0.707
	149	61321	0.261	-0.456	0.750	0.681	0.266	-0.466	0.766	0.696
	150	61323	0.457	-0.266	0.750	0.683	0.465	-0.271	0.764	0.696

Table C.5.: $\alpha = 3,\ \beta = 1$.

		Finite Element Analyses					New Proof			
	data point	run id	$R_{x,ult}$	$R_{y,ult}$	$R_{\tau,\ ult}$	Magnitude	$R_{x,ult}$	$R_{y,ult}$	$R_{\tau,\ ult}$	Magnitude
$\tau_{xy} = 0$	151	12303	0.605	0.243	0.000	0.652	0.572	0.230	0.000	0.617
	152	12305	0.293	0.331	0.000	0.442	0.298	0.337	0.000	0.450
	153	12309	-0.411	0.375	0.000	0.556	-0.407	0.371	0.000	0.551
	154	12311	-0.809	0.272	0.000	0.854	-0.831	0.279	0.000	0.877
	155	12321	0.380	-0.754	0.000	0.845	0.380	-0.754	0.000	0.845
	156	12323	0.686	-0.461	0.000	0.827	0.686	-0.461	0.000	0.827
$\tau_{xy} = 0.25{\cdot}\tau_{xy,ult}$	157	42301	0.721	0.000	0.244	0.735	0.711	0.000	0.241	0.725
	158	42303	0.580	0.233	0.244	0.641	0.542	0.218	0.228	0.599
	159	42305	0.278	0.314	0.244	0.442	0.280	0.317	0.247	0.447
	160	42307	0.000	0.357	0.244	0.384	0.000	0.350	0.240	0.377
	161	42309	-0.397	0.362	0.244	0.555	-0.384	0.351	0.237	0.538
	162	42311	-0.784	0.263	0.244	0.839	-0.804	0.270	0.251	0.861
	163	42321	0.368	-0.730	0.244	0.830	0.368	-0.731	0.245	0.831
	164	42323	0.664	-0.446	0.244	0.812	0.666	-0.447	0.245	0.814
$\tau_{xy} = 0.50{\cdot}\tau_{xy,ult}$	165	52301	0.617	0.000	0.488	0.679	0.609	0.000	0.482	0.669
	166	52303	0.497	0.200	0.489	0.606	0.470	0.189	0.461	0.572
	167	52305	0.250	0.282	0.488	0.471	0.242	0.274	0.474	0.456
	168	52307	0.000	0.320	0.489	0.427	0.000	0.304	0.464	0.405
	169	52309	-0.358	0.327	0.489	0.561	-0.335	0.306	0.457	0.525
	170	52311	-0.705	0.237	0.489	0.796	-0.720	0.242	0.499	0.812
	171	52321	0.329	-0.653	0.489	0.784	0.331	-0.657	0.492	0.788
	172	52323	0.596	-0.400	0.489	0.772	0.598	-0.402	0.490	0.774
$\tau_{xy} = 0.75{\cdot}\tau_{xy,ult}$	173	62301	0.428	0.000	0.733	0.602	0.428	0.000	0.732	0.601
	174	62303	0.338	0.136	0.733	0.558	0.332	0.134	0.721	0.549
	175	62305	0.193	0.218	0.733	0.514	0.183	0.206	0.694	0.486
	176	62307	0.000	0.265	0.732	0.499	0.000	0.240	0.663	0.452
	177	62309	-0.293	0.267	0.733	0.580	-0.264	0.241	0.660	0.523
	178	62311	-0.550	0.185	0.733	0.719	-0.557	0.187	0.742	0.727
	179	62321	0.248	-0.493	0.733	0.695	0.253	-0.502	0.746	0.708
	180	62323	0.458	-0.308	0.733	0.696	0.446	-0.299	0.713	0.676

Table C.6.: $\alpha = 3$, $\beta = 2$.

		Finite Element Analyses					New Proof			
	data point	run id	$R_{x,ult}$	$R_{y,ult}$	$R_{\tau,\ ult}$	Magnitude	$R_{x,ult}$	$R_{y,ult}$	$R_{\tau,\ ult}$	Magnitude
$\tau_{xy} = 0$	181	13303	0.434	0.160	0.000	0.462	0.412	0.152	0.000	0.439
	182	13305	0.222	0.227	0.000	0.317	0.218	0.223	0.000	0.311
	183	13309	-0.411	0.281	0.000	0.498	-0.384	0.262	0.000	0.465
	184	13311	-0.829	0.214	0.000	0.856	-0.869	0.224	0.000	0.897
	185	13321	0.352	-0.776	0.000	0.852	0.352	-0.776	0.000	0.852
	186	13323	0.646	-0.493	0.000	0.813	0.611	-0.467	0.000	0.769
$\tau_{xy} = 0.25 \cdot \tau_{xy,ult}$	187	43301	0.537	0.000	0.214	0.551	0.558	0.000	0.223	0.573
	188	43303	0.403	0.149	0.214	0.447	0.381	0.141	0.202	0.422
	189	43305	0.202	0.207	0.214	0.314	0.200	0.205	0.212	0.311
	190	43307	0.000	0.246	0.214	0.276	0.000	0.241	0.210	0.270
	191	43309	-0.393	0.268	0.214	0.492	-0.357	0.244	0.194	0.447
	192	43311	-0.805	0.208	0.214	0.841	-0.847	0.218	0.225	0.884
	193	43321	0.343	-0.758	0.214	0.841	0.344	-0.758	0.214	0.842
	194	43323	0.598	-0.456	0.214	0.762	0.566	-0.432	0.203	0.721
$\tau_{xy} = 0.50 \cdot \tau_{xy,ult}$	195	53301	0.450	0.000	0.429	0.513	0.457	0.000	0.436	0.522
	196	53303	0.361	0.133	0.429	0.457	0.326	0.120	0.387	0.413
	197	53305	0.178	0.181	0.429	0.354	0.169	0.172	0.407	0.337
	198	53307	0.000	0.214	0.428	0.327	0.000	0.203	0.407	0.310
	199	53309	-0.348	0.238	0.429	0.489	-0.307	0.210	0.378	0.431
	200	53311	-0.735	0.190	0.428	0.799	-0.755	0.195	0.440	0.820
	201	53321	0.316	-0.697	0.429	0.805	0.318	-0.701	0.431	0.809
	202	53323	0.538	-0.410	0.428	0.720	0.485	-0.370	0.386	0.649
$\tau_{xy} = 0.75 \cdot \tau_{xy,ult}$	203	63301	0.283	0.000	0.643	0.467	0.291	0.000	0.662	0.481
	204	63303	0.211	0.078	0.643	0.434	0.210	0.078	0.640	0.432
	205	63305	0.112	0.114	0.643	0.404	0.111	0.114	0.639	0.402
	206	63307	0.000	0.168	0.643	0.407	0.000	0.153	0.586	0.371
	207	63309	-0.277	0.189	0.643	0.500	-0.239	0.163	0.554	0.431
	208	63311	-0.611	0.158	0.643	0.732	-0.571	0.147	0.601	0.684
	209	63321	0.267	-0.590	0.643	0.746	0.269	-0.593	0.646	0.750
	210	63323	0.419	-0.320	0.642	0.645	0.370	-0.282	0.567	0.569

Table C.7.: $\alpha = 3$, $\beta = 3$.

		Finite Element Analyses					New Proof			
	data point	run id	$R_{x,ult}$	$R_{y,ult}$	$R_{\tau,\ ult}$	Magnitude	$R_{x,ult}$	$R_{y,ult}$	$R_{\tau,\ ult}$	Magnitude
$\tau_{xy} = 0$	211	14303	0.345	0.123	0.000	0.366	0.336	0.120	0.000	0.357
	212	14305	0.179	0.175	0.000	0.251	0.180	0.176	0.000	0.252
	213	14309	-0.415	0.241	0.000	0.480	-0.376	0.219	0.000	0.435
	214	14311	-0.843	0.187	0.000	0.864	-0.887	0.197	0.000	0.908
	215	14321	0.335	-0.789	0.000	0.858	0.335	-0.789	0.000	0.858
	216	14323	0.512	-0.424	0.000	0.665	0.541	-0.448	0.000	0.702
$\tau_{xy} = 0.25{\cdot}\tau_{xy,ult}$	217	44301	0.438	0.000	0.180	0.450	0.479	0.000	0.196	0.492
	218	44303	0.315	0.112	0.180	0.350	0.304	0.108	0.173	0.338
	219	44305	0.161	0.157	0.180	0.247	0.162	0.158	0.181	0.249
	220	44307	0.000	0.193	0.180	0.219	0.000	0.196	0.182	0.223
	221	44309	-0.386	0.225	0.180	0.459	-0.344	0.200	0.160	0.409
	222	44311	-0.820	0.182	0.180	0.846	-0.870	0.194	0.191	0.899
	223	44321	0.329	-0.776	0.180	0.850	0.330	-0.777	0.180	0.850
	224	44323	0.499	-0.413	0.180	0.656	0.488	-0.404	0.176	0.641
$\tau_{xy} = 0.50{\cdot}\tau_{xy,ult}$	225	54301	0.361	0.000	0.359	0.416	0.377	0.000	0.376	0.435
	226	54303	0.281	0.100	0.360	0.363	0.254	0.090	0.325	0.329
	227	54305	0.140	0.136	0.359	0.285	0.133	0.130	0.342	0.271
	228	54307	0.000	0.161	0.359	0.263	0.000	0.159	0.353	0.258
	229	54309	-0.330	0.192	0.359	0.434	-0.289	0.168	0.315	0.381
	230	54311	-0.757	0.168	0.359	0.803	-0.724	0.161	0.344	0.768
	231	54321	0.312	-0.735	0.359	0.825	0.313	-0.737	0.360	0.827
	232	54323	0.454	-0.376	0.359	0.624	0.410	-0.339	0.325	0.564
$\tau_{xy} = 0.75{\cdot}\tau_{xy,ult}$	233	64301	0.230	0.000	0.538	0.386	0.236	0.000	0.553	0.397
	234	64303	0.155	0.055	0.538	0.351	0.155	0.055	0.539	0.352
	235	64305	0.080	0.078	0.539	0.331	0.081	0.079	0.545	0.334
	236	64307	0.000	0.102	0.538	0.327	0.000	0.102	0.536	0.326
	237	64309	-0.251	0.146	0.539	0.426	-0.217	0.126	0.466	0.368
	238	64311	-0.643	0.143	0.539	0.728	-0.561	0.125	0.470	0.635
	239	64321	0.282	-0.663	0.539	0.785	0.270	-0.635	0.516	0.752
	240	64323	0.369	-0.306	0.539	0.572	0.316	-0.261	0.461	0.489

Table C.8.: $\alpha = 3$, $\beta = 4$.

		Finite Element Analyses					New Proof			
	data point	run id	$R_{x,ult}$	$R_{y,ult}$	$R_{\tau,\ ult}$	Magnitude	$R_{x,ult}$	$R_{y,ult}$	$R_{\tau,\ ult}$	Magnitude
$\tau_{xy} = 0$	241	11503	0.966	0.441	0.000	1.062	0.938	0.428	0.000	1.031
	242	11505	0.455	0.602	0.000	0.755	0.460	0.608	0.000	0.762
	243	11509	-0.423	0.552	0.000	0.696	-0.466	0.608	0.000	0.766
	244	11511	-0.771	0.349	0.000	0.847	-0.777	0.351	0.000	0.853
	245	11521	0.415	-0.726	0.000	0.836	0.415	-0.726	0.000	0.836
	246	11523	0.721	-0.420	0.000	0.835	0.721	-0.420	0.000	0.835
$\tau_{xy} = 0.25 \cdot \tau_{xy,ult}$	247	41501	0.947	0.000	0.250	0.958	0.949	0.000	0.251	0.960
	248	41503	0.929	0.424	0.250	1.031	0.909	0.415	0.245	1.009
	249	41505	0.448	0.591	0.250	0.756	0.445	0.589	0.249	0.752
	250	41507	0.000	0.596	0.250	0.613	0.000	0.589	0.247	0.606
	251	41509	-0.414	0.540	0.250	0.696	-0.448	0.585	0.271	0.753
	252	41511	-0.747	0.338	0.250	0.833	-0.752	0.340	0.251	0.838
	253	41521	0.401	-0.702	0.250	0.821	0.402	-0.703	0.250	0.822
	254	41523	0.697	-0.406	0.250	0.820	0.698	-0.407	0.250	0.821
$\tau_{xy} = 0.50 \cdot \tau_{xy,ult}$	255	51501	0.844	0.000	0.500	0.892	0.848	0.000	0.502	0.896
	256	51503	0.820	0.374	0.500	0.947	0.814	0.372	0.497	0.940
	257	51505	0.423	0.559	0.500	0.758	0.404	0.534	0.477	0.724
	258	51507	0.000	0.563	0.500	0.633	0.000	0.535	0.475	0.601
	259	51509	-0.384	0.501	0.500	0.694	-0.398	0.519	0.519	0.720
	260	51511	-0.669	0.303	0.500	0.789	-0.672	0.304	0.502	0.792
	261	51521	0.356	-0.623	0.500	0.773	0.359	-0.627	0.503	0.779
	262	51523	0.619	-0.361	0.500	0.772	0.623	-0.363	0.503	0.778
$\tau_{xy} = 0.75 \cdot \tau_{xy,ult}$	263	61501	0.645	0.000	0.750	0.777	0.647	0.000	0.752	0.779
	264	61503	0.638	0.291	0.750	0.824	0.630	0.288	0.741	0.814
	265	61505	0.375	0.496	0.749	0.757	0.339	0.448	0.676	0.684
	266	61507	0.000	0.494	0.750	0.657	0.000	0.447	0.678	0.594
	267	61509	-0.313	0.409	0.750	0.673	-0.311	0.406	0.744	0.668
	268	61511	-0.514	0.232	0.750	0.711	-0.514	0.232	0.750	0.711
	269	61521	0.261	-0.456	0.750	0.681	0.266	-0.466	0.767	0.696
	270	61523	0.456	-0.266	0.750	0.683	0.465	-0.271	0.764	0.696

Table C.9.: $\alpha = 5,\ \beta = 1$.

		Finite Element Analyses					New Proof			
	data point	run id	$R_{x,ult}$	$R_{y,ult}$	$R_{\tau,\ ult}$	Magnitude	$R_{x,ult}$	$R_{y,ult}$	$R_{\tau,\ ult}$	Magnitude
$\tau_{xy} = 0$	271	12503	0.619	0.216	0.000	0.656	0.582	0.203	0.000	0.617
	272	12505	0.286	0.273	0.000	0.395	0.296	0.284	0.000	0.410
	273	12509	-0.394	0.300	0.000	0.495	-0.391	0.298	0.000	0.492
	274	12511	-0.802	0.229	0.000	0.834	-0.855	0.244	0.000	0.890
	275	12521	0.380	-0.754	0.000	0.845	0.380	-0.754	0.000	0.845
	276	12523	0.687	-0.461	0.000	0.827	0.687	-0.461	0.000	0.827
$\tau_{xy} = 0.25{\cdot}\tau_{xy,ult}$	277	42501	0.721	0.000	0.244	0.734	0.712	0.000	0.241	0.725
	278	42503	0.599	0.210	0.244	0.650	0.552	0.193	0.224	0.599
	279	42505	0.275	0.263	0.244	0.406	0.279	0.266	0.247	0.411
	280	42507	0.000	0.288	0.244	0.321	0.000	0.281	0.237	0.312
	281	42509	-0.383	0.291	0.244	0.501	-0.369	0.281	0.235	0.484
	282	42511	-0.780	0.223	0.244	0.823	-0.826	0.236	0.258	0.872
	283	42521	0.368	-0.731	0.244	0.830	0.369	-0.731	0.244	0.831
	284	42523	0.666	-0.447	0.244	0.814	0.666	-0.447	0.244	0.814
$\tau_{xy} = 0.50{\cdot}\tau_{xy,ult}$	285	52501	0.616	0.000	0.487	0.677	0.609	0.000	0.481	0.669
	286	52503	0.507	0.177	0.487	0.607	0.478	0.167	0.459	0.572
	287	52505	0.254	0.243	0.487	0.450	0.242	0.232	0.465	0.429
	288	52507	0.000	0.266	0.487	0.387	0.000	0.246	0.451	0.358
	289	52509	-0.353	0.268	0.487	0.525	-0.324	0.247	0.448	0.483
	290	52511	-0.709	0.202	0.487	0.789	-0.737	0.210	0.507	0.821
	291	52521	0.329	-0.653	0.487	0.784	0.331	-0.657	0.490	0.789
	292	52523	0.597	-0.401	0.487	0.772	0.599	-0.402	0.489	0.775
$\tau_{xy} = 0.75{\cdot}\tau_{xy,ult}$	293	62501	0.428	0.000	0.731	0.601	0.428	0.000	0.730	0.601
	294	62503	0.327	0.114	0.729	0.545	0.328	0.115	0.732	0.547
	295	62505	0.195	0.187	0.730	0.500	0.183	0.175	0.686	0.470
	296	62507	0.000	0.231	0.731	0.481	0.000	0.200	0.635	0.418
	297	62509	-0.301	0.229	0.731	0.566	-0.262	0.200	0.637	0.494
	298	62511	-0.564	0.161	0.731	0.722	-0.573	0.163	0.743	0.734
	299	62521	0.249	-0.493	0.731	0.695	0.253	-0.503	0.745	0.709
	300	62523	0.461	-0.309	0.731	0.697	0.447	-0.300	0.709	0.676

Table C.10.: $\alpha = 5$, $\beta = 2$.

		Finite Element Analyses					New Proof			
	data point	run id	$R_{x,ult}$	$R_{y,ult}$	$R_{\tau,\ ult}$	Magnitude	$R_{x,ult}$	$R_{y,ult}$	$R_{\tau,\ ult}$	Magnitude
$\tau_{xy} = 0$	301	13503	0.436	0.130	0.000	0.455	0.418	0.125	0.000	0.436
	302	13505	0.215	0.172	0.000	0.276	0.217	0.173	0.000	0.278
	303	13509	-0.393	0.204	0.000	0.443	-0.373	0.193	0.000	0.419
	304	13511	-0.818	0.163	0.000	0.834	-0.898	0.179	0.000	0.916
	305	13521	0.352	-0.776	0.000	0.852	0.352	-0.776	0.000	0.852
	306	13523	0.647	-0.494	0.000	0.814	0.611	-0.467	0.000	0.769
$\tau_{xy} = 0.25 \cdot \tau_{xy,ult}$	307	43501	0.578	0.000	0.205	0.590	0.563	0.000	0.199	0.575
	308	43503	0.412	0.123	0.205	0.446	0.387	0.115	0.192	0.419
	309	43505	0.200	0.160	0.205	0.282	0.199	0.159	0.204	0.281
	310	43507	0.000	0.184	0.205	0.218	0.000	0.178	0.198	0.211
	311	43509	-0.380	0.196	0.205	0.444	-0.346	0.179	0.187	0.404
	312	43511	-0.798	0.159	0.205	0.823	-0.875	0.175	0.224	0.902
	313	43521	0.344	-0.759	0.205	0.842	0.345	-0.760	0.205	0.843
	314	43523	0.614	-0.469	0.205	0.782	0.567	-0.433	0.189	0.722
$\tau_{xy} = 0.50 \cdot \tau_{xy,ult}$	315	53501	0.474	0.000	0.410	0.530	0.465	0.000	0.402	0.520
	316	53503	0.371	0.111	0.409	0.454	0.332	0.099	0.366	0.406
	317	53505	0.182	0.145	0.409	0.331	0.169	0.135	0.382	0.309
	318	53507	0.000	0.165	0.410	0.288	0.000	0.151	0.376	0.265
	319	53509	-0.346	0.179	0.409	0.455	-0.300	0.155	0.355	0.395
	320	53511	-0.740	0.148	0.409	0.790	-0.733	0.146	0.405	0.783
	321	53521	0.320	-0.705	0.409	0.809	0.321	-0.708	0.411	0.813
	322	53523	0.562	-0.429	0.409	0.746	0.491	-0.375	0.357	0.651
$\tau_{xy} = 0.75 \cdot \tau_{xy,ult}$	323	63501	0.296	0.000	0.614	0.461	0.300	0.000	0.623	0.469
	324	63503	0.207	0.062	0.614	0.415	0.209	0.062	0.618	0.418
	325	63505	0.124	0.099	0.614	0.388	0.118	0.094	0.587	0.371
	326	63507	0.000	0.140	0.614	0.381	0.000	0.120	0.528	0.328
	327	63509	-0.294	0.152	0.614	0.485	-0.242	0.125	0.506	0.399
	328	63511	-0.638	0.127	0.614	0.741	-0.573	0.114	0.551	0.665
	329	63521	0.274	-0.604	0.614	0.752	0.276	-0.609	0.620	0.759
	330	63523	0.464	-0.354	0.614	0.683	0.390	-0.298	0.516	0.574

Table C.11.: $\alpha = 5$, $\beta = 3$.

		Finite Element Analyses					New Proof			
	data point	run id	$R_{x,ult}$	$R_{y,ult}$	$R_{\tau,\ ult}$	Magnitude	$R_{x,ult}$	$R_{y,ult}$	$R_{\tau,\ ult}$	Magnitude
$\tau_{xy} = 0$	331	14503	0.342	0.094	0.000	0.354	0.339	0.093	0.000	0.352
	332	14505	0.173	0.126	0.000	0.214	0.179	0.130	0.000	0.221
	333	14509	-0.398	0.165	0.000	0.430	-0.366	0.152	0.000	0.396
	334	14511	-0.832	0.134	0.000	0.843	-0.918	0.148	0.000	0.930
	335	14521	0.334	-0.790	0.000	0.858	0.334	-0.790	0.000	0.858
	336	14523	0.509	-0.424	0.000	0.662	0.537	-0.447	0.000	0.699
$\tau_{xy} = 0.25{\cdot}\tau_{xy,ult}$	337	44501	0.503	0.000	0.166	0.512	0.485	0.000	0.160	0.494
	338	44503	0.318	0.087	0.166	0.343	0.306	0.084	0.160	0.331
	339	44505	0.158	0.115	0.166	0.218	0.160	0.117	0.168	0.221
	340	44507	0.000	0.137	0.166	0.167	0.000	0.136	0.165	0.166
	341	44509	-0.375	0.155	0.166	0.417	-0.335	0.139	0.148	0.372
	342	44511	-0.812	0.131	0.166	0.828	-0.842	0.135	0.172	0.858
	343	44521	0.329	-0.779	0.166	0.851	0.329	-0.779	0.166	0.851
	344	44523	0.497	-0.413	0.166	0.653	0.484	-0.403	0.162	0.637
$\tau_{xy} = 0.50{\cdot}\tau_{xy,ult}$	345	54501	0.406	0.000	0.332	0.449	0.393	0.000	0.321	0.434
	346	54503	0.291	0.080	0.333	0.358	0.259	0.071	0.296	0.318
	347	54505	0.143	0.104	0.333	0.261	0.133	0.097	0.310	0.244
	348	54507	0.000	0.120	0.332	0.226	0.000	0.113	0.312	0.213
	349	54509	-0.332	0.137	0.332	0.407	-0.284	0.118	0.285	0.349
	350	54511	-0.760	0.122	0.332	0.793	-0.705	0.113	0.308	0.736
	351	54521	0.315	-0.744	0.332	0.830	0.315	-0.745	0.333	0.831
	352	54523	0.468	-0.389	0.332	0.638	0.412	-0.343	0.293	0.562
$\tau_{xy} = 0.75{\cdot}\tau_{xy,ult}$	353	64501	0.247	0.000	0.498	0.380	0.248	0.000	0.498	0.380
	354	64503	0.161	0.044	0.499	0.333	0.159	0.044	0.494	0.329
	355	64505	0.094	0.069	0.498	0.310	0.090	0.066	0.475	0.296
	356	64507	0.000	0.098	0.499	0.304	0.000	0.086	0.437	0.267
	357	64509	-0.275	0.114	0.499	0.414	-0.225	0.093	0.407	0.338
	358	64511	-0.674	0.108	0.499	0.741	-0.564	0.091	0.417	0.620
	359	64521	0.289	-0.683	0.499	0.795	0.273	-0.646	0.472	0.752
	360	64523	0.399	-0.332	0.499	0.593	0.327	-0.273	0.409	0.487

Table C.12.: $\alpha = 5$, $\beta = 4$.

C.2. Graphical Results

In this section the results of finite element analyses used in the evaluation of proofs are plotted. Results obtained with the new proof are also included.

Note: In this appendix all graphical results of the new proof are shown for fixed levels of shear equal to those of the finite element analyses (i.e. $\tau_{xy} = 0.25 \cdot \tau_{xy,ult}$, $\tau_{xy} = 0.50 \cdot \tau_{xy,ult}$ *or* $\tau_{xy} = 0.75 \cdot \tau_{xy,ult}$*). Accordingly, any differences between the new proof and finite element analyses are shown fully in the x-y planes, but are therefore magnified compared to tabular results where the unit vectors for the new proof and finite element analyses are the same (i.e. the levels of shear are not fixed).*

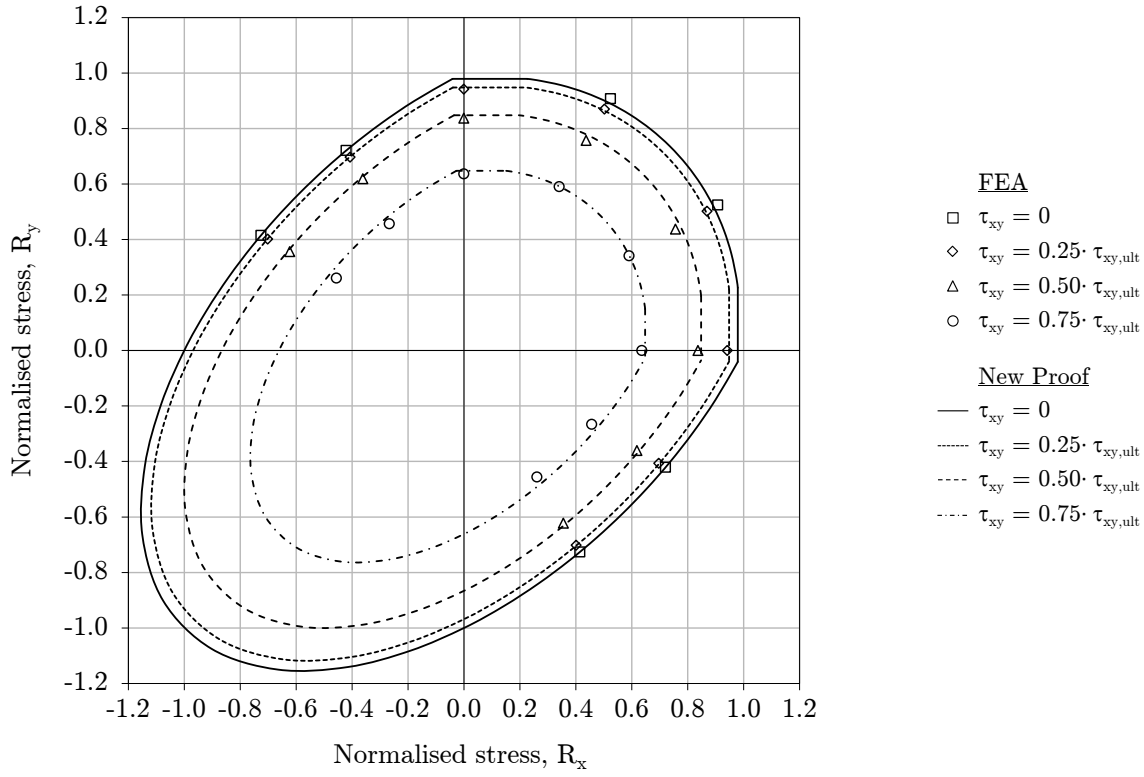

Figure C.1.: $\alpha = 1$, $\beta = 1$.

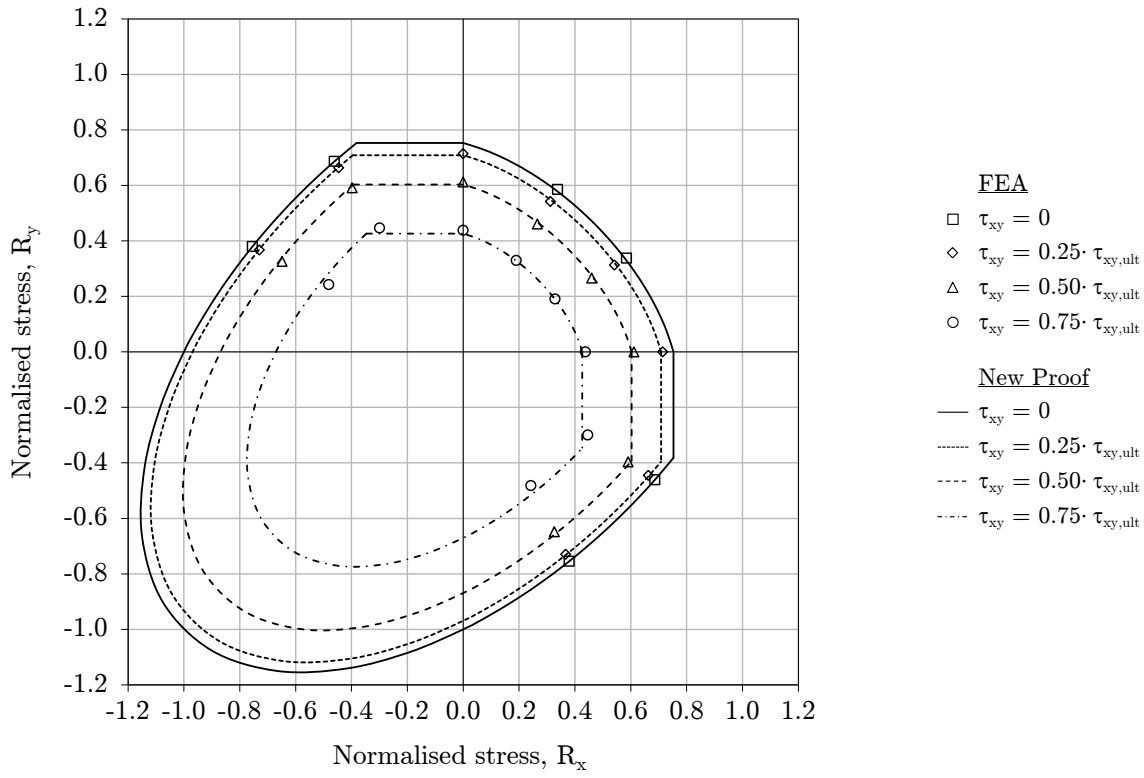

Figure C.2.: $\alpha = 1$, $\beta = 2$.

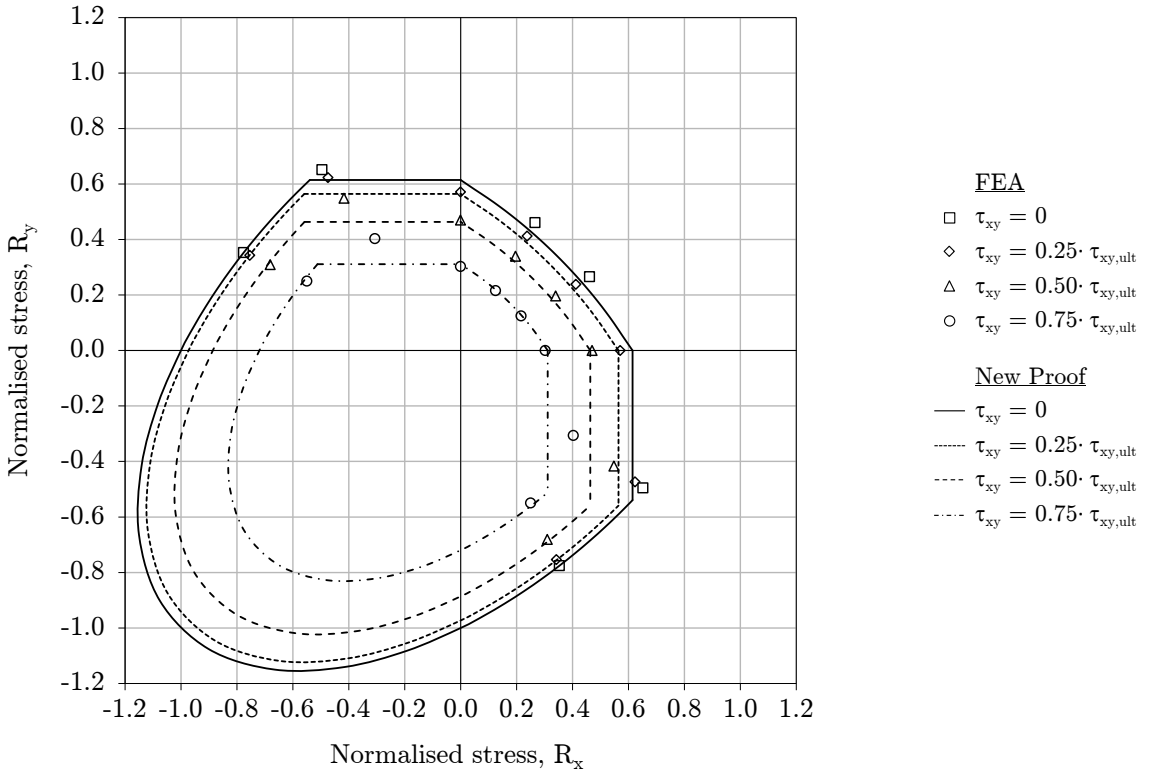

Figure C.3.: $\alpha = 1$, $\beta = 3$.

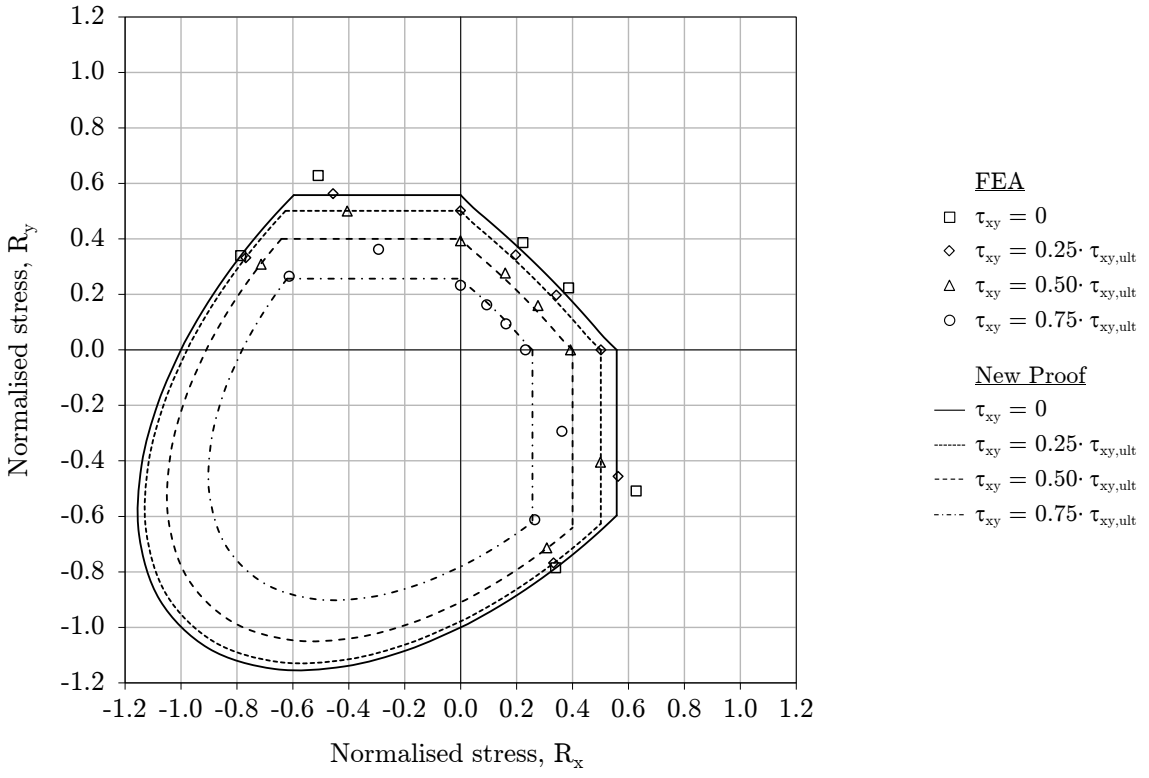

Figure C.4.: $\alpha = 1$, $\beta = 4$.

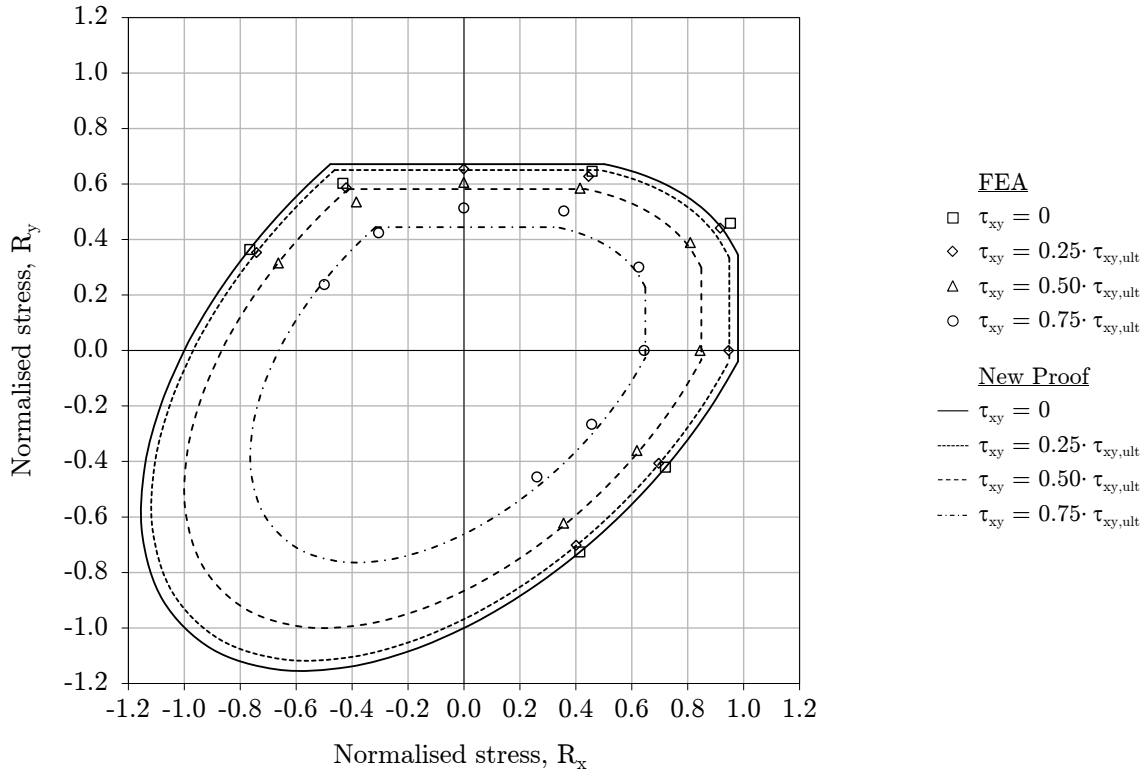

Figure C.5.: $\alpha = 3$, $\beta = 1$.

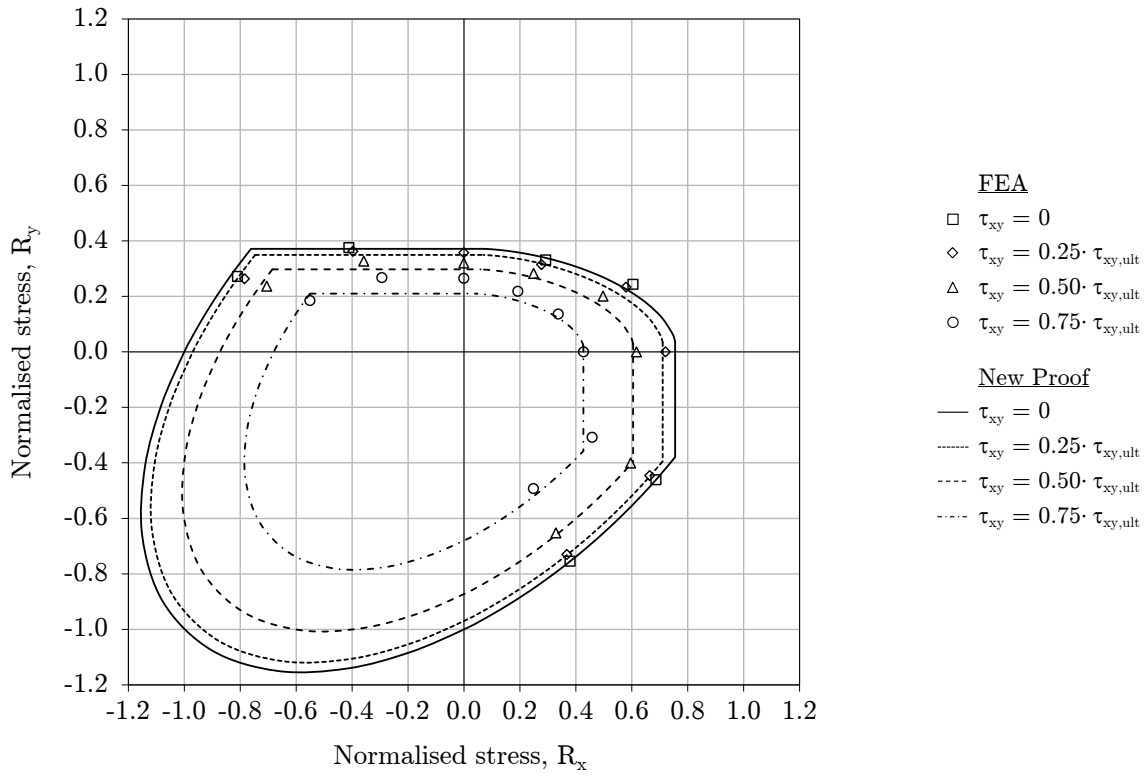

Figure C.6.: $\alpha = 3$, $\beta = 2$.

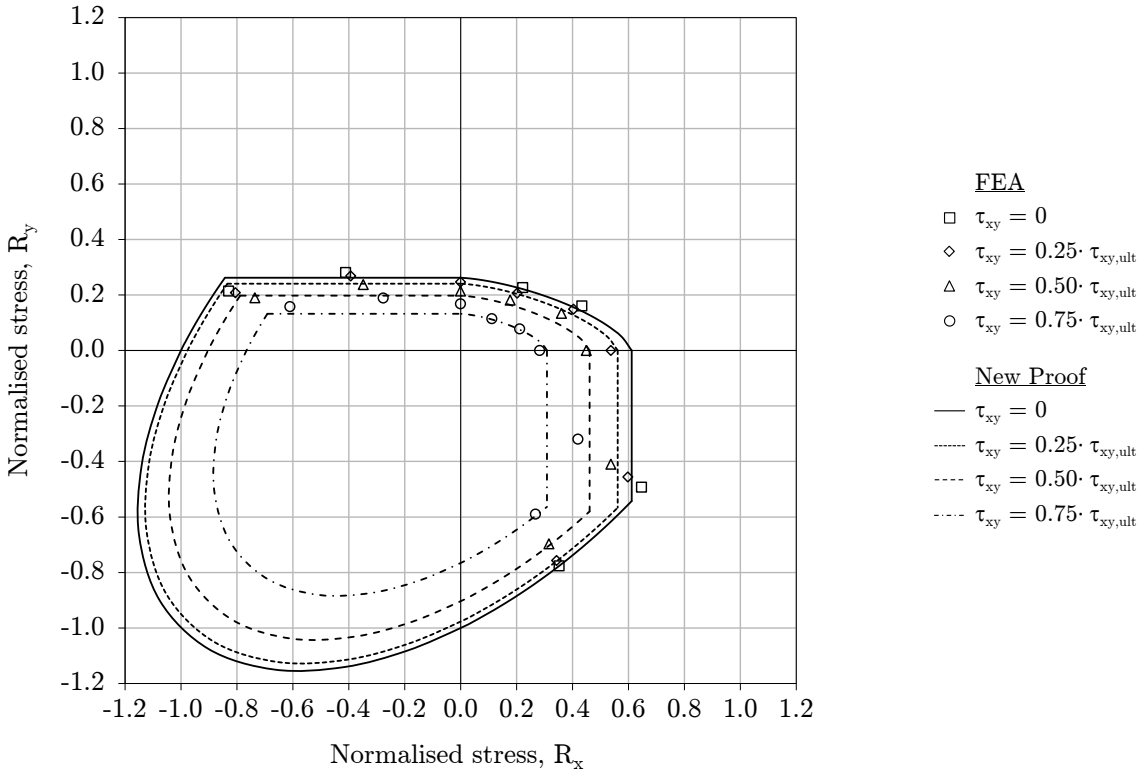

Figure C.7.: $\alpha = 3$, $\beta = 3$.

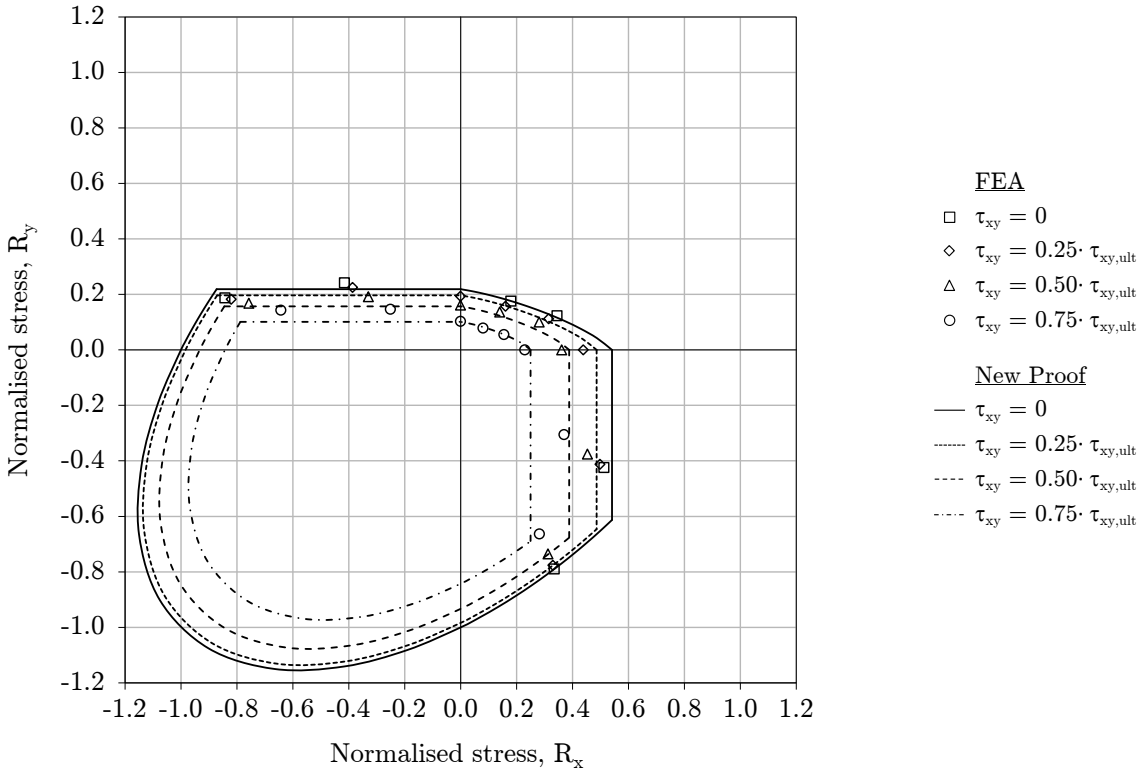

Figure C.8.: $\alpha = 3$, $\beta = 4$.

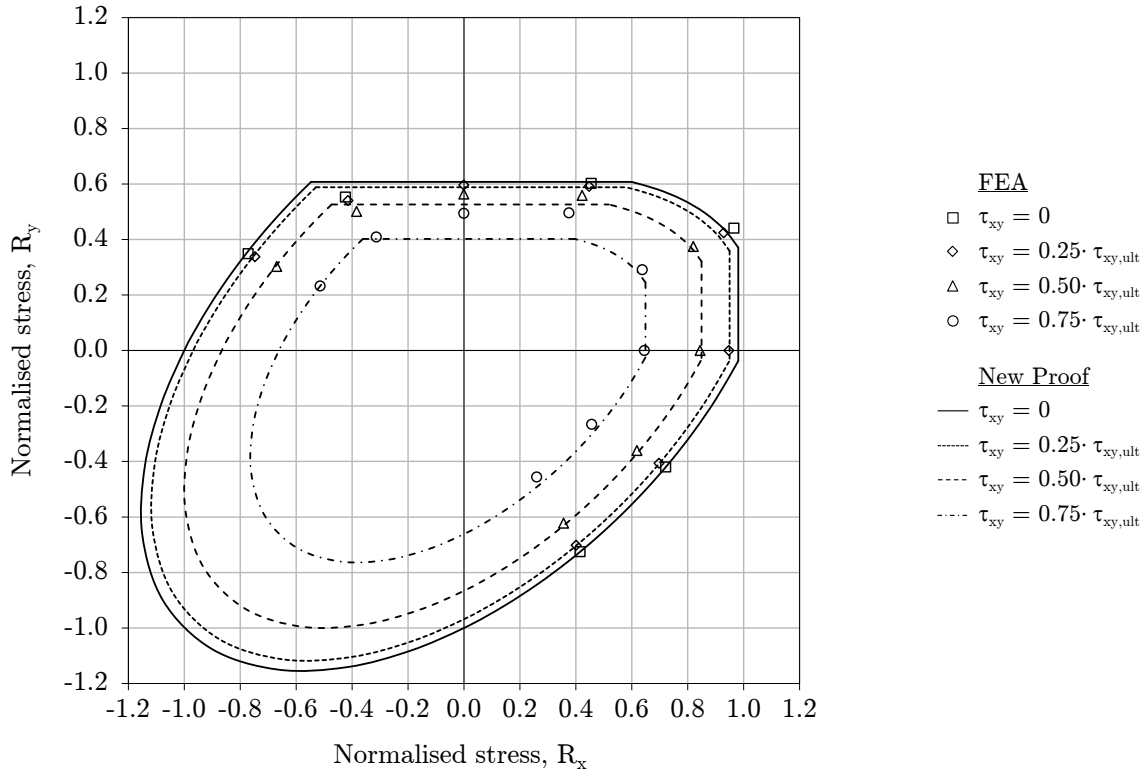

Figure C.9.: $\alpha = 5,\ \beta = 1$.

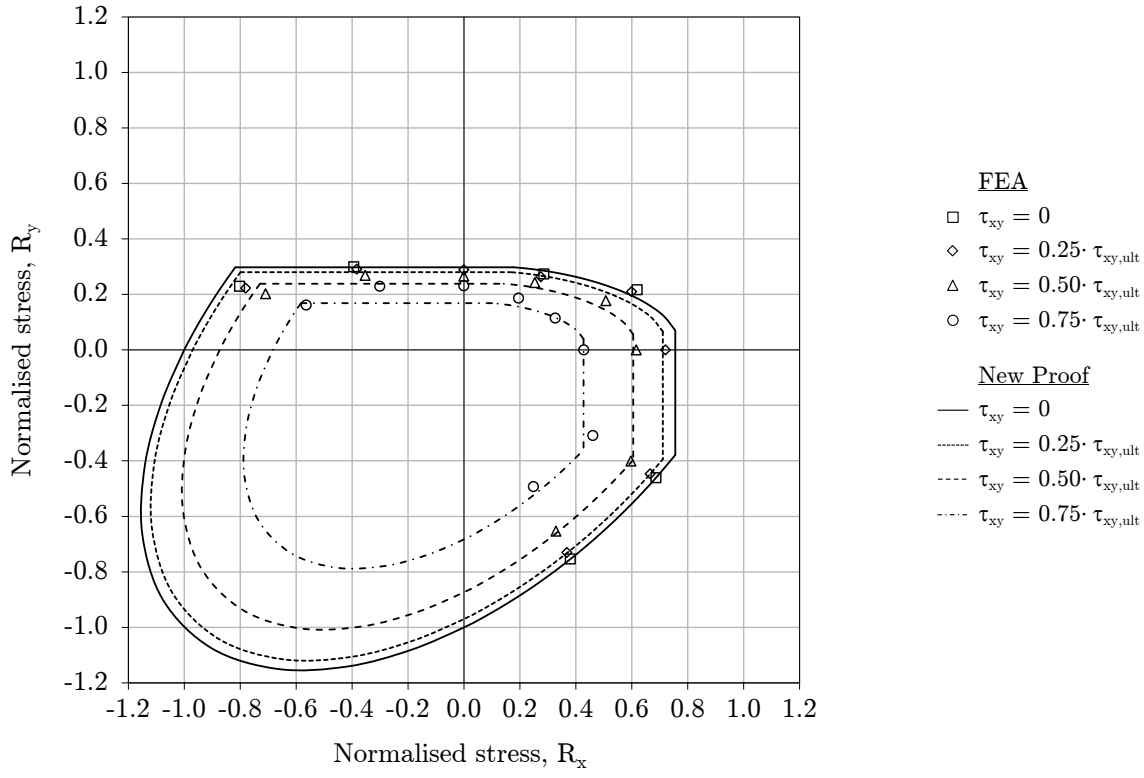

Figure C.10.: $\alpha = 5,\ \beta = 2$.

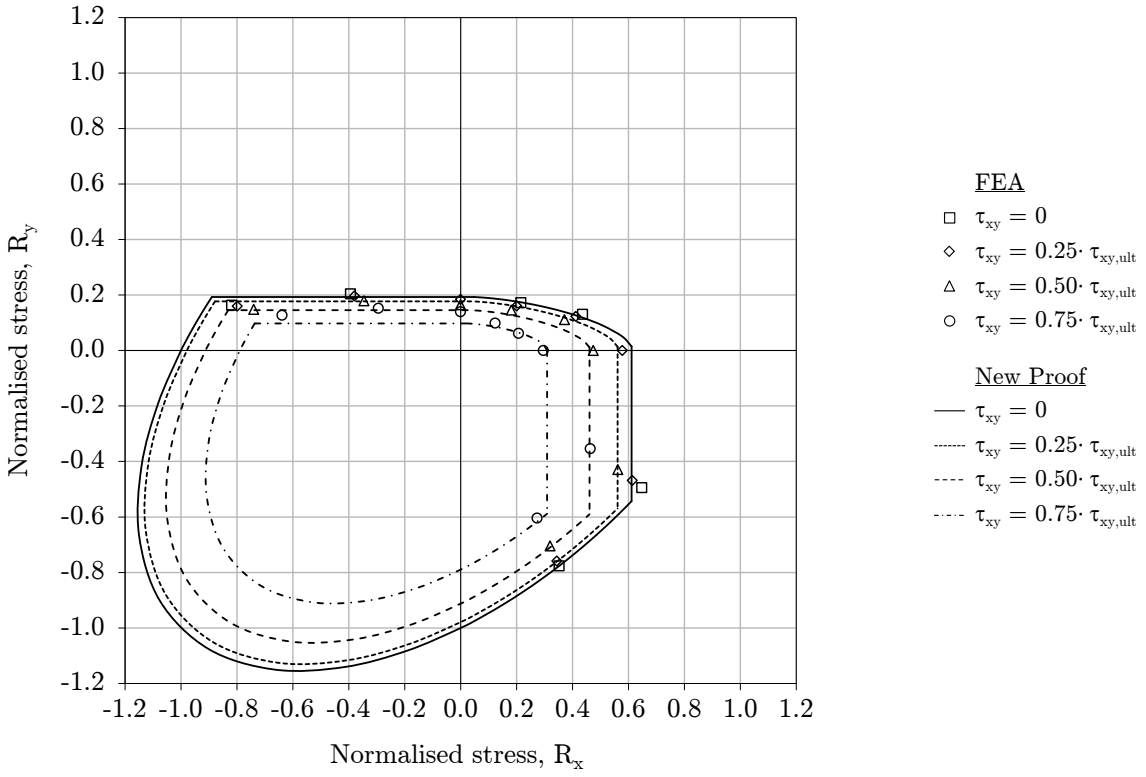

Figure C.11.: $\alpha = 5$, $\beta = 3$.

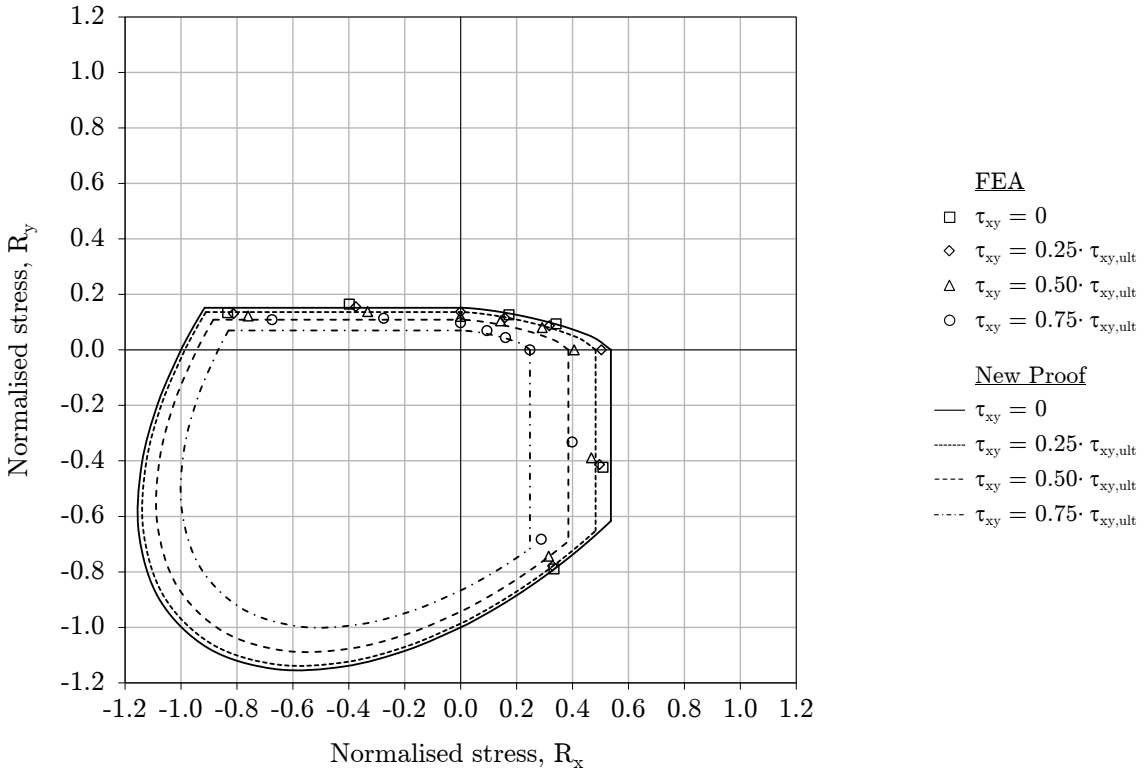

Figure C.12.: $\alpha = 5$, $\beta = 4$.

Appendix D. Calibration Data

D.1. Tabular Results

In this section the results of finite element analyses used in the calibration of the exponent e_0 and interaction coefficient B are tabulated. Results obtained with the new proof are also included.

		Finite Element Analyses					New Proof			
	data point	run id	$R_{x,ult}$	$R_{y,ult}$	$R_{t,\ ult}$	Magnitude	$R_{x,ult}$	$R_{y,ult}$	$R_{t,\ ult}$	Magnitude
$\beta = 0.5$	1	15101	1.000	0.000	0.000	1.000	1.000	1.000	0.000	1.000
	2	15102	1.115	0.299	0.000	1.155	1.000	1.000	0.000	1.035
	3	15103	1.113	0.643	0.000	1.285	1.000	1.000	0.000	1.155
	4	15104	0.936	0.936	0.000	1.324	1.000	1.000	0.000	1.414
	5	15105	0.643	1.113	0.000	1.285	1.000	1.000	0.000	1.155
	6	15106	0.299	1.115	0.000	1.155	1.000	1.000	0.000	1.035
	7	15107	0.000	1.000	0.000	0.000	1.000	1.000	0.000	0.000
$\beta = 1$	8	11101	0.979	0.000	0.000	0.979	0.979	0.226	0.000	0.979
	9	11102	1.007	0.270	0.000	1.043	0.974	0.261	0.000	1.009
	10	11103	0.908	0.524	0.000	1.048	0.894	0.516	0.000	1.032
	11	11104	0.736	0.736	0.000	1.041	0.736	0.736	0.000	1.041
	12	11105	0.524	0.908	0.000	1.048	0.516	0.894	0.000	1.032
	13	11106	0.270	1.007	0.000	1.043	0.261	0.974	0.000	1.009
	14	11107	0.000	0.979	0.000	0.000	0.226	0.979	0.000	0.000
$\beta = 2$	15	12101	0.753	0.000	0.000	0.753	0.753	0.000	0.000	0.753
	16	12102	0.688	0.184	0.000	0.712	0.679	0.182	0.000	0.703
	17	12103	0.585	0.338	0.000	0.676	0.580	0.335	0.000	0.670
	18	12104	0.467	0.467	0.000	0.660	0.466	0.466	0.000	0.659
	19	12105	0.338	0.585	0.000	0.676	0.335	0.580	0.000	0.670
	20	12106	0.184	0.688	0.000	0.712	0.182	0.679	0.000	0.703
	21	12107	0.000	0.753	0.000	0.000	0.000	0.753	0.000	0.000
$\beta = 3$	22	13101	0.614	0.000	0.000	0.614	0.614	0.000	0.000	0.614
	23	13102	0.554	0.148	0.000	0.574	0.519	0.139	0.000	0.537
	24	13103	0.461	0.266	0.000	0.532	0.431	0.249	0.000	0.497
	25	13104	0.366	0.366	0.000	0.518	0.343	0.343	0.000	0.485
	26	13105	0.266	0.461	0.000	0.532	0.249	0.431	0.000	0.497
	27	13106	0.148	0.554	0.000	0.574	0.139	0.519	0.000	0.537
	28	13107	0.000	0.614	0.000	0.000	0.000	0.614	0.000	0.000
$\beta = 4$	29	14101	0.558	0.000	0.000	0.558	0.558	0.000	0.000	0.558
	30	14102	0.467	0.125	0.000	0.484	0.447	0.120	0.000	0.463
	31	14103	0.386	0.223	0.000	0.446	0.365	0.211	0.000	0.421
	32	14104	0.307	0.307	0.000	0.434	0.289	0.289	0.000	0.409
	33	14105	0.223	0.386	0.000	0.446	0.211	0.365	0.000	0.421
	34	14106	0.125	0.467	0.000	0.484	0.120	0.447	0.000	0.463
	35	14107	0.000	0.558	0.000	0.000	0.000	0.558	0.000	0.000

Table D.1.: σ_x-σ_y, $\alpha = 1$.

		Finite Element Analyses					New Proof			
	data point	run id	$R_{x,ult}$	$R_{y,ult}$	$R_{t,\ ult}$	Magnitude	$R_{x,ult}$	$R_{y,ult}$	$R_{t,\ ult}$	Magnitude
$\beta = 0.5$	36	15301	1.000	0.000	0.000	1.000	1.000	0.938	0.000	1.000
	37	15302	1.113	0.289	0.000	1.150	1.000	0.938	0.000	1.033
	38	15303	1.121	0.627	0.000	1.284	1.000	0.938	0.000	1.146
	39	15304	0.934	0.905	0.000	1.301	1.000	0.938	0.000	1.347
	40	15305	0.587	0.984	0.000	1.145	1.000	0.938	0.000	1.092
	41	15306	0.272	0.983	0.000	1.020	1.000	0.938	0.000	0.973
	42	15307	0.000	0.938	0.000	0.000	1.000	0.938	0.000	0.000
$\beta = 1$	43	11301	0.980	0.000	0.000	0.980	0.980	0.343	0.000	0.980
	44	11302	1.015	0.230	0.000	1.041	0.980	0.343	0.000	1.004
	45	11303	0.953	0.458	0.000	1.057	0.920	0.442	0.000	1.021
	46	11304	0.732	0.601	0.000	0.947	0.726	0.596	0.000	0.939
	47	11305	0.459	0.646	0.000	0.792	0.501	0.672	0.000	0.824
	48	11306	0.221	0.666	0.000	0.702	0.501	0.672	0.000	0.708
	49	11307	0.000	0.672	0.000	0.000	0.501	0.672	0.000	0.000
$\beta = 2$	50	12301	0.755	0.000	0.000	0.755	0.755	0.036	0.000	0.755
	51	12302	0.709	0.140	0.000	0.723	0.695	0.137	0.000	0.708
	52	12303	0.605	0.243	0.000	0.652	0.572	0.230	0.000	0.617
	53	12304	0.441	0.295	0.000	0.530	0.439	0.293	0.000	0.528
	54	12305	0.293	0.331	0.000	0.442	0.298	0.337	0.000	0.450
	55	12306	0.148	0.356	0.000	0.385	0.152	0.364	0.000	0.395
	56	12307	0.000	0.371	0.000	0.000	0.074	0.371	0.000	0.000
$\beta = 3$	57	13301	0.611	0.000	0.000	0.611	0.611	0.000	0.000	0.611
	58	13302	0.567	0.105	0.000	0.577	0.515	0.096	0.000	0.524
	59	13303	0.434	0.160	0.000	0.462	0.412	0.152	0.000	0.439
	60	13304	0.324	0.197	0.000	0.379	0.315	0.192	0.000	0.369
	61	13305	0.222	0.227	0.000	0.317	0.218	0.223	0.000	0.311
	62	13306	0.116	0.251	0.000	0.277	0.114	0.247	0.000	0.272
	63	13307	0.000	0.262	0.000	0.000	0.000	0.262	0.000	0.000
$\beta = 4$	64	14301	0.541	0.000	0.000	0.541	0.541	0.000	0.000	0.541
	65	14302	0.449	0.081	0.000	0.457	0.427	0.077	0.000	0.434
	66	14303	0.345	0.123	0.000	0.366	0.336	0.120	0.000	0.357
	67	14304	0.259	0.151	0.000	0.300	0.258	0.150	0.000	0.298
	68	14305	0.179	0.175	0.000	0.251	0.180	0.176	0.000	0.252
	69	14306	0.096	0.198	0.000	0.219	0.096	0.199	0.000	0.221
	70	14307	0.000	0.219	0.000	0.000	0.000	0.219	0.000	0.000

Table D.2.: σ_x-σ_y, $\alpha = 3$.

		Finite Element Analyses					New Proof			
	data point	run id	$R_{x,ult}$	$R_{y,ult}$	$R_{t,\ ult}$	Magnitude	$R_{x,ult}$	$R_{y,ult}$	$R_{t,\ ult}$	Magnitude
$\beta = 0.5$	71	15501	1.000	0.000	0.000	1.000	1.000	0.906	0.000	1.000
	72	15502	1.111	0.284	0.000	1.147	1.000	0.906	0.000	1.032
	73	15503	1.126	0.619	0.000	1.285	1.000	0.906	0.000	1.141
	74	15504	0.941	0.896	0.000	1.299	1.000	0.906	0.000	1.314
	75	15505	0.581	0.956	0.000	1.119	1.000	0.906	0.000	1.060
	76	15506	0.268	0.951	0.000	0.988	1.000	0.906	0.000	0.941
	77	15507	0.000	0.906	0.000	0.000	1.000	0.906	0.000	0.000
$\beta = 1$	78	11501	0.981	0.000	0.000	0.981	0.981	0.371	0.000	0.981
	79	11502	1.016	0.221	0.000	1.040	0.981	0.371	0.000	1.004
	80	11503	0.966	0.441	0.000	1.062	0.938	0.428	0.000	1.031
	81	11504	0.742	0.574	0.000	0.938	0.731	0.566	0.000	0.925
	82	11505	0.455	0.602	0.000	0.755	0.598	0.608	0.000	0.762
	83	11506	0.216	0.610	0.000	0.647	0.598	0.608	0.000	0.645
	84	11507	0.000	0.608	0.000	0.000	0.598	0.608	0.000	0.000
$\beta = 2$	85	12501	0.755	0.000	0.000	0.755	0.755	0.070	0.000	0.755
	86	12502	0.715	0.128	0.000	0.726	0.709	0.127	0.000	0.720
	87	12503	0.619	0.216	0.000	0.656	0.582	0.203	0.000	0.617
	88	12504	0.439	0.251	0.000	0.506	0.442	0.252	0.000	0.509
	89	12505	0.286	0.273	0.000	0.395	0.296	0.284	0.000	0.410
	90	12506	0.142	0.288	0.000	0.321	0.178	0.298	0.000	0.332
	91	12507	0.000	0.298	0.000	0.000	0.178	0.298	0.000	0.000
$\beta = 3$	92	13501	0.611	0.000	0.000	0.611	0.611	0.015	0.000	0.611
	93	13502	0.582	0.092	0.000	0.589	0.523	0.083	0.000	0.530
	94	13503	0.436	0.130	0.000	0.455	0.418	0.125	0.000	0.436
	95	13504	0.320	0.154	0.000	0.355	0.318	0.153	0.000	0.353
	96	13505	0.215	0.172	0.000	0.276	0.217	0.173	0.000	0.278
	97	13506	0.111	0.187	0.000	0.217	0.111	0.188	0.000	0.219
	98	13507	0.000	0.193	0.000	0.000	0.047	0.193	0.000	0.000
$\beta = 4$	99	14501	0.537	0.000	0.000	0.537	0.537	0.002	0.000	0.537
	100	14502	0.453	0.067	0.000	0.458	0.429	0.063	0.000	0.434
	101	14503	0.342	0.094	0.000	0.354	0.339	0.093	0.000	0.352
	102	14504	0.254	0.111	0.000	0.277	0.259	0.114	0.000	0.283
	103	14505	0.173	0.126	0.000	0.214	0.179	0.130	0.000	0.221
	104	14506	0.091	0.139	0.000	0.166	0.094	0.144	0.000	0.172
	105	14507	0.000	0.152	0.000	0.000	0.006	0.152	0.000	0.000

Table D.3.: σ_x-σ_y, $\alpha = 5$.

		Finite Element Analyses					New Proof			
	data point	run id	$R_{x,ult}$	$R_{y,ult}$	$R_{t,\ ult}$	Magnitude	$R_{x,ult}$	$R_{y,ult}$	$R_{t,\ ult}$	Magnitude
$\beta = 1$	106	11001	0.983	0.000	0.000	0.983	0.983	0.406	0.000	0.983
	107	11002	1.017	0.215	0.000	1.039	0.983	0.406	0.000	1.005
	108	11003	0.978	0.430	0.000	1.069	0.966	0.425	0.000	1.055
	109	11004	0.751	0.557	0.000	0.935	0.747	0.554	0.000	0.930
	110	11005	0.457	0.577	0.000	0.736	0.703	0.567	0.000	0.724
	111	11006	0.214	0.577	0.000	0.616	0.703	0.567	0.000	0.605
	112	11007	0.000	0.567	0.000	0.000	0.703	0.567	0.000	0.000
$\beta = 2$	113	12001	0.757	0.000	0.000	0.757	0.757	0.099	0.000	0.757
	114	12002	0.721	0.115	0.000	0.731	0.736	0.117	0.000	0.745
	115	12003	0.651	0.196	0.000	0.680	0.605	0.182	0.000	0.632
	116	12004	0.448	0.217	0.000	0.498	0.455	0.221	0.000	0.506
	117	12005	0.284	0.229	0.000	0.365	0.309	0.242	0.000	0.385
	118	12006	0.139	0.237	0.000	0.275	0.309	0.242	0.000	0.280
	119	12007	0.000	0.242	0.000	0.000	0.309	0.242	0.000	0.000
$\beta = 3$	120	13001	0.611	0.000	0.000	0.611	0.611	0.035	0.000	0.611
	121	13002	0.591	0.076	0.000	0.596	0.545	0.070	0.000	0.550
	122	13003	0.457	0.106	0.000	0.469	0.437	0.101	0.000	0.449
	123	13004	0.326	0.120	0.000	0.347	0.330	0.121	0.000	0.352
	124	13005	0.214	0.130	0.000	0.251	0.222	0.135	0.000	0.260
	125	13006	0.108	0.138	0.000	0.175	0.151	0.141	0.000	0.178
	126	13007	0.000	0.141	0.000	0.000	0.151	0.141	0.000	0.000
$\beta = 4$	127	14001	0.537	0.000	0.000	0.537	0.537	0.015	0.000	0.537
	128	14002	0.502	0.055	0.000	0.505	0.449	0.050	0.000	0.452
	129	14003	0.356	0.070	0.000	0.363	0.357	0.070	0.000	0.363
	130	14004	0.259	0.080	0.000	0.271	0.271	0.083	0.000	0.284
	131	14005	0.173	0.088	0.000	0.194	0.185	0.094	0.000	0.207
	132	14006	0.089	0.095	0.000	0.130	0.081	0.101	0.000	0.138
	133	14007	0.000	0.101	0.000	0.000	0.081	0.101	0.000	0.000

Table D.4.: σ_x-σ_y, $\alpha = 10$.

		Finite Element Analyses					New Proof			
	data point	run id	$R_{x,ult}$	$R_{y,ult}$	$R_{t,\ ult}$	Magnitude	$R_{x,ult}$	$R_{y,ult}$	$R_{t,\ ult}$	Magnitude
$\beta = 0.5$	134	25101	1.000	0.000	0.000	1.000	1.000	0.000	0.000	1.000
	135	25102	0.939	0.000	0.344	0.960	0.939	0.000	0.344	0.960
	136	25103	0.795	0.000	0.606	0.869	0.795	0.000	0.606	0.869
	137	25104	0.614	0.000	0.789	0.765	0.614	0.000	0.789	0.765
	138	25105	0.416	0.000	0.909	0.670	0.416	0.000	0.909	0.670
	139	25106	0.210	0.000	0.978	0.602	0.210	0.000	0.978	0.602
	140	25107	0.000	0.000	1.000	0.000	0.000	0.000	1.000	0.000
$\beta = 1$	141	21101	0.979	0.000	0.000	0.979	0.979	0.000	0.000	0.979
	142	21102	0.912	0.000	0.339	0.933	0.920	0.000	0.342	0.941
	143	21103	0.771	0.000	0.601	0.845	0.778	0.000	0.607	0.853
	144	21104	0.595	0.000	0.785	0.748	0.599	0.000	0.791	0.753
	145	21105	0.404	0.000	0.908	0.661	0.405	0.000	0.911	0.663
	146	21106	0.204	0.000	0.979	0.601	0.204	0.000	0.978	0.600
	147	21107	0.000	0.000	1.000	0.000	0.000	0.000	1.000	0.000
$\beta = 2$	148	22101	0.753	0.000	0.000	0.753	0.753	0.000	0.000	0.753
	149	22102	0.702	0.000	0.287	0.721	0.696	0.000	0.285	0.716
	150	22103	0.597	0.000	0.522	0.668	0.591	0.000	0.517	0.662
	151	22104	0.469	0.000	0.706	0.622	0.464	0.000	0.698	0.615
	152	22105	0.327	0.000	0.847	0.588	0.324	0.000	0.839	0.583
	153	22106	0.170	0.000	0.945	0.571	0.169	0.000	0.941	0.569
	154	22107	0.000	0.000	0.990	0.000	0.000	0.000	0.990	0.000
$\beta = 3$	155	23101	0.614	0.000	0.000	0.614	0.614	0.000	0.000	0.614
	156	23102	0.566	0.000	0.246	0.584	0.560	0.000	0.243	0.578
	157	23103	0.479	0.000	0.448	0.544	0.474	0.000	0.443	0.539
	158	23104	0.376	0.000	0.607	0.514	0.376	0.000	0.607	0.514
	159	23105	0.263	0.000	0.736	0.500	0.267	0.000	0.746	0.507
	160	23106	0.140	0.000	0.843	0.507	0.143	0.000	0.859	0.516
	161	23107	0.000	0.000	0.927	0.000	0.000	0.000	0.927	0.000
$\beta = 4$	162	24101	0.558	0.000	0.000	0.558	0.558	0.000	0.000	0.558
	163	24102	0.499	0.000	0.216	0.514	0.498	0.000	0.216	0.513
	164	24103	0.413	0.000	0.384	0.469	0.416	0.000	0.387	0.473
	165	24104	0.322	0.000	0.517	0.439	0.329	0.000	0.528	0.449
	166	24105	0.227	0.000	0.630	0.429	0.234	0.000	0.651	0.443
	167	24106	0.123	0.000	0.735	0.442	0.127	0.000	0.758	0.456
	168	24107	0.000	0.000	0.832	0.000	0.000	0.000	0.832	0.000

Table D.5.: σ_x-τ_{xy}, $\alpha = 1$.

		Finite Element Analyses					New Proof			
	data point	run id	$R_{x,ult}$	$R_{y,ult}$	$R_{t,\ ult}$	Magnitude	$R_{x,ult}$	$R_{y,ult}$	$R_{t,\ ult}$	Magnitude
$\beta = 0.5$	169	25301	1.000	0.000	0.000	1.000	1.000	0.000	0.000	1.000
	170	25302	0.939	0.000	0.344	0.960	0.939	0.000	0.344	0.960
	171	25303	0.795	0.000	0.606	0.869	0.795	0.000	0.606	0.869
	172	25304	0.614	0.000	0.789	0.765	0.614	0.000	0.789	0.765
	173	25305	0.416	0.000	0.909	0.670	0.416	0.000	0.909	0.670
	174	25306	0.210	0.000	0.978	0.602	0.210	0.000	0.978	0.602
	175	25307	0.000	0.000	1.000	0.000	0.000	0.000	1.000	0.000
$\beta = 1$	176	21301	0.980	0.000	0.000	0.980	0.980	0.000	0.000	0.980
	177	21302	0.918	0.000	0.341	0.938	0.921	0.000	0.342	0.942
	178	21303	0.776	0.000	0.604	0.851	0.779	0.000	0.606	0.854
	179	21304	0.599	0.000	0.788	0.752	0.600	0.000	0.790	0.754
	180	21305	0.405	0.000	0.910	0.664	0.406	0.000	0.910	0.664
	181	21306	0.204	0.000	0.979	0.601	0.204	0.000	0.978	0.600
	182	21307	0.000	0.000	1.000	0.000	0.000	0.000	1.000	0.000
$\beta = 2$	183	22301	0.755	0.000	0.000	0.755	0.755	0.000	0.000	0.755
	184	22302	0.708	0.000	0.288	0.727	0.697	0.000	0.283	0.716
	185	22303	0.598	0.000	0.520	0.669	0.591	0.000	0.513	0.661
	186	22304	0.465	0.000	0.694	0.614	0.464	0.000	0.692	0.612
	187	22305	0.323	0.000	0.829	0.577	0.323	0.000	0.830	0.578
	188	22306	0.168	0.000	0.927	0.561	0.169	0.000	0.930	0.563
	189	22307	0.000	0.000	0.977	0.000	0.000	0.000	0.977	0.000
$\beta = 3$	190	23301	0.611	0.000	0.000	0.611	0.611	0.000	0.000	0.611
	191	23302	0.534	0.000	0.225	0.550	0.554	0.000	0.233	0.570
	192	23303	0.458	0.000	0.413	0.516	0.466	0.000	0.420	0.525
	193	23304	0.362	0.000	0.564	0.487	0.367	0.000	0.571	0.493
	194	23305	0.250	0.000	0.672	0.461	0.259	0.000	0.696	0.478
	195	23306	0.132	0.000	0.762	0.459	0.138	0.000	0.797	0.480
	196	23307	0.000	0.000	0.857	0.000	0.000	0.000	0.857	0.000
$\beta = 4$	197	24301	0.541	0.000	0.000	0.541	0.541	0.000	0.000	0.541
	198	24302	0.438	0.000	0.180	0.450	0.478	0.000	0.196	0.492
	199	24303	0.376	0.000	0.330	0.422	0.395	0.000	0.348	0.443
	200	24304	0.302	0.000	0.456	0.401	0.310	0.000	0.468	0.411
	201	24305	0.212	0.000	0.553	0.384	0.219	0.000	0.570	0.396
	202	24306	0.113	0.000	0.630	0.381	0.118	0.000	0.659	0.398
	203	24307	0.000	0.000	0.719	0.000	0.000	0.000	0.719	0.000

Table D.6.: σ_x-τ_{xy}, $\alpha = 3$.

		Finite Element Analyses					New Proof			
	data point	run id	$R_{x,ult}$	$R_{y,ult}$	$R_{t,\ ult}$	Magnitude	$R_{x,ult}$	$R_{y,ult}$	$R_{t,\ ult}$	Magnitude
$\beta = 0.5$	204	25501	1.000	0.000	0.000	1.000	1.000	0.000	0.000	1.000
	205	25502	0.939	0.000	0.344	0.960	0.939	0.000	0.344	0.960
	206	25503	0.795	0.000	0.606	0.869	0.795	0.000	0.606	0.869
	207	25504	0.614	0.000	0.789	0.765	0.614	0.000	0.789	0.765
	208	25505	0.416	0.000	0.909	0.670	0.416	0.000	0.909	0.670
	209	25506	0.210	0.000	0.978	0.602	0.210	0.000	0.978	0.602
	210	25507	0.000	0.000	1.000	0.000	0.000	0.000	1.000	0.000
$\beta = 1$	211	21501	0.981	0.000	0.000	0.981	0.981	0.000	0.000	0.981
	212	21502	0.918	0.000	0.341	0.939	0.921	0.000	0.342	0.942
	213	21503	0.776	0.000	0.604	0.851	0.780	0.000	0.607	0.855
	214	21504	0.600	0.000	0.789	0.753	0.601	0.000	0.790	0.754
	215	21505	0.406	0.000	0.911	0.664	0.406	0.000	0.910	0.664
	216	21506	0.205	0.000	0.979	0.601	0.204	0.000	0.978	0.601
	217	21507	0.000	0.000	1.000	0.000	0.000	0.000	1.000	0.000
$\beta = 2$	218	22501	0.755	0.000	0.000	0.755	0.755	0.000	0.000	0.755
	219	22502	0.708	0.000	0.287	0.727	0.698	0.000	0.283	0.717
	220	22503	0.597	0.000	0.518	0.668	0.591	0.000	0.512	0.661
	221	22504	0.465	0.000	0.692	0.613	0.464	0.000	0.690	0.611
	222	22505	0.323	0.000	0.828	0.577	0.323	0.000	0.828	0.577
	223	22506	0.168	0.000	0.924	0.559	0.169	0.000	0.927	0.561
	224	22507	0.000	0.000	0.974	0.000	0.000	0.000	0.974	0.000
$\beta = 3$	225	23501	0.611	0.000	0.000	0.611	0.611	0.000	0.000	0.611
	226	23502	0.568	0.000	0.234	0.583	0.552	0.000	0.228	0.567
	227	23503	0.470	0.000	0.415	0.528	0.462	0.000	0.408	0.518
	228	23504	0.361	0.000	0.549	0.481	0.362	0.000	0.551	0.482
	229	23505	0.254	0.000	0.664	0.460	0.255	0.000	0.668	0.463
	230	23506	0.133	0.000	0.746	0.450	0.136	0.000	0.763	0.461
	231	23507	0.000	0.000	0.819	0.000	0.000	0.000	0.819	0.000
$\beta = 4$	232	24501	0.537	0.000	0.000	0.537	0.537	0.000	0.000	0.537
	233	24502	0.489	0.000	0.195	0.502	0.472	0.000	0.188	0.484
	234	24503	0.400	0.000	0.340	0.446	0.387	0.000	0.329	0.431
	235	24504	0.306	0.000	0.446	0.400	0.302	0.000	0.439	0.394
	236	24505	0.211	0.000	0.528	0.371	0.213	0.000	0.532	0.374
	237	24506	0.112	0.000	0.601	0.365	0.114	0.000	0.611	0.371
	238	24507	0.000	0.000	0.665	0.000	0.000	0.000	0.665	0.000

Table D.7.: σ_x-τ_{xy}, $\alpha = 5$.

		Finite Element Analyses					New Proof			
	data point	run id	$R_{x,ult}$	$R_{y,ult}$	$R_{t,\ ult}$	Magnitude	$R_{x,ult}$	$R_{y,ult}$	$R_{t,\ ult}$	Magnitude
$\beta = 1$	239	21001	0.983	0.000	0.000	0.983	0.983	0.000	0.000	0.983
	240	21002	0.919	0.000	0.338	0.939	0.924	0.000	0.340	0.945
	241	21003	0.781	0.000	0.601	0.854	0.784	0.000	0.603	0.858
	242	21004	0.605	0.000	0.786	0.756	0.606	0.000	0.787	0.758
	243	21005	0.411	0.000	0.908	0.666	0.411	0.000	0.908	0.666
	244	21006	0.207	0.000	0.978	0.602	0.207	0.000	0.978	0.601
	245	21007	0.000	0.000	1.000	0.000	0.000	0.000	1.000	0.000
$\beta = 2$	246	22001	0.757	0.000	0.000	0.757	0.757	0.000	0.000	0.757
	247	22002	0.708	0.000	0.287	0.727	0.699	0.000	0.284	0.718
	248	22003	0.599	0.000	0.520	0.670	0.592	0.000	0.513	0.662
	249	22004	0.469	0.000	0.698	0.618	0.464	0.000	0.692	0.613
	250	22005	0.324	0.000	0.831	0.579	0.324	0.000	0.830	0.578
	251	22006	0.169	0.000	0.927	0.561	0.169	0.000	0.929	0.562
	252	22007	0.000	0.000	0.977	0.000	0.000	0.000	0.977	0.000
$\beta = 3$	253	23001	0.611	0.000	0.000	0.611	0.611	0.000	0.000	0.611
	254	23002	0.568	0.000	0.232	0.584	0.551	0.000	0.225	0.566
	255	23003	0.470	0.000	0.411	0.527	0.460	0.000	0.402	0.515
	256	23004	0.364	0.000	0.546	0.481	0.361	0.000	0.541	0.477
	257	23005	0.249	0.000	0.643	0.447	0.254	0.000	0.656	0.456
	258	23006	0.131	0.000	0.728	0.440	0.135	0.000	0.747	0.452
	259	23007	0.000	0.000	0.801	0.000	0.000	0.000	0.801	0.000
$\beta = 4$	260	24001	0.537	0.000	0.000	0.537	0.537	0.000	0.000	0.537
	261	24002	0.491	0.000	0.192	0.503	0.470	0.000	0.183	0.481
	262	24003	0.400	0.000	0.332	0.443	0.384	0.000	0.318	0.426
	263	24004	0.308	0.000	0.436	0.398	0.298	0.000	0.423	0.385
	264	24005	0.210	0.000	0.510	0.361	0.210	0.000	0.509	0.361
	265	24006	0.110	0.000	0.573	0.349	0.112	0.000	0.583	0.355
	266	24007	0.000	0.000	0.633	0.000	0.000	0.000	0.633	0.000

Table D.8.: σ_x-τ_{xy}, $\alpha = 10$.

		Finite Element Analyses					New Proof			
	data point	run id	$R_{x,ult}$	$R_{y,ult}$	$R_{t,\ ult}$	Magnitude	$R_{x,ult}$	$R_{y,ult}$	$R_{t,\ ult}$	Magnitude
$\beta = 0.5$	267	35101	0.000	1.000	0.000	0.000	0.000	1.000	0.000	0.000
	268	35102	0.000	0.939	0.344	0.960	0.000	0.939	0.344	0.960
	269	35103	0.000	0.795	0.606	0.869	0.000	0.795	0.606	0.869
	270	35104	0.000	0.614	0.789	0.765	0.000	0.614	0.789	0.765
	271	35105	0.000	0.416	0.909	0.670	0.000	0.416	0.909	0.670
	272	35106	0.000	0.210	0.978	0.602	0.000	0.210	0.978	0.602
	273	35107	0.000	0.000	1.000	0.000	0.000	0.000	1.000	0.000
$\beta = 1$	274	31101	0.000	0.979	0.000	0.000	0.000	0.979	0.000	0.000
	275	31102	0.000	0.912	0.339	0.933	0.000	0.920	0.342	0.941
	276	31103	0.000	0.771	0.601	0.845	0.000	0.778	0.607	0.853
	277	31104	0.000	0.595	0.785	0.748	0.000	0.599	0.791	0.753
	278	31105	0.000	0.404	0.908	0.661	0.000	0.405	0.911	0.663
	279	31106	0.000	0.204	0.979	0.601	0.000	0.204	0.978	0.600
	280	31107	0.000	0.000	1.000	0.000	0.000	0.000	1.000	0.000
$\beta = 2$	281	32101	0.000	0.753	0.000	0.000	0.000	0.753	0.000	0.000
	282	32102	0.000	0.702	0.287	0.721	0.000	0.696	0.285	0.716
	283	32103	0.000	0.597	0.522	0.668	0.000	0.591	0.517	0.662
	284	32104	0.000	0.469	0.706	0.622	0.000	0.464	0.698	0.615
	285	32105	0.000	0.327	0.847	0.588	0.000	0.324	0.839	0.583
	286	32106	0.000	0.170	0.945	0.571	0.000	0.169	0.941	0.569
	287	32107	0.000	0.000	0.990	0.000	0.000	0.000	0.990	0.000
$\beta = 3$	288	33101	0.000	0.614	0.000	0.000	0.000	0.614	0.000	0.000
	289	33102	0.000	0.566	0.246	0.584	0.000	0.560	0.243	0.578
	290	33103	0.000	0.479	0.448	0.544	0.000	0.474	0.443	0.539
	291	33104	0.000	0.376	0.607	0.514	0.000	0.376	0.607	0.514
	292	33105	0.000	0.263	0.736	0.500	0.000	0.267	0.746	0.507
	293	33106	0.000	0.140	0.843	0.507	0.000	0.143	0.859	0.516
	294	33107	0.000	0.000	0.927	0.000	0.000	0.000	0.927	0.000
$\beta = 4$	295	34101	0.000	0.558	0.000	0.000	0.000	0.558	0.000	0.000
	296	34102	0.000	0.499	0.216	0.514	0.000	0.498	0.216	0.513
	297	34103	0.000	0.413	0.384	0.469	0.000	0.416	0.387	0.473
	298	34104	0.000	0.322	0.517	0.439	0.000	0.329	0.528	0.449
	299	34105	0.000	0.227	0.630	0.429	0.000	0.234	0.651	0.443
	300	34106	0.000	0.123	0.735	0.442	0.000	0.127	0.758	0.456
	301	34107	0.000	0.000	0.832	0.000	0.000	0.000	0.832	0.000

Table D.9.: σ_y-τ_{xy}, $\alpha = 1$.

		Finite Element Analyses					New Proof			
	data point	run id	$R_{x,ult}$	$R_{y,ult}$	$R_{t,\ ult}$	Magnitude	$R_{x,ult}$	$R_{y,ult}$	$R_{t,\ ult}$	Magnitude
$\beta = 0.5$	302	35301	0.000	0.938	0.000	0.000	0.000	0.938	0.000	0.000
	303	35302	0.000	0.893	0.335	0.914	0.000	0.884	0.332	0.905
	304	35303	0.000	0.773	0.609	0.849	0.000	0.754	0.594	0.828
	305	35304	0.000	0.599	0.800	0.756	0.000	0.585	0.782	0.739
	306	35305	0.000	0.402	0.916	0.664	0.000	0.397	0.906	0.657
	307	35306	0.000	0.201	0.980	0.600	0.000	0.200	0.977	0.599
	308	35307	0.000	0.000	1.000	0.000	0.000	0.000	1.000	0.000
$\beta = 1$	309	31301	0.000	0.672	0.000	0.000	0.000	0.672	0.000	0.000
	310	31302	0.000	0.649	0.283	0.670	0.000	0.645	0.281	0.665
	311	31303	0.000	0.591	0.554	0.672	0.000	0.568	0.533	0.646
	312	31304	0.000	0.489	0.792	0.670	0.000	0.454	0.736	0.622
	313	31305	0.000	0.329	0.923	0.626	0.000	0.315	0.883	0.599
	314	31306	0.000	0.163	0.983	0.590	0.000	0.161	0.971	0.583
	315	31307	0.000	0.000	1.000	0.000	0.000	0.000	1.000	0.000
$\beta = 2$	316	32301	0.000	0.371	0.000	0.000	0.000	0.371	0.000	0.000
	317	32302	0.000	0.360	0.212	0.381	0.000	0.355	0.209	0.375
	318	32303	0.000	0.333	0.420	0.411	0.000	0.319	0.403	0.395
	319	32304	0.000	0.291	0.629	0.466	0.000	0.269	0.582	0.430
	320	32305	0.000	0.217	0.800	0.510	0.000	0.203	0.748	0.477
	321	32306	0.000	0.117	0.911	0.539	0.000	0.115	0.894	0.529
	322	32307	0.000	0.000	0.977	0.000	0.000	0.000	0.977	0.000
$\beta = 3$	323	33301	0.000	0.262	0.000	0.000	0.000	0.262	0.000	0.000
	324	33302	0.000	0.251	0.172	0.270	0.000	0.247	0.169	0.266
	325	33303	0.000	0.230	0.334	0.300	0.000	0.221	0.322	0.289
	326	33304	0.000	0.201	0.495	0.349	0.000	0.189	0.465	0.328
	327	33305	0.000	0.154	0.634	0.397	0.000	0.146	0.604	0.378
	328	33306	0.000	0.087	0.742	0.437	0.000	0.088	0.746	0.440
	329	33307	0.000	0.000	0.857	0.000	0.000	0.000	0.857	0.000
$\beta = 4$	330	34301	0.000	0.219	0.000	0.000	0.000	0.219	0.000	0.000
	331	34302	0.000	0.199	0.137	0.214	0.000	0.203	0.140	0.219
	332	34303	0.000	0.180	0.263	0.235	0.000	0.180	0.263	0.235
	333	34304	0.000	0.156	0.385	0.272	0.000	0.152	0.376	0.265
	334	34305	0.000	0.121	0.501	0.313	0.000	0.118	0.489	0.306
	335	34306	0.000	0.070	0.600	0.353	0.000	0.072	0.610	0.360
	336	34307	0.000	0.000	0.719	0.000	0.000	0.000	0.719	0.000

Table D.10.: σ_y-τ_{xy}, $\alpha = 3$.

		Finite Element Analyses					New Proof			
	data point	run id	$R_{x,ult}$	$R_{y,ult}$	$R_{t,\ ult}$	Magnitude	$R_{x,ult}$	$R_{y,ult}$	$R_{t,\ ult}$	Magnitude
$\beta = 0.5$	337	35501	0.000	0.906	0.000	0.000	0.000	0.906	0.000	0.000
	338	35502	0.000	0.869	0.331	0.890	0.000	0.856	0.326	0.877
	339	35503	0.000	0.764	0.613	0.842	0.000	0.733	0.588	0.807
	340	35504	0.000	0.590	0.805	0.751	0.000	0.570	0.777	0.725
	341	35505	0.000	0.394	0.919	0.661	0.000	0.388	0.904	0.650
	342	35506	0.000	0.197	0.980	0.599	0.000	0.196	0.976	0.597
	343	35507	0.000	0.000	1.000	0.000	0.000	0.000	1.000	0.000
$\beta = 1$	344	31501	0.000	0.608	0.000	0.000	0.000	0.608	0.000	0.000
	345	31502	0.000	0.594	0.271	0.615	0.000	0.585	0.267	0.606
	346	31503	0.000	0.554	0.545	0.637	0.000	0.522	0.513	0.600
	347	31504	0.000	0.470	0.801	0.659	0.000	0.422	0.719	0.592
	348	31505	0.000	0.316	0.934	0.625	0.000	0.296	0.873	0.585
	349	31506	0.000	0.155	0.986	0.590	0.000	0.152	0.968	0.579
	350	31507	0.000	0.000	1.000	0.000	0.000	0.000	1.000	0.000
$\beta = 2$	351	32501	0.000	0.298	0.000	0.000	0.000	0.298	0.000	0.000
	352	32502	0.000	0.291	0.200	0.313	0.000	0.286	0.196	0.307
	353	32503	0.000	0.275	0.401	0.359	0.000	0.260	0.379	0.340
	354	32504	0.000	0.249	0.615	0.434	0.000	0.223	0.551	0.389
	355	32505	0.000	0.198	0.819	0.513	0.000	0.174	0.717	0.449
	356	32506	0.000	0.107	0.912	0.537	0.000	0.103	0.874	0.515
	357	32507	0.000	0.000	0.974	0.000	0.000	0.000	0.974	0.000
$\beta = 3$	358	33501	0.000	0.193	0.000	0.000	0.000	0.193	0.000	0.000
	359	33502	0.000	0.187	0.156	0.208	0.000	0.183	0.152	0.203
	360	33503	0.000	0.175	0.308	0.250	0.000	0.165	0.291	0.236
	361	33504	0.000	0.158	0.468	0.313	0.000	0.143	0.422	0.283
	362	33505	0.000	0.130	0.632	0.388	0.000	0.114	0.552	0.339
	363	33506	0.000	0.075	0.717	0.421	0.000	0.073	0.691	0.406
	364	33507	0.000	0.000	0.819	0.000	0.000	0.000	0.819	0.000
$\beta = 4$	365	34501	0.000	0.152	0.000	0.000	0.000	0.152	0.000	0.000
	366	34502	0.000	0.141	0.120	0.157	0.000	0.142	0.121	0.158
	367	34503	0.000	0.130	0.236	0.188	0.000	0.127	0.230	0.184
	368	34504	0.000	0.117	0.354	0.236	0.000	0.109	0.330	0.220
	369	34505	0.000	0.099	0.490	0.300	0.000	0.087	0.432	0.264
	370	34506	0.000	0.059	0.570	0.334	0.000	0.056	0.545	0.320
	371	34507	0.000	0.000	0.665	0.000	0.000	0.000	0.665	0.000

Table D.11.: σ_y-τ_{xy}, $\alpha = 5$.

		Finite Element Analyses					New Proof			
	data point	run id	$R_{x,ult}$	$R_{y,ult}$	$R_{t,\ ult}$	Magnitude	$R_{x,ult}$	$R_{y,ult}$	$R_{t,\ ult}$	Magnitude
$\beta = 1$	372	31001	0.000	0.567	0.000	0.000	0.000	0.567	0.000	0.000
	373	31002	0.000	0.559	0.262	0.579	0.000	0.548	0.257	0.568
	374	31003	0.000	0.530	0.534	0.613	0.000	0.492	0.497	0.570
	375	31004	0.000	0.460	0.804	0.653	0.000	0.403	0.704	0.572
	376	31005	0.000	0.310	0.937	0.624	0.000	0.286	0.864	0.575
	377	31006	0.000	0.151	0.987	0.590	0.000	0.148	0.965	0.577
	378	31007	0.000	0.000	1.000	0.000	0.000	0.000	1.000	0.000
$\beta = 2$	379	32001	0.000	0.242	0.000	0.000	0.000	0.242	0.000	0.000
	380	32002	0.000	0.239	0.191	0.263	0.000	0.233	0.187	0.257
	381	32003	0.000	0.230	0.390	0.322	0.000	0.214	0.362	0.299
	382	32004	0.000	0.215	0.612	0.414	0.000	0.186	0.530	0.358
	383	32005	0.000	0.179	0.837	0.515	0.000	0.148	0.693	0.427
	384	32006	0.000	0.099	0.919	0.540	0.000	0.092	0.857	0.503
	385	32007	0.000	0.000	0.977	0.000	0.000	0.000	0.977	0.000
$\beta = 3$	386	33001	0.000	0.141	0.000	0.000	0.000	0.141	0.000	0.000
	387	33002	0.000	0.138	0.146	0.162	0.000	0.134	0.142	0.157
	388	33003	0.000	0.132	0.295	0.215	0.000	0.122	0.273	0.199
	389	33004	0.000	0.123	0.458	0.291	0.000	0.107	0.397	0.253
	390	33005	0.000	0.107	0.637	0.383	0.000	0.087	0.520	0.312
	391	33006	0.000	0.063	0.708	0.413	0.000	0.058	0.655	0.383
	392	33007	0.000	0.000	0.801	0.000	0.000	0.000	0.801	0.000
$\beta = 4$	393	34001	0.000	0.101	0.000	0.000	0.000	0.101	0.000	0.000
	394	34002	0.000	0.096	0.110	0.115	0.000	0.095	0.109	0.114
	395	34003	0.000	0.091	0.220	0.156	0.000	0.086	0.208	0.148
	396	34004	0.000	0.084	0.339	0.213	0.000	0.075	0.300	0.189
	397	34005	0.000	0.075	0.479	0.286	0.000	0.061	0.393	0.235
	398	34006	0.000	0.046	0.553	0.323	0.000	0.042	0.499	0.291
	399	34007	0.000	0.000	0.633	0.000	0.000	0.000	0.633	0.000

Table D.12.: σ_y-τ_{xy}, $\alpha = 10$.

D.2. Graphical Results

In this section the results of finite element analyses used in the calibration of the exponent e_0 and interaction coefficient B are plotted. Results obtained with the new proof are also included.

Stress combination	Plate aspect ratio, α	Figure	Page
σ_x-σ_y	1	D.1	238
	3	D.2	
	5	D.3	239
	10	D.4	
σ_x-τ_{xy}	1	D.5	240
	3	D.6	
	5	D.7	241
	10	D.8	
σ_y-τ_{xy}	1	D.9	242
	3	D.10	
	5	D.11	243
	10	D.12	

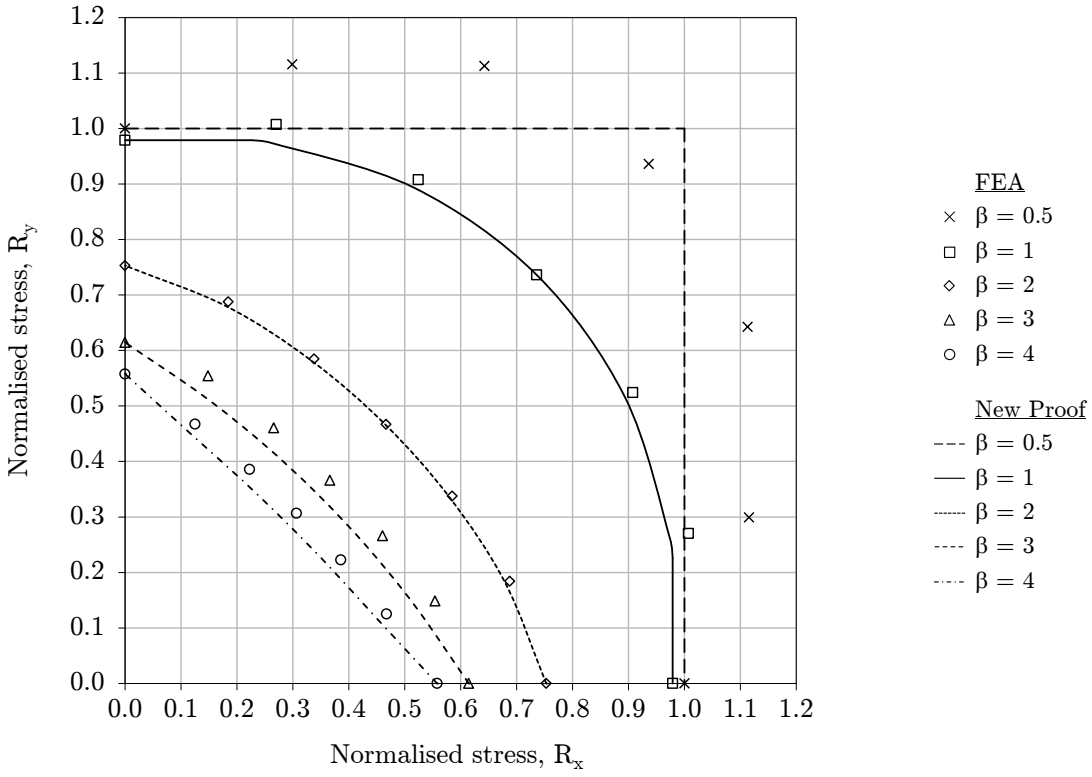

Figure D.1.: σ_x-σ_y, $\alpha = 1$.

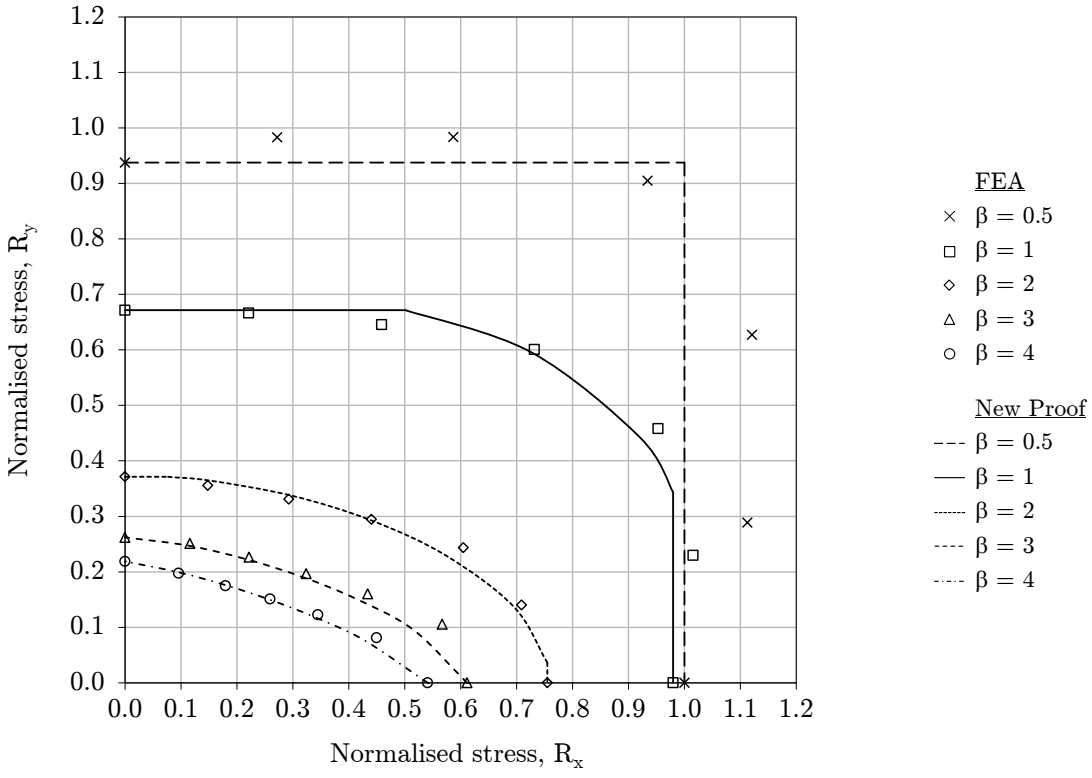

Figure D.2.: σ_x-σ_y, $\alpha = 3$.

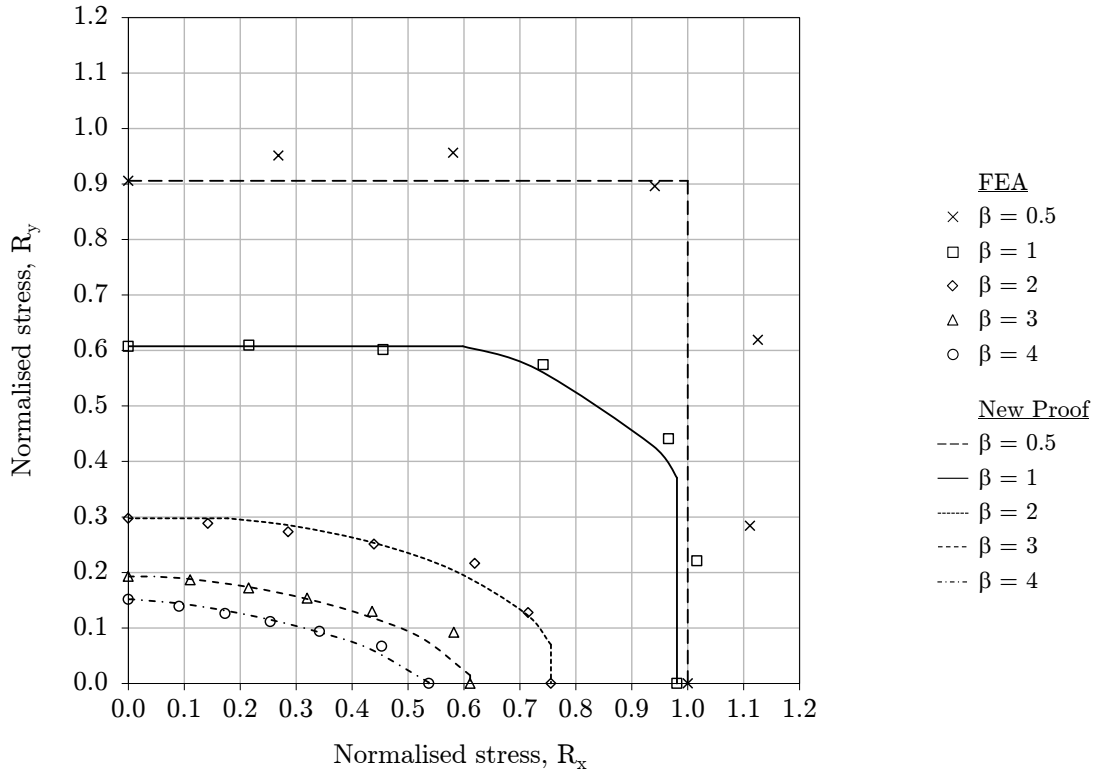

Figure D.3.: σ_x-σ_y, $\alpha = 5$.

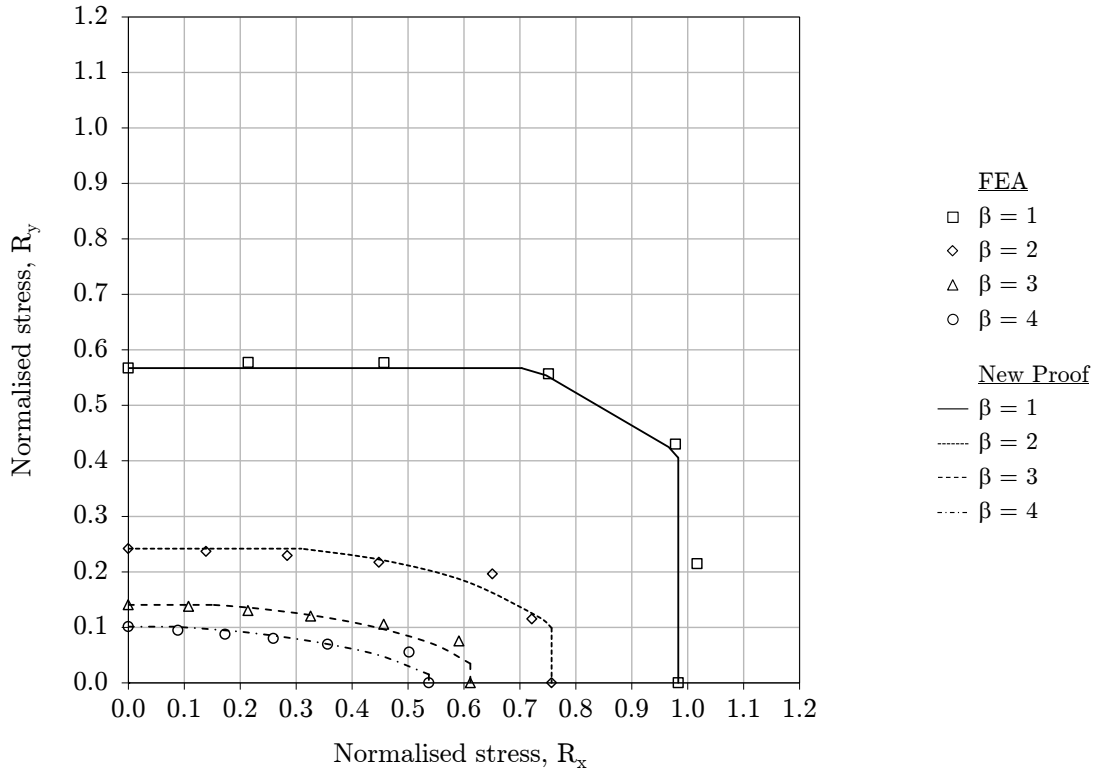

Figure D.4.: σ_x-σ_y, $\alpha = 10$.

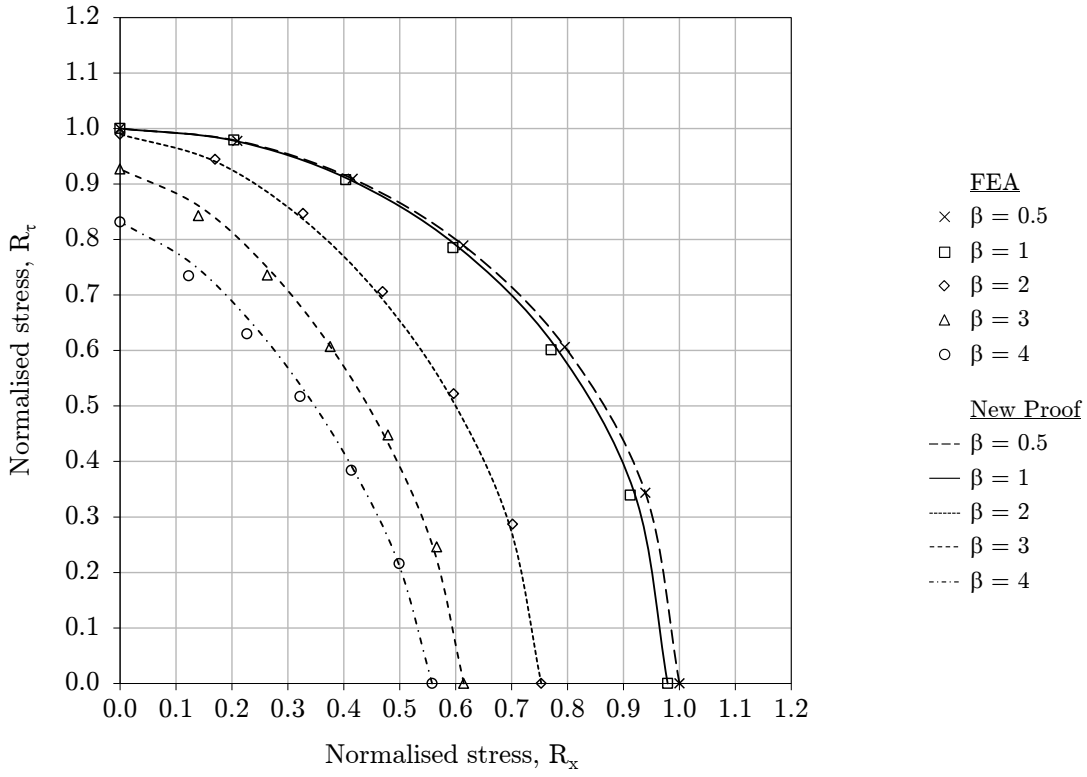

Figure D.5.: σ_x-τ_{xy}, $\alpha = 1$.

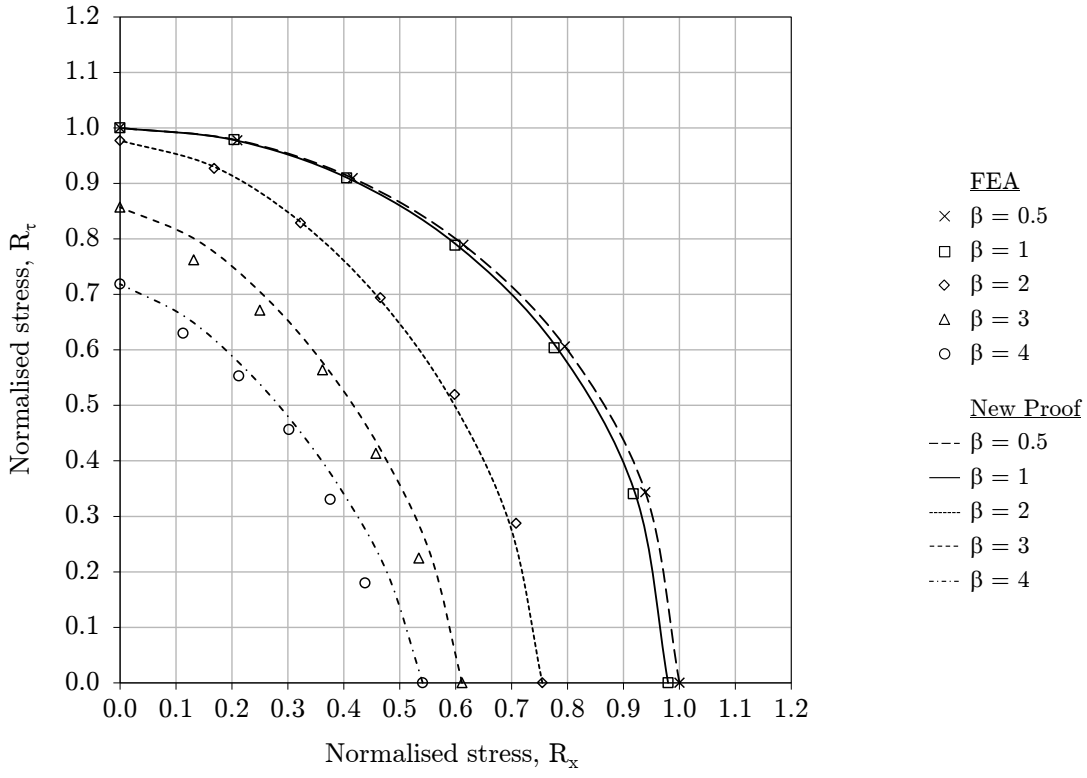

Figure D.6.: σ_x-τ_{xy}, $\alpha = 3$.

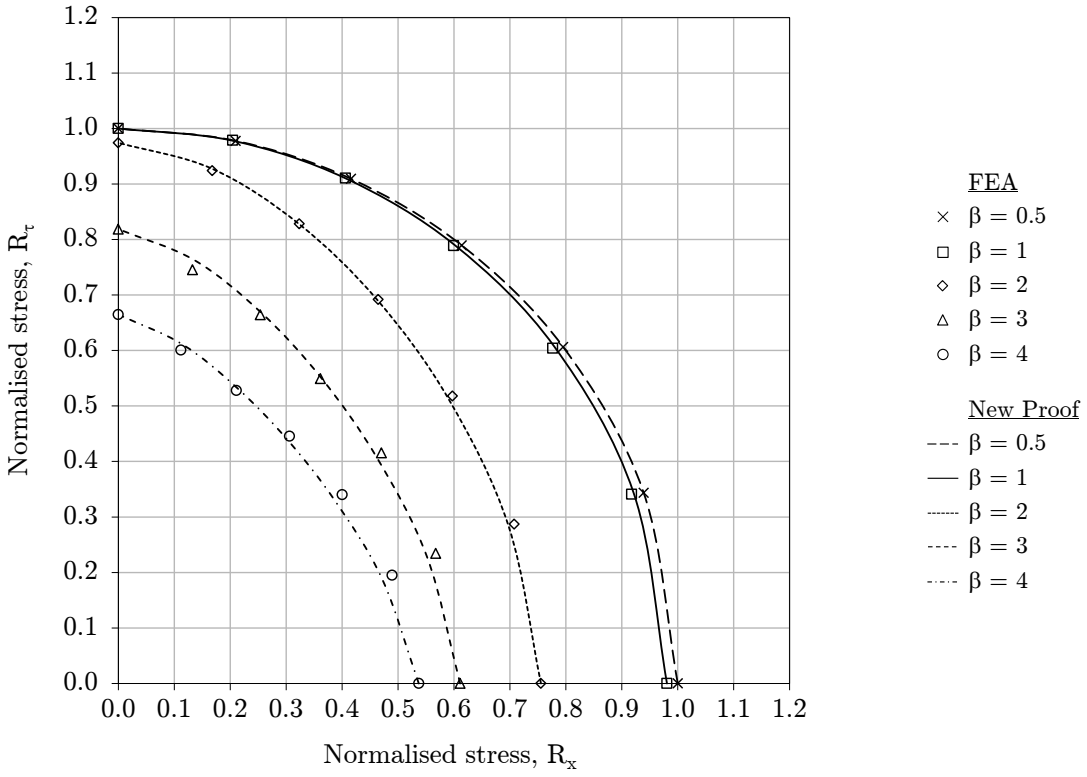

Figure D.7.: σ_x-τ_{xy}, $\alpha = 5$.

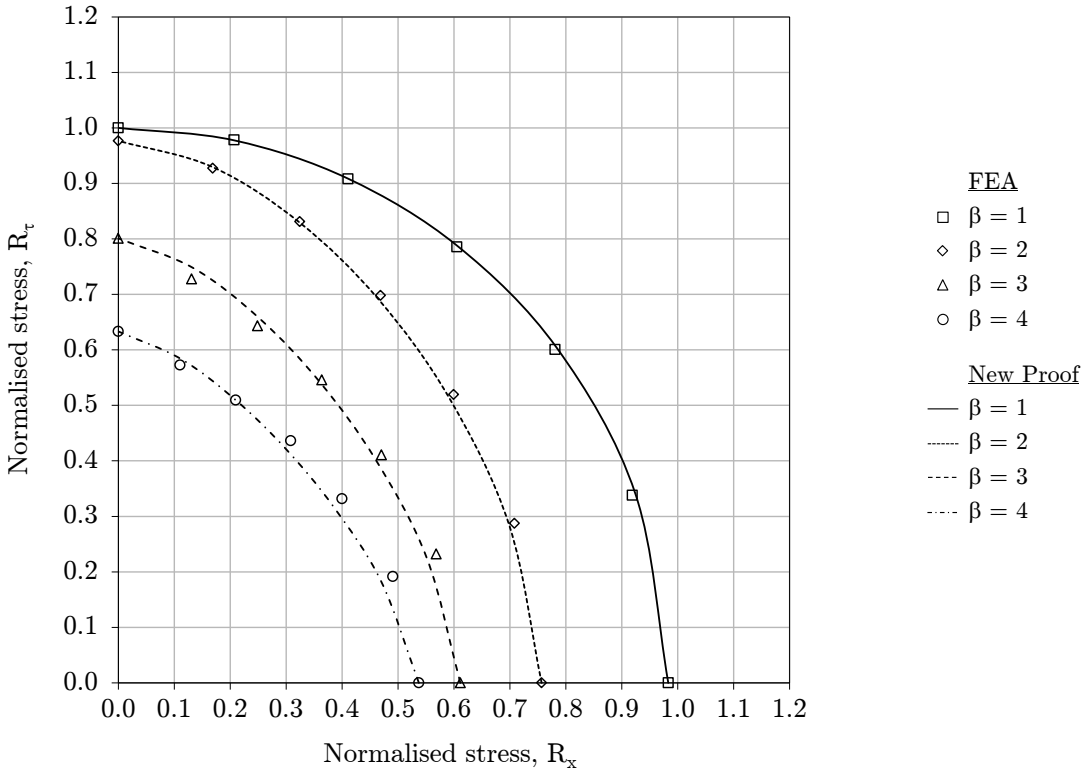

Figure D.8.: σ_x-τ_{xy}, $\alpha = 10$.

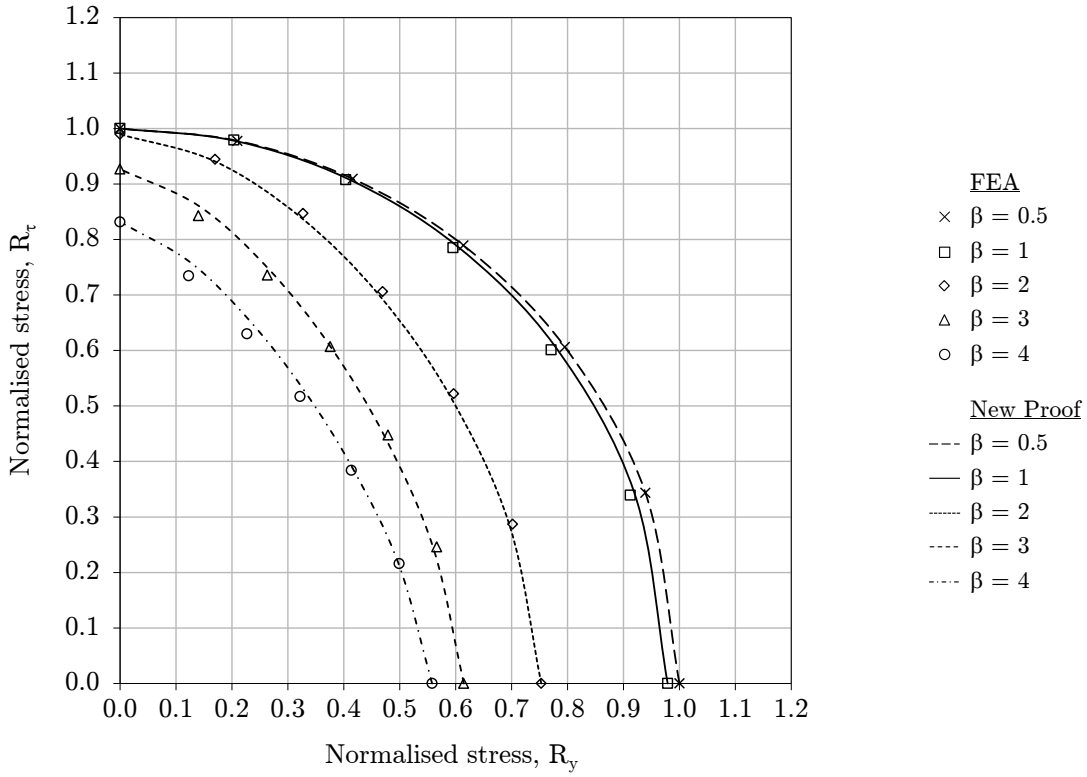

Figure D.9.: σ_y-τ_{xy}, $\alpha = 1$.

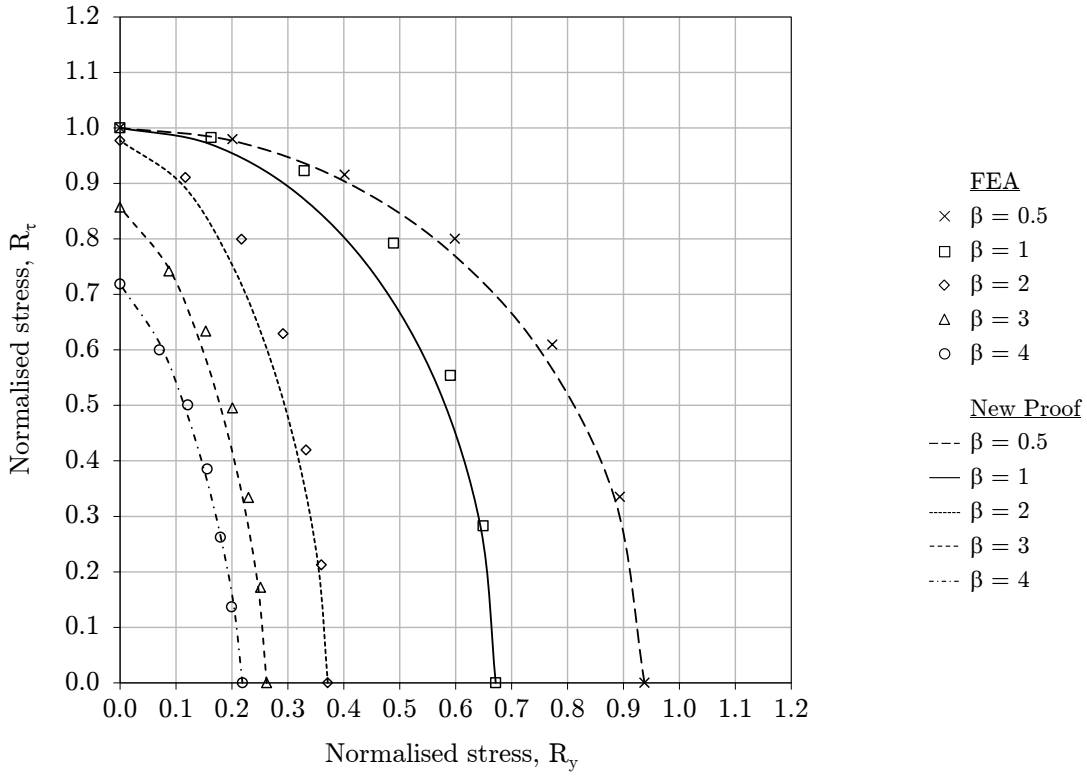

Figure D.10.: σ_y-τ_{xy}, $\alpha = 3$.

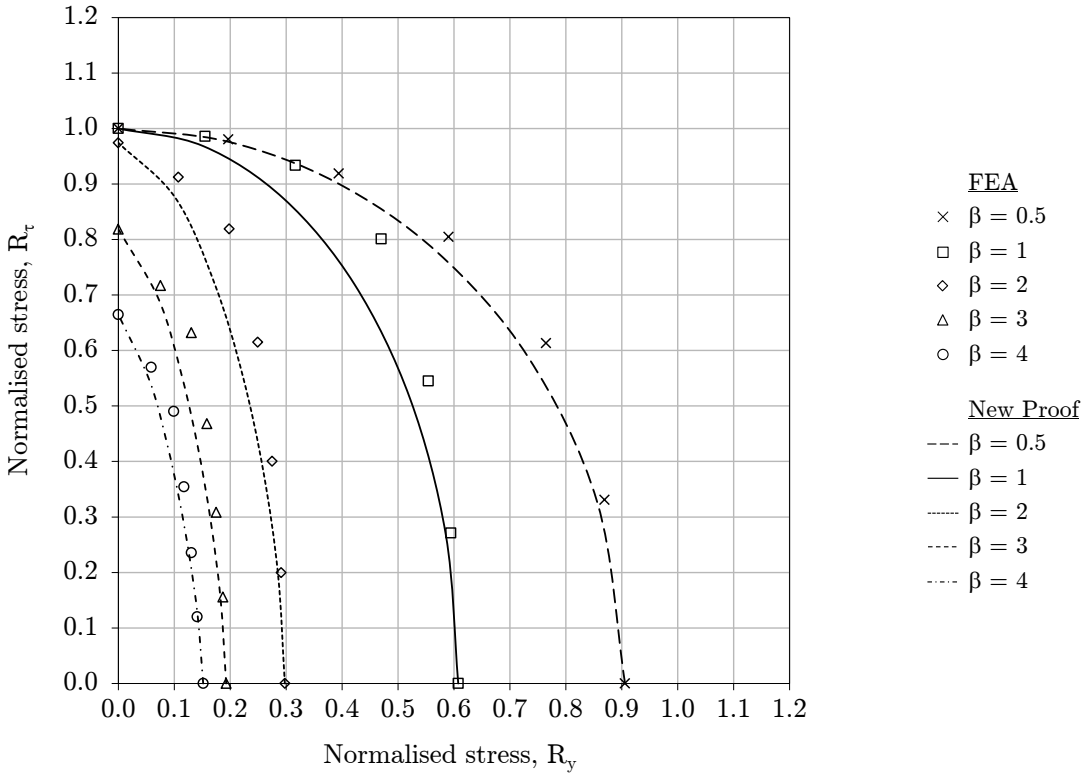

Figure D.11.: σ_y-τ_{xy}, $\alpha = 5$.

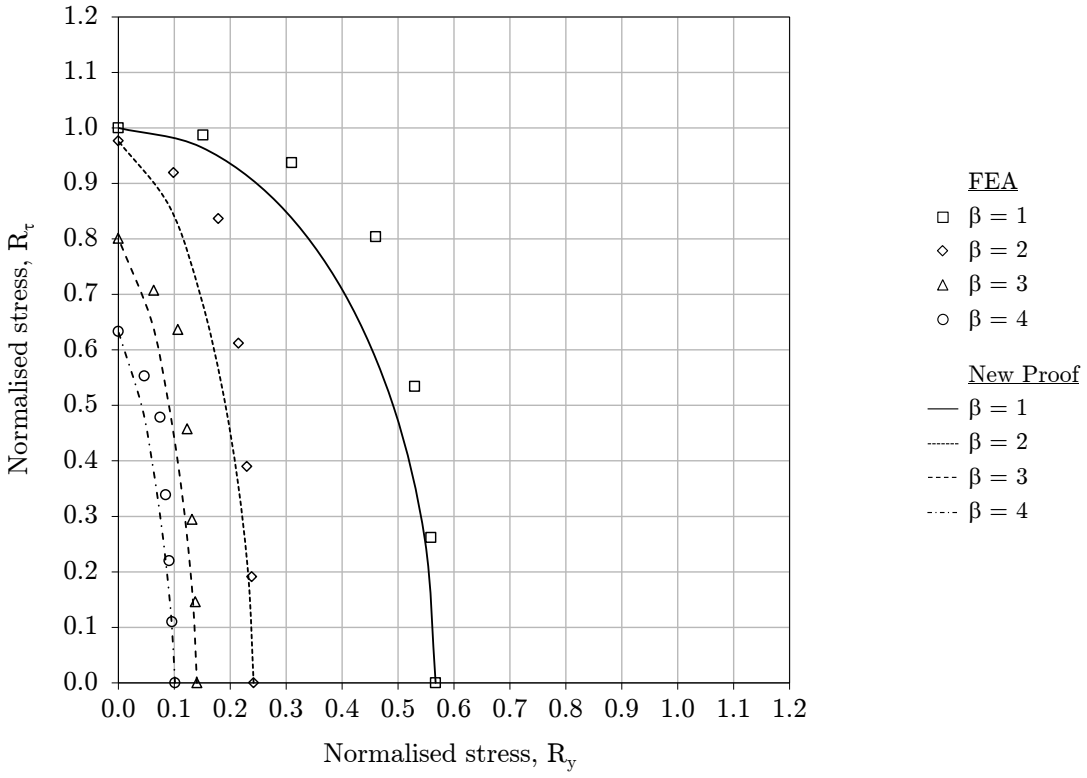

Figure D.12.: σ_y-τ_{xy}, $\alpha = 10$.

ISBN: 978-3-89220-699-6